efzn

Energie-Forschungszentrum
Niedersachsen

TU Clausthal

Numerical study of physico-chemical interactions for CO$_2$ sequestration and geothermal energy utilization in the Ordos Basin, China

Hejuan Liu

Promotion an der Technischen Universität Clausthal
Arbeitsgruppe Rock Mechanics in Petroleum Engineering
Prof. Dr.-Ing. habil. Michael Z. Hou

Band 24

Cuvillier Verlag Göttingen

Schriftenreihe des Energie-Forschungszentrums Niedersachsen (EFZN)

Band 24

Numerical study of physico-chemical interactions for CO₂ sequestration and geothermal energy utilization in the Ordos Basin, China

Dissertation

zur Erlangung des Doktorgrades
der Ingenieurwissenschaften

vorgelegt von

HejuanLiu

aus Hebei, VR China

genehmigt von der Fakultät für Energie- und Wirtschaftswissenschaften

der Technischen Universität Clausthal

Tag der mündlichen Prüfung

22.10.2014

D 104

Vorsitzender der Promotionskommission

Prof. Dr. rer. pol. W. Pfau

Betreuer

apl. Prof. Dr.-Ing. habil. M. Z. Hou

Gutachter

Prof. Dr.-Ing. habil. O. Kolditz

Acknowledgements

I would like to express my sincere thanks to all the people who kindly offered me help during my PhD study at EFZN, one research center of the Clausthal University of Technology, Germany.

First and foremost, I would like to express my gratitude to my supervisors, Professors Zhengmeng Hou and Olaf Kolditz for entrusting me with the task of preparing this thesis under their untiring guidance. It was a great pleasure for me to work and learn from them.

Next, I would like to express my sincere appreciation to China SHENHUA Group Co. Ltd, Sichuan University and Institute of Rock and Soil Mechanics of the Chinese Academy of Sciences, for their great support on providing some invaluable data (e.g. geological stratigraphy, well test, formation water composition and reservoir pressure etc.) and their permissions to use those data in my PhD dissertation.

I would also like to appreciate the working group of my supervisor Prof. Hou at EFZN, including Dr. Patrick Were, Yang Gou, Ms. Dr. Martina J. Weichmann, Tobias Kracke, Dr. Lei Zhou, Dr. Lars Wundram, Ms Juan Zhao, Ms. Mengting Li, Xuan Luo, Wei Xing, Ms. Khatia Dzebisashvili, Ms. Qun Wang and Roger Sonwa, for a good sense of teamwork. I want to show special thanks to Dr. Patrick Were, who devoted more time to comprehensively review and revise my thesis for its content and grammatical order, and Mr. Yang Gou, for his great help in solving the technical problems related to the numerical simulations. Other staff at EFZN, especially Christoph Gröger, Pascal Heinichen and Marco Tödteberg also give me great help in solving the technical problems of some software. Olaf Franz and Ralf Peix give me a lot of suggestions for literature study.

I also want to express my appreciation to Prof. Tianfu Xu and Prof. Qi Li, for their tips on setting up the simulations properly. Discussions with them helped me acquire some skills for independently solving some scientific challenges.

I would like to extend my thanks to the teachers and students of Sichuan University, including Asso. Prof. Jianfeng Liu, Asso. Prof. Lingzhi Xie, Ms. Dr. Xiaoshuang Shi, Peng Zhao and Cunbao Li. They broadened my understanding in rock mechanics and hydraulic fracturing technology through the seminar discussions.

I am also grateful to all my friends at TU Clausthal, particularly Ms Jianing Cheng, Qian Zhang, Shengxia Zheng, Zhuo Ma, Jianying Cheng, Dr. Youping Wang, Dr. Mingxing Bai, Xiaosong Wang, Yizhou Qiu, Wenjun Zhang, and Wei Jian for making my life comfortable and interesting in Germany. They also gave me a lot of moral support and comfort, at times when I felt worried and confused.

I would like to show my special thanks to my family, especially my parents and in-laws, who have constantly given me their total support and took care of my son when I was abroad for study in Germany.

Last but not least, I would like to give my dearest thanks to my husband Xiaoling Sun. Without his well thought decision to allow me further my education, my life would be entirely different. Without his continuous moral support and encouragement, I could not have been able to finish my thesis in the stipulated time. I would like to give my heartfelt thanks and love to my son Haoxuan Sun, the most precious gift that God gave me during my PhD study. He inspired me to study very hard and finish my thesis as soon as possible, so I may find time to take care of him. I hope that I could be a good model for him.

Life becomes more beautiful after we overcome the difficulties one by one. After the continuous improvement, one can become the person whom one wants.

Abstract

The injection of CO_2 in geological formations for storage, especially in the widespread deep saline formations, is considered an optimal option to reduce CO_2 emissions in the atmosphere. However, geological sequestration of CO_2 in porous media must confront with comprehensive problems, for example, pollution of the shallow ground water, the damage of the caprock caused by overpressured effect, the corrosion of downhole equipments, which can only be addressed by synthetic solutions from studies of hydrology, geotechnology, geochemistry, rock mechanics, mathematics, computational technology and related sciences.

In order to understand the physical and chemical processes associated with CO_2 sequestration in the subsurface, numerical simulators, such as TOUGH2MP, TOUGHREACT, FLAC3D have been developed. These numerical investigations can provide important information on spatial and temporal evolution of CO_2 plume, pore pressure, effective stresses, formation uplifts, ion concentration, mineral volume fraction etc., under the consideration of reservoir heterogeneities at different scales, thus can provide an invaluable reference for a specific CCS project to ensure its safety and efficiency.

In this thesis, a pilot-scale (0.1 Mt/year) CO_2 sequestration site in the Ordos Basin of China has been selected to provide a case study of CO_2 storage in deep saline formations, by addressing a variety of aspects including two phase (CO_2 & water) flow, rock deformation, heat transport and CO_2-water-rock interactions. Besides, a simple case study for geothermal production associated with CO_2 sequestration in porous media has been carried out. In general, the basic research carried out in this thesis will be useful in assessing and evaluating the capacity, efficiency, safety, economics and feasibility of CO_2 sequestration in deep saline formations. To achieve these objectives, the study has further developed suitable criteria of site selection both for CO_2 sequestration and geothermal production utilizing CO_2 to enhance heat extraction.

In the course of this study, some general results have been obtained for the problems of coupled geo-processes that arise from CO_2 sequestration. The upward and lateral migration process of CO_2 is triggered off as soon as the injection starts, until it is restricted or stopped by some impermeable layers (caprocks) and structures for its storage, in the short-term. This is then, followed by its long-term trapping mechanisms, including solubility and mineralization, which may impart significant changes on the reservoir properties, especially in the vicinity of the injection well. If the multilayered injection strategy was used in a multilayered reservoir-caprock system, strong perturbation between aquifer layers may occur, especially if they are located close to each other. Sensitivity analysis shows that CO_2 plume migration can be affected by factors in the following sequence: injection rate, reservoir permeability and multi-layered injection strategy, while the impact of other parameters is not obvious. Under consideration of the coupled hydro-mechanical effect, the lateral movement of the CO_2 plume can be enlarged to some extent as a result of volumetric expansion of the reservoir. Among those factors that affect the uplift movement of formations, injection rate has the largest impact, followed by reservoir permeability. Furthermore, the risk of tensile or shear failure of rocks surrounding the injection wellbore can be induced due to use of a poorly designed injection scheme. With respect to the geological conditions at the pilot site in the Ordos Basin, simulation results suggest that the pressure buildup should be controlled not to exceed 13.7, 14.8, 17.0 and 17.5 MPa in the four injection layers from top to bottom, respectively, to achieve a safe long-term storage of CO_2. Geochemical interactions caused by CO_2 injection are complex and highly specific case-dependent (e.g. initial mineralogy and formation water chemistry, salinity, pH, temperature). In view of a short time (several tens of years), the impact of geochemical interactions on fluid flow can be negligible. Using the reservoir properties representative for the injected aquifers of the Ordos Basin, simulation results show that after 1000 years of chemical reactions, the maximum reduction of the reservoir porosity and permeability is about 3% and 8%, respectively.

In the case of CO_2-sequestration associated with geothermal production, some advantages can be achieved, i.e. an increased amount of heat extraction and additional CO_2-sequestration capacity of underground. After CO_2 breakthrough, the flowing enthalpy increases greatly, showing the great advantage of CO_2 as a heat extraction fluid. A favorable well configuration is achieved if geothermal production wells are perforated at the same depth of CO_2 injection wells or even deeper, because it can greatly delay the CO_2 breakthrough time if CO_2 is used as a pressure-driven fluid. Economical configuration of geothermal systems can also depend on other factors, including well spacing, completion depth, injection/production rate, reservoir temperature and pressure, etc. Therefore, further studies are still required before commercial applications.

Many uncertainties mar the evaluation of a suitable site for CO_2 sequestration and CO_2-associated geothermal production. These are, for instance, uncertainties in geological characteristics at the injection site and the simulation methods used. The site selection criteria further developed in this thesis, were based on different scales of the investigated site (e.g. basin scale, field scale, target formation scale, engineering operation scale). However, more studies in the future are still required to optimize the screening and ranking system. Under the guidance of the screening and ranking system, the optimization sequence of several sedimentary basins of China suitable for CO_2 sequestration and CO_2-associated geothermal production are studied. Bohaiwan, Songliao and Qiangtang Basins present the greatest potential for a geothermal production, while for only CO_2 sequestration purpose, top three sequences are the Ordos, Tarim and Bohaiwan Basins.

Keywords: CO_2 sequestration; numerical simulations; two phase flow; CO_2-water-rock interactions; geothermal production

Zusammenfassung

Die CO_2-Injektion zu Speicherungszecken in geologische Formationen, vor allem in weit verbreitete tiefe saline Formationen, kann als eine optimale Option für die Reduzierung des CO_2-Ausstoßes betrachtet werden. Jedoch muss die geologische CO_2-Sequestrierung in porösen Medien mit umfassenden Problemen konfrontiert werden, z. B. mit der Verschmutzung des flachen Grundwassers, dem Integritätsverlust des Deckgebirges, verursacht durch einen zu hohen Speicherdruck, der Korrosion einiger Bohrlochausrüstungen, die nur durch die kombinierte Anwendung von Hydrologie, Geotechnik, Geochemie, Felsmechanik, Mathematik, Computertechnologie und verwandten Fachdisziplien gelöst werden können.

Um die physikalischen und chemischen Geo-Prozesse im Zusammenhang mit einer CO_2-Sequestrierung im Untergrund zu verstehen und zu quantifizieren, wurden die numerischen Simulatoren TOUGH2MP, TOUGHREACT und FLAC3D entwickelt. Diese numerischen Untersuchungen können wichtige Information über die räumliche und zeitliche Entwicklung von CO_2-Verteilung, Porendruck, effektiven Spannungen, Formationshebungen, Ionenkonzentration, Volumenanteil von Mineralien usw., unter Berücksichtigung von Reservoirheterogenitäten im unterschiedlichen Maßstab liefern und somit eine unschätzbare Referenz für ein bestimmtes CCS-Projekt zur Verfügung stellen, um seine Sicherheit und Effizienz zu gewährleisten.

In dieser Doktorarbeit wurde ein CO_2-Speicher-Pilotprojekt (CO_2-Injektionsrate: 0.1 Mt/Jahr) im Ordos-Becken (China) als Fallstudie für die CO_2-Speicherung in tiefen salinen Formationen ausgewählt, in dem eine Reihe von damit verbundenen Aspekten einschließlich des Zweiphasenflussprozesses von CO_2 und Wasser, der Gesteinsdeformation, des Wärmetransports sowie der Wechselwirkungen von CO_2, Wasser und Gestein behandelt werden. Darüber hinaus wurde eine vereinfachte Fallstudie für die geothermische Produktion in Verbindung mit der CO_2-Sequestrierung in porösen Medien betrachtet. Im Allgemeinen wird die im Rahmen dieser Arbeit durchgeführte Grundlagenforschung für die Beuteilung und Auswertung der Kapazität, Effizienz, Sicherheit, Wirtschaftlichkeit und Machbarkeit der CO_2-Sequestrierung in tiefen salinen Formationen von Nutzen sein. Um diese Ziele zu erreichen, wurden im Rahmen dieser Arbeit geeignete Kriterien zur Standortauswahl sowohl für die CO_2-Sequestrierung als auch für eine geothermische Produktion unter Anwendung von CO_2 zur Steigerung der Wärmegewinnung weiterentwickelt.

Im Rahmen dieser Doktorarbeit wurden einige allgemeingültige Ergebnisse bezüglich der Fragestellungen im Zusammenhang mit den gekoppelten Geo-Prozessen in der geologischen CO_2-Sequestrierung erzielt. Für die CO_2-Speicherung gilt zuerst der kurzfristige Bindungsmechanismus, nämlich dass, die nach oben und seitlich gerichtete Migration unmittelbar nach dem Beginn der CO_2-Injektion ausgelöst wird und erst durch undurchlässige Schichten, die sogenannten Deckgebirges, oder Strukturen für die CO_2-Speicherung gestopt wird. Danach wirken dann die langfristigen Bindungsmechanismen, wie Löslichkeit und Mineralisierung, die, insbesondere in der Nähe der CO_2-Injektionsbohrung, positive oder negative Auswirkungen auf die Reservoireigenschaften haben können. Im Fall der Anwendung der Mehrschichtinjektionsstrategie in ein mehrschichtiges Reservoir-Caprock-System, können starke Störungen zwischen Aquiferschichten auftreten, insbesondere wenn sie nahe beieinander ligen. Die Sensitivitätsanalyse zeigt, dass die CO_2-Migration durch folgende Faktoren in folgender Reihenfolge beeinflusst werden kann: Injektionsrate, Reservoirpermeabilität und Mehrschichtinjektionsstrategie, während die Auswirkungen anderer Parametern nicht offensichtlich sind. Unter Berücksichtigung des gekoppelten hydromechanischen Effekts, kann die seitliche Bewegung der CO_2-Verteilung wegen der Volumenausdehnung des Reservoirs zu einem gewissen Grad vergrößert werden. Unter den Faktoren, die sich auf die Hebung von Formationen auswirken, hat die Injektionsrate den größten Einfluss, gefolgt von der Reservoirpermeabilität. Weiterhin kann sich das

Risiko eines Zug- oder Scherversagens der Gesteine im Nahbereich der Injektionsbohrung aufgrund eines schlecht ausgelegten Injektionsschemas erhöhen. Gemäß den geologischen Bedingungen am Pilotstandort in dem Ordos Becken zeigen die Simulationsergebnisse, dass die Druckerhöhung in den vier Injektionsformationen von oben bis unten so kontrolliert werden soll, jeweils 13.7, 14.8, 17.0 und 17.5 MPa nicht zu überschreiten, für eine sichere langfristige Speicherung von CO_2. Die durch CO_2-Injektion verursachten geochemischen Wechselwirkungen sind komplex und hochspezifisch fallabhängig (z. B. initiale Mineralogie und Formationenwasserchemie, Salzgehalt, pH, Temperatur). In Anbetracht eines kurzen Zeitraums (mehrere Jahrzehnte) ist der Einfluss der geochemischen Wechselwirkungen auf den geohydraulischen Prozess vernachlässigbar. Mit repräsentativen Reservoireigenschaften für die Injektionsaquiferen im Ordos Becken zeigen die Simulationsergebnisse, dass die maximale Reduzierung der Porosität und Permeabilität nach 1000 Jahren jeweils ca. 3% und 8% beträgt.

Die CO_2-Sequestrierung in Verbindung mit geothermischer Produktion bringt einige wesentliche Vorteile mit sich, wie z. B. ein erhöhtes Potential zur Wärmegewinnung und eine zusätzliche CO_2-Aufnahmekapazität des Untergrundes. Nach dem CO_2-Durchbruch, steigt die Fließenthalpie stark an, was den großen Vorteil von CO_2 als Wärmeextraktionsflüssigkeit zeigt. Eine günstige Bohrlochkonfiguration wird erreicht, wenn die geothermische Produktionsbohrung in der gleichen Teufe der Injektionsbohrung order noch tiefer perforiert wird, weil sich der Durchbruch von CO_2 verlangsamet, falls CO_2 als ein druckgetriebenes Fluid benutzt wird. Die Wirtschaftlichkeit geothermischer Systeme hängt darüber hinaus von weiteren Faktoren ab wie z. B. Bohrungsdurchmesser, Komplettierungstiefe, Injektions-/Produktionsrate, Reservoirtemperatur und Reservoirdruck usw. Aus diesem Grund sind vor einer kommerziellen Anwendung weitere Untersuchungen erforderlich.

Viele Unsicherheiten beeinträchtigen die Bewertung einer für die CO_2-Sequestrierung und CO_2-assoziierte geothermische Produktion geeigneten Lokalität, da sie beispielsweise hinsichtlich der Unwägbarkeit bezüglich der geologischen Gegebenheiten am Standort und damit der anzuwendenden Simulationsmethoden aufweisen. Die in dieser Arbeit weiterentwickelten und angewendeten Standortauswahlkriterien basieren auf verschiedenen Bewertungsmaßstäben für das Untersuchungsgebiet, wie z. B. auf den Maßstäben des Beckensystems, des Felds, der Zielformation sowie des ingenieurtechnischen Betriebes. Es werden jedoch auch zukünftig weitere Studien erforderlich sein, um das Screening- und Ranking-System zu optimieren. Nach diesem Screening-und Ranking-System, wurde mehrere Hauptsedimentbecken in China auf Eignung für die CO_2-Speicherung und CO_2-assoziierte geothermische Produktion untersucht. Das Bohaiwan, das Songliao und das Qiangtang Becken stellen das größte Potenzial für eine geothermische Produktion, während das Ordos-, Tarim- und Bohaiwan- Becken am besten für den Zweck der CO_2-Sequestrierung geeignet sind.

Keywords: CO_2-Sequestrierung; numerische Simulationen; Zweiphasenströmung; CO_2-Wasser-Gesteins-Wechselwirkungen; geothermische Produktion

Contents

List of Figures

List of Tables

Nomenclature

A	Cross sectional area, m^2
A_m	Specified surface area of mineral m, m^2
B	Biot's modulus, MPa
B_f	Fluid formation volume factor, bbl/STB for oil, bbl/scf for gas
B_g	Gas formation volume factor, bbl/scf
B_o	Oil formation volume factor, bbl/STB
B_s	Skempton coefficient (compressibility coefficient), -
C	Chemical component concentration, mol/L
C'	Internal cohesion of the rock, N
C_s	Mass of CO_2 dissolved per unit volume of water
c	Compressibility, 1/Pa
c_b	Compressibility of bulk rock, 1/Pa
c_{eff}	Effective compressibility, 1/Pa
c_f	Fluid compressibility, 1/Pa
c_o	Isothermal oil compressibility, 1/Pa
c_p	Pore compressibility, 1/Pa
c_s	Compressibility of solid skeleton material, 1/Pa
c_w	Water compressibility, 1/Pa
D	Diffusion coefficient, m^2/s
D_e	Effective molecular diffusion coefficient, m^2/s
E_a	Activation energy, J
E_b	Elastic modulus of bulk rock, Pa
E_s	Elastic modulus of solid skeleton, Pa
F	Mass flux term, kg/(m^2·s)
fr_m	Volume fraction of the reactive mineral m in the rock, -
fr_u	Volume fraction of of the nonreactive minerals, -
G	Shear modulus, N/m^2
g	Gravitational acceleration, m/s^2
$\Delta H^{\ominus}$	Standard enthalpy change, J/mol
h	Specific heat, J/(kg·^{o}C)
$\hat{h}$	Formation thickness, m
I	Ion strength= $0.5 \sum_j c_j \tilde{z}_j^2$, mol/L
IAP/Q	Ion activity product, -
J	Hydraulic gradient, -
J_d	Diffusion flux per unit area per unit time, $mol/m^2 s$
J_{inj}	Injectivity index, kg/ (Pa·s)
K	Drained bulk modulus, N/m^2
$\hat{K}$	Equilibrium constant in chemical reactions, -
K_c	Permeability coefficient/hydraulic conductivity, m/s
$K_{c\alpha}$	Permeability coefficient of phase α, m/s
K_f	Fluid bulk modulus, N/m^2
K_s	Solid bulk modulus, N/m^2
K_{sp}	Solubility product constant under a certain temperature, -
K_u	Bulk modulus under undrained state, N/m^2
k	Intrinsic permeability/absolute permeability, m^2

k_0	Permeability under zero stress condition, m^2
k_i	Initial permeability, m^2
k_α	Permeability of phase α, m^2
k^m	Permeability coefficient (mobility coefficient), $k^m = \frac{K_c}{\rho_f g}$, m^2/Pa/s
$k_{r\alpha}$	Relative permeability of phase α, -
k_{rg}	Relative gas permeability ratio, -
k_{rw}	Relative water permeability ratio, -
k_{rl}	Liquid phase relative permeability ratio, -
$\bar{k}$	Reaction rate constant, -
L	The distance between the two cross sections perpendicular to the flow direction, m
$\boldsymbol{M}$	Mass accumulation term, kg/m^3
$\bar{\bar{M}}$	Fluid mobility, kg/ (m^3.cP)
N	Number of chemical basic components, -
P_c	Capillary pressure, Pa
P_d	Air entry pressure, Pa
P_{fm}	Fracture margin pressure of rocks, Pa
P_g	Gas partial pressure, Pa
P_i	Initial reservoir pressure, Pa
P_l	Water partial pressure, Pa
P_{max}	Maximum capillary pressure, Pa
P_0	Strength coefficient, Pa
P_{sc}	Critical shear slip pore pressure, Pa
p	Pore pressure, Pa
Δp	Pressure difference, Pa
$\boldsymbol{q}$	Source/sink term, $kg/(m^3 \cdot s)$
$\hat{q}$	Total filtration amount per unit time, kg/s
q_c	Injection rate of CO_2, kg/s
R_e	Ion radius, m
R_s	Solution gas oil ratio, scf/stb
R_t	Formation electrical resistivity factor, -
R_w	Well radius, m
$\bar{R}_n$	Radius of capillary tubes of non-wetting phase, m
$\bar{R}_w$	Radius of capillary tubes of wetting phase, m
r_m	Dissolution/precipitation rate of mineral m
r_t	Throat radius, m
r_p	Pore radius, m
S	Saturation, -
S_{gr}	Residual gas saturation, -
S_l'	Critical liquid saturation for fluid flow, -
S_{lr}	Residual liquid saturation, -
$S_{r\alpha}$	Residual saturation of phase α, -
S_{wi}	Connate water saturation, -
S_{wr}	Residual water saturation, -
$\hat{S}$	Effective saturation, $\hat{S} = (S_w - S_{wr})/(1 - S_{wr})$

S_e	Normalized saturation, $S_e = \dfrac{(S_w - S_{wr})}{(S_w - S_{wr} - S_{gr})}$
$\bar{\bar{S}}$	Brine salinity, -
SI	Mineral saturation index, -
T	Temperature, ^oC
T_c	Temperature at critical point, ^oC
t	Time, s
U	Internal energy, J/kg
$\boldsymbol{u}$	Darcy velocity, m/s
$\hat{\boldsymbol{u}}$	Solid grain displacement, m
$\hat{u_i}$	Solid grain displacement vector, m
V	Volume, m^3
V_b	Volume of bulk rock, m^3
V_m	Molar volume (V/n), L/mol
V_t	Total volume of porous media, m^3
V_p	Pore volume of porous media, m^3
V_{p1}	Pore volume of matrix medium, m^3
V_{p2}	Pore volume of the fracture, m^3
X	Mass fraction, -
x	Distance, m
Z_c	Compressibility factor at the critical point, -
$\tilde{z}_j$	Ion charge, -
z	Gas compressibility factor, -
α	Biot's coefficient, -
$\bar{\bar{\alpha}}_j$	Activity of aqueous component j
β	Undrained thermal coefficient,1/^oC
Γ	Volumetric exchange rate (interporosity flow, transfer rate) between fractures and matrix blocks per unit bulk volume, m^3/s
γ_j	Activity coefficient of aqueous component j, -
δ_{ij}	Kronecker delta($i=j$, $\delta_{ij} = 1$)
ε_{ij}	Strain, $\varepsilon_{ij} = \frac{1}{2}(u_{i,j} + u_{j,i})$
ε_v	Volumetric strain, -
θ	Contact angle between solid and fluid, -
λ	Heat conductivity, W/(m·^oC)
μ	Fluid viscosity, cP or m.Pa/s
ν	Possion's ratio, -
ν_u	Possion's ratio of the undrained elastic rock skeleton, -
π	Variation of fluid content per unit volume of porous media, -
ρ	Density, kg/m^3
ρ_c	CO$_2$ density, kg/m^3
ρ_f	Fluid density, kg/m^3
ρ_o	Oil density, kg/m^3
σ	Stress, Pa
σ'	Effective stress, Pa
σ_{ij}	Total stress, $\sigma_{ij} = \sigma'_{ij} + \alpha P$, Pa

σ'_{ij}	Effective stress, Pa
σ_h	Minimum horizontal stress, Pa
σ_m	Mean stress, Pa
σ_{s1}	Interfacial tension between solid and fluid 1, N
σ_{s2}	Interfacial tension between solid and fluid 2, N
σ_{wg}	Interfacial tension between water and gas, N
σ_v	Vertical stress, Pa
σ_1	Maximum principal stress, Pa
σ_3	Minimum principal stress, Pa
σ_{12}	Interfacial tension between fluid 1 and fluid 2, N
τ	Maximum shear stress, Pa
$\hat{\tau}$	Medium tortuosity, -
ϕ	Porosity, -
$\hat{\phi}$	Porosity at reference pore pressure p_0, -
ϕ_e	Effective porosity, -
ϕ_r	Residual porosity under zero stress condition, -
ϕ_t	Total porosity, -
ϕ_0	Porosity under zero stress condition, -
ϕ_1	Porosity from matrix media, -
ϕ_2	Porosity from fracture part in the fractured media, -
φ'	Internal friction angle, °
Ω	Mineral saturation ratio, -
ω	Fugacity coefficient,-
$\tilde{\omega}$	Solubility,-
$\nabla \cdot$	Divergence, -
∇	Gradient, -

Superscripts

T	Under thermal mode condition
c	CO_2 component
i	Chemical aqueous ions
m	Pore size distribution index, -
n	Power term
o	Initial state
w	H_2O component
λ	Pore size distribution index, -
κ	Mass component (water, CO_2, NaCl, heat etc.)
nu, H, OH	Reaction is under neutral, acid and base mechanism
θ	Parameter used in the calculation of reaction rate of mineral
η	Parameter used in the calculation of reaction rate of mineral

Subscripts

g, l/w, s	Gas phase, liquid phase and solid phase, respectively
$n = 1,2$	Matrix and fracture media, respectively
α	Phase index

1. Introduction

1.1 The carbon challenge

Carbon dioxide (CO_2) is a chemical compound composed of carbon and oxygen. A small amount of CO_2 in the atmosphere will play an important role in the Earth's environment which is regarded as an essential ingredient in the photosynthesis of plants and the life activities of animals (www.ipcc.ch). Plants can absorb CO_2 and release O_2 through photosynthesis. CO_2 can also be released through natural or human activities, for example, volcanic activity, combustion of fossil fuels (e.g. oil, natural gas and coal) and other organic compounds, the breathing processes of humans and other animals, etc.

Carbon dioxide (CO_2) has attracted worldwide attention since the last decade for being the main reason for global warming and the consequent potential threats to human beings (IPCC, 2007). Based on many investigations on climate change, it has been confirmed that the balance of the carbon cycle has been changing since the mid-20th century caused by the rapid development of industrialization (Court, 2011). The observed increase in global temperatures, which corresponds to the evolution of the CO_2 concentration in atmosphere (Fig. 1.1), makes the carbon dioxide (CO_2) emission problems become more obvious (IPCC, 2007).
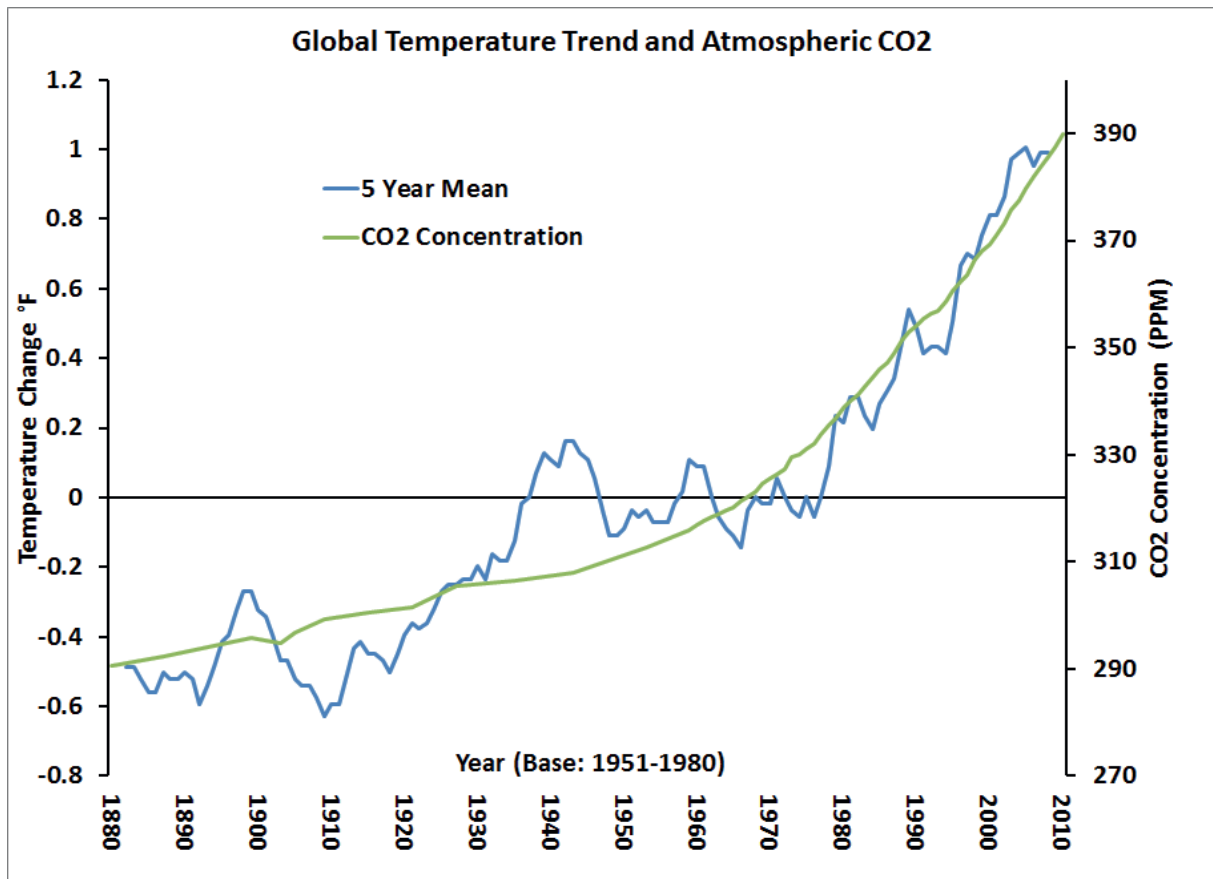
Fig. 1.1 Evolution of the concentration of atmospheric carbon dioxide with time over the past 130 years (from http://www.c2es.org/facts-figures/trends/co2-temp)

1.2 CCS introduction

1.2.1 CCS motivation

Aiming at the mitigation of global warming challenge, CO_2 emissions must be reduced through some strategies (Fig. 1.2), including the increase in energy efficiency, the use of renewable energy sources (i.e.

nuclear, wind, solar, geothermal, hydro power and marine energy) and clearner use of ordinary fossil fuels (De Visser et al., 2009). Based on the existing energy structure, coal still plays a dominant role in baseload electricity generation, satisfying 40% of the global electricity demand in 2010 (Court, 2011). In some countries, it may take a much higher percent. CO_2 emissions from large stationary sources, including power plants, cement factories, refineries etc., contributes almost 90% of the total amount of CO_2 in the atmosphere (IPCC, 2005). These point sources provide the possibility to reduce CO_2 emission by CO_2 Carbon Capture and Storage (**CCS**) technologies.

Reduce CO_2 emission methods

1. Efficient Energy use	2. Renewable Energy Resources	3. Cleaner Use of Fossil Fuels
-Consumer	-Wind energy	-Carbon Capture and Storage (CCS)
-Buildings	-Solar energy	-Hydrogen
-Industries	-Bio-energy	-Fuel Cells
-Transport	-Geothermal	
	-Hydro power	
	-Marine energy	
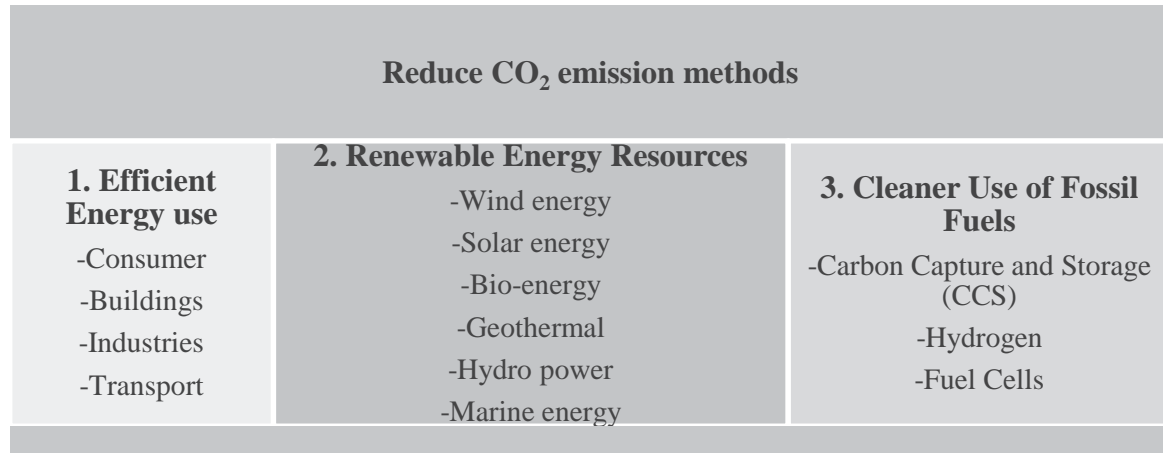
Fig. 1.2 Three strategies for reducing the CO_2 emission (modified from De Visser et al., 2009)

Table 1.1 Number of large point sources of CO_2 worldwide, with emissions of more than 0.1 million tonnes (Mt) per year (sourced from IPCC, 2005)

Process	Number of sources	Emissions (MtCO$_2$/yr)
Fossil fuels		
Power	4942	10539
Cement production	1175	932
Refineries	638	798
Iron and steel industry	269	646
Petrochemical industry	470	379
Oil and gas processing	Not available	50
Other sources	90	33
Biomass		
Bioehanol and bioenergy	303	91
Total	**7887**	**13466**

1.2.2 CO_2 capture and geological sequestration

CCS technology first emerged during the early 1990s and has since then become worldwide spread. Recently, a delivative of CCS, namely carbon capture utilization and storage (CCUS) has become more popular and created a stir among several states due to its ability to utilize underground resources and conditions to generate further economic benefits and therefore offset costs on CO_2 sequestration (Harrison and Falcone, 2014; Xie et al., 2014). CCUS technology may be divided into three classes, namely chemical, biological and geological utilization. Geological utilization may be further subdivided into several forms including the use of CO_2 to enhance the recovery of oil (EOR), natural gas (CO_2-EGR), coalbed methane (CO_2-ECBM), geothermal system (CO_2-EGS), shale gas (CO_2-ESG) and carbon mineralization utilization (CO_2-CMU) (Bachu et al., 2008; Xie et al., 2014).

In general, **CCS** technology proceeds in three steps from capture to storage (IPCC, 2005): (1) **C**apture of **CO$_2$** from a point source (i.e. a power plant, gasification synfuels plant, a cement or natural

gas factory, etc.); (2) Transport of CO_2 to a suitable field site by trucks or pipelines; and (3) Storage or Sequestration of CO_2 in a deep geological formation of sedimentary basins, such as deep aquifer formations, depleted oil and gas reservoirs, deep unmineable coal seams etc (Fig. 1.3).

The idea of CO_2 sequestration came from the presence of natural CO_2 reservoirs distributed in North America, Australia, China, and Europe, illustrating that CO_2 can be stored underground for millions of years or even longer (Benson, 2005). In addition, the fact that a large quantity of CO_2 can be kept intact in many oil and gas reservoirs over geologic time scales shows that oil and gas reservoirs can also be used as the repository sites for CO_2. Among all the potential sites for CO_2 repository, deep aquifer formations seem to be more promising due to its widespread distribution. The CO_2-EOR technology, which involves injection of CO_2 into depleted oil reservoirs to enhance production of oil, was started in 1972 in America (Mathiassen, 2003). Similarly, CO_2-EGR technology is another form of CCUS that has been proposed recently to enhance natural gas recovery by injecting CO_2 into depleted gas reservoirs.
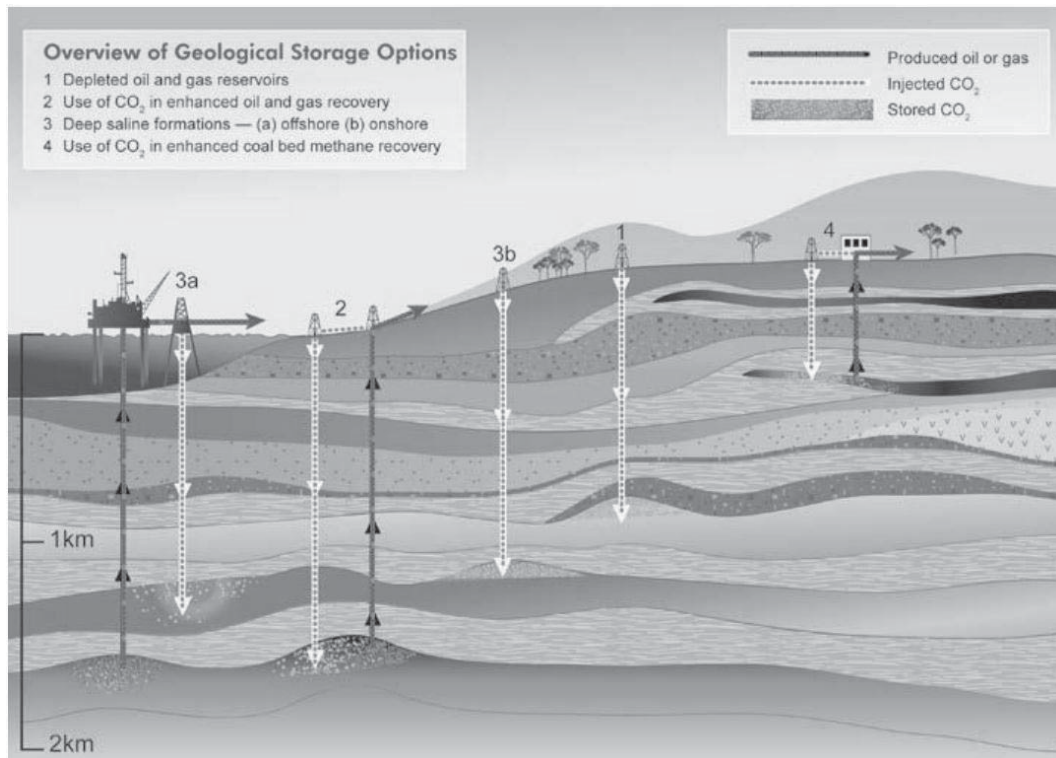
Fig. 1.3 Different CO_2 sequestration sites (IPCC, 2005)

Compared with hydrocarbon reservoirs, deep saline aquifers have the advantage that they are ubiquitous underground, and therefore possess the largest CO_2 sequestration capacity (Rutqvist, 2012). Moreover, it may be more economic if the CO_2 sequestration site in the deep saline formations can be launched close to a major CO_2 point source, saving the transport cost compared to other sites like depleted oil or gas reservoirs, coal beds, etc (Bennion and Bachu, 2005).

1.3 State-of-the-art and progress beyond

Based on ScienceDirect database, the number of the papers related to CO_2 sequestration has been analyzed. Fig. 1.4 shows the development trend of CCS technology during the last 20 years. The paper screening process has been carried out for three study categories: (1) total number of papers on studies about CO_2 storage, (2) papers on simulation studies related with CO_2 storage, and (3) papers on CO_2-rock-fluid interactions studies, see Fig. 1.4 A. In this dissertation, however, only study categories (2) and (3) have been considered, see Fig. 1.4 B. Furthermore, the two charts show that more attention has been paid on CCS sequestration particularly in the last 20 years.

3
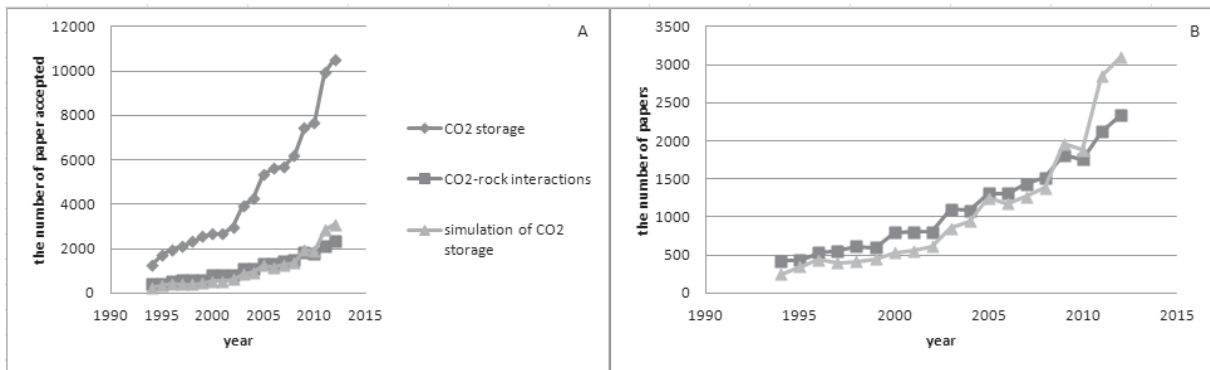
Fig. 1.4 Development of CCS technology in the last 20 years, (A) for all three study categories; (B) for only two study categories

CCS is a mature technology and can be applied immediately based, for example on the experiences already gained from almost 100 years of natural gas storage at numerous sites in North America and Europe (Perry, 2005). 30 years of CO_2-EOR in the USA and 15 years of acid gas (a mixture of CO_2 and H_2S) injection in western Canada (Bachu and Gunter, 2005b; Moritis, 2006), see Table 1.2. Carbon dioxide storage in depleted oil/gas reservoirs in conjunction with EOR and EGR are likely to be economically viable projects as the costs involved are likely to be offset by the production of the bypassed and residual oil and gas.

Governments, research centers, universities and several industries are working in conjuction to execute a large number of CCS projects for different purposes in various parts of the world. They cooperate with each other to ensure the successful running of the CCS projects. Usually, CO_2 sequestration projects are funded by different countries and companies, forming a close relationship with other countries and industries. From this point of view, CCS technology has already formed a big chain, connecting policy-makers, scientists, technologists and engineers together for a concrete solution.

Table 1.2 Examples of major CCS projects worldwide (adapted from IPCC, 2005)

Representative project	Country	Scale of project	Lead organizations	When Injection started	Injection rate	Total storage amount	Type of storage reservoir	Geological Storage formation	Age of storage formation	Lithology of storage formation
Sleipner	Norway	Commerical	Statoil, IEA	1996	3000 t/day	20 Mt planned	Saline aquifer	Utsira formation	Tertiary	Sandstone
Weyburn	Canada	Commerical	EnCana IEA	2000	3-5000 t/day	20 Mt planned	CO_2-EOR	Midale Formation	Mississippian	Carbonate
Fenn Big Valley	Canada	Pilot	Alberta Research Council	1998	50 t/day	200 t	CO_2-ECBM	Mannville Group	Cretaceous	Coal
Minami-Nagoaka	Japan	Demonstration	Japanese Ministry of Economy, Trade and Industry	2002	Max 40 t/day	10,000 t planned	Saline aquifer	Haizume Formation	Pleistocene	sandstone
Recopol	Poland	Pilot	TNO-NITG	2003	1 t/day	10 t	ECBM	Silesian Basin	Carboniferous	Coal
Qinshui Basin	China	Pilot	Alberta Research Council	2003	30 t/day	150 t	ECBM	Shanxi Formation	Carboniferous-Permian	Coal
In Salah	Algeria	Commercial	Sonatrach, BP, Statoil	2004	3-4000 t/day	17 Mt planned	Depleted hydrocarbon reservoirs	Krechba Formation	Carboniferous	Sandstone
K12B	The Netherlands	Demonstration	Gaz de France	2004	100-10000 t/day (2006+)	about 8 Mt	EGR	Rotleigendes	Permian	Sandstone
Frio	USA	Pilot	Bureau of Economic Geology of the University of Texas	4-13 Oct. 2004	Approx. 177 t/day for 9 days	1600 t	Saline formation	Frio formation	tertiary	Brine-bearing sandstone-shale
Otway	Australia	Pilot	CO2CRC	late 2005	160 t/day for 2years	0.1 Mt	Saline formation and depleted gas field	Waarre Formation	Cretaceous	Sandstone
Ketzin	Germany	Demonstration	GFZ Potsdam	2006	100 t/day	60 kt	Saline formation	Stuttgart Formation	Triassic	Sandstone
CLEAN	Germany	Demonstration	GFZ Potsdam	2008-2011	274 t/day	0.1 Mt	Depleted gas reservoir	Rotliegend formation	Permian	Sandstone
Ordos Basin	China	Pilot	Shenhua	2010	100 t/day	Planned 0.1 Mt/year	Saline formation	Shanxi formation, Shihezi formation	Permian	Sandstone

1.3.1 Research scope of CO2 geological sequestration

Papers concerning the conceptual framework of Carbon Capture and Sequestration (**CCS**) were first presented in the early 1990s (e.g. Van der Meer, 1992, 1993; Winter and Bergman, 1993; Gunter et al., 1993; Holloway and Savage, 1993; Hendriks and Blok, 1993; Koide et al., 1993, 1995; Bachu et al., 1994; Bergman and Winter 1995; Holt et al., 1995; Weir et al., 1995). The injection sites are various, including deep saline formations, depleted gas or oil reservoirs, deep coal-beds and so on (Gunter et al., 1996; Byrer and Guthrie, 1997, 1998a, 1998b; Stevens et al., 1998a, 1998b; Somomon et al., 2007).

While rapid progress has been made in the development of CO_2 geologic sequestration since its inception (Benson, 2005), many countries take part in the exploration and engineering activities of suitable reservoirs. Lohuis (1993), for example, has worked on the feasibility of CCS in the Netherlands and Korbol and Kaddour (1995) introduced the practical situation of CCS in Norway. Furthermore, great progress has been made in the Alberta Basin of Canada (Bachu et al., 1994; Law and Bachu 1996; Gunter et al., 1996, 1997; Xu et al., 2003).

The worldwide implementation of CCS demands a comprehensive knowledge of the geological processes, safety and efficiency of the specific engineering project, impact on the environment, policy and law support. The main topics related with CO_2 sequestration have been concluded in detail by Benson (2005).

Geological Processes caused by CO_2 injection

Additional knowledge is needed in order to understand the physical and chemical geological processes that affect the long-term storage of CO_2 underground (Benson, 2005). These include its physical trapping beneath low-permeability cap rocks, immobile residual phase trapping, CO_2 plume movement in the reservoir or cap rock and geochemical solubility trapping in form of aqueous ions in solution or precipitation of solid carbonate minerals.

After the injection of supercritical CO_2 gas injection into the aquifers, three trapping mechanisms (i.e. structural, solubility and mineral trapping) begin to work. Mineral trapping (a chemical process whereby CO_2 can react directly or indirectly with minerals and organic matter existed in the geologic formation leading to the deposition of secondary minerals and organic matter) is the most potential and safest way to withdraw CO_2 gas from the atmosphere (Xu et al., 2006), because it can immobilize CO_2 as solid minerals in the long-term.

Storage efficiency

Geological sequestration of CO_2 can be economically efficiency by combination with its application for enhanced oil and gas production (Benson, 2005). Extra income from oil and gas recovery can offset the costs of CO_2 sequestration. Optimization can also be achieved through the efficient use of storage space underground. In brief, monitoring technologies can help to ensure storage efficiency in the following aspects: ① sweep efficiency monitoring; ② optimization EOR and enhanced coalbed-methane recovery.

Storage safety (Risk assessment and mitigation)

Engineering safety consideration is the highest priority when CO_2 storage project proceeds. Risk assessment and mitigation are essential during site selection processes. This allows the application of monitoring technology to provide us more detailed information about, for instance, the evolution of the reservoir, including pressure, composition of aqueous components changes, injection and production rates, geological structure and so on, from pre-operational to closure stage (Tables 1.3 and 1.4).

Table 1.3 Monitoring technology used in the lifespan of a detailed CO_2 sequestration project
(adapted from Benson and Cole, 2008)

Basic monitoring program	Enhanced monitoring program
Pre-operational monitoring	*Pre-operational monitoring*
Well logs Wellhead pressure Formation pressure Injection- and production-rate testing Seismic survey Atmospheric-CO_2 monitoring	Well logs Wellhead pressure Formation pressure Injection- and production-rate testing Seismic survey Gravity survey Electromagnetic survey Atmospheric-CO_2 monitoring CO_2-flux monitoring Pressure and water quality above the storage formation
Operational monitoring	*Operational monitoring*
Wellhead pressure Injection and production rates Wellhead atmospheric-CO_2 monitoring Microseismicity Seismic surveys	Well logs Wellhead pressure Injection and production rates Wellhead atmospheric-CO_2 monitoring Microseismicity Seismic survey Gravity survey Electromagnetic survey Continuous CO_2-flux monitoring Pressure and water quality above the storage formation
Closure monitoring	*Closure monitoring*
Seismic survey	Seismic survey Gravity survey Electromagnetic survey CO_2-flux monitoring Pressure and water quality above the storage formation Wellhead pressure monitoring

Table 1.4 Monitoring methods and their purposes (adapted from Benson and Cook, 2005)

Surface devices	rates and compositions of injected and produced gases and liquids; atmospheric CO_2 concentration and flux monitoring; ecosystem monitoring;
Seismic methods	surface-to-borehole, single-well, and cross-borehole time-lapse seismic methods
Electrical methods	electrical resistance tomography and cross-well electromagnetic methods
Borehole Sensor methods	reservoir pressure and temperature measurements
Chemical tracers	quantify hydrodynamic, solubility, and mineral trapping rates and processes

Over the past few years, distinct progress has been made in risk assessment associated with CO_2 sequestration, especially with regard to the application of the features, events, and process (FEP) methodology (Benson, 2005). IPCC (2005) provides a detailed description of the potential environmental impacts caused by CO_2 leakage which can occur mainly through three ways: (1) abrupt leakage through injection well failure and abandoned wells; (2) gradual leakage through undetected faults and fractures; or (3) via diffusion leakage through bad qualified impermeable cap rock (Court, 2011).

Environmental friendly

Great progress has been made in understanding the severe consequences of CO_2 leakage on natural systems and human beings. Besides, some useful models have been applied to assess how CO_2 behaves after released into the near surface and the atmosphere (Benson and Cook, 2005; Morozova et al., 2011).

1.3.2 THMC geo-processes

A series of physical and chemical processes take place in the deep geological system (Fig. 1.5). The reaction rate for some of the processes, are fast, while others, require hundreds to thousands of years to complete. Overall, four processes are mainly recognized in the deep geological system as a result of CO_2 injection and storage: (1) heat transport (T), (2) geo-hydrological transport (H), (3) geomechanics (M) and (4) geochemical process (C). These processes couple or interact with each other, impacting changes to the petrophysical properties of the rock (Wang and Wang, 2004). For example, the petrophysical reservoir parameters including porosity, permeability, fluid composition, mineral content and rock stiffness may be spatially heterogeneous, depending on temperature, pressure, effective stress, chemical potential etc. In particular, fractured rocks that are characterized by dual porosity and permeability, may be altered during the THMC processes through many coupled mechanisms, such as stress-driven asperity dissolution (MC), thermal-hydro-mechanical asperity compaction/dilation (THM), and mineral precipitation/dissolution (HC) (Taron et al., 2009).
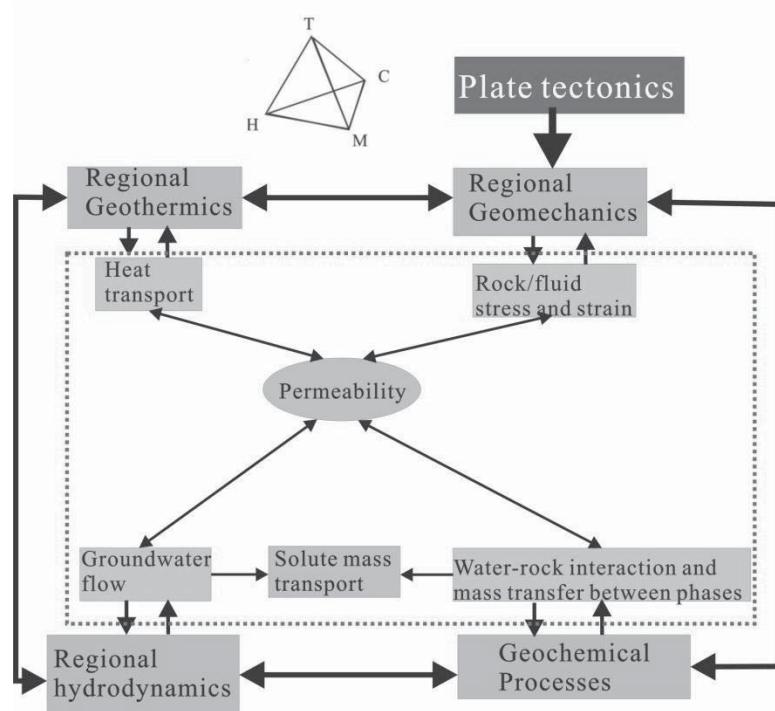
Fig. 1.5 Coupled thermo-hydro-chemo-mechanical effects in a large geosystem (after Stephansson et al., 2004)

Both experimental and simulation methods can be used in understanding the different scales of the T-H-M-C coupling processes (Schrefler and Gawin, 1996; Bower and Zyvoloski, 1997; Swenson et al., 2004; Taron et al., 2009). Within the context of numerical simulations, a diversity of complex T-H-M-C problems can be treated (e.g. coupling of different processes, consideration of heterogeneities under various geological conditions), although the development of efficiency and stability algorithms is always challenging (Goerke et al., 2011). Taron et al. (2009) proposed a method for fully THMC coupled study, using the simulators $FLAC^{3D}$ and TOUGHREACT. However, it is still very little to know about the complex processes that are strongly dependent on a specific field with a range of uncertainties and scales

.

(from micro_scale to macro_scale) of the geological model Furthermore, parameters of the physical structure of the reservoirs like permeability and strata geometries, description of multiphase fluid flow, behavior of the cap rock in response to CO_2-rich fluids etc., make it difficult to track the reality (Van der Meer et al., 2000; Huppert 2000; Rutqvist and Tsang, 2002; Johnson et al., 2001). Before the numerical model is used for prediction, the prescribed parameters must be adjusted to match the history of the real geological model. However, due to the limited availability of data, dubious parameters and the numerical dispersion problems make it hard to test the applicability of the assumptions inherent in simulation modeling (Bickle et al., 2007).

1.3.3 Geological model uncertainties

As regards to the site selection, suitable for CO_2 sequestration, it is essential to set up a 3-D geological model in terms of structure and heterogeneities (facies, mineral, petrophysical…) at different scales (basin, field, target formation). Structure information of the site can be understood using 2D or 3D seismic data. Different assumptions should be carefully used in light of the available data (Le et al., 2011). The heterogeneities at different scales cause the establishment of a geological model more difficult.

Petrophysical characteristics of a reservoir rock (Table 1.5) is mainly be composed of three main aspects: ① rock composition, including mineral composition and their relative contents, porosity, state of saturation state (unsaturated or saturated), properties of pore fluid (one phase/ multi-phase; one component or multi-component) and so on; ② rock structures, including grain size, grain shape, cementation, etc.; ③ thermodynamic environments, including temperature, pressure, stress fields etc (Wu and Yin, 2008).

Table 1.5 Petrophysical characteristics of a reservoir rock

Petrophysical properties	Parameters
Mechanical parameters	density, Young's modulus, bulk modulus, shear modulus, possion's ratio, compressive strength, tensile strength
Flow parameters	porosity, permeability, diffusion coefficient, dispersion
Electromagnetic parameters	magnetic conductivity, electric inductivity

To ensure the safety of a CCS project, more available data need to be added in the geological model. The geological uncertainties can be estimated using a statistical method, and the main risks associated with CO_2 storage should be assessed using key petrophysical characteristics of reservoir.

1.3.4 Dynamic simulation model

The injected CO_2 flows together with the other fluid components in the subsurface hydro-system which is a multiphase open system with changeable boundary conditions. Therefore, the flow and transport processes can occur at extremely different scales (see Fig. 1.6): including regional scale, geological structure scale, pore pace and molecular scale (Helmig, 1997).
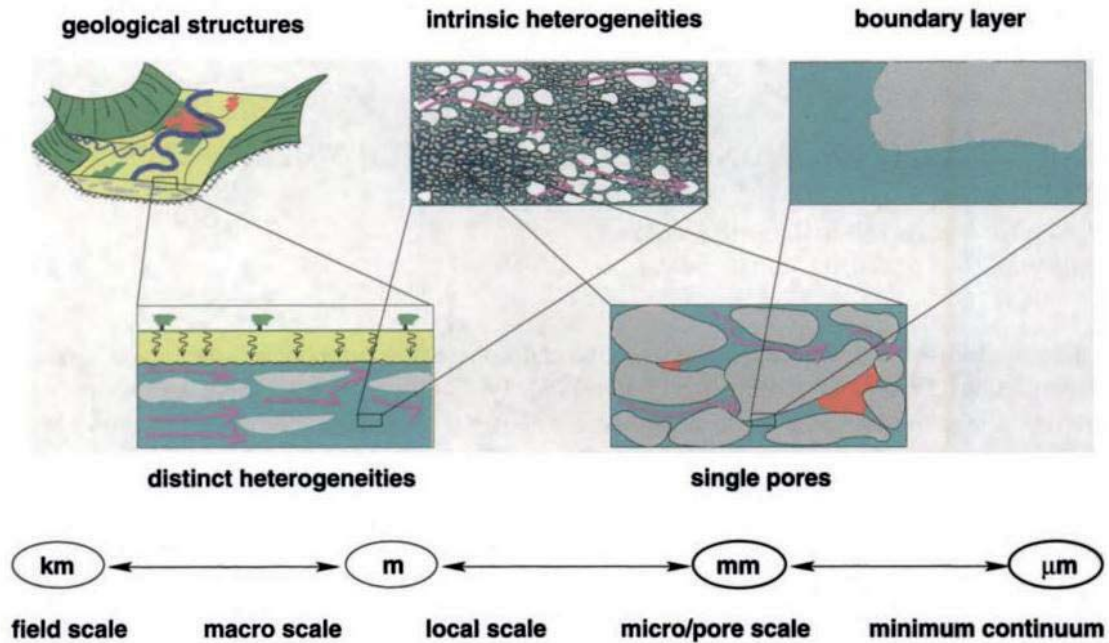
Fig. 1.6 Subsurface hydro-systems at different scales (Kobus and de Haar, 1995)

An optimal understanding of the complex physical, chemical and microbiological processes at different scales is fundamental to the efficient in-situ remediation techniques. Generation of the necessary model and of its corresponding prediction instruments is an interdisciplinary problem that combines several science research disciplines including many subjects from geology, geophysics, chemistry, hydrogeology, fluid mechanics, thermodynamics, mathematics and microbiology. The numerical models thus obtained, enable us to compare different hypotheses on the behavior of the complex system. Through numerical simulation, the following information about the geological processes can be obtained: (1) the CO_2 plume movement in porous media (as the CO_2 saturation changes); (2) the displacement of water, oil or gas by CO_2 in the pore space; (3) the pressure buildup during CO_2 injection; (4) the CO_2-water-rock interactions (the injected CO_2 can be immobilized in the form of dissolved aqueous phase-fraction of CO_2 dissolved in the water or mineral phase); (5) the variation of storage capacity and possibility of seismic events due to the changes in faults or failure stress field; (6) the potential risk of leakage through injection wells or abandoned wells.

Modeling of CO_2 sequestration processes involves the solutions of the component transport equations, the equations for thermodynamic equilibrium between the gas and aqueous phase, and the equations for geochemistry. The latter involves reactions between the aqueous species and mineral precipitation and dissolution. Modeling of reactive transport of components in the aqueous phase has also been a subject of the study in the field of hydro-geochemistry (Lasaga et al., 1993; Pruess et al., 2001). The main difficulties of the coupled modeling of transport and reactions are related to the size and nonlinearity of the resulting system of equations (Lichtner, 1985). There are mainly two approaches for solving the coupled system of equations: the **sequential solution method** and the **simultaneous solution method**. For the **sequential solution** approach, flow and chemical-equilibrium equations are solved separately and sequentially (Yeh et al., 1989, 1991; Mangold and Tsang, 1991; Sevougian et al., 1992; Reeves and Abriola, 1994; Steefel and MacQuarrie, 1996). Iteration methods are applied between the two systems until convergence is achieved. For the **simultaneous solution** approach (fully-coupled method), recognized as the most stable approach, all equations are solved simultaneously using Newton interation (Lichtner, 1992; Steefel and Lasaga, 1992, 1994).

The prediction model will be much precise when verifications are used. It is a step by step process from conceptual model to true 3D geological model, which can be described in detail in Fig. 1.7.
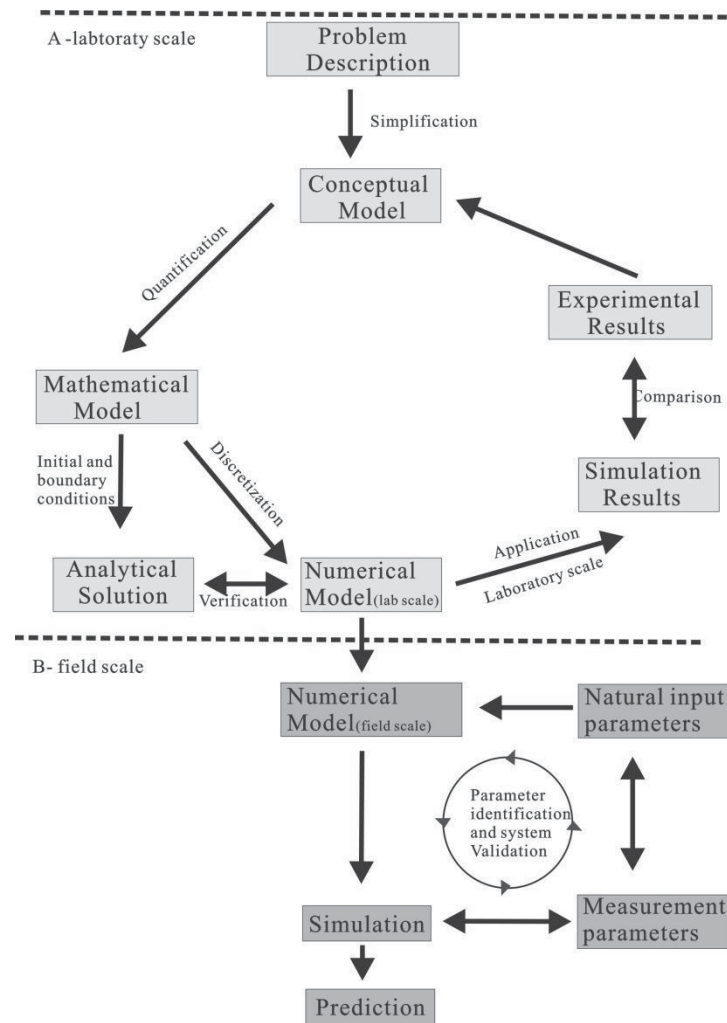
Fig. 1.7 Step by step processes from conceptual model to prediction (after Helmig, 1997)

Realistic 3D modeling of fluid flow in a sedimentary basin is almost impossible as the permeability distribution can not be predicted precisely due to the strong heterogeneity induced by the complicated sedimentary facies, diagenesis and tectonic development (Bjϕrlykke et al., 2004). Corresponding to the different scale of subsurface hydro-system, dynamic models for CO_2 sequestration can also be elaborated at different scales, for example, regional scale model, storage site model, near-well region model and pore-scale model (Table 1.6).

Table 1.6 Different scales of dynamic modeling and their targets

Scale of modeling	Problems to solve
Regional-scale	Estimate migration pathways and constraint boundary conditions
Field storage site	Estimate overpressure and CO_2 plume behavior
Near-well region	Estimate chemical induced effects
Pore-scale	Estimate microscopic mineral and fluid changes

1.3.4.1 Multi-phase, multi-component reactive transport simulation (TH^{2}C)

Due to the geological heterogeneity of porous media and the multiple components involved, single phase reactive tranport process is complex. When two or multiple phases (water/oil or gas) are considered, the flow properties (EOS-equation of state) become even more complicated. For instance, when CO_2 is injected into deep saline formations, it is always at a supercritical state and flows together with the connate water. The mass balance equations in such a multiphase system are described by more

11

complicated laws than in the case of single-phase condition (Bear, 1972; Lake, 1989; Pankow and Cherry, 1996).

In this dissertation, TOUGH2MP and TOUGHREACT codes have been used in the simulation of multiphase multicomponent fluid flow and derived multi-field coupled problems in the deep saline formation, e.g., CO_2 plume movement, pressure buildup, CO_2-water-rock interactions etc.

TOUGH2-MP is a product belonging to the family of TOUGH. TOUGH2MP is a numerical simulator for non-isothermal flow of multi-components, multi-phase fluids in one, two, and three-dimensional porous and fractured media (Pruess et al., 1999). The first TOUGH simulator, TOUGH2, was developed in 1991 (Pruess, 1991). Since then, more modules have been added. And TOUGH series products becomes more and more effective in handling scientific and engineering problems, including T2VOC, TMVOC, TOUGH2-MP, TOUGHREACT, TOUGH+, iTOUGH2. The TOUGHREACT simulator is a supplement to the TOUGH family and useful for geochemical reaction simulations. A wide range of complex subsurface thermo-physical-chemical heterogeneity processes are considered under various thermohydrological and geochemical conditions of pressure, temperature, water saturation, and ionic strength (Xu et al., 2003) inlcuding: (1) fluid flow in multiple phases under different pressure and gravity forces, (2) capillary pressure effects for the liquid phase, and (3) heat flow controlled by conduction, convection and diffusion mechanisms.

Many other computer code simulators have been developed to study the coupling effects of multi-scale, multi-phase, multi-physical, dynamic model in the geologically complex systems, for example, FEHM, COMSOL Multiphysics, SHEMAT, CMG- GEM and OGS etc (Table 1.7). The aim is to provide a flexible numerical framework for solving multifield problems in porous and fractured media for applications in geosciences and hydrology (Kolditz et al., 2012). Most of these simulators are able to solve partial differential equations that describe the complicated physical phenomenon, using either the finite element or finite difference theory.

Table 1.7 Simulators used in CO_2 sequestration

Simulator	Full name	Research scope	Solution method	Developer
FEHM	**F**inite **E**lement **H**eat and **M**ass	From single fluid/single phase to multi-fluid/multi-phase fluid flow	FEM (Finite Element Method)	Los Alamos National Laboratory (LANL)-1980s
TOUGH2	**T**ransport **O**f **U**nsaturated **G**roundwater and **H**eat	From single fluid/single phase to multi-fluid/multi-phase fluid flow (water, vapor, non-condensible gas and heat) in porous and fractured media	FDM (Finite Difference Method)	Lawrence Berkeley National Laboratory (LBNL) in the early 1980s
TOUGHREACT	Non-isothermal reactive geochemical transport model	Adding reactive geochemistry into the framework of TOUGH2	FDM (Finite Difference Method)	Lawrence Berkeley National Laboratory (LBNL) Version 1 at 1998
COMSOL Multiphysics	-	For various physical processes, especially coupled phenomena or multiphysics	FEM (Finite Element Method)	COMSOL GROUP, Sweden, 1986
SHEMAT	**S**imulator of **HE**at and **MA**ss **T**ransport	Simulating steady-state and transient processes in hydro-geothermal reservoirs in two and three dimensions, including fluid flow, heat convection and mass transport	FDM (Finite Difference Method)	RWTH Aachen, Germany,
CMG- GEM	**C**omputer **M**odeling **G**roup- **G**eneral **E**quation of state **M**odel	Thermodynamic properties, geochemical reactions and phase change during CO_2 sequestration in underground formation		Commercial software, CMG GROUP, 2008
ECLIPSE	**-**	Reservoir simulations: Black Oil module and Compositional module	FDM (Finite Difference Method)	Commercial software, Schlumberger Ltd.
OpenGeoSys	-	Numerical simulations of individual or coupled thermo-hydro-mechanical-chemical (**THMC**)processes in porous and fractured media	FEM (Finite Element Method)	UFZ, Germany,

1.3.4.2 Rock mechanics simulation (THM)

FLAC3D is a three-dimensional explicit finite difference program used for the computation of geotechnical engineering mechanics (Itasca, 2009). It can simulate the behavior of three-dimensional structures comprised of soil, rock or other materials that can undergo plastic flow after yield state. Explicit formulation is used in the simulation, which can be overcome by both automatic inertia scaling and automatic damping.

FLAC3D offers several models to represent the mechanical response of the geological materials (Itasca, 2009). For example, the "null" model; the three elasticity models (isotropic, transversely isotropic and orthotropic elasticity); and the nine plasticity models (Drucker-Prager, Mohr-Coulomb, strain-hardening/softening, ubiquitous-joint, bilinear strain-hardening/softening ubiquitous-joint, double-yield, modified Camclay, Cysoil and Hoek-Brown).

13

1.4 Research objectives, contents and structure

When injected deep into saline formations, supercritical CO_2 will be able to both migrate and reside within the aquifer. However, the migration or leakage of the CO_2 plume into potable groundwater reservoirs can lead to pollution of the groundwater resources. In order to estimate the potential risk of CO_2 infiltration, and eventually plan an appropriate remedial program, the characteristic temporal/spatial changes of the CO_2 plume in the storage aquifer must be well known.

The purpose of CO_2 sequestration is to immobilize CO_2 into suitable underground reservoirs, on long-term basis. Therefore, its characteristic migration of CO_2 in the reservoir and cap rock, together with its corresponding response to changes in the reservoir temperature (T), hydraulic field (H), mechanical field (M) and chemical field(C) should be adequately investigated, to ensure the safety (avoidance the possible leakage of CO_2), capacity, and injectivity of CO_2 for sequestration at any specific site. In this thesis, the deep saline formations in Ordos Basin of China have been selected targets for demonstration of CO_2 sequestration.

This thesis finds basis on the reviews of the progress and probable problems associated with CO_2 sequestration, at the demonstration site located in the Ordos Basin. The project has selected for study the deep multilayered saline formations as CO_2 injection points using basic experiments, analytical methods and numerical simulations. In this dissertation, the following topics have been studied and discussed in detail (see Table 1.8): (1) the review on CO_2 flow and distribution characteristics, and CO_2 sequestration mechanisms; (2) a detailed summary of the geological characteristics of the Ordos Basin, particularly the target injection aquifer layers; (3) description of the two phase (CO_2 and H_2O) fluid flow processes in the multilayered reservoir-cap rock systems and analysis of uncertainties due to the heterogeneity of the geology in the Ordos Basin; (4) description of the coupled hydro-mechanical processes induced by CO_2 injection; (5) simulation of the water-rock interactions caused by CO_2 injection; (6) simulation of geothermal production associated with CO_2 sequestration. Consequently, site selection criteria have been discussed in detail, including their application to CO_2 sequestration and geothermal production in China.

First, the relevant data was collected from literature about the pilot CO_2 sequestration project launched in Ordos Basin. Geological models were then set up according to the input data. To understand the characteristic distribution and storage mechanisms of CO_2, characteristic movement of the CO_2 plume in the multi-layered reservoir (by the multi-layer injection technique) was studied. This was followed by studying the impact of some relevant factors (e.g. permeability, boundary conditions, injection rate, geological structure, irreducible gas saturation etc.). CO_2 migration and the induced physic-chemical processes during injection and post-injection periods were discussed, including coupled processes of H^2, H^2M, H^2C, etc. The utilization of CO_2 (for e.g. EOR, EGR, and EGS) has attracted much attention for further research, mainly due to the economical benefits involved in the processes. For instance, when CO_2 is injected into a geothermal reservoir, it will act to enhance the pressure driving force. Though a lot of research has been carried out on this topic, only a fundamental understanding of the processes related with CO_2 sequestration has been obtained so far. The fully coupled THMC processes still require more research studies, especially the constitutive relationships between the various physical fields established during and after the sequestration. Furthermore, realistic 3D modeling of fluid flow in a sedimentary basin is nearly impossible as permeability distribution can not be predicted precisely, due to the strong heterogeneity of the sedimentary basins, with respect to primary sedimentary facies, diagenesis and tectonic development (BjΦrlzkke et al., 2004). Though faced with many difficulties (e.g. the strongly varied heterogeneity of the geology, limited access to geological and operation data, etc.), simulation results of this thesis may provide some invaluable understanding of sequestration processes and some guidance for future commercial /industrial scale CCS operation.

Table 1.8 Research structure of this thesis

Literature Review
• The relevant geological processes caused by CO_2 injection • CO_2 based geothermal production • Geological characteristics of the Ordos Basin

Numerical simulation of CO_2 sequestration		
CO_2-H_2O two phase fluid flow (H^2)-by TOUGH2MP	**The interaction of fluid flow and mechanical changes (H^2M)-TOUGH2MP+FLAC^{3D}**	**CO_2-water-rock interactions (H^2C) -by TOUGHREACT**
Geometric model: simplified 3D multilayered reservoir-caprock system **Input data source:** Ordos Basin **Uncertainties, parameters and analysis:** Injection strategy; Boundary effect; Reservoir permeability; Geological structures; Multiphase effect (relative permeability and capillary pressure)	**Geometric model:** simplified multilayered reservoir-cap rock system **Input data source:** Ordos Basin **Uncertainties, parameters and analysis:** In situ stress fields; Reservoir permeability; Biot coefficient; **Results analysis:** Pore pressure; In situ stress changes; Fluid migration; Vertical displacement, etc.	**Geometric model:** batch, 1D and 2D studies **Input data source:** Ordos Basin **Uncertainties, parameters and analysis:** Water chemistry; Mineral composition **Results analysis:** Ion concentration changes; Mineral volume fraction Changes; Porosity and permeability; Propagation distance

Simulation of CO_2 sequestration associated with geothermal production		
Geometric model: simplified 3D multilayered reservoir-caprock system	**Parameters Data source:** some are from Ordos Basin, some are just assumed	**Well configuration:** one injection well+ two production wells + two reinjection wells

Site selection criteria for CO_2 sequestration and geothermal production		
Evaluation processes: Country-level; Sedimentary basin-level; Target area of interest-level; Site-level	**Different scales of the selection criteria:** Basin scale; Field scale; Target formation scale; Engineering operation scale	**Screening and ranking methods and its application in China**

2. CO$_2$ sequestration project in Ordos Basin

2.1 CCS project in Ordos Basin of China

In recent years many large projects related with coal transformation energy have been constructed in Ordos Basin, including many large coal chemical industry projects (coal to liquid, coal to methanol, coal to olefins, coal liquefaction (DCL), coal to gas). As much as 8.7 Mt/year CO$_2$ will be released if all the existing projects are in operation. If all the planned projects are completed, the emission amount will rise to about 54 Mt/year (Table 2.1, Ren et al., 2010). Therefore, CCS technology has the potential advantage to reduce CO$_2$ emission in Ordos Basin.

Table 2.1 Large coal chemical industrial projects constructed in the Ordos Basin (Ren et al., 2010)

Company	Project name	Scale	City
Shenhua GROUP	Direct coal liquefaction(DCL)	1.08 Mt/year	Ordos
Shenhua GROUP	Substitute natural gas(SNG)	2B m^3/year	Ordos
Shenhua GROUP	Coal to olefins (CTO)	0.6 Mt/year	Baotou
Datang GROUP	SNG	4B m^3/year	Ordos
Yidong GROUP	Coal to methanol(CTM)	1.20 Mt/year	Ordos
Xin'ao GROUP	CTM	0.6 Mt/year	Ordos
Jiutai ENERGY	CTM	1.00 Mt/year	Ordos
Yitai GROUP	Indirect coal liquefaction(ICL)	0.16 Mt/year	Ordos
Shenhua Ningxia Coal Industry Group (SNCIG)	CTO	0.52 Mt/year	Yinchuan
SNCIG	CTM	0.85 Mt/year	Yinchuan
Rong Yu Shi Ye company	CTMO	1.80 Mt/year	Yulin

The Ordos Basin has been a favorite for the generation of several petroleum systems (Fig. 2.1), including four large gas fields (i.e. Yulin, Wushenqi, Sulige and Jingbian) in the Upper Paleozoic and one large oil field (Mizhi), with an estimated reserve of more than hundreds of billon cubic meter (Yang et al., 2004). The CO$_2$ sequestration project launched in the Ordos Basin, under the leadership of SHENHUA GROUP, is the first full scale (from capture to injection) CCS project in saline formation in China. The purpose of CO$_2$ sequestration is to immobilize the CO$_2$ produced during the processes of coal liquefaction to oil, thus reduce the emission of CO$_2$ to the atmosphere. The CCS pilot project was started in 2010, with an estimated injection capacity of 0.1 Mt/year (Table 2.2). Till 2014.8, about 220,000 tons of CO$_2$ has already been injected into underground saline formations. The wellhead injection pressure is at 4.98 MPa, with a flow rate 17.23 m^3/h. Under this condition (injection pressure and ambient temperature), CO$_2$ is at liquid state at the surface. The CO$_2$ sequestration site belongs to Wulanmulun town (Fig. 2.1), about 17 km away from coal direct liquefaction factory of Shenhua GROUP. Three wells have been drilled for demonstration purpose, i.e. 1 injection and 2 monitoring wells located 31 m and 70 m away from the injection well.

Table 2.2 Timelines for the pilot scale CO$_2$ sequestration project launched in Ordos Basin (Liu et al., 2014a)

Start time	Task
2008.10	First-phase involved the preparation of a feasibility study of CO$_2$ capture and sequestraiton
2009.12	Feasibility study completed
2010.05	3D exploration seismics of demonstration area completed
2010.06	Installation of the CO$_2$ capture equipment started
2010.08	Drilling of injection well started
2010.12	Capture equipment switched on at the Shenhua CTL plant
2011.01	Injection test carried out
2011.05	Started injection successfully
Till 2014.8	Injection amount of CO$_2$ about 220,000 tones
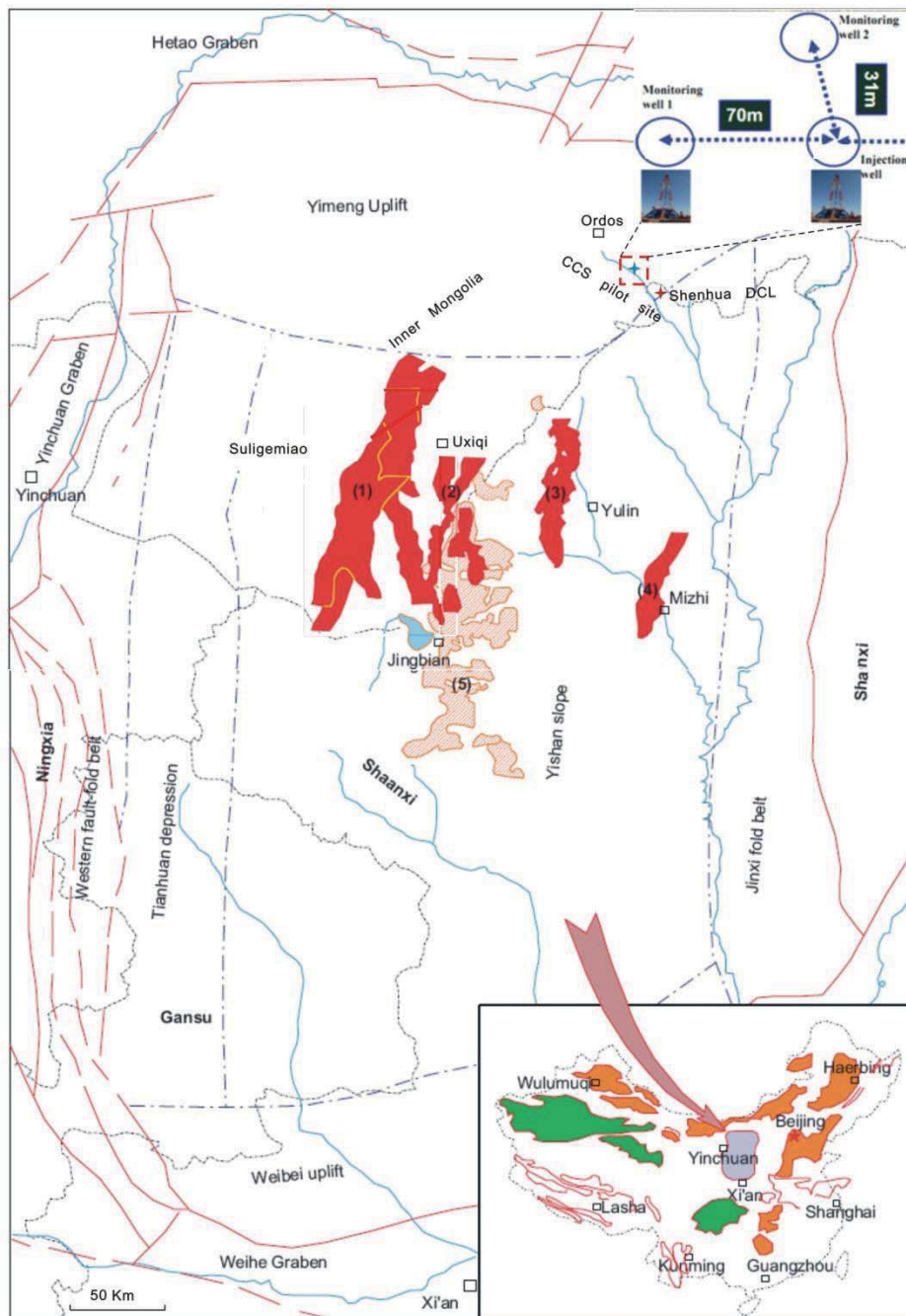
Fig. 2.1 Locations of CCS pilot project and some major oil/gas field in the Ordos Basin (Yang et al., 2008, modified), (1) Sulige; (2) Uxiqi; (3) Yulin; (4) Mizhi; (5) Jingbian

From the lithological stratigraphy at the pilot site (Fig. 2.2), there are mainly 6 reservoir-caprock systems of interest below the depth of 800 m (i.e. the Zhifang formation—Heshanggou, Liujiagou, Shiqianfeng, Shihezi, Shanxi—Taiyuan and Majiagou formation storage units), which are considered potential reservoirs for CO$_2$ storage. During the drilling processes, core (a total length of 98 m) and the formation water samples were simultaneously collected for laboratory experimental studies. Subsequently, four injection layers below the depth of 1690 m were selected for CO$_2$ injection. To improve the injectivity, hydraulic fracturing treatments was taken before injection.
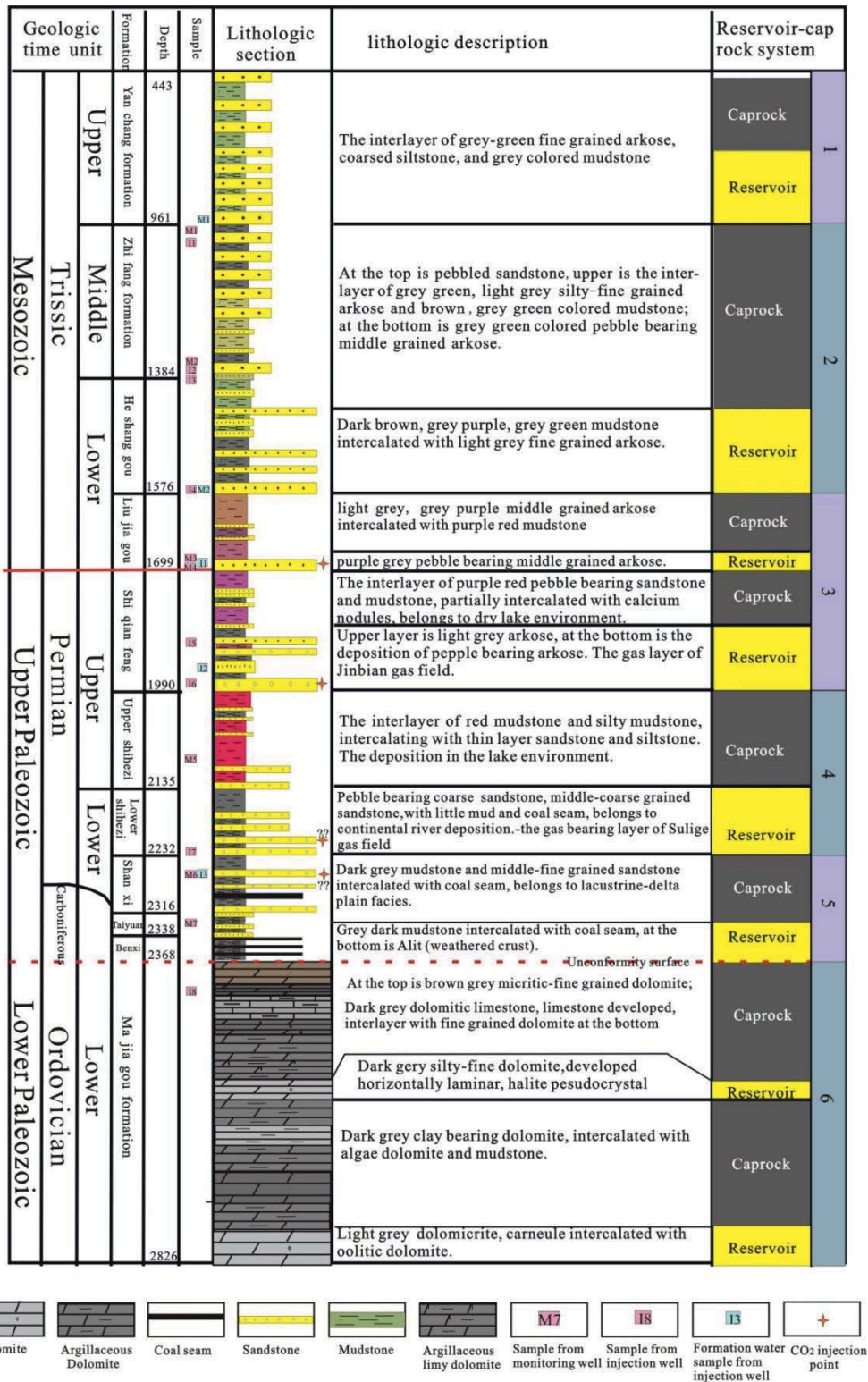
Fig. 2.2 Lithology and stratigraphic column at the approximate position of injection at CCS pilot site in the Ordos Basin, where core and formation water samples were simulataneously collected during well drilling (after Liu et al., 2014a)

2.2 Geological characteristics of the Ordos Basin

Selection of a specific site for CO$_2$ underground storage demands a careful study of the geological characteristics of the reservoir-caprock systems in order to guarantee environmental and operational safety during and after injection. The study should include petrographic, tectonic characteristics and properties of the reservoir strata (i.e. porosity, permeability, the composition of fluid and minerals,

18

pressure, temperature, salinity, etc.), which may affect the physical and chemical behavior of CO$_2$ in reservoir and cap rock, thus its storage safety and capacity. Injection of CO$_2$ can cause a series of problems, including the risk of leakage when the pressure buildup exceeds the fracture pressure of the reservoir rock (Fig. 2.3). Leakage paths could be along the injection or abandoned wells, faults or fractures, with hazardous consequences to human beings and the environment.
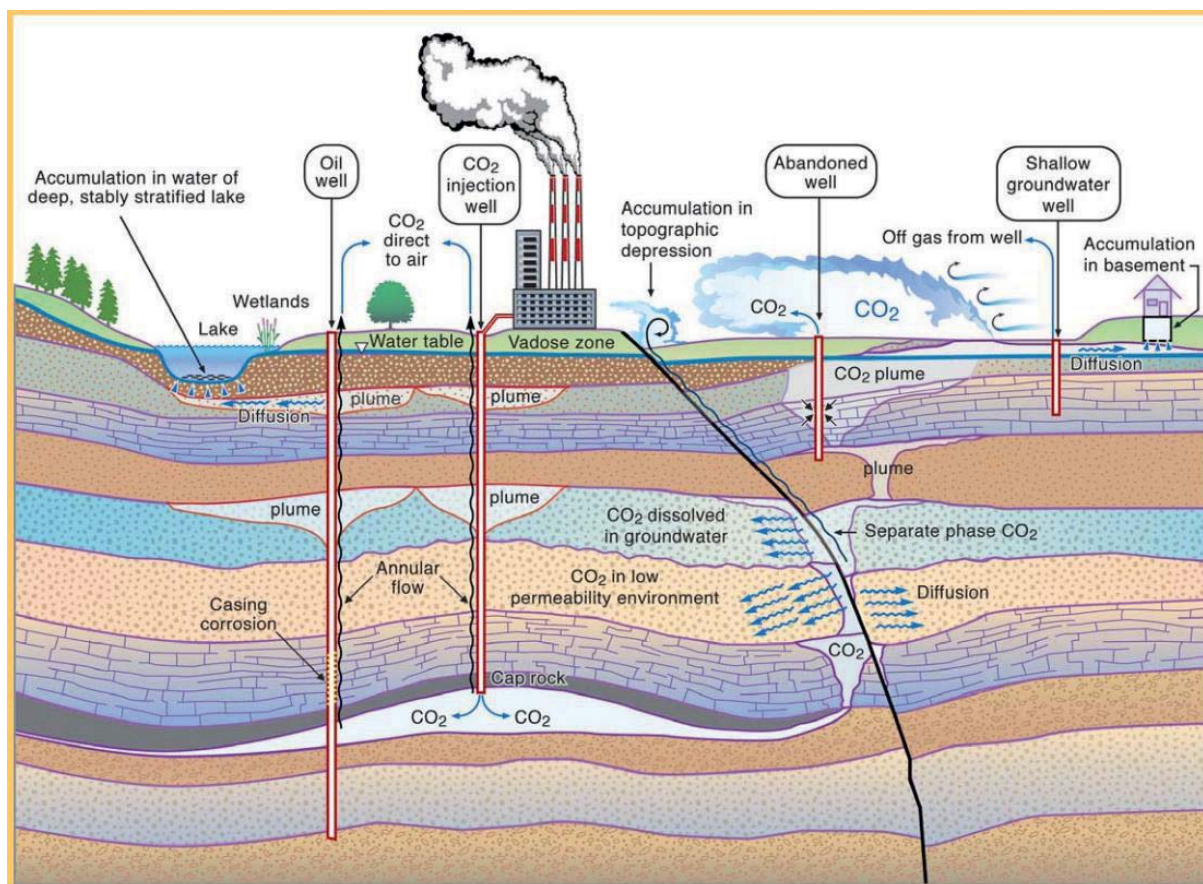
Fig. 2.3 CO$_2$ leakage paths during the post-injection period (after Benson and Hepple, 2005)

2.2.1 Tectonic evolution of the Ordos Basin

The Ordos Basin appeared as a south-north directional rectangle shape (Fig. 2.4A), with the dimensions of 640 km from south to north by 400 km from west to east. The Ordos Basin, with an area of about 2.5×10^5 km^2 (Yang et al., 2004; Xiao et al, 2005), is an intracontinental depression, which developed on the base of North China craton during Mesozoic period. According to the regional geology of China, the Ordos Basin is located at the transition zone between the Pacific and Tethys-Himalayan dynamic setting (Ren and Xiao, 2002). It differs from sedimentary basins in orogenic belt and classic cratons because of its tectonically active margins. The strata in the interior of the basin are generally horizontal or gently dipping (1°-3°), whereas those in the marginal parts of the basin were subjected to a significant degree of folding and faulting during Yanshanian (Jurassic and Cretaceous) orogeny (Guo et al., 1994, 2001; Xiao et al, 2005; Xue et al., 2011). The boundary faults and fold structures were developed during the formation and evolution process of the basin (Klimetz, 1983; Yang et al., 1991; Li et al., 1993; Zhou and Graham, 1996). The basin boundaries include the Yinshan piedmont fault zone in the north, Qinling piedmont fault zone in the south, Helan mountain—Pingliang fault zone—Qingtongxia—Guyuan fault zone in the west, and Lishi fault zone in the east (Li and Gao, 2010). The basin is surrounded by a series of mountain ranges, including the Innermongolia-Daxinganling Hercynian orogenic belt to the north, the Qilian-Qinling Indosinian orogenic belt to the south, Alashan block to the

west and Shanxi block to the east (Yang et al, 2004). According to its present tectonic characteristics (Fig. 2.4B), the basin can be divided into the following regions: 1) the West boundary Thrust Belt, 2) the Western Depression Belt/Tianhua Syncline, 3) the Eastern Slope Belt/Yishan Slope, 4) the Jinxi Flexure Zone, 5) the Yimeng Uplift Zone and 6) the Weibei Uplift Zone.

The Ordos basin is the second largest energy base (in terms of oil, gas and coal) in China (Yang et al., 2004; Wang et al., 2004; Wei and Wang, 2004; Chen et al., 2005; Deng et al., 2005; Xue et al., 2011), characterized by multiple petroleum source rocks (Lower Paleozoic carbonates, Upper Paleozoic coal measures and Mesozoic shales). The impermeable beds developed widely at the top and base of the Upper Paleozoic strata. Lack of large vertical faults resulted into the isolation of the Upper Paleozoic strata from the Lower Paleozoic and Mesozoic strata, in addition to and the formation of an independent petroleum system (Wei et al., 2003). Hydrocarbon source rocks have been discovered in the Upper and Lower Paleozoic strata (Fig. 2.4B and Fig. 2.4C). The large scale oil-bearing layers have been discoverd is in the Yanchang formation of Triassic age (Ren, 1996), while gas-bearing layers are prevalent in the Shanxi, Lower and Upper Shihezi and Shiqianfeng of Carboniferous and Permian (Yang et al, 2008). The Shihezi (He-8 member) and Shanxi (Shan-1 member and Shan-2 member) formations of the Upper Proterozoic period in Yishan slope zone are very rich in gas. The porous media in this area is gas saturated or gas dominated (Fig. 2.5). Tight gas, coalbed methane and shale gas are all abundant in the Upper Paleozoic formations of the Ordos Basin (Zhao et al., 2011). The Ordos Basin is not only an irregular rectangle block, but also surrounded by active or deep faults at the boundaries. There are also a lot of basement fractures in the basin. Generally, there are four groups of faults in the basin:

- The N-S trending boundary faults: occurring on the western and eastern boundaries of the basin, were mainly formed at the end of Proterozoic period, and reactivated during the Mesozoic (Fig. 2.6, [20, 21, 22]);
- The E-W trending faults: include boundary faults (Fig. 2.6, [23, 24]) and intracontinental faults (Fig. 2.6, [1, 2, 3, 4, 5, 25]) developed during the Early Archean period and were responsible for controlling the deposition and volcanic activities in the Early Archean period;
- The NE trending faults: developed during the Late Archean period – Early Proterozoic period (Fig. 2.6, [6, 7, 8, 9, 10, 11, 12, 13]);
- The NW trending faults: mainly appears in the Datong-Huachi ductile shear belt, which probably formed later or at the same time with the northeastern trending faults (Fig. 2.6, [14, 15, 16, 17, 18, 19]).
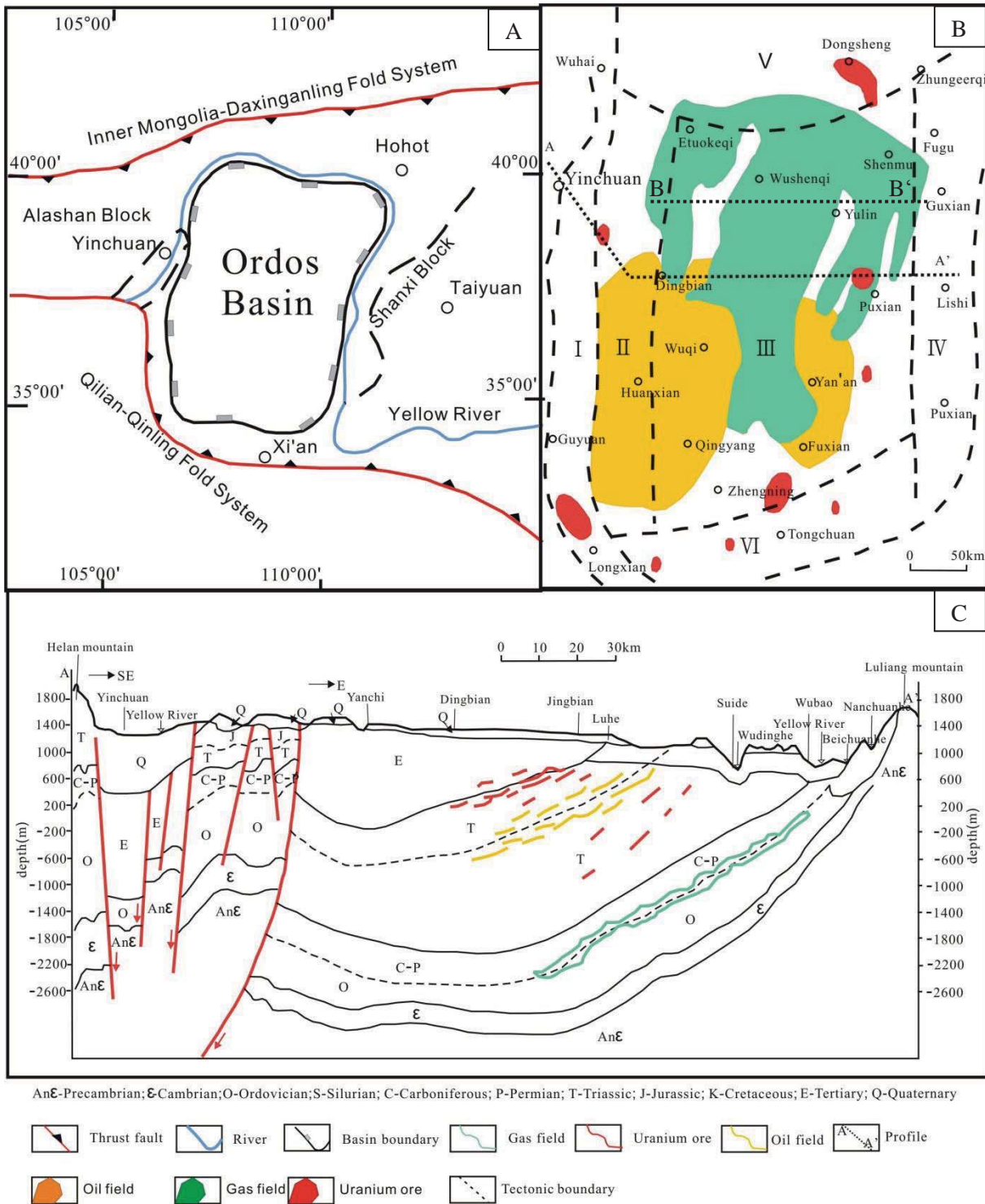
Fig. 2.4 Geological structures of the Ordos Basin, (A) Regional tectonic background; (B) Tectonic units including locations of major hydrocarbon fields; (C) W-E geological cross-sectional profile (modified after Xue et al., 2008)
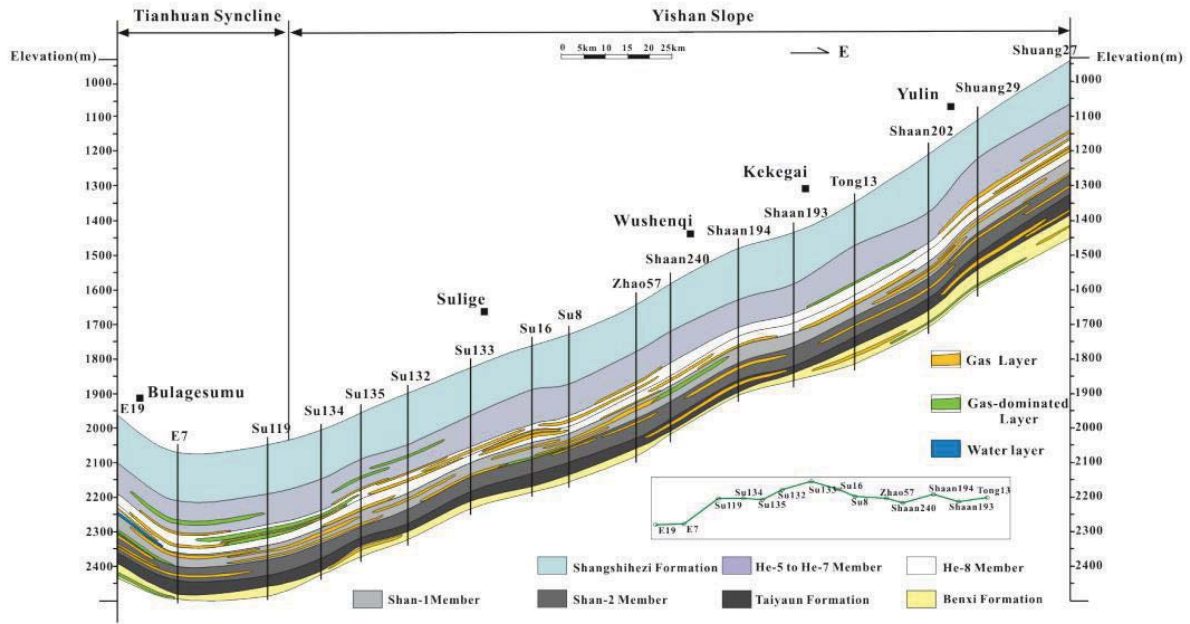
Fig. 2.5 Distribution of gas wells and reservoirs along the monocline limb in the Yishan Slope zone see Fig. 2.4 B, section B-B' for the approximate location in the basin (Zhao et al., 2011)
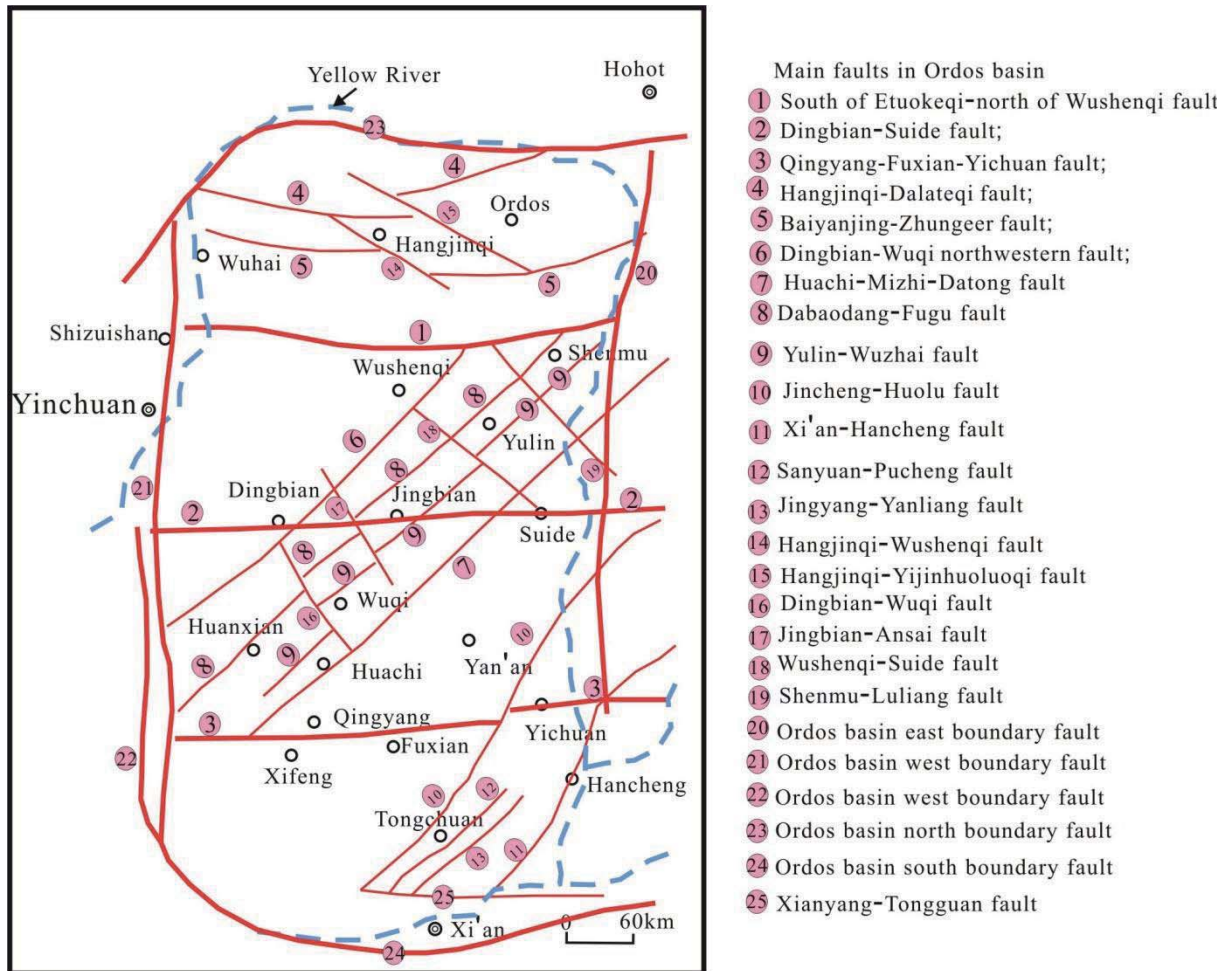
Fig. 2.6 Distribution of major fault systems in the Ordos Basin (modified after Ma et al., 2009)

2.2.1.1 Regional tectonic stress fields

The regional tectonic stress field is responsible for controlling the trends and extent of faults and fractures, including the re-activation of original sealing faults. Therefore it is very important to know the characteristic evolution of the tectonic stress field if safety of CCS project is taken into consideration. Due to the injection of large amounts CO$_2$, local stress state will be changed, which may trigger the movement of original faults and occurrence of seismic events.

Due to stress delivery effect from far-field and tectonic movements such as the subduction of Pacific Plate towards the NNE of Asian Plate, and the movement of Indian Plate towards the NE, the distribution of the present stress field in the Ordos basin (Fig. 2.7) has completely undergone different changeable characteristics compared to original stress field during the Neozoic Era (Zheng 2008; Zhou et al., 2009). Since 0.78 Ma, the Tibet Plateau has undergone a strong intermittent uplift movement and attained its current altitude of 3000-4000 m. During this period, the Pacific Plate has been subducted and spreaded along the NEE direction, with the middle stress directed towards the NNW. This means that the compressional stress was mainly towards the NNE-NEE direction (ca 50°-80°), with its tension nearly trending in the NNW direction (Zheng, 2008). Since the Neozoic Era, the driving force of the Ordos Basin comes from the synthetic results of far-field delivery force generated by the northward movement of Indian Plate, the uplift of the Tibet Plateau and the westward subduction of the Pacific Plate (Zheng, 2008).
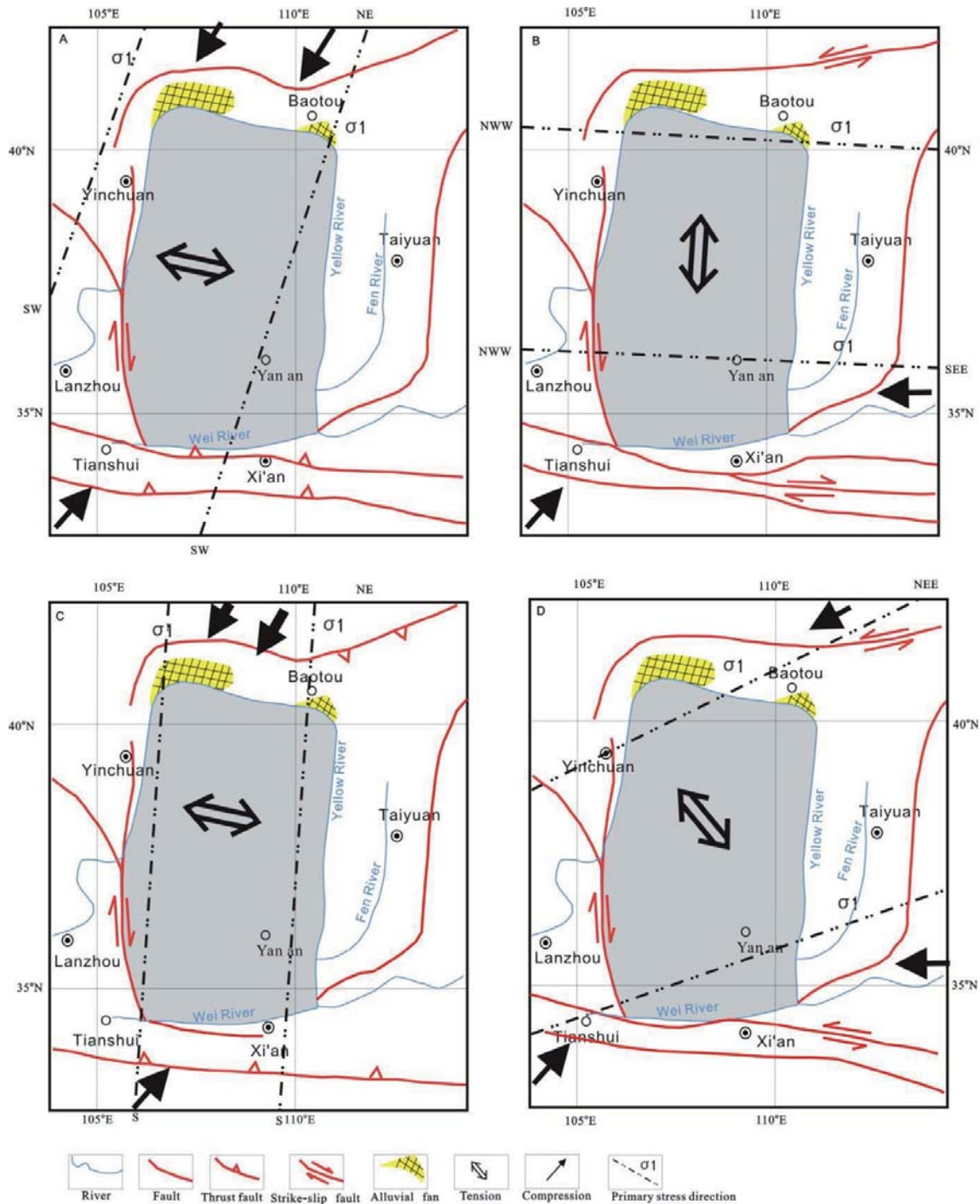
Fig. 2.7 Regional tectonic stress field in the Ordos Basin during the Neozoic Era (Zheng, 2008), (A) during the Late Cretaceous to Early Eocene, 65~45 Ma BP (before the present); (B) Middle-Late Eocene until end of Oligocene, 45~25 Ma BP; (C) Early Miocene, 25~0.78 Ma BP; and (D) Miocene (0.78 Ma BP) until the present

2.2.2 Sequence stratigraphy and sedimentary facies

Deposition of marine carbonates and mudstone in the Ordos Basin occurred during the Cambrian-Ordovician period. Very thick (ca. 4500 m) carbonates and marine clastics of Middle and Upper Ordovician turbidites can be found at the southern and northern parts of the basin (Feng et al., 1998; Wang and Al-Asam, 2002; Yang et al., 2008). Geological field mapping reveals missing strata for the period Silurian-Devonian (Ma et al., 1998; Yang et al., 2008). During the Carboniferous-Permian period, the sedimentary environment changed from offshore shallow water to fluvial-lacustrine facies, both

24

containing coal resources (Watson et al., 1987; Yin and Nie, 1996; Yang et al., 2008). During Triassic-Early Cretaceous period, the basin had formed and evolved independently by undergoing multi-cycled intracontinental depression processes with the subsequent deposition of fluvial-lacustrine facies (Zhou and Graham, 1996). By the Late Cretaceous-Paleogene, the tectonic regime of the basin had been transformed, with the occurrence of large-scale vertical uplift, followed by the formation of several Neozoic graben systems, e.g., Fen River, Wei River, Yinchuan and Hetao (Li and Lu, 2002; Yang et al., 2008).

The lithologic section in Fig. 2.2 shows that the rocks of Ordovician period are mainly composed of dolomite, argillaceous dolomite, limy dolomite, gypsum-bearing muddy dolomicrite, algalclastic and pebbles. The stratas for Silurian and Devonian are missing. During the Early Permian period, extensive delta and shallow lacustrine environments (see Fig. 2.8) were prevailing in the Ordos Basin (Fu et al., 2003). Uplift of the North China Plate during the Upper Paleozoic period caused a sudden retreat of the sea from the eastern and western parts of the Ordos Basin (Fu et al., 2003). The lower Permian strata, the Shanxi and Xiashihezi formations (see Figs. 2.2 and 2.8), occurring in the northern region of the Ordos Basin and both comprised of fluvial-lacustrine facies (sandstone interbedded with mudstone), constitute the target gas reservoirs of the Upper Paleozoic gas fields (Yang et al., 2008). In the central and southern regions of the basin, swamp and shallow lacustrine mudstones interbedded with coals are the main rock types, forming the target gas source rocks of the Paleozoic gas fields (Figs. 2.9 and 2.10). During the early stage of Shangshihezi deposition period, fluvial environment was predominant forming an interlayer of sandstone and mudstone. Uplift of North China Platform, at the inception of the Shiqianfeng period, led to the formation of an inland lake basin of the Ordos and a totally continental depositional environment, which is characterized by a combination of fluvial, delta and shallow lake (Fig. 2.11).
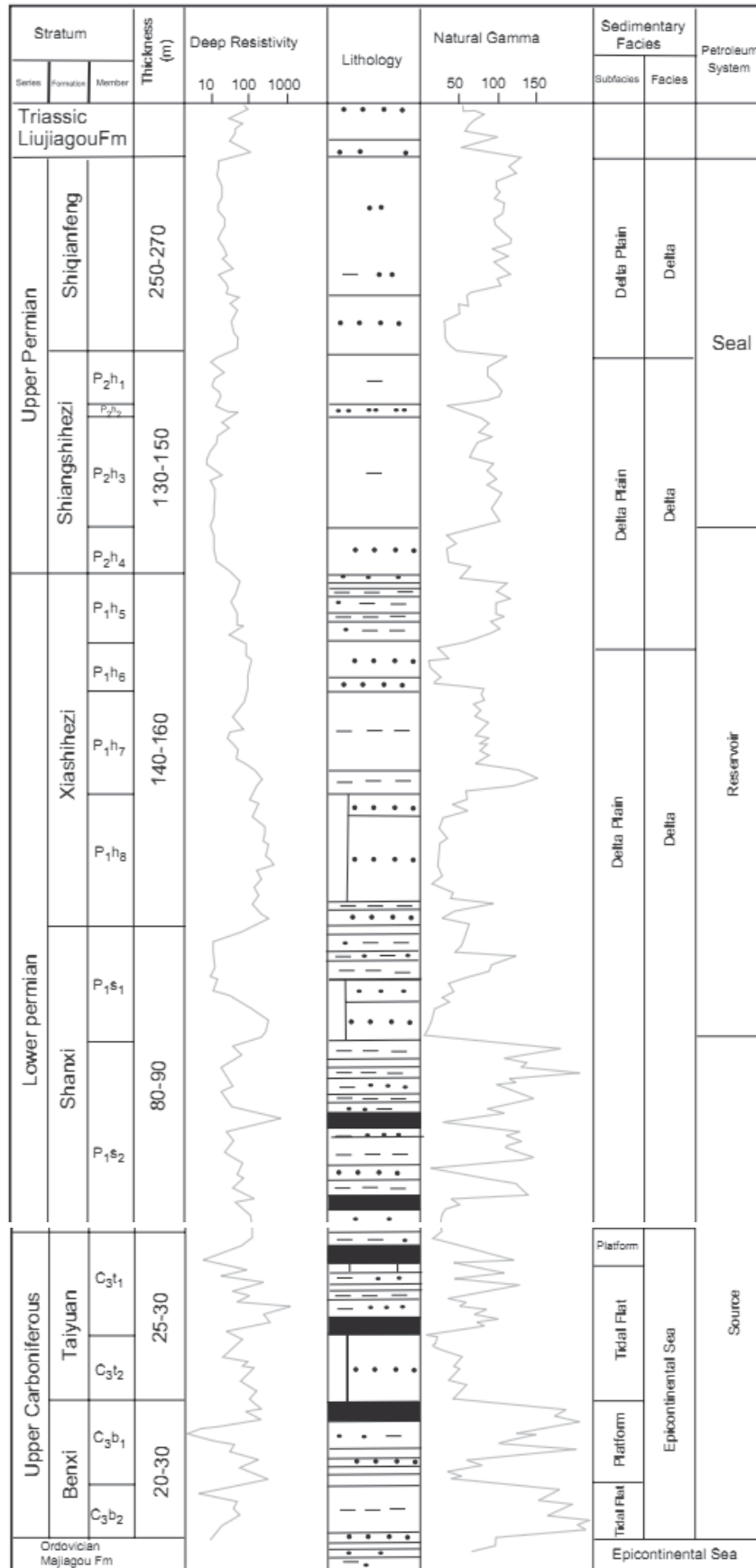
Fig. 2.8 Stratigraphy, deposition facies and typical well log response of Upper Paleozoic strata in the Ordos Basin (Yang et al., 2008)

26

Related to the target injection layers for CO$_2$ storage in Ordos Basin is the first section of the Shanxi Formation including the 8th section of the Shihezi formation, which are also the main gas reservoirs of the Sulige gas field (Wei et al., 2002; Yin et al., 2006; Yang et al., 2008), deposited mainly by meandering and braided river systems, respectively (Yang et al., 2008). The evolution of the micro-facies of the delta system can be illustrated pictorially by Figs 2.10, 2.11 and 2.12.
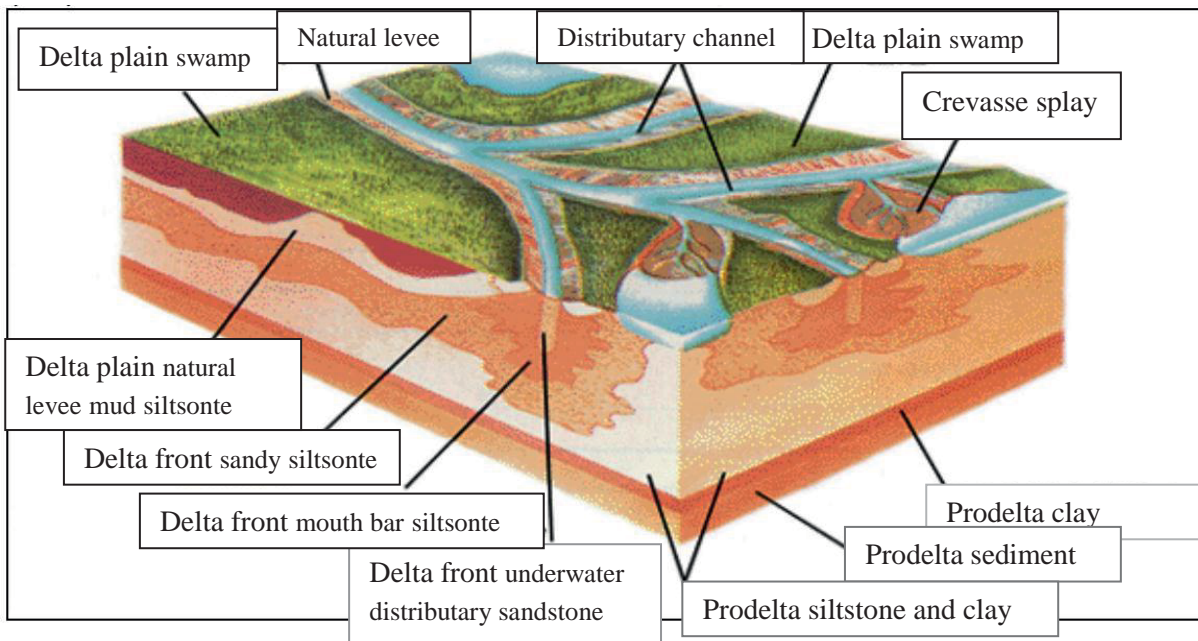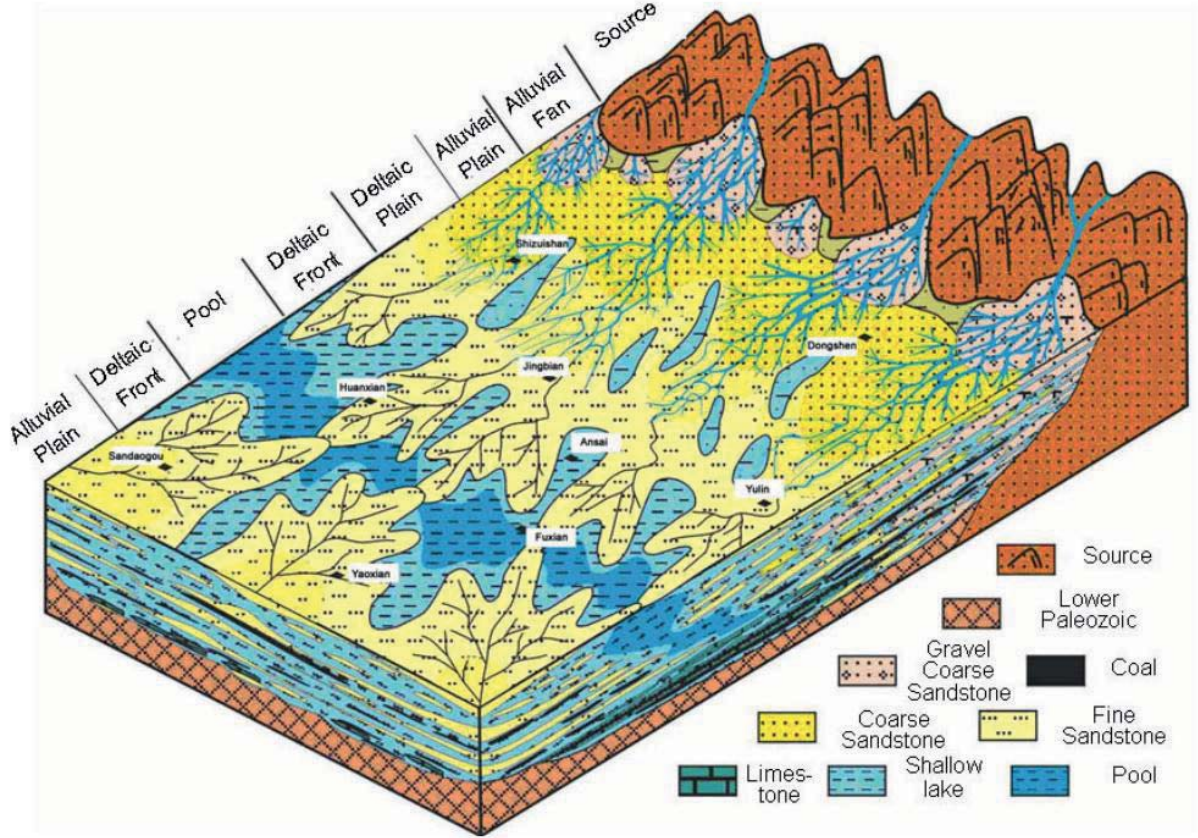
Fig. 2.9 Paleogeographic model of the delta system during the Upper Paleozoic period in the Ordos Basin (modified after Yang et al., 2009)

27
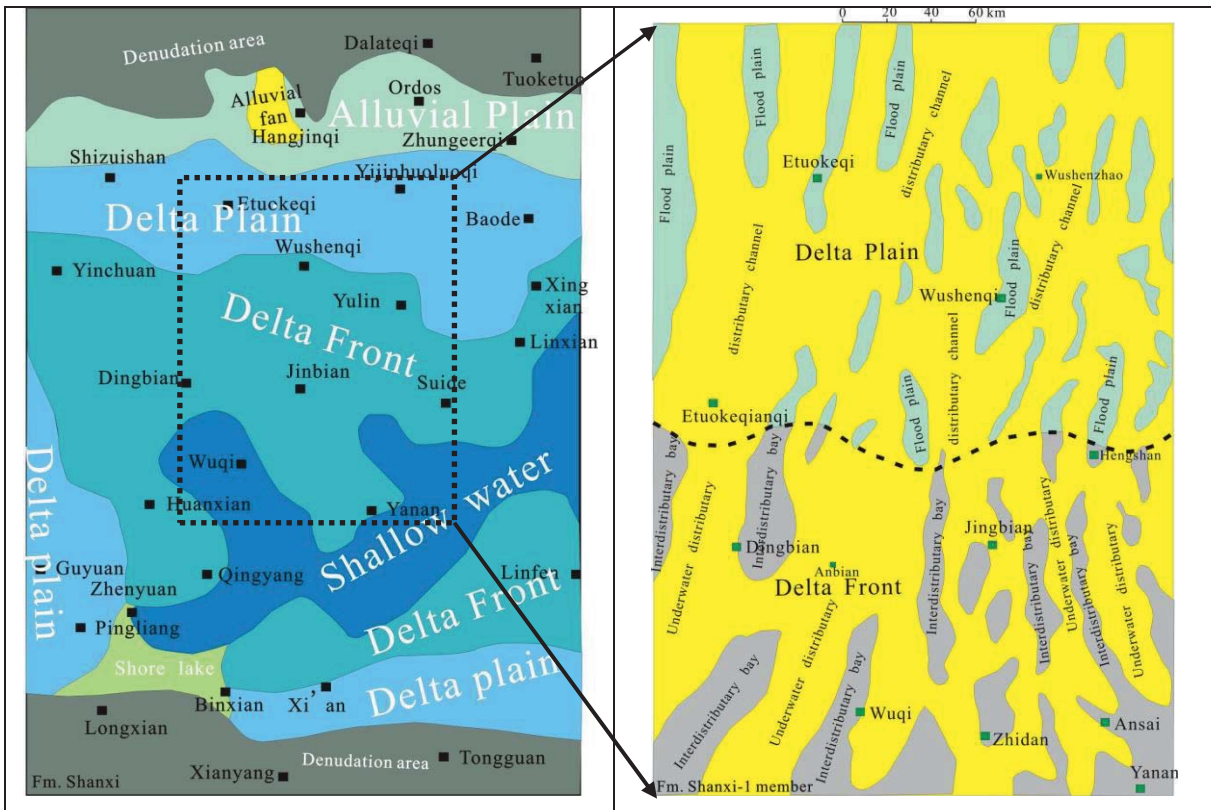
Fig. 2.10 The lithofacies paleogeographic map of the first section of Shanxi formation (modified after Zhang et al., 2009)
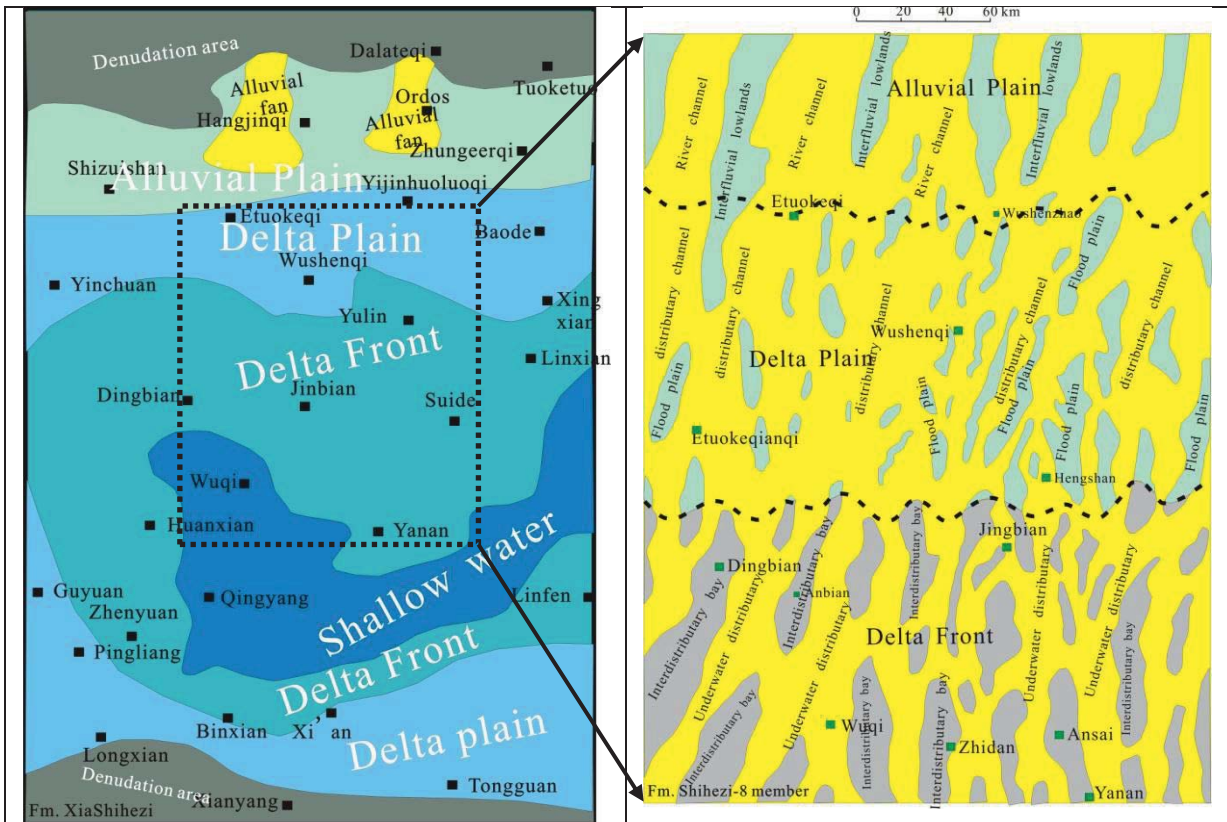
Fig. 2.11 The lithofacies paleogeographic map of the 8th section of Shihezi formation (modified after Fu et al., 2003)

28
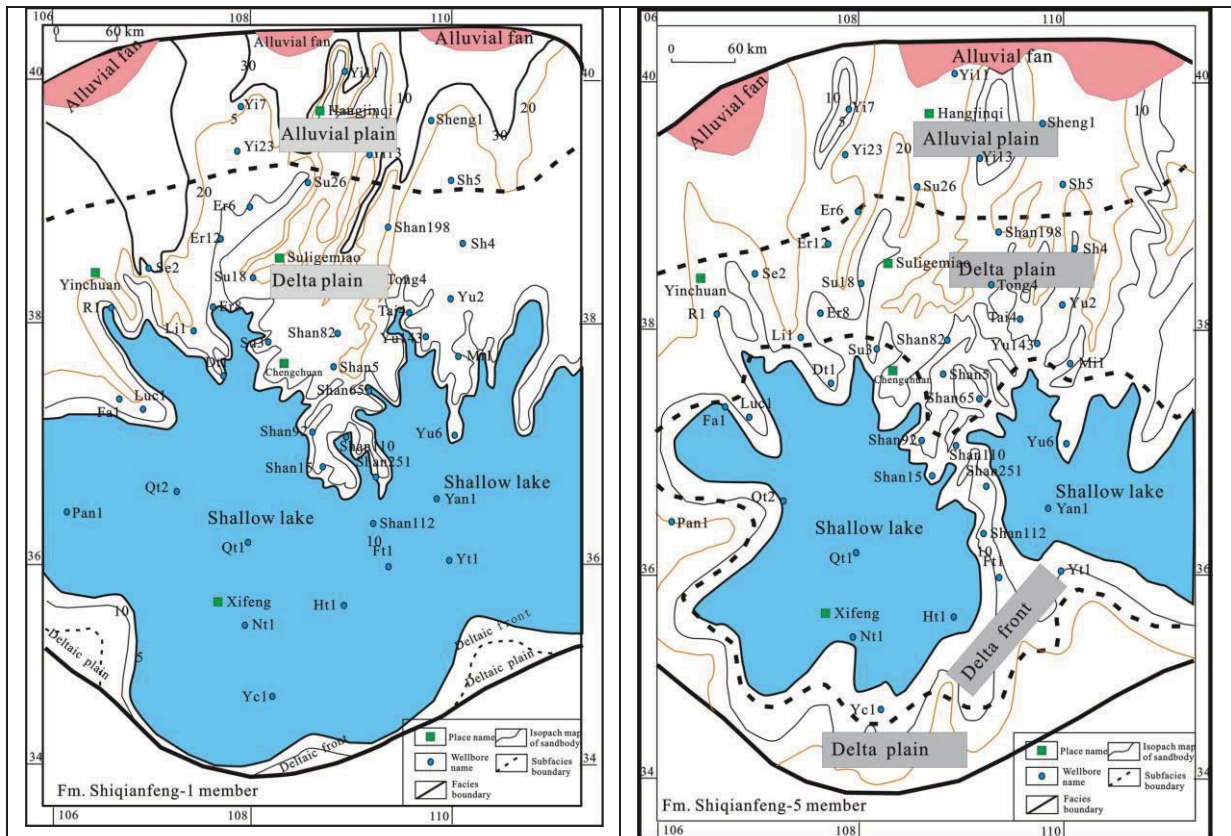
Fig. 2.12 The lithofacies paleogeographic map of Shiqianfeng formation (modified after Fu et al., 2003; Zhang et al., 2009)

2.2.3 Hydrogeological characteristics of the Ordos Basin

The Ordos Basin is composed of overlapping aquifer systems (Wang et al., 2005). The hydrostratigraphic units, from bottom to top, include the pre-Cambrian metamorphic rocks, Lower Paleozoic carbonate rocks, Upper Paleozoic to Mesozoic clastic rocks and Cenozoic deposits. It is a half open basin with different groundwater types circulating at different depths. Karstic and pore-fracture water circulation in the Cambrian-Ordovician and Cretaceous clastic rocks, respectively, is the thickest aquifer system (ca. 1200-1800 m) in the basin. The pore and pore-fracture water systems of the Cenozoic soil deposits and Carboniferous-Jurassic clastic rock formations, respectively, have a relatively smaller circulation distance (< 300 m).

Groundwater in the Ordos Basin can be divided into two systems: the shallow open and the deep closed groundwater systems. The boundary between these two systems is also considered as the boundary between fresh and saline water in the basin. This boundary, however, is not static and can be shifted by changes in climate evolution, tectonic activity, topography changes and human activity (e.g. water production). The shallow groundwater system includes a strong run-off and a weak half-open runoff belt, which often has some relationship with meteoric water. The deep closed groundwater system mainly consists of a slow viscous flow region.

According to Wang et al., 2005, the groundwater system, from basin boundary to the center, can be divided into 3 fields: 1) the karstic water zone along the basin boundary, 2) the clastic-fracture water field in the central-eastern loess region of the basin, and 3) the Cretaceous artesian basin groundwater field in the central western region of the basin (Fig. 2.13).
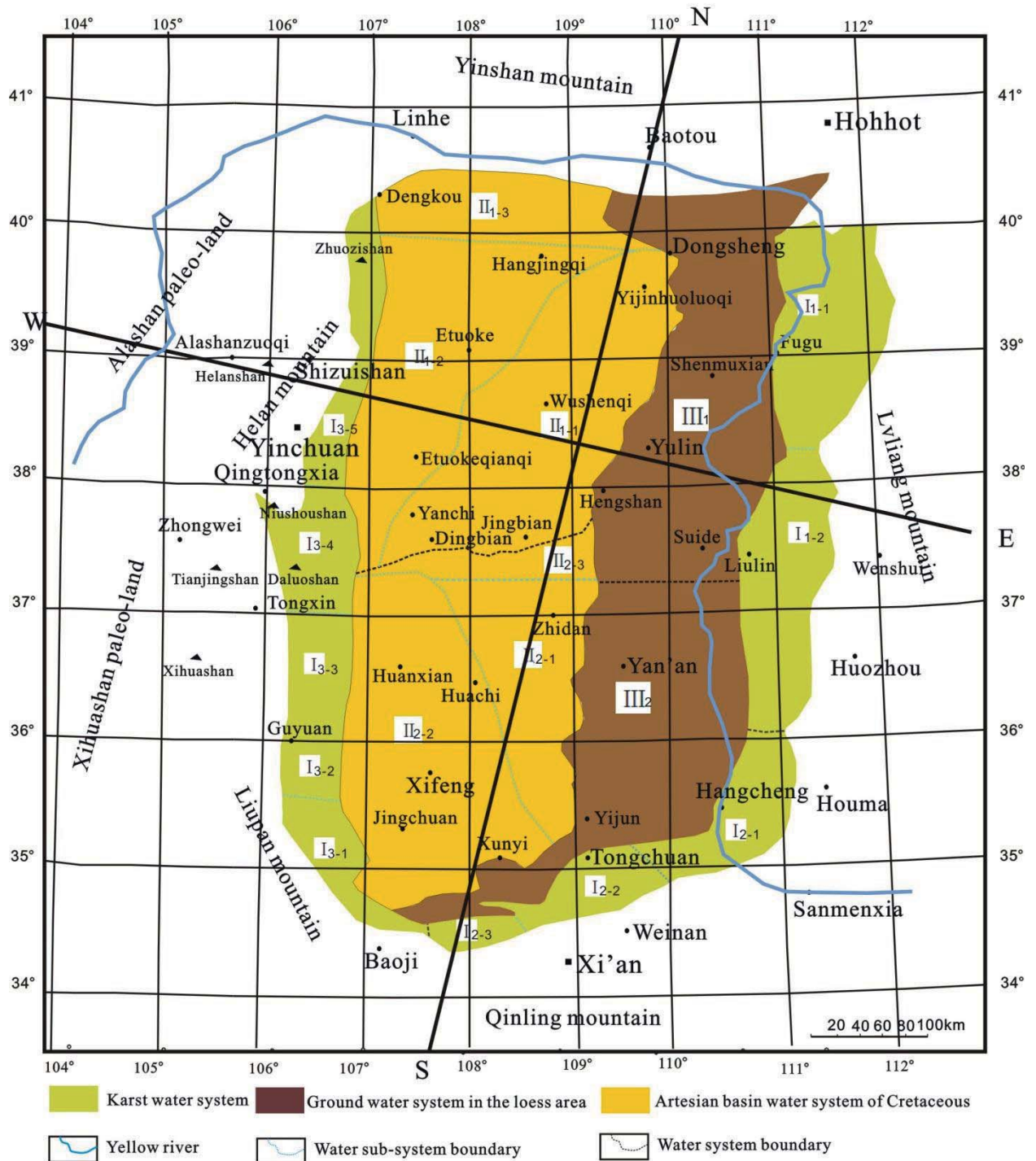
Fig. 2.13 Zonal distribution of the hydrogeological system in the Ordos Basin (modified from Wang et al., 2005)

In the plane view of the water head distribution map (Fig. 2.14A), it can be observed that the main directions of groundwater flow in the basin are the east- west, and the north- south. Its flow rate is in the range of about 0.0005-0.1 cm/year. Groundwater flows faster, to a maximum value of about 0.1 cm/year, in the northern and eastern regions of the basin, and slowest (almost to a state of detention) in the central part of the basin (Zhu et al., 2003). Logging results of water conductivity in the Upper Paleozoic formation illustrate an increasing trend towards the northern and eastern directions (Fig. 2.14C). The formation water pressure coefficient reflects the relationship between leak -off of natural gas and recharge of groundwater in this part of the basin (Fig. 2.14D). However, low pressure regions may have formed in some parts of the basin due to the leak-off of natural gas into the shallow formations.

30
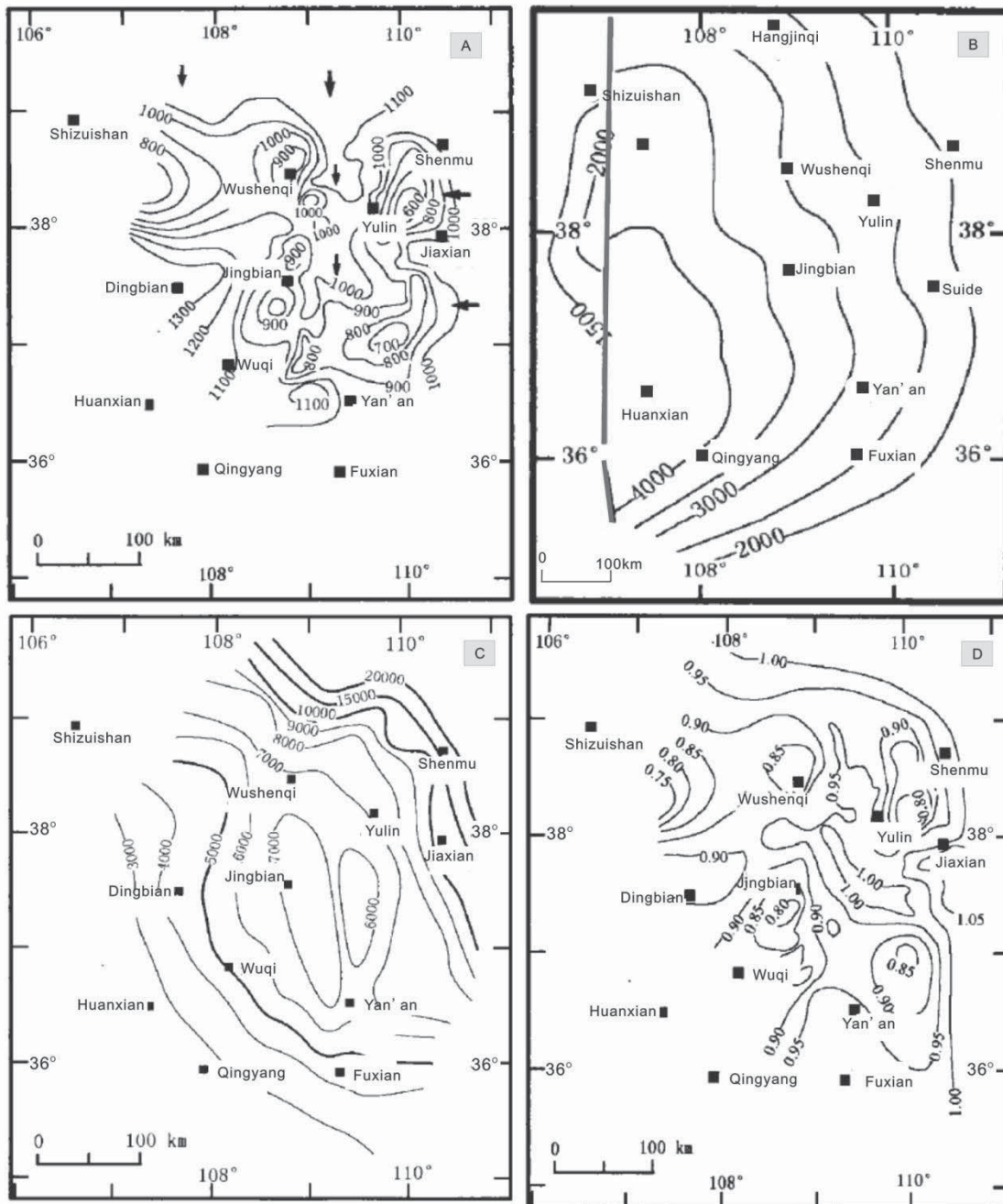
Fig. 2.14 Present planer distribution of hydrogeological structures in the Ordos Basin (A) groundwater heads (m); (B) top view of contour surface of Taiyuan formation; (C) water conductivity (m^2/s); and (D) fluid pressure coefficient (modified after Zhu et al., 2003)

Fig. 2.15 shows two superimposed vertical cross-sections in the basin through the aquifer systems along two profiles (the N-S and W-E, see Fig 2.13 for locations). The sections show groundwater systems, with their respective flow character and directions, including the aquifer, circulation, hydrodynamic, and aqueous chemical systems.

31
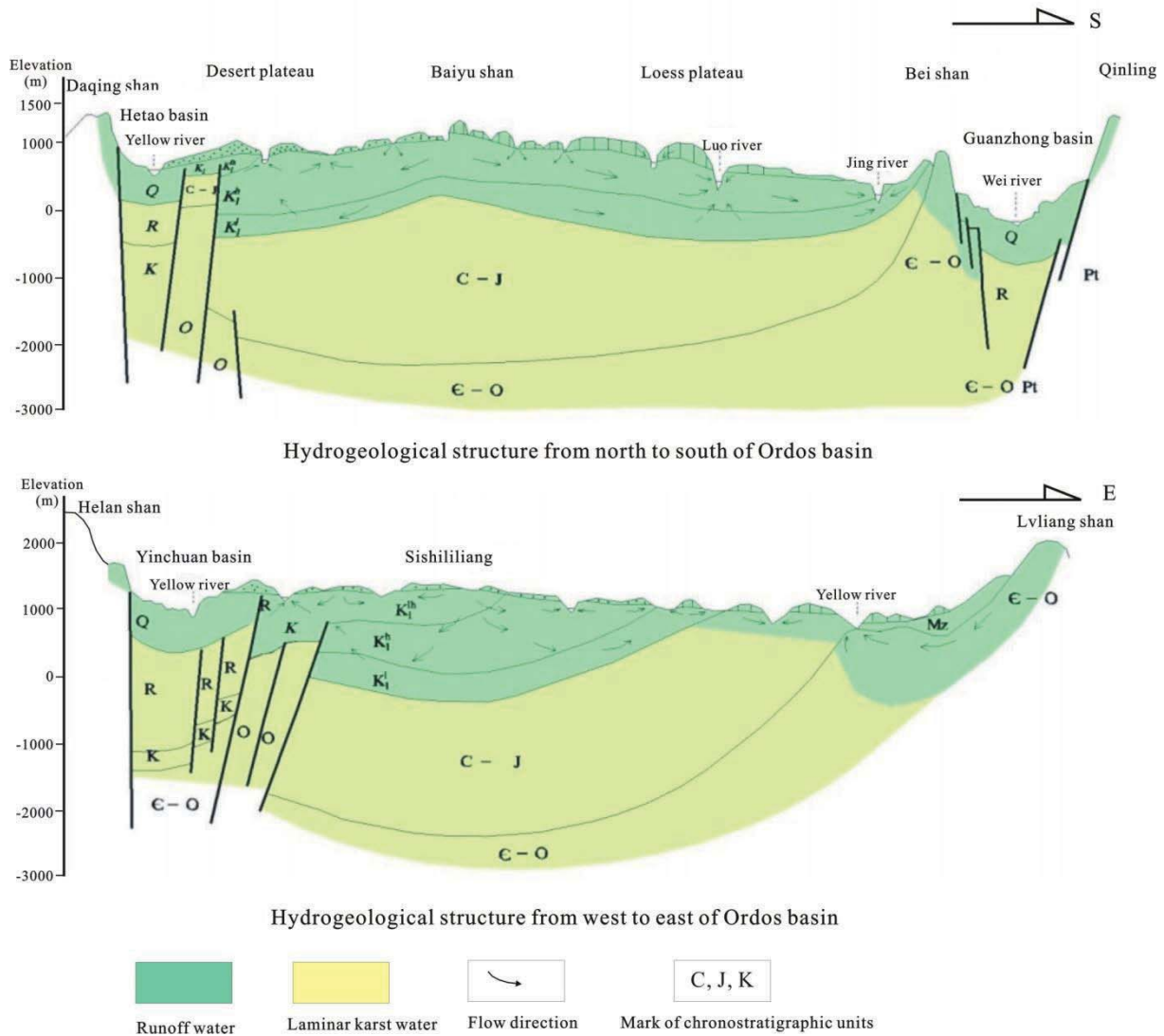
Fig. 2.15 Hydrogeological structures of the Ordos Basin (modified after Wang et al., 2005)

The Ordos Basin belongs to the scope of a cold basin, with a low geothermal flux (ca. 40-50 mW/m^2, Fig. 2.16A) and a low temperature gradient, Fig. 2.16B (Wang et al., 1990; Wang, 2001). Hot water reservoirs are mainly concentrated in the Zhidan Group of Cretaceous formations, the Yan'an formation of Jurassic, the Yanchang formation of the Triassic and Upper Permian (Chen et al., 1994).

The Cretaceous sandstone reservoir is deeply buried in the western part of the basin, and lies at a shallower depth in the eastern region of the basin (Chen et al., 1994). Temperature ranges mainly between 20 °C and 55 °C, and porosity is usually in the range of 16%-18%. The warm aquifer water is of good quality, with its salinity ranging from 0.5-3 g/L, and a maximum value of 5 g/L in some regions. In the middle part of the basin, artesian flow may occur at a rate of 100-3000 m^3/d, producing warm water with 25-30 °C.

The potential geothermal reservoirs in the Permian, Triassic and Jurassic formations are mainly well distributed in the eastern region of the basin at depths ranging from 500-1000 m. The salinity of the warm waters in the shallow reservoirs is often in the range between 1.5-3.0 g/L, with the tendency to increase with depth. For example, the salinity can attain 20-30 g/L when the buried depth is in the range of 1500-2000 m.
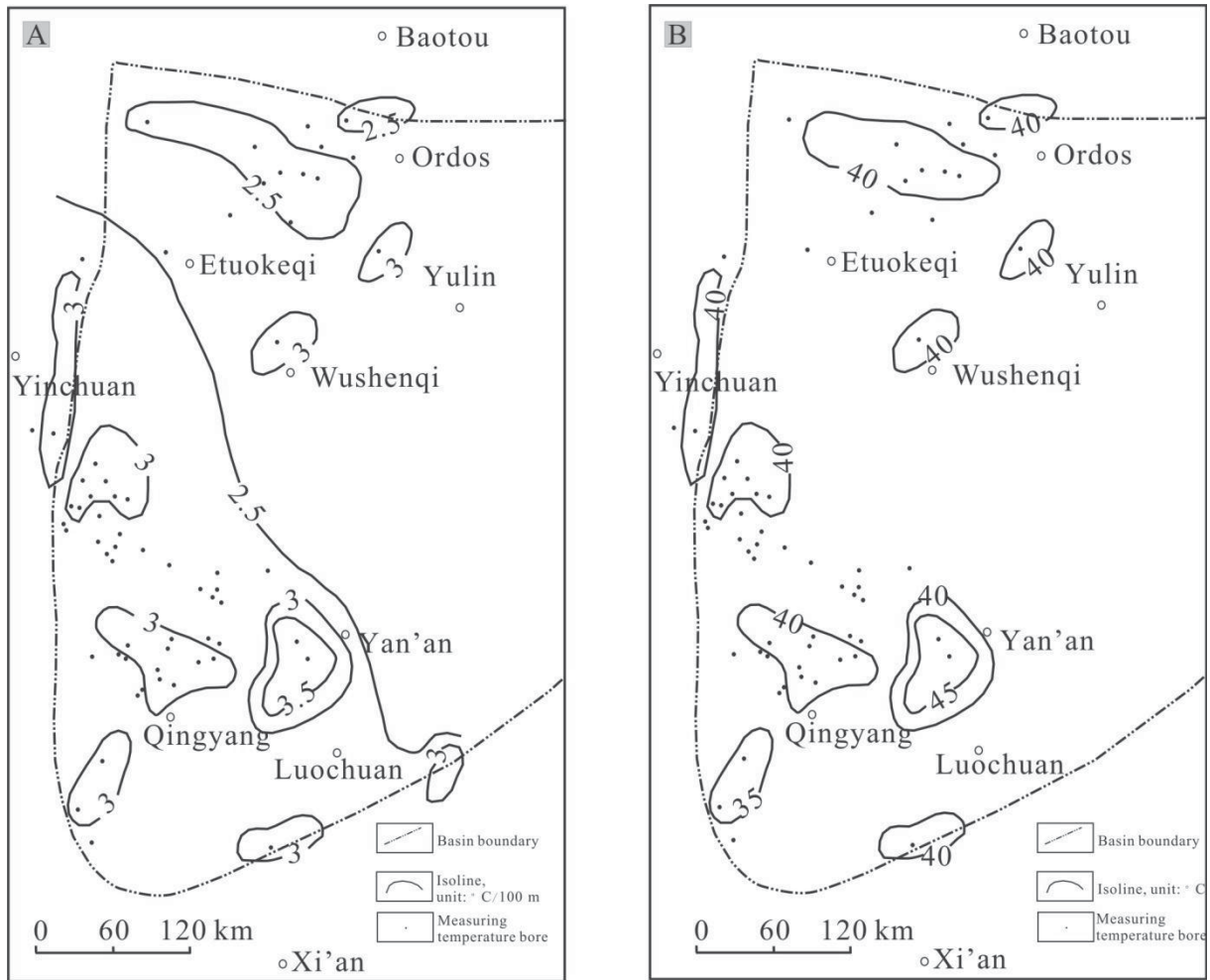
Fig. 2.16 Distribution of geothermal flux (A) and temperature (B) in a reservoir at 1000 m depth in the Ordos Basin (modified after Wang et al., 2005)

2.2.4 Characteristics of the Upper Paleozoic reservoir formations

It is necessary that the demonstration CCS project in the Ordos Basin acquires a thorough understanding of the geological features of the related strata, especially the Upper Paleozoic, for CO$_2$ storage. Nevertheless, prior knowledge of the characteristic features of the Upper Paleozoic reservoir formations in the northeastern part of the basin could be acquired from the oil and gas exploration and exploitation experience in that region. Data from the adjacent gas/oil fields is very helpful to supplement the meager geological information currently established at the CCS pilot site.

2.2.4.1 Porosity and permeability

Table 2.3 shows that each of the 4 target formations at the CCS pilot site has different effective reservoir properties (Li et al., 2013). These formations, belonging to the Upper Paleozoic, can be considered as tight sandstone reservoirs with low porosity (2-10.27%) and permeability (0.1-1.36 mD). Microscopic studies show that these sandstone reservoirs are now at their late diagenetic stage, with decreased primary pores (Table 2.3 and Table 2.4).

33

Table 2.3 Material parameters for the CO$_2$ storage saline formations (Li et al., 2013)

Properties	Fm. Liujiagou	Fm. Shiqianfeng	Fm. Shihezi	Fm. Shanxi
Total reservoir thickness (m)	10-15	60-80	50-60	10-20
Effective reservoir thickness (m) ϕ>4% for sandstone, ϕ>2% for dolomite	10-15	55-75	45-55	5-10
Maximum thickness of Single-layer sand body (m)	10-15	15-30	15-35	3-5
Average porosity (%)	4.5-7	6-8	6-9	2-3
Average permeability (mD)	0.1-0.3	0.2-0.5	0.5-0.6	0.3-0.5

Table 2.4 Analytical reservoir properties in the northeastern part of the Ordos Basin (Qin et al., 2005)

Layer	Average porosity/%	Average permeability/mD	Total number of samples
3 member of Fm. Shihezi	10.27	1.36	95
2 member of Fm. Shihezi	8.66	0.73	310
1 member of Fm. Shihezi	9.09	0.55	1604
2 member of Fm. Shanxi	7.94	0.58	1327
1 member of Fm. Shihezi	7.62	0.66	1080

Interpretation of data from well logs show good correlations of the effective porosity and mud content with permeability (Fig. 2.17). This graphics further illustrates the positive and negative exponential relationship respectively between porosity versus permeability and mud content versus permeability.
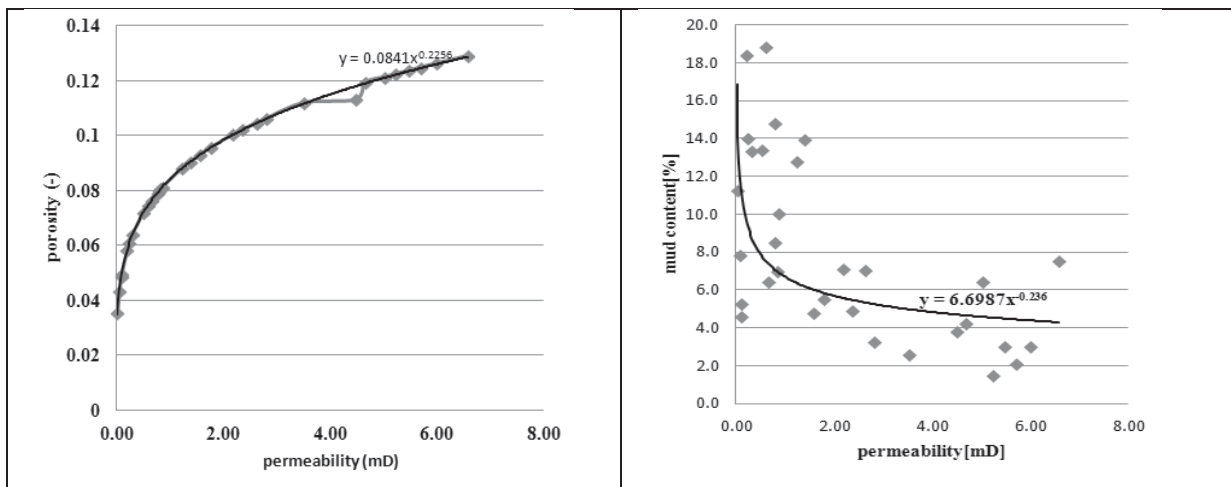
Fig. 2.17 Relationships of effective porosity (a) and shale content (b) permeability

Reservoir properties are mainly controlled by the structure of the pores, which are also affected by many factors including sedimentary microfacies, diagenesis (i.e. compression, cementation and dissolution) and so on. Measurement of porosity, permeability and water saturation for different sedimentary microfacies of 8th member of Shihezi formation in Ordos Basin (Yuan et al., 2009) demonstrates that channel sandbar has the best porosity and permeability, followed by distributary channel, while swampy and interfluvial lowlands have the worst values (Fig. 2.18).
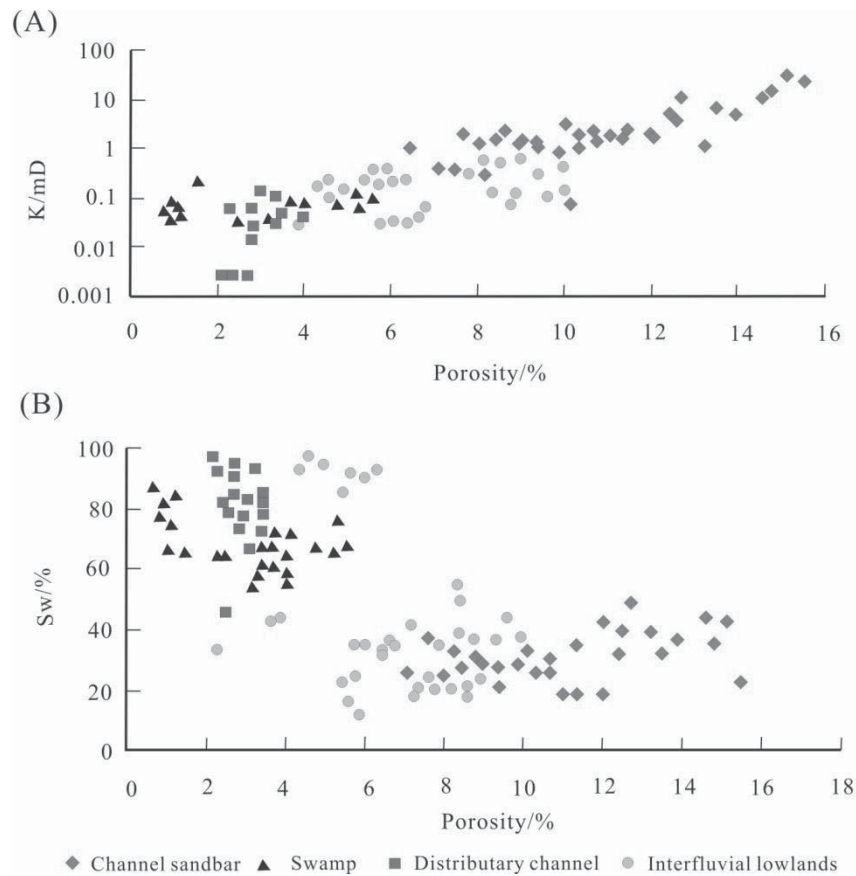
Fig. 2.18 Correlation between microfacies and reservoir properties (A) porosity-permeabiltiy and (B) porosity-water saturation (modified after Yuan et al., 2009)

2.2.4.2 Pore structure

Though characterized by low porosity and low permeability (Table 2.5) the Upper Paleozoic reservoirs contain three types of pores structures, i.e. the primary pores, secondary pores and micro fractures, Fig. 2.19 (Hu et al., 2001; Liu et al., 2001; Yang et al., 2001; Dong et al., 2006).

Table 2.5 Magnitude of micro-pores in various blocks of the Ordos Basin (Yang et al., 2001)

Layer	Sulige	Wushenqi	Mizhi	Yulin-Hengshan	Jinbian	Ansai
9th member of Fm. Shihezi (%)	28.2	74.4	93.9	91.7	57.7	92.9
8th member of Fm. Shihezi (%)	71	73.3	96.3	67.6	54.5	82.2
7th member of Fm. Shihezi (%)	79.5	87	89.1	81.7	72.7	74.7
6th member of Fm. Shihezi (%)	83.5	-	96.2	-	79.2	64.2
2nd member of Fm. Shanxi (%)	92.7	87.1	93.8	40.6	90.4	74.9
1st member of Fm. Shanxi (%)	94.1	72.2	100	21.7	47.1	84.4
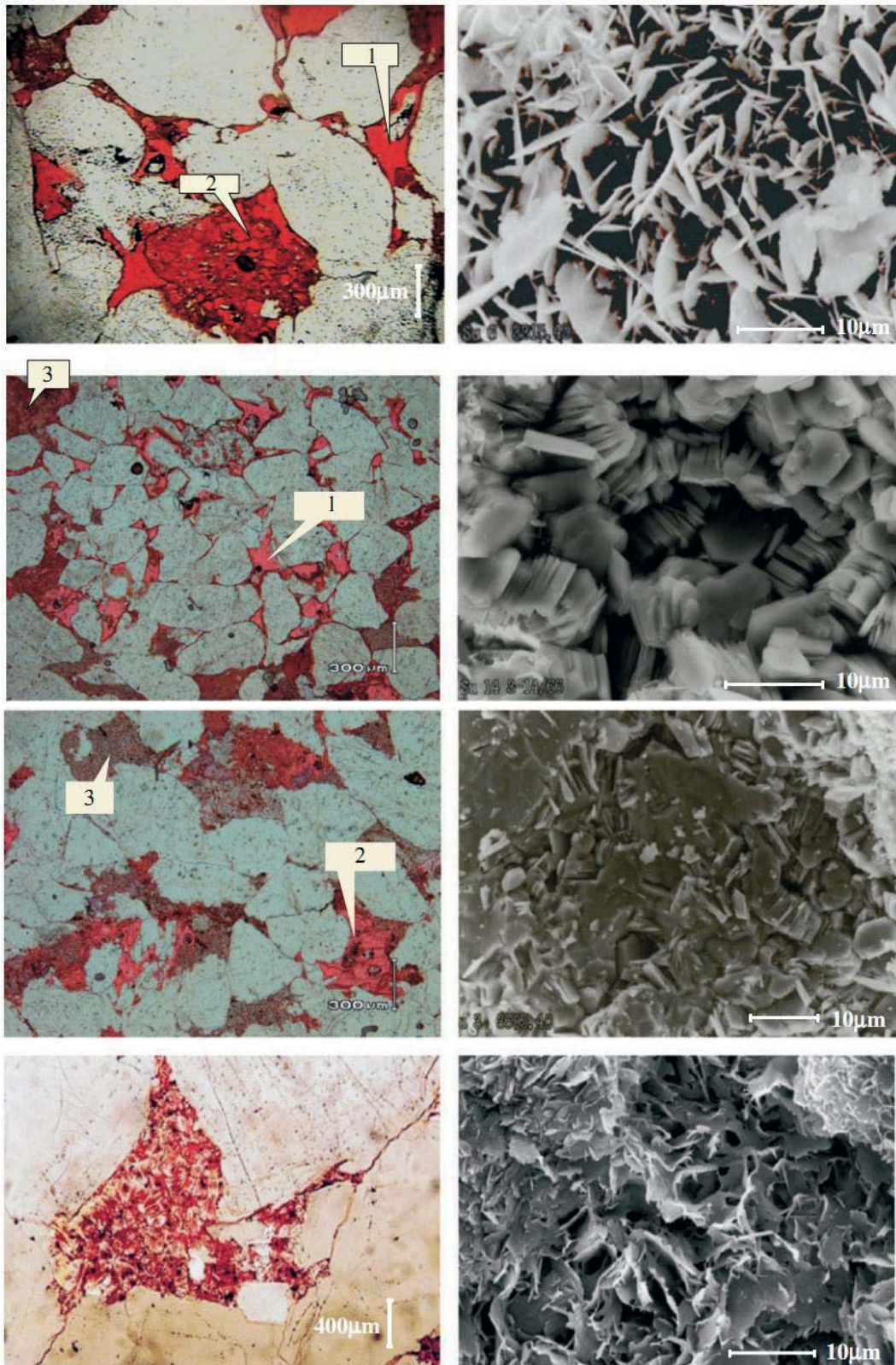
Fig. 2.19 Thin sections and scanning electron microphotographs of pore structure types in Ordos sandstone samples; i.e. (1) intergranular pore; (2) grain dissolution pore; and (3) kaolinite intercrystalline pore, right part of the Figure is an enlarged view of the left part at some pore space (after Yang et al., 2008)

(1) Primary pores

Primary pores comprise inter-grain pores, micro pores between clay grains, clay shrinkage pores and intergranular pores in rock debris.

Inter-grain pores: Their areal porosity is in the range between 0 ~ 2.5%, with an average of less than 1%. Meanwhile, their individual apertures are on the average very small, within the range of 50 ~ 150 μm, the largest measuring about 300 μm. Due to the increasing underground compression and cementation with burial depth, there is only a small percentage of inter-grain pores in the reservoir rock.

Micro-pores: They exist between clay grains, with an aperture of less than 1 μm. Micro-pores are predominant in tight reservoir rocks of the Upper Paleozoic in the basin. Optical microscopy reveals that about 50% ~ 70% of the pores available in the reservoir are micro-pores (Table 2.4), with their proportion rising to more than 90% in some parts of the basin.

Shrinkage pores: The apertures for shrinkage pores widely vary from 10 to 300 μm, and their areal porosity ranges between 2% ~ 4%. There is a high content of clay in the Upper Paleozoic sandstone formations in the Ordos Basin. Shrinkage pores in sandstones is usually caused by compaction during burial.

Inter-granular pores: Their individual apertures measure about 20 ~ 30 μm, with an areal porosity of less than 0.5%. Intergranular pores develop mainly in siltstone, metamorphic sandstone and schists (see lable 1 in Fig. 2.19). The morphology of intergranular pores is irregular, and can be enlarged during diagenesis.

(2) Secondary pores

The structure and type of secondary pores, also called vugular pore spaces, varies with rock types, e.g. feldspar, carbonate mineral, rock clastic and clay matrix; feldspar mold hole, intercrystalline pores of kaolinite, etc.

Vugular pore space in feldspar and mold hole: Under the favorable underground conditions of temperature and pressure feldspar minerals can easily be dissolved in formation brines, allowing the development of vugular pores and mold holes in the whole rock (see label 2 in Fig. 2.19). This pore space is irregular and characterized by poor sorting and connectivity.

Vugular pore space in carbonate minerals: Calcite and dolomite can be dissolved along the cleavage direction or along grain boundary, with varying morphologies of the pore spaces. The average aperture size is about 10 ~ 20 μm, with an areal porosity of less than 0.5%.

Vugular pore space in rock clastics: It is caused by the dissolution of unstable volcanic rocks. A large amount of clay minerals and quartz will exist in the pores, with the aperture size in the range of about 500 ~ 3000 μm and an areal porosity of 1% ~ 2%.

Intercrystalline pores of kaolinite: Given rise to high porosity in the reservoir rock, with an average aperture size of about 5 ~ 20 μm. This type of pores will particularly occur in kaolinite clay minerals that precipitate in the inter-grain pores of the primary rock grains (see type 3 in Fig. 2.19).

Vugular pore space in the rock matrix: The aperture of the vugular pore space in the rock matrix is in the range of 5 ~ 200 μm, with an areal porosity of between 1% ~ 3%. There is plenty of volcanic ash in the Upper Paleozoic sandstone reservoir in the Ordos Basin. Vugular pores in the matrix form by leaching of acid fluids from the volcanic ash.

(3) Micro fractures

Micro fractures are important pathways connecting the inter- and intra-grain pores in the low permeable sandstone reservoirs and thus, helping to enhance the production of oil and gas. According to their mechanism of formation, micro fractures may be divided into two groups (Zeng et al., 2008): 1)

structural fractures (e.g. tensile fracture, shear fracture) and 2) diagenetic fractures (e.g. grain-edge fractures, intragranular fractures, and planes between bedding layers). The aperture of grain-edge and intragranular fractures is about 10 μm. The permeability of the tight sandstone reservoir is significantly improved by the existence of micro fractures, ranging between 1.7 ~ 43.4 mD, when the aperture of the fractures attains a maximum value of 40 ~ 90 μm. This is the most encountered type of fracture observed in the thin sections (about 45% of the section) of the tight sandstone reservoirs from the Shenmu-Yulin area (Wang et al., 2004).

By using the mercury pore entry experiments, the following characteristics have been established for the sandstone reservoir rocks of the Upper Paleozoic in the Ordos Basin (Yang et al., 2001; Yuan et al., 2009; Yang et al., 2009; Liu et al., 2014b):

- Small apertures with very fine pore throats and a very low areal porosity. The aperture is in the range of 0.5 ~ 400 μm and the thinnest part of the average throat radius is only 0.0628 ~ 0.2485 μm for most sandstone samples. The aperture for the largest pore throat is about 2.5 ~ 7.5 μm and areal porosity is less than 4%;

- High displacement pressure. The displacement pressure for a good reservoir is usually less than 0.1 MPa, while the displacement pressure for the tight sandstone reservoir in Ordos Basin is between 0.75 ~ 5 MPa.

2.2.4.3 Mineral composition

The primary mineral composition of the Upper Paleozoic sandstones in the Ordos Basin include clastic grains of quartz, rock debris, feldspar and kaolinite, occupying about 85-95% of the whole rock minerals. The secondary minerals in the target sandstone formation mainly comprise siderite, kaolinite, overgrowth quartz, calcite, and little amount of chlorite, illite and hydro-mica. Both mineral and rock structural compositions are strongly dispersed and vary from sample to sample due to the formation characteristic heterogeneity (Figs. 2.20 and 2.21).
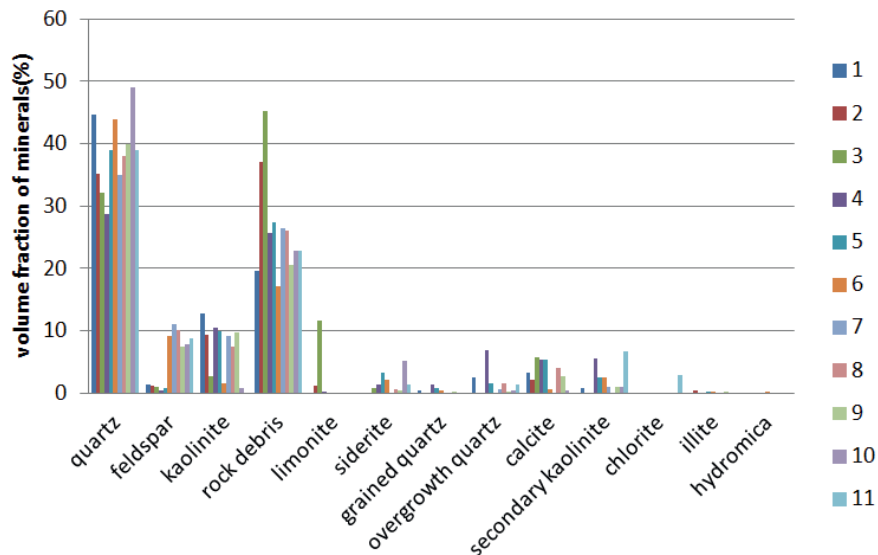
Fig. 2.20 Mineral compositions for 11 sandstone samples from the Upper Paleozoic formations in the Ordos Basin
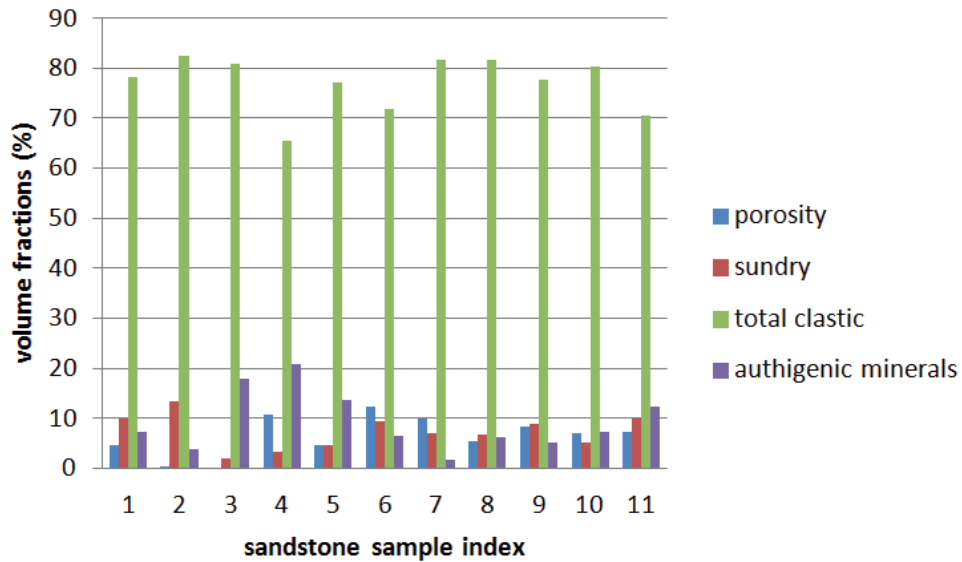
Fig. 2.21 Rock structural composition for 11 sandstone samples from the Upper Paleozoic formations in Ordos Basin

The clay minerals in the reservoir are mainly composed of kaolinite, illite and chlorite. The total content of clay minerals in the reservoir decreases with depth. Each type of clay mineral imparts varied properties to the reservoir rock. The content of chlorite reduces with depth, while that of illite increases with depth. The relative content of clay minerals is illustrated in Table 2.6.

Table 2.6 Relative content of clay minerals in 5 sandstone samples (Qin et al., 2005)

Layer	Absolute content	Relative content/%			
		illite	kaolinite	chlorite	Illite/smectite interbedded layer
P_{2sh}^3	5.85	17.00	17.00	54.50	11.50
P_{2sh}^2	5.85	17.00	17.00	54.50	11.50
P_{2sh}^1	5.37	28.89	27.11	37.00	7.00
P_{1s}^2	4.22	41.57	40.00	15.57	2.86
P_{1s}^1	4.69	69.19	24.81	0.81	5.29

2.2.4.4 Mechanical parameters

Based on the experimental results of the mechanical properties of the reservoir rock by Qin et al., 2005 and Tang et al., 2010 (see Table 2.7), the following has been established: (1) the values of Young's module and Possion's ratio are higher for mudstone than sandstone; (2) Young's module of the reservoir is intermediate, which is beneficial in hydraulic fracturing for extension of fractures; (3) variation of the mechanical properties of mudstone and sandstone in the reservoir is marginal.

Table 2.7 The experimental results of rock mechanical parameters (Qin et al., 2005 and Tang et al., 2010)

Layer	Number of samples	Lithology	Young's module/GPa	Possion's ratio
P_{2sh}^3	3	sandstone	23	0.16
	1	mudstone	26	0.23
P_{2sh}^2	2	sandstone	27	0.16
	1	mudstone	24	0.21
P_{2sh}^1	6	sandstone	20	0.22
	2	mudstone	20	0.24
P_{1s}^2	4	sandstone	32	0.21
	3	mudstone	25.6	0.24
P_{1s}^1	8	sandstone	23	0.23
	2	mudstone	25	0.28

2.2.5 Characteristics of mudstone

The characteristics of the cap rock including mudstone, tight limestone or dolomite, rock salt, silty mudstone etc., plays a vital role in the integrity and safety of geological CO$_2$ sequestration. The properties of cap rock can be different due to the variation in depositional environment. Mudstone, developed in Upper Paleozoic period, is the main caprock in the Ordos Basin. Its color is determined by the responsible sedimentary environments of deposition. It appears grey to dark grey in the Shanxi formation, grey green to purple red in Lower Shihezi formation, and predominantly purple red in the Upper Shihezi formation.

There are two main types of Upper Paleozoic mudstone in the Ordos Basin (Zheng et al., 1999). One that is associated with coal seams and the other that is associated with fluvial sandstones. The former is swamp mudstone, and is usually composed of black or grey mudstone, carbonaceous mudstone, silty mudstone, and coal seams, with plenty of plant fossil (Fig. 2.22). It mineralogical composition mainly consists of kaolinite (40%-80%), a relatively low amount of mixed-layer minerals of illite and smectite (25%-49%), and some little chlorite (0-12%). The latter is mainly composed of smectite, kaolinite (27%-35%) and mixed-layer clay minerals of illite and smectite (37%-42%).

Table 2.8 Mineral composition of swamp mudstone in the Upper Paleozoic strata (%) (Zheng et al., 1999)

Sample no	Rock name	mix-layer of illite and smectite	Kaolinite	Chlorite
1	Black mudstone	49	6	12
2	Black mudstone	43	24	0
3	Black mudstone	25	60	0
4	Dark grey mudstone	25	40	8
5	Grey mudstone	5	80	0
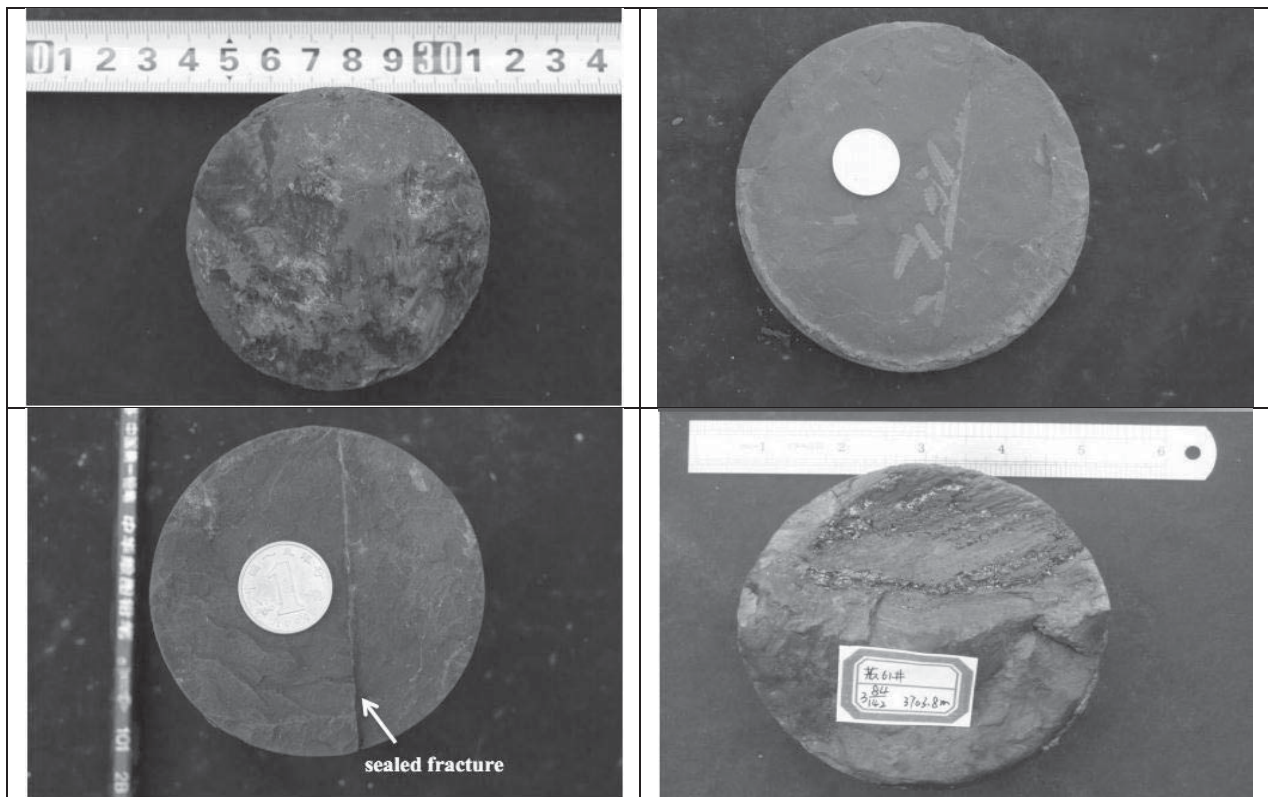
Fig. 2.22 Characteristics of swamp mudstone in the Fm. Shanxi in Ordos Basin (A) dark mudstone with carbonized plant; (B) shale with carbonized plant; (C) mudstone with sealed fracture; (D) shale with coal seam (from Zheng et al., 1999)

40

Table 2.9 Mineral composition of flood plain mudstone in the Upper Paleozoic strata (%) (Zheng et al., 1999)

Sample no	Rock name	mix-layer of illite and smectite	kaolinite
1	Grey mudstone	40	26
2	Black mudstone	42	35
3	Black mudstone	60	27
4	Dark grey mudstone	37	52

3. Theoretical background of CO_2 sequestration in porous media

Underground geological formations are made of rock grains (transported and motionless), organic matter and fluids (water, oil, gas). Subsurface porous medium (e.g. open fractures and cavities) are always filled with fluids. Injected CO_2 can displace the in situ fluids in the pore space and fractures of a permeable formation. Furthermore, part of the injected CO_2 may dissolve in the fluids with time, which in the long-term increases the water-rock interaction (Dawson et al., 2013).

At this stage, introducing the basic and theoretical concepts of CO_2 geological sequestration would make a worthwhile contribution toward understanding the coupling THMC processes that take place as a result of CO_2 sequestration into the deep saline formations. In this chapter, the CO_2 sequestration mechanism and capacity in saline formations will be reviewed and summarized. Besides, the basic characteristics of porous media, for example, compaction and compressibility will be described. CO_2 sequestration problems involve multi-phase and multi-component fluid flow in porous media. Therefore, the characteristics of flow systems at different scales have also been considered in this chapter. Equally important is the introduction of Darcy's law in its original and extensional forms. The relative permeability and capillary pressure are also included in the chapter for their important role in influencing the multi-phase fluid flow process.

The problem concept of CO_2 geological sequestration can be classified into a number of fields, all focusing on the study of fluid transport, either as a single phase fluid (gas or liquid), or as a two phase fluid (gas and liquid): (1) hydraulic field (H) for fluid flow in porous or fractured media, (2) temperature field (T), whereby temperature is distributed in solid grains and fluid by convection and conduction, (3) stress field (M) that consideres the mechanical deformation and damage of the rock skeleton, (4) chemical field (C), (5) microbial field (B), (6) geomagnetic field (G), etc. However, only a few fields should be considered to study a specific project. For example, fluid-mechanical coupling problem (HM) that is composed of rock deformation and seepage (Rutqvist et al., 2008; Hou et al., 2012a)**;** the heat-mechanics coupling problem (TM) that consists of rock deformation and heat conduction; and the heat-hydraulic-mechanical coupling problem (THM) that involves deformation, seepage, and heat transport processes in the reservoir and caprocks (Chen et al., 2009; Watanabe et al., 2009; Tong et al., 2010).

Mathematical constitutive relationships are fundamental for the transformation of physical-chemical problems into solutions of mathematical equations (Bear and Bachmat, 1990; Tong et al., 2010). Generally, there are four main categories constitutive laws relevant with CO_2 sequestration problems (Stephansson et al., 2004): (1) the constitutive law of rock mechanics, under which the action of fluid flow, heat transport and chemical reaction, deformation and yield criterion of porous/fracture media will be studied (Zhao et al., 2008); (2) the constitutive law of hydraulic mechanics, by which the infiltration characteristics of fluids (single gas/liquid phase or multi-phases) including synthetic effect of stress, chemical reaction and heat transport are considered; (3) the constitutive law of heat transport, which studies the characteristics of heat conduction, convection and thermal dilation under the influence of stress, chemical reaction and fluid seepage (Yin et al., 2012); (4) the constitutive law of mass transfer theory, which studies the dissolution of the solid rock skeleton and mass transfer rules under the influence of temperature, concentration, convection and fluid diffusion. Theoretically, the coupling terms must be added into the basic physical equation when coupling problems are studied. The coupling HM problem, for example, requires three main coupling physical equations: i.e. (1) the equation of permeability coefficient changes induced by the deformation of the solid skeleton caused by changes in the stress field ($\sigma \rightarrow k$) (Gou et al., 2014); (2) the effect of fluid flow on the deformation of porous rock skeleton ($k \rightarrow \sigma$); and (3) the effective stress equation (σ'_M).

A typical example of coupled THMC processes is shown in Fig. 3.1, with a complete cycle of thermal/stress loading paths in a chemically active fractured rock (Taron et al., 2009). During the

loading/unloading processes, reversible (elastic) and irreversible (e.g. pressure solution) changes occur in the rock fracture aperture. After the unloading process, an irreversible aperture reduction and its corresponding irreversible stress loss is observed.
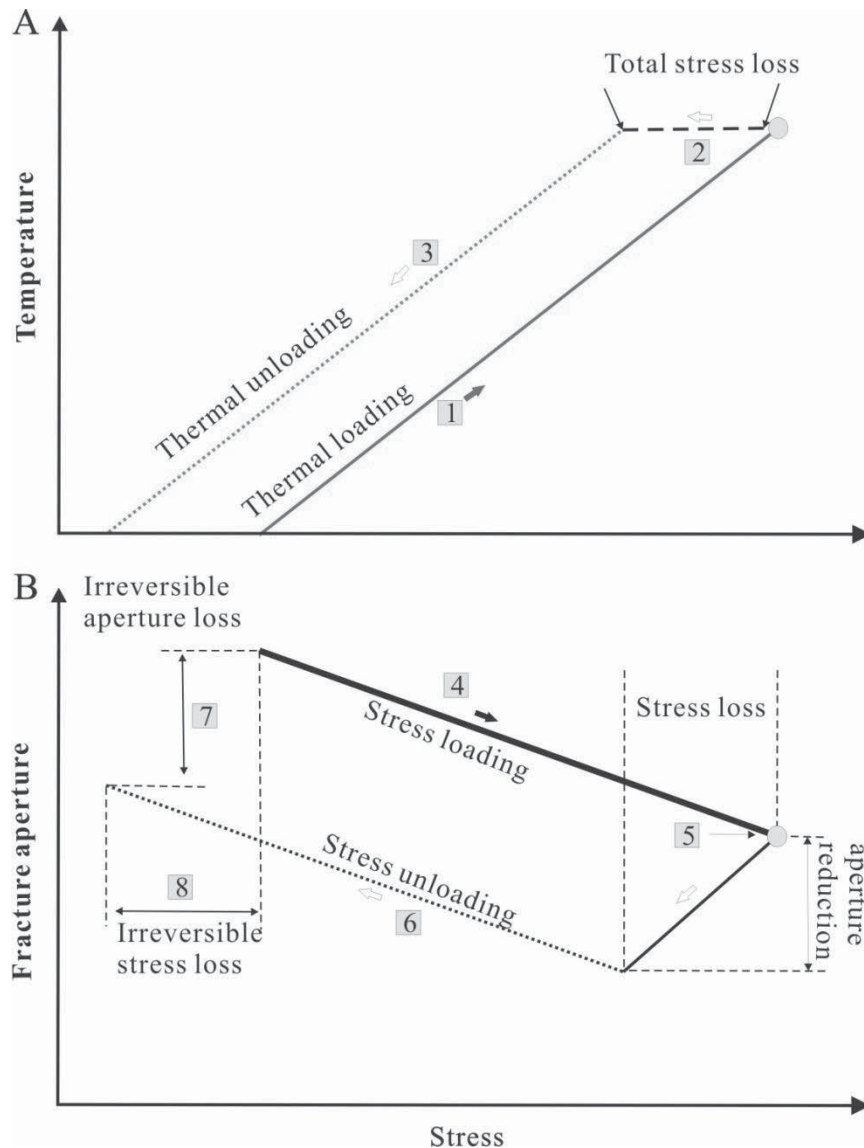
Fig. 3.1 Stress loading paths in a thermally loaded (A) and chemically active fractured (B) rock. (A) changes in temperature with stress during thermal loading and unloading processes, (1) stress buildup with increasing temperature; (2) irreversible strains accumulation in fracture due to reduced stress; (3) Thermal unloading path; (B) fracture aperture changes with stress during loading and unloading process (4) loading path during which linear fracture aperature decrease with increasing stress; (5) maximum stress loading value attained, at which chemical strain will cause a drop in stress; (6) unloading path, during which linear fracture aperture increases with decreasing stress; (7) irreversible aperture reduction; (8) irreversible stress loss (after Taron et al., 2009)

3.1 Feasibility of CO_2 sequestration

3.1.1 Mechanisms of CO_2 sequestration

CO_2 trapping mechanisms can be broadly grouped into two categories: physical and chemical trapping mechanisms. Physical trapping mechanisms are predominant during and shortly after the CO_2

injection, while chemical trapping may obly become important in the long-term after hundreds to thousands of years.

During the injection process, CO$_2$ is first trapped through primary mechanisms (i.e. static and hydrodynamic trapping) directly below the tight layer sealing the target storage reservoir (Fig. 3.2). The target layer could be either a depleted oil and gas reservoir or a deep saline aquifer (Bachu, 2008). In the long run, a series of secondary trapping mechanisms are triggered off to enhance the CO$_2$ storage capacity of the reservoir, hence decreasing the potential risk of leakage or migration. In other words, a combination of primary and secondary trapping mechanisms will increase the storage security for CO$_2$ due to the very long retention time for CO$_2$ solubility and mineral trapping mechanisms.

Many physical and chemical processes take place in the storage formation (Nooner et al., 2007; Benson and Cole, 2008), influencing the CO$_2$ plume movement and its immobilization (Table 3.1). Examples of such processes include (IPCC, 2005, 2007): 1) Fluid flow (migration) in response to pressure gradients caused by the injection of CO$_2$ or natural hydraulic gradients; 2) buoyancy and gravity flow caused by the density differences between CO$_2$ and the formation water; 3) molecular diffusion; 4) dispersion and fingering induced by formation heterogeneities and mobility difference between CO$_2$ and other fluids; 5) dissolution into the formation fluid; 6) adsorption of CO$_2$ on organic matter; 7) pore space (relative permeability) trapping; and 8) mineralization.

Several factors do influence the efficiency of CO$_2$ sequestration, including reservoir heterogeneity, the thermodynamic properties of the in situ fluids, and the injection strategy, see Table 3.1.
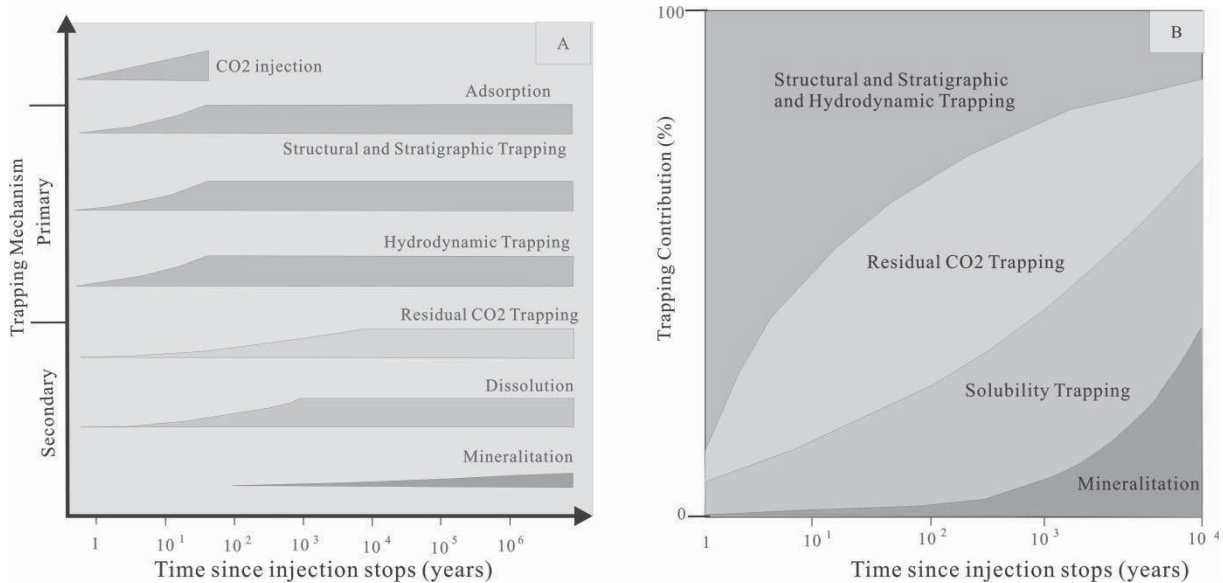
Fig. 3.2 Differences between various CO$_2$ trapping mechanisms in geological media (a) operating timeframe, and (b) contribution to storage security (after Bachu, 2008)

44

Table 3.1 CO_2 sequestration mechanisms and the corresponding influencing factors

CO_2 transport and sequestration mechanisms	Main factors affecting CO_2 transport and sequestration

Physical trapping:
• Structural trapping
  - Anticline
  - Fault
• Stratigraphic trapping
• Hydrodynamic trapping
  - Buoyancy and gravity
  - Natural hydraulic gradients
  - Molecular diffusion
  -Dispersion
• Residual gas trapping
	Reservoir heterogeneity (physical factors):
	
	-average permeability, ratio of vertical to horizontal permeability (K_v/K_h)
	- aquifer dip angle
	- lateral continuity of the reservoir
	- residual gas saturation(S_{gr})
	- temperature
	- pore space size and connectivity
	- pore pressure
	- mineral composition

Chemical trapping: • Solubility trapping • Mineralization trapping	*Formation water properties:* -pH, density, viscosity, salinity and composition of the brine
Other: • Adsorption (physical or chemical)	*Injection strategy:* -injection rate, total amount, time and temperature; injection target (single layer or multi-layer); bottomhole pressure (BHP); wellhead pressure

Physical trapping mechanisms:

Occur when CO_2 is immobilized as a free gas or supercritical fluid, as determined by the available storage volume. There are two kinds of physical trapping methods:

(1) **Static trapping of mobile CO_2** occurs in stratigraphic and structural traps, or in man-made caverns. The flow of CO_2 beyond the top reservoir boundary is impeded by a physical low-permeable barrier layer. If a pathway is found, CO_2 will flow along the pathway driven by its own buoyancy and gravity (Fig. 3.3);

Horizontal formation	Dipping formation
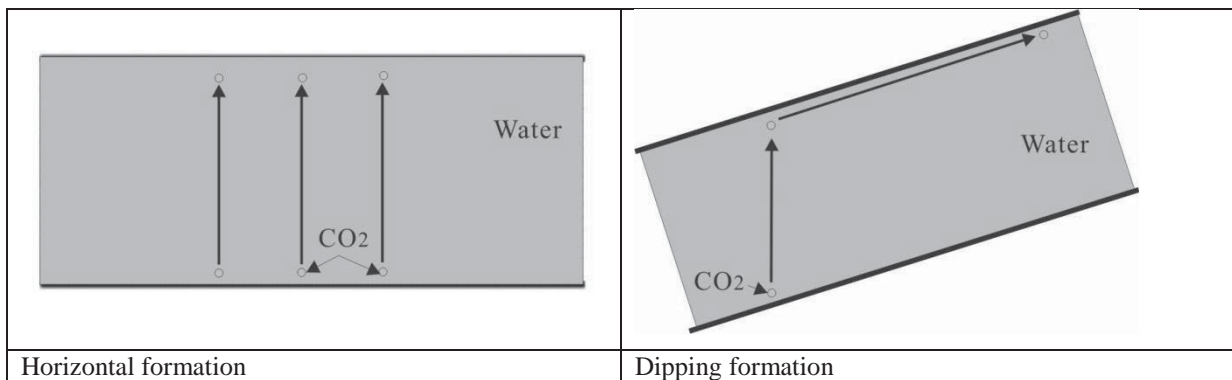
Fig. 3.3 CO_2 flow under the effect of buoyancy and gravity

(2) **residual-gas trapping in the pore space**- As CO_2 migrates through the porous medium some will be trapped in the pore space by capillary forces (Obdam et al., 2003; Kumar et al., 2005). When the migration pressure for CO_2 (P_d) is smaller than the capillary pressure difference (ΔP_c), CO_2 will be trapped in the pores as the residual gas (Fig. 3.4), i.e. $P_d < \Delta P_c = 2\sigma(\frac{1}{r_t} - \frac{1}{r_p})$, where σ, r_t, r_p are the capillary surface tension, radius of the pore throat and pore space, respectively.

Residual gas trapping is strongly formation-specific and the residual CO_2 saturations may be as high as 15–25% for many typical storage formations (Holtz, 2002).
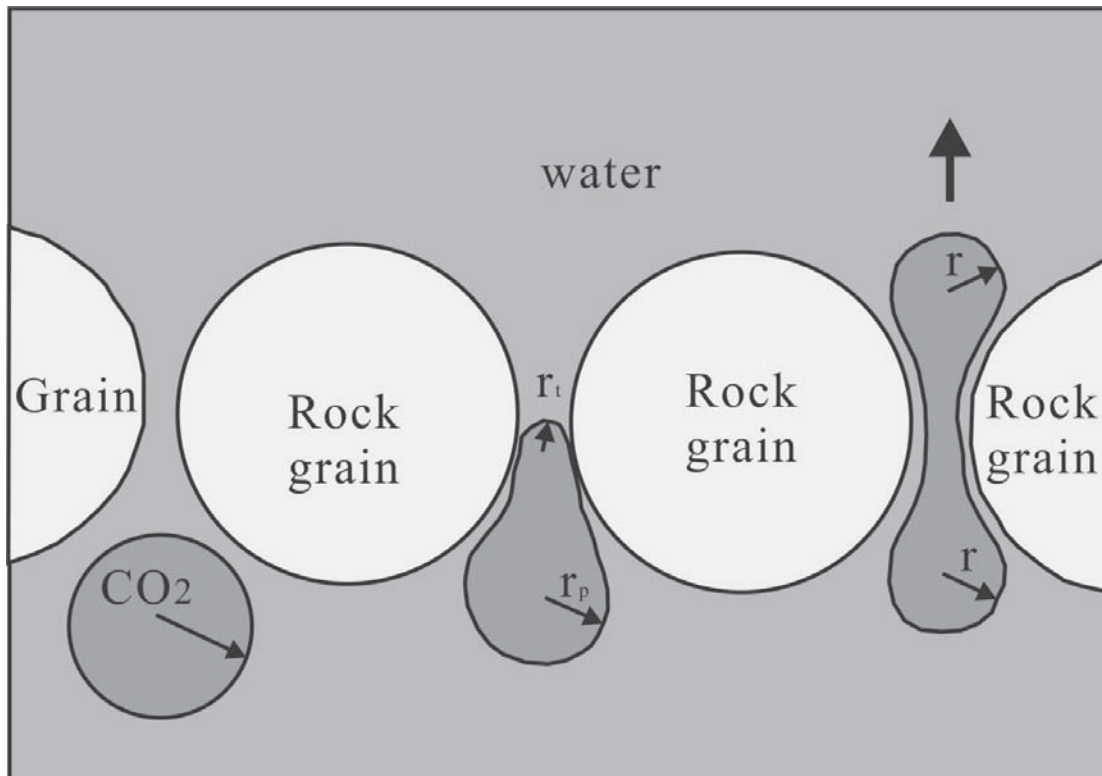
Fig. 3.4 Illustration of capillary forces responsible for the migration of CO_2 across throat to pore space (modified after IEA, 2011)

(3) **Hydrodynamic trapping in porous media-**this considers the seepage of fluid in the storage formation including molecular diffusion, hydrodynamic dispersion and advection (De Silva and Ranjith, 2012). CO_2 and water will flow at their own respective rates, but the flow of one phase will be restricted by the existence of the other (Pentland et al., 2008). This phenomenon can be described by the concepts of relative permeability and capillary pressure.

In the aquifer, groundwater flows in the direction from high to low relative piezometric levels (Fig. 3.5). The flow path of the injected CO_2 is affected by the dynamic water pressure state, which in turn may change the flow path of water.
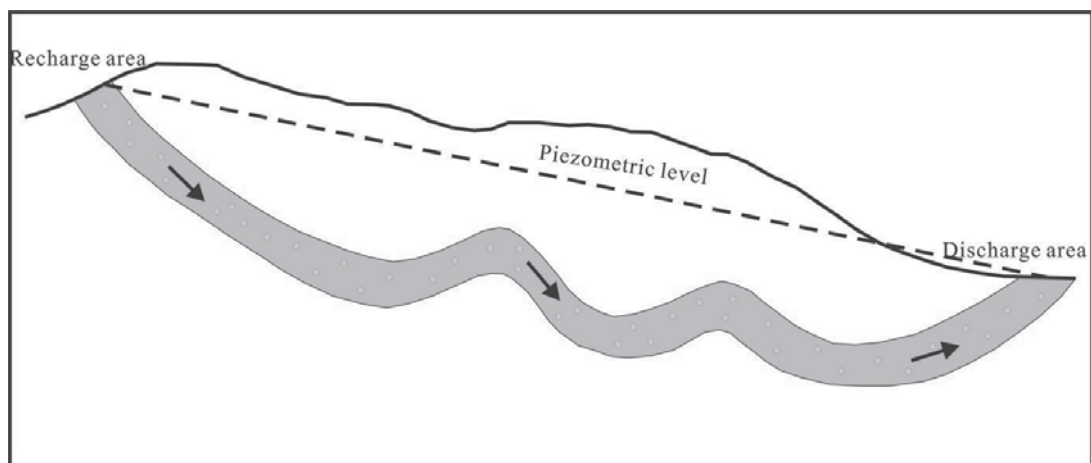
Fig. 3.5 Dynamic water pressure state and aquifer fluid flow path (modified after Zhang et al., 2011)

Fluid advection and flow direction will be affected by the buoyancy and gravity caused by the difference in density of CO_2 and the formation brine. The injected CO_2 will migrate vertically and horizontally. On one hand, buoyancy forces will promote the CO_2 to move towards the upper part of the reservoir, until stopped by the non-permeable and low-permeable mudstone or shale confining layers. On the other hand, downward movement of CO_2, though not evenly distributed, can occur due to gravity (IPCC, 2005; Solomon, 2006). The shape of the CO_2 plume rising through the rock matrix is greatly affected by formation heterogeneities (Flett et al., 2005), such as the presence of relative low permeable siltstone and shale lenses. These may act as barriers to fluid flow and cause lateral migration of CO_2, blocking by any stratigraphic or structural trap it encounters. Therefore the presence of low-permeable layers within the storage formation can slowdown the upward migration of CO_2, causing CO_2 to bypass the lower regions of the storage formation (Doughty et al., 2001).

The density differences occur when some CO_2 dissolves in the saline formation, forcing the heavier CO_2 bearing brine to migrate downwards. In addition, a horizontal dispersion of CO_2 can also take place due to the layering structure of the reservoir, the diffusion, lateral pressure differences and capillary pressure effects (IPCC, 2005).

The rate of buoyant forces driving vertical flow of CO_2 is determined by the type of fluid in the formation (Solomon, 2006). In saline formations, the relative larger density contrast (30–50%) between CO_2 and formation water occurs. In oil reservoirs, the density difference and buoyancy forces are not that large, particularly when the oil and CO_2 are miscible (Kovscek, 2002; IPCC, 2005, 2007). In natural gas reservoirs, however, downward migration of CO_2 takes place because CO_2 is much denser (Oldenburg et al., 2001).

Chemical trapping mechanisms:

(4) **Solubility trapping** (intra-aqueous species reactions): CO_2 can react with water to form carbonic acid (H_2CO_3), which exists for tens to hundreds of years (Ennis-King and Paterson, 2003; IPCC, 2005; Keith et al., 2005). This depends on many factors, such as pressure, temperature, sweep efficiency, heterogeneity etc.

(5) **Mineral trapping** (mineral dissolution and precipitation): Fluid-rock (minerals and organic matter) interaction will be enhanced if CO_2 dissolves in the subsurface fluid, causing the dissolution of some unstable minerals, e.g., feldspar and some carbonate minerals. Meanwhile, new carbonates minerals that trap the injected CO_2 will form, including calcite, siderite, dawsonite and so on. Mineral trapping mechanism may be effective for over thousands to millions of years (IPCC, 2005).

3.1.2 CO_2 sequestration capacity in saline formation

If water is produced during CO_2 injection or the aquifer is connected to an open source (i.e. an open saline formation reservoir), the storage capacity of of the aquifer can be calculated using the following equation (Xie and Economides, 2009):

$$C_{saline} = \rho_{CO2}(1 - S_{wi})\phi + S_{wi}\phi C_s, \tag{3.1}$$

where C_{saline} is the specific storage capacity of the saline formations (kg/m^3); ρ_{CO2} is the density of CO_2 at reservoir temperature and pressure conditions (kg/m^3); S_{wi} is connate water saturation (-); ϕ is the porosity of the reservoir (-); C_s is the mass of CO_2 dissolved per unit volume of water (kg), which can be neglected since it takes hundreds to tens of thousands years for CO_2 to dissolve in formation water.

In a closed saline formation reservoir, the storage capacity or the injectivity of CO_2 solely depends on the compressibility of the rock and water (about 6×10^{-6} psi^{-1}). The injectivity index of the reservoir will remain constant if the near-well zone is not damaged. Under the same injection pressure conditions, the injection rate will decrease with time, depending on the size of the aquifer, formation permeability and

pressure build-up (Xie and Economides, 2009). Under unsteady state, injectivity may be calculated using the following mathematical equation:

$$J_{inj} = \frac{q_c}{\Delta p} = \frac{2\pi kh}{\mu \ln(0.472\, R_e/R_w)}, \quad (3.2)$$

where J_{inj} is injectivity index (kg/s/Pa); q_c is the injection rate of CO$_2$ (kg/s); Δp is pressure gradient (difference between the injection and formation pressures); k is permeability of reservoir rock (m^2); h is thickness of reservoir (m); μ is viscosity of CO$_2$ (cP); R_w is well radius (m); R_e is equivalent closed formation radius.

To ensure safety and integrity of the reservoir and cap rock, the CO$_2$ injection pressure must not be allowed to exceed the reservoir fracture pressure. The available maximum reservoir volume for CO$_2$ storage, considering fracture pressure limitations, can be calculated as follows (Xie and Economides, 2009):

$$V_{max} = c_t \pi (R_e^2 - R_w^2) h \phi (P_{fm} - P_i), \quad (3.3)$$

where c_t is the total compressibility of the reservoir (Pa^{-1}); P_{fm} is the fracture margin pressure of reservoir rock (Pa); P_i is initial reservoir pressure (Pa).

3.2 Characteristics of porous media

Porous media can be characterized mainly by the following parameters:

- Scale of reservoir (basin, regional, pore scale, etc.);
- Flow regime (non-steady state, including transient state and pseudo steady state; steady state);
- Driving mechanism (gravity- or topography-driven, thermal-driven, tectonic-driven, etc.);
- Fluid properties (including compressible, slightly compressible, incompressible; nonviscous or viscous; laminar or turbulent; miscible or immiscible);
- Reservoir geometry (linear, radial, spherical, etc.);
- Number of phases (single phase, two phases, multi-phase)

3.2.1 Fundamentals

Based on void geometric structure, the porous media can be divided into two main groups:

• *intergranular-intragranular porous media (single porosity)*

• *fractured media (dual-porosity)*

Mechanical porous media can be divided into two main categories:

• *consolidated porous media*

• *unconsolidated porous media*

In a consolidated porous medium (e.g. sandstone, granite, mudstone etc.) the grains are usually connected to each other through means of intergranular cement (Heinemann, 2005). While in an unconsolidated porous media, the grains are loosely packed and may easily deform or collapse through the loading process.

3.2.1.1 Concepts of volume fractions, porosity and saturation

Fluid flow through porous media is largely dependent on research scale (Jambhekar, 2011). On a small scale (e.g. micro-scale or pore-scale), the conventional fluid mechanics approach can be used to describe the multiphase fluid flow problems. On a large scale, however, application of conventional fluid

mechanics approach may meet with some difficulties because of the complicated flow paths. Nevertheless, today there are a number of methods that can be used to simplify the physical properties of flow in a porous medium. The molecular properties, for example, may be transferred into the micro-scale or pore-scale through the continuum approach. Furthermore, the volume averaging method (also called the continuum approach) can be used to transform the micro-scale properties into macro-scale parameters.

The continuum description of multiphase flow in a porous medium at Darcy's scale (i.e. the macro scale) implies that the relevant effective physical parameters (e.g., porosity, saturation, intrinsic permeability etc.), defined at a given point x represent the average value taken over a pore-scale representative elementary volume (REV) associated with that point (Fig. 3.6). At Darcy scale the same point can be occupied simultaneously by all three phases (gas, liquid and solid), which is represented by the concepts of volume fractions and saturations.
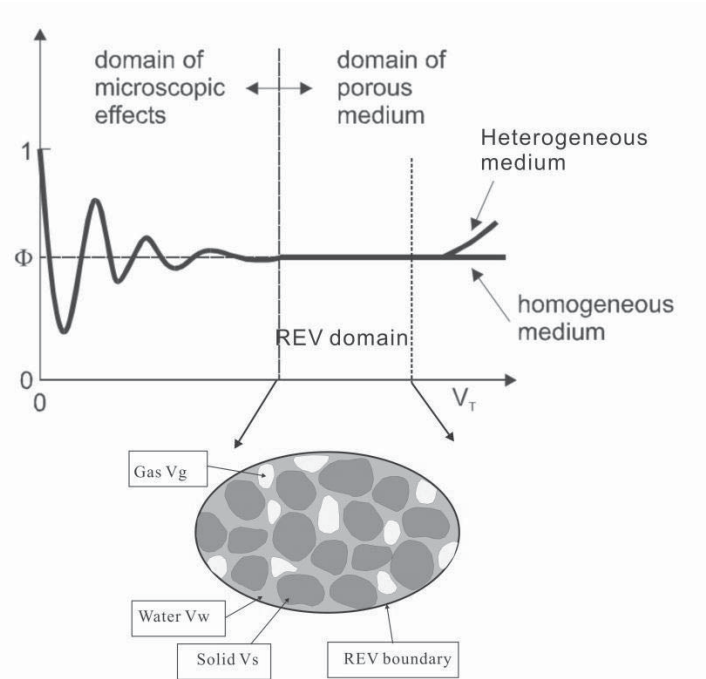
Fig. 3.6 Pore-scale representative elementary volume (REV) (modified after Szymkiewicz, 2013)

(1) Single-porosity matrix media

A matrix block, when common in natural system, is usually called a porous medium, without consideration of its fractures. The volume of the porous medium (matrix blocks) is divided into two parts, i.e. the pore and solid volumes:

$$V_t = V_p + V_s, \tag{3.4}$$

where V_p is the pore volume (m^3); V_s is the solid grain volume (m^3) and V_t is the total volume of the matrix (m^3). Porosity (ϕ) is then expressed as follows:

$$1 = \phi + V_s/V_t, \tag{3.5}$$

$$\phi = (V_g + V_w)/V_t, \tag{3.6}$$

The saturation of each phase α (S_α) can be defined as the fraction of the pore space occupied by a given fluid:

$$S_\alpha = \frac{V_\alpha/V_t}{\phi}, \tag{3.7}$$

The sum of the gas (S_g) and water saturation (S_w) must be equal to 1:

$$S_g + S_w = 1, \tag{3.8}$$

49

(2) Dual-porosity fractured media

A fractured medium is also refered to as a dual-porosity medium. In this case, two overlapping continua are usually considered: i.e. the matrix and fractured medium. The bulk fractured medium, V_t, is therefore composed of three parts:

$$V_t = V_{p1} + V_{p2} + V_s, \tag{3.9}$$

where V_{p1} is the pore volume of matrix medium (m^3); V_{p2} is the pore volume of the fractures (m^3); and V_s is the solid skeleton volume (m^3). In terms of porosity, this can be expressed as follows:

$$\phi_1 + \phi_2 + V_s/V_t = 1, \tag{3.10}$$

where $\phi_1 = V_{p1}/V_t$, and $\phi_2 = V_{p2}/V_t$.

Fractures can be observed on drilling cores, and may be characterized as filled, semi-filled and open. Fractures can be described by their orientation as horizontal, vertical or oblique. Filled fractures, however, do not contribute to porosity.

3.2.1.2 Compaction of porous medium

The porosity of the porous media will be affected by the packing pattern of its grains. The cubic pack pattern of sphere yields maximum porosity, while the rhombohedral pack pattern presents the minimum porosity. Different forms of sphere arrangements (in Figs. 3.7 and 3.8) illustrate the effect of compaction, which is irreversible and changes with depth (Heinemann, 2005).
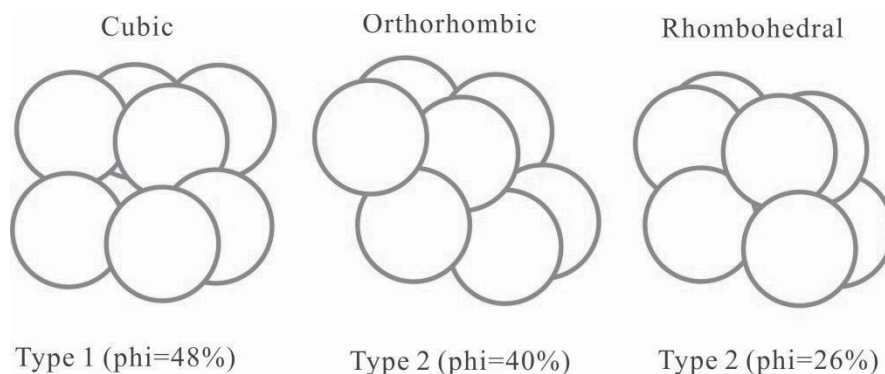
Fig. 3.7 Packing of spheres and porosity (after Heinemann, 2005)
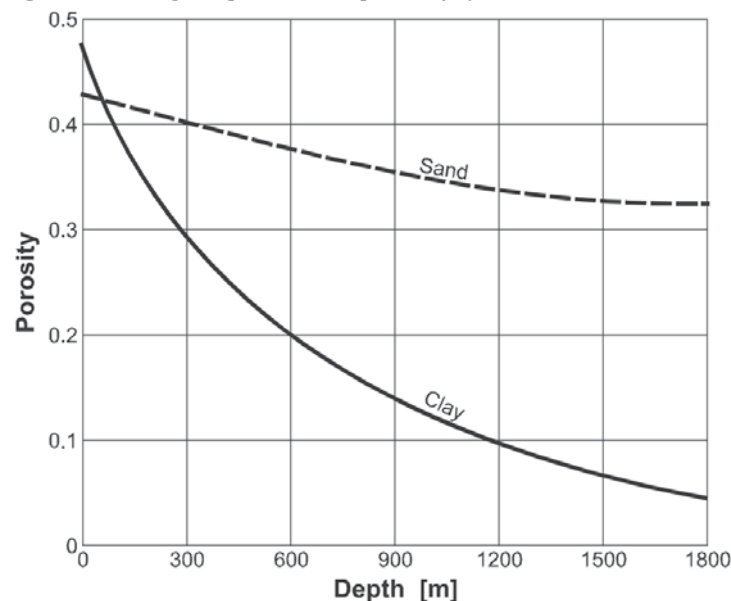
Fig. 3.8 The porosity changes in clay and sand with depth due to compaction (Heinemann, 2005)

3.2.1.3 Compressibility

A reservoir is considered to be incompressible if both its solids and the fluid cannot be compressed. In the processes of fluid flow, the parameters ρ and ϕ are considered constant when the chemical interaction between fluid and rock is neglected.

Under the circumstances, however, it is reasonable to consider the reservoir rock as a compressible medium. Compressibility is then defined as the ratio of relative volume change of fluid or solid skeleton to the pressure (or effective stress) change. When the pore pressure drops, the reservoir rock becomes compressible, thus the pore volume is changed (Jalalh, 2006). Compressibility can provide an extra driving force for oil or gas production. Therefore, many experimental and theoretical studies are conducted on the compressional property of rocks (Hall, 1953; Geertsma, 1957; Fatt, 1958; Li et al., 1999; Li et al., 2004).

Based on the objectives of the research on porous media, three kinds of compressibilities are usually defined: matrix, bulk, and pore compressibility. Pressure in this case may be described as the pore pressure or confining pressure. Besides, fluid can also be compressed under pressure effect.

(1) Compressibility of solid skeleton or matrix

The compressibility of solid skeleton material (c_s) is defined as:

$$c_s = \frac{dV_s}{V_s \, d\sigma'}, \tag{3.11}$$

where V_s is the solid volume (m^3); σ' is the effective stress acting on the solid skeleton grains (Pa).

According to rock mechanics, the compressibility of solid skeleton materials can be obtained by using the following empirical equation (Li et al., 2004),

$$c_s = \frac{3(1 - 2\nu)}{E_s}, \tag{3.12}$$

where ν is Possion's ratio, with an average value of 0.3 for most solid materials (-); and E_s is the elastic modulus of solid skeleton material (MPa), which varies in the range of 1-2$\times$10^4 MPa for most solid grains. Therefore, the compressibility of solid skeleton materials varies between 0.1-1$\times$10^{-4} /MPa.

The elastic modulus of skeleton materials (E_s) is often correlated with the elastic modulus of the bulk rock (E_b) through the equation,

$$E_s = \frac{E_b}{1 - \phi}, \tag{3.13}$$

(2) Bulk compressibility

When the confining pressure is held constant, the compressibility of bulk rock (c_b) can be expressed as (Zimmerman, 1991; Suman, 2009):

$$c_b = \frac{dV_b}{V_b \, dp}, \tag{3.14}$$

The relationship of bulk rock compressibility and solid skeleton compressibility can be written as:

$$c_b = \frac{\phi}{1 - \phi} \times c_s, \tag{3.15}$$

(3) Pore compressibility

The widely used rock compressibility under isothermal condition can be defined as the ratio of pore volume (or porosity) changes to pore pressure (Zimmerman, 1991; Suman, 2009):

$$c_p = \frac{dV_p}{V_p\,dp} \approx \frac{1}{\phi}\left(\frac{\partial \phi}{\partial p}\right)_T, \tag{3.16}$$

By integration of Eq 3.16,

$$\phi = \phi_0 e^{(p-p_0)c_\phi} \approx \phi_0[1 + c_p(p-p_0)], \tag{3.17}$$

where ϕ_0 is porosity at the reference pore pressure p_0 (-); and c_p is the pore compressibility (Pa^{-1}).

The most popular correlation between pore compressibility and porosity can be dated back to Hall (1953) and Horne (1990). Hall (1953) obtained a general relationship between pore compressibility and porosity from the experimental data:

$$c_p = \frac{2.587 \times 10^{-4}}{\phi^{0.4358}}\,(1/MPa), \tag{3.18}$$

Based on the lithology of the rocks, Horne (1990) presented the relationship between pore volume compressibility and porosity as follows:

$$c_p = \exp(44.28\phi^2 - 23.07\phi + 4.026) \times 10^{-6}\left(\frac{1}{psi}\right), \quad \text{(for consolidated limestone)} \tag{3.19}$$

$$c_p = \exp(63.98\phi^2 - 36.26\phi + 5.118) \times 10^{-6}\left(\frac{1}{psi}\right), \quad \text{(for consolidated sandstone)} \tag{3.20}$$

$$c_p = \exp(534.01(\phi - 0.2)) \times 10^{-6}\left(\frac{1}{psi}\right), \quad \text{(for unconsolidated sandstone)} \tag{3.21}$$

In fact, the empirical functions of pore compressibility have a great uncertainty due to a variety of factors, including overburden pressure, confining stress, pore pressure condition, pore structure etc. Fig. 3.9 illustrates the scatter distribution of the relationship between pore volume compressibility and porosity of different rocks.
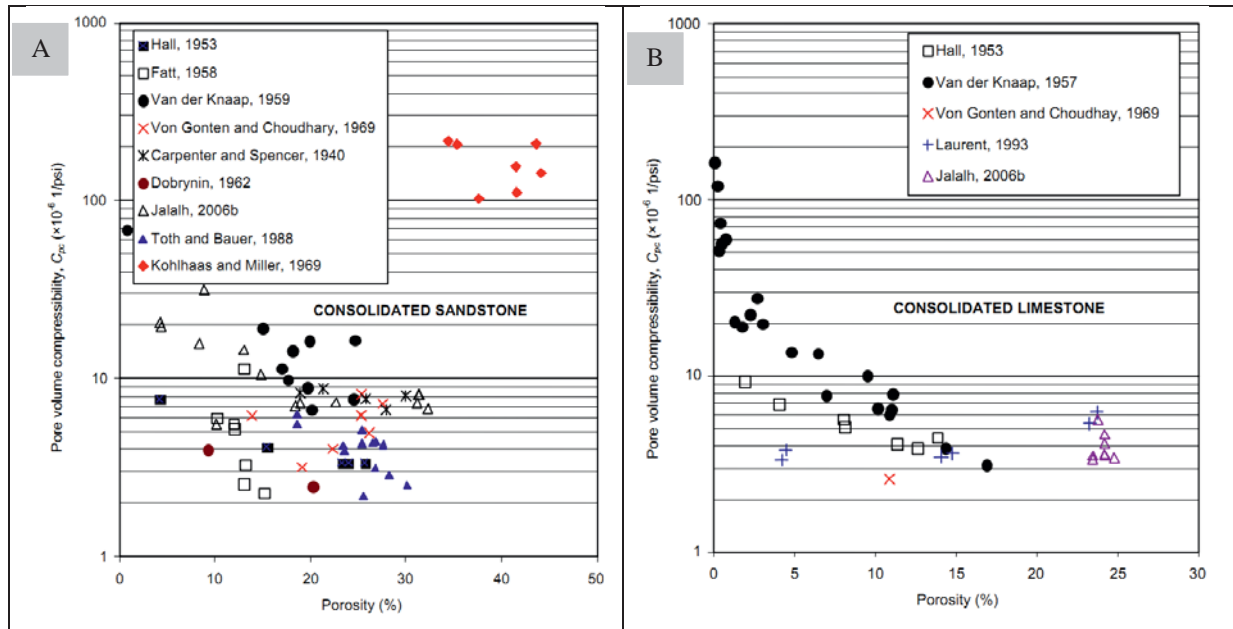
Fig. 3.9 Pore compressibilities of different rock types (Jalalh, 2006), (A) for consolidated sandstone; and (B) for consolidated limestone

(4) Fluid compressibility

Fluid compressibility (c_f) can be expressed as the ratio of fluid volume changes to pressure change under isothermal conditions:

$$c_f = -\frac{1}{V_f}(\frac{dV_f}{dp})_T = -\frac{1}{B_f}(\frac{\partial B_f}{\partial p})_T = -\frac{1}{\rho_f}(\frac{\partial \rho_f}{\partial p})_T, \tag{3.22}$$

where c_f is isothermal fluid compressibility (1/Pa); B_f fluid formation volume factor (bbl/STB) for oil, (bbl/scf) for gas; ρ_f fluid density (lb/ft³); p reservoir pressure (psi).

The compressibility of fluids can change with fluid type, temperature and pressure. For **water**, the compressibility is very small ($c_w = 4 \sim 5 \times 10^{-4} \text{ MPa}^{-1}$) and therefore can be assumed to be an incompressible fluid.

For **oil**, when the reservoir pressure is below the bubble point pressure, Eq 3.22 can not be used. Under this condition, gas will come out of the oil solution (McCaln, 1991), thus,

$$c_o = -\frac{1}{B_o}(\frac{\partial B_o}{\partial p})_T + \frac{B_g}{B_o} \times \frac{\partial R_s}{\partial p}, \tag{3.23}$$

where c_o is isothermal oil compressibility (MPa^{-1}), usually be used as a constant equal to 6.0×10^{-4}; B_o is the oil formation volume factor (bbl/STB); ρ_o is the oil density (lb/ft³); B_g is the gas formation volume factor (bbl/scf); and R_s is the solution gas oil ratio (scf/stb).

For a two phase system, e.g. water-oil, total and effective compressibility can also be expressed as (Adepoju, 2006):

$$c_t = c_o S_o + c_w S_w + c_p, \tag{3.24}$$

$$c_{eff} = \frac{c_t}{B_{oi}(p_i - p)}, \tag{3.25}$$

where c_w is water compressibility, equal to $4.0 \sim 5.0 \times 10^{-4} \text{MPa}^{-1}$; c_p is pore compressibility (1/Pa); c_t is total compressibility (1/Pa); c_{eff} is effective compressibility (1/Pa); S_o and S_w are oil and water saturation, respectively; B_{oi} is the initial oil formation volume factor (bbl/STB); p_i is the initial reservoir pressure (psi).

Gas has a large compressibility compared to water and oil (Adepoju, 2006). It can be described as follows,

$$c_g = \frac{1}{p} - \frac{1}{z}\frac{\partial z}{\partial p}, \tag{3.26}$$

where c_g is gas compressibility (1/Pa); z is gas compressibility factor, $z = \frac{V_{actual}}{V_{ideal\,gas}}$

3.2.1.4 Wettability

When two fluids are present in a reservoir, the one that is preferentially attracted by the surface of the solid skeleton (Szymkiewicz, 2013) is called the wetting fluid (or phase), while the other is the non-wetting phase. If saturation of wetting fluid decreases, the cross-sectional area available for its flow will also decrease. Accordingly, the wetting phase will occupy the larger pore spaces which were initially filled with the non-wetting fluid phase. Generally, because of the existence of capillary pressure, the wetting fluid will tend to occupy the smaller pores, while the non-wetting fluid will occupy pores with a larger radius (Hillel, 1998).

The porous media can be divided into two categories based on wettability: hydrophilic and hydrophobic. The degree of wetting ability of solids by liquids can be determined by the contact angle between solid-fluid interface and fluid-fluid interface (Fig. 3.10).
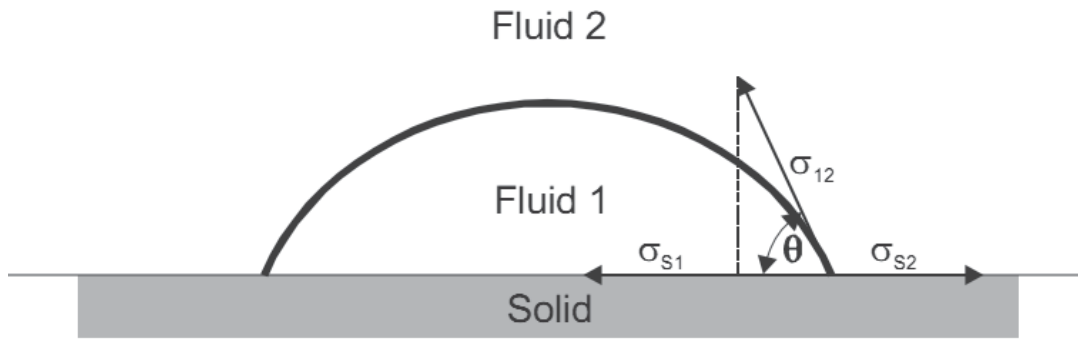
Fig. 3.10 The schematic diagram of the contact angle (after IEA, 2011)

The contact angle (θ) can be expressed using the Young's equation as follows (Subedi, 2011):

$$cos\,\theta = \frac{\sigma_{s2} - \sigma_{s1}}{\sigma_{12}}, \tag{3.27}$$

Where, σ_{12} is the interfacial tension between fluid 1 and fluid 2 (N); σ_{s1} and σ_{s2} are the interfacial tensions between solid and fluid 1 and fluid 2, respectively.

When the contact angle is smaller than 90°, fluid 1 is said to be wetting (Yuan and Lee, 2013). On the contrary, fluid 1 is regarded as non-wettability when its contact angle is larger than 90°. Normally, water acts as a wetting fluid in most reservoirs. In carbonate reservoirs oil is the wetting fluid, while in sandstones, both water and oil wet have the similar probability of wetting (Treiber et al., 1972), see in Table 3.2.

Table 3.2 Reservoir wettability based on contact angle results (Treiber et al., 1972)

Contact angle ($^\circ$)	Number of reservoir rock investigated		wettability
	Sandstone (30)	Carbonate (25)	
0-75	13	2	Water wet
75-105	2	1	Intermediate wet
105-180	15	22	Oil wet

For the two phase system, brine-CO_2, the interfacial tension between CO_2 (fluid 2) and the brine (fluid 1) appears to vary relatively with the reservoir pressure, temperature, salinity etc. It has been e that σ_{wg} decreases with increased reservoir pressure, but has a positive correlation with temperature and salinity, though water salinity effect is small (Bennion and Bachu, 2006a, 2006b, 2008).

Wettability plays an important role in oil and gas production as it can affect fluid distribution by changing some infiltration parameters, such as end point relative permeability (Fig. 3.11), capillary pressure and waterflood/CO_2-flooding behavior, etc (Heinemann, 2005). Wettability of rock is affected by many factors, including mineral composition and formation water chemistry (ion components and pH). Wettability has a great impact on flow processes and the distribution of fluids (oil, water, gas) in the reservoir.
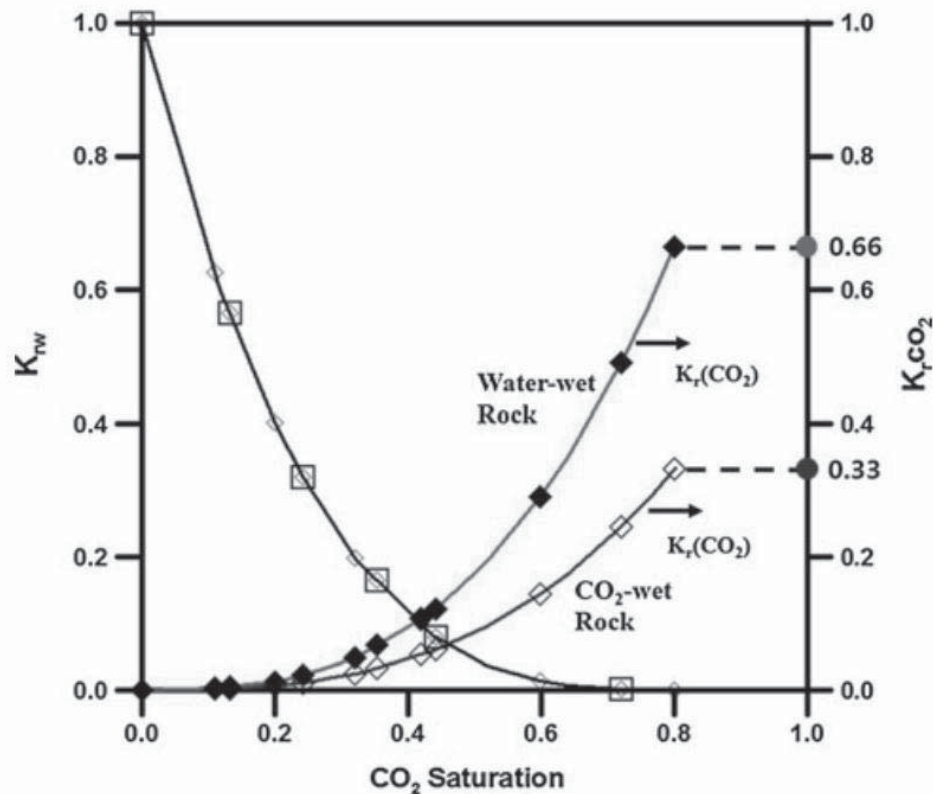
Fig. 3.11 The impact of wettability on endpoint relative permeability of CO_2 in brine-CO_2 system (Sung et al., 2011)

3.3 Multiphase fluid flow

Understanding of the multiphase phenomena dates back to the mid of 20th century when the parallel flow of oil, gas, and water in oil reservoirs was first investigated in petroleum engineering (Muskat and Meres, 1936; Leverett, 1939; Graf, 2004). At that time the model was based on the assumption of local equilibrium, by which the relative phase permeability and the capillary pressure could be expressed through the universal functions of local saturation (Graf, 2004).

Due to a pressure gradient, forces acting on the fluid will induce a flow motion through the porous media. Fluid flow can be described at the pore scale by the Navier-Stokes equation and by Darcy's law at a continuum scale (Graf, 2004). In a saturated porous medium (water-saturated), the resistance to fluid flow is established between the solid matrix (pore geometry) and fluid mobility. In an unsaturated porous medium, additional resistance exists in the presence of other fluids (e.g. air or oil) destined to share the same pore space.

It is also important to distinguish mass flow and filtration in this study. In case of mass flow, all grains move together with the fluid (e.g. river), whereas for filtration, only a portion of the mass grains will move and the rest comprise the rock framework.

Scientific terms like *convection*, *advection*, *dispersion*, *diffusion* can be used to describe the mass flow*;* while for heat transport, *advection*, *diffusion* and *conduction* are often used (Logan, 2001).

Convection/advection: is a process whereby mass grains are transport due to bulk flow (mass flow). Advection of aqueous and gaseous species can be described by Darcy's law of extended multiphase flow (Logan, 2001). In this case, the flow rate is related with the number and properties of the fluid phases present in the formation. When two or more fluid phases of any proportions can mix completely, they are

55

referred to as miscible fluids (Booth, 2008). On the other hand, they are called immiscible if no homogeneous mixture is attained.

In the presence of more than one fluid phase in a porous or fracture media, the flow behavior of one phase will affect that of the other. The two phase system, CO_2 and water, for example, its fluid properties are very complicated in all the various storage sites considered in Table 3.3. Because the supercritical CO_2 is much less viscous compared to water and oil (by an order of magnitude or more), fluid migration is greatly controlled by the mobility difference between CO_2 and the in situ formation fluid (Celia et al., 2005; Nordbotten et al., 2005). Because the CO_2 has a relative higher mobility, when it displaces the in situ oil or water, an average saturation of CO_2 in the range of 30–60% will be left in the porous media. Viscous fingering can induce CO_2 to bypass much of the pore space, depending on the heterogeneity of formation and anisotropy of rock permeability (van der Meer, 1995; Ennis-King and Paterson, 2001; Flett et al., 2005). In natural gas reservoirs, CO_2 is more viscous than CH_4, thus the 'plume front' will be stable and the viscous fingering effect can be limited to some extent (IPCC, 2005, 2007).

Table 3.3 Fluid properties caused by the injection of CO_2 into different storage sites

CO_2 storage sites	Fluid properties
Depleted gas reservoirs	Miscible gas phase
Deep saline formations	Supercritical phase (immiscible with water)
Oil reservoirs	Miscible/immiscible(depending on oil composition, pressure, temperature)
Coal bed seams	Miscible gas phase (adsorption and desorption occur)

Dispersion/Diffusion: are terms usually used to describe the mixing of soluble fluid. Dispersion can occur in two ways: microscopic and macroscopic (Logan, 2001; Roht et al., 2012). The former is usually used in describing the tortuous flow behavior in inter-granular porous media; while the latter is caused by permeability differences. Dispersion is another form of molecular diffusion for flow in a porous medium. Molecular diffusion, as described by Fick's law (Hassanizadeh, 1986a, 1986b; Bennethum et al., 1997), is the random movement of aqueous or gaseous molecular species, i.e.:

$$J_d^i = -D^i A \frac{dC^i}{dx},$$
(3.28)

where A is the cross sectional area for diffusion (m^2); C is the concentration of the aqueous, (moles/m^3); J_d^i is the molar flux of diffusion, per unit area per unit time (mol/(m^2.s)); t is time (s); x is distance (m); D is the molecular diffusion coefficient (m^2/s); and the superscript i stands for ion index (-).

Diffusion in rocks occurs along the indirect zigzag paths through the intergranular porous medium. Therefore, the diffusion coefficient has to be adjusted to account for this feature (Liu et al., 2007). For simplicity, however, an average diffusion coefficient at the 50% saturation concentration can be used to obtain the following equation:

$$\frac{D_e}{D} = \frac{1}{R_t \phi},$$
(3.29)

Where, R_t formation electrical resistivity factor ($\Omega \cdot$ m); D_e is the effective molecular diffusion coefficient (m^2/s); ϕ' effective porosity (-).

3.3.1 Different scales of fluid flow systems

3.3.1.1 Fluid flow at basin scale

From basin scale point of view, the direction of flow of formation fluids varies with the present hydrogeologic and tectonic characteristics of the topographic and underground geology of the basin (Fig. 3.12). The flow system is complicated being influenced by several factors including gravity, thermal, tectonic, seismic events etc (Garven, 1995).
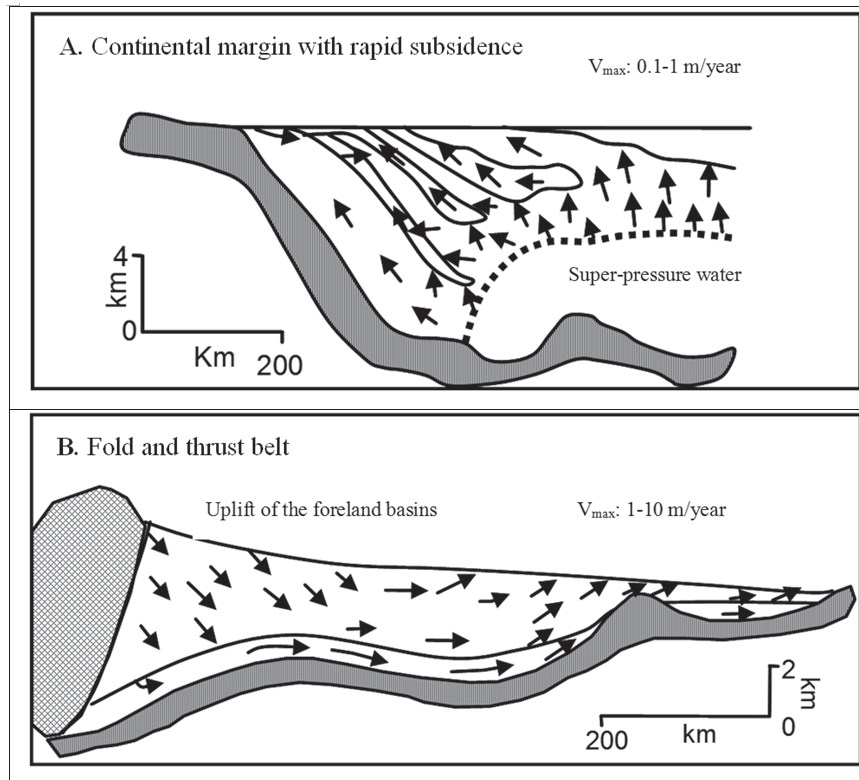
Fig. 3.12 Basin scale groundwater flow pattern due to different hydrogeologic and tectonic regimes, (A) in a continental margin; and (B) in a fold and thrust belt (Garven, 1995)

3.3.1.2 Fluid flow at regional scale

The regional scale fluid flow can be described using Darcy's law (Hassanizadeh, 1986b). However, considering the complicated nature of fluid flow systems, different researchers develop different equations (e.g. different form of Darcy's law) to describe the fluid flow and filtration in porous media (Whitaker, 1986; Garcia, 2003; Jambhekar, 2011). In order to find a suitable solution to the filtration problem, fluid flow regime must be established (Scatter et al., 2007): i.e. whether it is a steady state or a non-steady state flow regime (Fig. 3.13).

Steady-state fluid flow

Steady state flow occurs when the pressure at any point in the reservoir remains constant, i.e., does not change with time (Tallakstad et al., 2009). During oil/gas production processes, steady state regime begins to play a role after the late transient period. This condition is applicable when the production rate is constant and fluid withdrawal will be exactly balanced by fluid inflow across the open boundary, so that there is no change in pressure with time in the whole reservoir (Scatter et al., 2007). The composition at a point in space also does not change with time.

Non-steady state fluid flow

This is subdivided into the following: early-transient; late-transient and pseudo-steady state (semi-steady state) flow.

Transient flow occurs during drilling, workover and gas/oil production processes (Li et al., 2012). At the beginning of production, pressure in the wellbore drops sharply forcing the fluid near the wellbore to expand and move toward the well bottom. This movement of fluid is retarded by friction against the pore walls and the fluid viscosity. The process continues until the drop in pressure is equal to that dissipated during production (Scatter et al., 2007). This condition is valid for a short period of time as the pressure response in the reservoir is not affected by the presence of an outer boundary, thus the reservoir is considered to be infinitely large.

Late transient flow occurs when boundary effects start to work. For example, if the reservoir is smaller than expected or when the well test period takes a longer time, it will occur (Scatter et al., 2007).

The pseudo- (or semi) steady state fluid flow occurs when the withdrawl lasts a long time (Ostrowski, 2011). The outer boundary could be a constant pressure boundary (open boundary, Fig. 3.13) or impermeable to fluids (closed boundary, Fig. 3.14).
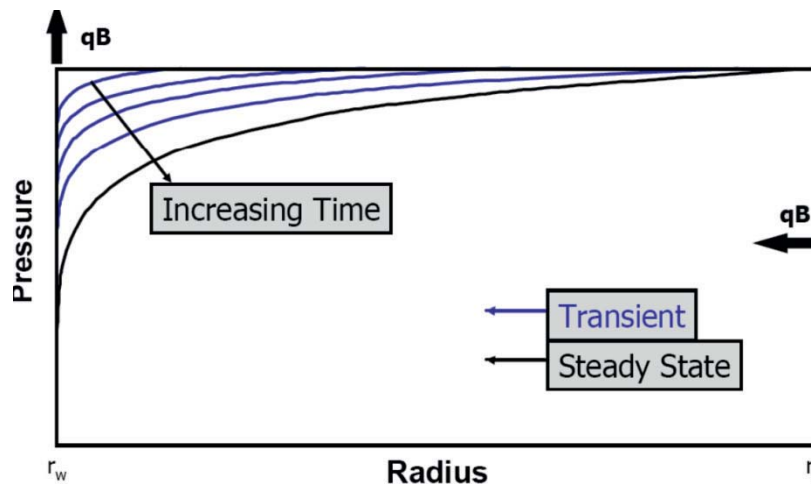
Fig. 3.13 Transient and steady state of fluid flow with an open boundary (Ostrowski, 2011)
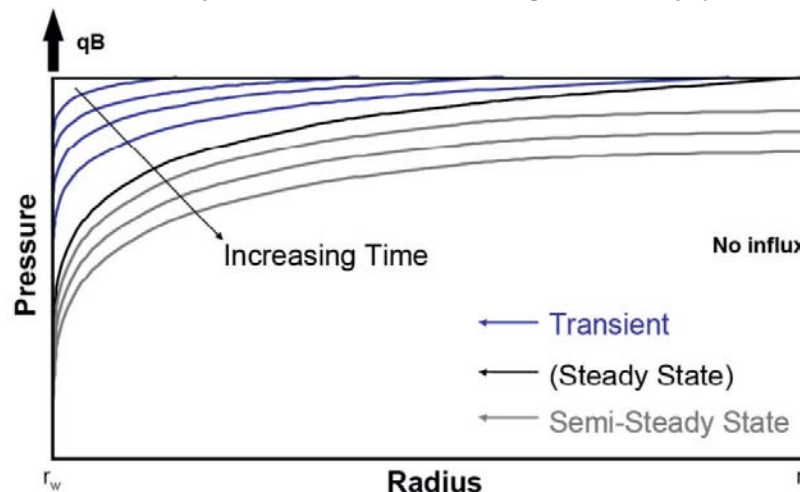
Fig. 3.14 Transient and steady state of fluid flow in a closed system (Ostrowski, 2011)

3.3.1.3 Fluid flow at pore scale

Depending on the proportions of water and gas in a porous medium, different spatial configurations of fluid will occur. With increased water content, water thin film → isolated capillary pendular water → capillary funicular water → isolated gas bubble → fully saturated water will occur in sequence (Szymkiewicz, 2013).

When water content is very low in porous media, it will always exist in the form of thin film covering the surface of the solid grain as a result of the force of attraction between water molecules and solid surface. This type of water is always considered immobile (Fig. 3.15a). As the proportion of water increases, it will be adsorbed onto the solid surface by the cohesion force. This type of water is called capillary water and forms capillary pendular rings (Szymkiewicz, 2013). Capillary or pendular water distributes itself nearly along all the corners of the solid grains (Fig. 3.15b). It is considered macroscopically immobile because it cannot form the continuous flowpaths. When more water enters into the pore system, the pendular water units will merge to form a thick continuous film (funicular water) along the boundary of the solid grains (Fig. 3.15c). From this stage on, continuous flow of water will dominate. As the amount of water in the pore system increases further, there only isolated gas bubble will exist in the center of water film (Fig. 3.15d). With time, no more gas can dissolve in water, leading to the occurrence of a fully water saturated state (Fig. 3.15e).
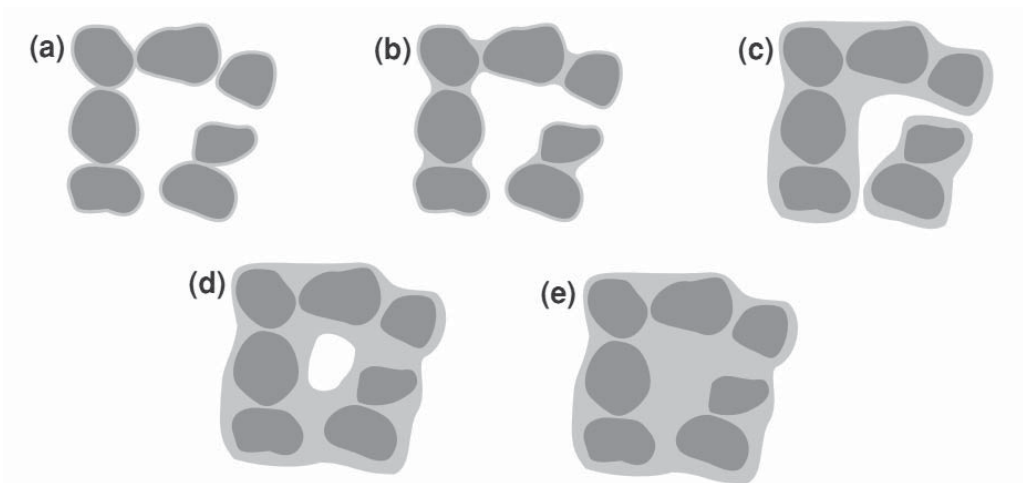
Fig. 3.15 Spatial distribution of different proportions of water and gas in an unsaturated porous medium: with (a) thin adsorbed water films; (b) pendular capillary water; (c) funicular capillary water; (d) isolated gas bubbles in dominated water; (e) fully saturated water(Szymkiewicz, 2013)

3.3.2 Darcy's law

The earliest investigations on filtration can trace its history to the year 1825 when Chaumont excavated a trench parallel to river Garonne, which he dewatered using an Archimedian screw. It was realized that the water level in the trench increased to a new height after a period of time due to infiltration (Heinemann, 2005).

In 1856, Henri Darcy performed the filtration experiment by using a vertical cylinder filled with sand (Fig. 3.16) to solve the water supply problems. This established the foundation of infiltration by using the mathematical formula, later named *Darcy's law*, to describe the fluid flow phenomenon in a porous medium. This formula has been employed in solving a wide range of problems in groundwater hydrology, sanitary engineering and petroleum engineering (Hassanizadeh and Gray, 1980). The scientific term "*permeability*" was defined at the first World Oil Congress in 1933. In the same year, "*Darcy*" was selected as the unit of permeability (Heinemann, 2005).
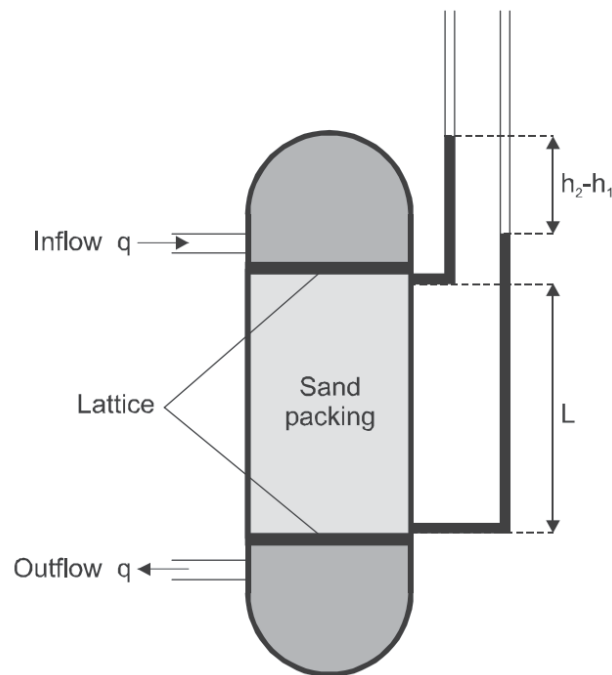
Fig. 3.16 Schematic diagram of *DARCY's* experiment (Heinemann, 2005)

3.3.2.1 Assumptions in Darcy's law

To simplify complex problems, assumptions are often used in the description of physical and chemical problems. Assumptions with respect to the application of the original *Darcy's law* can be summarized as follows (Teng and Zhao, 2000):

- The flow is laminar
- Inertial effects are neglected and quasi-steady fluid flow is assumed
- The fluid has to be largely incompressible
- One-phase fluid flow

The assumptions used in the derivation of *Darcy's law* based on the mathematical form of the pore scale Navier-Stokes equations can be summarized as follows (Teng and Zhao, 2000):

- The flow is laminar
- Inertial effects are neglected, e.g. quasi-steady fluid flow is assumed
- The fluid behavior satisfies Newton's law

Bachmat and Bear (1986) derived *Darcy's law* by making the following assumptions:

- Any inertial terms may be ignored. This is due to the assumption of a slow moving fluid where inertial effects are neglected.
- The momentum transfer between phases due to mass transfer is assumed to be zero
- The momentum transfer by viscous shear force within a phase is considered to be negligible
- Gravity is considered to be the only external force
- The viscous stress is assumed to obey Newton's law for an incompressible fluid
- The no-slip condition applies at the interface between the solid rock and the fluid. Additionally, the rock phase is rigid.

Hassanizadeh and Gray (1980), however, made no assumptions regarding incompressibility or the constitutive relationship between stress and shear when deriving Darcy's law for single-phase flow.

Extensions to multiphase flow have been developed by Gray (1983), further to multi-component flow by Hassanizadeh and Gray (1979, 1980).

3.3.2.2 Mathematical equations

The initial form of *Darcy's law* can be expressed as follows,

$$\hat{q} = K_c A \frac{\hat{h}_1 - \hat{h}_2}{L} = K_c A \frac{\Delta \hat{h}}{L}, \tag{3.30}$$

where $\hat{q}$ is the total filtration amount per unit time (m^3/s); Kc is the permeability coefficient, and also be called hydraulic conductivity coefficient (m/s); A is the cross section area (m^2); $\hat{h}_1$ and $\hat{h}_2$ are the hydraulic heads at the two flow cross-sections (m); $\Delta \hat{h}$ is the altitude difference between $\hat{h}_1$ and $\hat{h}_2$ (m); L is the distance between the two cross sections perpendicular to the flow direction (m).

The above equation can be rewritten as:

$$u = K_c \boldsymbol{J} = -K_c \frac{d\hat{h}}{dL}, \tag{3.31}$$

with

$$\boldsymbol{J} = \frac{\Delta \hat{h}}{L} \ and \ u = \frac{\hat{q}}{A}, \tag{3.32}$$

where $\boldsymbol{J}$ is the hydraulic gradient (-), which is also the loss of hydraulic head a unit length of infiltration path and u is the infiltration rate (m/s).

For a general case of three-dimensional single-phase fluid flow in a porous medium characterized by arbitrary pore network, a mathematical form of the pore scale *Navier-Stokes* equations yields the following extension form of *Darcy's law*, using volume averaging technology (Bear, 1972; Hassanizadeh and Gray, 1980; Whitaker, 1986; Auriault et al., 2009):

$$u = -K_c \nabla \hat{h} = -\frac{k}{\mu} \frac{\Delta p}{L}, \tag{3.33}$$

where k is the permeability (m^2), which represents the intrinsic permeability as a parameter characterizing the porous media; μ is the viscosity of the fluid (cP).

For a multi-phase system, the Darcy's law can be rewritten as,

$$u_\alpha = -K_{c\alpha}(S_\alpha) \nabla \hat{h}_\alpha = -\frac{k_\alpha(S_\alpha)}{\mu_\alpha} (\nabla p_\alpha - \rho_\alpha \boldsymbol{g}), \tag{3.34}$$

$K_{c\alpha}$, the hydraulic conductivity of phase α, is a macro-scale parameter, which accounts for the influence of viscosity and adhesion at the soil grain surfaces, and can be expressed as,

$$K_{c\alpha} = \frac{k k_{r\alpha}}{\mu_\alpha}, \tag{3.35}$$

$$k_\alpha(S_\alpha) = k k_{r\alpha}(S_\alpha), \tag{3.36}$$

where the product of k and $k_{r\alpha}$ is called the *effective permeability of phase* α, $k_{r\alpha}$ is the relative permeability of phase α (-), which depends on the phase saturation S_α:

$$0 \le \sum_{\alpha=1}^{\mathbf{nphas}} k_{r\alpha}(S_\alpha) \le 1, \tag{3.37}$$

Darcy formula can be extended according to phase mobility:

$$u_\alpha = -k\lambda_\alpha(S_\alpha)(\nabla p_\alpha - \rho_\alpha \boldsymbol{g}), \tag{3.38}$$

61

where $\lambda_\alpha(S_\alpha) = k_{r\alpha}(S_\alpha)/\mu_\alpha$ is the mobility of phase α.

When interfacial forces are considered, the driving forces for the flow of a phase are the gradients of Gibbs free energy of the phase plus gravity (Hassanizadeh and Gray, 1986b; Joekar-Niasar and Hassanizadeh, 2011). The extended Darcy's law can be expressed as,

$$u_\alpha = -K_{c\alpha}(S_\alpha)\nabla h_\alpha = -\frac{k_\alpha(S_\alpha)}{\mu_\alpha}(\nabla p_\alpha - \rho_\alpha \boldsymbol{g} - \Psi_{\alpha a}\nabla a^{nw} - \Psi_{\alpha S}\nabla S^w), \tag{3.39}$$

where the parameters $\Psi_{\alpha a}$ and $\Psi_{\alpha S}$ are material properties; a^{nw} is the specific area of phase interfaces; the superscripts n and w stand for non-wetting and wetting phase, respectively.

3.3.3 Relative permeability

The concept of relative permeability describes the simultaneous multiphase flow of fluids in a porous medium using Darcy's law. The proposed parameterization of the relative permeability-saturation relationships for a two-phase system can be divided into two groups: one based on pore-scale network models and the other on purely empirical models.

3.3.3.1 Capillary models (pore-scale network) used in relative permeability

A system of pores is assumed to be equivalent to a bundle of uniform capillary tubes (same or different radius). In this model, the tubes are drained in the centers and water exists only at the walls (Averjanov, 1950). Relative permeability depends on the the nature of the existing pore network, for example, their distribution, radius and so on. The influence of tortuosity on the permeability is based on the fact that the actual flow and direction are much more complex than the physical description depicted by *Darcy's law*. Therefore, it is better to calculate the pressure gradient with respect to the effective length of the pore system. In this case, rock samples with a higher fraction of micro pores tend to have a better uniform displacement effect and higher endpoint relative permeability values (Bennion et al., 2006a).

Early representative models assumed that pore systems are comprised of bundles of parallel capillaries (Burdine, 1953; Mualem, 1976). The relationships between relative permeability, tortuosity and the mean hydraulic radius of the wetting phase ($\bar{R}_w$) and non-wetting phase ($\bar{R}_n$) for the Burdine model are shown in Table 3.4. In the Mualem model, the capillary pressure-saturation relationship is used for calculating the relative permeability for the wetting and non-wetting phase.

3.3.3.2 Empirical models

To simplify the complex problems, some empirical models describing the relationship between relative permeability and saturation, such as Brooks-Corey model and combined Van Genuchten-Mualem model (see Table 3.4) have become the basis of rock hydraulic functions. Besides, direct fits from experimental data or mathematical theoretical functions are also used (for more details see Court, 2011).

Much progress has been made in describing the hydraulic properties, especially for the multiphase porous system (Stone, 1973; Dane et al., 2011; Szymkiewicz, 2013). However, all functions in the above models impose strong constraints in fitting with the experimental data.

Table 3.4 The representative models of relative permeability functions

Representative models	equations
Capillary model	
Burdine model (1953)	$$k_{rw} = \frac{S_w \overline{R}_w^2}{\hat{\tau}}$$ $$k_{rn} = \frac{(1 - S_w)\overline{R}_n^2}{\hat{\tau}}$$
Mualem model (1976)	$$k_{rw} = \sqrt{\hat{S}}\left[\frac{\int_0^{\hat{S}} p_c(S_e)^{-1} dS_e}{\int_0^1 p_c(S_e)^{-1} dS_e}\right]^2$$ $$k_{rn} = \sqrt{1 - \hat{S}}\left[\frac{\int_{\hat{S}}^1 p_c(S_e)^{-1} dS_e}{\int_0^1 p_c(S_e)^{-1} dS_e}\right]^2$$ $$S_e = \frac{S_w - S_{wr}}{1 - S_{wr} - S_{gr}}; \hat{S} = \frac{S_w - S_{wr}}{1 - S_{wr}}$$
Empirical model	
Brooks and Corey model (1964)	$$k_{rw} = \hat{S}^{\frac{2+3\lambda}{\lambda}}$$ $$k_{rn} = \left(1 - \hat{S}\right)^2 (1 - \hat{S}^{\frac{2+\lambda}{\lambda}})$$
Van Genuchten-Mualem model(1980)	$k_{rw} = \sqrt{\hat{S}}\{1 - (1 - \hat{S}^{1/\lambda})^\lambda\}^2$ if $S_w < S_{wr}$ $\quad = 1$ if $S_w \geq S_{wr}$ $k_{rn} = 1 - k_{rw}$ if $S_{gr} = 0$ $\quad = (1 - S_e)^2(1 - S_e^2)$ if $S_{gr} > 0$

Reservoirs in deep sedimentary basins are characterized by low permeability and high salinity. Under these conditions, groundwater flow velocities are very low, typically on the order of mm-cm/year (Bachu et al., 1994). Thus, migration rates of dissolved CO_2 are obviously lower than single phase CO_2. The understanding of hydraulic characteristics in such kinds of systems is essential in ascertaining CO_2 injectivity and migration rate, thus in assessing the suitability and safety of CO_2 sequestration (Bennion et al., 2006a). For the two phase system of CO_2-saline, the endpoint relative permeability of CO_2 is consistent with the maximum CO_2 saturations, which has the same trend in both sandstone and carbonate reservoirs (Bennion et al., 2005, Fig. 3.17). Table 3.5 lists the hydraulic functions of relative permeability and saturation in the recent simulation runs for CO_2 sequestration problems.
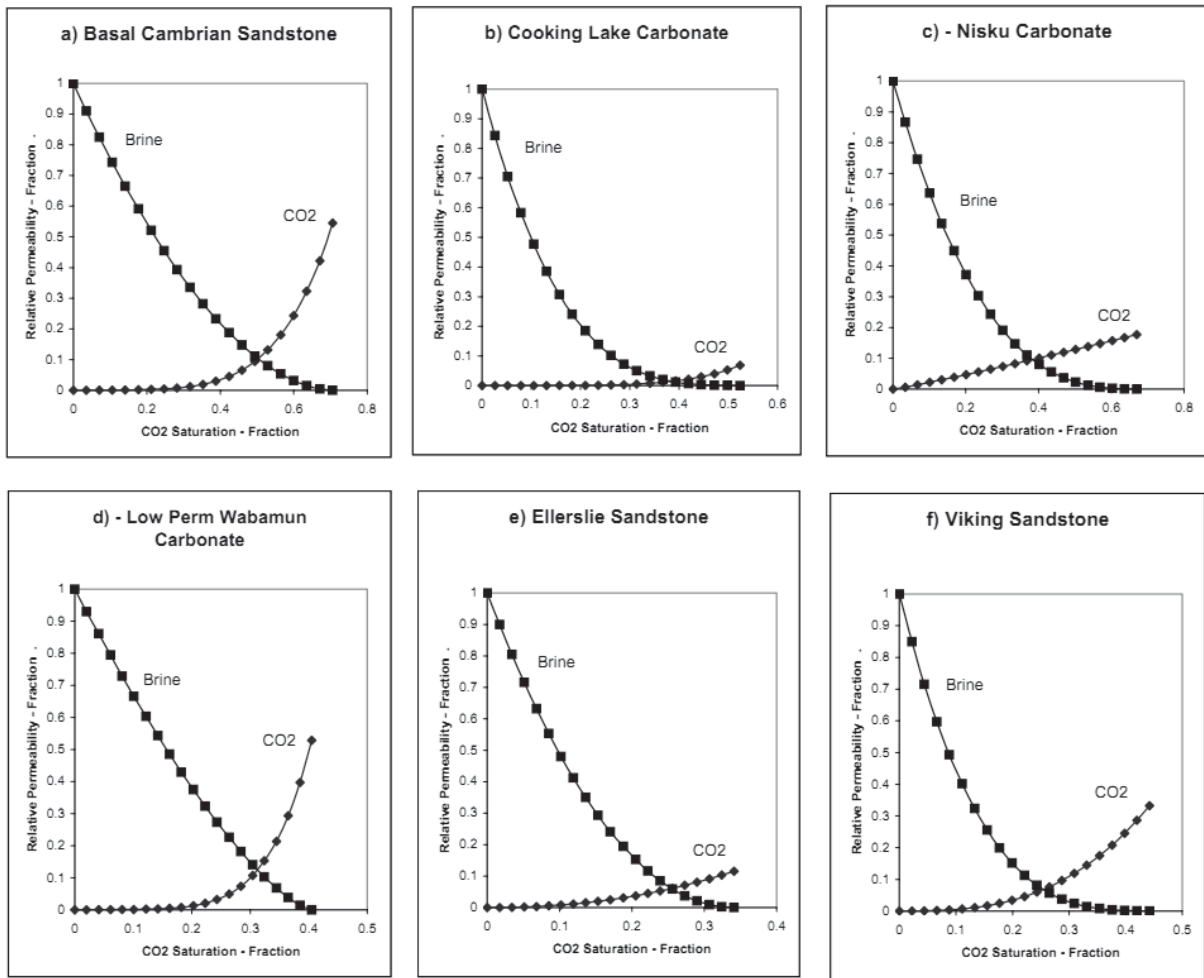
Fig. 3.17 Evolution of relative permeability and CO_2 saturation at in situ conditions for CO_2-brine systems for different rock samples (Bennion et al., 2005)

Table 3.5 Literature review of relative permeability and saturation relationships in CO_2 geological sequestration modeling literatures (Court, 2011)

References	Functions	Parameters	S_{wr}	Endpoint k_{rg}	Formation thickness (m)
(Nordbotten and Celia, 2006)	Linear: $k_{rg}=S_g$; $k_{rl}=S_w$	-	0	1.0	-
(Class et al., 2009)		-	0.2	1.0	90-140
(Dentz and Tartakovsky, 2009)		-	0	1.0	-
(Gasda et al., 2010)		-	0.2	1.0	90-140
(Lu et al., 2009)	VGM: $k_{rl} = \sqrt{S_w}[1-(1-S_w^{1/m})^m]^2$ $k_{rg} = \sqrt{1-S_w}[1-S_w^{1/m}]^{2m}$ Experimental: $k_{rl} = \sqrt{\hat{S}}[1-(1-\hat{S}^{1/m})^m]^2$ $k_{rg} = \sqrt{1-S_w}[1-S_w^{1/m}]^{7m}$ Cubic: $k_{rw} = S_w^3$; $k_{rg} = S_g^3$	$m=0.75$	0	1.0	62
(Bennion and Bachu, 2008)	Fit of experimental data-Nisku 1 Fit of experimental data-Basal	-	0.3 0.3	0.2 0.55	72 23
(Zhou et al., 2008) (Birkholzer et al., 2009) (Zhou et al., 2010)	VG: $k_{rl} = \sqrt{\hat{S}}[1-(1-\hat{S}^{1/m})^m]^2$ $k_{rg} = \sqrt{1-\hat{S}}[1-\hat{S}^{1/m}]^{2m}$	$m=0.46$	0.3	1.0	250 60 300-700
(Pruess et al., 2002) (Doughty, 2007) (Doughty et al., 2008) (Pruess and Muller, 2009) (Doughty, 2010)	$k_{rl} = \sqrt{\hat{S}}[1-(1-\hat{S}^{1/m})^m]^2$ $k_{rg} = (1-S_e^2)(1-S_e)^2$	-	0.3 0.3 0.0-0.45 0.3 0.2	1.0 1.0 1.0 1.0 1.0	100 100 5.5-8.0 100 & 10 160
(Ebigbo et al., 2007)	$k_{rl} = S_e^{(2+3\lambda)/\lambda}$ $k_{rg} = (1-S_e)^2\left(1-S_e^{(2+\lambda)/\lambda}\right)$	$\lambda=2$	0.2	1.0	30
(Dahle et al., 2009)	$k_{rl} = S_e^4$ $k_{rg} = 0.4(1-S_e^2)(1-S_e)^2$	-	0.2	0.4	50
(Alkan et al., 2010) case 1 case 2	$k_{rl} = S_e^4$ $k_{rg} = (1-S_e^2)(1-S_e)^2$	-	0.2 0.3	1.0 1.0	100 100

3.3.4 Capillary pressure

Capillary pressure offers the main resistance when gas is transported through a porous medium. Ideally, however, capillary pressure (P_c) is the pressure difference between the gas (P_g) and liquid (P_l) pressures (Garcia, 2003). Gas will only flow continuously through the large pores and even the pore throats if the gas and liquid pressure difference is larger than the capillary pressure. Since P_c is a function of saturation, pressure gradients between gas and liquid phases are coupled. According to Laplace capillary pressure is formulated as follows:

$$P_c = P_g - P_l = \frac{2\sigma_{wg} cos\theta}{r},$$
(3.40)

where σ_{wg} is the interfacial tension of water with respect to gas (N); θ is the contact angle (°); and r is the radius of the observed meniscus (m).

From capillary pressure equation the following may be concluded:

- A decrease of the meniscus radii corresponds to an increase of the capillary pressure
  If a water-saturated soil/rock is **drained** (water displacing oil), the wetting phase retreats to smaller pores or fractures (Faigle, 2009),
- An increase of the meniscus radii corresponds to a decrease of the capillary pressure
  If **imbibition** (water displaced by oil) occurs, the wetting phase penetrates into larger pores. The water in the smaller pores will form an irreducible phase.

For the different wettability characteristics of rocks with respect to a specific fluid, there is a hydrophilic channel and an oil-wet channel in the reservoir system. In the hydrophilic capillary channel, the direction of capillary pressure P_c is equal to the displacement pressure, and capillary pressure acts as the driving force. The smaller the pores, the larger the driving force becomes. Water will flow through smaller pores, while oil tends to stay in the larger pore channel. On the contrary, capillary pressure P_c acts as the resistance when water displaces oil in the oil-wet channel system. Under this situation, the direction of P_c is just opposite to that of the displacement pressure direction (Fig. 3.18).
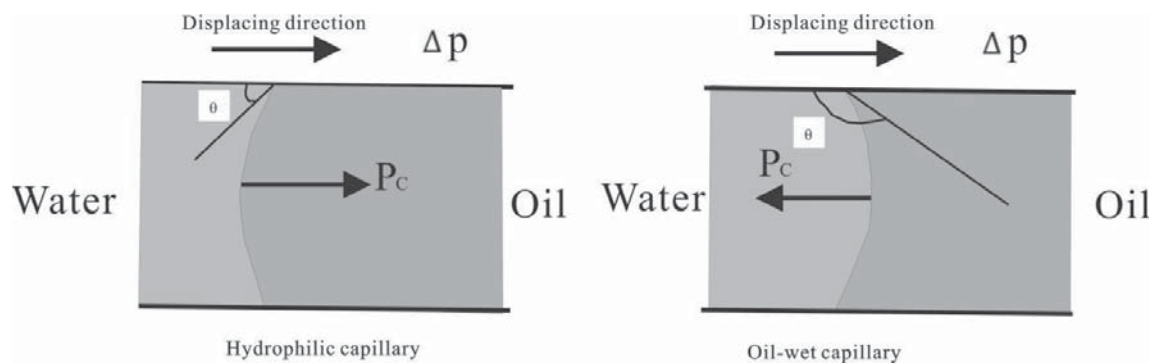
Fig. 3.18 Relationship between wettability and capillary pressure

Several models are today used to describe the relationship between capillary pressure and saturation (e.g. Brooks and Corey, 1964; Brutsaert, 1967; Campbell, 1974; Mualem, 1974; Parlange, 1976; van Genuchten, 1980; Scott et al., 1983; Kool and Parker, 1987; Lenhard et al., 1993). These models can fit experimental data by using different material parameters (e.g. pore space distribution, air entry pressure, etc.) to reflect the geometric structure of the pore space. Although the Brooks and Corey model was better related to physical principals, the van Genuchten model has been used widely because of its better numerical applicability.

During the drainage process in a porous medium, saturation of the wetting fluid decreases with capillary pressure (Brooks and Corey, 1964). Depending on the mathematical model used, capillary pressure is often formulated as a function of *effective saturation*:

$$P_c(S_w) = P_d \hat{S}^{-1/\lambda}; for\ P_c \geq P_d \ , \tag{3.41}$$

where $\hat{S}$ is the effective saturation (-), $\hat{S} = \frac{S_w - S_{wr}}{1 - S_{wr}}$; S_w is the water saturation (-); S_{wr} is the residual water saturation (-); λ is the pore size distribution index (-); P_c is the capillary pressure (Pa); P_d is the air entry pressure (Pa).

All parameters used to characterize pore space geometry are determined by fitting to the experimental data. The parameter λ is related to the pore size distribution of the rock. For a typical porous medium, λ usually ranges between 0.2 and 3.0. For soil, λ is usually less than 2, while for sand λ is usually larger than 2 or even greater than 5 (Graf, 2004). A small value of λ implies a narrow pore size distribution (strong homogeneous material); large λ indicates a very heterogeneous pore structure (Graf, 2004; Rhodes et al., 2009). The entry pressure P_d is considered as the minimum pressure required to retreat the wetting phase from the largest pores.

The van Genuchten (1980) model describes the relationship between capillary pressure and saturation in the following way:

$$P_c(S_w) = -P_0(\hat{S}^{-1/\lambda} - 1)^{1-\lambda}; \text{ for } P_c > 0, \tag{3.42}$$

where P_0 is the strength coefficient (Pa).

In the CO$_2$-water system, typical capillary pressue and water saturation curves for different rocks are compared in Table 3.6. This is caused by the complicated pore network, for example, pore distribution, pore radius and so on (Fig. 3.19).
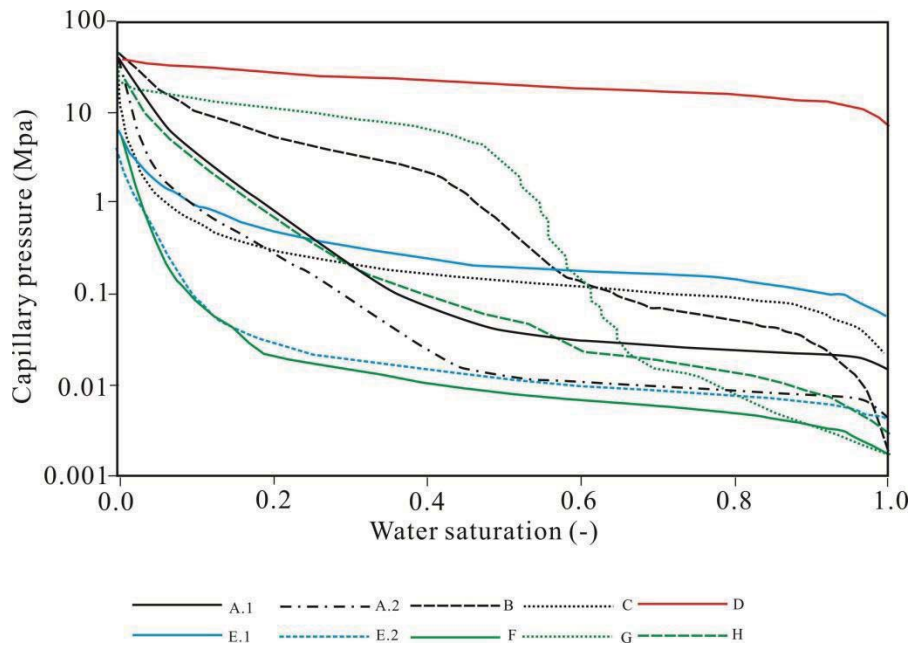
Fig. 3.19 The relationship between capillary pressure and water saturation for different CO$_2$-brine systems (data derived from Bennion and Bachu, 2006a). Experiments are based on different rock and different in-situ conditions: A, B, C-sandstones; D-shale; E, F, G, H-carbonate

Table 3.6 Literature review of capillary pressure-saturation relationships in CO_2 sequestration modeling (Court, 2011)

References	Functions	Parameters	P_d ($\times 10^5$ Pa)	S_{wr}	Formation thickness (m)
(Dahle et al., 2009) (Delshad, 2010) (Gasda et al., 2010)	$P_c = P_d \hat{S}^{-1/2}$	-	0.2	0.2	50 50 90-140
(Izgec et al., 2006) (Ebigbo et al., 2007) (Class et al., 2009)	Brooks-Corey: $P_c = P_d \hat{S}^{-1/\lambda}$	λ=0.4 λ=2 λ=2	1.1 0.1 0.1	0.13 0.2 0.2	70 30 90-140
(Lu et al., 2009)	Linear: $P_c = P_d(1 - S_w)$	-	1.0	0	62
(Bennion and Bachu, 2008)	Fit of experimental data-Nisku 1 Fit of experimental data-Basal	-	-	0.3 0.3	72 23
(Olafuyi, 2008) -Berea -Bentheim -Mt. Gambier	Brooks-Corey/VG fit of experiment	λ/m = 1.1/0.45 1.7/0.65 1.0/0.45	0.06 0.048 0.048	0.15 0.10 0.10	- - -
(Zhou et al., 2008) (Birkholzer et al., 2009) (Zhou et al., 2010) (Alkan et al., 2010) case 1 case 2	VG: $P_c = P_d(\hat{S}^{-\frac{1}{m}} - 1)^{1-m}$	m =0.46 m =0.46 m =0.41 m =0.40 m =0.25	0.19607 0.2 0.21 0.1 1.0	0.3 0.3 0.3 0.2 0.3	250 60 300-700 100 100
(Pruess et al., 2002) (Doughty, 2007) (Doughty et al., 2008) (Pruess and Muller, 2009) (Doughty, 2010)	VG $P_c = P_d[(\frac{S_w - 0.03}{1 - 0.03})^{-1.7/(1-1.7)}]^{1/1.7}$ VG VG	m =0.45 - - m =0.45 m =0.416	0.1961 0.133 0.065 0.1961 0.188	0.3 0.3 0.0- 0.45 0.3 0.2	100 100 5.5-8.0 100 & 10 160

3.4 Mathematical model for fluid flow in a porous medium

3.4.1 Single-phase single component fluid flow [H]

When describing the single phase fluid flow through a porous medium, different mathematical forms can be used considering the heterogeneity of the porous medium (e.g. single/dual porosity) and some other conditions, such as the deformable or non-deformable properties, compressible or incompressible of fluid, isothermal or non-isothermal conditions, saturated or unsaturated, whether chemical reactions of the fluid-rock interaction are considered or not, EOS of the fluid, etc (Bastian, 1999; Heinemann, 2005; Chen et al., 2006).

The general governing equation (for mass and heat conservation) can be expressed as (Pruess et al., 1999):

$$\frac{\partial M^\kappa}{\partial t} = -\nabla \cdot F^\kappa + q^\kappa, \tag{3.43}$$

where F-is the mass flux (kg); M-is the mass accumulation term (kg/s); q- is the source or sink term (kg/s); t-is time (s); $\nabla \cdot$ is the divergence and κ-is a superscript for component, e.g. H_2O, CO_2.

For isothermal, single phase fluid flow in a non-deformable single porosity porous medium, the mass conservation equation can be rewritten as (Chen et al., 2006),

$$\frac{\partial(\phi\rho_l)}{\partial t} = -\nabla \cdot (\rho_l \phi \boldsymbol{u}_l) + q_l, \tag{3.44}$$

where ϕ-is the porosity (-); ρ-is the density (kg/m^3); $\boldsymbol{u}$ – is the superficial Darcy velocity (kg/s); the total fluid mass term $M_l = \phi\rho_l$; the flux term $F_l = \rho_l\phi\boldsymbol{u}_l$ and l- is a subscript for liquid phase.

When non-isothermal mode is considered, the heat conservation equation can be expressed as (Pruess et al., 1999),

$$\frac{\partial(\phi\rho_l U_l)}{\partial t} = -\nabla \cdot (h_l\rho_l\boldsymbol{u}_l) - \lambda\nabla T, \tag{3.45}$$

where U-is internal energy (J); h-is the specific heat (J/kg ^{o}C); T-is temperature (^{o}C); λ-is heat conductivity (W/m ^{o}C) and ∇ is the gradient.

The momentum conservation can be expressed by Darcy's law as (Heinemann, 2005),

$$\boldsymbol{u}_l = -\frac{k}{\phi\mu}\nabla P, \tag{3.46}$$

where k- is the permeability (m^2); μ- is the viscosity (cP); P- is the pressure (Pa).

The main equations for state of fluid include density, viscosity, heat conductivity and so on. When, however, only isothermal conditions are considered, both fluid density and viscosity are assumed to be a function of fluid pressure (Chen et al., 2006), i.e., $\rho = \rho(p)$ and $\mu = \mu(p)$.

$$\rho_l = \rho_l(P_l)_T, \tag{3.47}$$

$$\mu_l = \mu_l(P_l)_T, \tag{3.48}$$

$$\lambda = \lambda_l(P_l)_T, \tag{3.49}$$

From Eqns 3.44- 3.49, a single porosity, non-deformable porous medium model is used, whereas for a dual porosity, non-deformable porous medium, the equations for mass, heat and momentum conservation can be written, respectively, as follows (Chen and Teufel, 1997):

$$\text{fluid: } \frac{\partial(\phi_{ne}\rho_l)}{\partial t} = -\nabla \cdot (\rho_l\phi_{ne}\boldsymbol{u}_l) + (-1)^n \rho_l\Gamma, \tag{3.50}$$

69

$$\text{solid:} \quad \frac{\partial((1-\phi_t)\rho_s)}{\partial t} = -\nabla\cdot(\rho_s(1-\phi_t)\boldsymbol{u}_s), \tag{3.51}$$

$$\text{heat conservation:} \quad \frac{\partial}{\partial t}\left(\sum_{n=1,2}\phi_{ne}\,\rho_l U_l + (1-\phi_t)\rho_s U_s\right) = -\nabla\cdot\left(\sum_{n=1,2}\phi_{ne}h_l\rho_l\boldsymbol{u}_l\right) - \lambda\nabla T, \tag{3.52}$$

$$\text{Darcy's law:} \quad \boldsymbol{u}_n - \boldsymbol{u}_s = -\frac{k_{ne}}{\phi_e\mu}\nabla P_n, \tag{3.53}$$

where the inter-porosity flow term Γ, is a function of fluid pressure both in the matrix-blocks and fractures, i.e., $\Gamma = \Gamma(p1,p2)$, is a unique aspect of the dual-porosity concept. All dual-porosity models contain large uncertainties due to the complex conditions in the configuration, distribution, and connectivity of fracture and matrix blocks; ρ_l- is the fluid density representing the actual microscopic density, i.e., fluid mass per unit fluid volume (kg/m^3); the term $\rho_l\phi_{ne}$ is the apparent macroscopic fluid density, i.e. fluid mass per unit bulk volume (kg/m^3); note that the subscript n represens the type of pores, n=1 for the matrix pores and n=2 for fractures; the subscript e represents the effective value of a parameter, for instance, ϕ_e means the effective porosity, while k_e stands for effective permeability; ρ_s and $(1-\phi_t)\rho_s$ are the actual microscopic solid density and apparent macroscopic solid density, respectively; the subscript s -solid phase, as used here, includes both real solid grains and the non-connected pores; both n-th fluid velocity vector $\boldsymbol{u}_n$ and the solid velocity $\boldsymbol{u}_s$ are local volumes, averaged values, with respect to a stationary coordinate, note that for a non-deformable porous media, $\boldsymbol{u}_s = 0$, while for a deformable porous medium, the movement of fluid velocity relative to the moving solid skeleton must be considered (Biot, 1955; Verruijt, 1969, 2008); the term $\phi_n\boldsymbol{u}_n$ is the fluid bulk volumetric flux (fluid-flow rate per unit bulk area; the term $(1-\phi_t)\boldsymbol{u}_s$ represents the solid bulk volumetric flux and ϕ_t is the total porosity.

3.4.2 Water-gas two phase flow [H^2]

Simulation of the unsteady state two phase fluid flow processes was first proposed by West and Garvin in 1954 (Guo et al., 2012), while the earliest demonstration of the concepts relative permeability and capillary pressure, used today, was carried out and documented by Coat et al. (1967). Since then, the theory of multiphase fluid flow has been largely developed and finds wide application in reservoir engineering (Stone, 1973; Pruess et al., 1999; Rutqvist et al., 2002; Xu et al., 2006; Freiboth et al., 2009; Kolditz et al., 2011).

When two immiscible fluids flow through a porous medium (e.g., the two phase system, water-CO_2), the governing equations will be significantly different from those of a single phase flow, under the assumptions that no mass transfer occurs at the boundary between the two phases, and phase equilibrium prevails in the system.

According to Chen et al., 2006, the mass conservation equation Eq 3.43 (mainly advection) for the water component (M^w) can be stated as follows:

$$M^w = \phi(S_l\rho_l X_l^w + S_g\rho_g X_g^w), \tag{3.54}$$

$$F^w = X_l^w\rho_l\boldsymbol{u}_l + X_g^w\rho_g\boldsymbol{u}_g, \tag{3.55}$$

$$q^w = q_l^w + q_g^w, \tag{3.56}$$

where S is the saturation (-); X is the mass fraction (kg/kg); the superscript w denotes for H_2O component; the subscripts l, g stand for liquid and gas phase, respectively.

The combined partial differential equation that accounts for transport of the **water** component, without considering molecular diffusion and hydrodynamic dispersion, can be written as follows:

$$\frac{\partial}{\partial t}\left(\phi\left(X_l^w S_l \rho_l + X_g^w S_g \rho_g\right)\right) = -\nabla\cdot\left\{X_l^w \rho_l\left(-k\frac{k_{rl}}{\mu_l}(\nabla P_l - \rho_l g)\right) + X_g^w \rho_g\left(-k\frac{k_{rg}}{\mu_g}(\nabla P_g - \rho_g g)\right)\right\} + (q_l^w + q_g^w),$$
(3.57)

where k_{rl} and k_{rg} are the relative permeability for liquid and gas phase, respectively (-); g is the gravational accrelation rate (m/s^2).

For **CO_2**: $\quad M^c = \phi(S_l \rho_l X_l^c + S_g \rho_g X_g^c),$ (3.58)

$$F^c = X_l^c \rho_l \boldsymbol{u}_l + X_g^c \rho_g \boldsymbol{u}_g,$$
(3.59)

$$q^c = q_l^c + q_g^c + q_s^c,$$
(3.60)

Combined partial differential form of the transport of **CO_2** component, without considering molecular diffusion and hydrodynamic dispersion, can be expressed as:

$$\frac{\partial}{\partial t}\left(\phi\left(X_l^c S_l \rho_l + X_g^c S_g \rho_g\right)\right) = -\nabla\cdot\{X_l^c \rho_l\left(-k\frac{k_{rl}}{\mu_l}(\nabla P_l - \rho_l g)\right) + X_g^c \rho_g\left(-k\frac{k_{rg}}{\mu_g}(\nabla P_g - \rho_g g)\right)\} + (q_l^c + q_g^c + q_s^c),$$
(3.61)

where the superscript c stands for the CO_2 component.

Heat conservation equations (advection and conduction) as quoted from Pruess et al., 1999:

Heat: $M^h = \phi(S_l \rho_l U_l + S_g \rho_g U_g),$ (3.62)

$$F^h = \sum_{\alpha=l,g} h_\alpha \rho_\alpha \boldsymbol{u}_\alpha - \lambda \nabla T,$$
(3.63)

$$q^h = 0,$$
(3.64)

where the superscript h stands for the heat component; the subscript α denotes for phases (e.g. liquid, gas).

Combined partial differential form of **heat** component transport:

$$\frac{\partial}{\partial t}\left(\phi\left(S_l \rho_l U_l + S_g \rho_g U_g\right) + (1-\phi)\rho_s U_s\right)$$
$$= -\nabla\cdot\left(h_l \rho_l\left(-k\frac{k_{rl}}{\mu_l}(\nabla P_l - \rho_l g)\right) + h_g \rho_g\left(-k\frac{k_{rg}}{\mu_g}(\nabla P_g - \rho_g g)\right)\right) - \lambda\nabla T, \quad (3.65)$$

Based on Chen et al., 2006, **momentum conservation/Darcy's Law** can be written as follows:

$$\boldsymbol{u}_l = -\frac{kk_{rl}}{\mu_l}(\nabla P_l + \rho_l \boldsymbol{g}),$$
(3.66)

$$\boldsymbol{u}_g = -\frac{kk_{rg}}{\mu_g}(\nabla P_g + \rho_g \boldsymbol{g}),$$
(3.67)

In these conservation equations, the relative permeability of liquid and gas phase can be calculated by the van Genuchten-Mualem (1980) model, while capillary pressure can be calculated using the Corey (1954) model.

$$k_{rl} = \sqrt{\hat{S}}\{1 - (1 - [\hat{S}]^{1/m})^m\}^2 \qquad S_l < S_l', \qquad (3.68)$$

$$k_{rl} = 1 \qquad\qquad\qquad S_l \geq S_l', \qquad (3.69)$$

$$k_{rg} = 1 - k_{rl} \qquad\qquad\qquad S_{gr} = 0, \qquad (3.70)$$

$$k_{rg} = (1 - S_e)^2(1 - S_e^2) \qquad S_{gr} > 0, \qquad (3.71)$$

$$P_c = -P_d([\hat{S}]^{-1/m} - 1)^{1-m}, \tag{3.72}$$

Where P_c is the capillary pressure (Pa); P_d is the entry pressure (Pa); m is the exponent; the normalized saturation, $\hat{S} = (S_l - S_{lr})/(S_l' - S_{lr})$; S_l' is the effective liquid saturation and $S_e = (S_l - S_{lr})/(1 - S_{lr} - S_{gr})$.

3.5 Mathematical model for coupled hydro-mechanical process

A mathematical model (eqn. 3.73) involving Biot's coefficient (α) has been established for coupling between fluid flow and mechanical deformation of rocks. In this model, a large value of α simplies a less compressible porous medium. However, if α is less or equal to 1, the grains are considered to be totally incompressible (ITASA, 2009).

Fluid diffusivity in a deformable porous medium can be expressed as,

$$D = \frac{k}{1/B + \alpha^2/\alpha_1}, \tag{3.73}$$

where D is fluid diffusivity (m/s); k is permeability (m^2); B is Biot's modulus (N/m^2), α is Biot's coefficient. In this equation the terms $\frac{1}{B}$ and α_1 are expressed as:

$$\frac{1}{B} = \frac{\phi}{K_f} + \frac{1-\phi}{K_s} - \frac{1-\alpha}{K_s}$$

where K_f is the fluid bulk modulus (N/m^2); K_s is the solid bulk modulus (N/m^2); ϕ is porosity (-). and

$$\alpha_1 = K + 4/3G$$

where K is the drained bulk modulus (N/m^2); G is the shear modulus (N/m^2).

For flow-only calculations (considered as rigid material), fluid diffusivity is expressed as follows:

$$D = k^m B, \tag{3.74}$$

where k^m is the permeability coefficient (or mobility coefficient) of the fluid. This term can also be expressed as:

$$k^m = K_c/\rho_f g, \tag{3.75}$$

Where ρ_f and g are the fluid density and gravity, respectively.

The permeability coefficient k^m used in FLAC^{3D} must be derived after conversions from other forms in literatures, e.g.:

k^m (m^2/Pa/s) = κ (intrinsic permeability, in cm^2) $\times$ 9.9×10^{-2}

k^m (m^2/Pa/s) = k_h (hydraulic conductivity, in m/s) $\times$ 1.02×10^{-6}

k^m (m^2/Pa/s) = permeability k in mD $\times$ 9.8×10^{-13}

3.5.1 Mass balance equations

The governing equations for non-isothermal multiphase flow of water and CO$_2$ in a porous medium have been presented in detail in Chapter 3.4, i.e.:

$$\frac{\partial}{\partial t}\left(\phi\left(X_l^\kappa S_l \rho_l + X_g^\kappa S_g \rho_g\right)\right) = -\nabla \cdot \left\{X_l^\kappa \rho_l\left(-k\frac{k_{rl}}{\mu_l}(\nabla P_l - \rho_l g)\right) + X_g^\kappa \rho_g\left(-k\frac{k_{rg}}{\mu_g}(\nabla P_g - \rho_g g)\right)\right\}$$

$$-\nabla \cdot \left(D_l^\kappa + D_g^\kappa\right) + (q_l^\kappa + q_g^\kappa), \tag{3.76}$$

According to Klubertanz et al., 2003, the mass balance for the solid phase present in the medium can be described as:

$$\frac{\partial}{\partial t}\left((1-\phi)\rho_s\right) = -\nabla \cdot (\rho_s(1-\phi)\frac{d\hat{\boldsymbol{u}}}{dt}), \tag{3.77}$$

where S_l, S_g are the phase saturations for liquid and gas, respectively; X_l^κ, X_g^κ are the mass fractions of component κ in liquid and gas phase, respectively; ρ_l, ρ_g, ρ_s are the densities for the three phases; μ_l, μ_g are viscosities for liquid and gas, respectively; k is the intrinsic permeability of rock; k_{rl}, k_{rg} are the relative permeability of liquid and gas, respectively; $\nabla P_l, \nabla P_g$ are the partial pressure gradients in each phase; $\nabla \cdot$ is the divergence; g is gravity acceleration; D_g^κ, D_l^κ are the diffusion terms of component κ in gas and liquid phases; q_l^κ, q_g^κ are the sink and source terms of component κ in liquid and gas phases; $\hat{\boldsymbol{u}}$ is the displacement of the solid grain; and ϕ is porosity.

Combining the mass balance equations of solids and fluids, the total form of fluid flow in a deformable porous medium can be written as (Bear and Bachmat, 1990; Kolditz, 2002),

$$\frac{\partial}{\partial t}\left(\phi\left(X_l^\kappa S_l\rho_l + X_g^\kappa S_g\rho_g\right) + (1-\phi)\rho_s\right) - \nabla$$
$$\cdot\left\{X_l^\kappa\rho_l\left(-k\frac{k_{rl}}{\mu_l}(\nabla P_l - \rho_l g)\right) + X_g^\kappa\rho_g\left(-k\frac{k_{rg}}{\mu_g}(\nabla P_g - \rho_g g)\right) + \rho_s(1-\phi)\frac{d\hat{\boldsymbol{u}}}{dt}\right\} - \nabla$$
$$\cdot\left(D_l^\kappa + D_g^\kappa\right) + (q_l^\kappa + q_g^\kappa), \tag{3.78}$$

Where the volumetric deformation term (ε_v) couples the mass balance equations with the deformations of the porous media ($d\varepsilon_v/dt = \nabla \cdot (d\hat{\boldsymbol{u}}/dt)$).

3.5.2 Constitutive laws

The changes in fluid mass are related to the changes in other parameters, including pore pressure P, saturation S, mechanical volumetric strains $\varepsilon_v(\varepsilon_{kk})$ and temperature T. The corresponding formulation can be expressed as follows:

$$\frac{1}{B}\frac{\partial P}{\partial t} + \frac{\phi}{S}\frac{\partial S}{\partial t} = \frac{1}{S}\frac{\partial \pi}{\partial t} - \alpha\frac{\partial \varepsilon_v}{\partial t} + \beta\frac{\partial T}{\partial t}, \tag{3.79}$$

where π is the variation in fluid content per unit volume of porous media; β is undrained thermal coefficient, $1/^\circ C$; T is temperature, $^\circ C$; B is Biot's modulus (N/m^2) and α is Biot's coefficient.

The isotropic stress-strain relations for poroelasticity are expressed according to Settari et al. (1999) as follows:

$$\sigma_{ij} - \alpha P\delta_{ij} = 2G\varepsilon_{ij} + \left(\frac{2Gv}{1-2v}\right)\varepsilon_{kk}\delta_{ij}, \tag{3.80}$$

where σ_{ij} is the total stress, is also expressed as $\sigma_{ij} = \sigma_{ij}' + \alpha P$, in which σ_{ij}' is the effective stress; and ε_{ij} the strain is expressed as $\varepsilon_{ij} = \frac{1}{2}\left(u_{i,j} + u_{j,i}\right)$, where u is the solid displacement vector; G and v are the shear modulus of the drained elastic rock skeleton and the Possion's ratio respectively; δ_{ij} is the Kronecker delta; P is pore pressure; α is Biot's coefficient $\alpha = 1 - \frac{K}{K_S}$, where K is the bulk modulus of the porous medium under drained state, and K_s is the bulk modulus of the solid grain.

Considering the thermal effect, Wang, 2000, expressed the relationship between effective stress and strain (under small strain conditions) as:

$$\sigma_{ij} - \sigma_{ij}^o - \alpha(p - p^o)\delta_{ij} = 2G\left(\varepsilon_{ij} - \varepsilon_{ij}^T\right) + \left(K - \frac{2G}{3}\right)(\varepsilon_{kk} - \varepsilon_{kk}^T), \tag{3.81}$$

where the superscript o refers to the initial state, T is under thermal mode condition; K is the bulk modulus of the drained elastic rock skeleton as in Eq 3.80.

By introducing compressibility coefficient (also called the Skempton coefficient, B_s) into the fluid content (π)-stress (σ) relationship:

$$2G\pi = \alpha \left(\frac{1-2v}{1+v}\right)(\sigma_{kk} + \frac{3P}{B_s}), \tag{3.82}$$

The elastic moduli (K and v) used in the above equation varies greatly between drained and undrained circumstances. Under undrained state, according to Plotkowiak (2005), the bulk modulus (K_u) and Possion's ratio (v_u) are as follows:

$$K_u = K[1 + \frac{\alpha^2 K_f}{\phi K + (1-\alpha)(\alpha-\phi)K_f}], \tag{3.83}$$

$$v_u = \frac{3v + B_s(1-2v)(1-(K/K_S))}{3 - B_s(1-2v)(1-(K/K_S))}, \tag{3.84}$$

In eqn. 3.84, B_s is the linkage of the drained and undrained solid properties and the fluid properties, where

$$B_s = \frac{\alpha K_f}{[\alpha - \phi(1-\alpha)]K_f + \phi K} = \frac{3(v_u - v)}{\alpha(1-2v)(1+v_u)}, \tag{3.85}$$

Substitution of the fluid mass balance in the constitutive equations produces the following fluid constitutive formulation:

$$\frac{1}{B}\frac{\partial p}{\partial t} + \frac{\phi}{S}\frac{\partial S}{\partial t} =$$

$$\frac{1}{S}[-\nabla \cdot \left\{X_l^\kappa \rho_l \left(-k\frac{k_{rl}}{\mu_l}(\nabla P_l - \rho_l g)\right) + X_g^\kappa \rho_g \left(-k\frac{k_{rg}}{\mu_g}(\nabla P_g - \rho_g g)\right) + \rho_s(1-\phi)\frac{d\boldsymbol{u}}{dt}\right\} - \nabla \cdot (D_l^\kappa + D_g^\kappa)$$

$$+ (q_l^\kappa + q_g^\kappa)] - \alpha\frac{\partial \varepsilon_v}{\partial t} + \beta\frac{\partial T}{\partial t}, \tag{3.86}$$

3.5.3 Failure criteria

The in-situ stress field and fluid pressure can cause induced shearing and hydraulic fracturing or reactivation of faults and their orientation in the caprock. CO_2-injection will lead to the buildup of pore pressure in the reservoir and bottom of caprock, thus causing a decrease in the effective stress. When predicting the integrity of the caprock for a specific CO_2 sequestration project, two main mechanical failure mechanisms are considered: 1) tensile and 2) shear failure. According to Rutqvist et al. (2002), potential failure of the caprock can be analyzed using the critical pressure initializing tensile and shear failures. The potential for tensile failure is calculated using the conservative assumption that a tensile fracture could occur when the pore fluid pressure exceeds the minimum principal stress:

$$P > \sigma_3 \text{ or } P > \sigma_3/n, \tag{3.87}$$

where P is the pore pressure (Pa); σ_3 is the minimum principle stress (Pa); and n is the safety factor (usually, $n = 1.25$).

According to Jaeger and Cook (1979), the condition for shear failure of pre-existing fractures or faults in the principal stress plane can be defined based on the Coulomb criterion as follows:

$$|\tau| = -(\sigma_m + P_{sc})\sin\varphi' + C'\cos\varphi', \tag{3.88}$$

where τ is the maximum shear stress (Pa); σ_m is the mean stress (Pa); P_{sc} is the critical shear slip pore pressure (Pa); C' and φ' are the internal cohesion and internal friction angle of the faults, respectively. φ' is usually in the range from 15 to 30° (Byerlee, 1978; Rutqvist et al., 2002; Streit and Hillis, 2004).

Expressing $|\tau|$ and σ_m in the form of the principal stress:

$$|\tau| = \frac{\sigma_1 - \sigma_3}{2}, \tag{3.89}$$

$$\sigma_m = \frac{\sigma_1 + \sigma_3}{2}, \tag{3.90}$$

When pore pressure (P) exceeds the critical slip failure pressure (P_{sc}), reactivation of pre-existing faults or fractures will occur, i.e.

$$P > -\frac{\sigma_1 + \sigma_3}{2} - \frac{\frac{\sigma_1 - \sigma_3}{2} - C' \cos \varphi'}{\sin \varphi'} = P_{sc}, \tag{3.91}$$

Based on the calculation equations in Hou et al. (2009), the maximal storage pressure necessary to avoid shear failure of the reservoir can be written as follows,

$$max\, P = P_r + max\Delta P_t = P_r + \frac{UCS - \sigma_H' + N_\phi * \sigma_v'}{\gamma - \alpha(1 - N_\phi)}, \tag{3.92}$$

where P_r is the primary reservoir pressure (Pa); σ_v' is the primary effective vertical stress (Pa); σ_H' is the primary effective maximum horizontal stress (Pa); the uniaxial compressional strength of the rock $UCS = 2C' * \frac{\cos\varphi'}{\sin\varphi'} = 2c\sqrt{N_\phi}$, in which N_ϕ is the triaxial factor in dimensionless, $N_\phi = \frac{1+sin\varphi}{1-sin\varphi}$; stress path $\gamma = \alpha \frac{1-2\nu}{1-\nu}$; and α, ν are Biot's coefficient and Possion's ratio, respectively.

The safe maximum storage pressure must satisfy both the Mohr-Coulomb's shear failure criterion for the reservoir rock and the integrity criterion for the caprock. Therefore, the smallest values from Eqs 3.87, 3.91 and 3.92 can be used as the most reasonable estimation.

A large number of variables for a specific site may affect the changes and distribution of pore pressure, thus the failure mechanism of the reservoir and caprock, such as Young's modulus of reservoir and caprock, Poisson's ratio, porosity, permeability, geometry of model, initial stress regime (extensional, compressional, slip state), lithostatic vertical total stress gradient, the injection pressure and so on (Rohmer and Bouc, 2010). In an extensional stress regime (when $S_v > S_H > S_h$), where, σ_2 and σ_3 are in the lateral direction, σ_1 is in the vertical direction, the faults located overlying and underlying the injected layer tend to be reactivated, while in a compressional stress regime (when $S_H > S_h > S_v$), where, σ_1 and σ_2 are in the lateral direction, σ_3 is in the vertical direction. Under this condition, compressional thrust faults easily occur and the pre-existing faults in the reservoir are easily to reactivated (Soltanzadeh and Hawkes, 2009; Rohmer and Bouc, 2010).

Mohr-Columb failure criteria with the failure envelop line (Fig. 3.20) is often used to analyze the shear failure of one material, which can be written as:

$$\tau_f = \sigma' tan\varphi' + C', \tag{3.93}$$

where τ_f is the shear stress when the shear failure occurs (Pa); σ' is the effective principle stress (Pa); C' and φ' are the internal cohesion and internal friction angle of the faults, respectively.

At the time of failure, the relationship between the effective maxium (σ_1') and minimum principal stresses (σ_3') can be presented as:

$$\sigma_1' = \sigma_3' tan^2(45^o + \varphi'/2) + 2C'tan(45^o + \varphi'/2), \tag{3.94}$$

When the effective mean stress (σ_m') is used to evaluate the yield of the material, it can be rewritten as:

$$\sigma_1' - \sigma_3' = \sigma_m' sin\varphi' + 2C'cos\varphi', \tag{3.95}$$
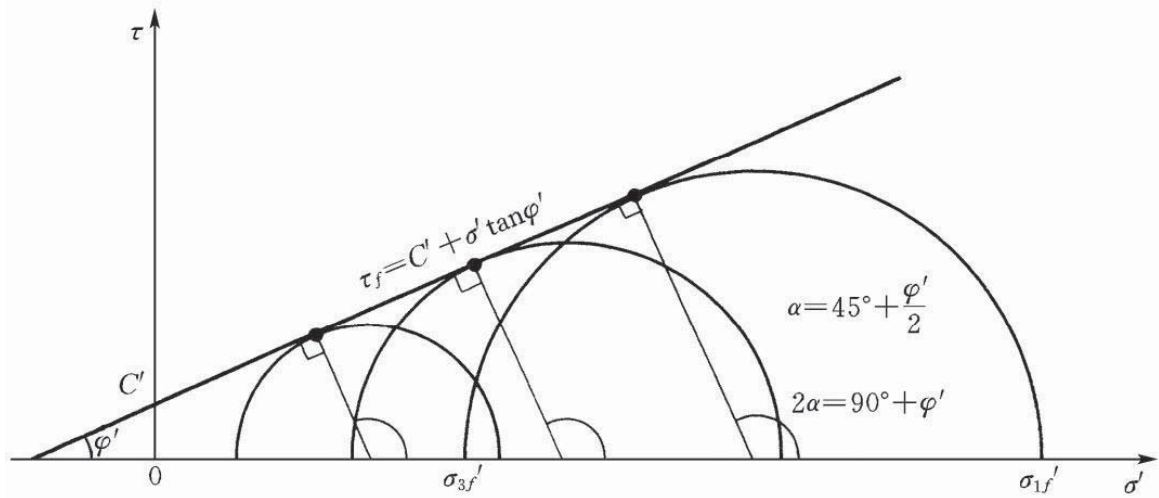
Fig. 3.20 The mohr circle under failure conditions and its envelop line (modified after Meyer, 2012)

3.6 Mathematical model for reactive fluid flow

3.6.1 Mass conservation of chemical components in liquid phase

Mass conservation of chemical components in the liquid phase can be written as:

$$\frac{\partial}{\partial t}\left(\phi S_l C_l^i\right) = -\nabla \cdot \{C_l^i\left(-k\frac{k_{rl}}{\mu_l}\left(\nabla P_l - \rho_l g\right)\right) - (\hat{\tau}\phi S_l D_l)\nabla C_l^i\} + (q_l^i + q_g^i + q_s^i), \tag{3.96}$$

where ϕ is porosity (-); S is saturation (-); C is concentration of chemical component (mol/L); k is permeability (m^2); k_{rl} is relative permeability of liquid phase (-); μ is viscosity (cP); P is pressure (Pa); ρ is density (kg/m^3); g is gravity acceralation rate (m/s^2); $\hat{\tau}$ is tortuosity (-); D is diffusion coefficient, (m^2/s); q is sink (kg); $\nabla \cdot$ is divergence (-); ∇ is gradient (-); superscript i is chemical ion type; subscript l, g, s are for liquid, gas and solid phases respectively.

If the flow path is long enough, the water (or saline fluid) attains equilibrium with the rock and the composition of the aqueous phase will not change with time (Edmunds et al., 1982). In other words, at a sufficient distance along the flow path, there is no change in the composition of the pore fluid resulting from n reactions between fluid and rock. In a multiple minerals system, the terminal concentration of component i can be written in the following form:

$$C_f^i = \sum_{m=1}^{n} A_m \bar{k}_m C_m^i / \sum_{m=1}^{n} A_m \bar{k}_m, \tag{3.97}$$

where C_m^i is concentration of component i necessary for attaining equilibrium between pore fluid and the mineral m (mol/L); C_f^i is the final concentration of component i in pore water at some point along its flow path (mol/L); A_m is the specified surface area of mineral m (m^2); and $\bar{k}_m$ represents the kinetic rate constant for mineral m (m/s) and n is the number of minerals.

In a complex system of mineral assemblage, where more than one mineral contribute the same ion to the pore fluid, the least stable mineral in the system will dissolve once the terminal concentration for the component ion i reached (Edmunds et al., 1982). The behavior of thermodynamically unstable mineral

mixtures in the presence of a moving fluid leads to dissolution of the least stable minerals and precipitation of the more stable phases. Although the system is initially not in its most stable state, it will evolve towards a more stable state (with respect to the initial pore fluid composition), as the meta-stable mineral is removed, one after another.

3.6.2 Equation of state for CO$_2$

At first, the Redlich–Kwong equation was applied in TOUGH2 (Spycher and Pruess, 2005). Afterwards, there was a small modification in ECO2N module, by which CO$_2$ molar volumes may be computed using a tabular EOS based on Altunin's correlation (Pruess, 2005). In the field of physics and thermodynamics, the Redlich–Kwong equation of state is an empirical equation that changes with temperature, pressure, and volume of gases.

The Redlich-Kwong equation of state can be written as follows:

$$P = \frac{RT}{V_m - b} - \frac{a}{\sqrt{T}V_m(V_m + b)},$$

(3.98)

where P is the gas pressure (Pa); R is the gas constant (-); T is temperature (°C); V_m is the molar volume (V/n) (L/mol); a and b are constants used to calibrate attractive potential of molecules and volume, respectively.

At critical points of temperature and pressure, Redlich-Kwong defined the compressibility factor, Z_c, as follows:

$$Z_c = \frac{PV_m}{RT} = \frac{V_m}{V_m - b} - \frac{a}{RT(V_m + b)},$$

(3.99)

Considering Z_c at critical point, the parameters a and b in equation (6.18) are often given as:

$$a = \frac{0.4275R^2 T_c^{5/2}}{P_c}, b = \frac{0.4275RT_c}{P_c}, Z_c = 1/3,$$

(3.100)

where Tc and Pc are the temperature and pressure at the critical point, respectively.

3.6.3 Chemical reaction equations (Equilibrium and Kinetics)

Thermodynamic and kinetic mechanisms can be used to describe chemical reactions. However, both have advantages and challenges. Thermodynamics is particularly useful for predicting whether a chemical reaction in a given system can possibly take place or not. However, it does not relate to the reaction time and reaction rate of the chemical process. The aqueous complexation and gas solubility in aqueous phase can be described at local equilibrium. Dissolution and precipitation of minerals can be controlled either under local equilibrium (thermodynamics theory) or kinetic conditions (Andre et al., 2006). Generally, dissolution of primary minerals is considered to be kinetically-controlled. The kinetic rate constants and specific surface areas are used. Similarly, precipitation of secondary minerals is described using the same equation as dissolution (Xu et al., 2007). Both precipitation and dissolution processes of a specific mineral are largely determined by its solubility. When the activity of the dissolving component is smaller than its solubility, the aqueous phase is undersaturated with respect to the component, and the dissolution process will continue, until attainment of equilibrium between activity and solubility.

3.6.3.1 Thermodynamics mechanisms

The van't Hoff equation is the basis of chemical thermodynamics, which relates the change in the equilibrium constant, $\widehat{K}$, of a chemical equilibrium to the change in temperature, T, given the standard enthalpy change, $\Delta H^{\ominus}$, as follows:

$$\frac{dln\widehat{K}^{\ominus}}{dT} = \frac{\Delta_r H_m^{\ominus}}{RT^2}, \tag{3.101}$$

where R is the gas constant (-); superscript $\ominus$ stands for standard state, which is, 0$^{\text{o}}$C and 1 atm; subscript m stands for minerals,.

Mineral saturation ratio can be expressed as,

$$\Omega_m = X_m^{-1}\gamma_m^{-1}\widehat{K}_m^{-1}\prod_{j=1}^{Nc} C_j^{vmj}\gamma_j^{vmj} \qquad m = 1 \dots Np, \tag{3.102}$$

where X_m is the mole fraction of the m-th mineral phase (-); γ is the thermodynamic activity coefficient (-), for pure mineral phases, X_{m} and γ_m are taken equal to one; $\widehat{K}$ is the equilibrium constant (-); N_c is the number of chemical components(-); superscript vmj stands for stoichiometric number of component j in a chemical reaction (-); subscript m is the equilibrium mineral index (-).

(1) Activity and activity coefficient

For a real solution, the activity of an aqueous species is used instead of concentration in thermodynamic calculations. It is equivalent to the product of the activity coefficient and molar concentration (mol/kg H$_2$O). Except for aqueous CO$_2$, the activity coefficients for other aqueous species can be calculated using the extended Debye-Hückel equation or Pitzer model (Helgeson et al., 1981; De Lucia et al., 2012). For CO$_2$ (aq), activity coefficient is a function of pressure, temperature and salinity (Xu et al., 2001). The activities of mineral phases and pure H$_2$O are assumed to be one in the simulation processes (Xu et al., 2001).

Activity of aqueous species ($\bar{\bar{\alpha}}$) can be defined as:

$$\bar{\bar{\alpha}}_j = \gamma_j C_j, \tag{3.103}$$

where γ is activity coefficient (-);C is concentration of a chemical component (mol/L); subscript j stands for chemical component (-).

Activity coefficient (γ) of charged aqueous species:

$$
\begin{aligned}
log(\gamma_j) = &-\frac{A_\gamma \tilde{z}_j^2 I^{0.5}}{1 + \mathring{a}B_\gamma I^{0.5}} + log(1 + 0.0180153m) \\
&- \left[b_{NaCl}\eta\frac{\tilde{z}_j^2}{r_{e,j}} + b_{Na+,Cl-} - 0.19(|\tilde{z}_j| - 1)\right] I,
\end{aligned} \tag{3.104}
$$

where

- A_γ , B_γ , b_{NaCl}, $b_{Na+,Cl-}$,m ,are Debye-Huckel constants (-),
- $\tilde{z}$ is the ion charge (-),
- r_e is the ion radium (m^2),
- η is a constant equal to 1.66027 (Å cal/mol),
- I is the ion strength, $I = 0.5\sum_j c_j \tilde{z}_j^2$,

- subscript j is the aqueous species index (-),
- å stands for Debye-Huckle parameter, which is related with radius and charge of ion.

Activities coefficient (γ) of the neutral CO_2 (aq) species:

$$log(\gamma_{CO2}) = \left(-1.0312 + 0.0012806T + \frac{255.9}{T}\right)I - (0.4445 - 0.001606T) * (\frac{I}{I+1}), \qquad (3.105)$$

where T is temperature (^oC) .

(2) Aqueous complexation

These aqueous complexation reactions are assumed to be at local equilibrium. The concentrations of aqueous complexes (C_i) can be expressed as functions of the concentrations of basis species (C_j):

$$C_i = \widehat{K}_i^{-1}\gamma_i^{-1}\prod_{j=1}^{Nc} C_j^{vij}\gamma_j^{vij}, \qquad (3.106)$$

where:

- C_i - molal concentration of the i-th aqueous complex (mol/L);
- C_j - molal concentration of the j-th basis species (mol/L);
- γ_i and γ_j - thermodynamic activity coefficients of species i and j (-);
- $\widehat{K}$ - the equilibrium constant (-),
- superscript vij stands for stoichiometric number in a chemical reaction (-).

(3) CO_2 solubility in water

Reactions involving aqueous and gaseous phases can be assumed to be at equilibrium state. In this regard, CO_2 solubility in water can be described according to mass-action law:

$$P_g\omega_g\widehat{K}_g = C_l\gamma_l \quad (CO_2(aq) \leftrightarrow CO_2(g)), \qquad (3.107)$$

$$log\widehat{K} = b_1 lnT + b_2 + b_3T + \frac{b_4}{T} + \frac{b_5}{T^2}, \qquad (3.108)$$

$$ln\omega = \left(\frac{a}{T^2} + \frac{b}{T} + c\right)P + (\frac{d}{T^2} + \frac{e}{T} + f)\frac{P^2}{2}, \qquad (3.109)$$

where,
- P- pressure (Pa),
- ω-fugacity coefficient of CO_2 (-),
- $\widehat{K}$-equilibrium constant (-),
- C-chemical concentration (mol/kg H_2O),
- γ- activity coefficient (-),
- T- temperature (^oC),
- b1, b2, b3, b4, b5 and a, b, c, d, e, f are fitted constants to calculate $\widehat{K}$ and ω (Table 3.7).
- subscripts g and l stand for gas and liquid phase, respectively.
-

Table 3.7 Parameters used in the calculation of $\widehat{K}$ and ω (Xu et al., 2004a)

parameters	value	parameters	value
b1	65.48	a	-1.43087×10^3
b2	-4.255×10^2	b	3.598
b3	-5.301×10^{-2}	c	-2.27376×10^{-3}
b4	2.401×10^4	d	3.47644
b5	-1.22×10^6	e	-1.04247×10^2
		f	8.46271×10^{-6}

(4) Mineral dissolution and precipitation at local equilibrium

According to thermodynamics theory, the saturation index (SI) determines the dissolution and precipitation of various minerals:

$$SI = \lg(\Omega) = \log(IAP/Ksp), \tag{3.110}$$

where SI - the mineral saturation index (-); Ω - mineral saturation ratio (-); IAP - the ion activity product (-); K_{sp} - the solubility product constant under a certain temperature (-).

For the mineral A_nB_m, the equilibrium equation can be written as follows: $A_nB_m(s) \leftrightarrow nA^{m+}_{(aq)} + mB^{n-}_{(aq)}$

$$\hat{K} = \frac{(\bar{\bar{\alpha}}_{A^{m+}})^n (\bar{\bar{\alpha}}_{B^{n+}})^m}{\bar{\bar{\alpha}}_{A_nB_m}}, \tag{3.111}$$

$$K_{sp} = (C_{A^{m+}})^n \ (C_{B^{n-}})^m, \tag{3.112}$$

$$(\bar{\bar{\alpha}}_{A^{m+}})^n = (C_{A^{m+}})^n \times (\gamma_{A^{m+}})^n, \tag{3.113}$$

where $\hat{K}$ - the equilibrium constant (-), $\bar{\bar{\alpha}}$ represents activity of aqueous species, C represents ion concentration. According to the definition, the activity of solid is 1. If the concentration of liquid is very low, ion activity coefficient can be regarded as 1, and the equilibrium equation can be written as concentration form. But for real solutions, when the concentration of the solution is not low, and ion activity coefficient should be used in the modified equilibrium constant.

$$\hat{K} = \frac{(C_{A^{m+}})^n \ (C_{B^{n-}})^m}{C_{A_nB_m}} \times \frac{(\gamma_{A^{m+}})^n (\gamma_{B^{n-}})^m}{\gamma_{A_nB_m}}, \tag{3.114}$$

When $SI < 0$ ($IAP < K_{sp}$), the mineral in the formation water is not at equilibrium state and tends to dissolve; when $SI = 0$ ($IAP = K_{sp}$), the mineral and formation water are at an equilibrium state; when $SI > 0$ ($IAP > K_{sp}$), the mineral tends to precipitate. Generally, for an underground water system, it is common that $SI \geq 0$, as the precipitation of minerals needs the nucleation free energy to overcome the anti-nucleation resistance. The nucleation of minerals under general temperature state is very difficult, requiring the addition of atoms or molecules to a nucleus and the action of saturated driving force (Swanson, 1977). Furthermore, precipitation of secondary minerals only occur when $SI > 0$. When the SI reaches a critical value, the precipitation of the mineral will occur.

3.6.3.2 Kinetic mechanisms

Arrhenius's equation expresses the dependence of the rate constant $\bar{k}$ in a chemical reaction on the temperature T (in Kelvin) and forms the basis of kinetic reactions:

$$\frac{dln\bar{k}}{dT} = \frac{E_a}{RT^2}, \tag{3.115}$$

where E_a - the activation energy (J); R - the gas constant (-).

Based on Lasaga et al. (1994), the reaction rate of mineral dissolution or precipitation can be expressed by:

$$r_m = f(C_1, C_2, \dots, C_{N_c}) = \pm \bar{k}_m A_m |1 - \Omega_m^\theta|^\eta \quad m = 1 \dots Np, \tag{3.116}$$

where r is the dissolution/ precipitation rate of a mineral, positive values of r reveal dissolution, and negative for precipitation; $\bar{k}$ is the rate constant (in moles per unit mineral surface area and unit time) which is temperature and pH dependent (-); A is the specific reactive surface area per kg H_2O (m²); Ω_n is the kinetic mineral saturation ratio (-); θ and η are parameters determined from experiments (-), and

usually considered unity; N_c and Np are the number of chemical and mineral components, respectively and the subscript m is mineral index for the kinetic rate condition (-).

(1) Reaction rate constant

The reaction rate constant, $\bar{k}$, used in the above equation, depends mainly on temperature, but can also be affected by pH, reaction mechanism (acid, neutral and base) and aqueous composition. Arrhenius equation (Lasaga, 1984; Steefel and Lasaga, 1994) can be used to describe the temperature dependent rate constant of a specific mineral-$\bar{k}_m$:

$$\bar{k}_m = \bar{k}_{25} \, exp\left[\frac{-E_a}{R}\left(\frac{1}{T} - \frac{1}{298.15}\right)\right],$$
(3.117)

where $\bar{k}_{25}$ is the rate constant at 25 °C (-); E_a - the activation energy (J); R - the gas constant (-); T - temperature (°C).

When the effect of pH is considered, the reaction rate constant should be modified to k'_m:

$$k'_m = \bar{k}_m (10^{-pHc}/10^{-pH1})^{slope1} \qquad (pHc < pH_1),$$
(3.118)

$$k'_m = \bar{k}_m (10^{-pHc}/10^{-pH2})^{slope2} \quad (pHc > pH_2),$$
(3.119)

where superscripts $pHc, pH1, pH2$ are current, below and above which the rates are adjusted using *slope1* and *slope 2*, respectively; *slope1* and *slope 2* are two different gradients of the log ($\bar{k}_m$) versus pH.

And when the effect of reaction mechanism is considered (Lasaga et al., 1994; Palandri and Kharaka, 2004), reaction rate constant should be modified to $\bar{\bar{k}}$.

$$\bar{\bar{k}} = \bar{k}_{25}^{nu} \exp\left[\frac{-E_a^{nu}}{R}\left(\frac{1}{T} - \frac{1}{298.15}\right)\right] + \bar{k}_{25}^{H} \exp\left[\frac{-E_a^{H}}{R}\left(\frac{1}{T} - \frac{1}{298.15}\right)\right] a_H^{n_H}$$
$$+ \bar{k}_{25}^{OH} \exp\left[\frac{-E_a^{OH}}{R}\left(\frac{1}{T} - \frac{1}{298.15}\right)\right] a_{OH}^{n_{OH}},$$
(3.120)

where the superscripts *nu, H, OH* signify that the reaction is under neutral, acid and base mechanism, respectively; and n is the power term.

The most complex form of reaction rate constant is the expression considering multiple reaction mechanisms and multiple species (the addition of many species may affect the reaction rate greatly):

$$\bar{\bar{k}} = \bar{k}_{25}^{nu} \exp\left[\frac{-E_a^{nu}}{R}\left(\frac{1}{T} - \frac{1}{298.15}\right)\right] + \sum_i \bar{k}_{25}^{i} \exp\left[\frac{-E_a^{i}}{R}\left(\frac{1}{T} - \frac{1}{298.15}\right)\right] \prod_j a_{ij}^{n_{ij}}$$
(3.121)

where i represents the additional reaction mechanisms (acid and base); j represents the species considered in the aqueous phase, which affects the reaction rate.

3.6.4 Fluid flow changes by chemical reactions

(1) Change in porosity

Variations in the mineral volume fraction caused by chemical reactions allow the changes in porosity. The porosity (ϕ) in the medium (fracture or porous media) can be calculated using the following equation:

$$\phi = 1 - \sum_{m=1}^{n} fr_m - fr_u,$$
(3.122)

where n is the number of minerals; fr_m and fr_u are volume fraction of the reactive mineral m in the rock and volume fraction of the nonreactive mineral u, respectively.

(2) Change in permeability

The changes of porosity can result in changes of permeability (k). The simplified cubic law can be used to describe the relationship between porosity and permeability (Steefel and Lasaga, 1994):

$$k = k_i(\frac{\phi}{\phi_i}),$$

(3.123)

where, k_i and ϕ_i are initial permeability and porosity, respectively.

4. Simulation of water-CO$_2$ (two phase) fluid flow in saline formations in the Ordos Basin [H^2]

Storage of CO$_2$ into deep geological formations is achieved by its injection into a well. The lower section of the well, located in the storage zone, is either perforated or covered with a permeable zone to enable CO$_2$ to enter into the surrounding formations (IPCC, 2005). The perforated interval is usually 10–100 m thick, up to the permeability and thickness of the reservoir formations. Injection of fluids increases the reservoir pressure, particularly in the near well region, allowing CO$_2$ to enter the pore spaces which were originally occupied by in situ formation fluids, e.g. water, oil or natural gas (Zhou et al., 2010; Cihan et al., 2013). The amount and spatial distribution of pressure buildup in the reservoir or caprock formations relate with the injection rate, permeability, thickness, geological structure, boundary conditions (i. e. open or closed), injection well patterns, etc (Heath et al., 2014). Besides, pressure buildup is also influenced by the presence of permeability barriers and geometry of the regional underground water (hydro-geological) system (IPCC, 2005, 2007).

Two stages can be used to describe the migration of the CO$_2$ plume in a deep saline formation: the injection and post-injection period (Kabera and Li, 2011). The migration and distribution pattern of CO2 are complex and varied during these two periods, and can only be analysed by simulation.

Injection period: Supercritical CO$_2$ (see white region in Fig. 4.1) is injected into a deep saline formation at high flow rate. It displaces the in situ brine (dark blue parts in Fig. 4.1) to an irreducible saturation. Due to buoyancy, the injected CO$_2$ forms a gravity tongue (Szulczewski, 2009).

Post-injection period: Once injection is stopped, the CO$_2$ plume continues to migrate due to buoyancy and the hydraulic gradient. At the trailing edge of the plume, CO$_2$ is trapped in residual form (light blue part in Fig. 4.1). At the leading edge of the plume, migration continues laterally and plume thickness continuously decreases until all the CO$_2$ is trapped (Szulczewski, 2009).
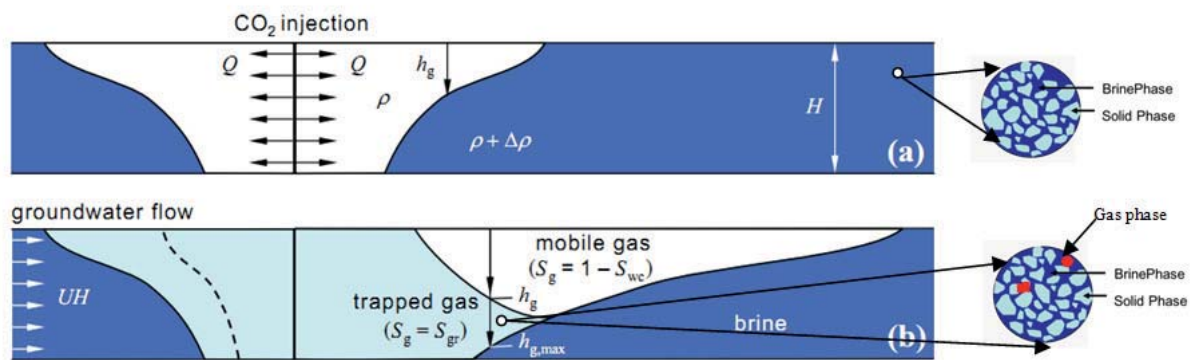
Fig. 4.1 Conceptual model of CO$_2$ migration during two different periods: (a) injection period; (b) post-injection period (after Szulczewski, 2009)

4.1 Modeling approach for two phase fluid flow

The TOUGH2MP code has been used in this dissertation to simulate the two phase (CO$_2$-water) fluid flow processes for CO$_2$ sequestration in a saline formation. TOUGH2MP is a massive parallel version of the previous TOUGH2 code, designed for efficient computation during the simulation of isothermal and non-isothermal multiphase multicomponent fluid flow in a one, two or three-dimensional porous and fractured medium (Zhang et al., 2008; Gou et al., 2014).

Integral finite difference method (FDM) is used for space discretization (Pruess et al., 1999). For each volume element (grid block), there are NEQ equations (component number κ = 1, 2 ..., NEQ; usually, NEQ = NK + 1 for non-isothermal condition), where NEQ stands for the number of equations, NK is the

number of components. Therefore, a geological model with NEL grid blocks has a total number of NEL×NEQ coupled non-linear equations, where NEL is the number of elements. The unknowns are the NEL×NEQ independent primary variables {x_i; i = 1, 2 ..., NEL×NEQ}, which completely define the state of the flow system at time step t^{k+1}. These equations are solved by Newton/Raphson iteration. Iteration is continued until the residuals $R_n^{\kappa,k+1}$ are reduced below a preset convergence tolerance like 10^{-5} (Pruess et al., 1999).

4.2 Numerical model setup and parameters

4.2.1 System geometry

The simulations in this thesis are based on the CO$_2$ sequestration project in the Ordos Basin in China (SHENHUA Group, personal communication, Oct 2012). To study the two phase (water-CO$_2$) fluid flow processes, a simplified 3D model was set up (1/4 model), with a length of 1 km in the horizontal direction and 830 m in the vertical direction. The top and bottom of the model are at depths -1690 and -2400 m, respectively (Fig. 4.2). Grids in the near wellbore region are fine, but gradually increase in size with distance away from the borehole.

The simulations consider four aquifer layers suitable for CO$_2$ injection, with thickness 10, 10, 30 and 15 m from bottom to top, respectively. Their corresponding injection points are at -2242.3, -2175.9, -1877.1 and -1694.5 m, respectively (for geometrical details, see Fig. 4.2). In this simulation model, the layers are simply assumed to be parallel and horizontal. The entire vertical extent of reservoir-caprock formations is assumed to measure about 830 m thick, with the thinner sandstone (aquifer) and siltstone layers of relatively high permeability sandwiched by the thicker mudstone units of lower permeability. The respective thicknesses of the formations (mudstone, siltstone and aquifer sandstones) were determined from the actual drilling well logging data of one injection and two monitoring wells. They were simplified lumped into the layers in this model. Aquifer 1 hosting the injection point A09 is 15 m thick. It is overlaid by a thick caprock layer of low permeable mudstone and directly underlaid by a thin layer of relatively high permeable siltstone. Aquifer 2, contains the injection point A020 and is vertically 30 m thick. It is overlaid and underlaid by mudstone layers of thickness 130 and 230 m, respectively. Aquifer 3, with injectin point A033, has a vertical thickness of 10 m. It is underlaid by a layer of mudstone with 60 m thick, and a very thin caprock layer of mudstone, 15 m thick. Aquifer 4, with injection point A036 is underlaid by a layer of siltstone of 25 m vertical thickness. It is overlaid by a layer of mudstone, 60 m thick (Liu et al., 2014a).
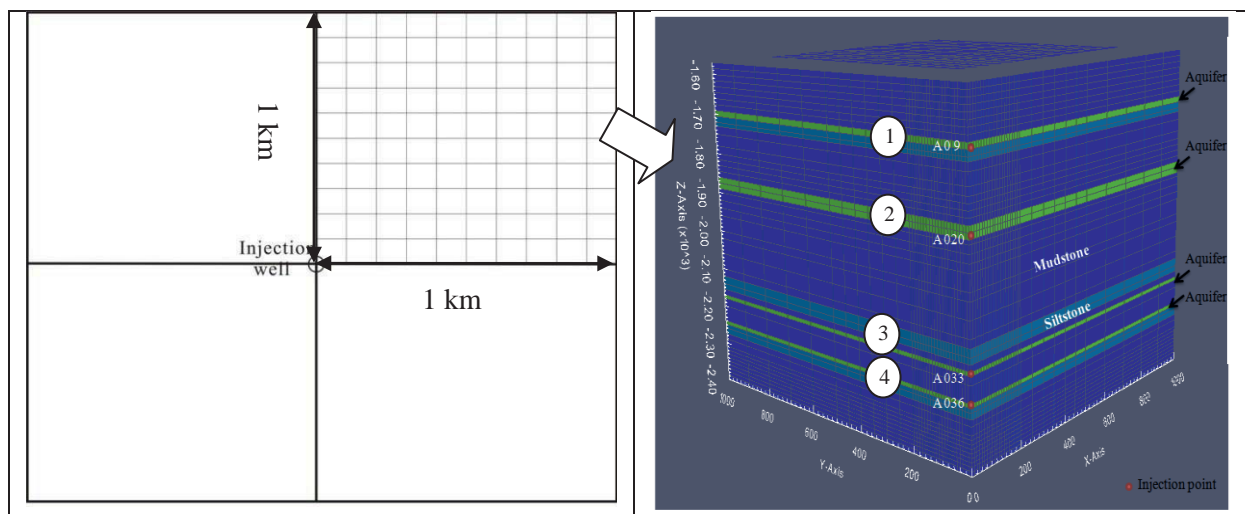
Fig. 4.2 Simplified plane and 3D geological model for the Ordos CCS project with a distance of 1 km (1/4 model) (Liu et al., 2014a)

4.2.2 Boundary conditions

Two boundary conditions can be considered in the two phase, CO$_2$-water, fluid flow system: (1) closed boundary, which means that no heat or mass flux is allowed to pass through any of the boundaries; (2) open boundary-this boundary is fixed at hydrostatic pressure, thus allowing fluids flow into and out of the domain so as to avoid overpressure damage to the formation. The latter situation is more reliable and closer to the natural condition of the reservoir.

4.2.3 Initial conditions

Initial conditions of the multilayered reservoir-cap rock system are critical for fluid flow and distribution characteristics of different phases. In the base case simulation study of CO$_2$-water two phase system, all the initial conditions are prescribed in Table 4.1, including the rock skeleton properties (e.g. thickness of the various layers, their porosity, permeability, density, specific heat, thermal conductivity and compressibility), formation fluid characteristics (e.g. saturation, fluid type, salinity, temperature and pore pressure), injection scheme (injection rate, injection fluid temperature, injection fluid enthalpy and etc.). A fully water saturated condition is prescribed before CO$_2$ injection (Liu et al., 2014a). Density, viscosity, and solubility of CO$_2$ in water are considered functions of pressure and temperature (Span and Wagner, 1996). Besides, vapor-liquid equilibrium property of water is assumed.

Table 4.1 Formation, injection condition parameters for CO$_2$-water system in base case

Parameter	Value
Geological Formation	
Thickness	830 m
Porosity	$\phi_{sandstone}=0.30$ $\phi_{siltstone}=0.08$ $\phi_{mudstone}=0.01$
Permeability	$k_{sandstone}=50$ mD $k_{siltstone}=1$ mD $k_{muddstone}=1\mu$D
Vertical and horizontal permeability ratio	$k_v = k_h$
Rock grain density	$\rho_{sandstone} = 2450$ kg/m^3 $\rho_{siltstone} = 2500$ kg/m^3 $\rho_{muddstone} = 2400$ kg/m^3
Rock specific heat	1000 J/kg/ ^{o}C
Thermal conductivity	2.1 W/m/^{o}C
Compressibility	4.5×10^{-10} Pa^{-1}
Initial Hydrogeological Condition	
Fluid in pore spaces	All H$_2$O
Temperature	75 ^{o}C
Pressure	Hydrostatic pressure
salinity	0.91% NaCl
Injection Condition	
Formation map-view area	4 km^2
Enthalpy of injected CO$_2$	508 kJ/kg
Injection rate	0.1981 kg/s
Injection strategy	Four layers simultaneously

The correlations among the permeability, porosity, irreducible water saturation and maximum residual gas saturation are described by Holtz (2002):

$$\phi = (\frac{k}{7 \times 10^7})^{1/9.606}, \tag{4.1}$$

$$S_{wr} = 5.6709(\frac{\log(k)}{\phi})^{-1.6349}, \tag{4.2}$$

$$S_{gr}^{max} = 0.5473 - 0.9696\phi, \tag{4.3}$$

where S_{gr}^{max} is the maximum residual gas saturation (-).

In Table 4.2, capillary pressure and liquid relative permeability of sandstone, siltstone and mudstone in this simulation model are described using van Genuchten (1980) functions and gas relative permeability after Corey (1954).

Table 4.2 Relative permeability and capillary pressure parameters used in base case simulation

Parameters	sandstone	siltstone	mudstone
Relative permeability (van Genuchten and Corey model)			
Exponent (m)	0.4	0.4	0.4
Irreducible water saturation (S$_{lr}$)	0.20	0.20	0.20
Residual gas saturation(S$_{gr}$)	0.05	0.05	0.05
Capillary pressure(van Genuchten model)			
Irreducible water saturation (S$_{lr}$)	0	0	0
Exponent (m)	0.4	0.4	0.4
Strength coefficient (P$_0$)-kPa	3.58	10.4	62.1

4.2.4 The maximum capacity for CO$_2$ in the simulation model

In multi-layered formations, the calculation of maximum storage capacity of CO$_2$ for each aquifer is essential for the safety of the injection strategy. Using the specified parameters in Table 4.1 and Table 4.2, i.e. $c_t = 4.5 \times 10^{-10}$ Pa^{-1}; $r_w = 0.1\,m$; $r_e = 1000\,m$; $\hat{h}_1 = 15\,m$; $\hat{h}_2 = 30\,m$; $\hat{h}_3 = 10\,m$; $\hat{h}_4 = 10\,m$; $\phi = 30\%$; P_{fm} is estimated to be 37 MPa, 42 MPa, 48 MPa, 49 MPa from the top aquifer to bottom aquifer layer, based on well test results.

The initial pore pressures at the injection points from top to bottom are also estimated to be 19, 21, 24.4 and 25.1 MPa, respectively, with a pressure gradient of 1.12 MPa/100 m.

Using Eq 3.3 in Chapter 3, the maximum storage capacities of CO$_2$ in each of the four injection reservoirs in the ¼ model may be calculated as follows:

$$V_{max1} = 4.5 \times 10^{-10} \times 3.14 \times (1000^2 - 0.1^2) \times 15 \times 0.3 \times \frac{(37 - 19)}{4} = 28613\ \mathrm{m}^3$$

$$V_{max2} = 4.5 \times 10^{-10} \times 3.14 \times (1000^2 - 0.1^2) \times 30 \times 0.3 \times \frac{(42 - 21)}{4} = 66764\ \mathrm{m}^3$$

$$V_{max3} = 4.5 \times 10^{-10} \times 3.14 \times (1000^2 - 0.1^2) \times 10 \times 0.3 \times \frac{(48 - 24.4)}{4} = 25010\ \mathrm{m}^3$$

$$V_{max4} = 4.5 \times 10^{-10} \times 3.14 \times (1000^2 - 0.1^2) \times 10 \times 0.3 \times \frac{(49 - 25.1)}{4} = 25328\ \mathrm{m}^3$$

Using an averaged CO$_2$ density of 700 kg/m^3, under 75 ^{o}C and 23 MPa, the maximum mass of CO$_2$ stored in each of the four layers can be calculated to be: M_{max1}=20 kt, M_{max2}=47 kt, M_{max3}=17.5 kt, M_{max4}=17.7 kt. Therefore, an injection rate of 0.1981 kg/s (equivalent to 0.1million tones per year) is reasonable for use in the simulation studies.

4.3 Results and discussion

4.3.1 Isothermal two phase fluid flow (H^2)

The simulated development of the CO$_2$ plume movement since injection start can be observed in Figs. 4.3 and 4.4. In particular, the Figures show changes in the evolution of the CO$_2$ saturation plume during injection and post-injection periods both in the vertical profile and plane views. As depicted in the Figures, the CO$_2$ plume front moves radially outward during the injection period, growing in both the lateral and vertical directions. However, the plume shape does not change significantly during the post-injection period, as depicted by the simulation results in Zhou et al. (2010). Furthermore, different injection layers will show differences in the characteristic distribution patterns of the gas saturation plumes due to the differences in reservoir structure, thickness, upper or bottom rock property, initial pressure and temperature, etc. In aquifer 2, for example, the thickest of all injection layers considered here, vertical migration of the plume will to some extent restrict its lateral movement. The distribution of CO$_2$ saturation in the plane view demonstrates a radial structure of the plume, with the lowest concentration of CO$_2$ at the plume front, while the highest concentration remains behind in the near-wellbore region (Fig. 4.4).
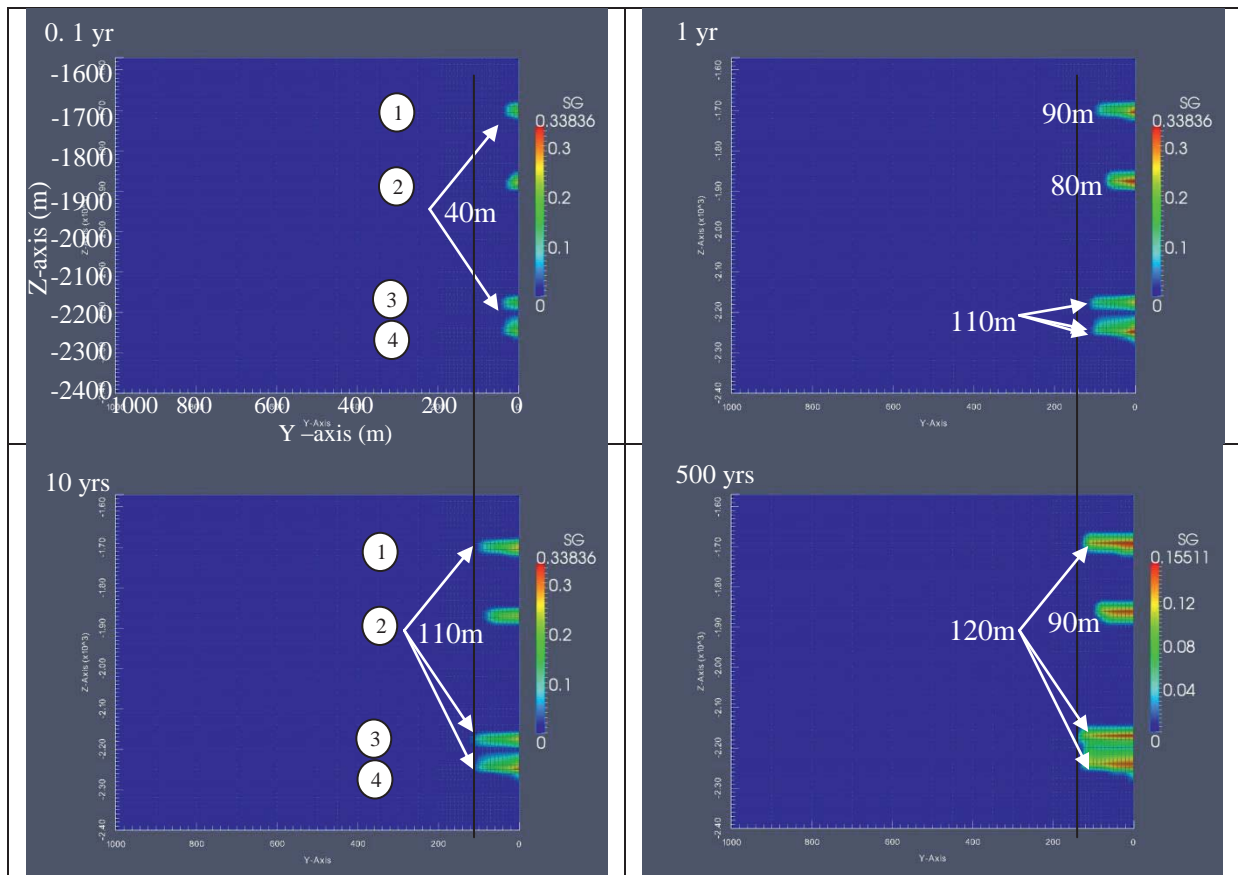
Fig. 4.3 Evolution of gas saturation since CO$_2$ injection start in base case
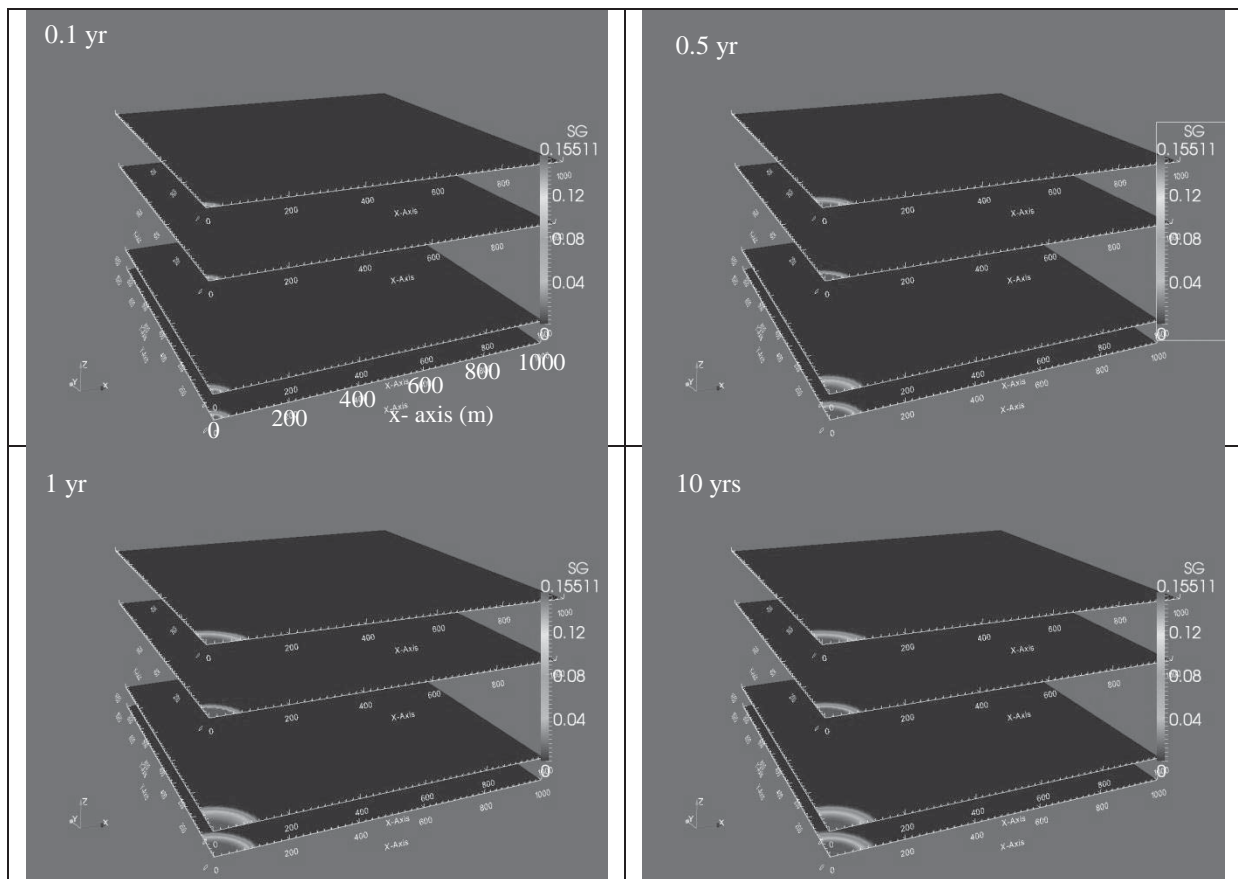
Fig. 4.4 Plane evolution of gas saturation at different layer in base case

The perturbation scope of the pressure pulse is much larger and faster than that of the CO_2 plume movement. One possible reason for this is that pressure transmission is far away from the injection zones (Nicot et al., 2008). In a fully water saturated closed system, the water can not flow outward through a physical boundary. Therefore, pressure buildup will increase greatly due to CO_2 injection. Three profile lines are drawn in the model, i.e. the two vertical profiles, one across the injection points (aǎ), and the other along the outer boundary (AǍ) and the third profile (hǐ) trending across aquifer layer 4 (see Fig. 4.5).

The model curves attained in Figs. 4.6, 4.7 and 4.8 illustrate the characteristics of pressure accumulation and dissipation in the system during and after CO_2 injection. A gradual continuous pressure buildup occurs in the near-wellbore region at the beginning of CO_2 injection. However, as the injection process continues, migration of the CO_2 plume will enhance pressure propagation, resulting in a simulataneous sharp increase of pressure at the boundary of the region and a decrease of plume thickness in the near-wellbore region. Henceforth, the pressure in the reservoir-cap rock system will be changed due to the advection of CO_2 and water.
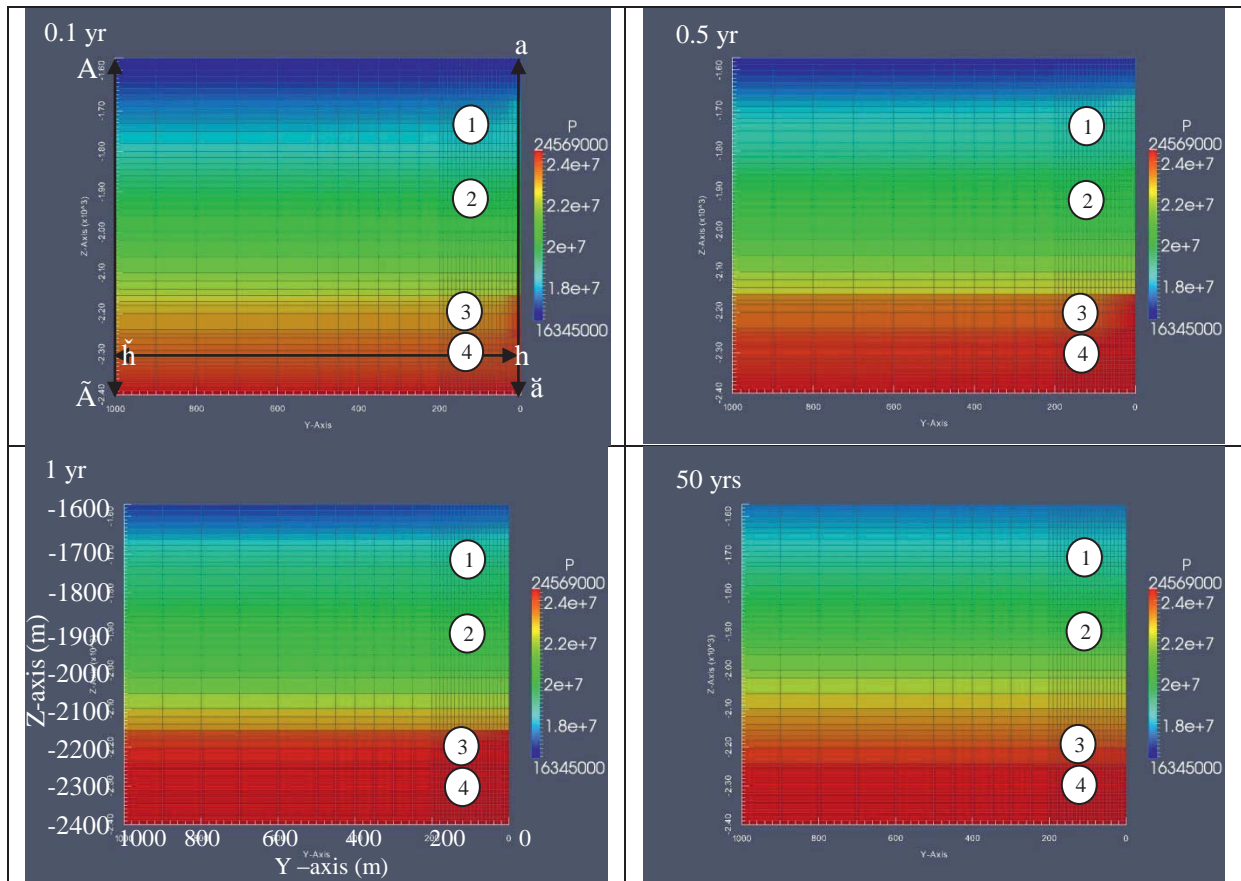
Fig. 4.5 Evolution of pressure since injection of CO$_2$ in base case
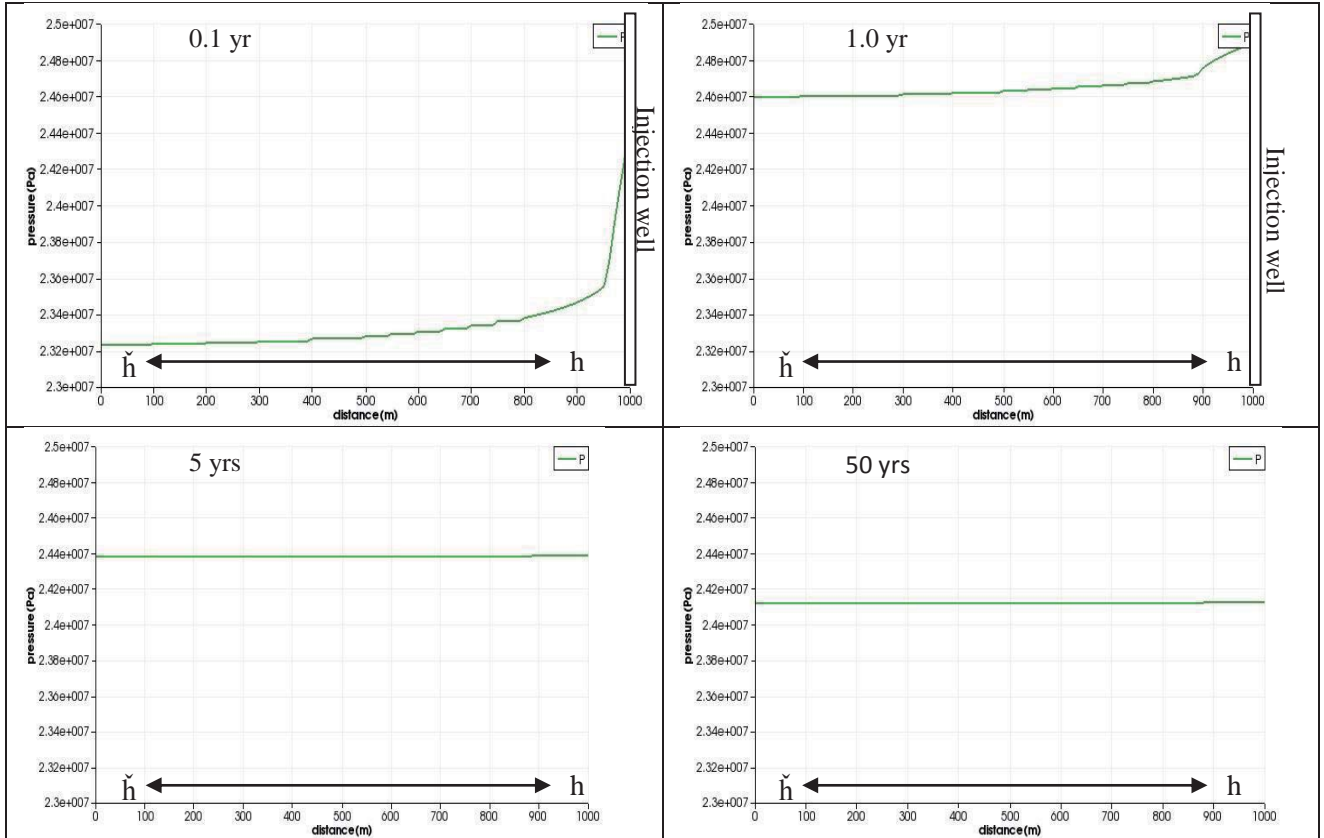
Fig. 4.6 Evolution of pressure since injection of CO$_2$ through the bottom injection point (at -2245m) in base case

89
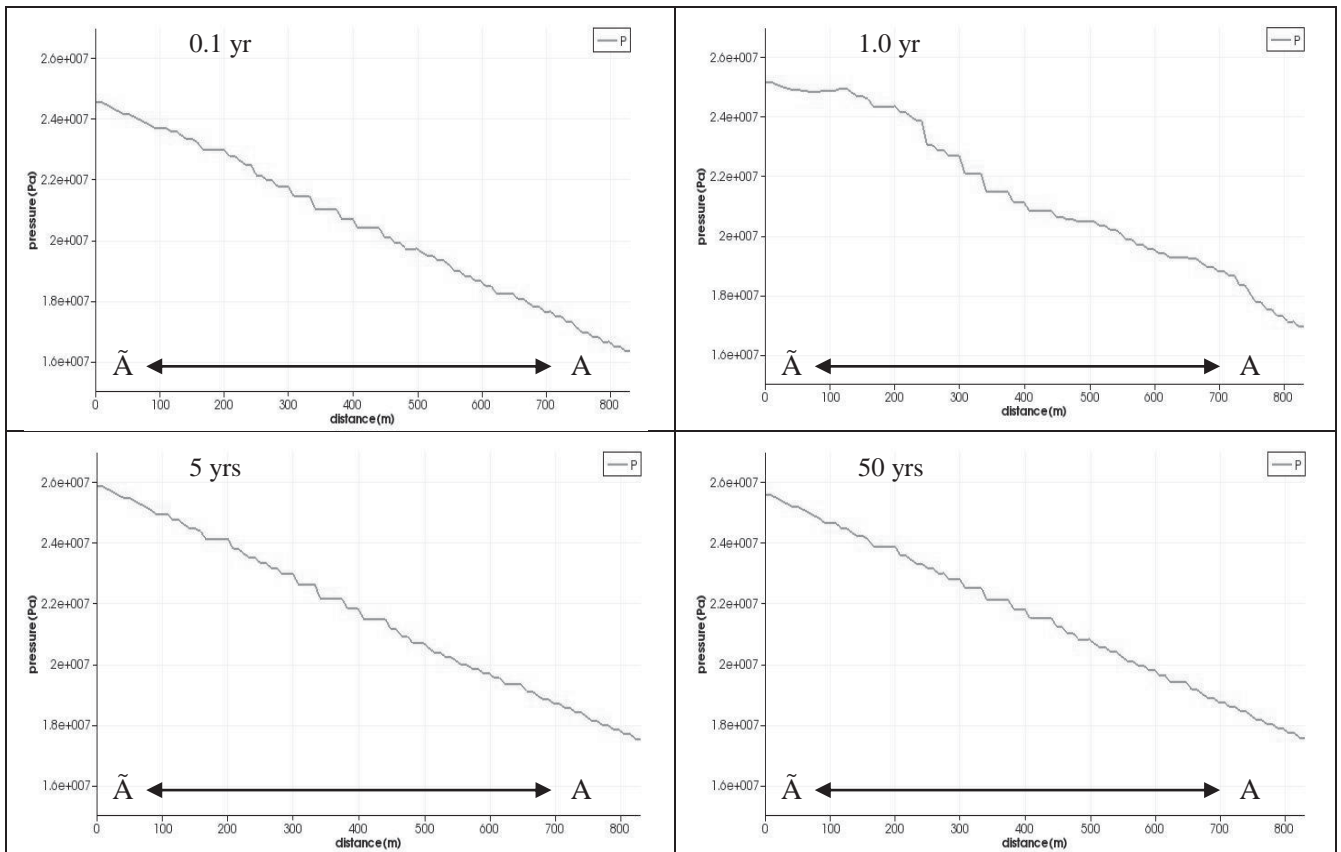
Fig. 4.7 Evolution of pressure since injection of CO$_2$ across the outer vertical boundary in base case
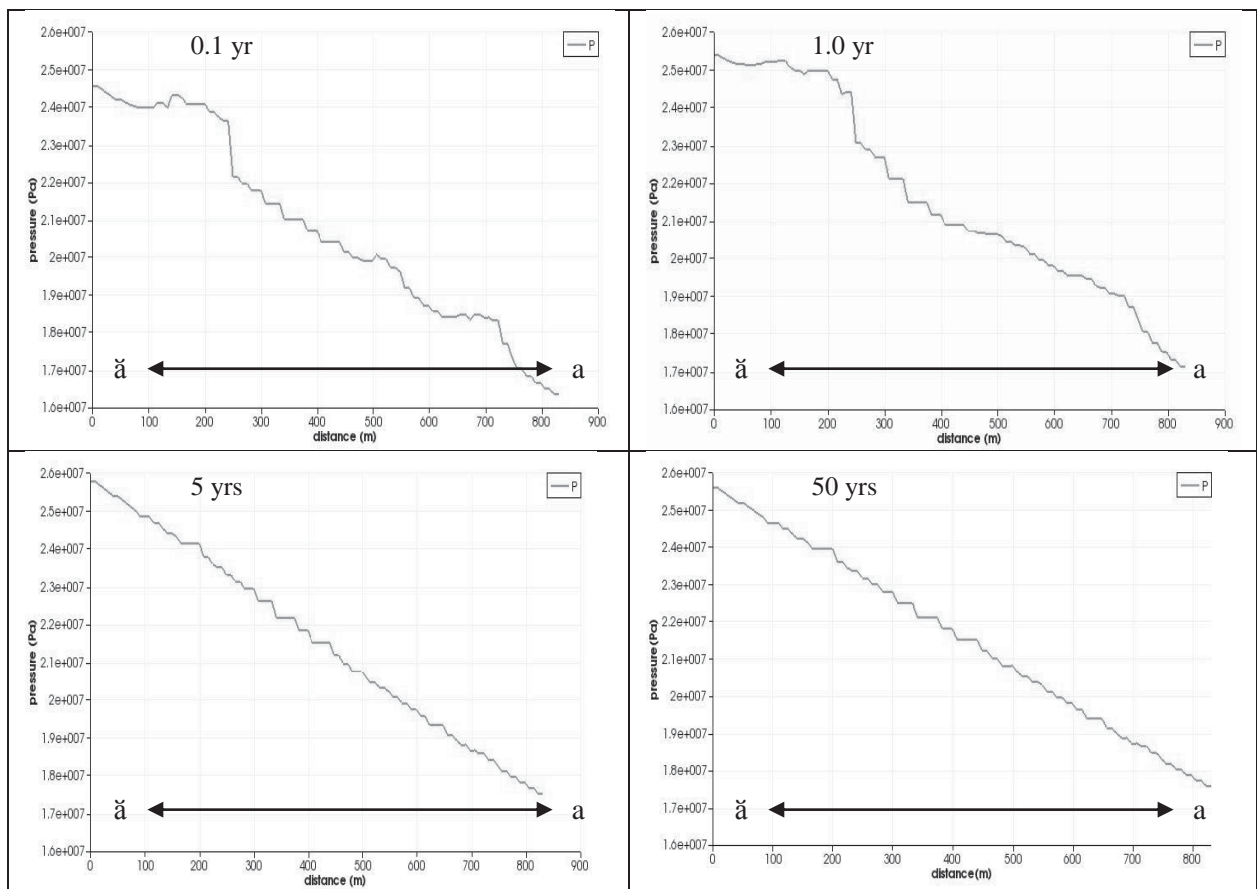
Fig. 4.8 Evolution of pore pressure since injection of CO$_2$ across the vertical injection points in base case

90

The solubility of CO_2 in water varies with time and space. During the injection period, more and more CO_2 will be dissolved in the brine, until the maximum solubility is reached under the prevailing reservoir pressure and temperature conditions. During the post-injection period, the shape of plume front changes when more CO_2 dissolves. The advection of pure brine water and water with dissolved CO_2 (with a different density) makes the plume shape more complex (Fig. 4.9). It should be noted that CO_2 plume in different vertical layers, above or below, presents distinct characteristics which may rely on the pressure dissipation characteristics of the different stratigraphic sequence and properties including porosity, permeability and thickness, etc. From the liquid density distribution chart (Fig. 4.10), it can be seen clearly that the vertical connection of CO_2 bearing brine occurs between the two bottom layers. This is because of the thin sealing layers between the two injection point can not completely hinder the vertical migration of CO_2 (Zweigel et al., 2000). This is called the accumulation-penetration-breakthrough processes, which means that when the pressure buildup at the interface between the aquifer and the low-permeability layer exceeds the entry capillary pressure, CO_2 starts to penetrate into the overburden layer, and finally breaks through into the overlying relatively high permeable aquifer layer (Zhou et al., 2010). As time goes by, the boundary of brine with dissolved CO_2 and gravity effect become more obvious (Nordbotten et al., 2005).
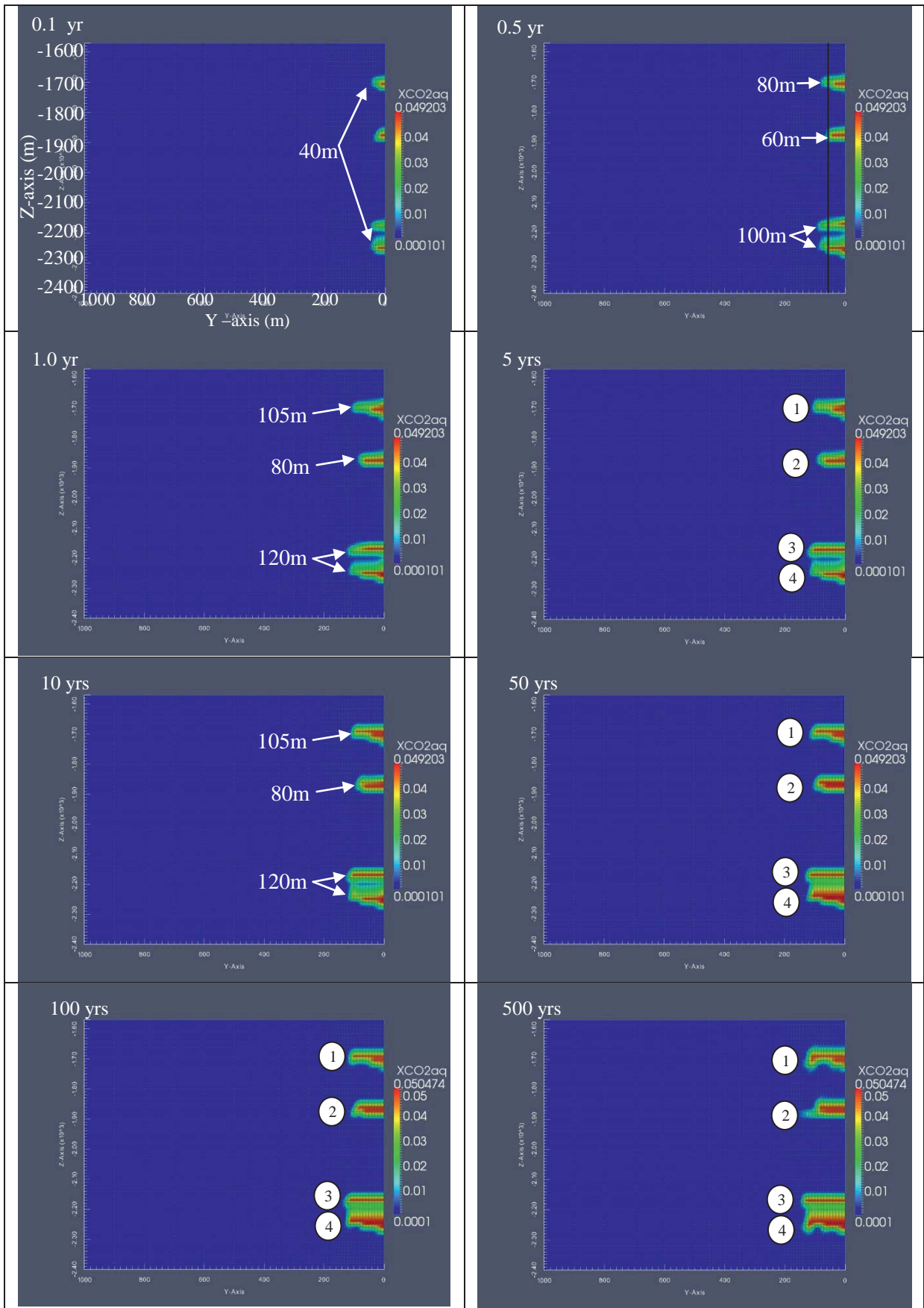
Fig. 4.9 Evolution of CO$_2$ mass fraction in brine since the injection of CO$_2$ in base case
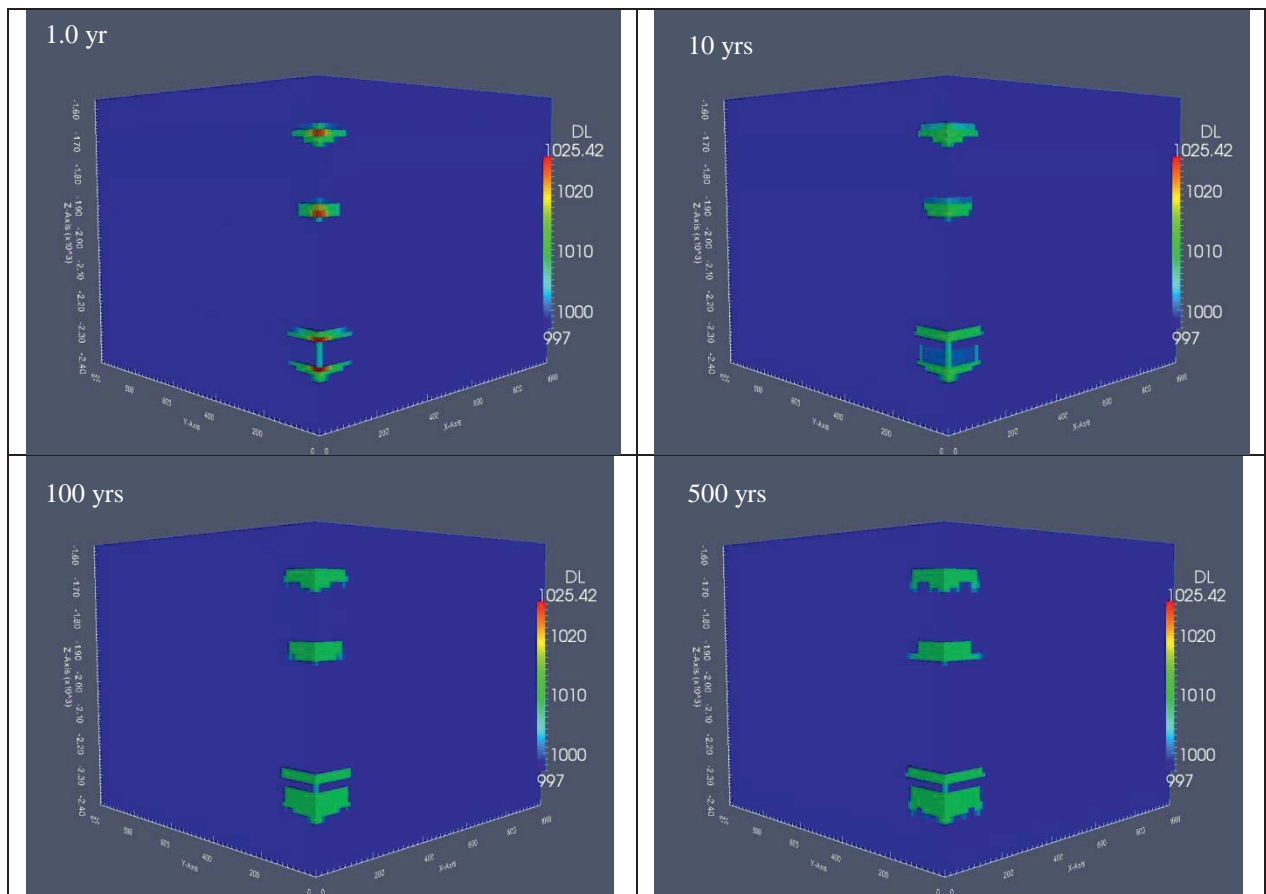
Fig. 4.10 Time evolution of liquid density in base case

4.3.2 Non-isothermal two phase fluid flow (TH[2])

Temperature evolution in the formation is another factor that influent subsurface processes during CO_2 injection. The behavior of the local temperature field depends on many factors (Kopp et al., 2006), such as the enthalpy of the injected CO_2, the heat capacity and heat conductivity of the formation and the expansion of the fluid coupled with a temperature lowering effect (Joule-Thomson cooling). When temperature is considered during the study of CO_2 plume transport processes, pressure, gas saturation and the amount of CO_2 dissolved in the aqueous phase may show some different characteristics compared with those under isothermal conditions.

The geothermal gradient is evaluated to be about 3.1 ^{o}C/100 m based on regional studies in the Ordos Basin (Fig. 4.11). Consideraing the geothermal gradient and the injection temperature of CO_2 (31 ^{o}C), there will be minor changes in gas saturation and pressure (Fig. 4.12), but the impact on the concentration of CO_2 in the aqueous phase is obvious, especially in the vertical direction around the injection zones (Fig. 4.13). The temporal and spatial-dependent migration characteristics of injected CO_2 can be seen in this figure. Compared with the isothermal condition, more gaseous CO_2 will dissolve into the water, promoting the propagation processes of aqueous CO_2. This is in accordance with the solubility rules of CO_2 in water, which shows inverse relationships with the increasing temperature (Kohl and Nielsen, 1997).

93
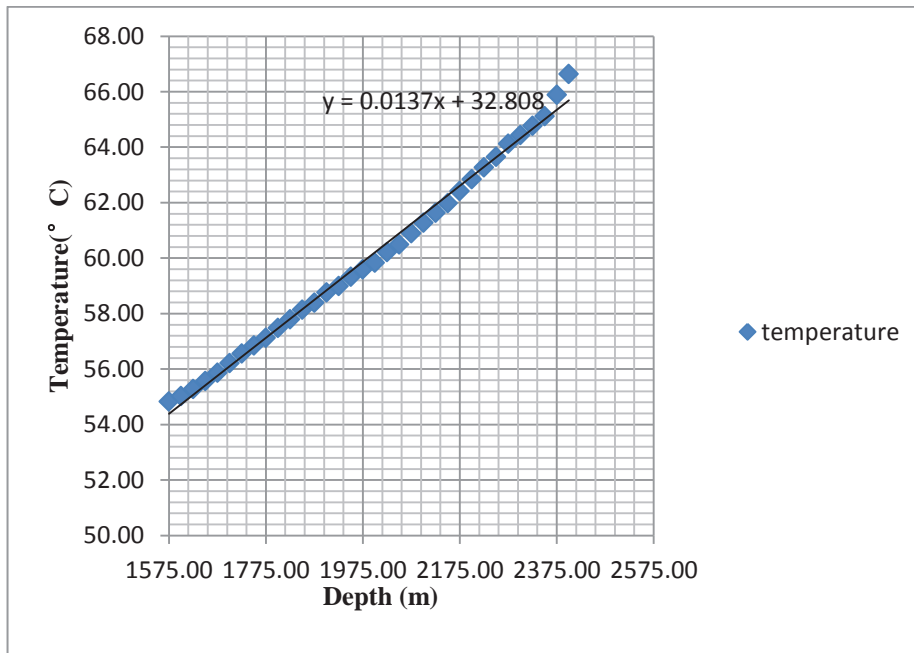
Fig. 4.11 Averaged temperature profile in the Ordos Basin
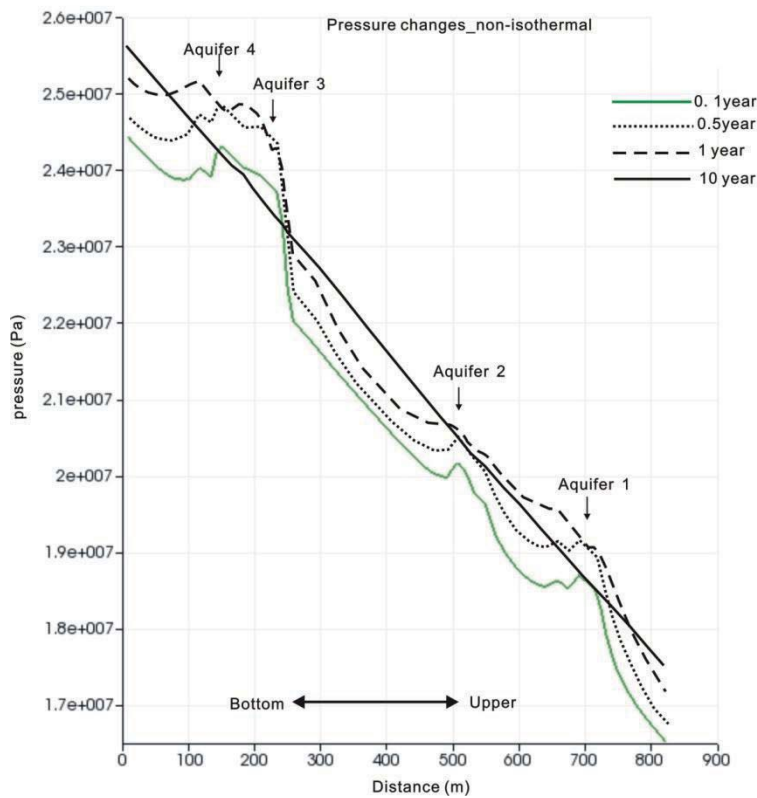
Fig. 4.12 Pressure changes for non-isothermal conditions in case 10 after CO$_2$ injection (520 kJ/kg) (Liu et al., 2014), during CO2 injection period, pressure increase will occur close to the injection points, while during post-injection period, pressure dissipation starts till to a state of hydro-equilibrium
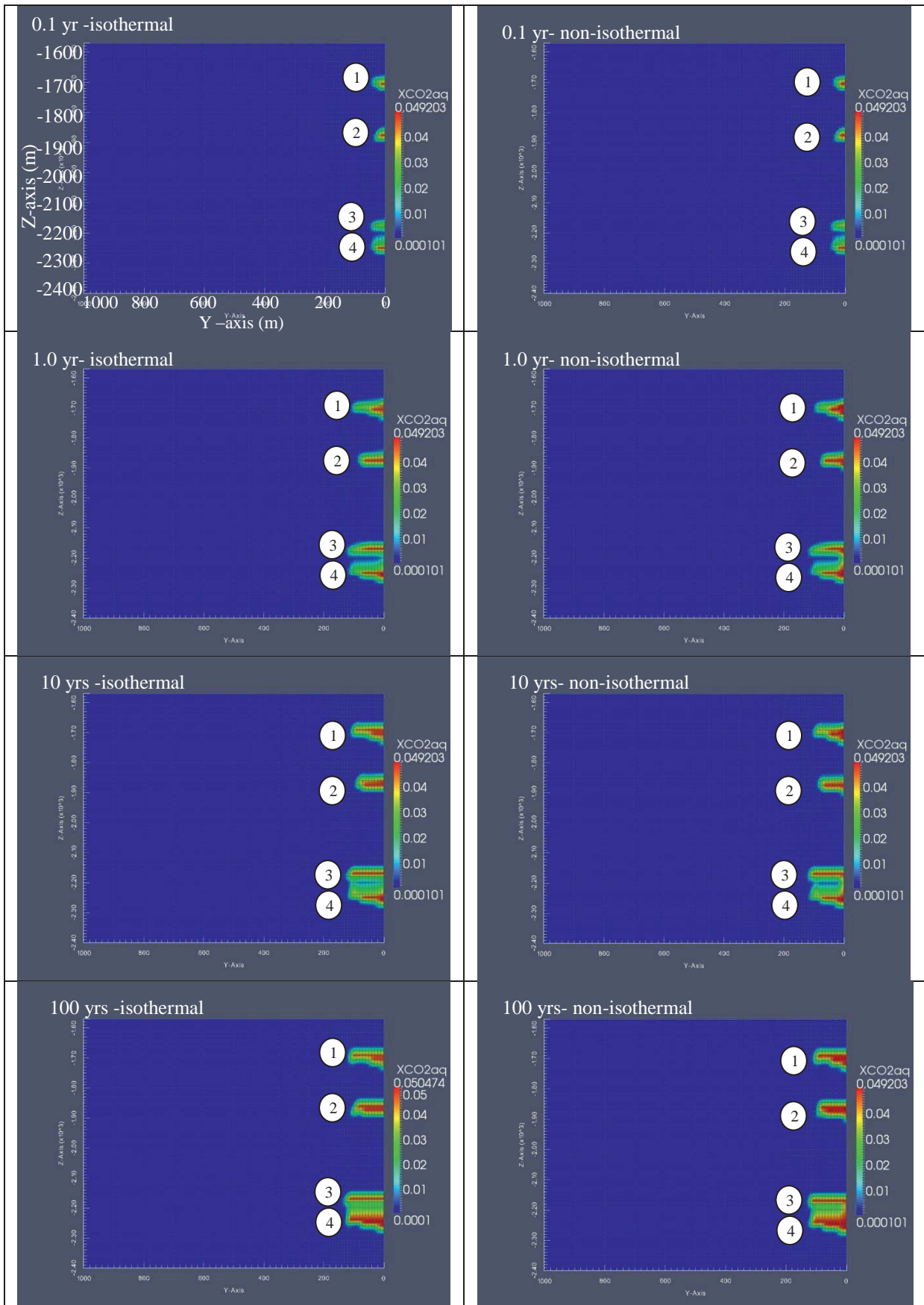
Fig. 4.13 The distribution of CO$_2$ mass fraction in saline under isothermal and non-isothermal condition (520 kJ/kg), for the latter condition, the vertical aquifer connections become much more obvious

The injected CO$_2$ has a strong influence on the evolution of the local temperature field which also spreads in a radially symmetrical manner away from the injection well (Fig. 4.14). Because the temperature of the injected fluid is colder than the initial reservoir temperature, the reservoir gets cooled down around the injection point during injection period. At the injection point of layer 1, a decreased temperature of 22.09 ^{o}C is attained after 0.1 year of CO$_2$ injection. The maximum temperature decrease occurs after CO$_2$ injection has stopped, with a decline of 42 ^{o}C compared with the initial reservoir temperature (Fig. 4.15). Large temperature perturbation occurs in the near wellbore region (Fig. 4.16). At the front of the plume, a slight increase in temperature occurs. Temperature effect does not spread to distances far away from the injection point. After injection stops, a long period is required for the temperature to recover to its initial value.

Apart from the cold CO$_2$ injection zone, several other factors affect the temperature distribution of the CO$_2$ plume (Riano, 2012), including the upward flow of the bottom warmer CO$_2$, the downward movement of the upper colder brines, CO$_2$ cooling down due to Joule –Thomson effect (Kopp et al., 2006) and temperature increase due to the exothermal reaction of CO$_2$ dissolution into the brine.

The effect of the injection CO$_2$ temperature on the local temperature field and fluid flow field is revealed through two case studies, which confirm that the higher the temperature of the injection fluid, the weaker the Joule-Thomson effect (Fig. 4.16).
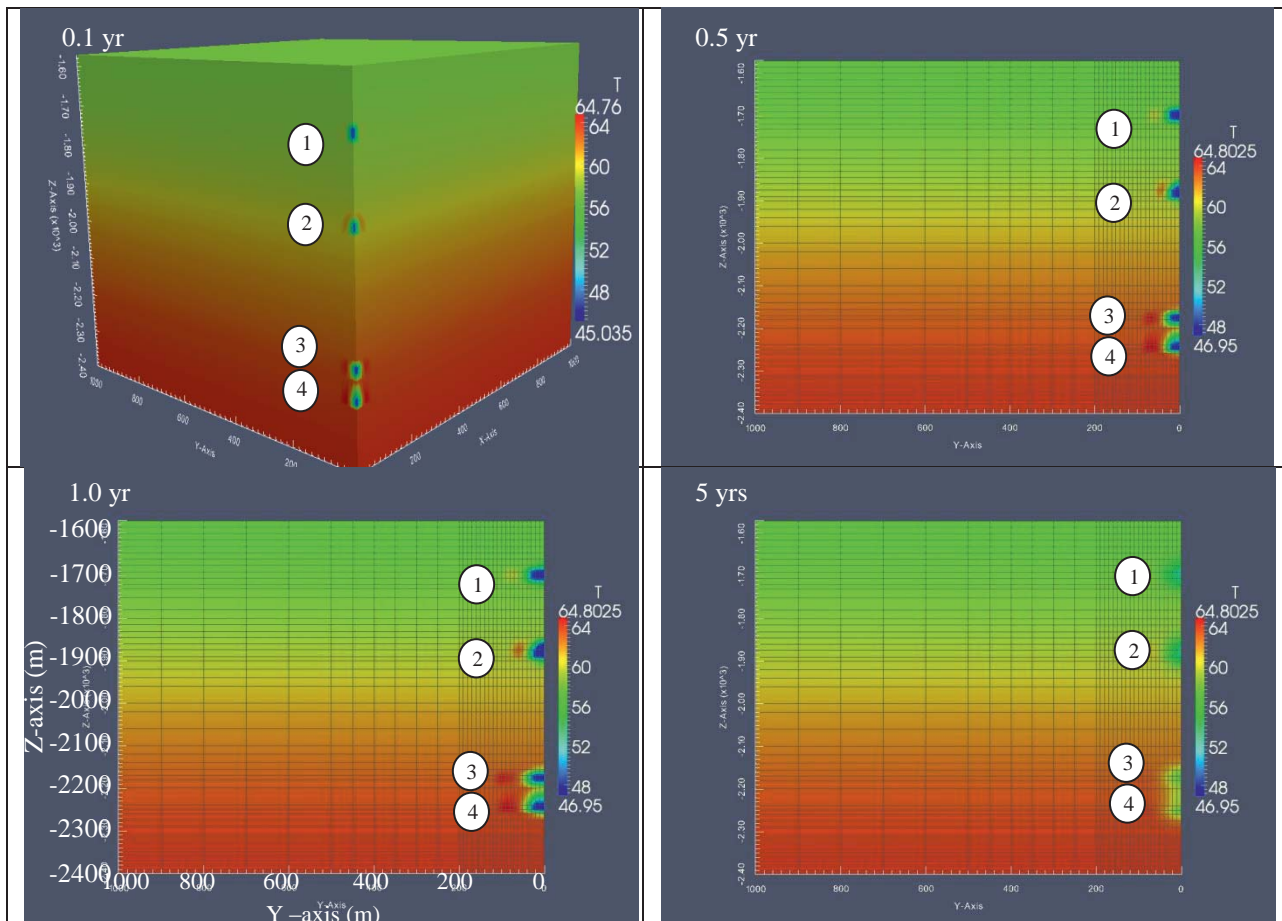
Fig. 4.14 Temporal development of temperatures for non-isothermal conditions after CO$_2$ injection (520kJ/kg)

96
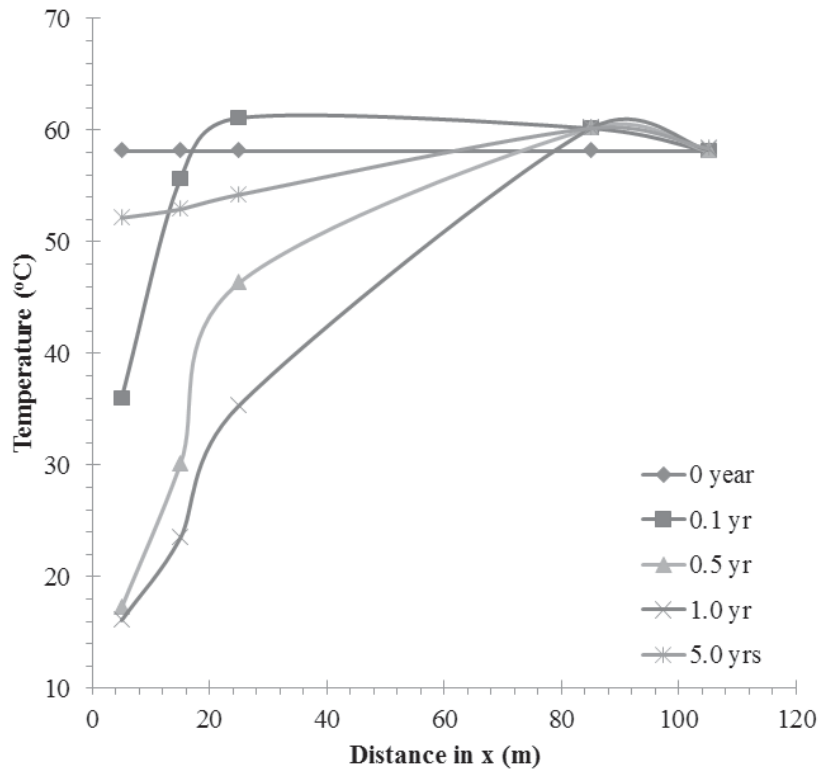
Fig. 4.15 Temperature evolution of aquifer layer 1 along fluid flow direction (520kJ/kg)
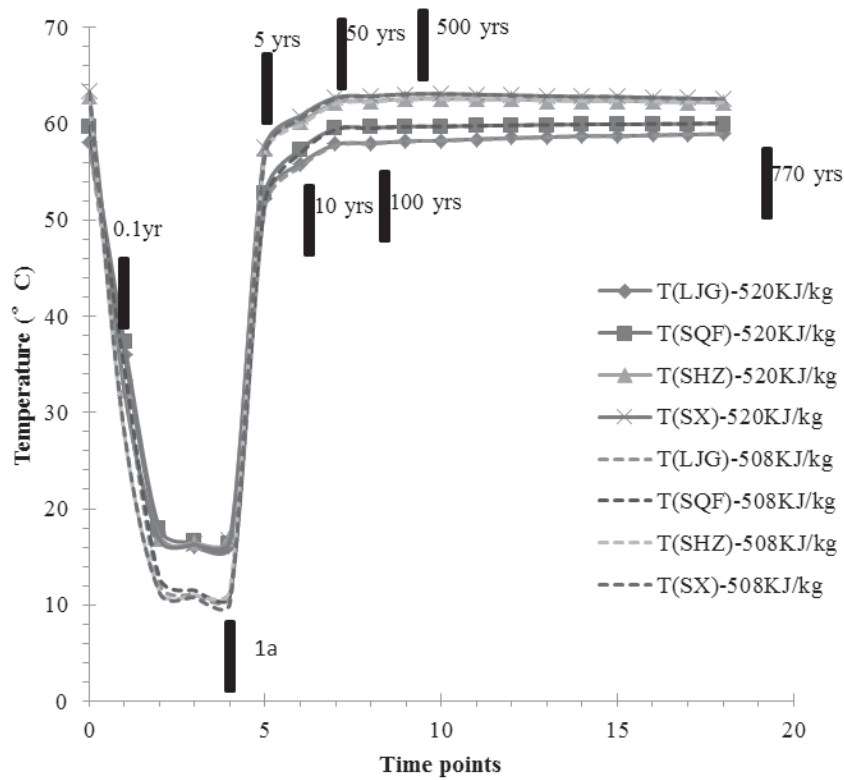
Fig. 4.16 Temperatures changes at different injection points under non-isothermal conditions after CO_2 injection (508 kJ/kg and 520 kJ/kg)

4.4 Sensitivity analysis of CO$_2$ sequestration

With the exception of the base case studied above, a number of scenarios have been simulated to predict the response of a multilayered reservoir-caprock system to CO$_2$ injection. These include (1) the injection strategy effect and (2) reservoir heterogeneity effect, consisting of formation structural heterogeneity and fluid properties. The detailed simulation models with modified parameters are shown in Table 4.3:

Table 4.3 Parameter changes in the comparative cases of sensitivity analysis caused by CO$_2$ storage in saline formation

Case number	Purpose	Changed parameters in simulations
Case 1	One layer injection	One layer; Injection rate: 0.7952 kg/s
Case 2	Injection rate effect	Case 2-1 Injection rate: 0.7952 kg/s Case 2-2 Injection rate: 3.17 kg/s
Case 3	Boundary effect	Open boundary
Case 4	Porosity and permeability effect	Tight sandstone and tight mudstone: $\phi_{sandstone}= 0.12$, $k_{sandstone}=5$ mD $k_{mudstone}=0.1$ μD
Case 5	Vertical and horizontal permeability ratio (k_v / k_h)	$k_v / k_h = 0.1$
Case 6	High permeable zone effect (Horizontal fracture zone length 300m, vertical thickness 0.1m)	case 6-1 fracture zone $\phi = 0.5$, $k = 1$ D case 6-2 fracture zone $\phi = 0.5$, $k = 10$ D
Case 7	Geological structure effect	Gentle slope anticline structure is considered
Case 8	Capillary pressure effect	No capillary pressure
Case 9	Relative permeability effect	Residual gas saturation 0 and 0.3
Case 10	Non-isothermal effect	Geothermal gradient is considered Case 10-1 injection enthalpy = 508 kJ/kg Case 10-2 injection enthalpy = 520 kJ/kg

4.4.1 Effect of injection strategy

The injectivity index is a key factor for evaluating the efficiency of CO$_2$ injection into formations in a closed system. Injectivity value can be increased greatly when the rock is more water wet (Fig. 4.17). Inflow performance relationship (IPR) can be used to define the relationship between the well bottomhole pressure (BHP) and fluid flow rate (Economides and Boney, 2000).
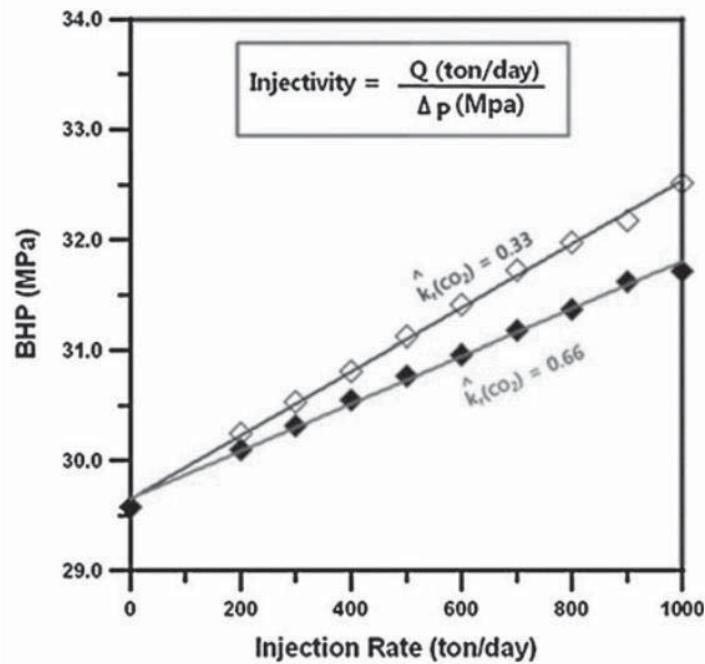
Fig. 4.17 The relationship between BHP and injection rate under different CO_2 relative permeability conditions (Sung et al., 2011)

Under a constant injection pressure, the injection rate will decrease due to the pressure buildup in reservoir, thus resulting into changes of the formation permeability (Fig. 4.18). However, injectivity increase also occured in some simulation results (Burton et al., 2008).
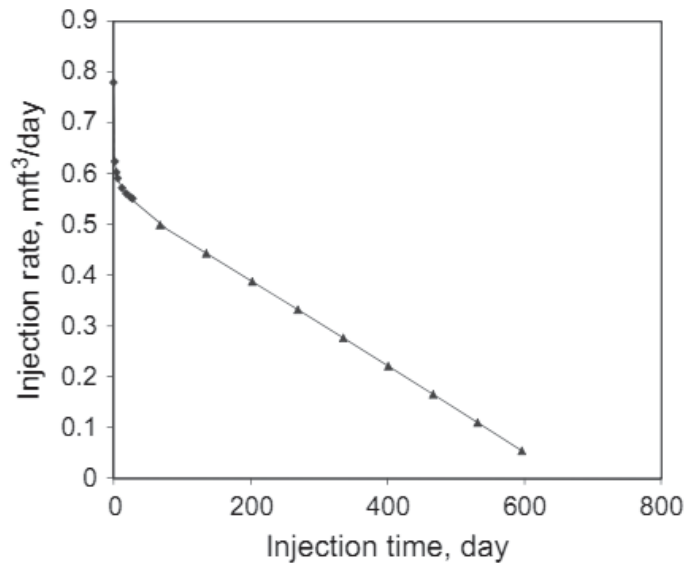
Fig. 4.18 The relationship between injection rate vs. time (Xie and Economides, 2009)

4.4.1.1 Comparison of multi-layer and one layer injection strategy

Injection strategy can have great impact on the propagation of CO_2 in the reservoir. The factors include well head pressure, well bottom-hole pressure, temperature of the injection fluid, injection rate, single-layer or multi-layer injection strategy, etc.

In comparison with the results in the base case, at the injection rate of 0.7925 kg/s the CO_2 plume front for the bottom layer will arrive at the 200 m mark after one year in a one layer injection scenario (Fig. 4.19). This is different from the expectations of four times further in distance than that of the base case, which may be due to the reason that the volume of supercritical CO_2 will be decreased when pore

99

pressure is increased. Therefore, when CO$_2$ is injected into a much higher pressure formation, the CO$_2$ plume volume will be small than in a shallower formation, thus greatly increasing the capacity of CO$_2$ storage.
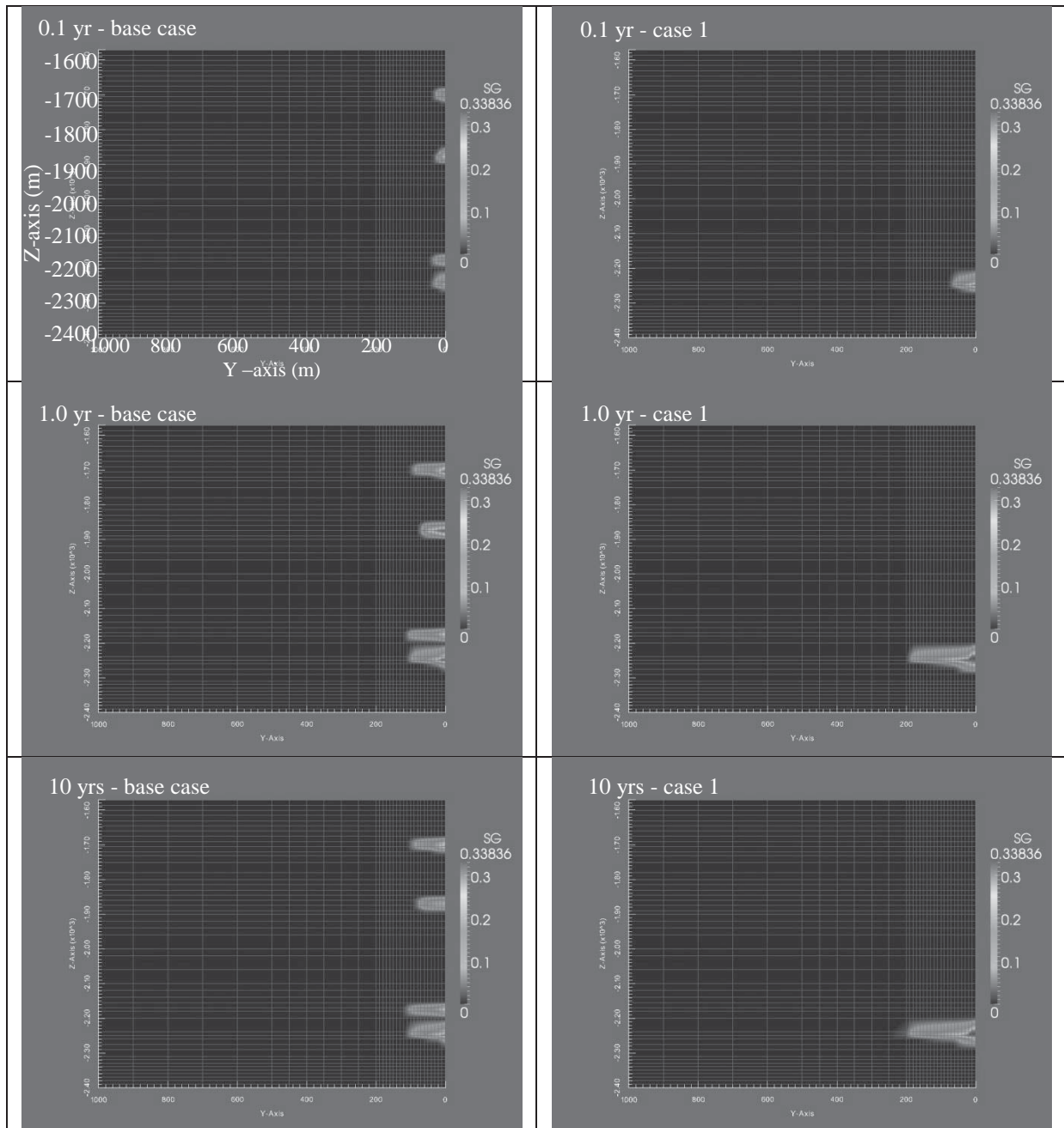
Fig. 4.19 Gas saturation under the condition of multi-layer and one layer (case 1) injection strategy

4.4.1.2 Effect of injection rate

The effect of injection rates on CO$_2$ plume growth can be demonstrated through three cases (i.e. at 0.1981 kg/s, 0.7925 kg/s and 3.17 kg/s) in Figs. 4.20, 4.21 and 4.22. The higher the CO$_2$ injection rate, the larger the lateral distance the CO$_2$ plume will migrate in an over-pressured reservoir (Mcpherson, 2001; Hussain et al., 2013). The responses of different injection layers on increased injection rate are different. The CO$_2$ plume in the relative thick sandstone layer is much closer to the injection point due to the relatively low pressure difference, induced by the distribution of CO$_2$ in the whole reservoir (Liu et al., 2014). Note that the CO$_2$ plume front normally shows a positive correlation with the injection rate. At lower injection rates, lateral migration and formation water displacement are the main processes.

100

However, at higher injection rates, vertical displacement of formation water dominates. When the injection amount of CO_2 is larger than the maximum capacity of the reservoir, that is, the injection pressure is larger than the fracture pressure, CO_2 penetration or eventually breakthrough will occur in the vertical direction through the thin caprock layer (Fig. 4.23).
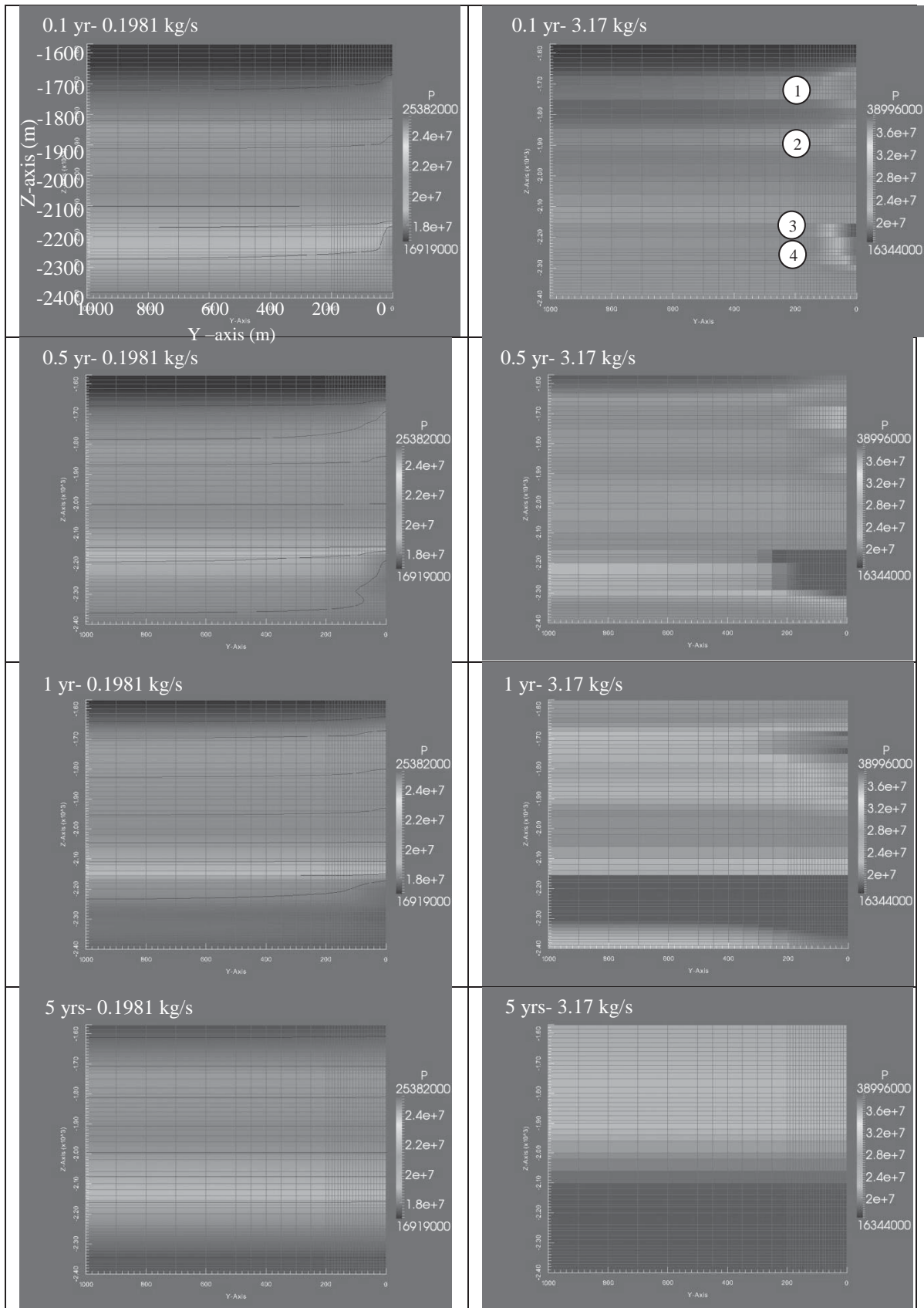
Fig. 4.20 Pore pressure distribution due to injection rate effect

101
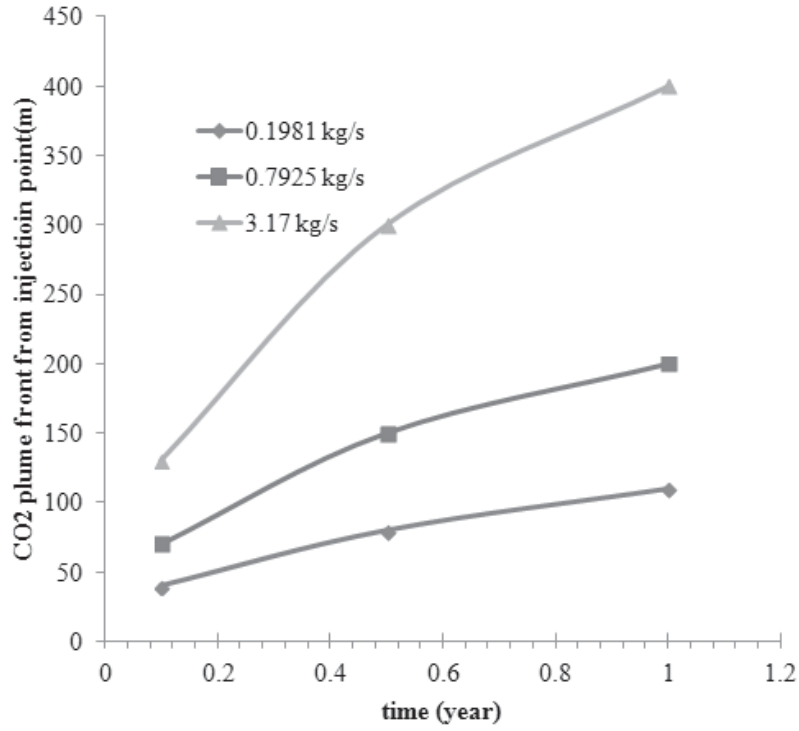
Fig. 4.21 Injection rate effect on CO_2 plume front of Fm. Shihezi
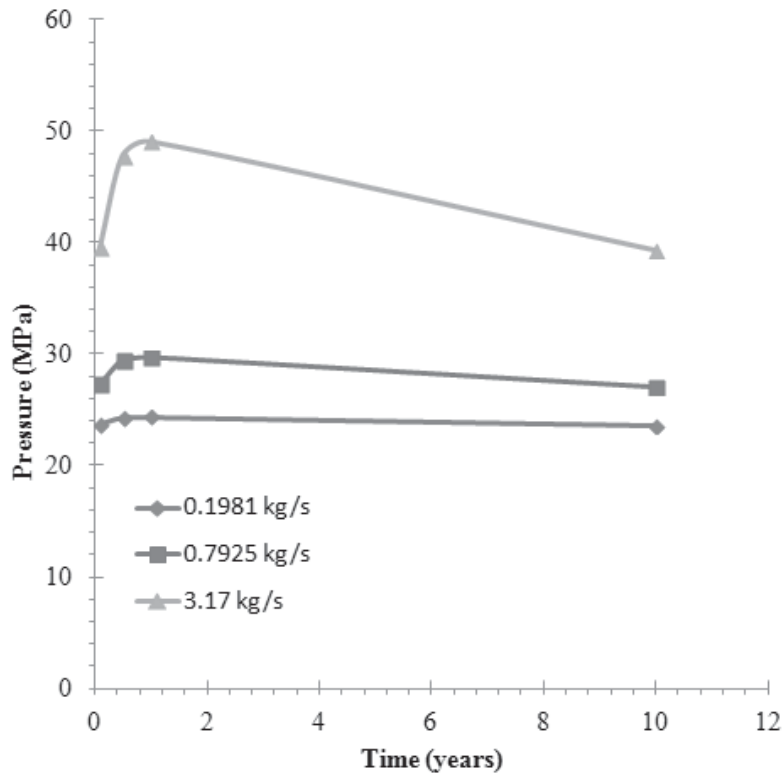
Fig. 4.22 Injection rate effect on injection zone pressure of Fm. Shihezi

102
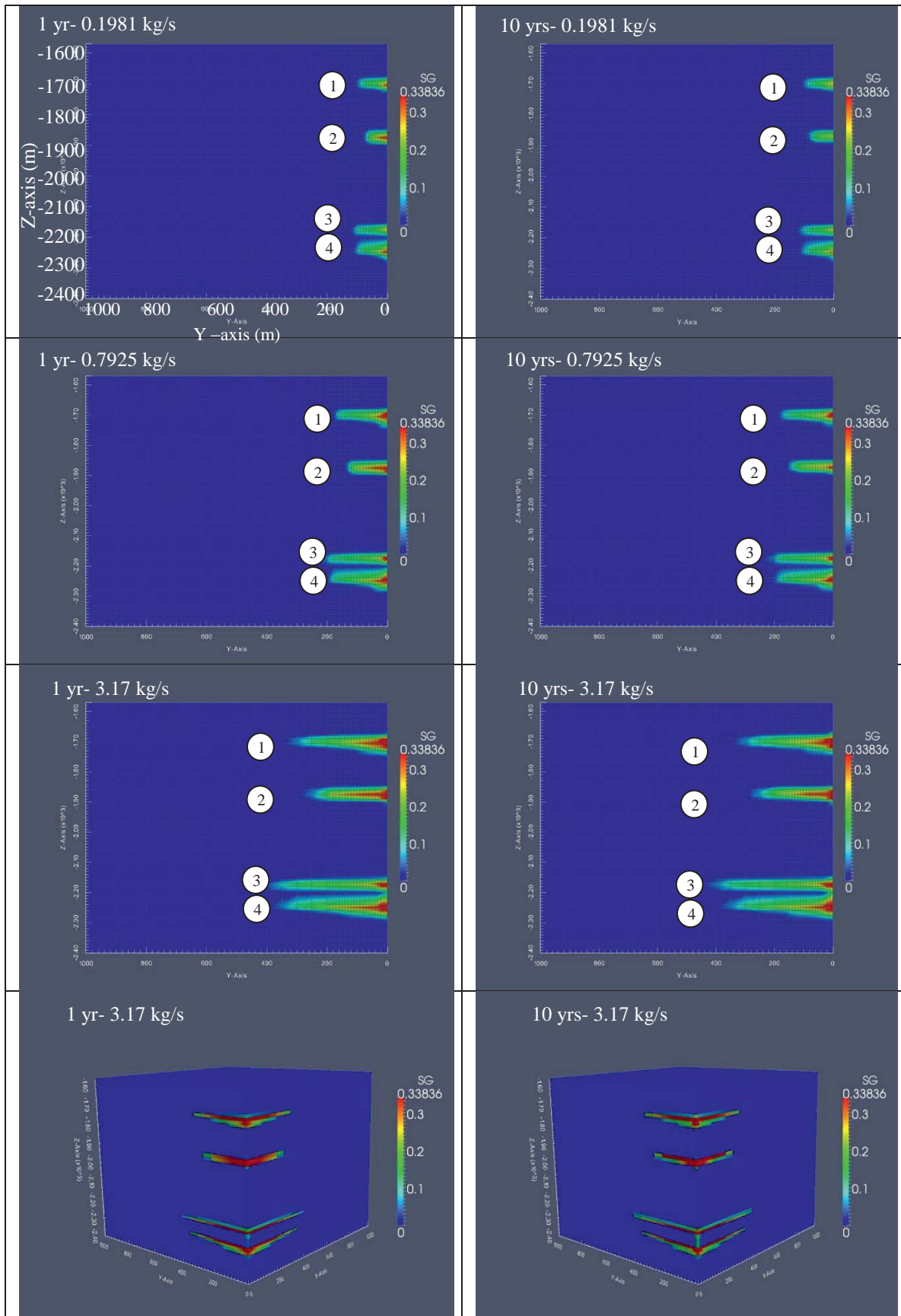
Fig. 4.23 Gas saturation changes due to injection rate effect (Liu et al., 2014a, modified)

103

4.4.2 Boundary effect

4.4.2.1 Boundary type

CO_2 storage in deep saline aquifers will either induce a pressure build-up in the formation through compression of rocks and water in a closed reservoir (Flett et al., 2008; Yang, 2008; Alkan et al., 2010; Neal et al., 2011; Oldenburg and Rinaldi, 2011) or displace formation water into adjacent formations toward the surface in an open reservoir (Zhou et al., 2008). Aquifers can be classified as open, semi-closed and closed systems, depending on the nature of the boundaries (Fig. 4.24). The evolution of pore pressure during and after CO_2 injection greatly varies under different boundary conditions, thus the accuracy of safety evaluation of the caprock may be infringed. Besides, the assessment of storage capacity of CO_2 in a particular aquifer layer varies by using different boundary models. For example, in closed and semi-closed aquifers, the CO_2 storage capacity is basically controlled by rock and fluid compressibility (Ehlig-Ecomomides and Economides, 2010; Vilarrasa, 2012), unlike in open aquifers, in which capacity has no limitations. Therefore, boundary type is a significant factor affecting the safety and capacity of CO_2 sequestration, and demands intensive investigations through simulation studies.
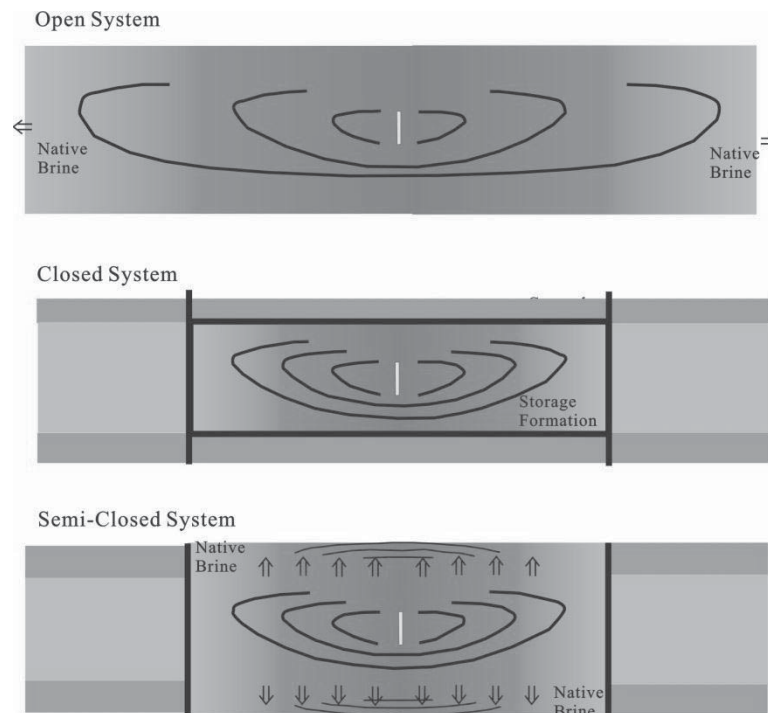
Fig. 4.24 Three potential storage systems with different boundary conditions (Zhou et al., 2008, modified)

In open systems, fluids can flow across the lateral boundaries of the geologic formations. The pore pressure buildup induced by CO_2 injection will be minimal as pore water flows through the boundary to the neighboring formations (Birkholzer et al., 2009; Zhou and Birkholzer, 2011; Wang et al., 2012). By comparing cases 2 and 1 (Fig. 4.25), it can be concluded that the pressure buildup in the open system will mainly affects a very narrow range around the injection point, and not the thick mudstone or siltstone layers away from injection zones (Fig. 4.25B). Once CO_2 injection stops, the pore pressure at the injection zone will quickly return to its initial hydrostatic pressure state (Hussain et al., 2013).
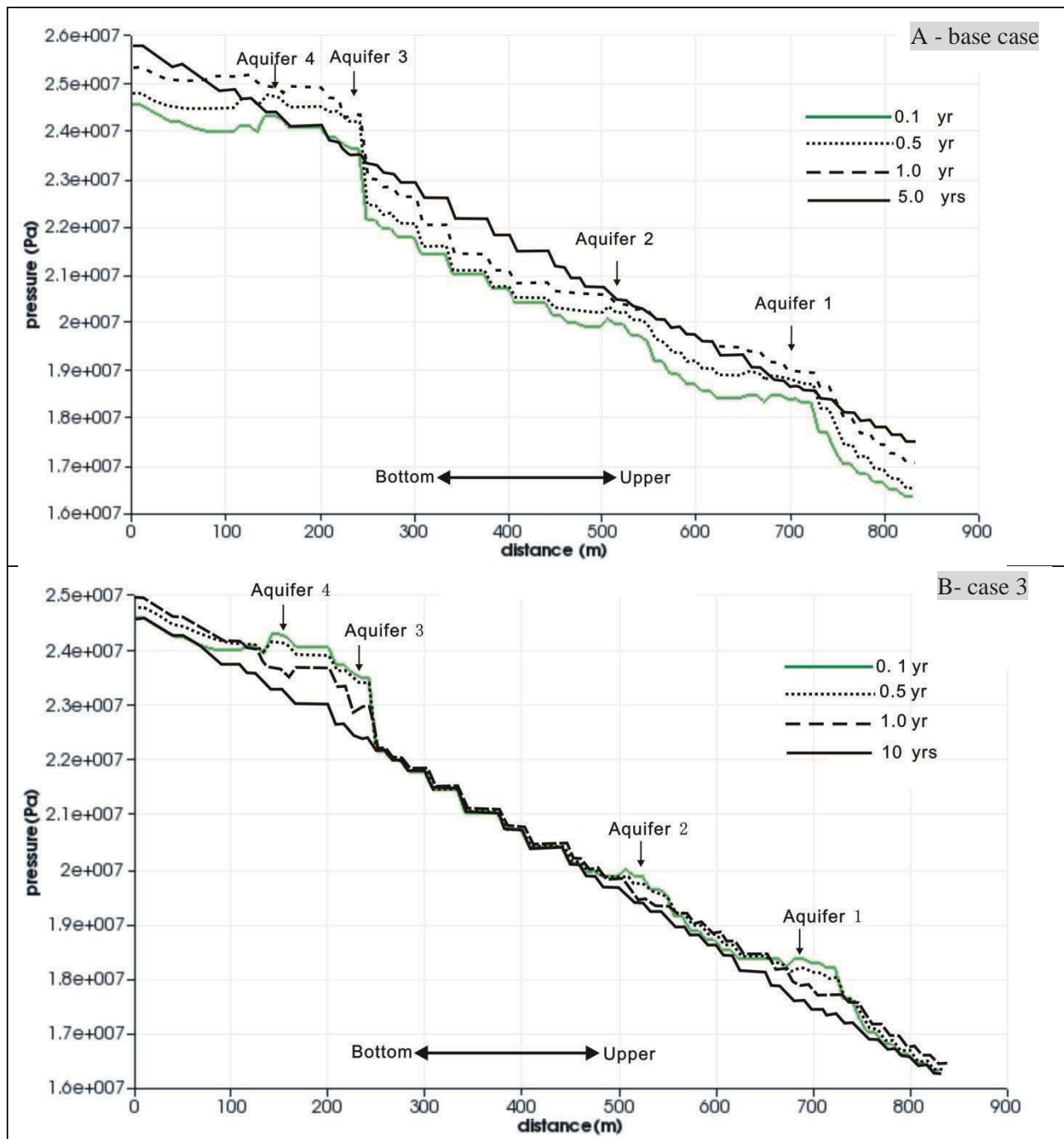
Fig. 4.25 The pressure changes in the vertical direction through the injection points at different time, over 0.1, 0.5, 1.0, 10 years after CO$_2$ injection, (A) closed and (B) open lateral boundary systems (Liu et al., 2014a)

Fig. 4.26 shows the variation of CO$_2$ gas saturation and CO$_2$ mass fraction dissolved in the aqueous phase at four injection points, including their upper and below contact layers in both closed and open lateral boundary cases. The variation trends for gas saturation in both cases are very similar because of the minimal pore pressure difference due to the small amount of CO$_2$ injected (Fig. 4.26A and B). Pressure buildup stops with the cessation of CO$_2$ injection and gas saturation in the aquifers correspondingly register an instantaneous decline, as seen at injection points A 0 9, A 020, A 033 and A 036. The thicker sandstone formation has the buffering effect, especially in the upper layer A 019 of aquifer 2, which allows maintainance of a relatively higher concentration of CO$_2$ in comparison with its bottom counterpart layer A 020 (Liu et al., 2014a). In addition, a small amount of CO$_2$ saturation (ca. 2%) occurs in the uppermost mudstone caprock A 08 overlying the sandstone aquifer 1.

On the other hand, however, the high mass fraction of dissolved CO_2 instantly attained by the aquifer layers during injection in both cases is maintained throughout the post-injection period (see Figs. 4.26C and D). In the closed lateral boundary system, the increased pressure of the system causes a relatively stronger dissolution of CO_2 in the saline water. In the injection aquifers, the solubility of CO_2 comes to a saturated state (4.7%-5.0%) almost instantly, while in the directly overlying mudstones, such as A 0 8 and A 035, it takes quite a while to reach the final saturated state of CO_2 in saline water (Liu et al., 2014). Dissolution of CO_2 in the mudstone layers below the injection aquifers is negligible small (ca. 0.1% or less). This is possibly due to the buoyant effect that allows more CO_2 gas to be conveyed more easily in the upward than downward directions.
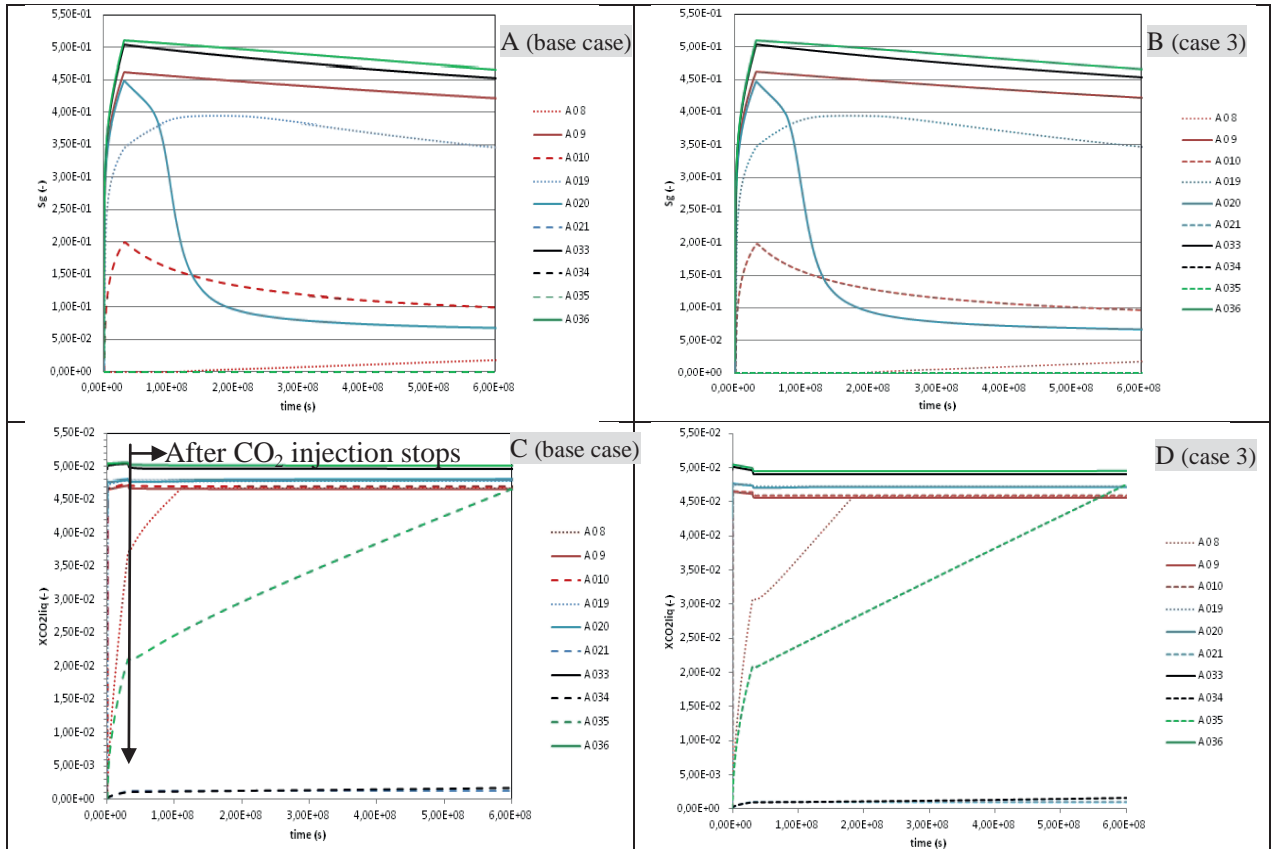
Fig. 4.26 CO_2 saturation and CO_2 mass fraction in aqueous phase with time at different points under base case (closed boundary) and case 3(open boundary) conditions, (A) and (B) gas saturation; (C) and (D) dissolved CO_2 amount in aqueous phase (Liu et al., 2014a)

4.4.2.2 Boundary position

In a closed reservoir system, the position of the boundary will affect fluid flow rate and pressure build-up (Fig. 4.27), thus amount of sequestrated CO_2 may be concentrated in a reservoir with the boundary position near to the injection point. Under a constant pressure injection scheme, the injection rate of CO_2 will be different before and after flow reaches the reservoir boundary (Xie and Economides, 2009).

(a) before CO2 plume reaches reservoir boundary   (b) after CO2 plume reaches reservoir boundary
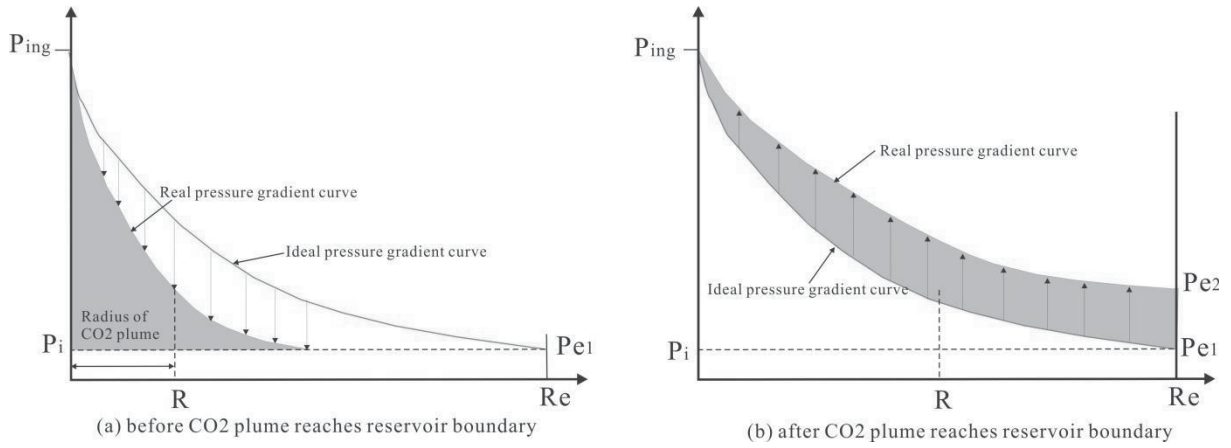
Fig. 4.27 The pressure changes in the reservoir away from the injection point under a constant pressure injection condition (Xie and Economides, 2009)

Before CO_2 plume reaches the reservoir boundary ($R_w < R < R_e$):

$$q = \frac{2\pi kh(P_{inj} - P_i)}{\mu \ln(0.472R_e/R_w)}, \tag{4.4}$$

where q – is the injection rate of CO_2 (kg/s); k – is the permeability of reservoir rock (m^2); h – is the thickness of reservoir; μ – is the viscosity of CO_2 (cP); R_w – is the well radius (m); R_e – is the equivalent closed formation radius (m), which is also the radius of the reservoir at the boundary; P_{inj} – is the injection pressure; P_i – is the initial reservoir pressure and P_{e1} and P_{e2} (in Fig. 4.27) are the reservoir pressure at boundary before and after the injected CO_2 reaches the boundary.

After fluid flow reaches the reservoir boundary ($P_i < P_{e2} < P_{inj}$), the injection rate can be calculated as follows (Economides et al., 1994):

$$q_t = \frac{kh(P_{ing} - pP_i)}{29\mu}(\log t + \log \frac{k}{\phi \mu c_t R_w^2} - 3.23), \tag{4.5}$$

By using a comparative case study with the outer lateral boundary closed at a distance of 10 km away from the injection point, it is observed that when 100 kt CO_2 is injected, the CO_2 plume will move much more faster in the lateral direction (Fig. 4.28), about 10 m farther, than in the base case (see Fig. 4.3). The difference in CO_2 induced pressure changes, with a total offset of 0.5 MPa, is obvious. The pressure concentration in layers between Aquifer 2 and Aquifer 3 in the base case is almost the same with the 10 km boundary condition (Fig. 4.29). It implies that boundary effect should be considered in the simulations of commercial scale CO_2 storage operations.
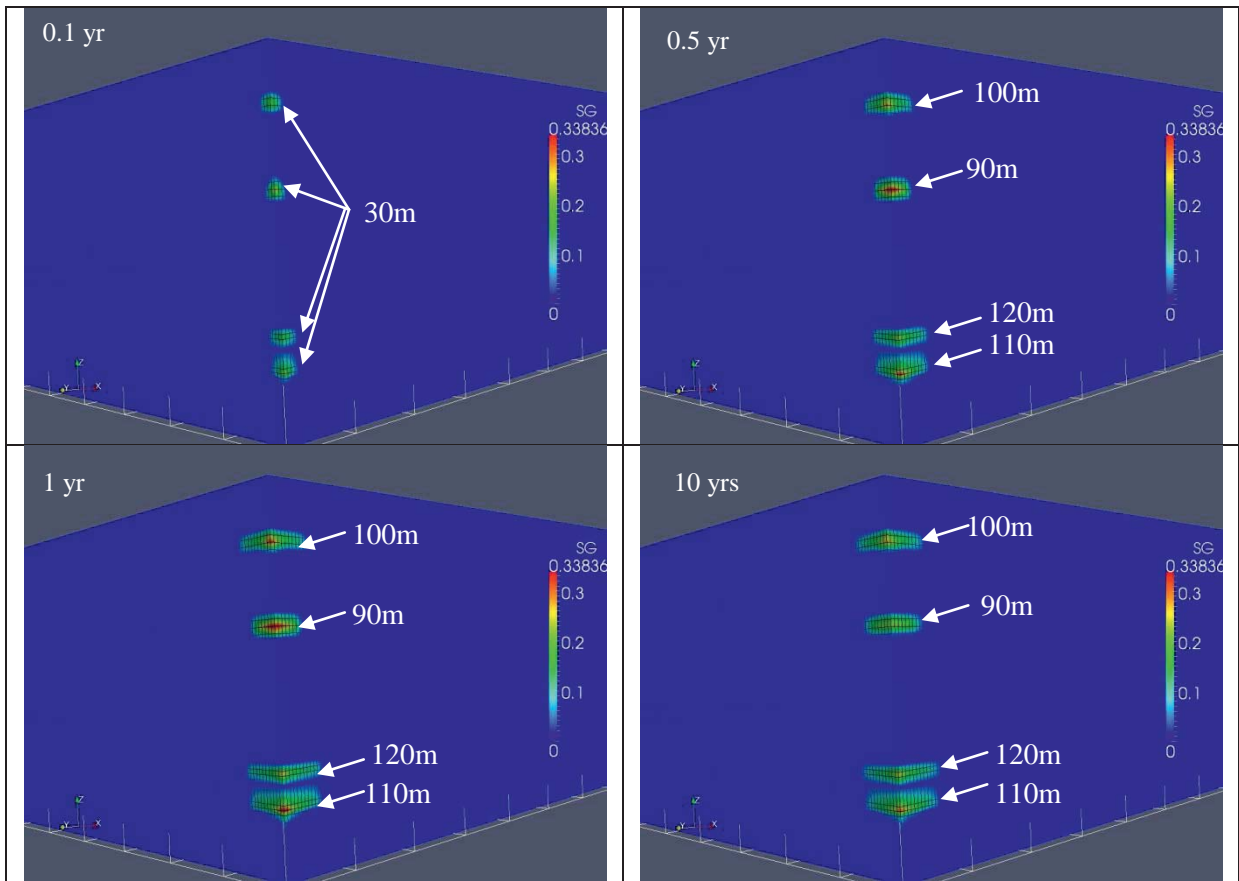
Fig. 4.28 Gas saturation changes in a 10 km model (case 3)
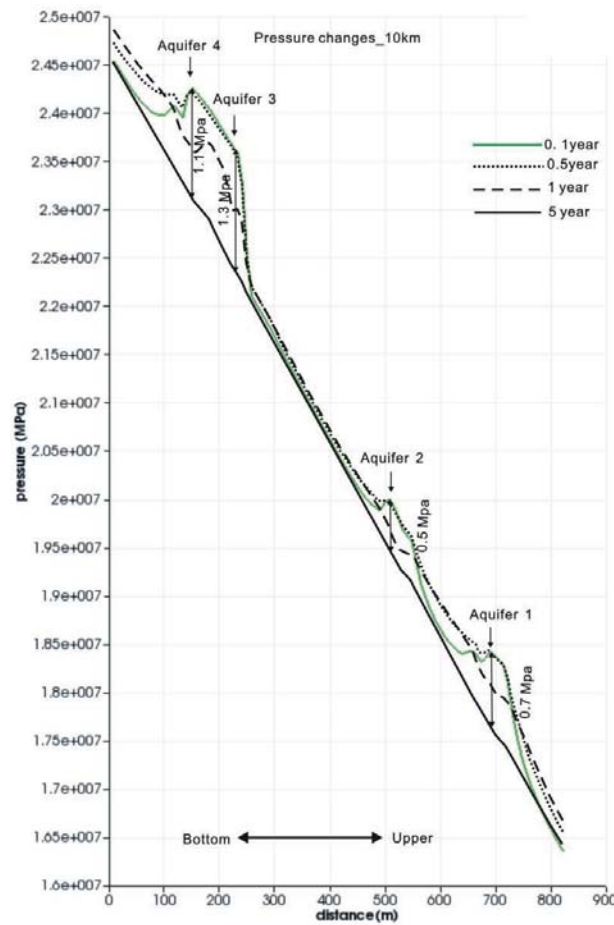
Fig. 4.29 Pressure changes in vertical direction across injection points in 10 km model

108

4.4.3 Anisotropy of the reservoir permeability

The anisotropy of the reservoir permeability established during deposition, presenting the variation in pore shape, size, connectivity (Meyer, 2002). The anisotropy has been modified during diagenetic processes, due to different scale of heterogeneity in formations in terms of mineral composition, matrix content and cementation content, etc, including intraformational heterogeneity, interlayer heterogeneity and areal heterogeneity (Halvorsen, 1993).

Anisotropy of permeability may have strong effect on the proesses in the two phase (water-CO$_2$) fluid flow system. It can be evaluated through numerical simulation by changing the permeability distribution in the reservoir-caprock system. Anisotropy of permeability could produce different reservoir segments, which may cause the infiltration process much complex (Fig. 4.30, Szulczewski, 2009).

(a) Plume migration in a homogeneous reservoir

(b) Plume migration in a reservoir with discontinuous, low-permeability beds

(c) Plume migration in a reservoir with extreme permeability channeling
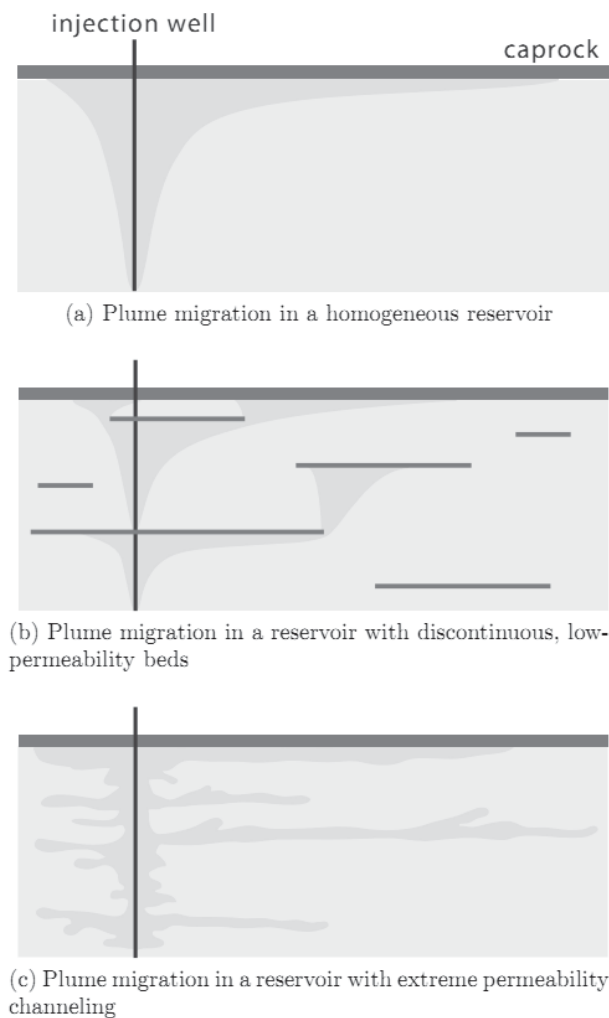
Fig. 4.30 Effect of vertical capillary barriers on the migration of the injected CO$_2$ (Szulczewski, 2009)

4.4.3.1 Tight sandstone and mudstone

When the porosity and permeability of the reservoir-caprock system changes, the distribution of gas saturation, the solubility of CO$_2$ in brine and pore pressure will show different characteristic patterns. In this sensitivity case study, the permeability of the mudstone is assumed to be 0.1 μD, with porosity and permeability of the sandstone modified to 12% and 5 mD, respectively (i.e. typical parameters for a tight sandstone). Figs. 4.31, 4.32 and 4.33 illustrate that the lateral movement of CO$_2$ plume is promoted in the tight reservoir-tight caprock system. A higher permeable seal enables the brine to move upwards. This is in accordance with the simulation results of Hussain et al. (2013).
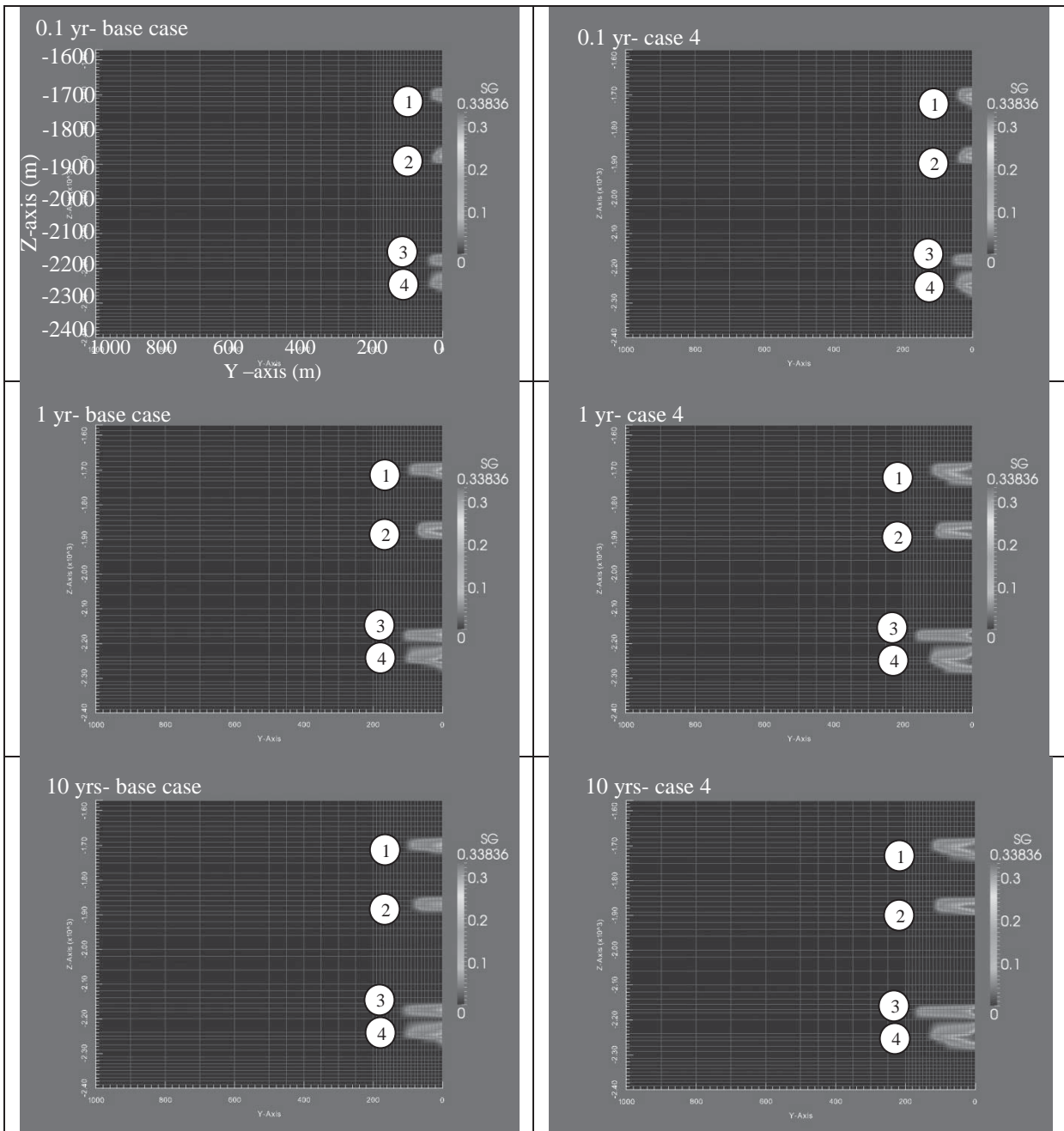
Fig. 4.31 Gas saturation changes in normal and tight reservoir-caprock system
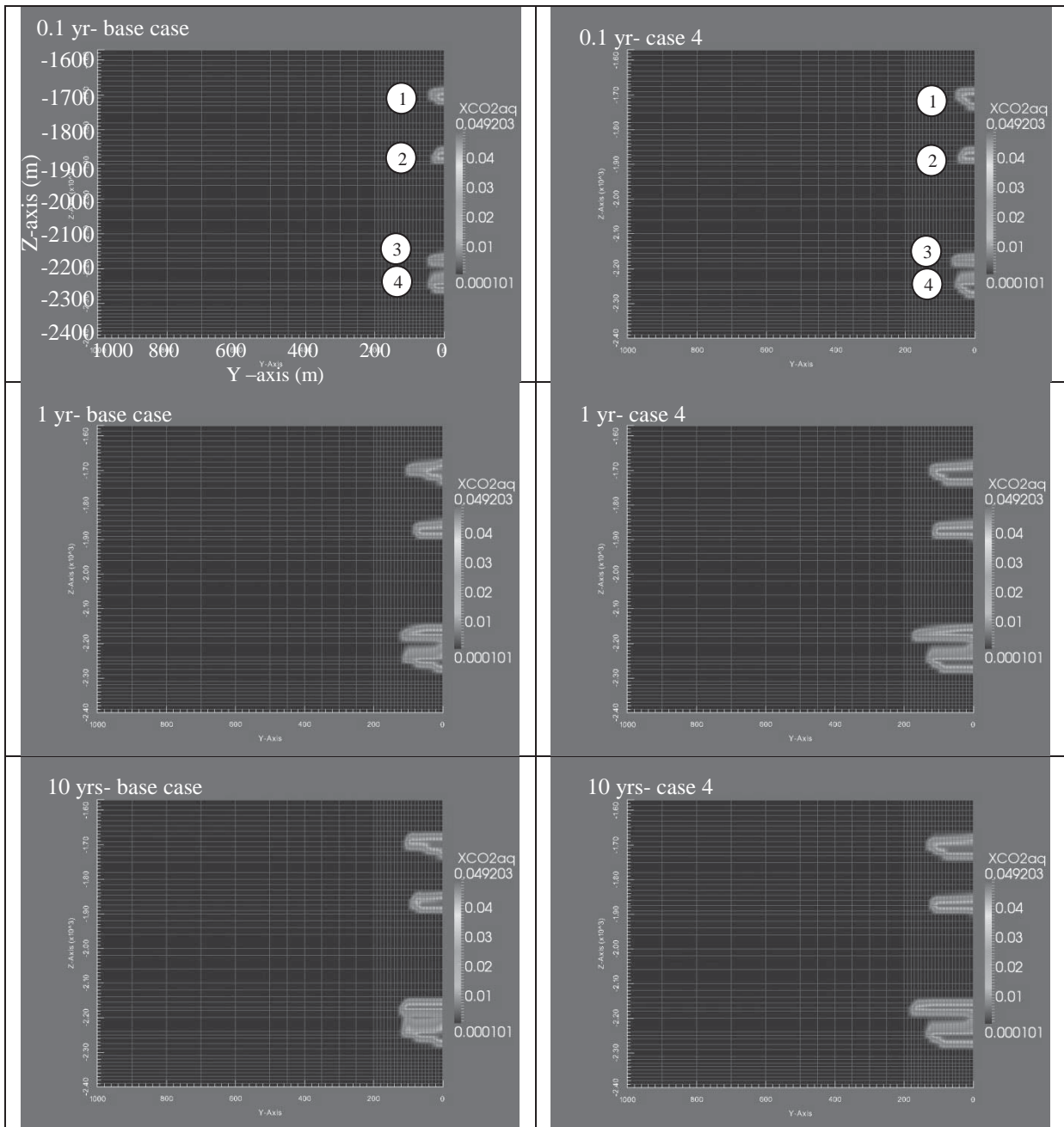
Fig. 4.32 The mass fraction of CO$_2$ in the formation water in base case (left) and tight reservoir-caprock system (right)
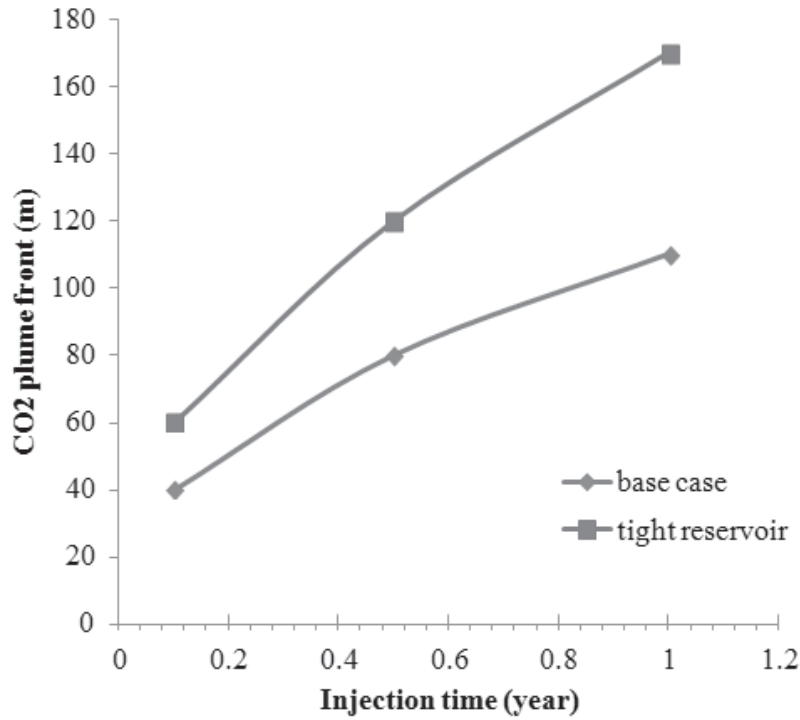
Fig. 4.33 Reservoir properties of the CO_2 plume front in Shihezi formation (layer 3)

4.4.3.2 K_h/K_v

The anisotropy of intact rock permeability is primarily a function of the preferred orientation of mineral particles and micro-discontinuities (Lewis, 1988). The permeability of a porous medium is usually larger in the parallel (K_h) than in the perpendicular (K_v) direction. Table 4.4 lists the ratios of K_h to K_v for different rocks. The CO_2 breakthrough can occur much earlier in the case of a higher horizontal permeability (Ganjdanesh et al., 2012).

Table 4.4 The ratios K_h to K_v for different rocks (Zhang 2013)

Rock	K_h/K_v	References
Crab Orchard sandstone	2.2	Walsh et al., 1979
Berea sandstone	4.0	Wei et al., 1988
Triassic Sherwood sandstone	2.0-3.3	Ayan et al., 1994
Granite	2.5	Wei et al., 1995
Sandstone	1.3-5.9	Bieber et al., 1996
Limestone	1.6-8.3	Bieber et al., 1996
Andesite	4.0	Bieber et al., 1996
Rothbach sanstone	5.3	Louis et al., 2005
Bentheim sandstone	1.2	Louis et al., 2005

Here, two scenarios are studied in this simulation. One with the ratio K_h/K_v=10 (case 5), and the other, a comparative case, with the ration K_h/K_v =1 in the base case. It is shown that pressure buildup will be much higher in the case of a larger K_h/K_v than in a smaller ratio case (Figs. 4.34 and 4.12).
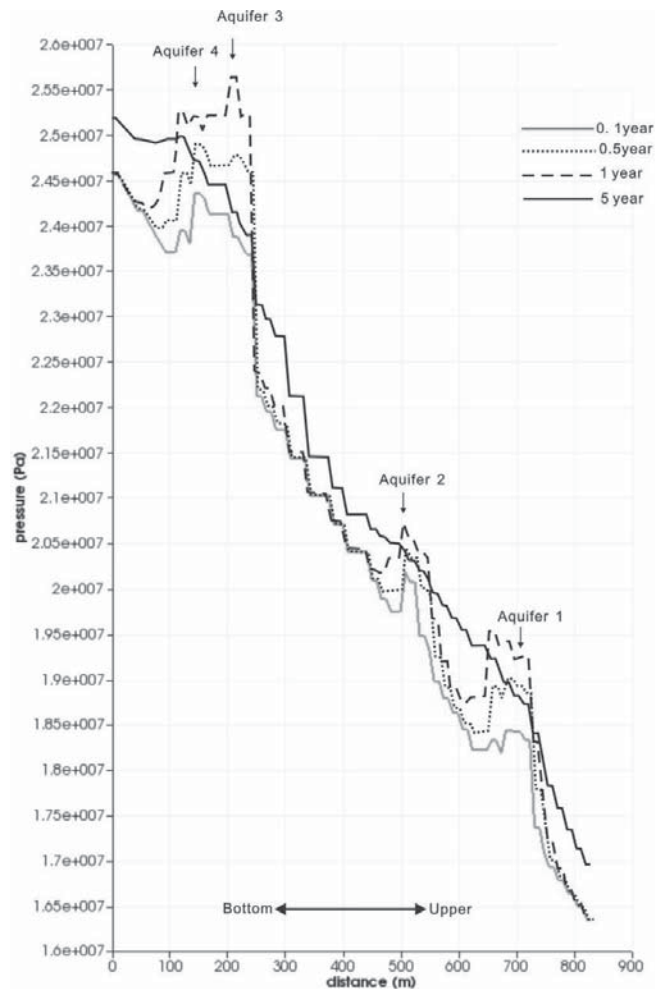
Fig. 4.34 Pressure changes along the vertical line through injection point in case 4 (K_h/K_v =10)

4.4.3.3 High permeable layer effect

Hydraulic fracturing technology has already been widely used in tight oil/gas reservoir or shale gas production. It has been proved that this technology can greatly enhance oil or gas recovery (El-Naqa, 2001; Bunger et al., 2013). In CO$_2$ sequestration project, hydraulic fracturing technology is also useful in increasing the injectivity of reservoir.

Here, the initiation, propagation and termination processes of hydraulic fractures are not the research point. The purpose is to study the migration of CO$_2$ in a relative higher permeable zone, which stands for a fracture zone. A fractured zone (high permeable layer) is created in this simulation study, with a size of 300 m × 300 m in the plane and an aperture of 10 cm. Two cases with different permeability are used in the fractured zone, one with 1 D, and the other 10 D.

Comparative studies (base case and case 6) show that CO$_2$ will flow much faster in the fractured zone due to enhanced fluid infiltration. This phenomenon also occurs in the natural system characterized by the ubiquitous occurrence of brecciated textures (Boschi et al., 2009). The higher the permeability in the fractured zone, the farther the CO$_2$ plume front will migrate (Fig. 4.35). This is in accordance with Mcpherson et al. (2001) that the lateral migration rate of supercritical CO$_2$ is a function of the matrix permeability. The brine with dissolved CO$_2$ will flow along the fracture path and form a larger zone than CO$_2$ plume (Figs. 4.36 and 4.37).

113
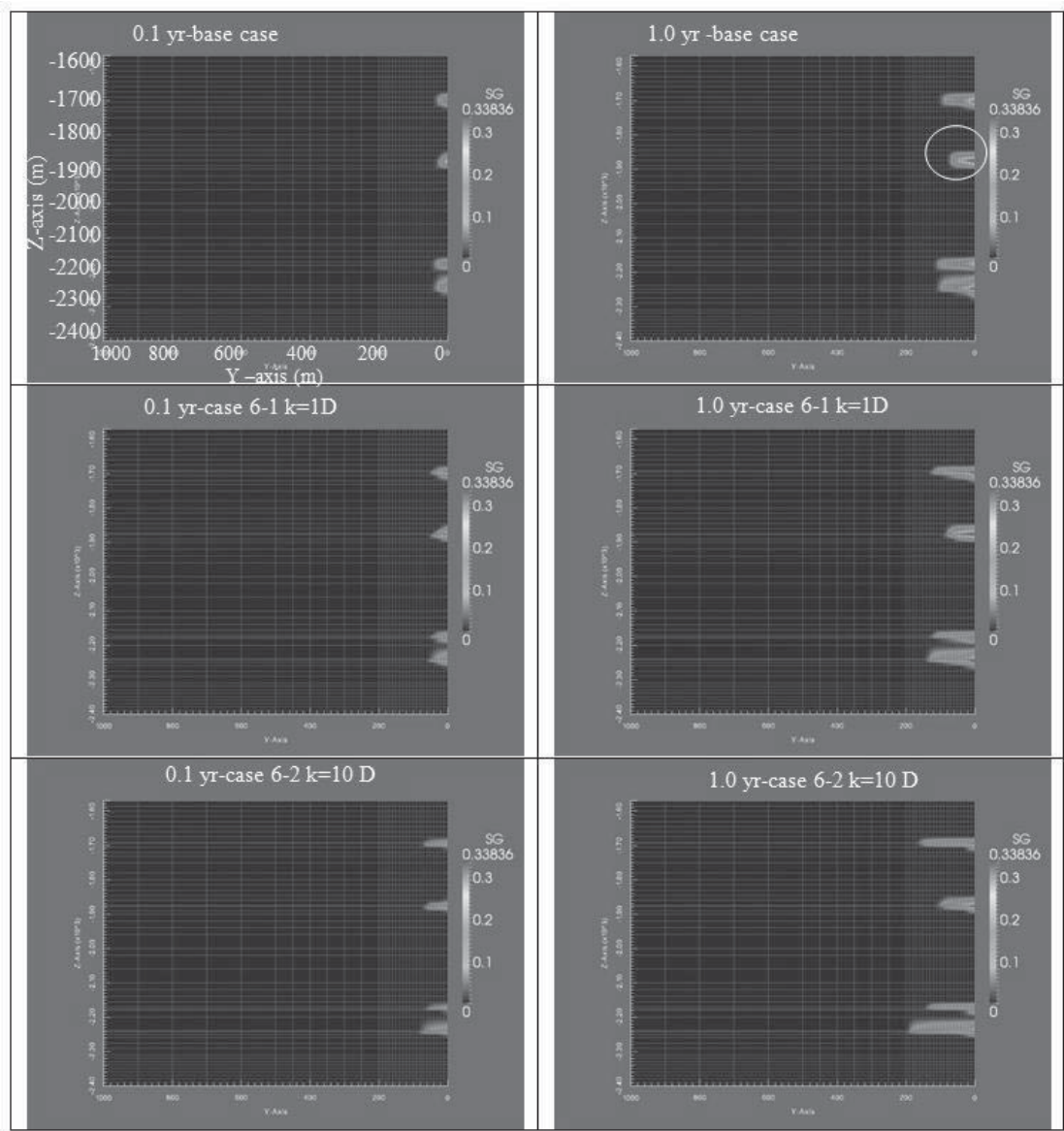
Fig. 4.35 Gas saturation changes due to different hydraulic conductivity effect
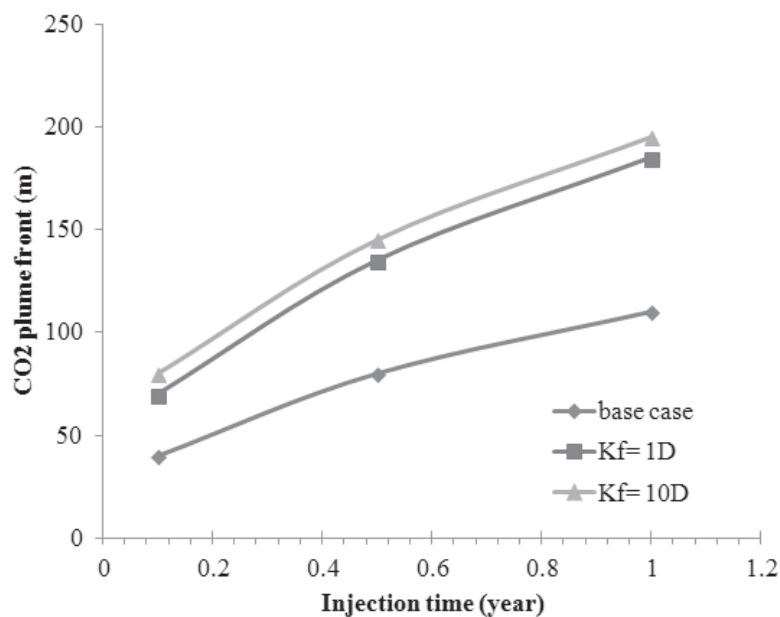
Fig. 4.36 The effect of high permeable layers on CO$_2$ plume front of Shanxi formation (layer 4)

114
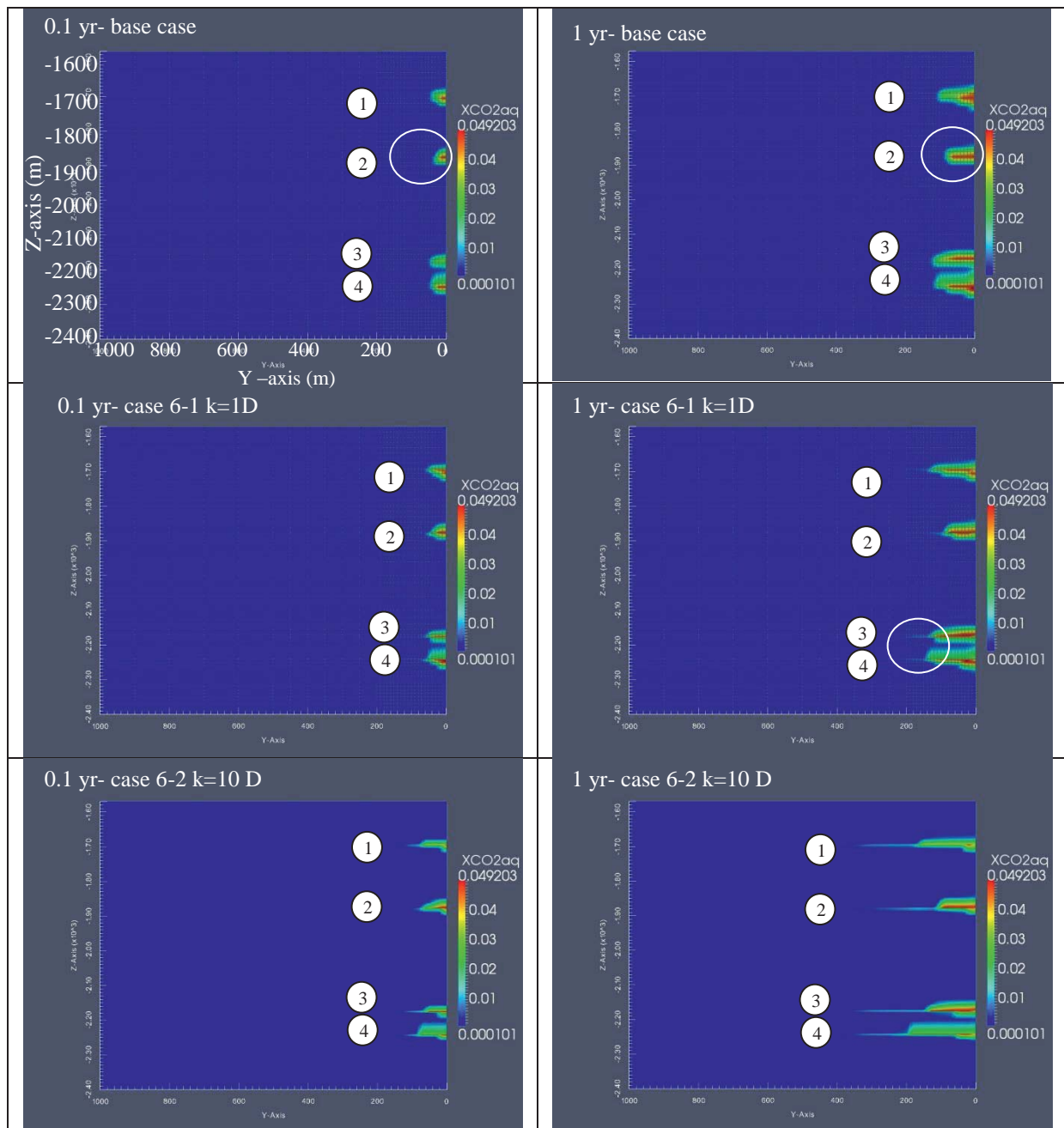
Fig. 4.37 The distribution changes of CO$_2$ mass fraction in aqueous phase due to the existence of high permeable layers

4.4.4 Effect of geological structures

Based on the structural setting of the pilot sites, CO$_2$ can be injected into a horizontally layered formation, an anticline or in a pinch-out sandstone body. These structures testify the greatest impact on CO$_2$ plume distribution pattern. In two case studies, where different injection positions and dip angles of the slope are used, the former model is simplified from Ketzin CO$_2$ injection project (Förster et al., 2006; Martens et al., 2012), with the injection position at the top of the model, while the latter is simplified from Ordos CO$_2$ injection project, with the injection position at the bottom, both of which are a 10 km in the lateral direction. The spatial and temperal evolutions of CO$_2$ plume are demonstrated (Fig. 4.38). When injection point is at the top of the reservoir, the radial scope starts from the upper injection zone, and a gravity tongue forms (Flett et al., 2003). The lateral movement below the caprock becomes more and more time-dependent. At the bottom of the reservoir, nearly no free gas exists due to the strong buoyancy effect of CO$_2$.

When the injection point is at the bottom of the reservoir (latter case), the continuous buildup of pressure caused by injected CO$_2$ at the injection zone drives the plume front forward. When injection stops, buoyancy effect starts to play a role, until the movement of CO$_2$ arrives at the bottom of the impermeable layer (Fig. 4.39). The pressure difference between at the CO$_2$ plume front and the initial reservoir will promote the continuous migration of CO$_2$ along the slopy boundary.
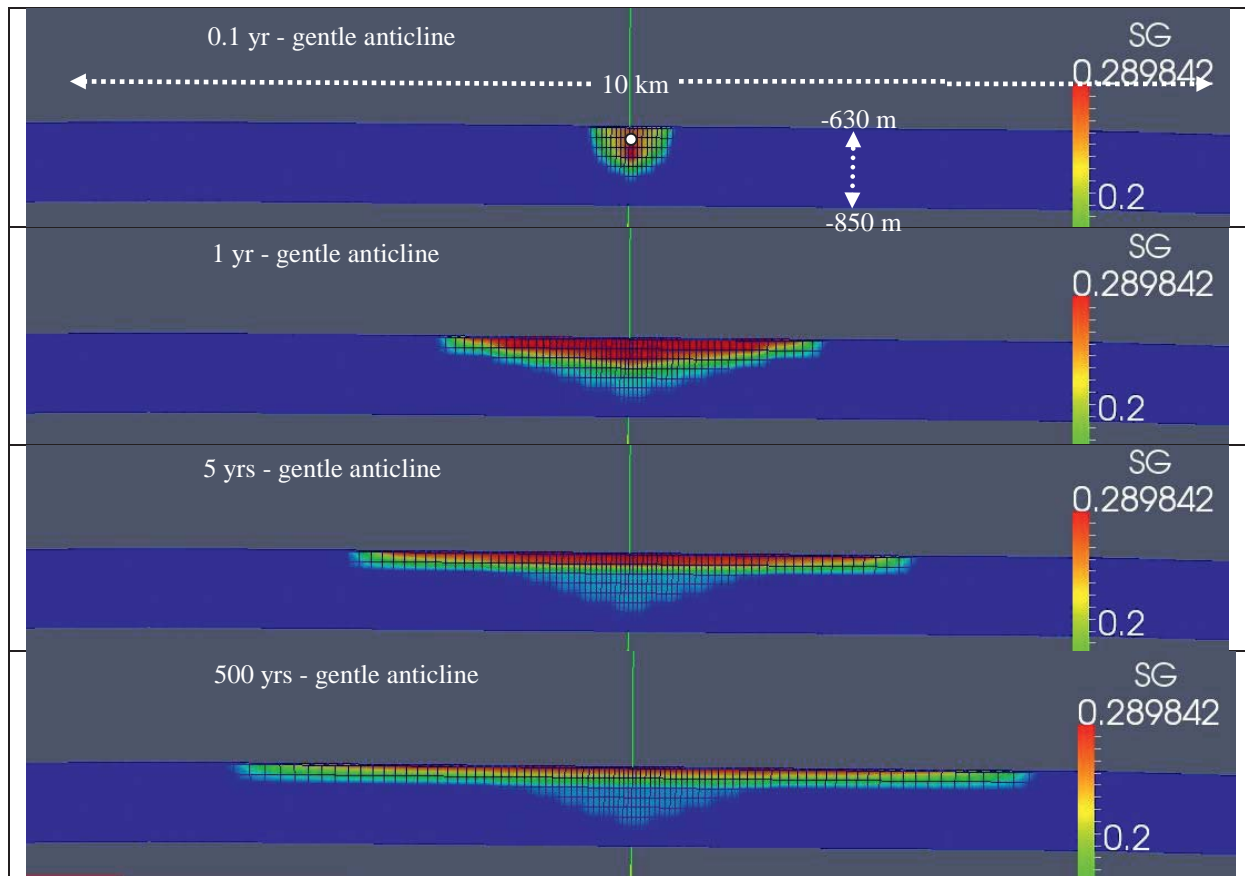
Fig. 4.38 Time evolution of CO$_2$ plume in gentle anticlines of different levels (based on geological structure of Ketzin)
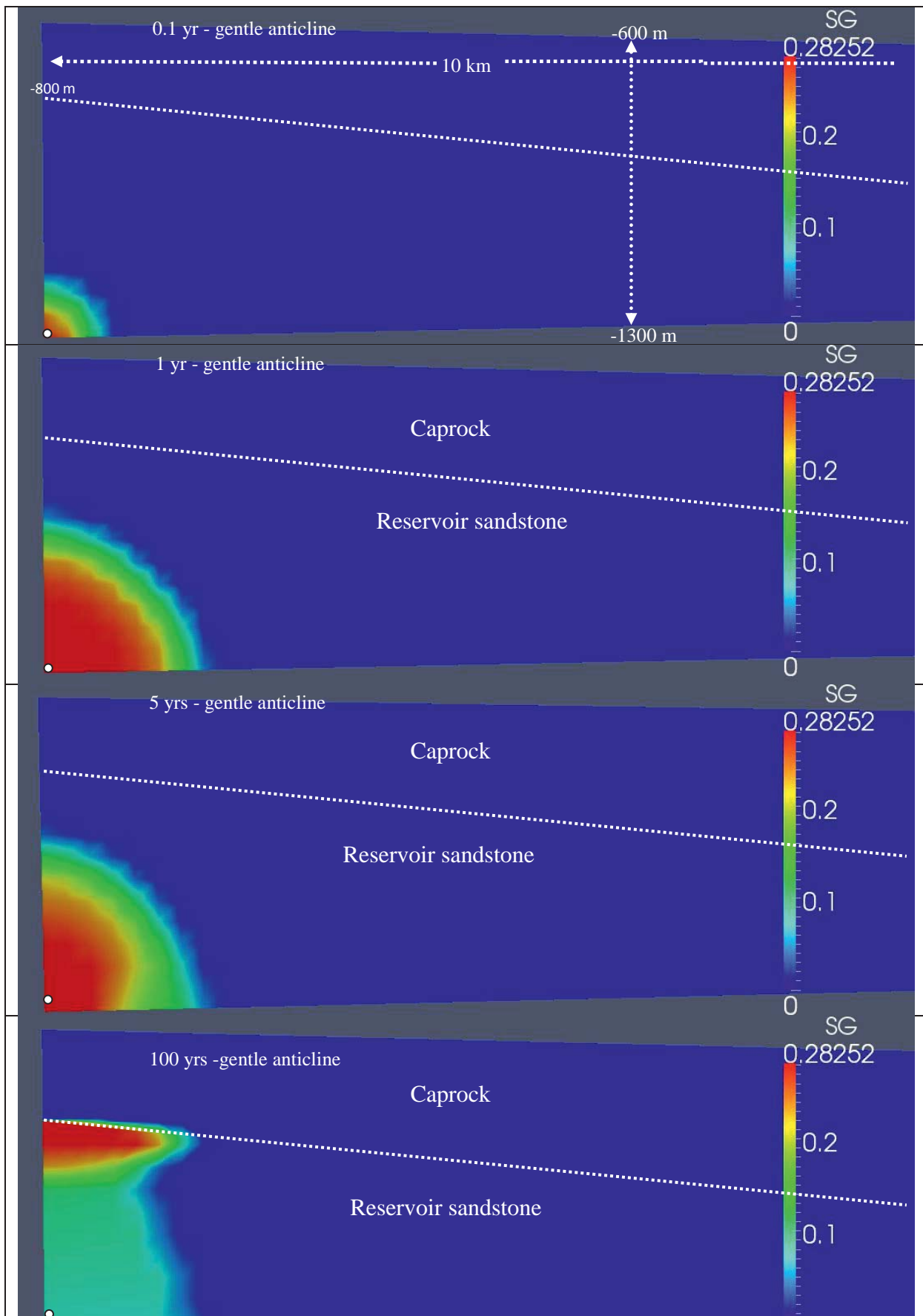
Fig. 4.39 Time evolution of CO$_2$ plume in gentle anticline with a bottom injection point

4.4.5 Capillary pressure and relative permeability effect

Caprock integrity is an important aspect in the study of CO_2 sequestration. CO_2 invasion in the caprock may occur through different physical processes: *diffusion* of the CO_2 molecules in the water-saturated cap rock; *capillary breakthrough* of the CO_2 phase and *hydraulic or thermal fracturing* of the cap rock consecutive to the pressure buildup and temperature decrease resulting from CO_2 injection (Chiquet et al., 2005). Therefore, the capillary pressure and relative permeability functions are investigated to show the impact on the CO_2 plume shape, migration distance, pressure buildup and so on.

4.4.5.1 Capillary pressure effect

Capillary leakage will occur when the pressure in the CO_2 phase increased to a value (P_0). This pressure is defined as the minimum pressure needed to initiate the displacement of water in the cap rock by the CO_2 phase. This means that it is difficult for CO_2 to enter into the caprock under a high capillary entry pressure condition or the vice versa.

In this case study (case 8), it will be demonstrated that only minor differences occur between gas saturation and mass fraction of CO_2 in aqueous phase in cases with and without capillary capillary effect. The reason for this phenomenon can be explained with the concept of CTZ (Capillary Transition Zone) in Court (2011). It assumed that capillary forces can be ignored when the CTZ is small relative to the thickness of the formation.

When capillary forces are significant, they need to be considered. Because the capillary pressure effect is not obvious in this simulation, information about its impact on gas migration has been obtained from previous literature. Two representative industrial and pilot scale injection scenarios are described in Court (2011) and Lu et al. (2009), with their simulation parameters summarized in Table 4.5.

Table 4.5 Numerical simulation parameters for capillary pressure effect study (Court et al., 2012)

Parameters	Court (2011) problem set up	Lu et al. (2009) problem set up
Top depth	2000	2000
Thickness (m)	50	62
Intrinsic permeability (mD)	100	10
Porosity (-)	0.15	0.15
Injection rate	0.939 Mt/y for 50 years	0.1 Mt/y for 10 years
Grid discretization	Horizontal: 5 m in radial direction to 6 km; Gradually increasing to 1 km block until 60 km Vertical: 1m in z	Horizontal: 2 m in radial direction to 1024 m; Vertical: 2 m in z
Outer boundary condition	Fixed hydrostatic pressure	Fixed hydrostatic pressure

From the simulation results in Figs. 4.40 and 4.41, it can be concluded that, in the high permeability reservoir, when capillary pressure takes effect, more water will be left in the water-gas two phase zones. The buoyancy effect becomes stronger when capillary pressure is ignored. In the tight reservoir, for example, the restriction of capillary pressure on vertical migration of CO_2 is weak.
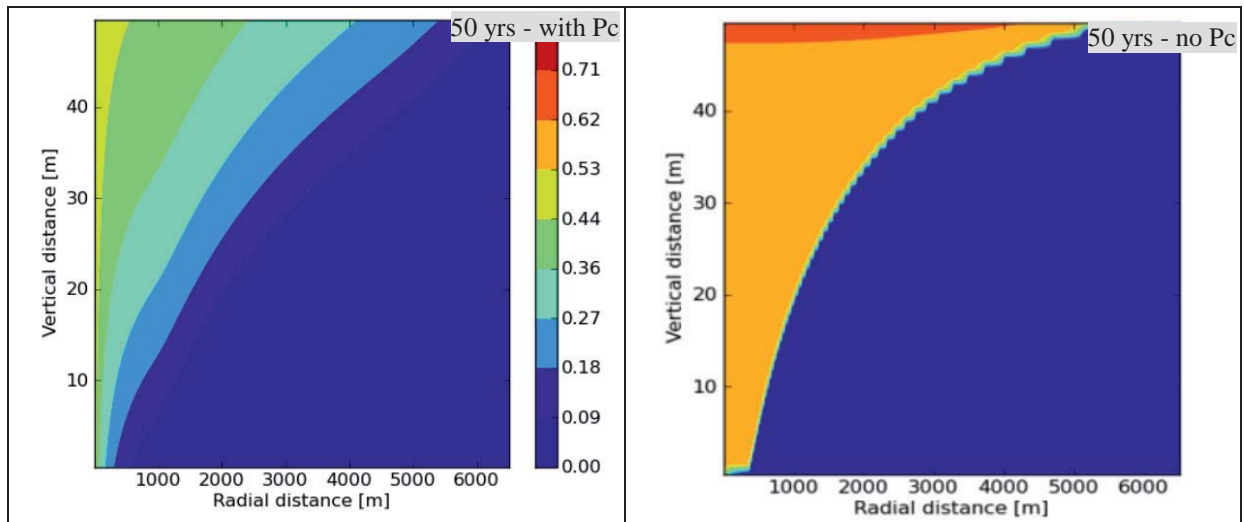
Fig. 4.40 Gas saturation profiles in high permeability reservoir under conditions with and without capillary pressure effect (Court, 2011)
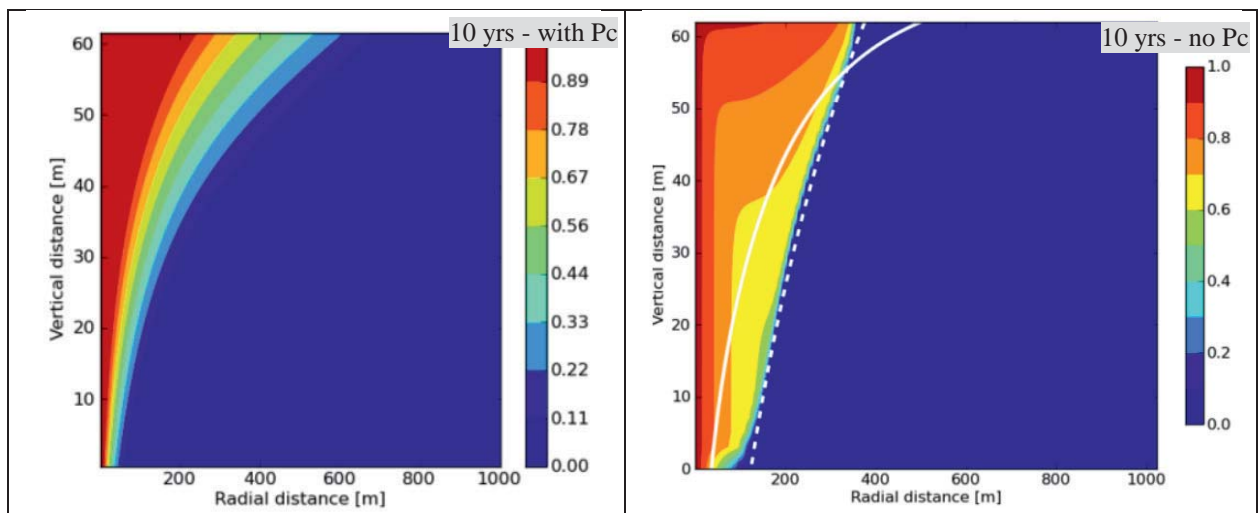
Fig. 4.41 Gas saturation profiles in low permeability reservoir under conditions with and without capillary pressure effect (Lu et al., 2009)

4.4.5.2 Relative permeability effect

In petroleum engineering, a reasonable relative permeability (k_{rel})-saturation (S) curve is vital in the prediction of oil and water distribution. A lot of k_{rel}-S functions have already been applied in the simulation study for CO_2 sequestration problems (Court, 2011). Some sensitivity studies about the effect of k_{rel}-S functions on CO_2 plume movement and CO_2-water distribution are necessary for selection of optimal parameters for simulations (Cinar et al., 2009).

Van Genuchten-Mualem model (Mualem, 1976; van Genuchten, 1980) is used in the water relative permeability calculation, while gas relative permeability calculation is due to Corey (1954). Residual liquid saturation (S_{lr}), determined by wettability of rock, pore structure, is an important factor in determing relative permeability, hence, its consideration in the sensitivity analysis. In this case study, the exponent m and residual gas saturation are assigned to be 0.4 and 0.05, respectively. In comparison, $S_{lr} = 0.2$ in the base case, while in case 9 two values 0 and 0.3 are used in their simulations.

The gas saturation distribution characteristics during injection and post-injection period indicate that the spreading scope of the CO_2 plume is even larger when the residual liquid saturation is low (Fig. 4.42).

119
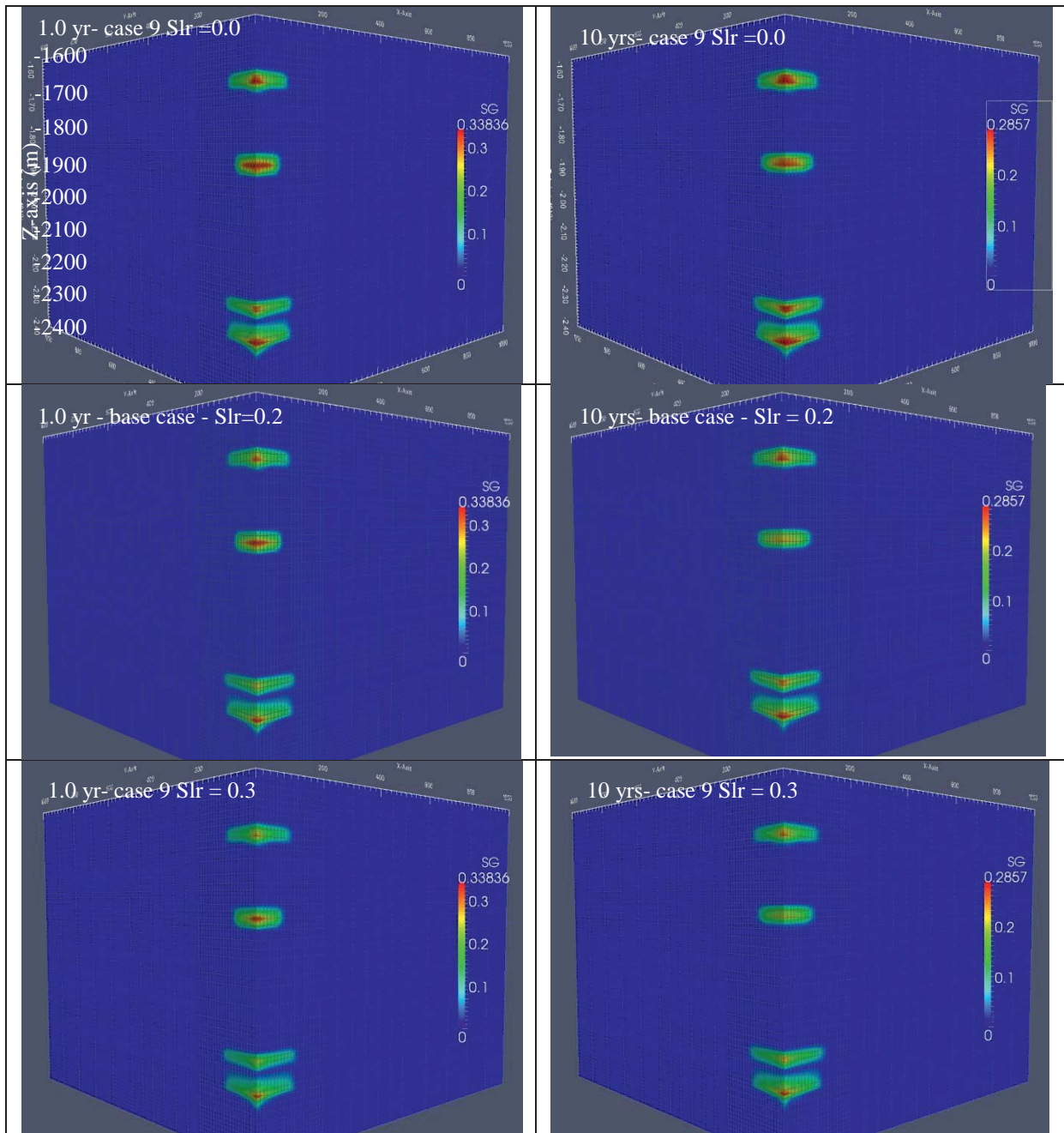
Fig. 4.42 Gas saturation profiles in different residual liquid saturation conditions

The choices of different k_{rel}-S relationships may also lead to very distinct results (Fig. 4.43). Therefore, more field data should be obtained before the selected functions are used in the long term prediction study.
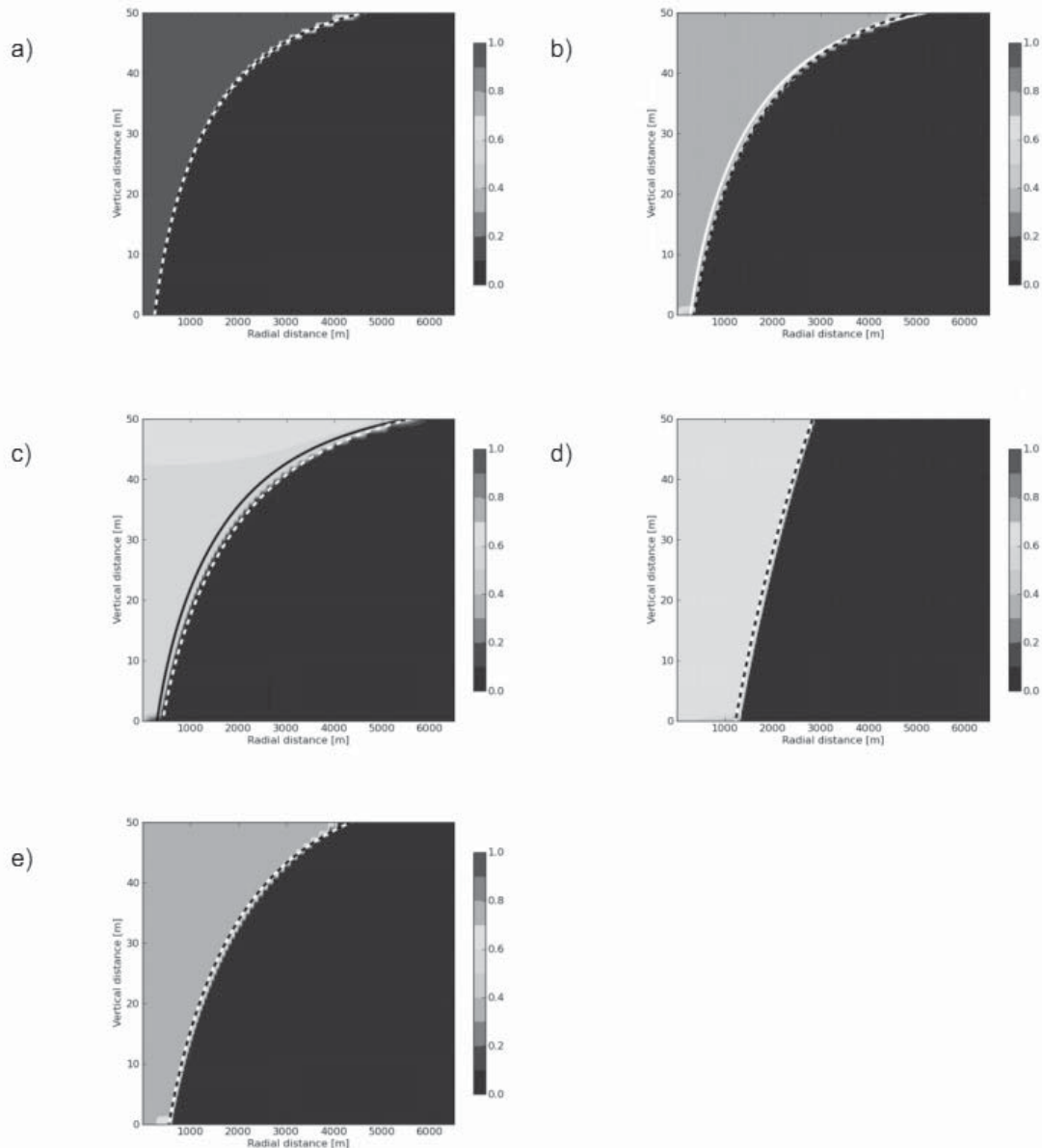
Fig. 4.43 Comparison of CO$_2$ saturation profiles at the end of injection with different k_{rel}-S functions   (Court, 2011) (a) linear, (b) Ebigbo, (c) Zhou, (d) Nisku, and (e) Basal

The numerical model is able to provide many insights into the overall system behavior. It is clearly limited in the scope by the restricted assumptions. After the sensitivity analysis based on different parameters modifications, some cognition about the whole systems can be obtained. The influence of parameters on CO$_2$ plume front migration from the injection point may be ranked in the following sequence: injection rate > hydraulic fracturing > multi-layer injection > tight sandstone and mudstone properties. The effect of other parameters on CO$_2$ plume front movement is not obvious. As time goes by, the distribution and movement of the CO$_2$ plume adjust with respect to pressure dissipation.

121

5. Simulation of fluid flow and mechanical response in Ordos saline formations [H^{2}M]

When a fluid infiltrates through the porous media, the complex interaction processes between rock and fluid are triggered off. The changes in pore pressure induced by CO_2 injection will in turn cause changes in effective stress of the formation. A reduction in effective stress due to fluid injection, for example, may induce plastic yield. Furthermore, a change in pore pressure may lead to changes in the mechanical volume of the rock grain framework, consequently affecting the porosity and permeability of the entire reservoir (Hou et al., 2009).

In practice, hydro-mechanical (HM) coupling studies can help to determine conditions under which mechanical failure may occur so as to guide to the safe injection strategy (i.e. injection or storage pressure < fracturing pressure of rock) (Riano, 2012; Vilarrasa, 2012). During CO_2 injection into deep saline formations, reduction of the effective stress initiates strongly coupled hydromechanical effects imposing a great risk to the integrity of the rocks in the lower part of the caprock (Rutqvist and Tsang, 2002). Shear and tensile failures are likely to occur during the CO_2 injection period. In-situ stress field and fluid pressure together with the induced shear may lead to hydraulic fracturing or reactivation and re-orientation of the old faults in the caprock. The shear failure usually happens much earlier than the tensile failure. Rutqvist et al. (2008) established that when the small horizontal stress is larger than the vertical stress ($\sigma_h > \sigma_v$), shear failure will occur more easily in the form of gently dipping fractures before damage to the upper caprock takes place. When the horizontal stress is smaller than the vertical stress ($\sigma_h < \sigma_v$), propagation of the steeply dipping fractures tends to occur. If fluid pressure exceeds the minimum principle stress (σ_3), extensional hydraulic fracturing will take place in the direction perpendicular to σ_3.

The aim of the hydro-mechanical coupling study is to investigate the stress and strain changes during the CO_2 injection and post-injection periods in order to assess caprock integrity (Riano, 2012). In this Chapter, literature review will involve the previous THMC coupling research on CO_2 sequestration, especially the hydro-mechanical coupling effect. Then the mathematical theories of hydro-mechanical coupling are described, followed by the HM modeling with respect to Ordos CO_2 sequestration using a simplified 3D multilayered model. Case studies will be used to study the sensitivity of different factors on HM coupling effects, including the in-situ primary stress state, Biot's modulus, injection rate and permeability. Finally, vertical displacement, pore pressure, stress state variation and hydrological characteristics changes due to CO_2 injection are analyzed in the results and discussion section.

5.1 Literature review

From the scientific, engineering and environmental point of view the technology of CO_2 sequestration, though complicated, remains a significant option for the reduction of greenhouse gas emission in the atmosphere (Solomon et al., 2007). It involves a multiphase fluid flow in porous media, including the complex multi-field interactions, especially the coupling effects of thermal (T), hydraulic (H), mechanical (M) and chemical (C) fields (Taron et al., 2009). All variants in these fields will be changed in space and time. Furthermore, property variations in one field can be more or less affected by other fields (Stephansson et al., 2004). For example, infiltration parameters in the hydraulic field, such as porosity and permeability, will be affected by the local temperature, water-rock interactions, in situ stress fields, etc. To reduce risks in a specific engineering project, such as hydrocarbon production, geothermal extraction, CCS and general civil engineering projects, closer attention must be paid to the interactions of the coupled THMC processes (Bachu and Dusseault, 2005a; Taron et al., 2009).

Researchers are making a great effort toward understanding the scope of coupled processes involved in a number of fields including thermo-hydrological, thermo-mechanical, thermo-chemical, hydro-

mechanical, thermo-hydro-mechanical, thermo-hydro-chemical, or the fully coupled THMC fields (Louis et al., 1977; Rutqvist et al., 2002; Pruess et al., 2004; Hawkes et al., 2004; Stephansson et al., 2004; Bachu and Dusseault, 2005a; Taron et al., 2009; Celia and Nordbotten, 2009; Yin et al., 2008, 2012; Hou et al., 2012a; Gou et al., 2014). Nevertheless, very little is known about the coupled mechanisms of THMC processes. Sophisticated mathematical models, numerical algorithms and software tools (Kolditz et al., 2012), such as TOUGH2, STOMP, HydroGeoSphere, FEFLOW, SUTRA, DUMUX, MIN3P, MT3D and OGS have been developed taking into account all the relevant physic-chemical phenomena that occur during migration and storage of CO_2. Such physic-chemical phenomena may include multiphase flow and transport of dissolved and mixed phases, viscous fingering effect, heat transport, rock deformation and failure (Goerke et al., 2011).

Based on the problems we are interested in, for example, CO_2 migration, deformation/uplift of rock, long-term integrity and safety of project, in this paper, the coupled hydro-mechanical effects are considered, involving two aspects (Settari and Walters, 1999; Hou et al., 2012a): geomechanical modeling (mainly for stress and strain behavior) and reservoir simulation (multiphase multi-component fluid flow and heat transfer in porous media). Except CO_2 sequestration (Rutqvist et al., 2008; Hou et al., 2012a; Gou et al., 2014), the coupled hydro-mechanical behavior studies can also be extended to other application in hydrocarbon production (McKee et al., 1988; Hettema et al., 1998; Hou and Zhou 2013; Zhou and Hou 2013) and geothermal production (Hou et al., 2012b).

5.2 Numerical model setup and parameters

5.2.1 Modeling methods

The linkage of TOUGH2MP/ECO2N to FLAC3D has been used for simulations in this part of the thesis. The simulations are based on the coupling concepts discussed in Rutqvist et al. (2002, 2003a, 2003b) and the previous works by Hou et al. (2012a). The linkage structure is shown in Fig. 5.1. At each time step, TOUGH2MP obtains the variables from each processor, including pressure, temperature and saturation, then transfers them to FLAC3D to calculate the deformation and stress distribution in the rock formations. The recalculated stresses and deformations of each element are then transferred back to TOUGH2MP and redistributed onto each processor to calculate the corresponding changes of flow properties (Gou et al., 2014).
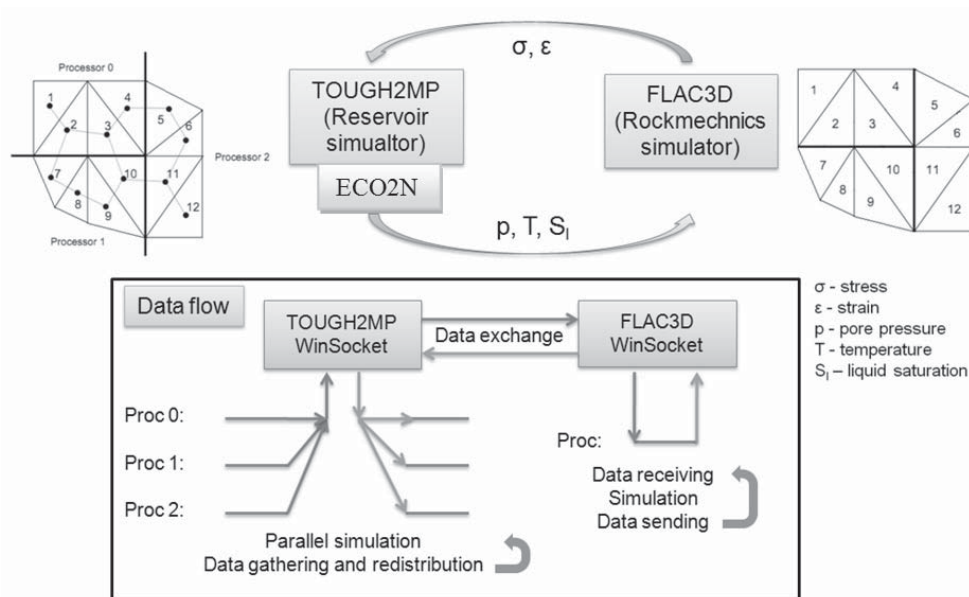
Fig. 5.1 The linkage between TOUGH2MP and FLAC3D (Hou et al., 2012a)

123

Linkage of TOUGH2MP/ECO2N and FLAC3D is through some coupling functions between the hydraulic and stress fields. Eqs 5.1 and 5.2, from Rutqvist and Tsang (2003), are used to calculate the relationships between porosity, permeability and effective stress for the four injection layers of the multiple reservoir-caprock system in the CO_2 sequestration site of the Ordos Basin:

$$\phi = (\phi_0 - \phi_r) \cdot exp(a \times \sigma_M') + \phi_r, \tag{5.1}$$
$$k = k_0 \cdot exp[b \times (\phi/\phi_0 - 1)], \tag{5.2}$$

where, $\sigma_M' = (\sigma_M - \alpha P)$ is the effective mean stress (Pa), in which σ_M is the total mean stress; α is the Biot's coefficient (-); ϕ is porosity under a random stress condition (-); ϕ_0 is the porosity under zero stress (-); ϕ_r is the residual porosity (-); a, b are the correction coefficients with the values of 5×10^{-8} (1/Pa) and 22.2, respectively.

For siltstone and mudstone layers, the following two functions (Eqs 5.3 and 5.4) obtained from experiments can be used to express the relationship between normalized permeability (k/k_0) and effective stress:

$$\begin{cases} k_0 = \alpha(\phi_e)^\beta & (\sigma_M' = 0), \\ k = Ak_0(\sigma_M')^B + C & (\sigma_M' \neq 0), \end{cases} \tag{5.3} \tag{5.4}$$

where ϕ_e is effective porosity (-); and the regression coefficients A, B, C, α and β can be assigned to be 1.5, -0.175, 0, 5.78×10^4, 4.4288 respectively.

5.2.2 Geometry

Based on the practical experiences of CO_2 sequestrated into saline formations of the Ordos Basin (Li et al., 2013; Liu et al., 2014a), a simplified multilayered reservoir-caprock model consisting of 4 layers of sandstone, interbedded with layers of low permeable mudstone and siltstone is set up. The system is idealized as a three dimensional symmetric domain of dimensions 1×1 km $\times$ 830 m, with a total brick zones of 47089. The thicknesses of the studied aquifers are 10, 10, 30 and 15 m in that sequence from bottom to top. In this simulation model, the layers are simply assumed to be parallel and horizontal, see Fig. 5.2. The entire vertical extent of reservoir-caprock formations is assumed to be comprised of the thinner sandstone (aquifer) and siltstone layers of relatively high permeability sandwiched by the thicker mudstone units of lower permeability. The respective thicknesses of the formations (mudstone, siltstone and aquifer sandstones in the simulation section) were determined from actual drilling well logging data (Liu et al., 2014). In the model, aquifer 4 is underlain by a siltstone layer and overlain by mudstone. Aquifer 3 is sandwiched between mudstone layers. Similarly, aquifer 2 is sandwiched between mudstone layers, and aquifer 1, like aquifer 4 is underlain and overlain by siltstone and mudstone layers, respectively, see Fig. 5.2.
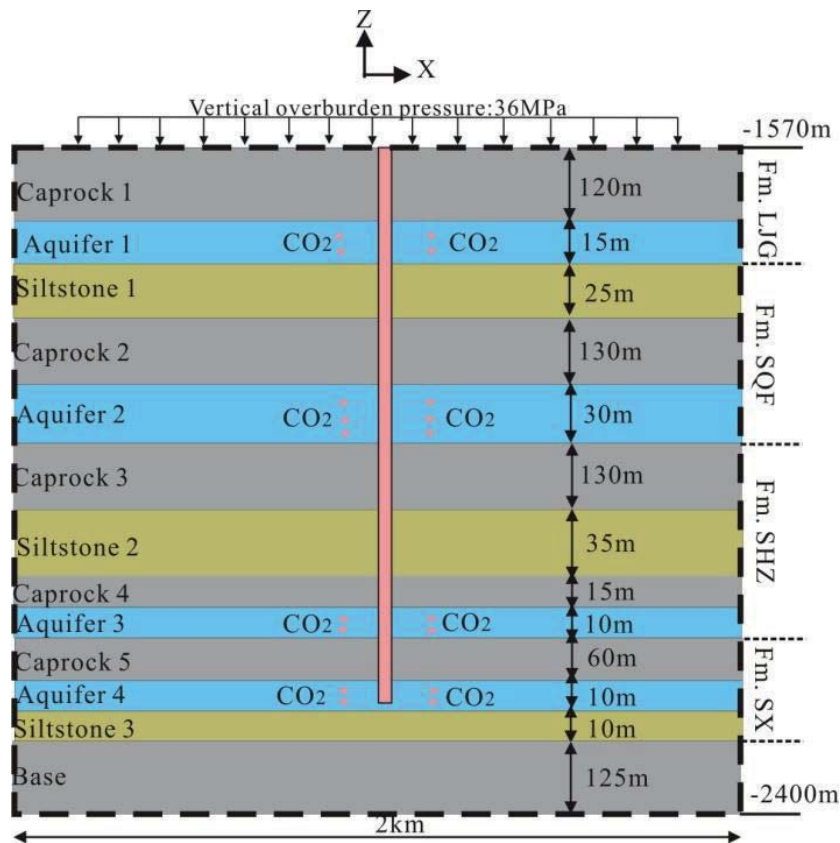
Fig. 5.2 A simplified multilayered geological model used for simulation runs

5.2.3 Hydrogeological and mechanical parameters

The hydrological parameters, reservoir conditions and material properties used in coupled hydro-mechanical simulation are shown in Table 5.1, for more details see Liu et al. (2014a). Three types of rock units have been used in this simplified model: i.e. the aquifer sandstone, siltstone and mudstone. To reflect the possibility of hydraulic fracturing treatment in the near wellbore region, in the aquifer sandstones, porosity and permeability are specified as 30 % and 50 mD, respectively. For siltstone, the porosity and permeability are much lower than that of sandstone, with the values of 10 % and 0.8 mD, respectively. Other parameters, such as Young's Modulus (E), Poisson's ratio (v), Cohesion (c), Internal friction angel (φ), etc., are based on the data obtained from the Daniudi gas field which is next to the CCS pilot site (Qin et al., 2005; Tang et al., 2010). Different values of Young's modulus and Poisson's ratio are used for different layers based on the parameters from Qin et al (2005) and Tang et al (2010). For example, for sandstones from top to bottom layers of the simulation model, the values of Young's modulus used are 23.0, 20.0, 27.0 and 23.0, respectively.

125

Table 5.1 Material properties used in the base case coupled hydro-mechanical simulation (data from Qin et al., 2005; Tang et al., 2010). (Aq: is aquifer sandstone; M: is mudstone; Ss: is siltstone)

Property	Fm. LJG		Fm. SQF			Fm. SHZ			Fm. SX		
	Aq	M	Aq	Ss	M	Aq	Ss	M	Aq	Ss	M
Young's modulus, E (GPa)	23.0	26.0	20.0	20.0	20.0	27.0	27.0	24.0	23.0	23.0	25.0
Poisson's ratio, ν (-)	0.16	0.23	0.22	0.22	0.24	0.16	0.16	0.21	0.23	0.23	0.28
Cohesion (MPa)	20.0	34.8	20.0	20.0	34.8	20.0	20.0	34.8	20.0	20.0	34.8
Saturated rock density, ρ_s (kg/m^3)	2450	2000	2450	2500	2000	2450	2500	2000	2450	2500	2000
Internal friction angel (°)	40.0	14.4	40.0	40.0	14.4	40.0	40.0	14.4	40.0	40.0	14.4
Biot's coefficient, α (-)	0.85	1.00	0.85	0.77	1.00	0.85	0.77	1.00	0.85	0.77	1.00
Porosity-stress function	$\phi = (\phi_0 - \phi_r) \exp(5 \times 10^{-8} \times \sigma'_M) + \phi_r$										
Zero stress porosity, ϕ_0 (-)	0.30	0.01	0.30	0.08	0.01	0.30	0.08	0.01	0.30	0.08	0.01
Residual porosity ϕ_r (-)	0.29	0.009	0.29	0.072	0.009	0.29	0.072	0.001	0.29	0.072	0.009
Permeability-Porosity function	$k = k_0 \times 7 \times 10^{-10} \times \exp(22.2 \times \phi/\phi_0)$										
Permeability in H, k_0 (m^2)	$5e^{-14}$	$1e^{-18}$	$5e^{-14}$	$1e^{-15}$	$1e^{-18}$	$5e^{-14}$	$1e^{-15}$	$1e^{-18}$	$5e^{-14}$	$1e^{-15}$	$1e^{-18}$
High zero stress Permeability in HM, k_0 (m^2)	$9.5e^{-13}$	$6.1e^{-18}$	$1.0e^{-12}$	$9.1e^{-15}$	$6.6e^{-18}$	$1.2e^{-12}$	$1.1e^{-14}$	$6.8e^{-18}$	$1.2e^{-12}$	$1.1e^{-14}$	$7.e^{-18}$
Low zero stress Permeability in HM, k_0 (m^2)	$8.1e^{-14}$	$4.1e^{-18}$	$8.3e^{-14}$	$6.2e^{-15}$	$4.4e^{-18}$	$8.6e^{-14}$	$7.5e^{-15}$	$4.8e^{-18}$	$8.6e^{-12}$	$7.9e^{-15}$	$5.e^{-18}$
Corey's (1954) relative permeability function parameters											
Residual gas (CO$_2$) saturation S$_{gr}$ (-)	0.05	0.05	0.05	0.05	0.05	0.05	0.05	0.05	0.05	0.05	0.05
Residual liquid saturation S$_{lr}$ (-)	0.40	0.40	0.40	0.40	0.40	0.40	0.40	0.40	0.40	0.40	0.40
Van Genuchten's (1980) capillary pressure function parameters											
Irreducible liquid saturation	0	0	0	0	0	0	0	0	0	0	0
entry pressure P$_0$ (kPa)	3.58	62.1	3.58	10.4	62.1	3.58	10.4	62.1	3.58	10.4	62.1
exponent m (-)	0.457	0.457	0.457	0.457	0.457	0.457	0.457	0.457	0.457	0.457	0.457

Based on the characteristics of the regional stress field near the pilot project zone, where strike faults are the dominant structural setting, the initial stress field should be used in anisotropic state. The direction of the maximum horizontal stress is along the NE-NEE-EW at present, and it gradually offsets from the southwest to northeast (Zhou et al., 2009). The stress regime at different places and depths are different. In the coal reservoir located in the southern region of the Ordos Basin (Meng et al., 2013), extensional stress regime ($\sigma_V > \sigma_H > \sigma_h$) is displayed at depths shallower than 1000 m, however, this transforms into a compressional state at depth deeper than 1000 m ($\sigma_H > \sigma_V > \sigma_h$ or $\sigma_H \sim \sigma_V \sim \sigma_h$). On the other hand, in the Yishan slope belt of the Ordos Basin, in the southwest, the present stress regime is compressional ($\sigma_H > \sigma_V > \sigma_h$) and the maximum horizontal stress can be determined by Eqn. 5.5 (Zhou et al., 2009):

$$\sigma_H = 0.0149H + 22.859 \ (Ma), \tag{5.5}$$

In the simplified numerical model for this study, vertical stress (36 MPa) is based on an average value at the top of the model (1570 m), and its distribution calculated using the density of the available rock type units in the model. A compressional stress regime is considered in the analysis of hydro-

126

mechanical coupling effect. To simplify the simulation process, the difference of the stresses in three directions is specified at 20% ($\sigma_H = 1.2\ \sigma_V$, $\sigma_h = 0.8\ \sigma_V$).

The injection of CO_2 lasts 1 year and simulation is stopped after 10 years since the beginning of injection. About 100,000 tonnes CO_2 are injected into the four layers (Formation Liujiagou, Shiqianfeng, Shihezi and Shanxi) in the Northeastern part of the Ordos Basin. Some case studies have been carried out to investigate the sensitivities of different parameters in the model, see simulation conditions in Tabel 5.2.

Table 5.2 Case studies in the HM coupled model

	Initial stress field	Biot's coefficient of mudstone	Injection rate (kg/s)	Zero stress perm-k_0
Case 1 (Base case)	Anisotropic ($\sigma_H > \sigma_v > \sigma_h$)	$\alpha_{mud} = 0.65$	0.1981	In **Table 5.1** high values
Case 2	Anisotropic ($\sigma_H > \sigma_v > \sigma_h$)	$\alpha_{mud} = 0.65$	0.1981	In **Table 5.1** low values
Case 3	Isotropic ($\sigma_H = \sigma_v = \sigma_h$)	$\alpha_{mud} = 1.00$	3.17	In **Table 5.1** low values
Case 4	Transverse anisotropic ($\sigma_v > \sigma_H = \sigma_h$)	$\alpha_{mud} = 1.00$	3.17	In **Table 5.1** low values

5.3 Results and discussion

In hydro-mechanical coupled simulations, profiles for several principal field variables including gas saturation, total CO_2 mass, vertical displacement, pore pressure, mean effective stress, minimum principal stress may be determined at various times.

5.3.1 Changes of CO_2 mass fraction in gas and liquid phased due to HM coupling effect

Changes in fluid fields occur in accordance with the mechanical field changes caused by CO_2 injection. To observe the CO_2 migration phenomenon more clearly, a higher injection rate (case 3) is used. The most obvious characteristics are the changes of CO_2 saturation in the porous medium and CO_2 concentration in aqueous phase (Figs. 5.3 and 5.4). When HM coupled effect is taken into account, the migration of CO_2 plume moves faster in the lateral direction (Fig. 5.4), especially the high CO_2 concentration zone. In this case, propagation of the CO_2 plume is slightly promoted due to the volumetric expansion of the porous medium (Fig. 5.4B), hence increasing the storage capacity of the reservoir for CO_2 (Goerke et al., 2011 and Arsyad et al., 2013). The difference in CO_2 distribution in various injection layers (Fig. 5.4A) may be caused by the formation structural influence of both the overlying and underlying layer (in terms of thickness, porosity and permeability), as already explained in Chapter 4 and by Liu et al. (2014a).

On the other hand, more CO_2 will be dissolved in the formation water in a pure hydraulic case than in the coupled HM condition (Fig. 5.5), especially in the vicinity of the injection points. This is due to the increased pressure in the near injection zone that enables a larger CO_2 solubility in the formation water. When deformation or mechanical effect is taken into account, the pressure gradient is a little smaller than in the case under pure hydraulic field effect. Volume expansion is in proportion with fluid pressure changes (Morris et al., 2011). Moreover, reduction of the effective stress, pore pressure difference and increased volumetric strain in coupled hydromechanical conditions promotes the increase in reservoir porosity and permeability.
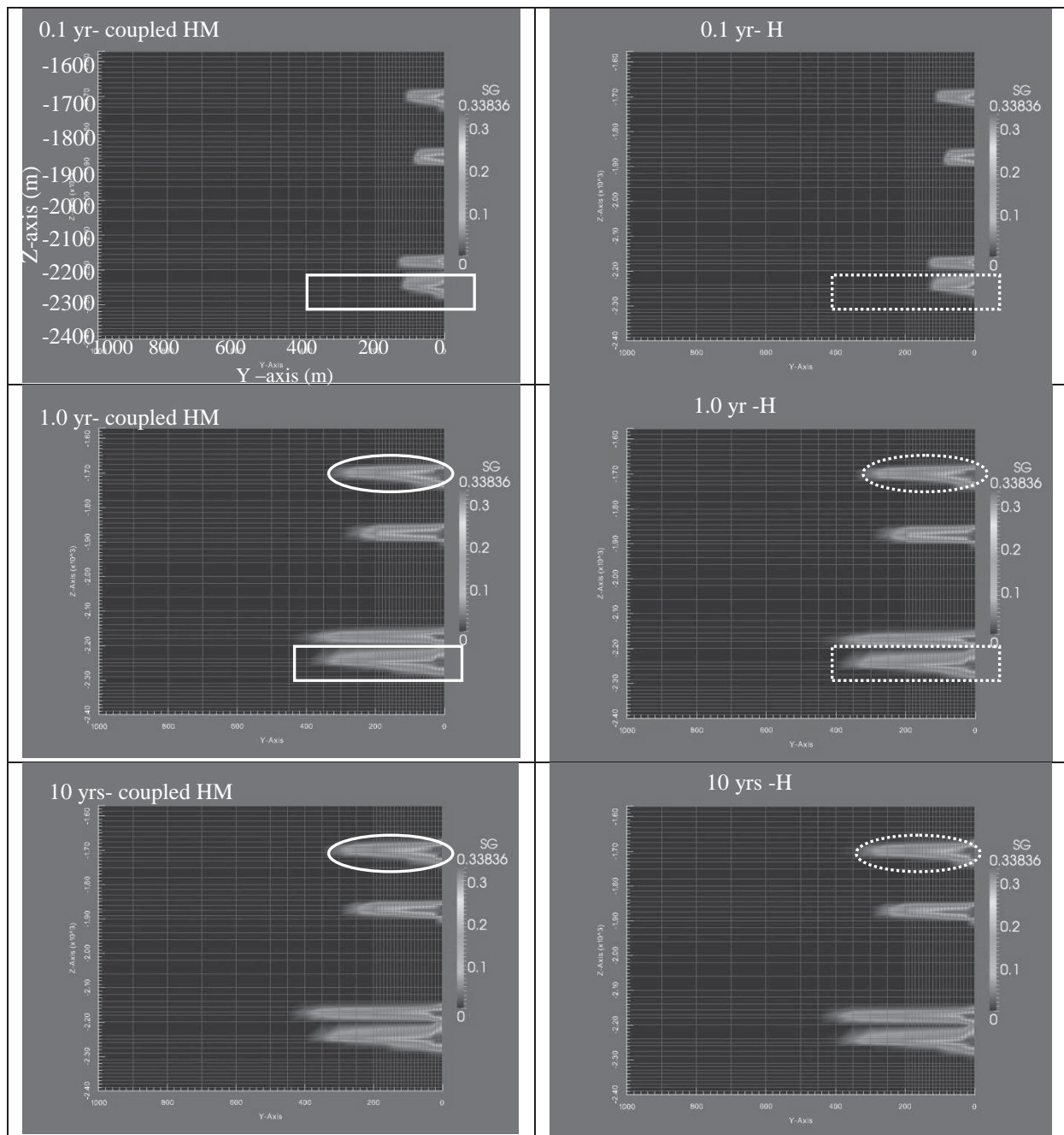
Fig. 5.3 The spatial and temporal evolution of gas saturation with (left column) and without (right column) coupled HM effect for an injection rate of 3.17 kg/s

128
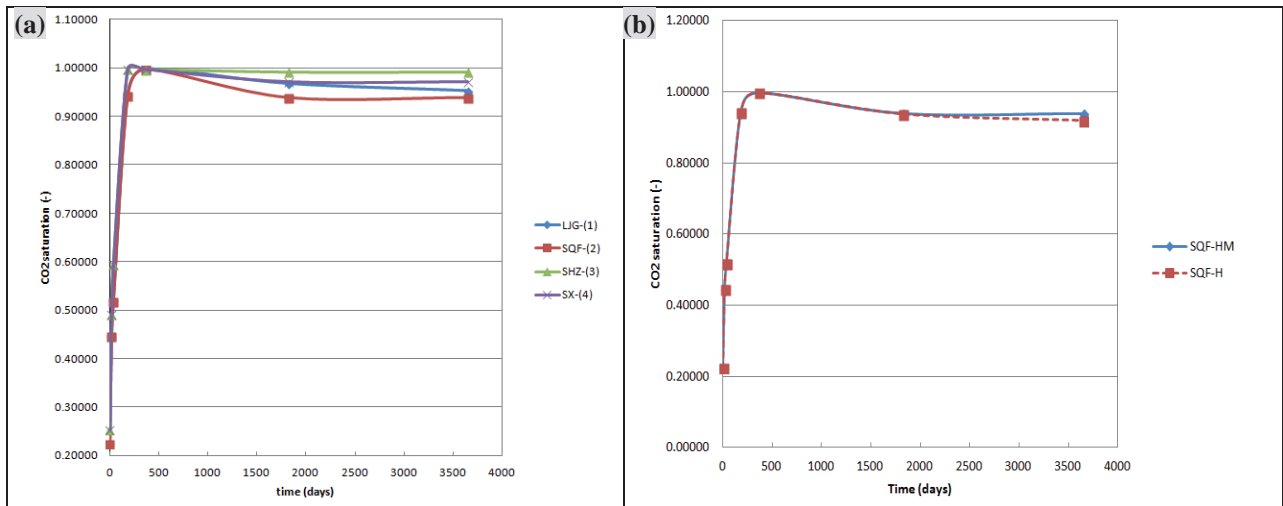
Fig. 5.4 (a) Temperal evolution of CO_2 saturation due to hydro-mechanical coupling effect at different injection points and (b) comparison of the temporal CO_2 saturation changes with hydro-mechanical (HM) and hydro(H) effects at the SQF injection point in case 3
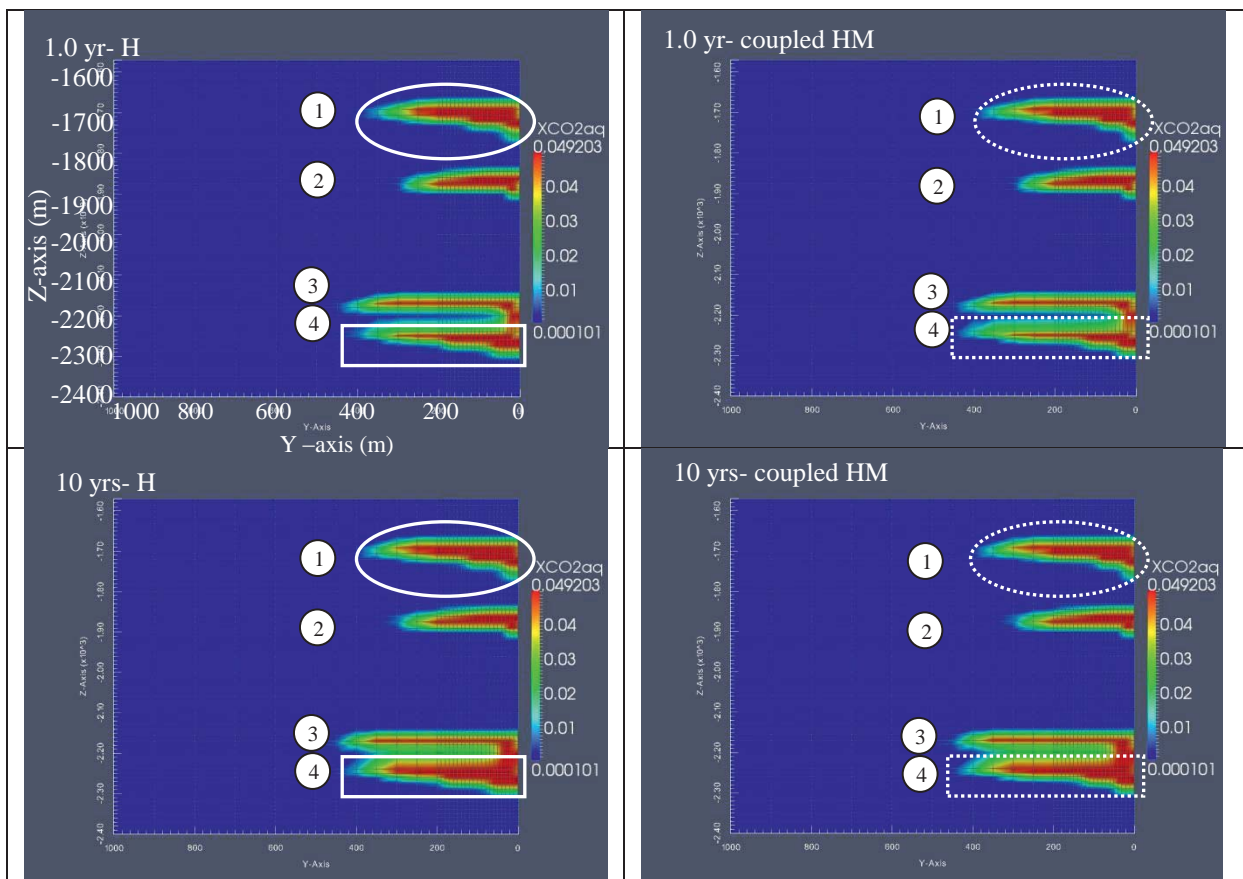
Fig. 5.5 The spatial and temporal evolution of CO_2 concentration in aqueous phase with (left column) and without (right column) HM effect in case 3

5.3.2 Pore pressure changes during and after CO_2 injection

Fig. 5.6 illustrates the evolution of pore pressure changes in the uppermost reservoir-caprock system during the injection period, under purely hydraulic (H) and hydromechanical (HM) conditions. In both formations pore pressure developments under the effect of coupled hydro-mechanical conditions are less than those due to a purely hydraulic state. HM simulation involves porosity changes in the formation in proportion with the increase in the rock volumetric strain during CO_2 injection (Riano, 2012). Across the entire simulation reservoir-caprock units, Fig. 5.7 demonstrates that during the injection period, the trend

129

of pressure buildup values under hydromechanical conditions will always be less than those under purely hydraulic field conditions by 0-1.5 MPa. Since the cap rock has very low permeability and porosity the magnitude of pressure increase due to CO_2 entry will be slightly higher than that in the adjacent sandstone. However, when the deformation of the formation system is taken into account, less CO_2 will enter the upper caprock. It is therefore more appropriate to take into consideration the coupled hydro-mechanical effect, when accurate evaluation of caprock integrity is required.
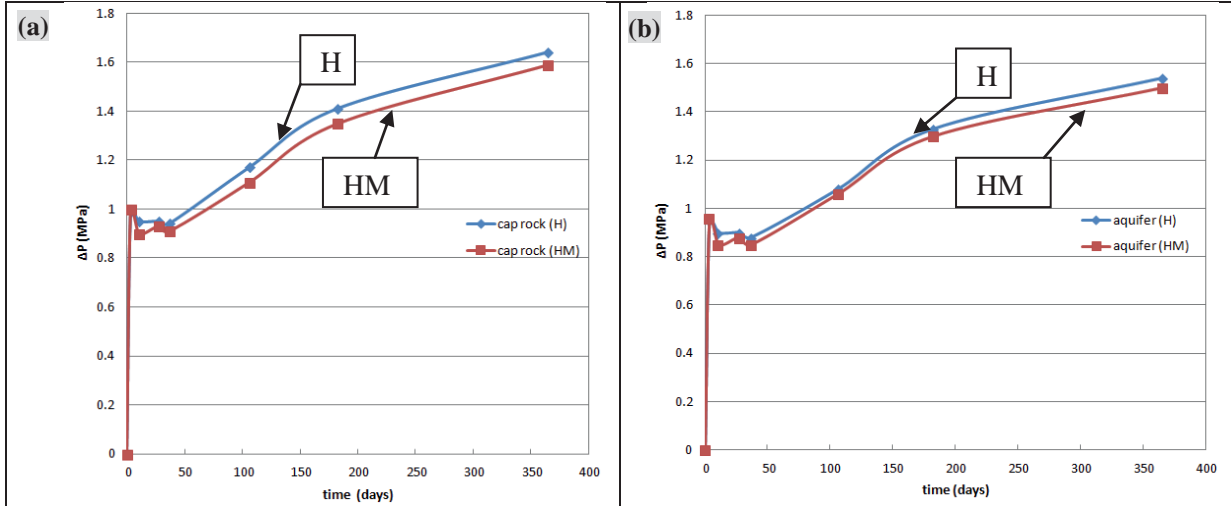
Fig. 5.6 Comparison of the temporal evolution of pore pressure buildup in the LJG sandstone (b) and its caprock (a) due to the effect of purely hydraulic (H) with coupled hydromechanical (HM) conditions during the CO_2 injection period (365 days) in base case (0.1981 kg/s)
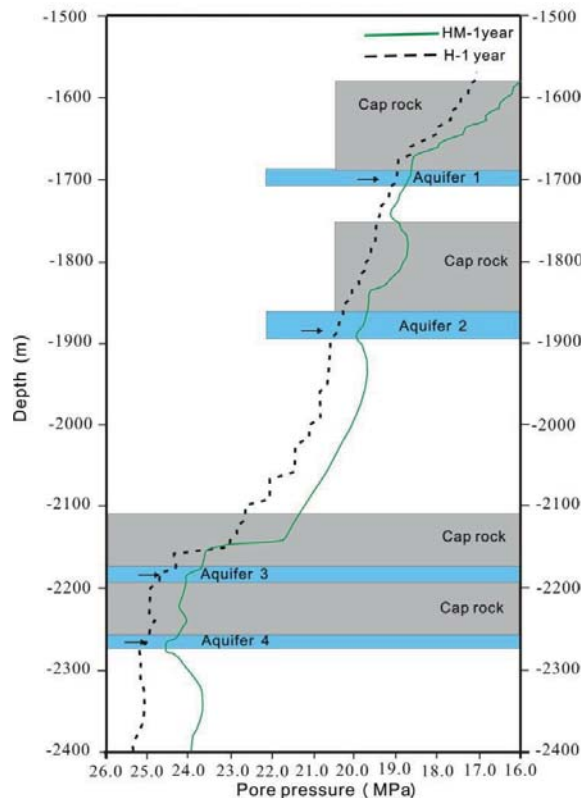
Fig. 5.7 Pore pressure distribution in the vertical direction across the injection points in base case

The primary stress state plays a significant role in the evolution of the pore pressure. Fig. 5.8 presents the pore pressure changes under consideration of different primary stress states, demonstrating that the scope of pore pressure region is larger in the isotropic stress state (case 3) than in the compressional stress condition (case 4). As time goes by during the injection process, pore pressure

130

gradually increases and the affected zone largely expands. Considering the large amount of CO_2 injected (0.8 Mt for these two layers), the most strongly affected zones are the aquifer layers 3 and 4, separated by a mudstone layer, at the bottom of the simulation zone.
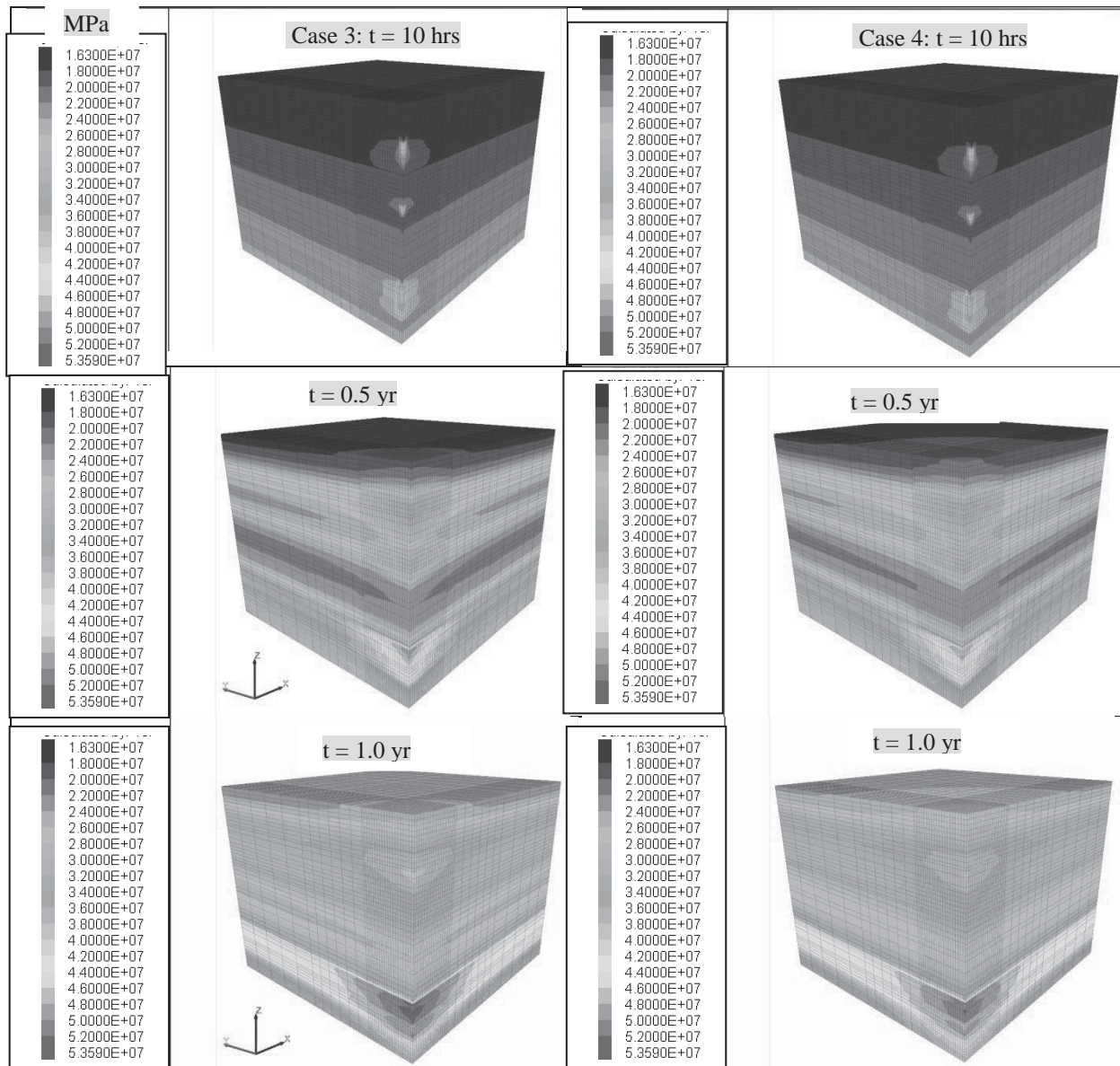
Fig. 5.8 The evolution of pore pressure in case 3 (left column: *Sx=Sz)* and case 4 (right column: *Sx=0.8Sz*) during CO_2 injection period (3.17 kg/s)

5.3.3 Primary stress state changes during and after CO_2 injection

The primary stress state, especially in the near-well region, will be affected due to CO_2 injection. Variations in the spatial distribution of the minimum principal stress concentration with time during and after injection are presented in Fig. 5.9. The primary stress state increases with time during injection period, in accordance with the results of Goerke et al. (2011). After injection stops, the stress state gradually tends to return to its original state.

131
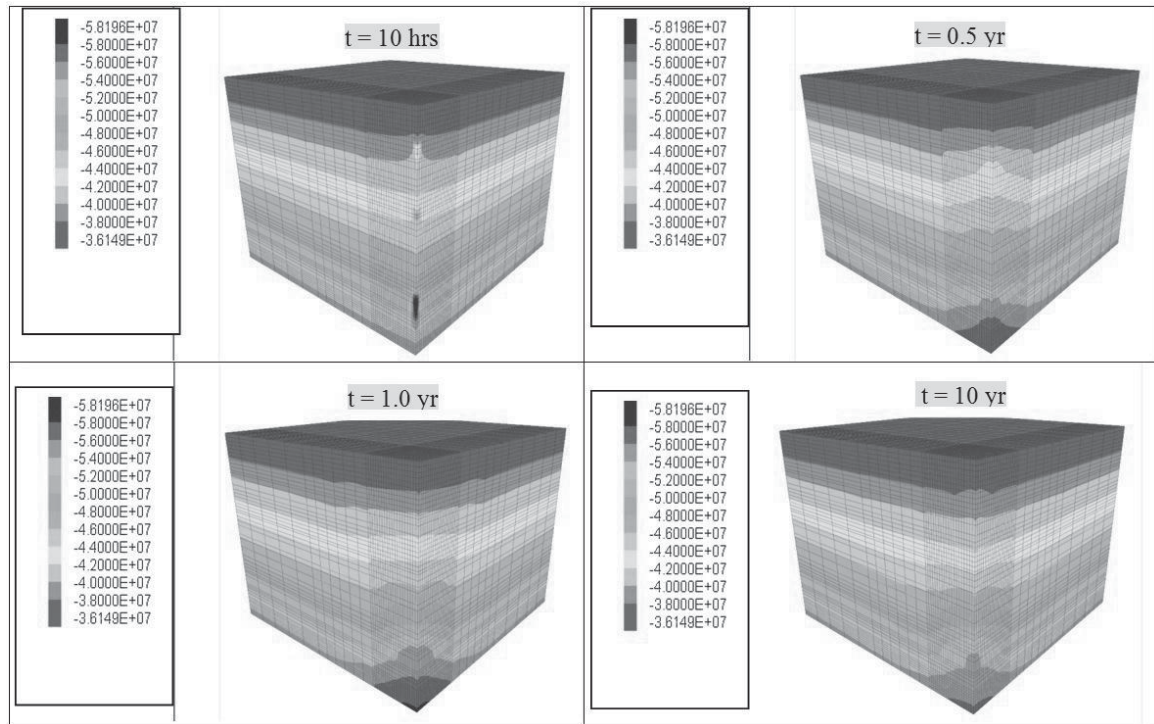
Fig. 5.9 The evolution of minimum principal stress with time in case 3

The characteristic evolution of the effective mean stress with time is different for each injection layer and the uppermost caprock layer (Fig. 5.10). In the short term period (< 0.1 year), the effective mean stress presents minor or no changes, after an instant rise in the first few days of injection. After injection stops (1 year), the effective mean stress in each layer will then instantly decline to a constant level that is still higher than the initial value. It should be noted that the uppermost caprock layer only experiences a minor flicky decline after the injection stop, which is subsequently, but gradually recovered to a constant level above that attained by its associate aquifer layer. The evolutionary trends of the effective mean stresses can be explained by the poro-elastic theory in which the variation of effective stress is controlled by total stress and pore pressure. With continued CO_2 injection into the reservoir, both pore pressure and total primary stress buildup will occur, however, at different rates and magnitudes.

Based on the definition of stress path by Hou et al. (2009), it can be derived that,

$$\Delta\sigma_{ht} = \gamma\Delta p_{t},$$ (5.6)

where γ is the stress path; σ_{ht} is the minimum principle stress under tensile state (Pa); p_t is the pore pressure under tensile stress state (Pa); Δ is the gradient.

As the stress path is γ less than 1, the increased magnitude of total stress is smaller than that of pore pressure. Hence, the effective mean stress will decrease with time. The abrupt decrease is due to the reason that once injection stops the pore pressures at the injection points will not increase but somehow decrease. Therefore the overall value will to some extent tend to sharply retract (Fig. 5.10). However, the existing injection CO_2 pressure effect hinders a complete recovery to the initial primary stress state.
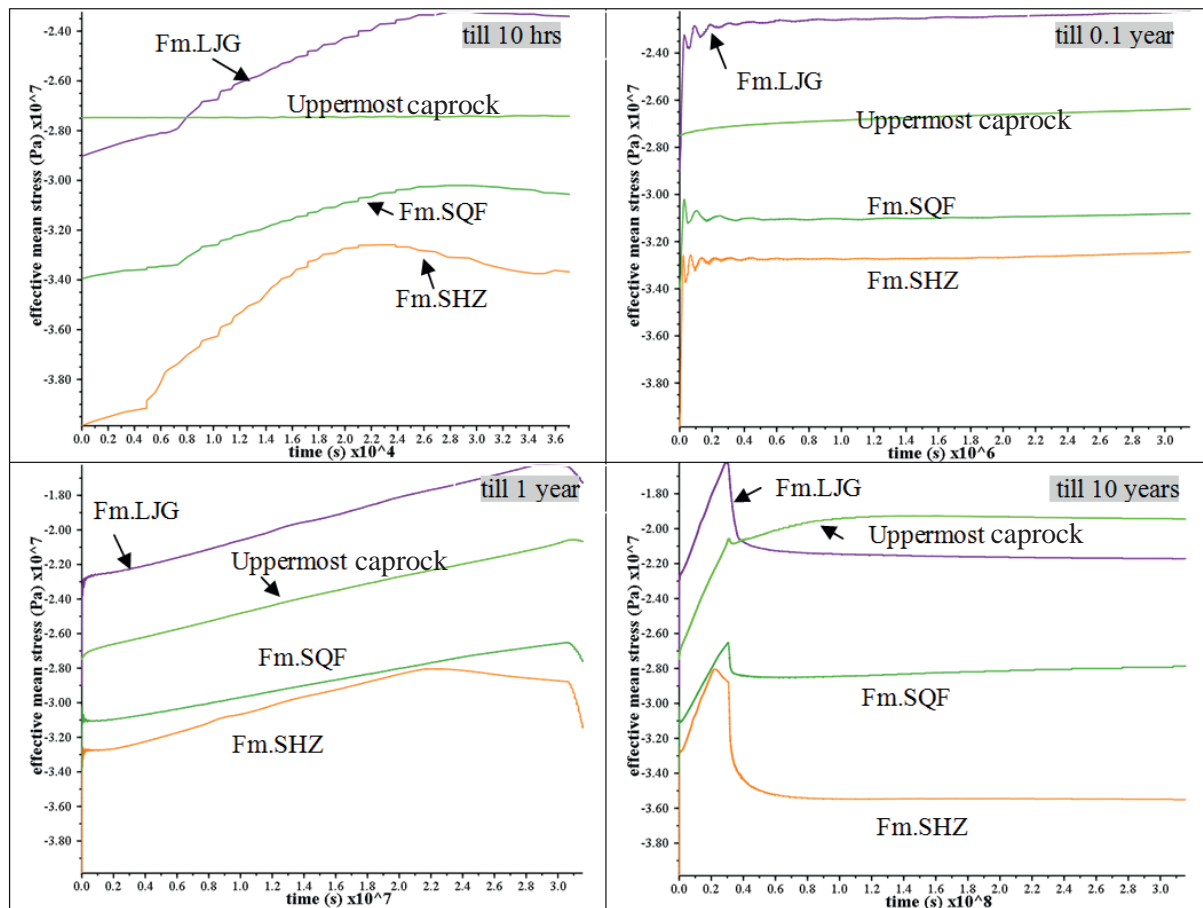
Fig. 5.10 The development of effective mean stress at the injection points and in the uppermost caprock layer, in case 3

Fig 5.11 portrays the evolution history of the von mises stress for each injection layers. CO_2 injection causes a slight increase of the von mises stress. The larger it is, the more easily plastic failure of the material occurs. It can be seen that the uppermost caprock undergoes the largest increase of the von mises stress, and therefore has the greatest potential for plastic failure. Both illustrations for the effective mean stress (Fig. 5.12) and the total minimum principal stress (Fig. 5.13) show that the local stress field changes due to CO_2 injection. Take the top LJG aquifer formation for example, during CO_2 injection process, the effective mean stress decreases by 0.75 MPa at the end of injection. After that, the stress field will instantly decline by 0.5 MPa to a constant level that is still lower than the initial stress (Fig. 5.12). As for the total minimum principal stress (Fig. 5.13), the same variation trend occurs with a maximum decreased value of 0.5 MPa under 100,000 tonnes's CO_2 injection in contrast to initial stress field before CO_2 injection.

133
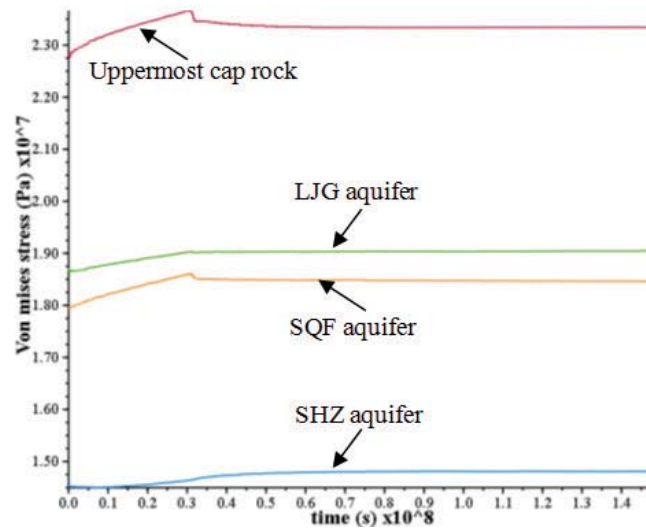
Fig. 5.11 Von mises stress evolution in each layer caused by CO_2 injection in the base case (0.1981 kg/s)
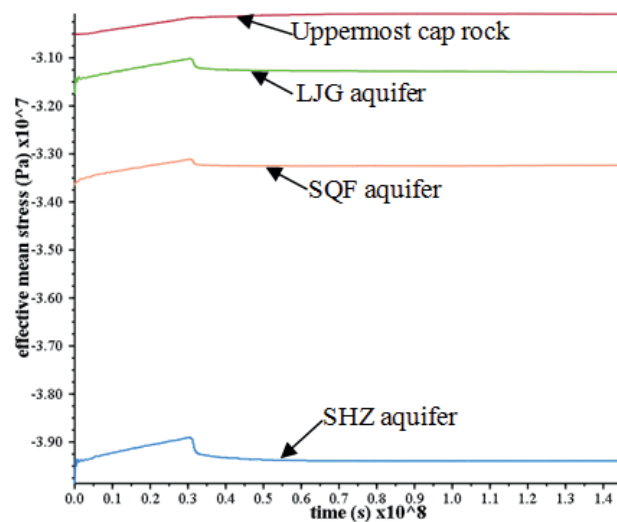
Fig. 5.12 Effective mean stress evolution in each layer caused by CO_2 injection in the base case (0.1981 kg/s)
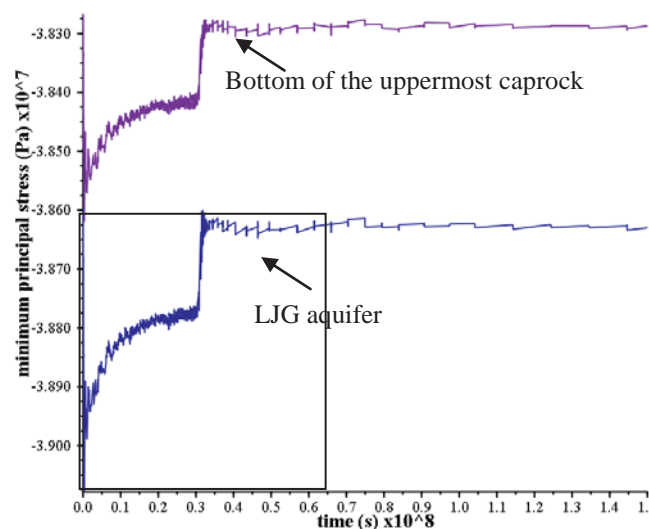
Fig. 5.13 Evolution of the total minimum principal stress evolution in the top caprock- aquifer system caused by CO_2 injection in the base case (0.1981 kg/s)

The effect of chemical reaction and temperature on stress and pore pressure changes (Fig. 5.14) due to CO_2 injection into saline formations has not been discussed in this thesis, more details can be seen in Yin et al. (2012).
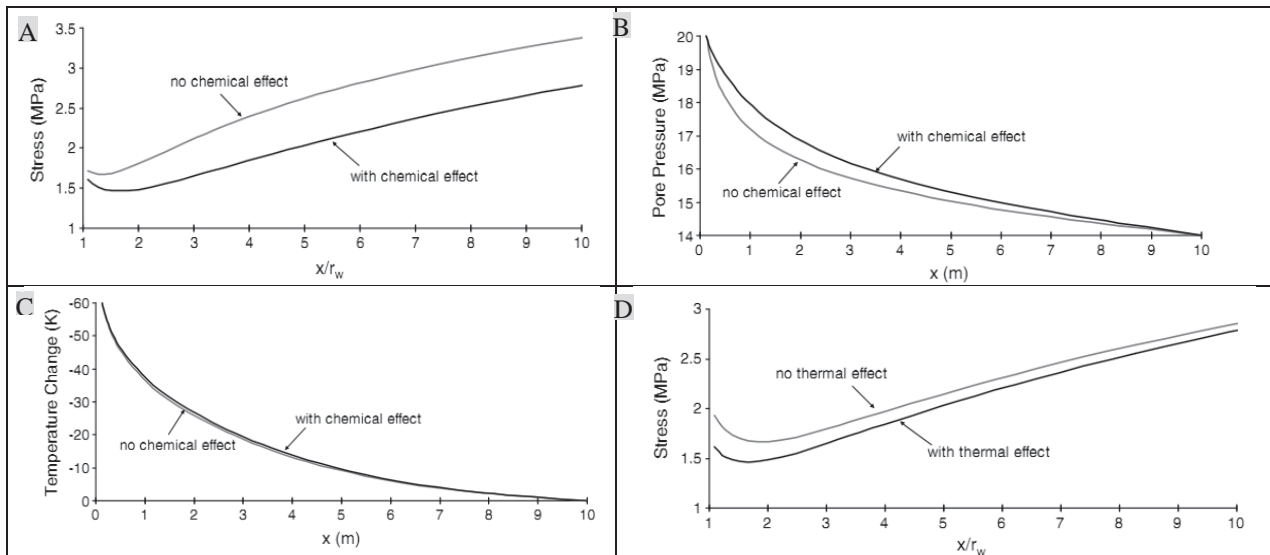
Fig. 5.14 Evolution tangential stress (A and D), pore pressure (B) and temperature (C) with lateral distance away from the injection wellbore for cases with and without chemical (in A, B, and C) and thermal effects (Yin et al., 2012)

5.3.4 Vertical displacement caused by CO$_2$ injection

Fig. 5.15 portrays the vertical uplift of the injection aquifer layers and the uppermost mudstone layer in the model. When a total amount of 100 kt CO$_2$ is injected into the multilayer reservoir-caprock system, uplift of the formations will occur. During the first one month of CO$_2$ injection process, the vertical uplift of each layer is less than 0.1 cm, after that, till the end of the injection (1 year), uplift increases sharply linearly with time, attaining values of 1.95, 1.70, 1.10, 0.60, 0.38 cm, for the responsible formations from top to bottom, respectively. It should be noted that vertical displacement will not instantly cease with injection stop. It will continue to rise for a certain period of time, however, at a relatively low rate until respective maximum values of 2.30, 1.97, 1.40, 0.62, 0.40 cm are attained. This is equivalent to ascending amounts of 18%, 16%, 27%, 3%, 5% compared with the values at the moment injection was stopped. The uplift of the formation due to CO$_2$ injection occurs because of increased pore pressure (Morris et al., 2011), which is in contrast to the depletion of reservoir or withdraw of ground water process, when the subsidence will happen caused by pore pressure decrease. The linear uplift during CO$_2$ injection is caused by the continuous increased pore pressure, while the transformation and subsequent gentle change is due to the residual increased pore pressure absent in the initial state before injection. The magnitude of the uplift will depend on Biot's coefficient, Poisson's ratio, Young's Modulus, changed pore pressure etc. Further information about estimation of uplift can be found in Hou et al. (2009).
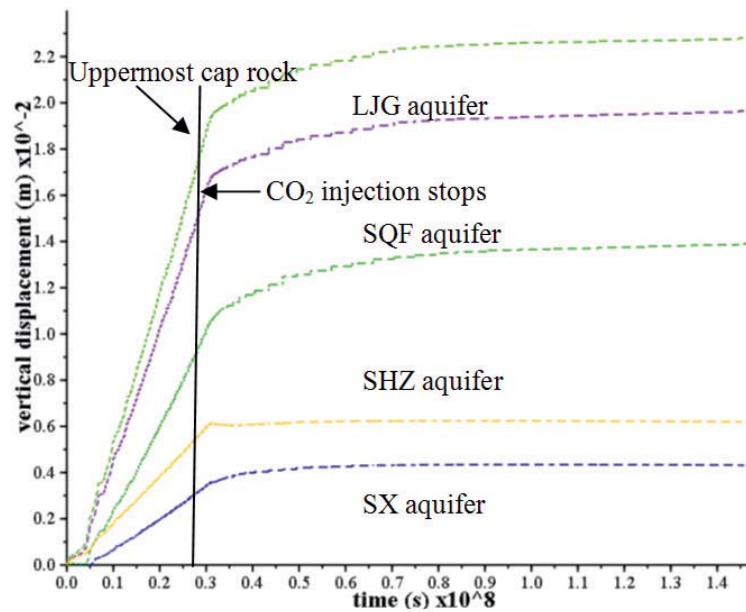
Fig. 5.15 The vertical displacement in each layer caused by CO_2 injection in base case (0.1981 kg/s)

Reservoir permeability and injection rate show great impact on the vertical displacement of the layers. When the injection rate is 3.17 kg/s, the maximum vertical uplift caused by CO_2 injection is 0.45 m for the uppermost cap rock layer after injection stop (Fig. 5.16). This unexpected uplift amplitude under only 16 million tons of CO_2 injection occurs because there is obvious tensile failure in the caprock, Under this condition, the previous constitutive relationship between effective stress and permeability will become invalid in describing the realistic changes in stress, strain, pore pressure etc. In real condition after the yield occurs in the caprock, the pore pressure will dissipate greatly along the fractures, restricting the uplift movement of the reservoir and caprock. When the initial zero stress reservoir permeability is smaller than that in the base case state, the variation trend of the vertical uplift will as illustrated in Fig. 5.18. Under this case (case 4), the vertical uplift is different for each layer with their respective maximum values being 2.6 cm, 2.3 cm, 1.5 cm, 1.1 cm and 0.5 cm, which means 13%, 16.8%, 7%, 48% and 25% larger than that of their corresponding values in the base case. This confirms that the permeability of the reservoir has a great impact on the mechanical displacement of the multiple reservoir-cap rock system. By comparing the uplift results for the two different reservoir permeability conditions (base case and case 4), it can easily be explained why the injected CO_2 can migrate much faster in the high permeable reservoir, thus causing a continuous pore pressure rise and a magnified and uniform uplift in the lateral zone (Arsyad et al., 2013). On the other hand, in a tight reservoir, the injected CO_2 will linger near the well-region, more difficult to dissipate outwards (Arsyad et al., 2013), and once the driving force disappears (i.e. by stopping the injection), the continuous uplift of the formation also stops, or even decreases to some extent.
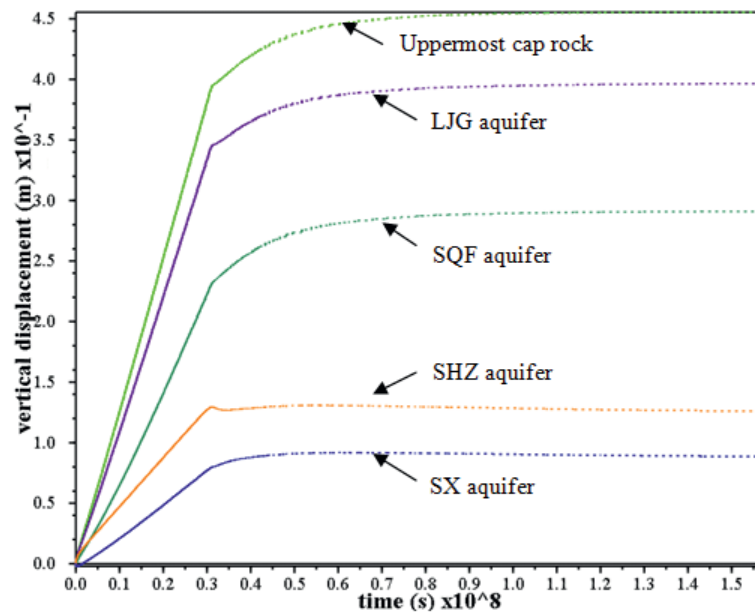
Fig. 5.16 Injection rate effect on the vertical displacement for each layer in case 3 (3.17 kg/s)
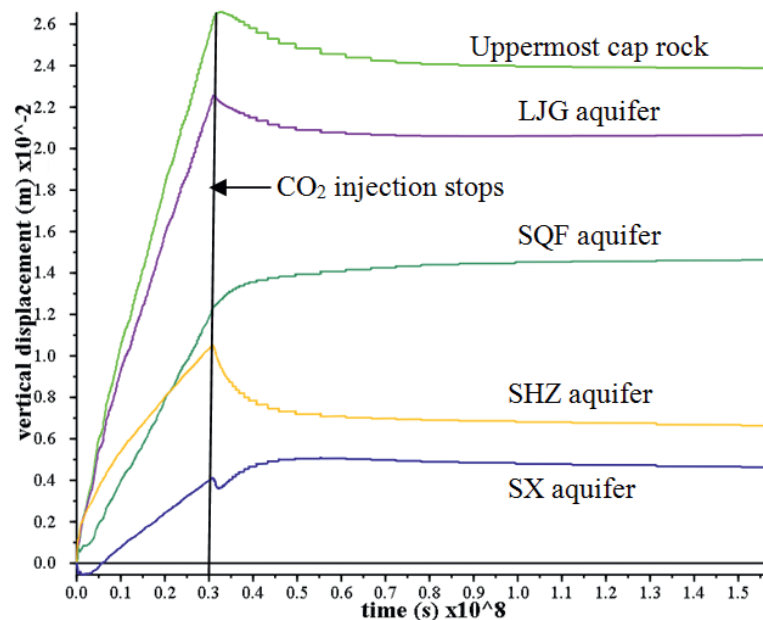
Fig. 5.17 The effect reservoir permeability on the vertical displacement for each layer in case 2 (0.1981 kg/s)

5.3.5 Maximum storage pressure increase

Tensile failure occurs during CO_2 injection processes in case 3. It is initiated at the bottom of the caprock with a large amount of CO_2 injection (3.17 kg/s). Under the isotropic in situ stress regime and mechanical property conditions, tensile failure occurs first in caprock 4, and then in caprock 1 during this simulation (Fig. 5.18). During CO_2 injection period, the yield zone significantly enlarges, but does not propagate throughout the entire caprock. Therefore, the sealing capacity of the cap rock can be maintained at some extent.

137
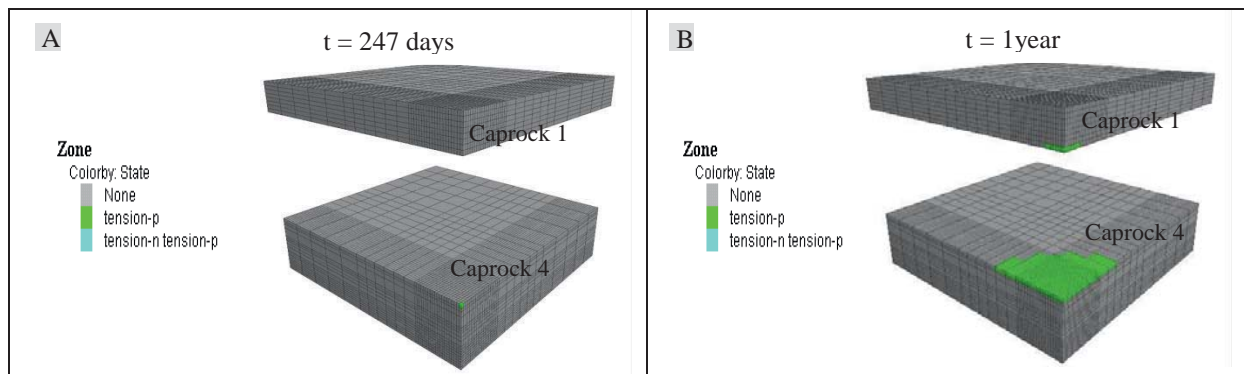
Fig. 5.18 The evolution of tensile yield zone with time in cap rock-reservoir system of case 3 (3.17kg/s)

Fig. 5.19 shows the relationship between the effective minimum and maximum stresses at the bottom of the uppermost caprock. It is observed that the variation trend is complex during CO_2 injection process. At the beginning of CO_2 injection (before 0.5 day), the effective minimum stress (σ_3') largely increases, and then decreases to a minimum value, but still higher than the initial σ_3' value. A minor change in injection rate, from 3.17 to 3.1701 at the time between 354 day and 365 day, will result in an abrupt increase in σ_3' (by about 0.4 MPa), which is beyond the initial expectation. Under the stress field and initial reservoir properties condition, shear failure does not occur.
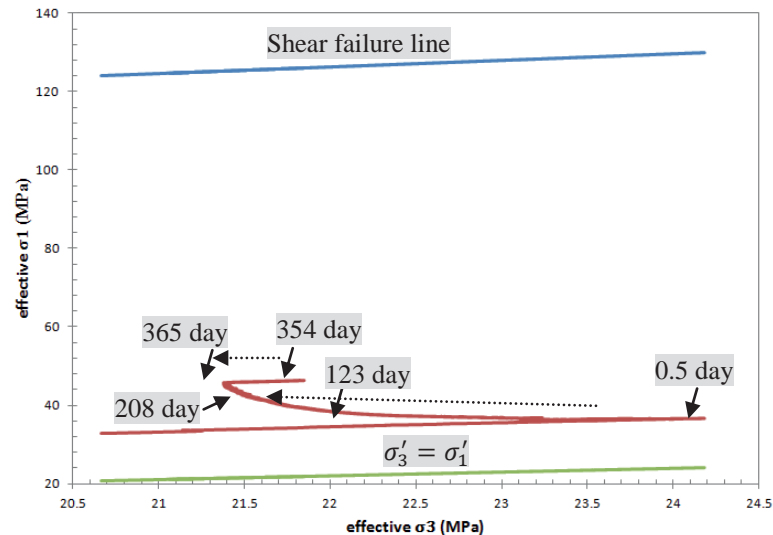
Fig. 5.19 The evolution of stress path at the bottom of the uppermost cap rock in case 3 (3.17 kg/s)

By using the geological and hydro-mechanical parameters in Table 5.1, the safe maximum reservoir pressure calculated from Eqs 3.87 and 3.92 is as shown in Table 5.3. It can be seen from the analytical results that the integrity of the caprock is much easier to be disturbed by CO_2 injection. Different layers have different maximum storage pressure, implying that the deeper the injection layer is, the much safer the operation. Based on the simulation runs in this paper (Table 5.4), the maximal pressure buildup is at the end of the injection with a rate of 3.17 kg/s, especially in the caprock of SHZ formation, SX formation and the uppermost caprock. The great divergence in pressure buildup in different layers is mainly affected by the thickness of the aquifer layer, demonstrating that failure of overlying caprock begins first overlying a much thinner aquifer layer. Furthermore, it should be noted that the pressure increase occurred at the bottom of caprock and reservoir is the same before a large amount of CO_2 enters into the caprock.

Table 5.3 Safe maximum storage pressure related with CO_2 storage in base case

Criterion	Primary pore pressure [MPa]	Used equation	Calculated maximum storage pressure increase ΔP [MPa]	Safe maximum storage pressure increase ΔP [MPa]
Mohr-Coulomb's shear failure criterion for reservoir sandstone	LJG: 17.0	3.92	LJG: 46.1	LJG: 25.0, n=1.5
	SQF: 18.8		SQF: 49.4	SQF: 26.7, n=1.5
	SHZ: 21.8		SHZ: 51.8	SHZ: 27.3, n=1.5
	SX: 22.5		SX: 54.0	SX: 28.5, n=1.5
Integrity criterion for cap rock	LJG: 16.9	3.87	LJG: 21.4	LJG: 13.7, n=1.25
	SQF: 18.6		SQF: 23.2	SQF: 14.8, n=1.25
	SHZ: 21.7		SHZ: 26.7	SHZ: 17.0, n=1.25
	SX: 22.4		SX: 27.5	SX: 17.5, n=1.25
Both	–	Eqs 3.87 and 3.92	LJG: 21.4	LJG: 13.7
			SQF: 23.2	SQF: 14.8
			SHZ: 26.7	SHZ: 17.0
			SX: 27.5	SX: 17.5

Table 5.4 Pressure buildup in cap rock and reservoir caused by CO_2 injection in case 3 and case 2

	Pressure increase in cap rock ΔP (MPa)			Pressure increase in reservoir ΔP (MPa)		
	Case 3 (0.5 yr)	Case 3 (1.0 yr)	Case 2 (1.0 yr)	Case 3 (0.5 yr)	Case 3 (1.0 yr)	Case 2 (1.0 yr)
LJG	16.8	21.3	6.1	16.8	19.2	4.8
SQF	11.6	14.4	4.1	11.6	14.4	3.4
SHZ	26.4	31.4	12.0	26.4	27.0	9.0
SX	22.2	28.8	8.9	22.2	24.5	6.4

6. Simulation of reactive transport of CO_2-fluid in Ordos saline formations [H^{2}C]

In a natural reservoir system, leaching of rocks will result in dissolution and precipitation of minerals with transfer of some elements during this process (Bachu, 2002). Throughout geological history, leaching of reservoir rocks has been caused mainly by CO_2 bearing fluids or hydrocarbons (Dawson et al., 2013). This phenomenon warns that the reservoir rocks may be very sensitive to the injection of supercritical CO_2, thus threatening the safety of CCS projects.

When CO_2 is injected into a deep saline aquifer, it will partially dissolve in the water phase (brine), forming carbonic acid, which lowers the pH of the aquifer in the near wellbore region. The rock-water-gas system will lose chemical equilibrium due to the injection of CO_2. In order to attain a new equilibrium, chemical reactions will take place, with the concomitant dissolution of unstable minerals and precipitation of secondary minerals. This results into the evolution of the underground aqueous components (Gunter et al., 1997; Rosenbauer et al., 2005). If these reactions take place at sufficiently high rates, transport and mechanical properties of the reservoir rock, including the injectivity activities and long-term integrity of the reservoir and caprock, will be highly affected. Therefore, it is important to investigate the impact of reactions between CO_2-rich fluids and reservoir rock.

The complex chemical interactions between injected CO_2-water-rock, is site specific and controlled by a number of factors, including pH of the mixed fluids, temperature, pore pressure, fluid composition, mineral composition, rock structure etc (Dawson et al., 2013). Therefore, to understand the specific CO_2-water-rock interactions in Ordos CO_2 sequestration site, batch, 1D and 2D model simulation runs have been carried out and explained in this Chapter.

This Chapter has been organized in the following way: first, the laboratory-scale and simulations of CO_2-water-rock interactions are reviewed in detail; next, information about the chemical reactions as a result of CO_2 sequestration is reviewed; followed by the description of the modeling approach and the related mathematical model; then the simulations, with a sequence of batch simulation runs→1D→2D models; and finally the results and discussion part, which will explain the spatial and temperal evolution of minerals and aqueous phase and the changes of reservoir properties under a variety of conditions.

6.1 Literature review

6.1.1 Previous laboratory-scale experimental studies on CO_2-fluid-rock interaction

Many laboratory experiments have already been performed on a variety of formation brines and minerals interactins at various sites under different conditions of pressure, temperature, water saturation, ionic strength and pH to evaluate the impact of CO_2 storage through mineral precipitation (Dawson et al., 2013). The results, however, show a considerable diversity and more often than not present a challenge to generalize them for application on reservoir scale geochemical characterization. Furthermore, similar experiments will yield different results for samples from different sites, i.e. the results are both laboratory and site specific.

Considering the huge number of experiments and countries where the CO_2-water-rock interaction studies have been launched, all with the intention to broaden the scope for understanding processes involved, significant interest and attention has been disclosed about the need to further develop the technology of CO_2 sequestration worldwide. In some countries, for instance, Australia (Remoroza et al., 2012), Belgium (Bertier et al., 2006), Brazil (Ketzer et al., 2009), Canada (Gunter et al., 1997), China (Fan et al., 2007; Wang et al., 2011; Wan, 2012), France (Rimmelé et al., 2010; Scislewski and Zuddas, 2010), Germany (Wigand et al., 2008; Fischer et al., 2011; Heeschen et al., 2011; Pudlo et al., 2012),

Japan (Ueda, 2005), Norway (Hellevang, 2006), Poland (Labus and Bujok, 2011), UK (Pearce et al., 1996; Rochelle et al., 2002), U.S.A (Shiraki and Dunn, 2000; Kaszuba et al., 2003, 2005; Rosenbauer et al., 2005), intensive CO_2 sequestration activities and research studies have already taken place.

From the experiment scale aspect of view, both the test conditions and the materials can be changed. The test conditions include temperature, pressure and time. In a specific CO_2-water-rock interaction experiment, the test conditions can be set to represent the in situ characteristics of the rock buried, or to a specific requirement value (Fischer et al., 2011). The materials involve the rock sample (powder or cylindrical cores) from different sites, fluid (brine water or pure water), supercritical CO_2. The experimental results about mineral characteristics and ion concentration changes before and after CO_2 flooding can be analyzed by NMR (petrophysical parameters, porosity, pore radius distribution), XRD and SEM (standard optical petrography), SEM-EDS, TEM-EDX, ICP-OES, ICP-MS, EPMA, X-ray CT, Hg-porosimetry, pycnometry and so on (Dawson et al., 2013).

Results from most experiments show that alteration of some minerals may occur, for example, the pre-existing calcite and dolomite in Pearce et al. (1996), also the corrosion of feldspar and coupled precipitation of smectite-Na. When the reaction time is short, the variation of minerals is not obvious. From a long time period scale, about tens- to hundreds-of-thousands of years, the effective mineral trapping may occur (Gunter et al., 1997). The comparison experimental runs by using different fluid in Shiraki and Dunn (2000) demonstrate the different saturation state of minerals, such as dolomite and anhydrite. Ions will be released from the in situ reservoirs due to CO_2-water-rock interaction, resulting in the precipitation of new minerals when the ions are saturated with respect to the mineral (Ueda, 2005).

The previous experimental results clearly imply that geochemical reactions induced by CO_2 injection are strongly case and site specific and greatly depend on the mineralogy of the formation rock, reservoir pressure, temperature, and fluid composition (Sorensena et al., 2009; Fischer et al., 2011; Huq et al., 2012; Kühn et al., 2012). Therefore, the laboratory experiments for each individual reservoir system have to be investigated separately, and general conclusions are mostly imprecise.

The effect of supercritical CO_2-water-rock interaction on the porosity and permeability changes presents more complex under different reservoir conditions (pressure, temperature, mineral and fluid composition) and reaction time scale (Xu et al., 2005). According to the strong heterogeneity of rock, it is impossible to get the totally same results after CO_2 and solution treatment for the experimental core samples. The increased or decreased permeability of the rock depends on many factors, such as fluid composition, CO_2 injection pressure, distribution of the rock crystals (aragonite, calcite, dolomite and magnesite) and pore structures, etc.

Overall, three different results are shown:

Increased permeability: Due to the dissolution of carbonate minerals, the porosity and permeability of rock matrix are increased at different levels (Fischer et al., 2011). This phenomenon is more common for carbonate rock (Fig. 6.1 and Fig. 6.2), especially for dolomite (Fig. 6.3; Grigg et al., 2005).

Decreased permeability: After chemical reaction, the permeability of the core samples is decreased. This may be caused by the migration of fine grains (mainly illite) to pore throats. This phenomenon can occur in many experiments (Sayegh et al., 1990; Grigg et al., 2005; Beyer et al., 2012).

Unchanged permeability: The core permeability does not change substantially throughout the CO_2-water-rock interaction processes (Bowker and Shuler, 1991). This is due to the offsetting effect, which means that the increased permeability caused by the dissolution of carbonate minerals is offset by the reduction induced by migration of clay minerals into pore throats.
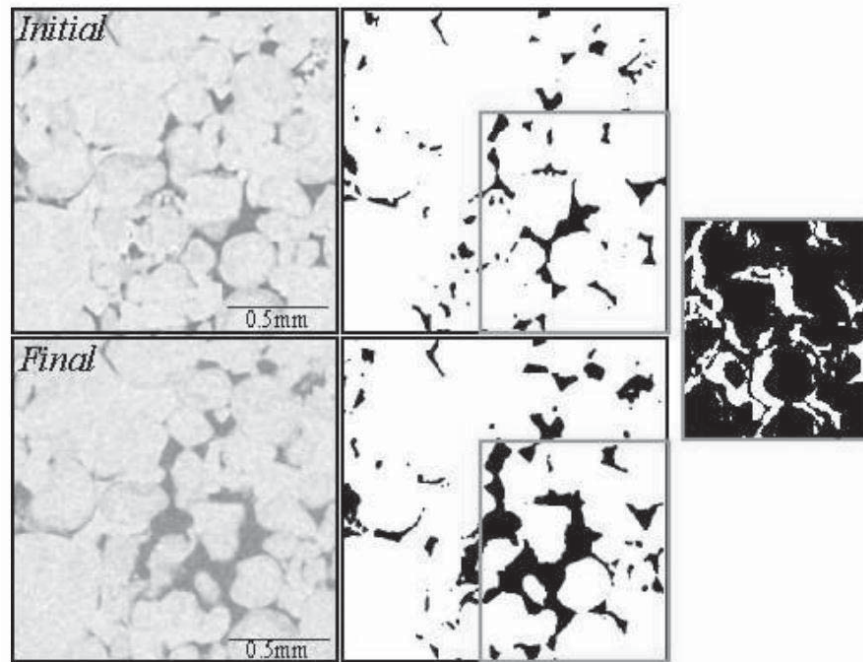
Fig. 6.1 XMT cross-section of the sample used for water-CO_2-rock interaction (Luquot and Gouze, 2009)- Black color represents pores, and calcite indicated in white
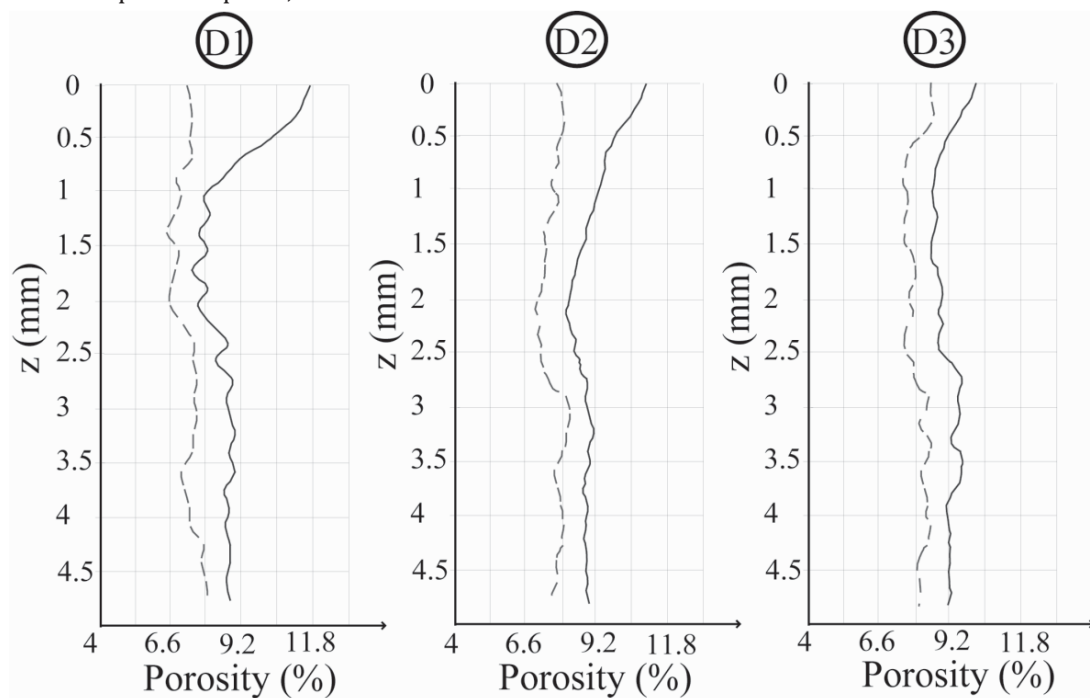
Fig. 6.2 Porosity changes along the flow direction before (dotted) and after (solid) the experiment (D1, D2, D3 are different samples with P_{CO2}=100bar, 60 bar, 25 bar, respectively) (Luquot and Gouze, 2009)
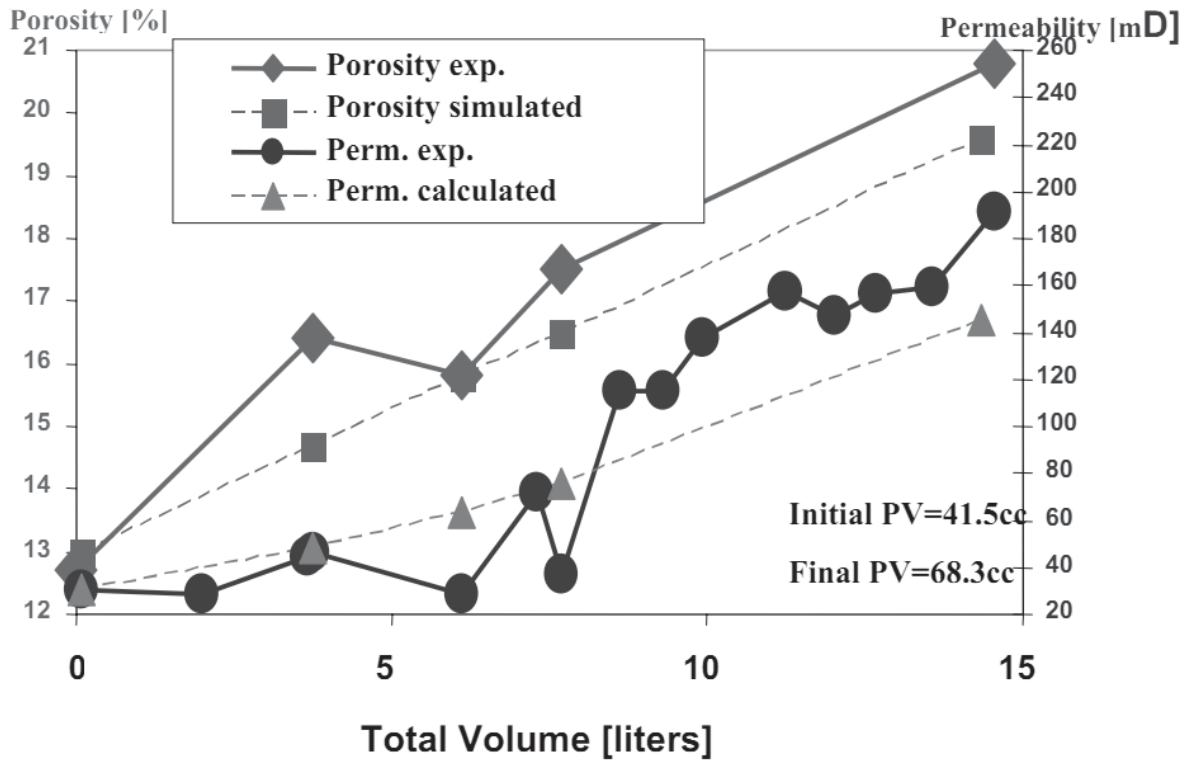
Fig. 6.3 Porosity and permeability changes due to CO_2 injection in dolomite cores (Grigg et al., 2005)

6.1.1.1 Sandstone core sample

Different kinds of reservoirs, such as sandstone and carbonate reservoirs, have different mineral assemblages (Von Eynatten et al., 2003). In sandstone reservoirs, for example, the clastic particles are mainly quartz, K-feldspar, alkali-feldspar, plagioclase, rock debris and sundries. The composition of cement is mainly quartz, calcite, chlorite, albite, illite, anhydrite and so on. Carbonate reservoirs are composed of calcite, dolomite, aragonite, ankerite, magnesite, siderite, etc.

Most of the CO_2-water-rock interaction experiments, especially on mineral sequestration mechanism studies are carried out for sandstone core samples. The experimental results show different characteristics, demonstrating strongly case and site specific features (Fischer et al., 2011). Supercritical CO_2-water-rock interactions can certainly cause the dissolution of some minerals, such as K-feldspar, albite, carbonate cements, etc, and also the precipitation of others, for example, Na-smectite, calcite, kaolinite, illite, chlorite, and so on. Different features occur in different cases (Pearce et al., 1996; Gunter et al., 1997; Shiraki and Dunn, 2000; Bateman et al., 2005; Rosenbauer et al., 2005; Bertier et al., 2006; Wigand et al., 2008; Ketzer et al., 2009; Gaupp et al., 2009; Grathwohl et al., 2009; Fischer et al., 2011).

6.1.1.2 Carbonate core sample

Different fluid compositions (pure supercritical CO_2, CO_2 saturated pure water, CO_2 saturated brine water) for the CO_2-water-carbonate rock interactions also show totally different results. Rosenbauer (2005) launched two experiments, in which CO_2 was injected into limestone cores either saturated with low-sulfate or high-sulfate brines. In the former, about 10% of the original calcite was dissolved and rock porosity increased by 2.6%; while in the latter, porosity decreased by 4.5%.

The experimental results will be affected by several factors including the CO_2 injection pressure, pressure gradient across the cores and the characteristics of the dolomite cores. Omole and Osoba (1983) carried out 3 sets of CO_2 flooding experiments at 27 °C, in which CO_2 was injected into dolomite cores saturated with a 0.1mol/L KCl solution. Results showed that the injection of CO_2 can increase the permeability of most dolomite cores, by 104 to 159% of the original value, although for some other

143

samples, the permeability remain unchanged or even decreased to an extent of about 77.5-83% of their orginal value (Table 6.1 and Fig. 6.4). For the similar core samples, the higher the injection pressure is, the higher the permeability will increase. Different core samples yield different results, which may be caused by the variations in pore structure and mineral distribution in the core. The pressure gradient across the core samples during experiment process can also have great impact on permeability changes.

Table 6.1 Permeability changes in dolomite cores caused by CO_2 injection (Omole and Osoba, 1983)

Core #	Length (inch)	Initial porosity (%)	CO_2 injection pressure (MPa)	Pressure gradient across core (MPa)	Initial permeability (mD)	Final permeability (mD)
# 1	9	24.98				
Run 1			7.24	<0.124	90.13	94.34
Run 2			7.31	<0.124	90.13	107.22
Run 3			8.41	<0.124	90.13	142.35
# 2	9	29.13				
Run 1			7.10	7.10	184.56	144.88
Run 2			7.10	0.69	184.56	152.91
Run 3			7.10	5.17	184.56	143.19
# 3	9	20.46	7.24	<0.124	86.90	86.90
# 4a	3	25.00	7.24	<0.034	103.27	108.43
# 4b	3	25.00	10.38	<0.034	103.27	119.57
# 4c	3	25.00	14.27	<0.034	103.27	121.10
# 4d	3	25.00	17.24	<0.034	103.27	126.10
# 5a	3	20.06	7.31	<0.034	77.60	81.56
# 5b	3	20.06	7.31	<0.034	77.60	81.55
# 5c	3	20.06	7.31	<0.034	77.60	81.00
# 5d	3	20.06	7.31	<0.034	77.60	81.72
# 6a	3	26.00	7.31	7.24	125.65	93.56
# 6b	3	26.00	7.31	3.45	125.65	119.23
# 6c	3	26.00	7.31	2.07	125.65	129.67
# 6d	3	26.00	7.31	0	125.65	123.10
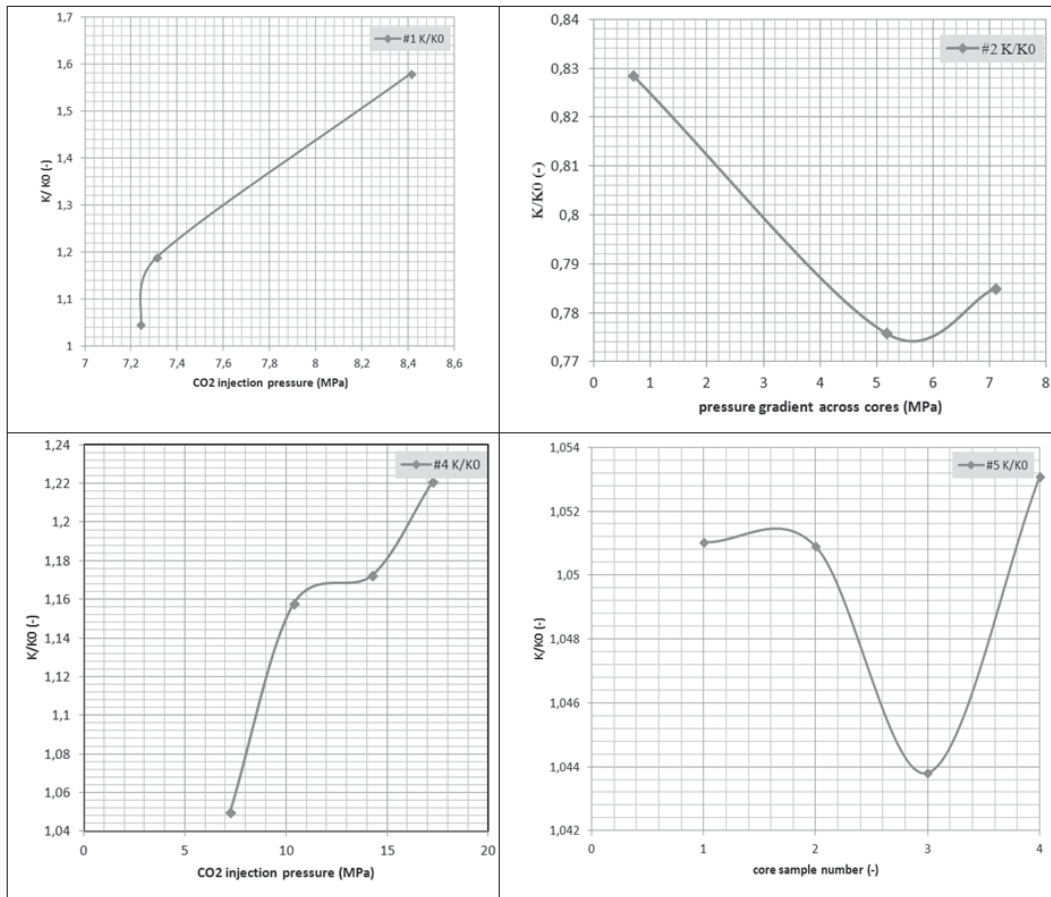
Fig. 6.4 Permeability changes in dolomite cores due to CO_2 injection (Omole and Osoba, 1983; modified)

6.1.2 Previous modeling studies on CO_2-fluid-rock interaction

Numerical modeling of geochemical processes is an essential tool to investigate the consequences of long-term disposal of CO_2 in deep formations due to the very slow reaction rate of underground reservoir minerals (Xu et al., 2005). The most common simulators that used in the CO_2- water-rock interaction modeling include PHREEQC, TOUGHREACT and EQ3/6. PHREEQC is a popular simulator developed by USGS and finds a wide application in the calculations of water chemistry, speciation of water and water-rock interactions (Van Pham et al., 2012). The major difference among the three simulators is the theoretical basis on which they relys. In PHREEQC simulations, individual reactions between the aqueous and mineral phases are controlled by chemical thermodynamics, while the reactions in TOUGHREACT and EQ3/6 simulations are predominantly controlled by a combination of thermodynamics and kinetics. The main input parameters for a PHREEQC model include pressure, temperature, mineral and fluid composition and volume ratio of water and rock, while a TOUGHREACT model demands extra input parameters (e.g. kinetic rate constants, activation energy and mineral reactive surface area) besides those mentioned above (Xu et al., 2005).

A large number of researchers have already worked on the modeling of CO_2 -water-rock reactions for CO_2 sequestration (e.g. Sonnenthal and Bodvarsson 1998; Dawson et al., 2013). Three 2D aquifer-caprock models (no intra-aquifer shales, continuous shales, non-lateral continous shales) are used in Johnson et al. (2001) to simulate mineral dissolution and precipitation, porosity, pH changes of the reservoir induced by CO_2 injection at Statoil North-Sea Sleipner facility, with three integrated simulators NUFT, GEMBOCHS and Xtool. When CO_2- water-rock reaction effect is considered, more CO_2 is sequestered through the ChemTOUGH2 simulator in a 2D unconfined saline reservoir system on the Colorado Plateau, White et al. (2001a and 2001b). Xu et al. (2005) used TOUGHREACT to perform

145

batch reaction modeling of the geochemical evolution in three aquifers of different mineralogies (i.e. glauconitic sandstone in Alberta sedimentary basin, sediments of Gulf Coast and dunite) with formation water in and without the presence of CO_2. Results showed that CO_2 sequestration by matrix minerals varies considerably with rock type. A series of kinetic batch simulation runs are discussed in Ketzer et al. (2009), to investigate the CO_2-water-rock interactions characteristics in Rio Bonito formation using PHREEQC. A more detailed review on the modeling of CO_2-water-rock interactions for CO_2 sequestration is treated in Dawson et al. (2013).

6.2 CO_2 sequestration by chemical reactions

The CO_2-bearing fluids will react with the original rock to release some elements into the saline brine, subsequently causing mineral dissolution, alteration, and re-crystallization. Below are proposed mechanisms that may affect the characteristics of reactive mineral surfaces and the availability of cations for carbonate precipitation. These features are essential in influencing the behavior of CO_2 bearing fluids in the reservoir and caprock (Gaupp et al., 2009).

6.2.1 Ionic trapping of CO_2

In general, injection of CO_2 into deep saline formations will cause a series of chemical reactions (Ortoleva et al., 1998), for instance, the dissolution of carbonate phases in limestones and the dissolution of silicates and precipitation of carbonates in plagioclase-rich arkosic sandstones. The chemical reactions caused by CO_2 injection take place in a series of sequence (Xu et al., 2004b). At first, CO_2 dissolves in formation water to generate carbonic acid:

$$CO_2 \text{ (g)} + H_2O \rightleftarrows H_2CO_3, \tag{6.1}$$

This process will be followed by rapid dissociation of carbonic acid and the formation of the bicarbonate ion:

$$H_2CO_3 \rightleftarrows H^+ + HCO_3^-, \tag{6.2}$$

The carbonic acid is unstable and easy to dissociate into a reactive hydrogen ion and a bicarbonate ions, which will potentially promote a complex series of reactions between aquifer fluids and formation rocks, resulting in the sequestration of CO_2 in aqueous and mineral phases. The increased acidity leads to the dissolution of some primary minerals constituting the formation rock, which in turn causes speciation of the dissolved cations with the bicarbonate ion (Xu et al., 2004b), for example:

$$CaCO_3 + H_2CO_3 \rightleftarrows Ca^{2+} + 2HCO_3^-, \tag{6.3}$$

$$Ca^{2+} + HCO_3^- \rightleftarrows CaHCO_3^+, \tag{6.4}$$

This is an example of ionic trapping of CO_2 by converting CO_2 into bicarbonate ions. A series of similar reactions can be written for the dissolution of other carbonates.

$$MgCO_3 + H_2CO_3 \rightleftarrows Mg^{2+} + 2HCO_3^-, \tag{6.5}$$

$$Mg^{2+} + HCO_3^- \rightleftarrows MgHCO_3^+, \tag{6.6}$$

$$FeCO_3 + H_2CO_3 \rightleftarrows Fe^{2+} + 2HCO_3^-, \tag{6.7}$$

$$Fe^{2+} + HCO_3^- \rightleftarrows FeHCO_3^+, \tag{6.8}$$

6.2.2 Mineral trapping of CO_2

The injected CO_2 can be trapped by minerals through mineral trapping mechanisms. For instance, chemical reactions between CO_2-saturated aquifer fluids and arkosic sandstone in the presence of H^+ ions

146

(from the dissociation of H_2CO_3) illustrate mineral trapping of CO_2 through the dissolution of silicates, especially the anorthitic component of plagioclase series (Rosenbauer et al., 2005): i.e.

$$2H^+ + CaAl_2Si_2O_8 \text{[anorthite]} + H_2O \rightleftarrows Ca^{2+} + 3Al_2Si_2O_5 (OH)_4 \text{[kaolinite]} \tag{6.9}$$
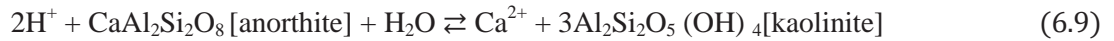
Unlike the ionic trapping process (Eqns 6.6-6.8), the dissolved bicarbonate species will react with divalent cations (Ca^{2+}, Mg^{2+}, Fe^{2+}) to precipitate carbonates. Formation of calcium, magnesium, and ferrous carbonates are expected to be the main means by which CO_2 is immobilized (Gunter et al., 1997) as mineral trapping mechanisms.

$$Ca^{2+} + HCO_3^- \rightleftarrows CaCO_3 \text{ (calcite)} + H^+, \tag{6.10}$$

$$Mg^{2+} + HCO_3^- \rightleftarrows MgCO_3 \text{ (magnesite)} + H^+, \tag{6.11}$$

$$Fe^{2+} + HCO_3^- \rightleftarrows FeCO_3 \text{ (siderite)} + H^+, \tag{6.12}$$
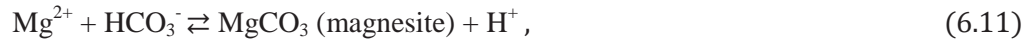
Mineral dissolution and re-precipitation can occur not only in porous media, but also in fractures and fault space. Water and gas flow between fractures and the adjacent matrix governs the mineral distribution within the medium (Gilbert and Pyrak-Nolte, 2004). There are many chemical reactions caused by the injection of CO_2. The type of chemical reaction that takes place in a reservoir depends on a number of factors, e.g. the relative content of appropriate minerals in the rock, cation/anion concentration in the aqueous phase, pH, temperature, CO_2 partial pressure, reservoir pressure, etc (Rosenbauer et al., 2005; Beyer et al., 2012; De Lucia et al., 2012). Among these factors, cation concentrations and partial pressures in the percolating water are the major controlling factors for the abundance of precipitated minerals and their stability. Besides, temperature is a very important factor. Take calcite as an example, the solubility of CO_2 in water will decrease with increasing temperature, resulting in the following degassing process:

$$HCO_3^- + H^+ \rightarrow CO_2 \text{ (g)} + H_2O, \tag{6.13}$$

The gaseous CO_2 is also redistributed by gas phase diffusive transport. Degassing increases the pH, this will then contribute to calcite precipitation:

$$Ca^{2+} + HCO_3^- \rightarrow CaCO_3 \text{ (calcite)} + H^+, \tag{6.14}$$

Calcite precipitation is also affected by other factors such as the dissolution and precipitation of alumino-silicate minerals (mainly through changing the pH and CO_2 partial pressure). Many other chemical reactions may also occur due to the injection of CO_2. Below, only a few chemical reactions have been listed in Table 6.2. They can be divided into two mineral groups: the unstable silicate minerals and the stable carbonate minerals.

Table 6.2 Some formulars of chemical reactions among CO_2-H_2O-minerals (modified from Xu et al., 2004b; Rosenbauer et al., 2005; Beyer et al., 2012; Liu et al., 2013a)

==============================

Unstable silicate minerals:

$NaAlSi_3O_8 + H_2O + CO_2 \rightleftarrows NaAlCO_3(OH)_2 + 3SiO_2$
 [albite]   [dawsonite]   [quartz]

$2NaAlSi_3O_8 + 3H_2O + 2CO_2 \rightleftarrows Al_2Si_2O_5(OH)_4 + 2Na^+ + 4SiO_2 + 2HCO_3^-$
[albite]   [kaolinite]   [quartz]

$CaAl_2Si_2O_8 + H_2CO_3 + H_2O \rightleftarrows CaCO_3 + Al_2Si_2O_5(OH)_4$
[anorthite]   [calcite]   [kaolinite]

$CaAl_2Si_2O_8 + 2Na^+ + 2CO_2 + 3H_2O \rightleftarrows 2NaAlCO_3(OH)_2 + 3CaCO_3 + 2SiO_2 + 2H^+$
[anorthite]   [dawsonite]   [calcite]

$2KAlSi_3O_8 + 3H_2O + 2CO_2 \rightleftarrows Al_2Si_2O_5(OH)_4 + 2K^+ + 4SiO_2 + 2HCO_3^-$
[K-feldspar]   [kaolinite]   [quartz]

$[Fe/Mg]_5Al_2Si_3O_{10}(OH)_8 + 5CaCO_3 + 2CO_2 \rightleftarrows 5Ca[Fe/Mg](CO_3)_2 + 2Al_2Si_2O_5(OH)_4 + SiO_2 + H_2O$
[chlorite]   [calcite]   [ankerite]   [kaolinite]   [quartz]

$3Na_{033}Al_{233}Si_{367}O_{12}H_2O + CO_2 + 4H_2O \rightleftarrows NaAlCO_3(OH)_2 + 3Al_2Si_2O_5(OH)_4 + 5SiO_2$
[smectite]   [dawsonite]   [kaolinite]   [quartz]

$NaAl_3Si_3O_{10}(OH)_2 + H_2O + CO_2 \rightleftarrows NaAlCO_3(OH)_2 + Al_2Si_2O_5(OH)_4 + SiO_2$
[paragonite]   [dawsonite]   [kaolinite]   [quartz]

$Al_2Si_2O_5(OH)_4 + H_2O + 2CO_2 + 2Na^+ \rightleftarrows NaAlCO_3(OH)_2 + 2SiO_2 + 2H^+$
[kaolinite]   [dawsonite]   [quartz]

$Al(OH)_3 + Na^+ + CO_2 \rightleftarrows NaAlCO_3(OH)_2 + H^+$
[gibbsite]   [dawsonite]

Carbonates:

$CaCO_3 + CO_2 + H_2O \rightleftarrows Ca^{2+} + 2HCO_3^-$
 [calcite]

$MgCO_3 + CO_2 + H_2O \rightleftarrows Mg^{2+} + 2HCO_3^-$
[magnesite]

$FeCO_3 + CO_2 + H_2O \rightleftarrows Fe^{2+} + 2HCO_3^-$
[siderite]

$Ca[Fe_{0.7}Mg_{0.3}](CO_3)_2 + 2H^+ \rightleftarrows Ca^{2+} + 0.7Fe^{2+} + 0.3Mg^{2+} + 2HCO_3^-$
[ankerite]

$CaMg(CO_3)_2 + 2H^+ \rightleftarrows Ca^{2+} + Mg^{2+} + 2HCO_3^-$
[dolomite]

$NaAlCO_3(OH)_2 + 2SiO_2 + 2H^+ \rightleftarrows Al_2Si_2O_5(OH)_4 + H_2O + 2CO_2 + 2Na^+$
 [dawsonite]   [quartz]   [kaolinite]

==============================

6.2.3 Dissolution and precipitation sequence of minerals

In the above section, the solubility product constant (K_{sp}), which is used to measure the dissolution/precipitation capacity of a mineral, has been introduced. It is only determined by the property of the mineral and temperature. The smaller K_{sp} is, the more difficult for this mineral to dissolve, but much easier to precipitate.

From the K_{sp} distribution diagrams for carbonate and silicate minerals (Figs 6.5 and 6.6), it can be observed that in the course of time, the K_{sp} for most minerals (except carbonate minerals, such as magnesite, calcite, dolomite, ankerite, siderite and chlorite) show positive correlations with temperature. This implies that with increasing temperature, the solubility of these minerals will increase, and therefore become more easily dissolvable (Wan, 2012). On the contrary, most carbonate minerals and some clay minerals (e.g. chlorite) will become more precipitable from solution with increasing temperature.

148

The K_{sp} distribution diagram for silicate minerals (Fig. 6.5), clearly illustrates a sequence of mineral dissolution, from the most to the least easily dissolved minerals, at 75 ^{o}C: chlorite → albite → anorthite → K-feldspar → kaolinite → Na-smectite → Ca-smectite → illite.

Except for dawsonite, the K_{sp} distribution curves for carbonate minerals in Fig. 6.6 show minor differences in their precipitation rates from solution. The relative dissolution sequence of carbonate minerals at 75 ^{o}C may be arranged as follows: magnesite → calcite → dolomite → ankerite → siderite → dawsonite.
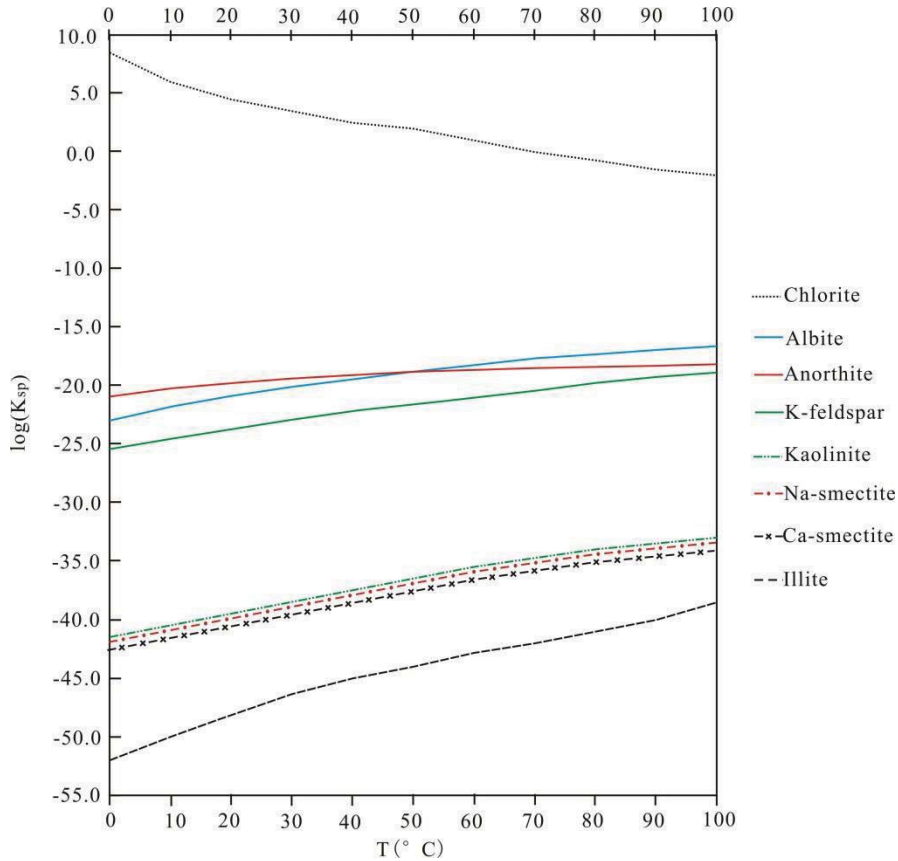
Fig. 6.5 K_{sp} for silicate minerals (modified after Wan, 2012)
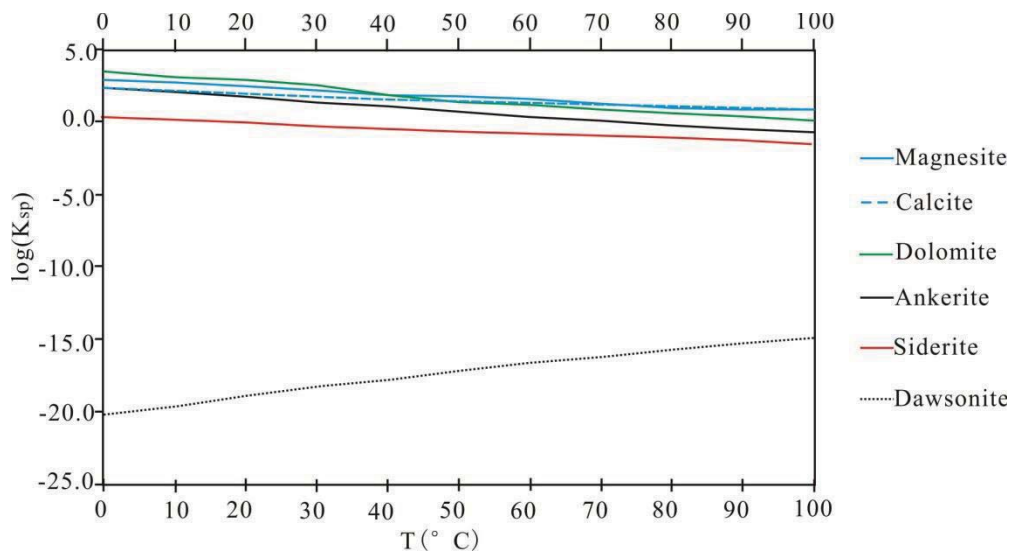
Fig. 6.6 K_{sp} for carbonate minerals (modified after Wan, 2012)

149

Minerals differ widely in their ability to maintain stability in a specific fluid environment (e.g., ion concentration and pH). Carbonate minerals, for example, are stable under alkaline environment, while chlorite can only maintain stability in a very strong alkaline environment, with fluids rich in Mg^{2+} cations, at a relatively high temperature. On the other hand, illites can stably exist under weak alkaline environment, in fluids with a high ratio of K^+/H^+ and smectite can stably exist under weak alkaline fluids with a high content of Na^+ and Ca^{2+}, but low content of K^+. Kaolinite can exist mainly under acid environment (Wan, 2012). Considering the K_{sp} of minerals and their respective stable environments, after the injection of CO_2, chlorite and most carbonate minerals will dissolve at first due to the decreased pH (acidic) conditions, followed by the dissolution of silicate minerals (e.g. albite, anorthite, K-feldspar). However, most clay minerals and dawsonite are stable and can hardly dissolve in the aqueous phase. Kaolinite may even precipitate, instead of dissolution, during CO_2 injection period. Due to the decreased leaching effect of in-situ rock minerals after stop of CO_2 injection, dissipation of the increased pH effect, caused by the neutralization of the dissolving minerals, can allow the precipitation of carbonate minerals (Gunter et al., 1997).

6.3 Modeling approach for reactive fluid flow

The modeling of CO_2 sequestration processes in saline formations involves the solution of a series of equations, including component transport equations, thermodynamic equilibrium equations in gas and aqueous phases or kinetic rate equations, and geochemistry equations. Geochemistry equations, however, involve reactions between aqueous species and mineral precipitation and dissolution.

The main problem in these processes is to find the solution to the coupled transport and reaction equations, which show strong nonlinear characteristics. Therefore, high performance computers are needed, especially for a specific CO_2 sequestration project. There are mainly two ways for solving the equations of a coupled system: the sequential solution method and the fully-coupled solution method. In the former, flow and chemical-equilibrium equations are solved separately and sequentially (Yeh et al., 1989, 1991; Mangold et al., 1991; Sevougian et al., 1992; Reeves et al., 1994; Steefel et al., 1996); while in the latter method, which is also recognized as the most stable method (Steefel and Lasaga, 1992, 1994), all equations are solved simultaneously using Newton's method.

The non-isothermal reactive transport simulator "TOUGHREACT" has been used in the simulations in this thesis. This simulator emerged by adding reactive chemistry into the preexisting multi-phase multi-component fluid and heat flow modeling code "TOUGH2" (Pruess, 1999; Xu et al., 2005). TOUGHREACT can simulate one-, two- or three dimensional reactive transport problems in both porous and fractured media with homogeneous or heterogeneous physical and chemical properties. It considers the complexation in aqueous phase, dissolution and degassing of gas in aqueous phase, local equilibrium and kinetic reactions of mineral dissolution and precipitation, etc. Pressure, temperature, water saturation, ionic strength, pH and Eh are considered in the chemical reactions (Xu et al., 2005).

Transport of aqueous and gaseous components through advection and molecular diffusion is considered in both liquid and gas phases. Complexation of aqueous species and gas (CO_2) dissolution and exsolution are assumed to be at local equilibrium. Mineral dissolution and precipitation can be controlled either local equilibrium or kinetic mechanisms (Xu et al., 2004a). For calcite and anhydrite, their dissolution and precipitation are assumed to be at local equilibrium because of their fast reaction rate, while other minerals, are assumed to be kinetically controlled.

Integral finite difference method is adopted in space discretization to solve differential equations using an implicit time-weighting method. A sequential iteration approach is adopted to solve the coupled problems of fluid flow, species transport and geochemical reactions (Xu et al., 2004a). Chemical reaction

equations in each grid-block are solved by Newton-Raphson iteration method, until convergence is achieved.

6.4 Numerical model setup for reactive fluid flow

6.4.1 Initial physical parameters

CO_2 solubility is very important for the estimating the CO_2 storage capacity of a specific geological formation by mineral and ion trapping mechanisms. Based on the experimental results of CO_2 solubility in different formation water corresponding to the multiple injection layers (Li, personal communication, Oct 2012) (Fig. 6.7), it can be observed that under a constant formation pressure (25 MPa), solubility increases with depth, i.e. from Liujiagou to Shihezi formation. However, the solubility in Shanxi formation (deeper) is a little smaller compared to that in Shihezi formation (shallower), illustrating that CO_2 solubility is not fully salinity-dependent.
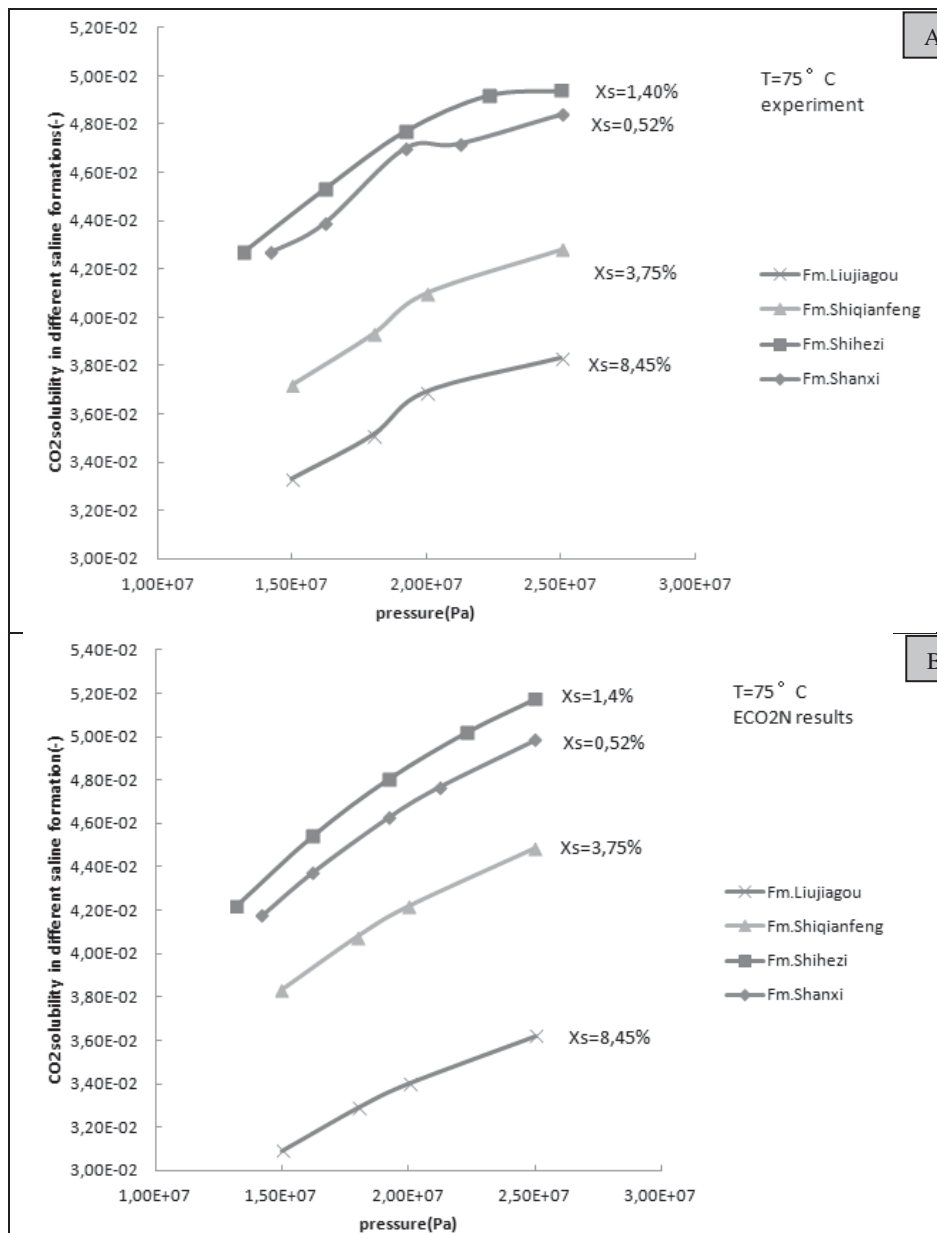
Fig. 6.7 Solubility of CO_2 in different formation water corresponding to four aquifer layers, A for experimental results, B for simulation results

By comparing experimental and simulation (using TOUGHREACT/ ECO2N simulator) results (Figs. 6.8 and 6.9), it can be seen that the two methods give a good match in formations with low salinity brines,

151

demonstrating the feasibility of the extended Debye-Hückel equation. However, when the salinity of the formation water increases, especially for Shiqianfeng and Liujiagou formations, the results difference is large and may need a calibration with Pitzer model (De Lucia et al., 2012).
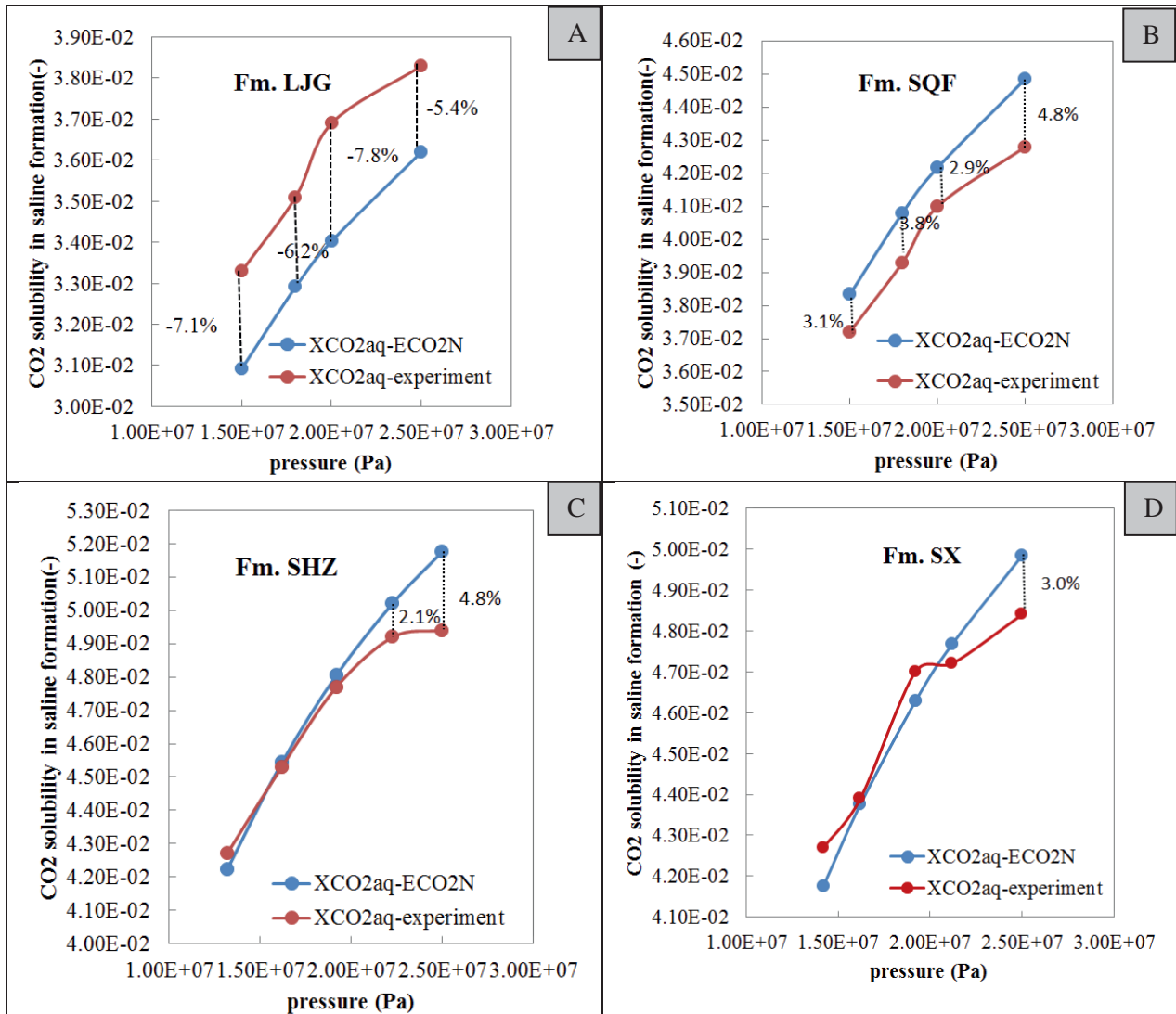
Fig. 6.8 Experimental and simulation (TOUGHREACT/ECO2N) results for the solubility of CO_2 in saline formation waters from different injection layers (Liu et al., 2014b)

6.4.2 Initial mineralogy and aqueous compositions

Data for initial mineral compositions and aqueous component concentrations used in the simulation is collected from gas fields adjacent to the sequestration site and other collaborators on the Ordos CCS project (Yang et al., 2001; Qin et al., 2005; Wan, 2012; Li X.C., personal communication, 2012), see Fig 6.9, Table 6.3, Fig 6.10.

152
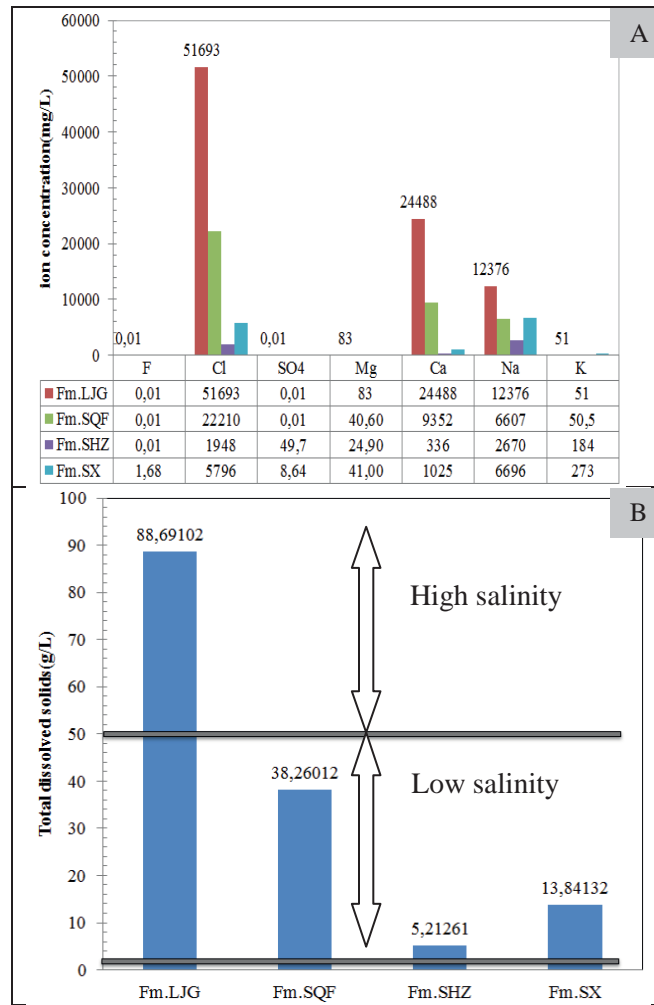
Fig. 6.9 Formation water chemistry characteristics of Upper Paleozoic strata in the Northern Ordos Basin (Liu et al., 2014b)

Table 6.3 Mineralogy of four formations in the Northern Ordos Basin (in volume fraction-%) (Yang et al., 2001; Qin et al., 2005; Wan, 2012)

Minerals	Chemical formula	Fm. LJG	Fm. SQF	Fm. SHZ	Fm. SX
Quartz	SiO_2	55	53	72	65
Hematite	Fe_2O_3	0	2	0	0
Oligoclase	$Na_{1-x}Ca_xAl_{1+x}Si_{3-x}O_8$	15	15	1	1
Low-albite	$NaAlSi_3O_8$	0	0	0	0
K-feldspar	$KAlSi_3O_8$	12	12	1	1
Smectite	$E_x(H_2O)_4 \{(Al_{2-x},Mg_x)_2 [(Si, Al)_4O_{10}] (OH)_2\}$; E is $Na^+/Ca^{2+}/K^+/Li^+$	0	0	1	0
Kaolinite	$Al_4Si_4O_{10} \cdot (OH)_8$	0	2	3.7	1.0
Illite	$K_{0.75}(Al_{1.75}R)[Si_{3.5}Al_{0.5}O_{10}](OH)_2$	2	7	7.0	1.0
Chlorite	$Y_3[Z_4O_{10}](OH)_2 \cdot Y_3(OH)_6$; Y is Mg/Fe/Al etc, Z is Si and Al	0	0	0.75	0.50
Calcite	$CaCO_3$	0	1	1.0	1.0
Dolomite	$CaMg[CO_3]_2$	0	0	0	0
Magnesite	$MgCO_3$	0	0	0	0
Siderite	$FeCO_3$	0	0	1.8	0
Ankerite	$Ca(Mg,Fe)(CO_3)_2$	0	0	1.3	0
Dawsonite	$NaAlCO_3(OH)_2$	0	0	0	0
Anhydrite	$CaSO_4$	0	0	0	0

153
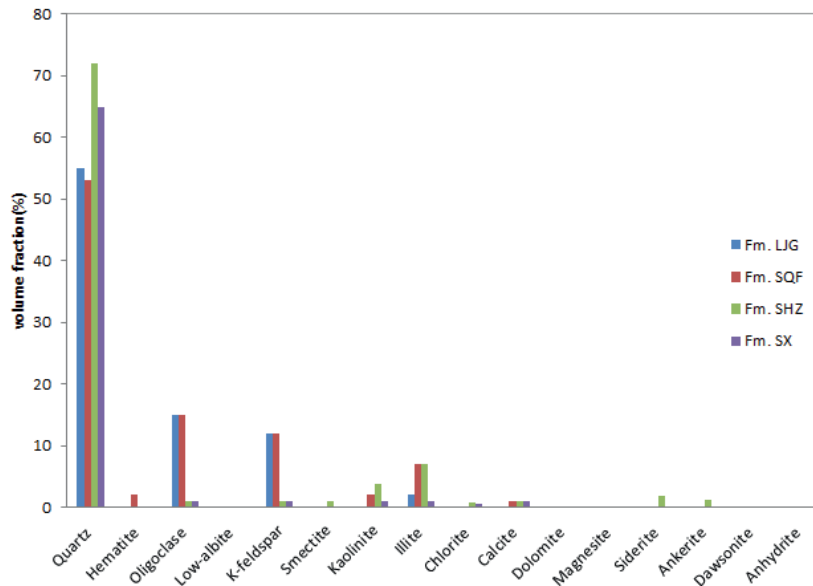
Fig. 6.10 Average volume fraction for minerals in the four aquifer formations (Liu et al., 2014b)

6.4.2.1 Initial mineralogy and aqueous compositions of the reservoir

The sandstone (lithic arkose) in Liujiagou formation is composed of framework grains that are partially rounded and poorly sorted. The detailed mineral composition of the arkose is as follows: detrital feldspar (20-40%), detrital quartz (24-50%); the cements, which are mainly composed of carbonate and clay minerals, i.e. calcite (0-20%), dolomite (0-2%), chlorite (5-10%), smectite (15-20%), illite (5-10%), kaolinite (0-5%); and other minerals including hematite (0-3%).

Based on the average mineralogy of arkose in the formation, the initial mineralogy and formation water chemistry characteristics of each aquifer layer in the simulation model are as shown in Tables 6.4-6.8, what should be noted, that the experimental results of formation water are from (Li, personal communication, Oct 2012):

Table 6.4 Initial mineral and formation water compositions in **Fm.Liujiagou sandstone** (data of mineral compositions are from Wan, 2012; while those for formation water are experimental)

Minerals	Chemical formula	Volume fraction (%)	Aqueous components of water	Concentration (moles/kg H_2O)
Quartz	SiO_2	55	Ca^{2+}	5.84×10^{-1}
Hematite	Fe_2O_3	0	Mg^{2+}	3.26×10^{-3}
Oligoclase	$Na_{1-x}Ca_xAl_{1+x}Si_{3-x}O_8$	15	Na^+	5.13×10^{-1}
Low-albite	$NaAlSi_3O_8$	0	K^+	1.25×10^{-3}
K-feldspar	$KAlSi_3O_8$	12	Iron	3.40×10^{-4}
Smectite	$E_x(H_2O)_4 \{(Al_{2-x},Mg_x)_2 [(Si, Al)_4O_{10}] (OH)_2\}$; E is $Na^+/Ca^{2+}/K^+/Li^+$	0	$SiO_{2(aq)}$	1.18×10^{-2}
Kaolinite	$Al_4Si_4O_{10} \cdot (OH)_8$	0	HCO_3^-	9.32×10^{-4}
Illite	$K_{0.75}(Al_{1.75}R)[Si_{3.5}Al_{0.5}O_{10}](OH)_2$	2	SO_4^{2-}	9.92×10^{-8}
Chlorite	$Y_3[Z_4O_{10}](OH)_2 \cdot Y_3(OH)_6$; Y is Mg/Fe/Al etc, Z is Si and Al	0	AlO_2^-	1.20×10^{-7}
Calcite	$CaCO_3$	0	Cl^-	1.38×10^0
Dolomite	$CaMg[CO_3]_2$	0	F^-	5.02×10^{-7}
Magnesite	$MgCO_3$	0		
Siderite	$FeCO_3$	0	$O_{2(aq)}$	5.03×10^{-10}
Ankerite	$Ca(Mg,Fe)(CO_3)_2$	0	pH	12.0
Dawsonite	$NaAlCO_3(OH)_2$	0		
Anhydrite	$CaSO_4$	0		

154

Table 6.5 Initial mineral and formation water compositions in **Fm.Shiqianfeng sandstone** (data of mineral and aqueous concentrations are from Wan, 2012)

Minerals	Chemical formula	Volume fraction (%)	Aqueous components	Concentration (moles/kg H_2O)
Quartz	SiO_2	53	Ca^{2+}	1.61×10^{-1}
Hematite	Fe_2O_3	2	Mg^{2+}	8.28×10^{-3}
Oligoclase	$Na_{1-x}Ca_xAl_{1+x}Si_{3-x}O_8$	15	Na^+	1.98×10^{-1}
Low-albite	$NaAlSi_3O_8$	0	K^+	6.27×10^{-4}
K-feldspar	$KAlSi_3O_8$	12	Iron	3.40×10^{-4}
Smectite	$E_x(H_2O)_4\{(Al_{2-x},Mg_x)_2 [(Si, Al)_4O_{10}] (OH)_2\}$; E is $Na^+/Ca^{2+}/K^+/Li^+$	0	$SiO_{2(aq)}$	1.18×10^{-2}
Kaolinite	$Al_4Si_4O_{10} \cdot (OH)_8$	2	HCO_3^-	9.32×10^{-4}
Illite	$K_{0.75}(Al_{1.75}R)[Si_{3.5}Al_{0.5}O_{10}](OH)_2$	7	SO_4^{2-}	2.02×10^{-2}
Chlorite	$Y_3[Z_4O_{10}](OH)_2 \cdot Y_3(OH)_6$; Y is Mg/Fe/Al etc, Z is Si and Al	0	AlO_2^-	1.20×10^{-7}
Calcite	$CaCO_3$	1	Cl^-	5.06×10^{-1}
Dolomite	$CaMg[CO_3]_2$	0	$O_{2(aq)}$	5.03×10^{-10}
Magnesite	$MgCO_3$	0	pH	6.0
Siderite	$FeCO_3$	0		
Ankerite	$Ca(Mg,Fe)(CO_3)_2$	0		
Dawsonite	$NaAlCO_3(OH)_2$	0		
Anhydrite	$CaSO_4$	0		

Table 6.6 Initial mineral and formation water compositions in **Fm. Shihezi sandstone** (data of mineral content data is from Yang, 2001; formation water data is from experiment)

Minerals	Chemical formula	Volume fraction (%)	Aqueous components	Concentration (moles/kg H_2O)
Quartz	SiO_2	72	Ca^{2+}	8.40×10^{-3}
Hematite	Fe_2O_3	0	Mg^{2+}	1.04×10^{-3}
Oligoclase	$Na_{1-x}Ca_xAl_{1+x}Si_{3-x}O_8$	1	Na^+	1.16×10^{-1}
Low-albite	$NaAlSi_3O_8$	0	K^+	4.72×10^{-3}
K-feldspar	$KAlSi_3O_8$	1	Iron	6.59×10^{-5}
Smectite	$E_x(H_2O)_4\{(Al_{2-x},Mg_x)_2 [(Si, Al)_4O_{10}] (OH)_2\}$; E is $Na^+/Ca^{2+}/K^+/Li^+$	1	$SiO_{2(aq)}$	1.57×10^{-4}
Kaolinite	$Al_4Si_4O_{10} \cdot (OH)_8$	3.7	HCO_3^-	2.51×10^{-3}
Illite	$K_{0.75}(Al_{1.75}R)[Si_{3.5}Al_{0.5}O_{10}](OH)_2$	7.0	SO_4^{2-}	5.18×10^{-4}
Chlorite	$Y_3[Z_4O_{10}](OH)_2 \cdot Y_3(OH)_6$; Y is Mg/Fe/Al etc, Z is Si and Al	0.75	AlO_2^-	1.29×10^{-9}
Calcite	$CaCO_3$	1.0	Cl^-	5.49×10^{-2}
Dolomite	$CaMg[CO_3]_2$	0	F^-	5.26×10^{-7}
Magnesite	$MgCO_3$	0		
Siderite	$FeCO_3$	1.8	$O_{2(aq)}$	5.03×10^{-10}
Ankerite	$Ca(Mg,Fe)(CO_3)_2$	1.3	pH	6.37
Dawsonite	$NaAlCO_3(OH)_2$	0		
Anhydrite	$CaSO_4$	0		

155

Table 6.7 Initial mineral and formation water composition in **Fm. Shanxi sandstone** (mineral content data from Yang, 2001; formation water data from experiment)

Minerals	Chemical formula	Volume fraction (%)	Aqueous components	Concentration (moles/kg H$_2$O)
Quartz	SiO_2	65	Ca^{2+}	2.55×10^{-2}
Hematite	Fe_2O_3	0	Mg^{2+}	1.70×10^{-3}
Oligoclase	$Na_{1-x}Ca_xAl_{1+x}Si_{3-x}O_8$	1	Na^+	2.90×10^{-1}
Low-albite	$NaAlSi_3O_8$	0	K^+	6.97×10^{-3}
K-feldspar	$KAlSi_3O_8$	1	Iron	8.96×10^{-11}
Smectite	$E_x(H_2O)_4 \{(Al_{2-x},Mg_x)_2 [(Si, Al)_4O_{10}] (OH)_2\}$; E is $Na^+/Ca^{2+}/K^+/Li^+$	0	$SiO_{2(aq)}$	1.39×10^{-4}
Kaolinite	$Al_4Si_4O_{10} \cdot (OH)_8$	1.0	HCO_3^-	1.43×10^{-9}
Illite	$K_{0.75}(Al_{1.75}R)[Si_{3.5}Al_{0.5}O_{10}](OH)_2$	1.0	SO_4^{2-}	8.96×10^{-5}
Chlorite	$Y_3[Z_4O_{10}](OH)_2 \cdot Y_3(OH)_6$; Y is Mg/Fe/Al etc, Z is Si and Al	0.50	AlO_2^-	2.96×10^{-5}
Calcite	$CaCO_3$	1.0	Cl^-	1.63×10^{-1}
Dolomite	$CaMg[CO_3]_2$	0	F^-	8.80×10^{-5}
Magnesite	$MgCO_3$	0		
Siderite	$FeCO_3$	0	$O_{2(aq)}$	2.59×10^{-20}
Ankerite	$Ca(Mg,Fe)(CO_3)_2$	0	pH	12.39
Dawsonite	$NaAlCO_3(OH)_2$	0		
Anhydrite	$CaSO_4$	0		

Table 6.8 Initial mineral and formation water compositions in **mudstone** (Zheng, 1999)

Minerals	Chemical formula	Volume fraction (%)	Aqueous components	Concentration (moles/kg H$_2$O)
Quartz	SiO_2	15	Ca^{2+}	1.61×10^{-1}
Hematite	Fe_2O_3	0	Mg^{2+}	8.28×10^{-3}
Oligoclase	$Na_{1-x}Ca_xAl_{1+x}Si_{3-x}O_8$	1	Na^+	1.98×10^{-1}
Low-albite	$NaAlSi_3O_8$	0	K^+	6.27×10^{-4}
K-feldspar	$KAlSi_3O_8$	1	Iron	3.40×10^{-4}
Smectite	$E_x(H_2O)_4 \{(Al_{2-x},Mg_x)_2 [(Si, Al)_4O_{10}] (OH)_2\}$; E is $Na^+/Ca^{2+}/K^+/Li^+$	20	$SiO_{2(aq)}$	1.18×10^{-2}
Kaolinite	$Al_4Si_4O_{10} \cdot (OH)_8$	35	HCO_3^-	9.32×10^{-4}
Illite	$K_{0.75}(Al_{1.75}R)[Si_{3.5}Al_{0.5}O_{10}](OH)_2$	20	SO_4^{2-}	2.02×10^{-2}
Chlorite	$Y_3[Z_4O_{10}](OH)_2 \cdot Y_3(OH)_6$; Y is Mg/Fe/Al etc, Z is Si and Al	1	AlO_2^-	1.20×10^{-7}
Calcite	$CaCO_3$	0	Cl^-	5.06×10^{-1}
Dolomite	$CaMg[CO_3]_2$	0	$O_{2(aq)}$	5.03×10^{-10}
Magnesite	$MgCO_3$	0	pH	4.64
Siderite	$FeCO_3$	0		
Ankerite	$Ca(Mg,Fe)(CO_3)_2$	0		
Dawsonite	$NaAlCO_3(OH)_2$	0		
Anhydrite	$CaSO_4$	0		

6.5 Results and discussion

6.5.1 Batch simulations: CO$_2$-fluid-rock interactions (CFRI)

Four batch simulation runs were performed in TOUGHREACT, under in-situ pressure conditions and a temperature of 75°C using mineral and water composition data from the four aquifer layers. CO_2 is injected in the formations during the first one year period and the total simulation lasts 100 years. Porosity and permeability of the sandstone samples is assumed to be 30% and 50 mD, respectively.

6.5.1.1 CFRI in Fm.LJG

In this batch simulation model, the samples were taken from the LJG sandstone formation. Parameters of supercritical CO_2 and water at 75^oC and 17.5 MPa were used. It can be seen from the simulation results (Fig. 6.11) that a sharp decrease in pH (about 3.1) occurs at the beginning of injection (i.e., only several days), which may significantly enhance mineral dissolution and precipitation (Xu et al., 2001). Maximum solubility of CO_2 in the formation water is maintained during the total simulation period. After the short-term decrease in pH, however, it will increase to an equilibrium state within a period of about 20 years, offsetting the acidification effect of CO_2 in formation water. This phenomenon is important in illustrating that the decrease in pH will not last a long period in the storage site due to the injected CO_2. The pH changes in the brine also dependent on the saturation state of the secondary minerals (Flaathen et al., 2009). However, a period of time is needed for the formation water to recover. As a result, the reaction rate promoted by CO_2 injection will slow down in the long term. Concentrations of the main ions (Fig. 6.11A), such as Ca^{2+}, Na^+ and Cl^-, remain almost unchanged during the entire simulation period. However, concentrations of other ions show a time-dependent characteristics (Fig. 6.11B), for instance, SiO_2 (aq) and HCO_3^- change proportionally with pH, while Mg^{2+} shows inverse characteristics with pH. The variation trends of K^+ and AlO_2^- present totally opposite characteristics, both showing non-linear changes with time. The time nodes at 4 year, 8 year, 18 year are the transition points of interactions between different minerals with the carbonic solution, showing the difference in chemical reaction kinitics (Friedmann, 2007).

(1) Ion concentration changes
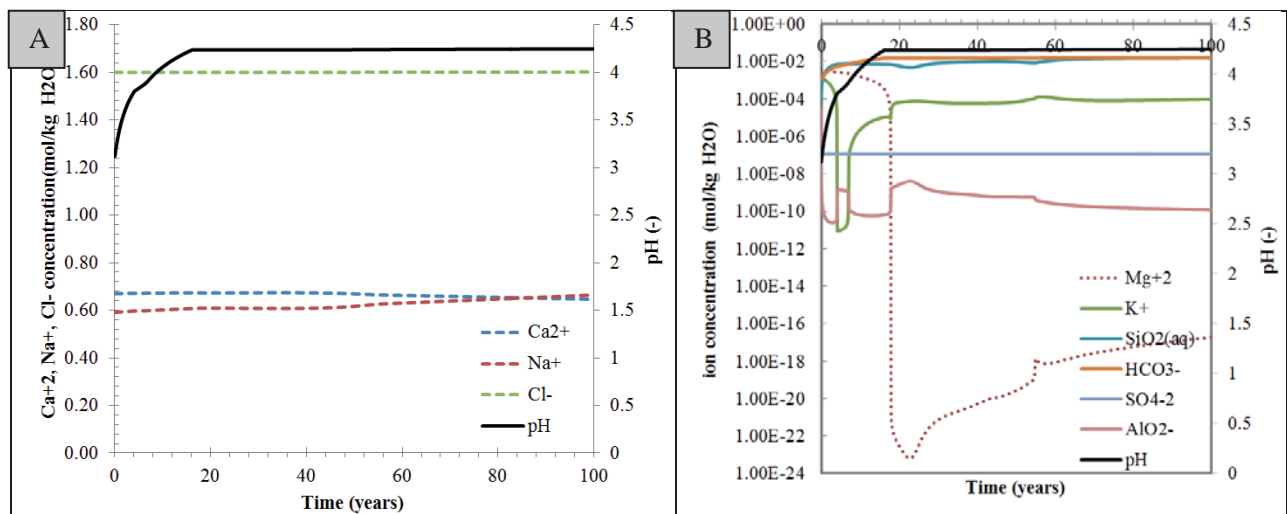
Fig. 6.11 Changes of aqueous components concentration with time in Fm. LJG sandstone sample due to CO_2 injection (Liu et al., 2014b)

(2) Mineral volume fraction changes

The volume fraction changes of minerals show time-dependent characteristics. Different minerals show various variation characteristics (Fig. 6.12). Some minerals, e.g. quartz and low-albite, precipitate during the simulation runs. Both oligoclase and k-feldspar tend to dissolve because they are more soluble in the presence of CO_2 (Xu et al., 2001; Rosenbauer et al., 2005). It should be stated that the distinction in reaction rates for different minerals results in a complex mineral assemblages with time. In the first few years, no carbonate minerals precipitate, while after about 26 years their chemical reactions strengthen greatly. Calcite starts to precipitate and increases with time, while dawsonite deposites for a time period (20-56 year). However, after 56 years, dawsonite disappears from the reaction system. Most clay minerals including kaolinite, illite and smectite-Ca precipitate, at different rates, causing a significant decrease in porosity (Xu et al., 2001). The above mentioned reaction characteristics of different minerals prove that

157

mineral trapping mechanisms occur at various rate for different minerals due to the difference in CO_2-water-rock interactions, which may require a much longer period to recovera chemical equilibrium state.
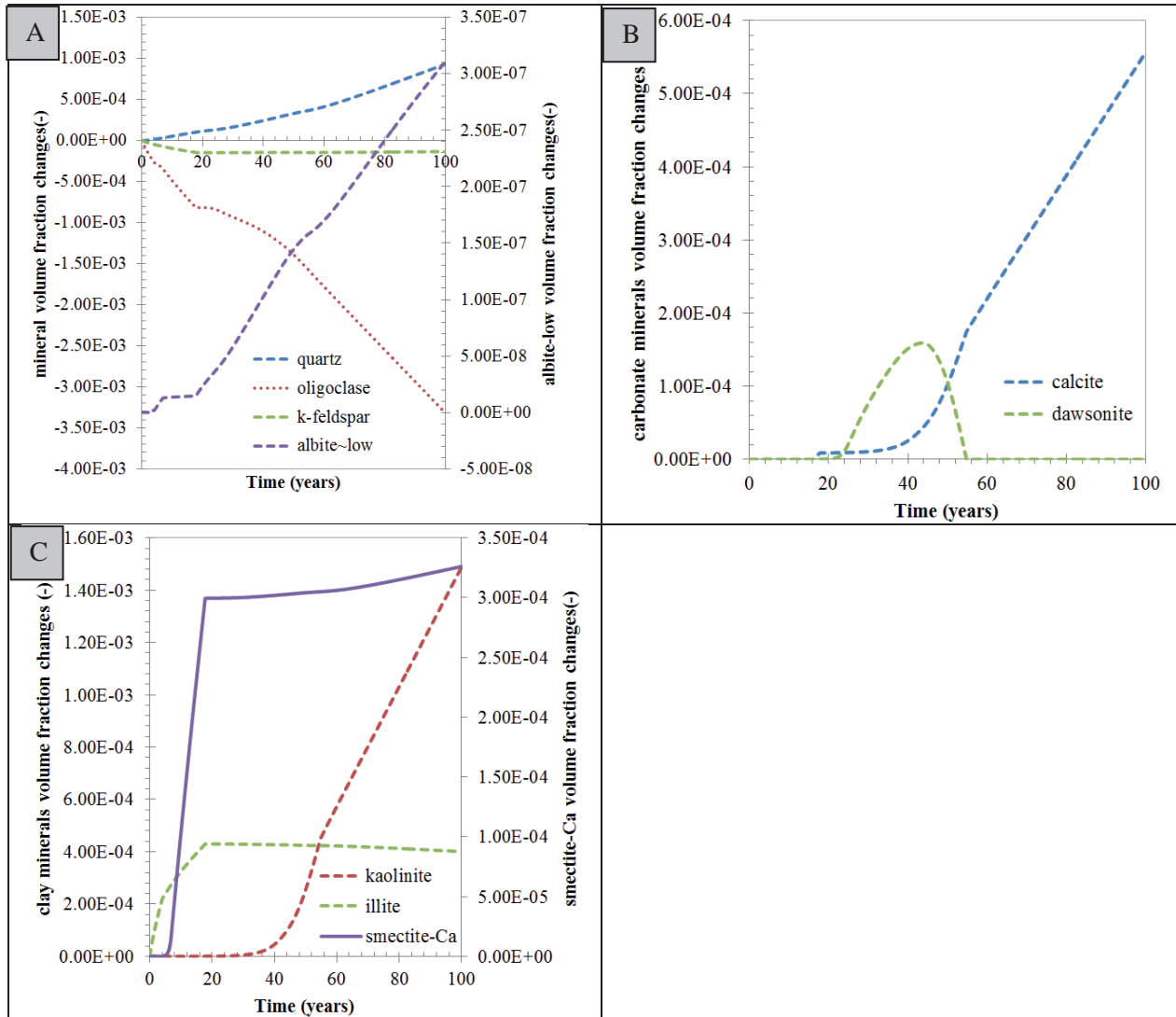
Fig. 6.12 Volume fraction changes in different minerals with time in Fm. LJG sandstone sample due to CO_2 injection (Liu et al., 2014b)

6.5.1.2 CFRI in Fm.SQF

The initial conditions prescribed for CO_2-water-rock interaction simulation runs in Fm. Shiqianfeng were 75°C and 19.2 MPa of temperature and in-situ formation pressure, respectively. There are obvious differences in the evolution of ions and minerals in Fm. SQF compared with that in the Fm. Liujiagou discussed above. Immediately after the injection begins, the injected CO_2 will cause a linear increase of Na^+ concentration and decrease in Ca^{2+} concentration, respectively (Fig. 6.13A). The variation trends for Mg^{2+}, K^+ and AlO_2^- ions are similar to those in the Liujiagou formation described above, however, with different jump or transition points (Fig. 6.13B).

158

(1) Ion concentration changes
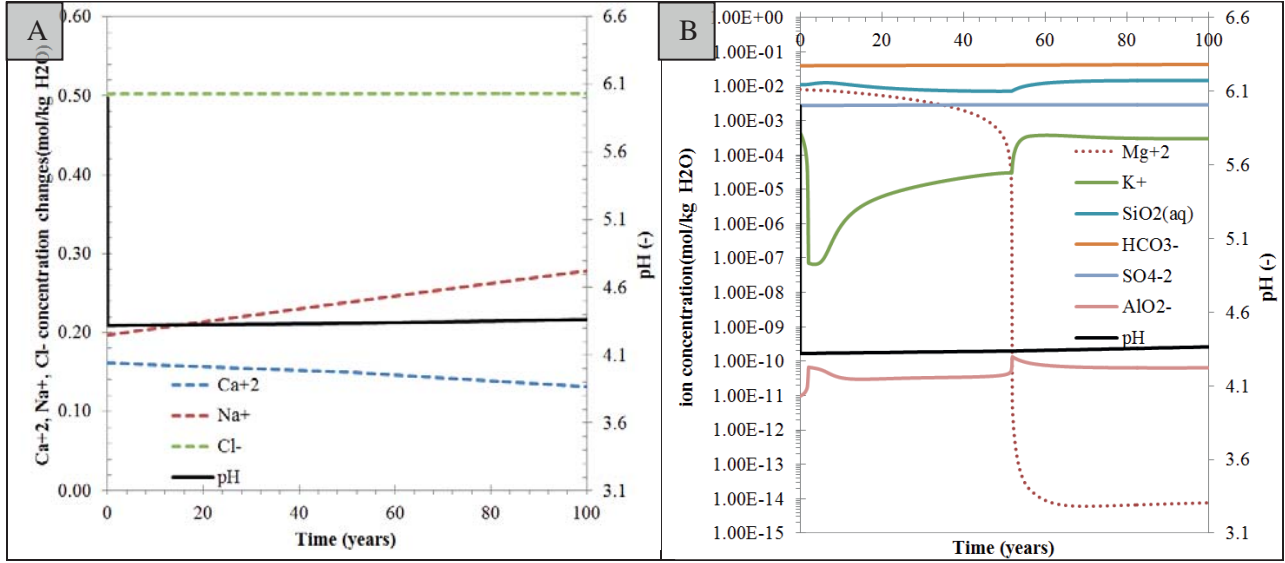
Fig. 6.13 Changes of aqueous components concentration with time in Fm. SQF sandstone sample due to CO_2 injection (Liu et al., 2014b)

(2) Mineral volume fraction changes

Considering the trends in volume fraction changes for different minerals (Fig. 6.14), it can be observed that calcite linearly dissolves in the first half of the simulation period (i.e. 50 years), while it starts to precipitate in the second half 50 years. The transition time point for calcite saturation state occurs at about 48 year. Unlike calcite, the transition time point for most clay minerals, from un-saturated to saturated state, including kaolinite, illite and smectite-Ca, occur at about 52 years since CO_2 injection (Fig. 6.14A). Illite and smectite-Ca deposit quickly before transition time, while the reaction rate slows down greatly afterward. Kaolinite presents a totally inverse variation characteristics compared to other clay minerals. Under the acidic solution conditions, oligoclase and K-feldspar generally show a dissolution trend, while low-albite will dissolve at first, but begins to deposit when the solution is saturated with respect to it (i.e. the accumulation of ions). Quartz shows a gradually increasing precipitation trend. It should be noted that the volume fraction of anhydrite does not change during the simulation time (Fig. 6.14B).
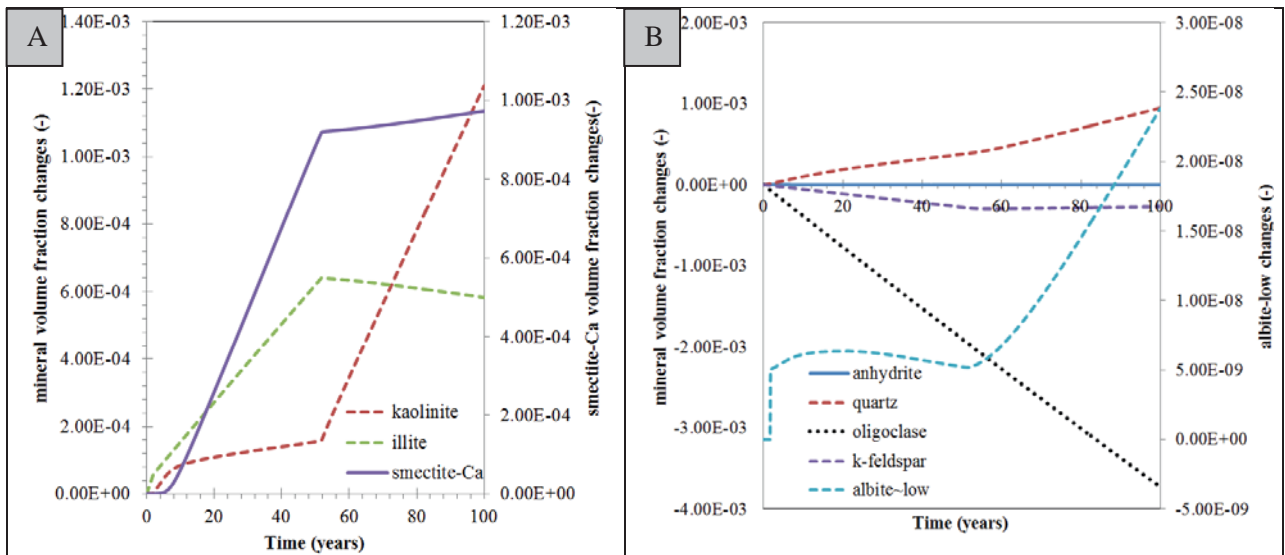
Fig. 6.14 Volume fraction changes in different minerals with time in Fm. SQF sandstone sample due to CO_2 injection

159

6.5.1.3 CFRI in Fm.SHZ

(1) Ion concentration changes

The initial simulation parameters used in the batch model for the SHZ formation were supercritical CO_2 and water at 75°C and 22.4 MPa formation pressure. The variation trends of concentration for some major ions (i.e. Ca^{2+}, Na^+ and Cl^-) in the Fm. SHZ (Fig. 6.15A) are similar to that in the Fm. LJG (Fig. 6.11A). Other ions, except SiO_2 (aq), AlO_2^- and K^+, show minor changes. The concentration of K^+ gradually decreases with time. In the first 10 years, the concentration of AlO_2^- decreases sharply with time, to an equilibrium state subsequently. In contrast to AlO_2^-, SiO_2 (aq) displays a reverse trend in concentration changes (Fig. 6.15B).
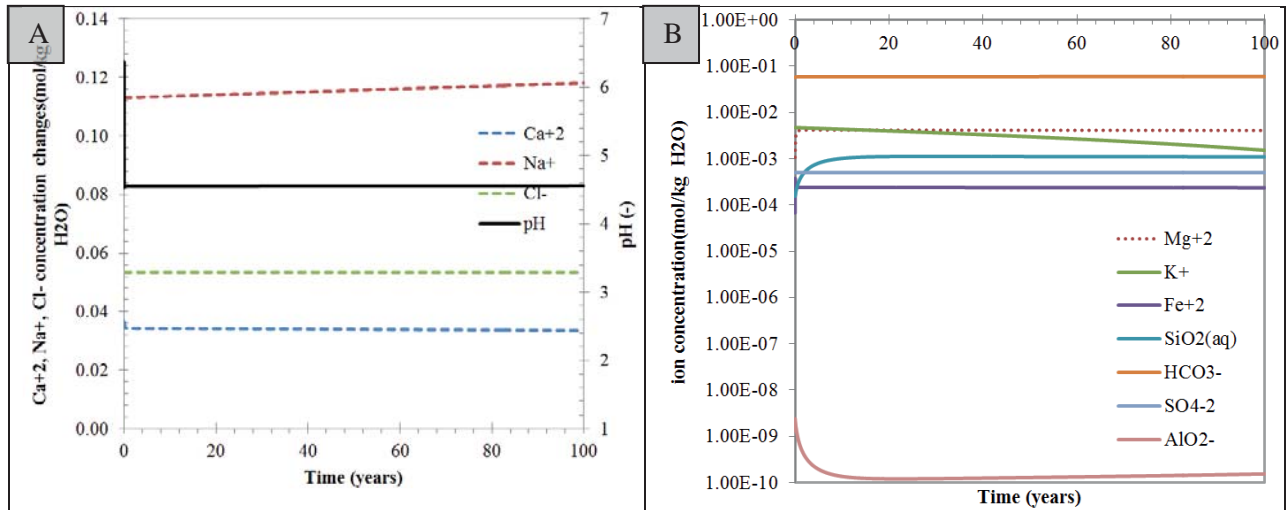
Fig. 6.15 Ion concentrations with time in Fm. SHZ sandstone sample due to CO_2 injection

(2) Mineral volume fraction changes

It is obvious that most feldspar minerals will stay as a dissolved state induced by CO_2 injection (Fig. 6.16). Considering the volume fraction changes for feldspars in the Fm. SHZ, the variation trend for oligoclase and k-feldspar can be distinguished because of their different reaction rates. Quartz, like in the other two injection formations described above, always shows a precipitation trend.
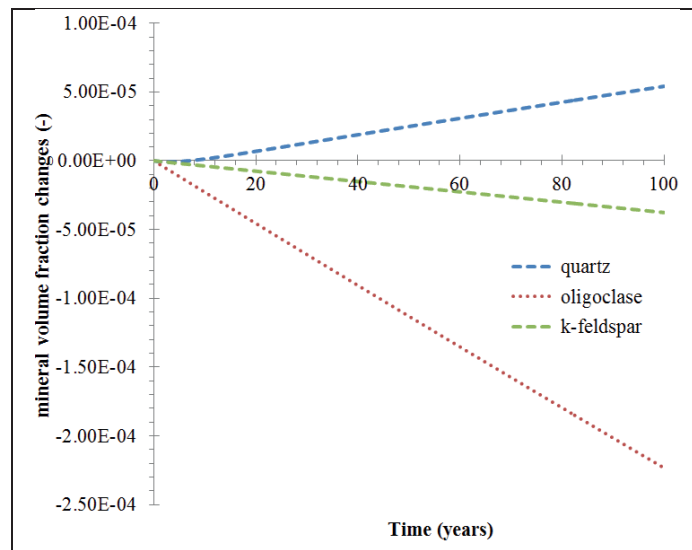
Fig. 6.16 Volume fraction changes of quartz and feldspar minerals with time in Fm. SHZ sandstone due to CO_2 injection (Liu et al., 2014b)

Simulation results of volume fraction changes for clay minerals demonstrate that time-dependent chemical reaction rates are obvious for different minerals (Fig. 6.17). Illite is the most easily deposited

clay mineral, with a volume fraction two orders of magnitude higher than kaolinite, which shows a non-linear relationship with time. During this simulation, both smectite-Ca and chlorite are always at a dissolved state in Fm.SHZ.
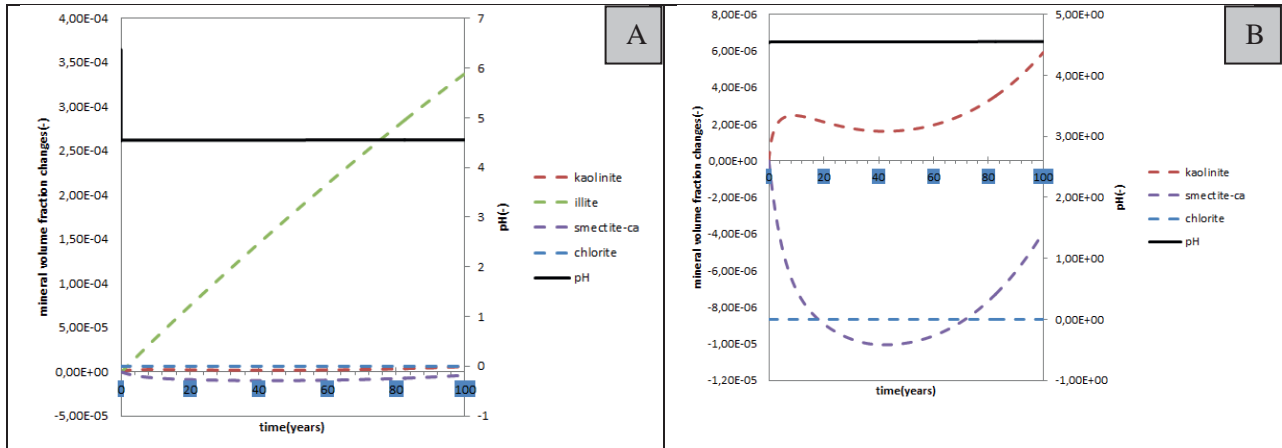
Fig. 6.17 Volume fraction changes of clay minerals with time in Fm. SHZ sandstone due to CO_2 injection. B is an expansion of the lower part of diagram A (note the changed scale of the y-axis), for a better visibility.

Similarly, the variation trends for dissolution and precipitation of carbonate minerals vary greatly. Considering different scales of x-axis (i.e. the simulation time) in Fig. 6.18, the results for mineral saturation states may be totally opposing in diagrams A and B. Take ankerite, for example, in diagram A it is seen to dissolve until about 40 years, when it starts to deposite at the same rate. On the contrary, however, when only a 1 year-period is considered, the long term changes in volume fractions of this mineral may be easily neglected. The transition from precipitation to dissolution of siderite is at 80 year. The calcite is always at the dissolution state, though the dissolution rate changes with time (Fig. 6.18).
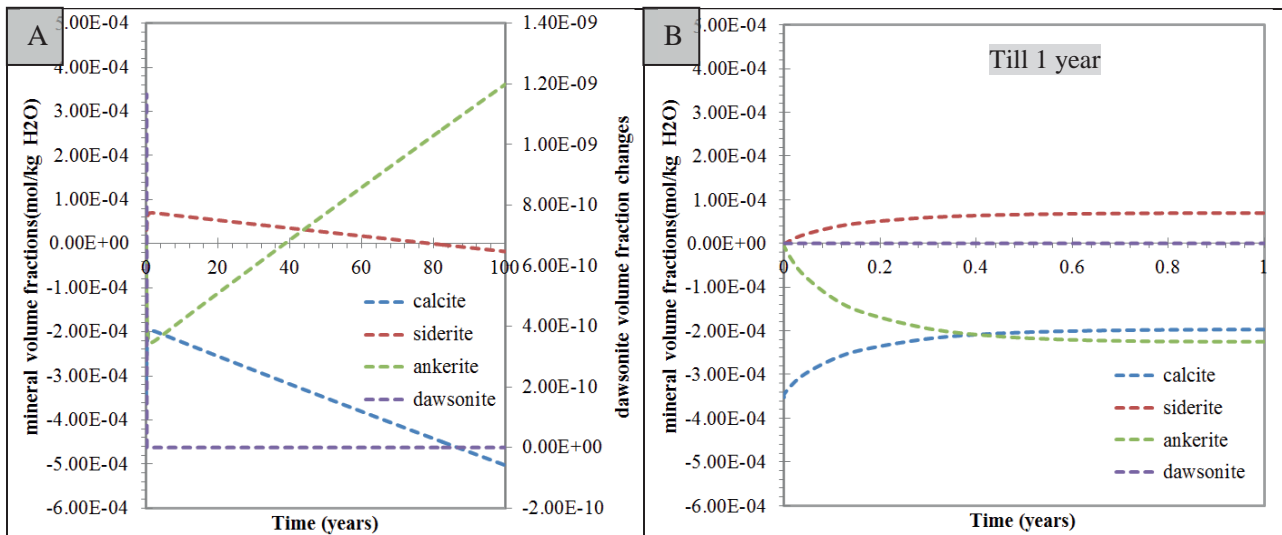
Fig. 6.18 Volume fraction changes of carbonate minerals with time in Fm. SHZ sandstone due to CO_2 injection

6.5.1.4 CFRI in Fm.SX

(1) Ion concentration changes

In this batch simulation model, the sandstone sample is taken from the SX formation. The parameters engaged in this simulation included supercritical CO_2, water at 75°C and 23.0 MPa, respectively. Like in the Fm. LJG, concentrations of some main ions (i.e. Ca^{2+}, Na^+ and Cl^-) in the Fm. SX remain almost unchanged during the total simulation period (Fig. 6.19A). Some ions, including HCO_3^-, Mg^{2+} and K^+, show minor changes, whereby HCO_3^- and Mg^{2+} tend to increase and K^+ decreases at

161

minimal rates. The increase in pH during the whole period is small, in the range of 4.55-4.575 (Fig. 6.19B).
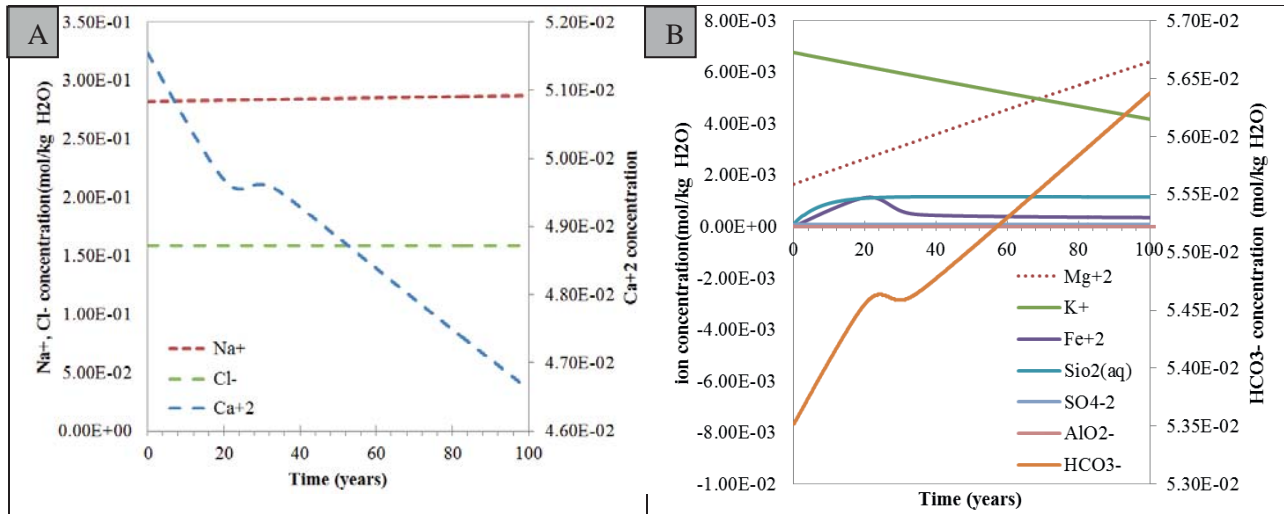
Fig. 6.19 Ion concentration changes with time in the Fm. SX sandstone sample due to CO$_2$ injection

(2) Mineral volume fraction changes

Illite and chlorite show significant variation trends due to their precipitation and dissolution reactions (Fig. 6.20A). The minor volume fraction changes in kaolinite and smectite-Ca can only be revealed using a larger scale of the Y-coordinate axis (Fig. 6.20B).
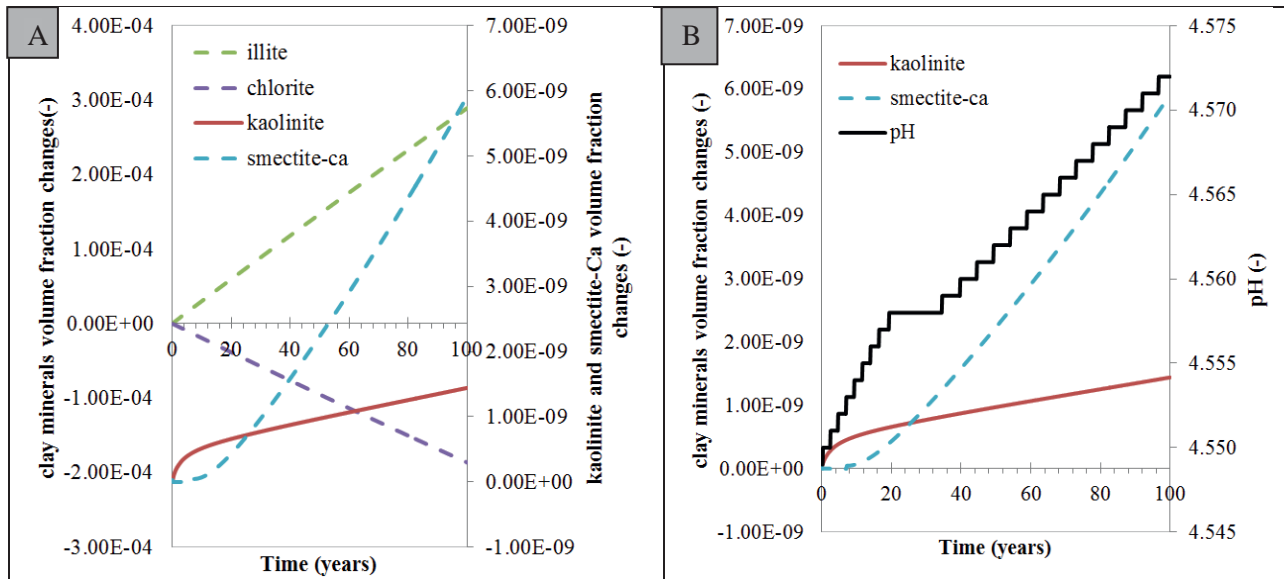
Fig. 6.20 Volume fraction changes with time for clay minerals in Fm. SX sandstone due to CO$_2$ injection

6.5.2 1D simulation for Fm. LJG sandstone

After these four batch simulations corresponding to the four injection layers, a 1D model was designed to investigate the reactive transport processes of the aqueous species and the subsequent mineral developments and distributions. RZ2D method is used for generating 1D radial grid blocks. In this model, the diameter of the wellbore is assigned a value of 0.3 m, with an increasing gradient of 19 successive radial grid blocks in the first 10 m from the wellbore. This is then followed by 10 radial grid blocks up to a radius of 500 m and finally another 10 grids to the boundary of the model, i.e. 1 km (Fig. 6.21). The thickness of the sandstone reservoir (i.e. the LJG formation layer) is set to be 15 m, just the same as that in Fig. 4.1. The parameters used in the model are shown in Table 6.9. Some geological parameters are randomly prescribed, e.g. density, specific heat, thermal conductivity, compressibility. The formation is assumed to be fully water saturated before CO$_2$ injection. The reservoir is regarded to be homogenerous,

162

at a temperature of 75 ^{o}C and a fluid pressure of 17 MPa. Water and average mineral compositions are assigned to be the same as that used in the batch simulations of LJG formation above. The injection rate is 0.1981 kg/s. The injection period is 1 year, while the entire simulation lasts over 100 years.
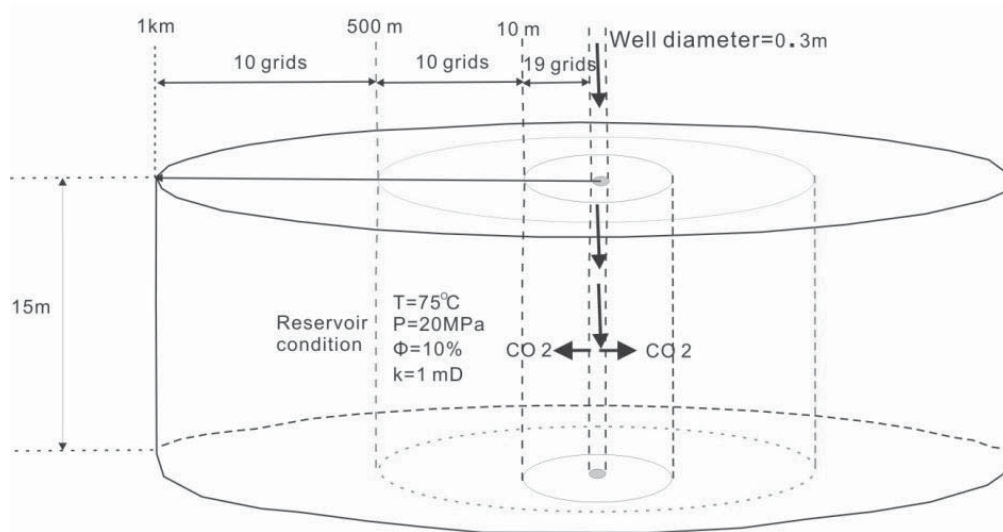
Fig. 6.21 Simplified radial grid model for 1D simulation

Table 6.9 Formation's initial, boundary and injection parameters in LJG formation for 1D simulation

Parameter	Value
Geological formation parameters	
Extension of the model	1 km
Thickness	H=15 m
porosity	ϕ=0.10
permeability	k=1 mD; $k_v = k_h$
Rock grain density	ρ= 2450 kg/m^3
Rock specific heat	1000 J/kg/^{o}C
Thermal conductivity	2.1 W/m/^{o}C
Compressibility	4.5×10^{-10} Pa^{-1}
Initial conditions	
Fluid in pore spaces	All H_2O
Temperature	75 ^{o}C
Pressure	17 MPa
salinity	88.69 g/L
Average mineralogy of LJG formation	See Table 6.5
Water chemistry of LJG formation	See Table 6.5
Boundary conditions	
Top/sides	No fluid or heat flow (closed)
Bottom	No fluid or heat flow (closed)
Injection parameters	
Injection rate	0.1981 kg/s
CO_2 injection enthalpy	5.08×10^6 J/kg

6.5.2.1 CO_2 propagation with time

After CO_2 injection, the near-wellbore region will be predominantly saturated with a pure CO_2 phase during the first 5 years since injection (Fig. 6.22A, B and C). Firstly, total displacement of the formation water by the injected CO_2 takes place, with a maximum displacement distance of about 3.1 m away from the core injection zone at the end of the injection. Once injection stops, imbibition of water will set off due to a pressure drop in the near-wellbore region (Flett et al., 2003). Thus, the single CO_2 phase zone will begin to contract with time, until 10 years when there will be no more area fully saturated with CO_2 (Fig. 6.22D). Overall, the CO_2 propagation distance can reach about 140 m away from the borehole (Fig. 6.22C and D).

163
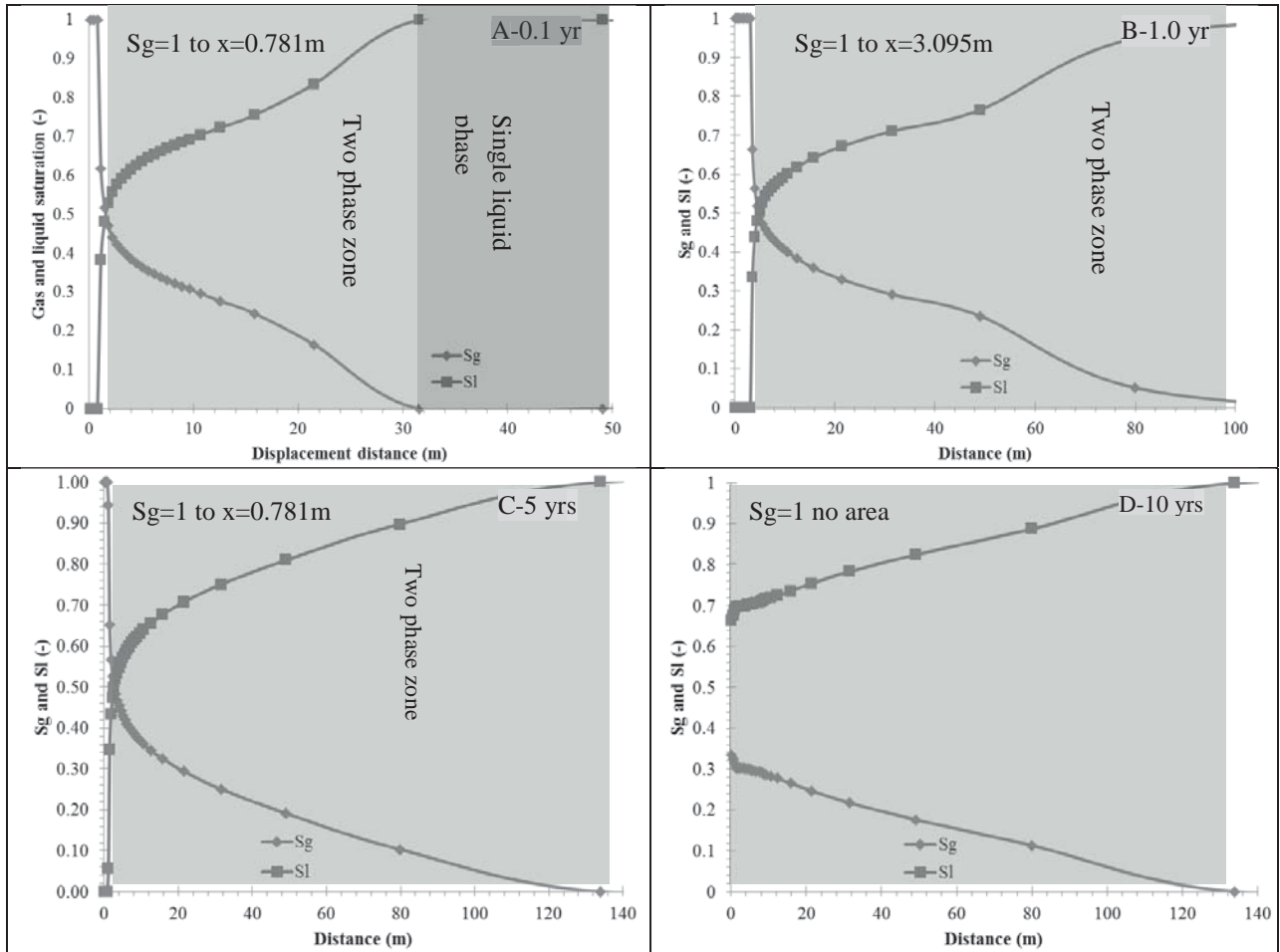
Fig. 6.22 Gas saturation changes with time in Fm.LJG sandstone reservoir

6.5.2.2 Ion concentration changes with time

The carbonic water derived from the dissolution of CO_2 into water will cause a decline of pH in the near-well region (Fig. 6.23), but not in the zone occupied by the single CO_2 phase (dry zone). As time goes by, the sweeping front of the carbonic water in the reservoir expands to a maximum distance of 70 m from injection zone. Between the propagation front and the intensive impact zone occupied by carbonic water, a transition region exists. Beyond that region, the initial formation water has not been affected. Note that the variation trends for different ions with time show significant differences (Figs. 6.23 to 6.28). The trends show positive correlation of the ions AlO_2^-, Mg^{2+}, Ca^{2+}, Na^+ and K^+ with pH. AlO_2^- is particularly sensitive to the changes in pH. As regards to some primary species, such as SiO_2 and HCO_3^-, a negative relationship with pH is displayed (Figs. 6.24 and 6.25). Note that the CO_2-water-rock interaction will change with time, but not in the single CO_2 phase region. The near well region is strongly affected by carbonic water and has the highest Ca^{2+} and Na^+ ion concentrations (at the boundary with the two phase zone), Fig. 6.23. The extent of the chemical reaction will result in the varied distribution of different species.
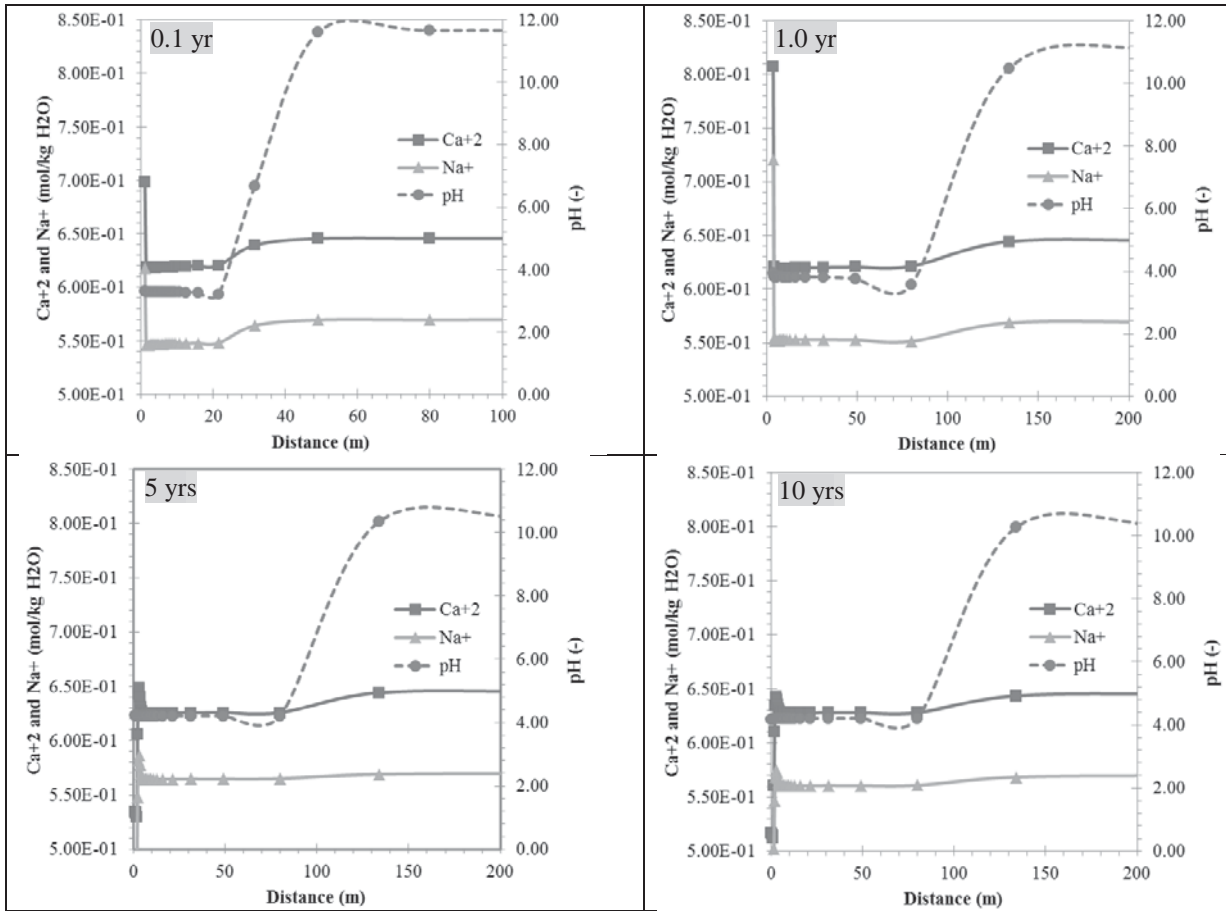
Fig. 6.23 Ca^{2+} and Na$^+$ concentration changes with time along the flow path in Fm.LJG sandstone reservoir
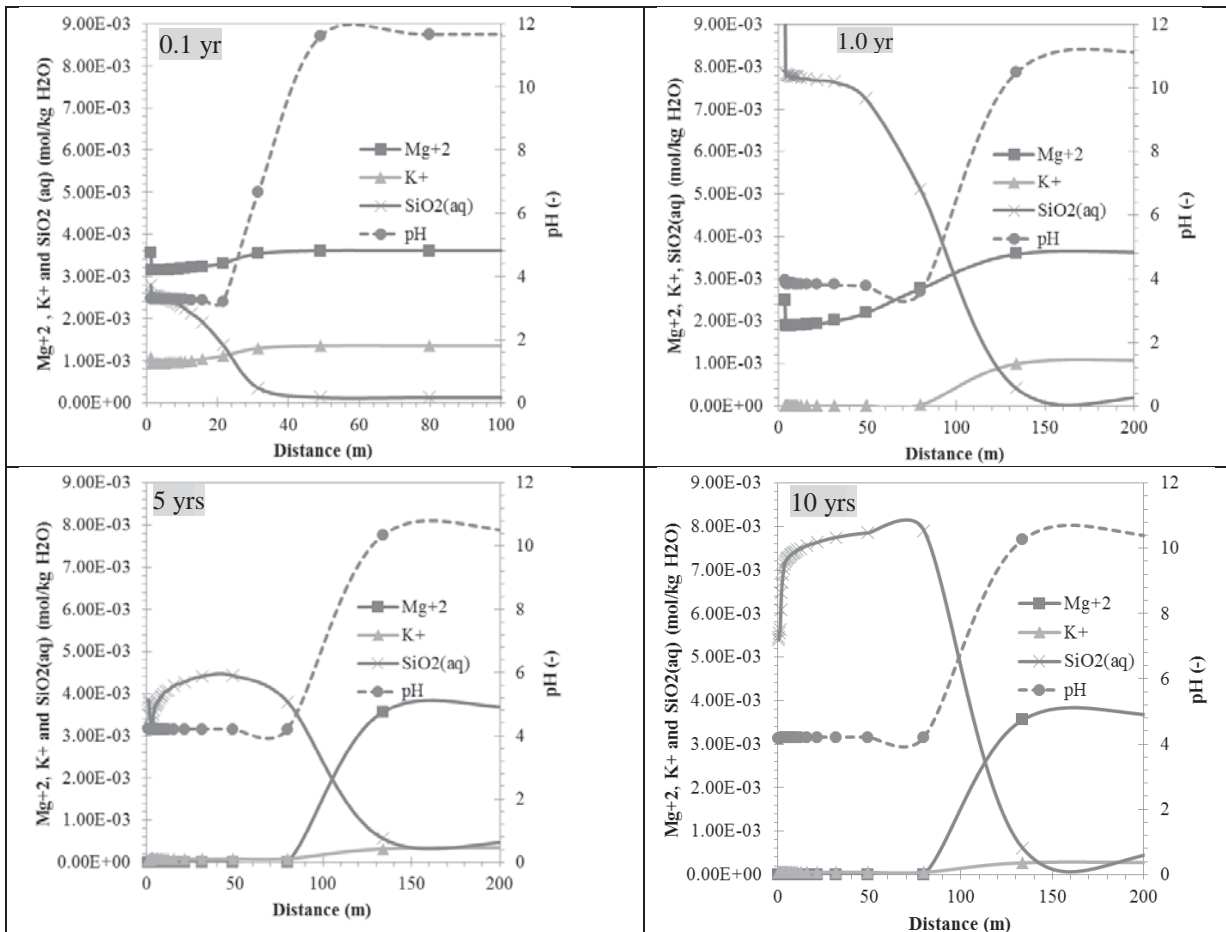
Fig. 6.24 Mg^{2+}, K$^+$ and SiO$_2$ (aq) concentration changes with time along the flow path

165
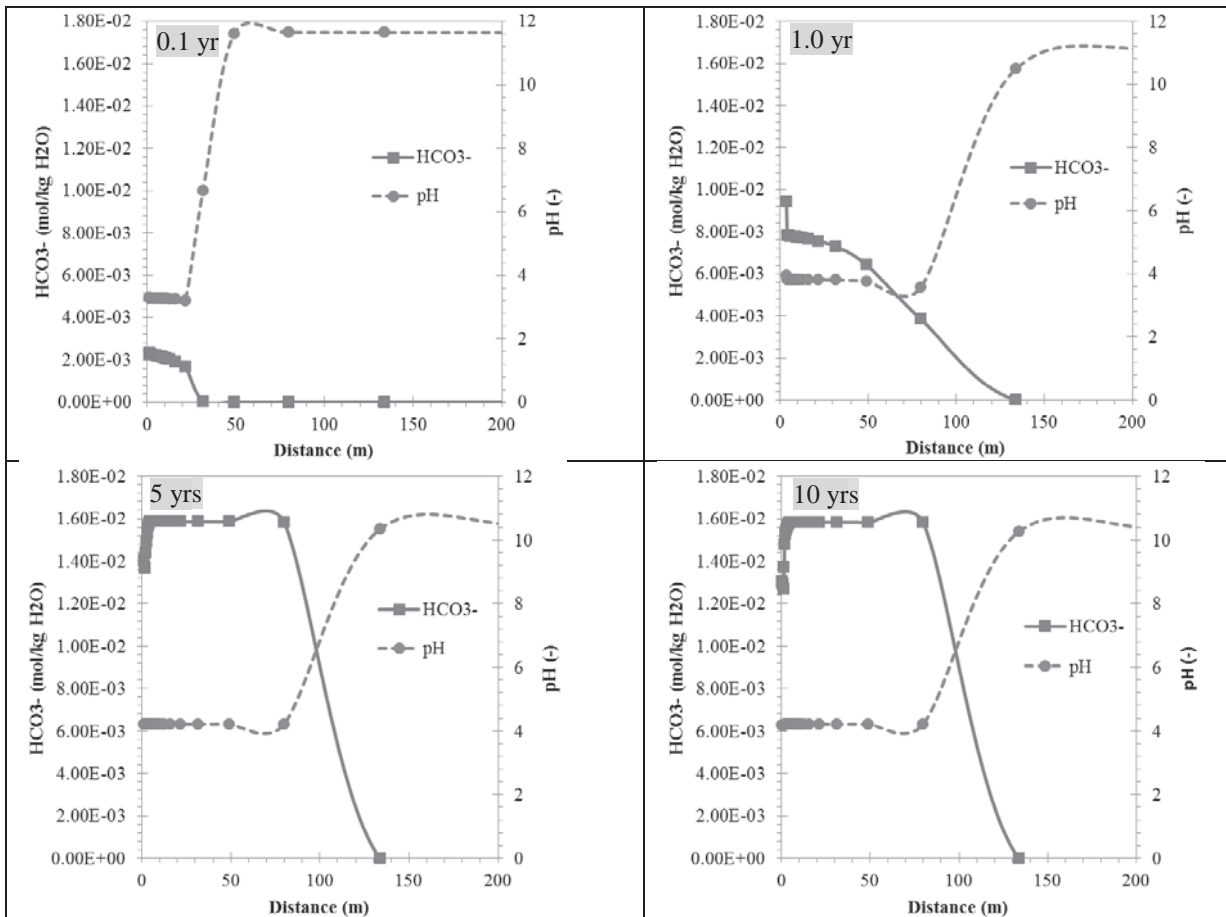
Fig. 6.25 HCO_3^- concentration changes with time along the flow path for Fm.LJG sandstone reservoir
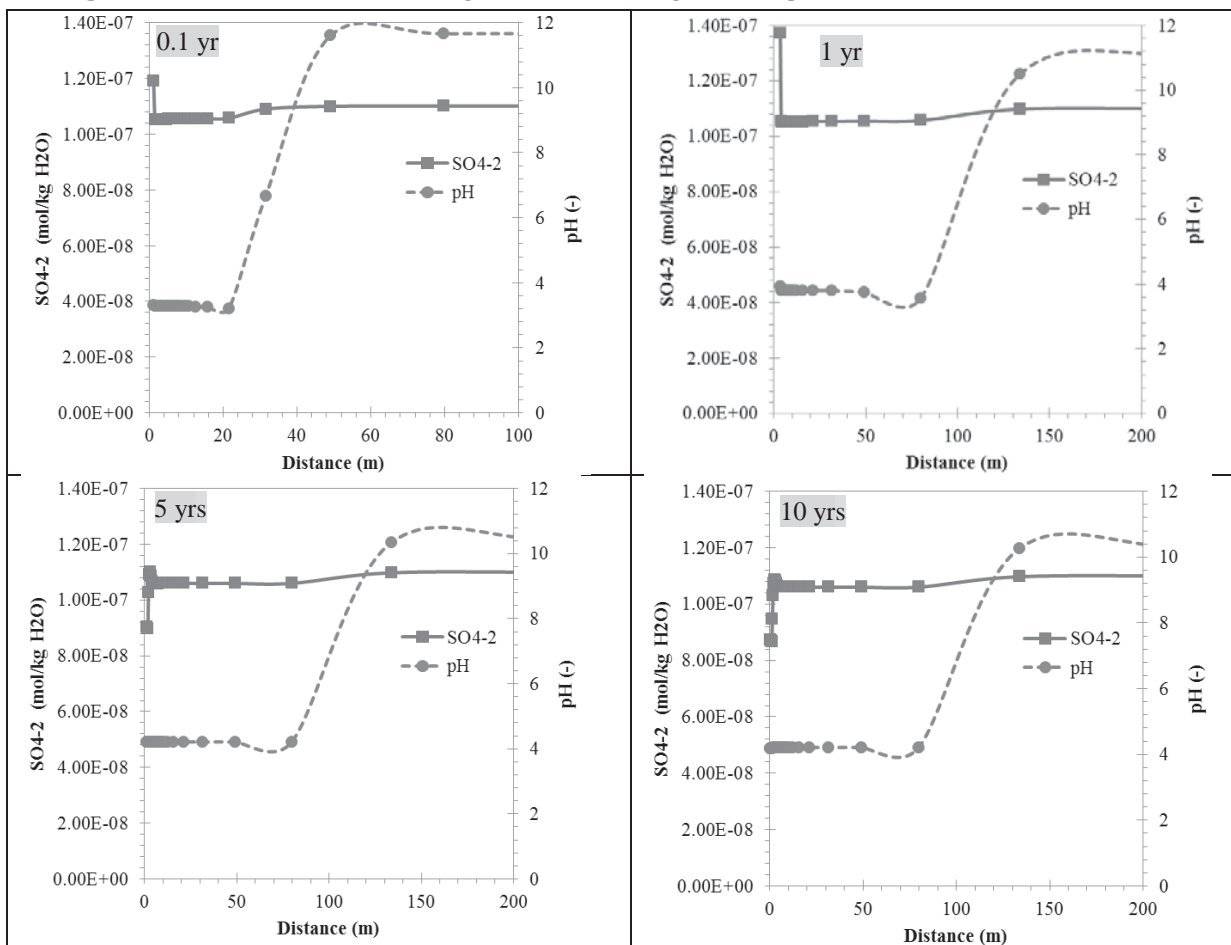
Fig. 6.26 SO_4^{2-} concentration changes with time along the flow path in Fm.LJG sandstone reservoir

166
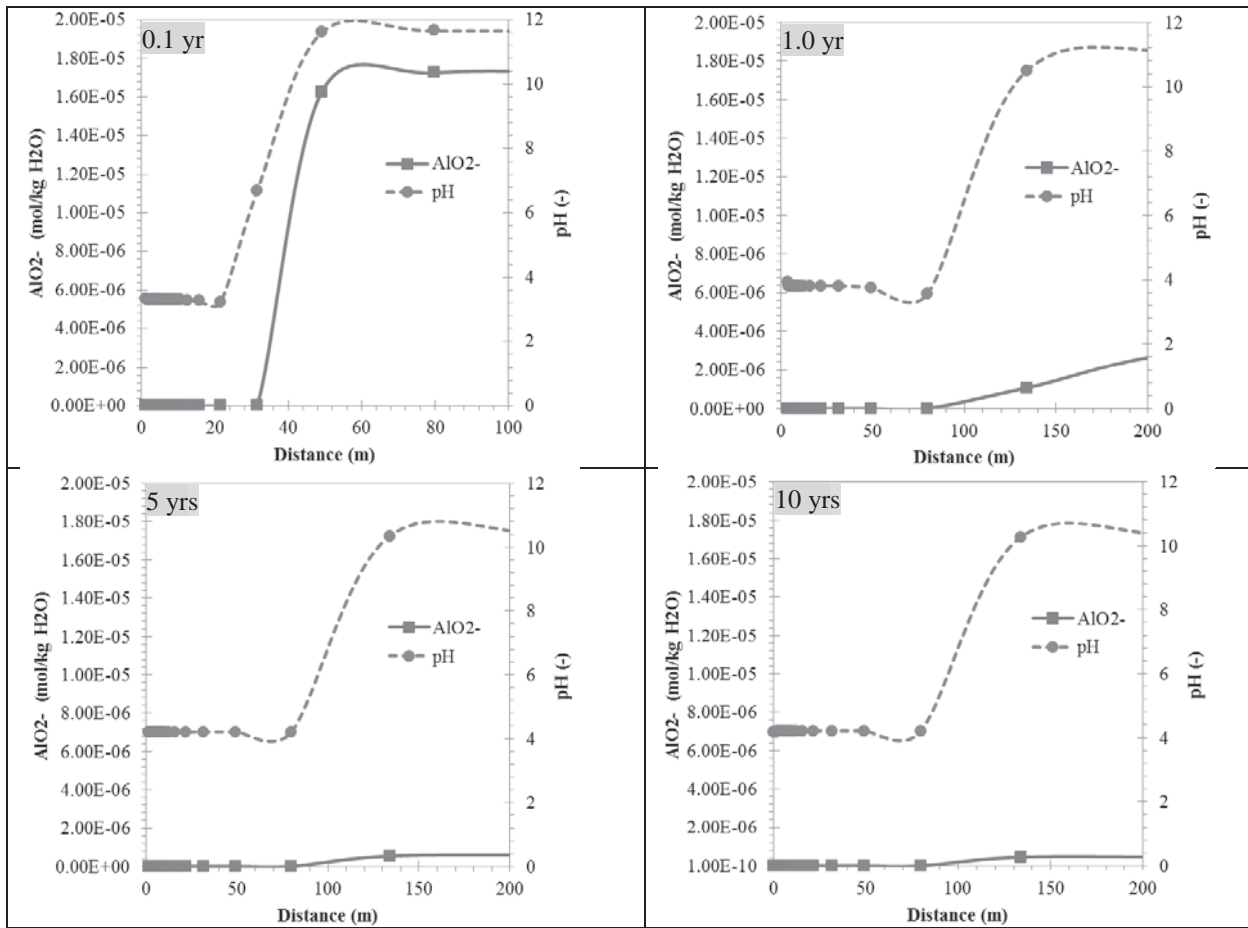
Fig. 6.27 AlO_2^- concentration changes with time along the flow path in Fm.LJG sandstone reservoir
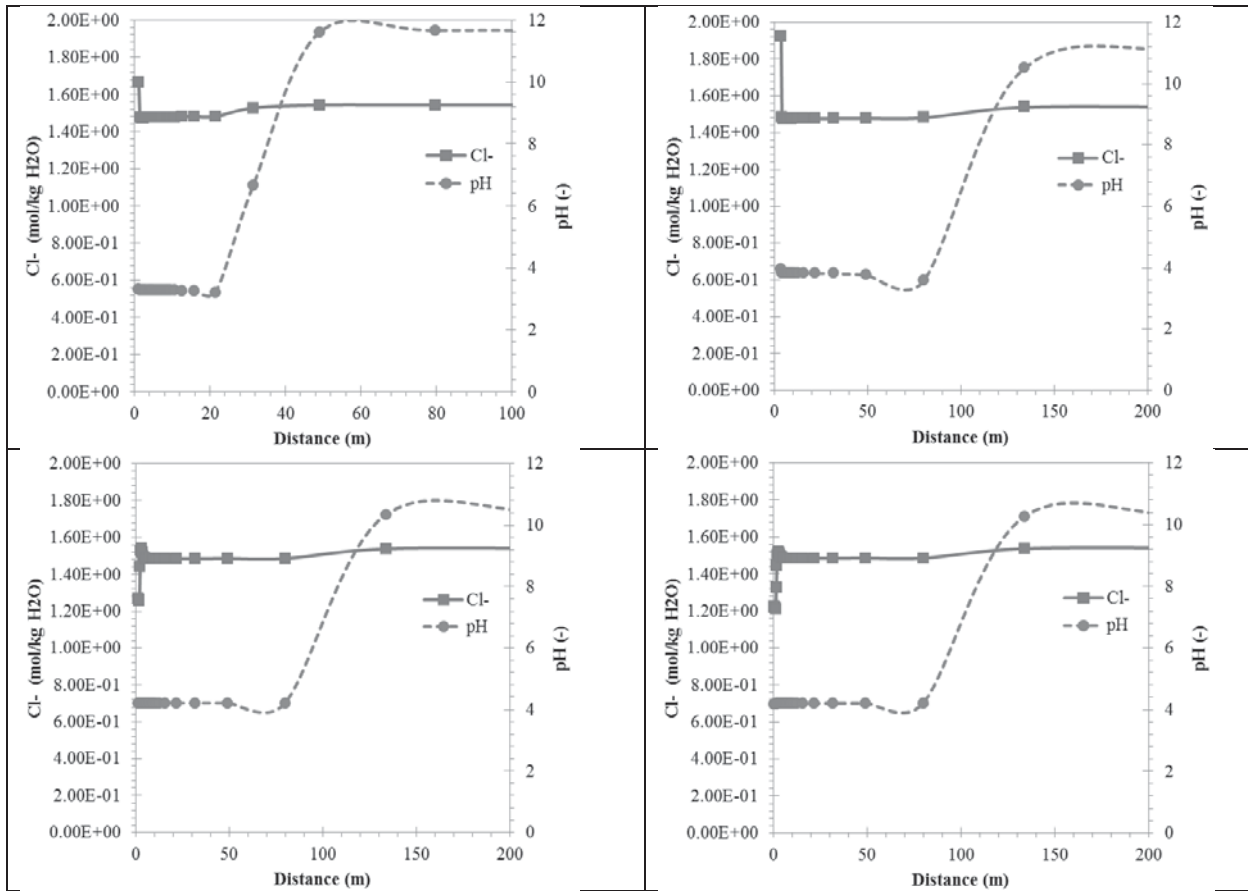
Fig. 6.28 Cl^- concentration changes with time along the flow path in Fm.LJG sandstone reservoir

167

6.5.2.3 Mineral volume fraction changes with time

In this 1D simulation model, varied dissolution and precipitation characteristics can be shown with respect to different minerals. For example, feldspar minerals (e.g. oligoclase and K-feldspars) and carbonates may dissolve, while quartz may show a typical precipitation state based on the initial water composition of the reservoir. In acidic aqueous environment, feldspar minerals can be dissolved to some extent, leading to the formation of secondary pores (Rosenbauer et al., 2005).

Fig. 6.29 depicts the temporal and spatial distribution of feldspar minerals. It shows clearly that without the perturbation of injected CO_2, all the feldspar minerals present a precipitation state. The reactive transport of CO_2 plays a significant role in the re-distribution of the minerals along the flow path (Johnson et al., 2001; Xu and Li, 2013), with an enlarged impact zone during CO_2 injection. The dissolution zones of oligoclase and K-feldspar increase with time and the reaction extent strengthens greatly. The albite precipitation characteristics show an inversed trend compared with other feldspar minerals.

Fig. 6.30 demonstrates the spatial distribution of quartz which is initially at a state of dissolution. Injection of CO_2 will lead to further contribution of SiO_2 aqueous species into the aquifer caused by the dissolution of other silicate minerals, such as K-feldspar, oligoclase, kaolinite, illite etc, present in the reservoir.

Fig. 6.31 illustrates that precipitation of carbonate minerals will occur due to the CO_2-water-rock interaction. Note that there is no calcite, smectite and dawsonite before CO_2 injection. The occurance of carbonate minerals in the reservoir demonstrates a sequential property, calcite and smectite-Ca first, then dawsonite. It should be mentioned that the precipitation rates of these minerals are also different. Initially, calcite occupies a large portion of the precipitates (Fig. 6.31A), about two orders of magnitude higher than smectite-Ca. In the long run, however, smectite-Ca will gradually dominate the precipitation process until after 5 years when dawsonite takes over (Fig. 6.31B to D).
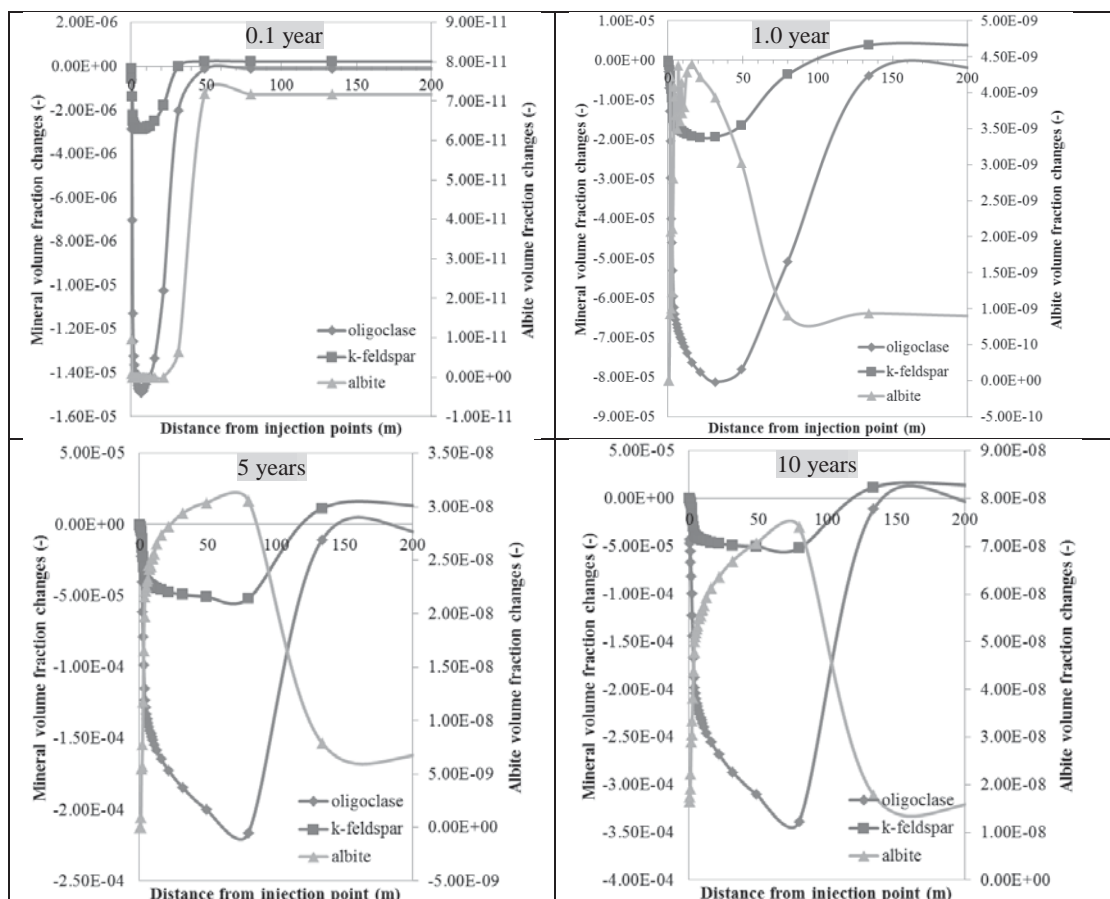
Fig. 6.29 Feldspar minerals volume fraction changes along the flow path at different time for Fm.LJG sandstone reservoir

168
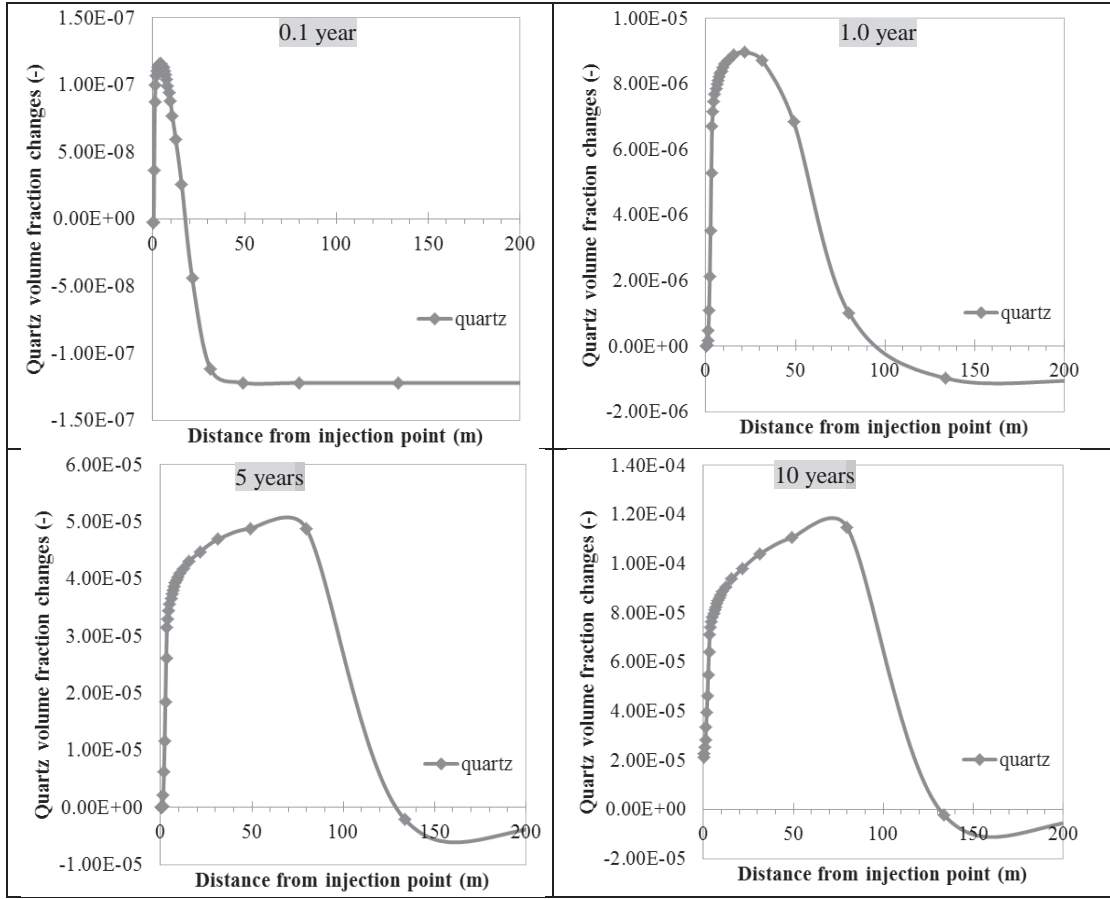
Fig. 6.30 Quartz volume fraction changes along the flow path at different time for Fm.LJG sandstone reservoir
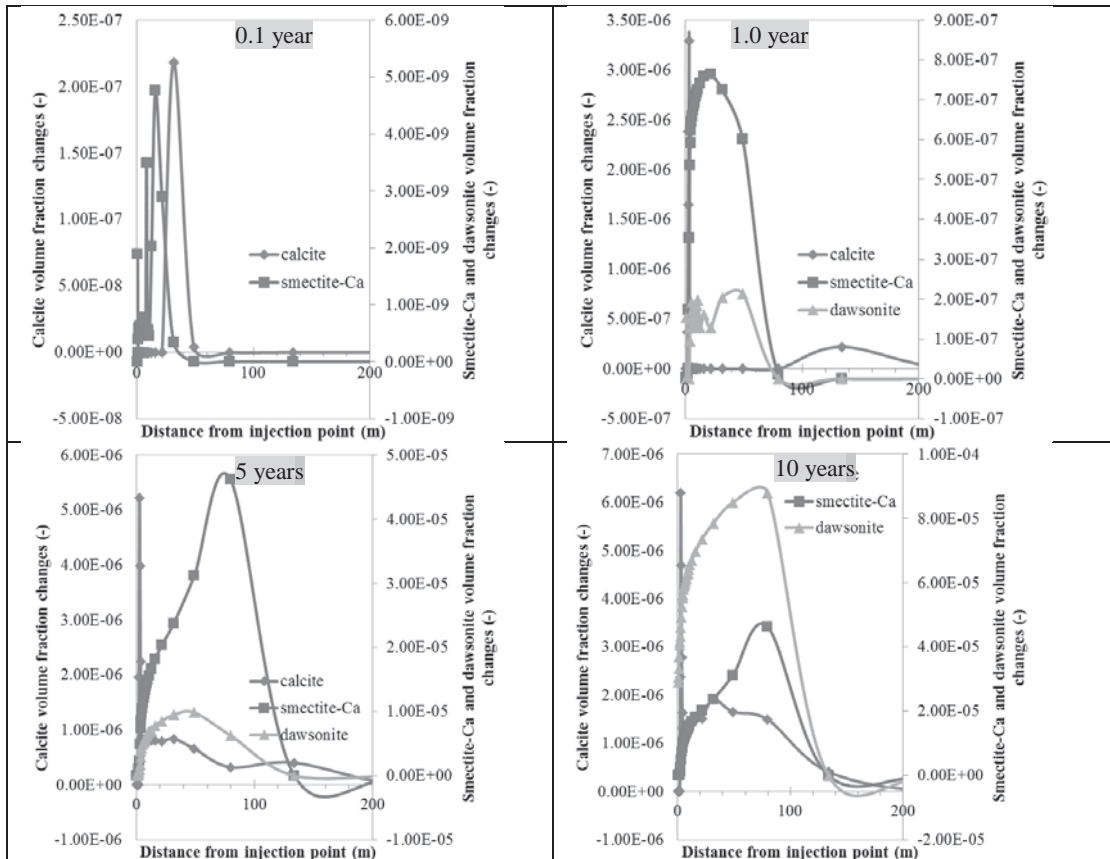
Fig. 6.31 Volume fraction changes with time in carbonate minerals along the flow path in the Fm.LJG sandstone reservoir

169

Both illite and kaolinite show strong precipitation characteristics due to CO_2 injection (Fig. 6.32). By comparison of results of the mineral volume fraction changes and aqueous species variation with time (Fig. 6.23, Fig. 6.29, Fig. 6.31, Fig. 6.32), for instance, for Na^+ and the minerals which can contribute Na^+ to the formation water (e.g. oligoclase, dawsonite, smectite, low-albite), it can be observed that after about 9 years since injection stopped, the Na^+ concentration reached an equilibrium state (i.e. at almost the same level as its initial value, 0.56 mol/kg H_2O). However, a relative higher ion concentration lies at the periphery of the wellbore (about 0.58 mol/kg H_2O). The dissolution of oligoclase can release Na^+ into the brine, while the deposition of illite and smectite-Ca will consume Na^+ from the brine. Dissolution effect is a little more intensive than precipitation with respect to Na^+ cation. Nevertheless, chemical deposition and dissolution reactions may show complex characteristics with respect to different aqueous species.
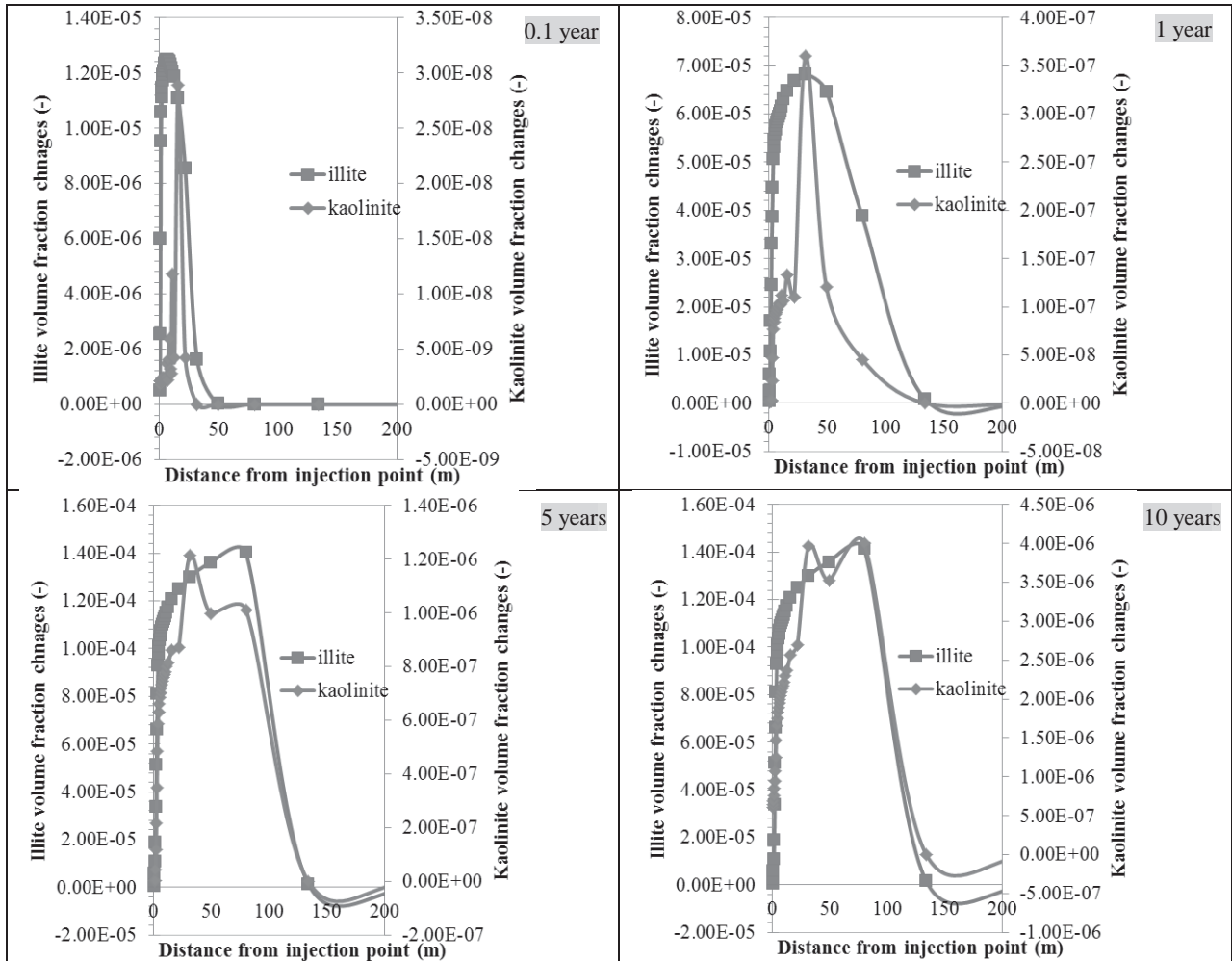
Fig. 6.32 Volume fraction changes with time for clay minerals along the flow path in the Fm.LJG sandstone reservoir

6.5.2.4 Porosity and permeability changes with time

The porosity and permeability of the reservoir will be changed due to CO_2 injection (Fig. 6.33). During the injection process, porosity and permeability are improved somewhat. However, at the 10 year time point since CO_2 injection, the evolution trends in porosity and permeability are reversed, progressively becoming smaller than the initial values toward the injection point. At the periphery of the injection well, less than 10 m from the borehole, a minimum reservoir property will be attained, which is partly the reason for the scaling effect. Away from the borehole, a transition zone indicates a strong CO_2-

170

water-rock interaction process. In the non-reactive zone, however, the reservoir properties will not be changed.
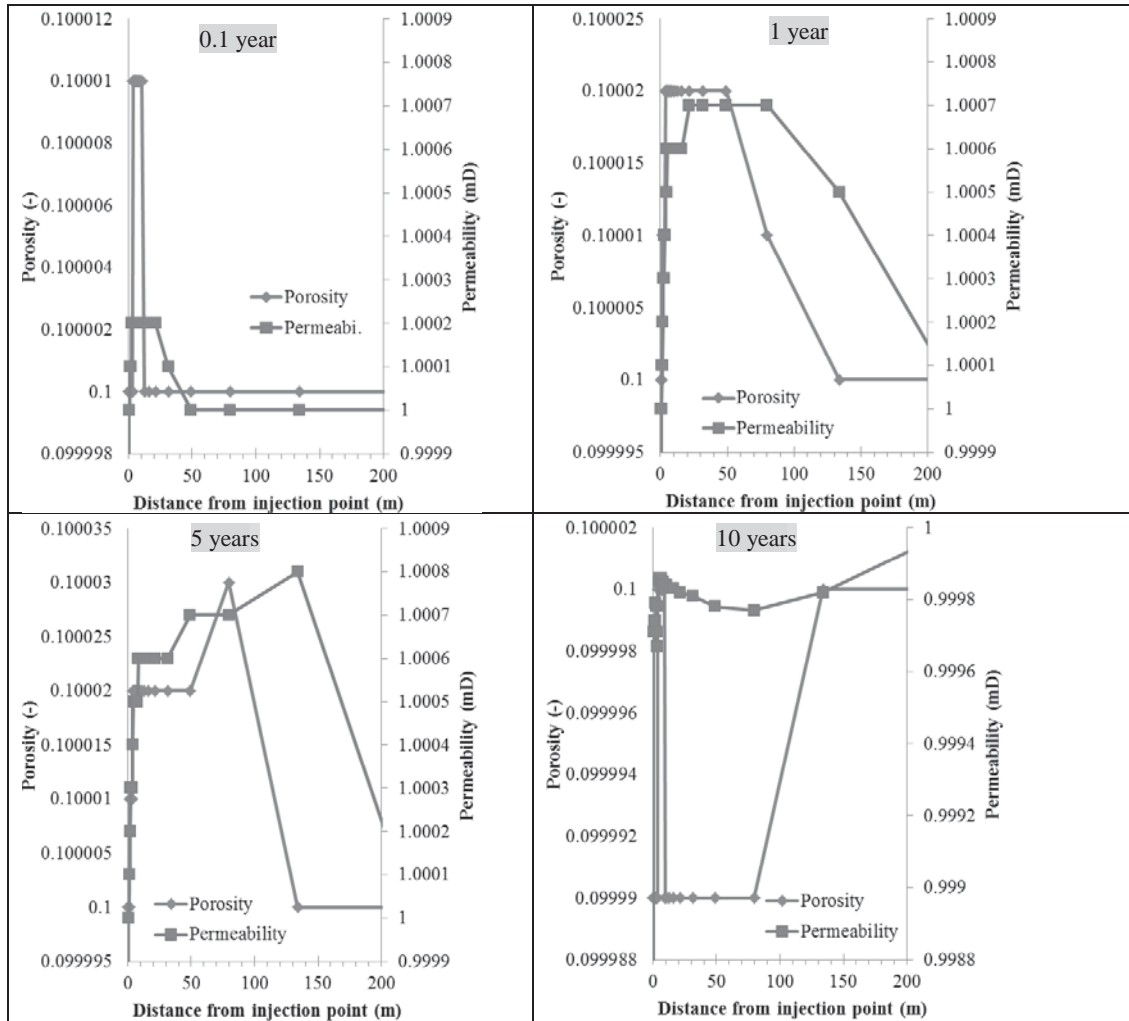
Fig. 6.33 Porosity and permeability changes along the flow path at different time frames in the Fm.LJG sandstone reservoir

6.5.2.5 Scaling effect in the near-well region

The near-well region, especially close to the wellbore, will be strongly affected by the CO_2 injection operation (Xu and Pruess, 2004b). During the supercritical CO_2 injection phase, mineral scales could form and lead to the decrease of injectivity. Scaling is a serious adverse effect in many petroleum and geothermal production wells. Scale deposits have a very large negative effect on reservoir porosity, permeability, injectivity, safety and heat transfer characteristics (Williams et al., 1999; Liu et al., 2013). Scaling problems caused by CO_2-water-rock interaction have been reported for many projects, such as Nag-67 of Tiwi field and wells in Hot Dry Rock research of the Soultz project (Charleston, 1968; Carrel, 1987; Hardy et al., 1992; Xu et al., 2004a, 2004b; Garcia et al., 2006; Taheri et al., 2011).

Fig. 6.34 depicts the gas and liquid saturation changes with time, 0.15 m away from the wellbore. During the displacement process, CO_2 begins to dominate in the fluid flow after about 12 hours since injection begins. After 5 days, the pore space at the periphery of well is totally saturated with the CO_2 phase. The imbibition process takes a long time before water reaches and dominates the pore space around the well, about 6.24 days. From this displacement-imbibition cycle, we can conclude that the CO_2 phase zone around the well will to some extent hinder the water fluid flow towards the well.
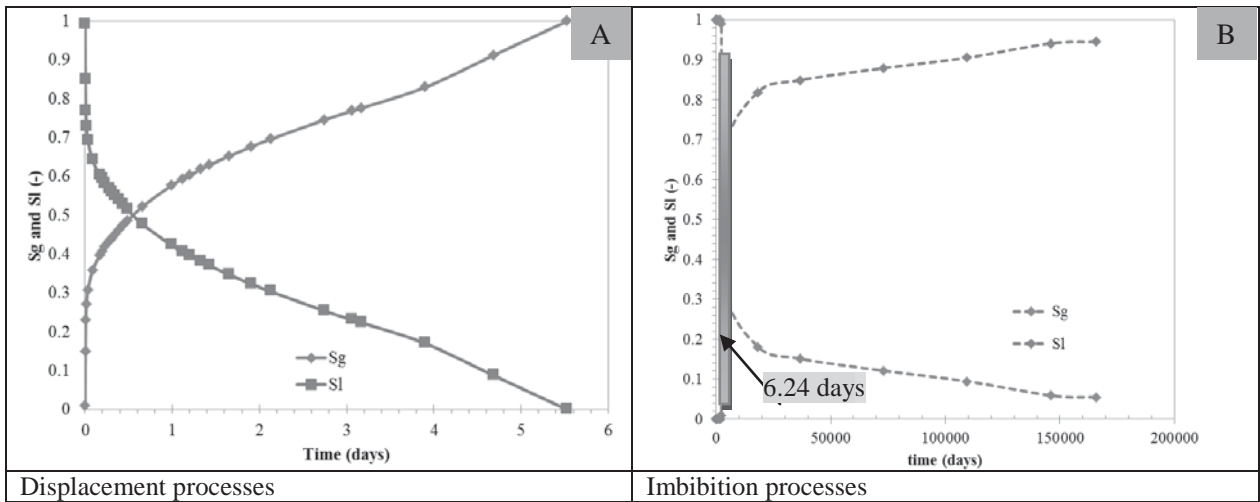
Fig. 6.34 Gas and liquid saturation changes with time caused by CO_2 injection in the near-well region (x=0.15 m)

In Figs. 6.35 to 6.37, evolution of the concentrations of the main aqueous species (including H^+ (pH), Mg^{2+}, K^+, Na^+, Ca^{2+}, SiO_2, HCO_3^-, AlO_2^-, SO_4^{2-}, Cl^-) at a fixed point in the reservoir, 0.15 m away from the injection wellbore, are shown. The pH and CO_2 partial pressure curves instantly evolve in inverse directions at the onset of the CO_2 injection and will each stay constant during the first few days of injection (Fig. 6.35A). The concentration of other species, including cations and anions, evolve differently at the fixed point in response to CO_2 injection. The equilibrium concentrations for Na^+ and Ca^{2+}, for example, during the displacement process, are about 1.3 and 1.7 mol/kg H_2O, respectively, while their respective equilibrium concentrations attained during imbibition process are about 1.7 and 0 mol/kg H_2O, illustrating the dissolution of Na bearing minerals and the precipitation of Ca-bearing minerals at the monitoring point in the long term. The CO_2-water-rock interactions present more intensive reactions during imbibition processes.
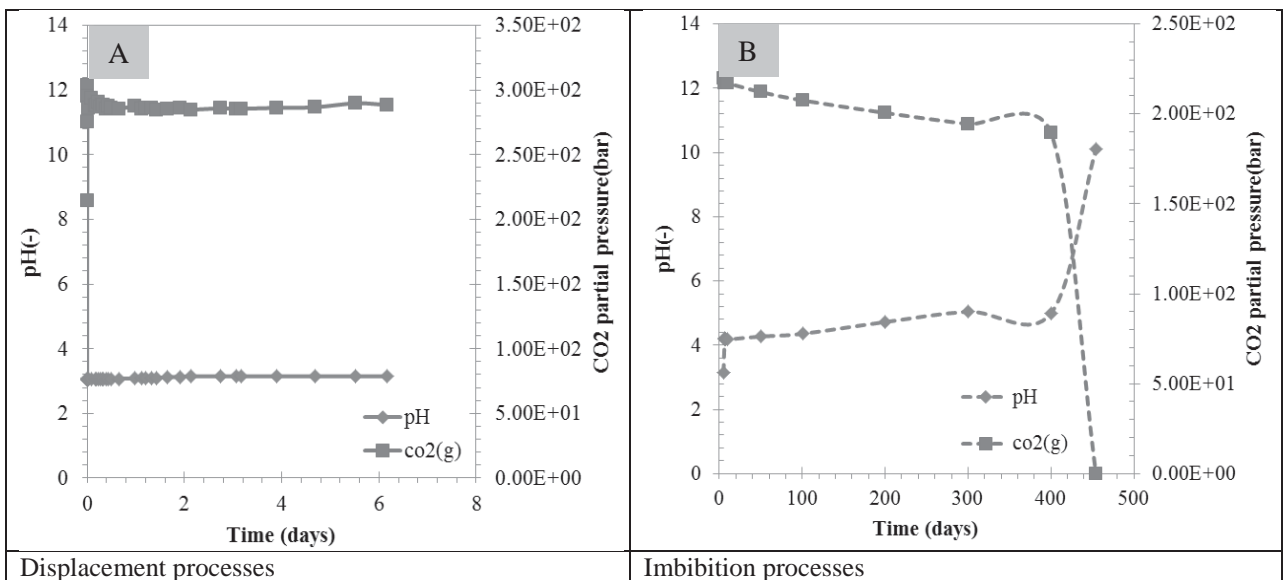
Fig. 6.35 pH changes with time caused by CO_2 injection(x=0.15m)
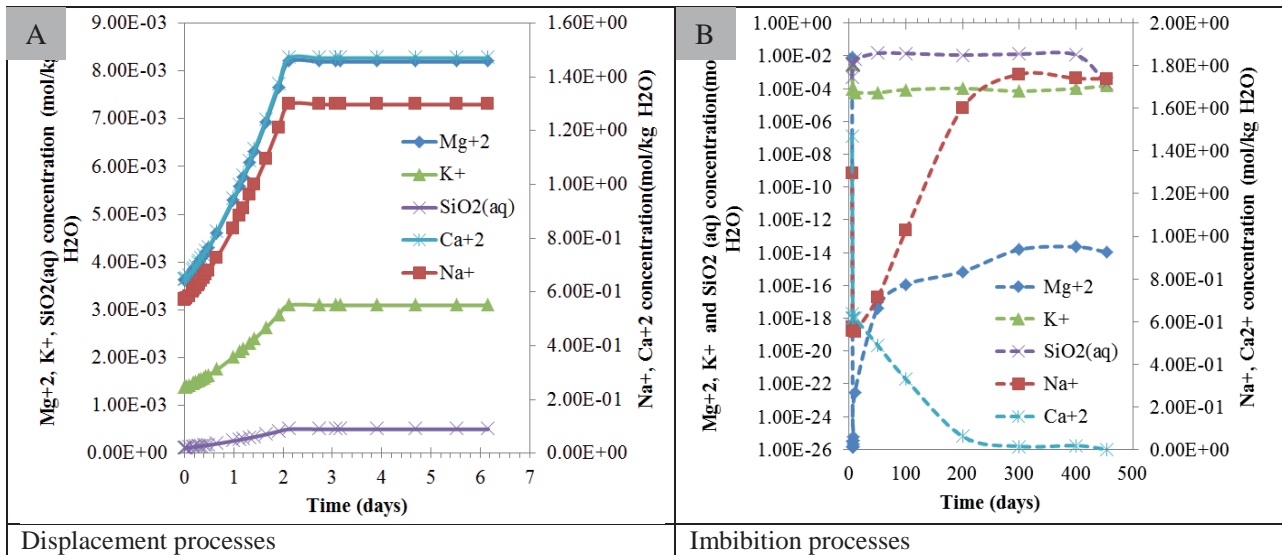
Fig. 6.36 Changes in concentration of major cations with time due to CO_2 injection(x=0.15 m)
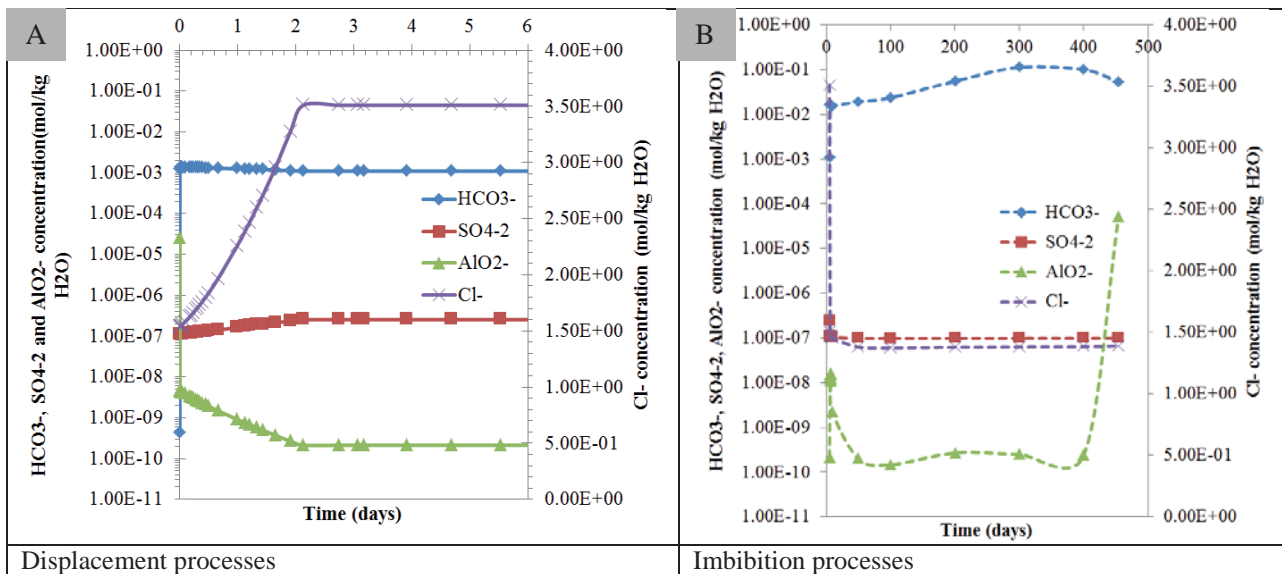
Fig. 6.37 Changes in concentration of major cations with time due to CO_2 injection (x=0.15 m)

In this simulation, minerals can be grouped into four classes based on their characteristic reactions: feldspar minerals, quartz, carbonate minerals and clay minerals (Figs. 6.38 to 6.41).The volume fractions of these minerals are mainly influenced by pH, but it will lag behind the pH variation. Based on the developments in the displacement stage, the CO_2-water-rock interaction can be divided into two sub-stages: CO_2 displaces water stage and water imbibitions stage. It shows that huge diversity occurs.

During displacement process, oligoclase and K-feldspar dissolve at a fast dissolution rate in the first 2 days of injection, before attaining an equilibrium state, while albite shows an inverse trend of variation. Like oligoclase and K-feldspar, quartz mineral dissolves in the first two days, before attaining an equilibrium state. As for the carbonate minerals, only a small amount of dawsonite precipitates, while other carbonate minerals, for instance, dolomite, ankerite, siderite, magnesite do not occur. Due to CO_2 injection, most clay minerals show depositional trends.

A time frame from 5 to 500 days has been chosen to show the results of imbibition processes. The dissolution of some minerals will supply the relevant cations for the precipitation of new minerals (Xu and Li, 2013). In comparison with the displacement process, the dissolution of oligoclase increases to about 5 orders magnitude during imbibition. K-feldspar and quartz minerals transform to precipitation

173

states during imbibition. Calcite appears for the first time in the system and its volumetric amount increases with time. Both kaolinite and illite undergo a transitional phase, the former from dissolution to precipitation state, while the latter transforms from precipitation to dissolution state.

From the figures for mineral volume fraction changes with time it can be concluded that any point in space is at a dynamic changeable state with respect to each mineral. Precipitation or dissolution state of a mineral is determined by the saturation index of the corresponding ions constituting that mineral in the aqueous phase (Edmunds et al., 1982).
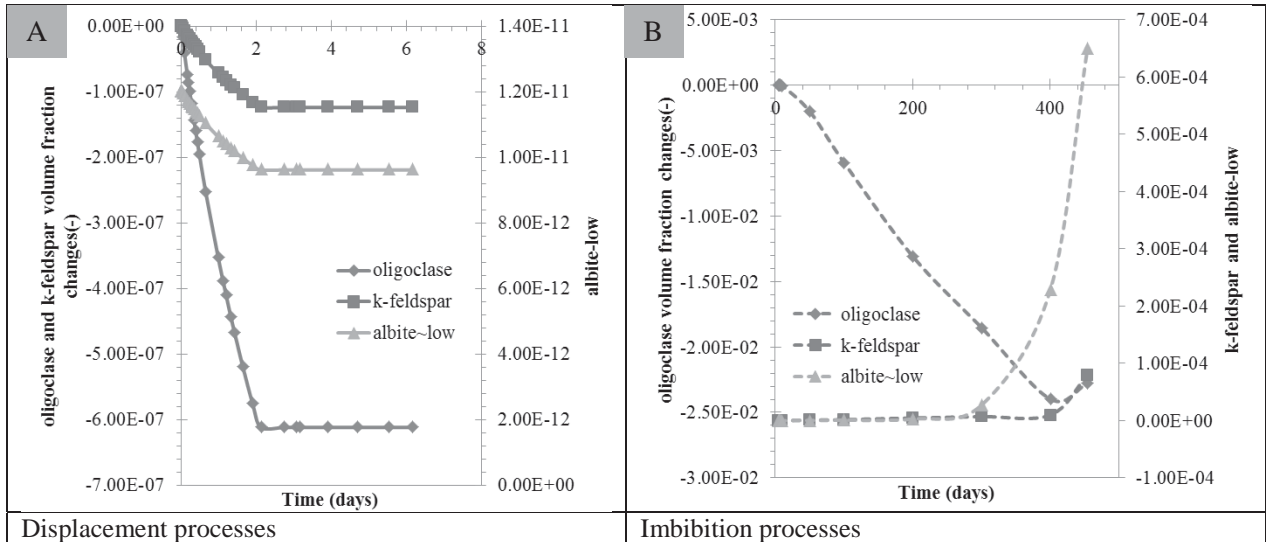
Fig. 6.38 Volume fraction changes of feldspar minerals with time in the near well region(x=0.15 m)
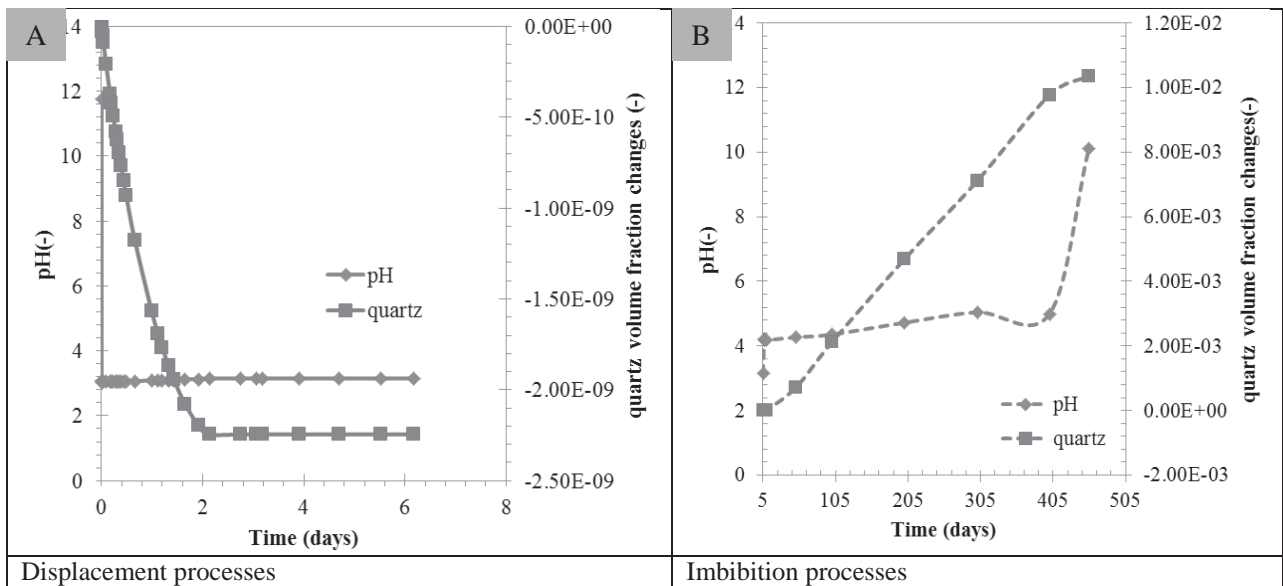
Fig. 6.39 Volume fraction changes of quartz with time in the near well region (x=0.15m)

174
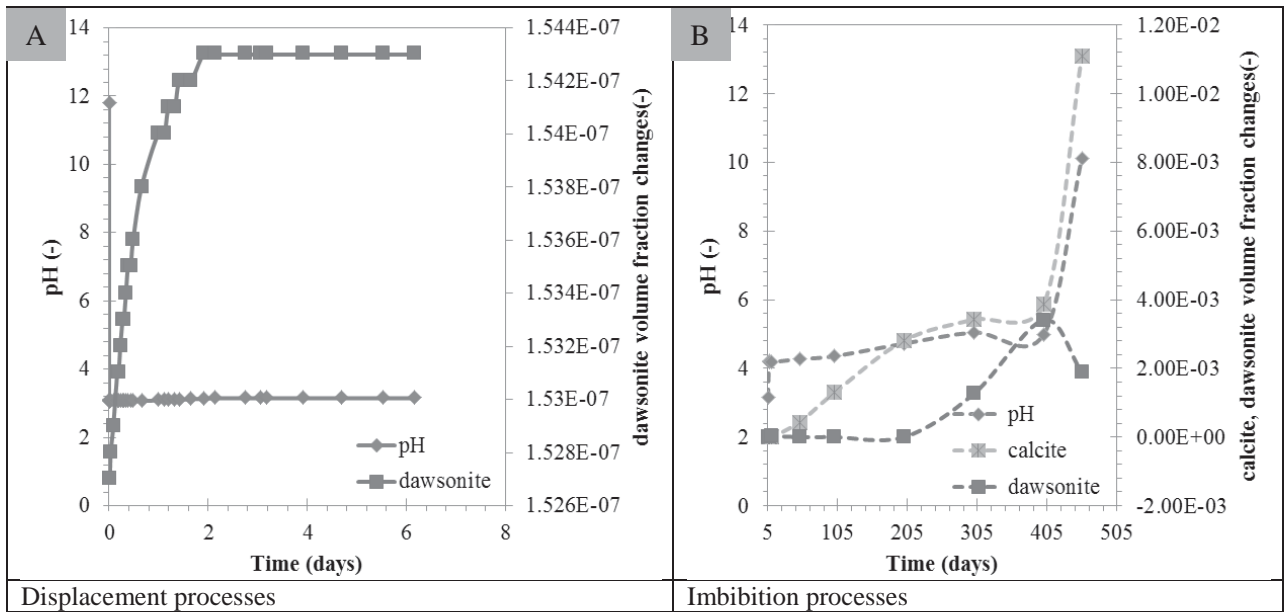
Fig. 6.40 Volume fraction changes of carbonate minerals with time in the near well region (x=0.15 m)
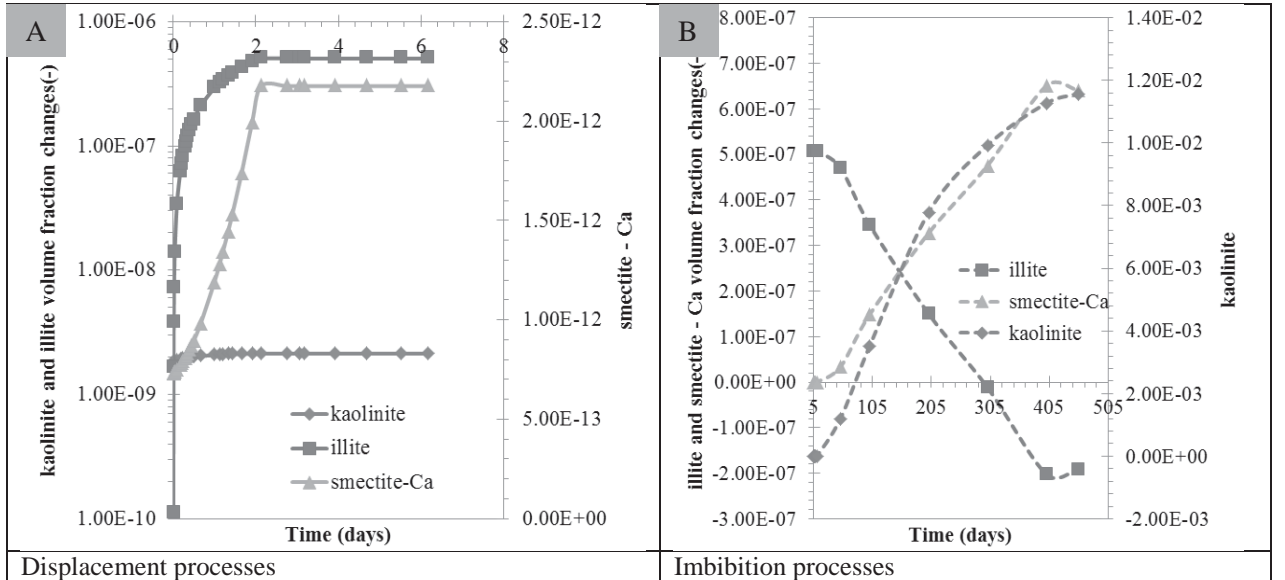
Fig. 6.41 Volume fraction changes of clay minerals with time in the near well region (x=0.15 m)

6.5.3 2D simulations for a sandstone reservoir representative of the four aquifer formations

In contrast to a 1D model, a 2D model offers a broader intuitive spatial distribution view. Therefore, a 2D model is set up to show how hydrogeological parameters and geochemical properties, such as porosity, permeability, ion concentration, pH and mineral volume fraction, spatially and temporally change as a result of CO_2-water-rock interactions triggered by injected CO_2.

The geometry of the 2D model is similar with that of 1D model (Fig. 6.42). However, the model size is significantly extended, from 1 to 10 km. The number of lateral grids is also increased to 50. In the vertical direction, a 10-layer structure, each layer with a thickness of 10 m is set up.

175
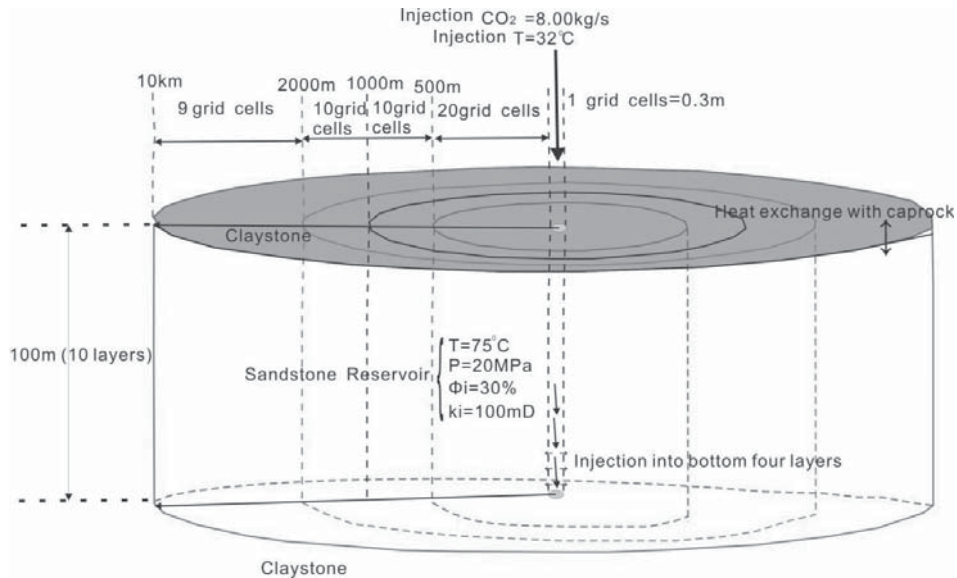
Fig. 6.42 Schematic representation of a geological model used in 2D simulation

Table 6.10 lists the detailed parameters assigned to the 2D simulation model. Porosity and permeability of the reservoir are assumed to be 30% and 100 mD, respectively. Based on the measured data of water samples from LJG, SQF, SHZ and SX formations, the average initial water composition used in the 2D model is listed in Table 6.11. The boundary conditions are also set to be closed as in the 1D model. Initial pore pressure is assumed to be hydrostatic pressure. The CO_2 injection period lasts 10 years at a rate of 8 kg/s for all the four bottom layers, which is equivalent to a commercial scale CO_2 sequestration project with a total amount of 10 M tonnes.

Table 6.10 Formation and injection parameters including initial and boundary reservoir conditions assigned to the 2D simulation model

Parameter	Value
Formation parameters	
Radial extension of the model	10 km
Thickness	H=100 meters
porosity	ϕ=0.30
permeability	k=100 mD; $k_v = k_h$
Rock grain density	ρ = 2450 kg/m^3
Rock specific heat	1000 J/kg/^{o}C
Thermal conductivity	2.1 W/m/^{o}C
Compressibility	4.5×10^{-10} Pa^{-1}
Formation initial conditions	
Fluid type in pore spaces	H_2O
Temperature	75 ^{o}C
Pressure	Hydrostatic pressure
salinity	88.69 g/L
Formation boundary conditions	
Top/sides	No fluid or heat flow (closed)
Bottom	No fluid or heat flow (closed)
Injection parameters	
Injection rate	8.0 kg/s
CO_2 injection enthalpy	5.08×10^6 J/kg

Table 6.11 Average mineral and water compositions used in the 2D simulation model

Minerals	Chemical formula	Average volume fraction (%)	Chemical aqueous components	Concentration (moles/kg H_2O)
Quartz	SiO_2	55	Ca^{2+}	6.54×10^{-1}
Hematite	Fe_2O_3	0	Mg^{2+}	3.66×10^{-3}
Oligoclase	$Na_{1-x}Ca_xAl_{1+x}Si_{3-x}O_8$	15	Na^+	5.77×10^{-1}
Low-albite	$NaAlSi_3O_8$	0	K^+	1.40×10^{-3}
K-feldspar	$KAlSi_3O_8$	12	Fe^{2+}	1.96×10^{-25}
Smectite-Ca/Na	$E_x(H_2O)_4\{(Al_{2-x},Mg_x)_2 [(Si, Al)_4O_{10}] (OH)_2\}$; E is $Na^+/Ca^{2+}/K^+/Li^+$	0	$SiO_{2(aq)}$	1.09×10^{-4}
Kaolinite	$Al_4Si_4O_{10} \cdot (OH)_8$	0	HCO_3^-	4.29×10^{-10}
Illite	$K_{0.75}(Al_{1.75}R)[Si_{3.5}Al_{0.5}O_{10}](OH)_2$	2	SO_4^{2-}	1.12×10^{-7}
Chlorite	$Y_3[Z_4O_{10}](OH)_2 \cdot Y_3(OH)_6$; Y is Mg/Fe/Al etc, Z is Si and Al	0	AlO_2^-	2.55×10^{-5}
Calcite	$CaCO_3$	0	Cl^-	1.56×10^0
Dolomite	$CaMg[CO_3]_2$	0	$O_{2(aq)}$	8.88×10^{-23}
Magnesite	$MgCO_3$	0	pH	9.5
Siderite	$FeCO_3$	0		
Ankerite	$Ca(Mg,Fe)(CO_3)_2$	0		
Dawsonite	$NaAlCO_3(OH)_2$	0		
Pyrite	FeS_2	0		

6.5.3.1 Gas saturation changes with time

Fig. 6.43 depicts the spatial distribution of CO_2 at different time points since CO_2 injection. It illustrates that CO_2 plume will propagate with time. Buoyancy plays a significant role in the migration processes of CO_2. At the beginning of injection, the plume appears like a long thin bud, close to the injection wellbore. During the injection the plume develops into a funnel shaped at its outer boundaries. After injection, as time goes by, the plume progressively shrinks back and migrates upward to the injection zone. After 1000 years, the residual CO_2 concentrates at the top of the reservoir within a lateral radial distance of 2000 m from the injection zone.
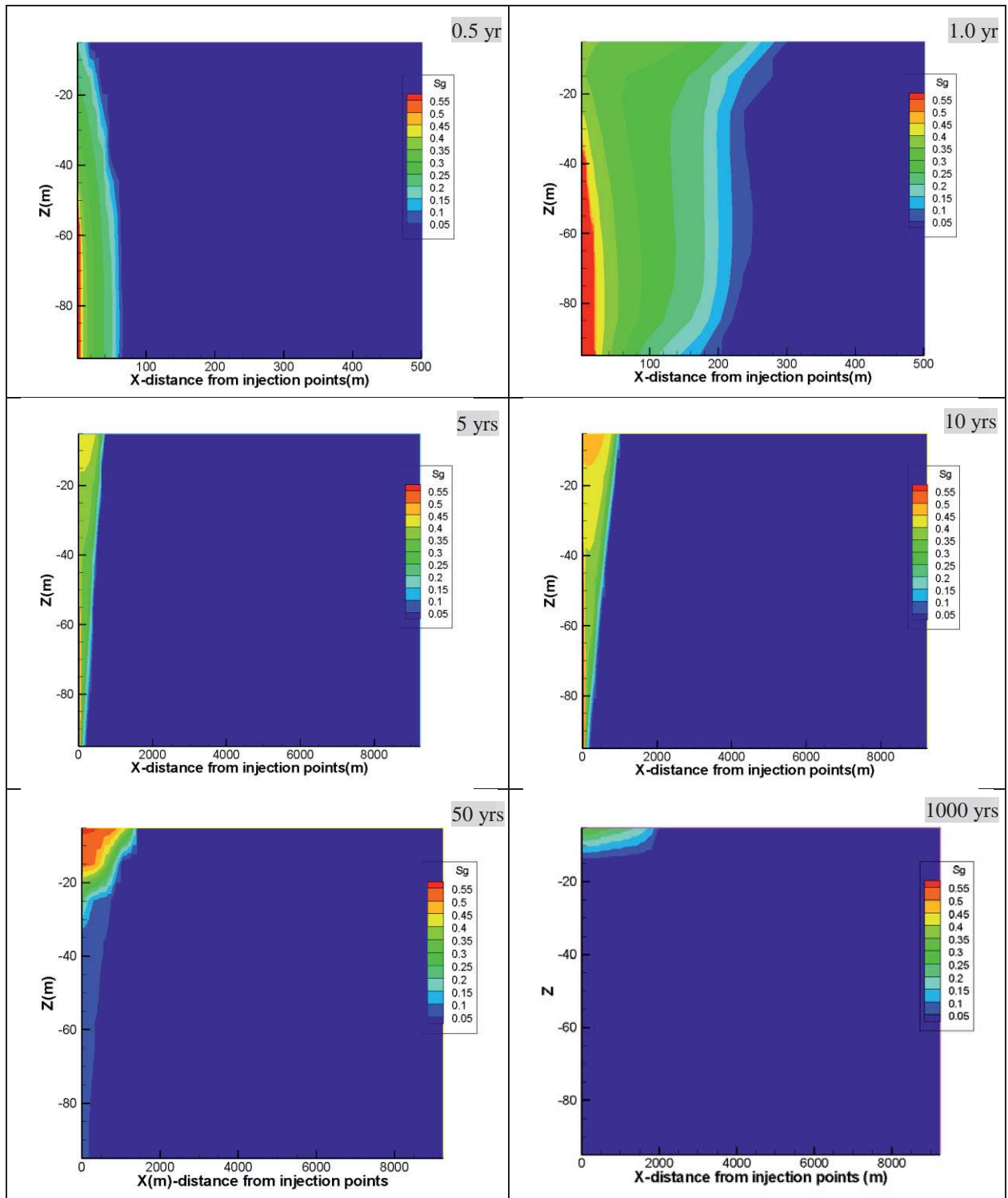
Fig. 6.43 Gas saturation changes with time in a sandstone reservoir (x-axis is exaggereted to show details)

6.5.3.2 Ion concentration changes with time

The changes of ion concentration have been described in detail in the 2D model. From Figs. 6.44 to 6.49, the spatial distribution of some aqueous species including H^+ (pH), Ca^{2+}, Mg^{2+}, HCO_3^-, AlO_2^- and Cl^- are presented with time. With the continuous injection of CO_2, the spreading zone extends outwards from the injection zone and ions concentration will be changed due to the CO_2-water-rock interactions. However, their variation extent and spatial distribution pattern show considerable diversity, depending on the rates of dissolution and precipitation of the relevant minerals (Xu and Li, 2013). Due to the dissolution of CO_2 in water, the chemical interactions are enhanced. The difference in density between CO_2 bearing water and initial formation water promotes the convective flow of fluid, especially at the

178

transition region between the CO_2 plume front and initial water zone. Ca^{2+} and Cl^- show similar variation trends in the first 50 years, while major divergence appears in the long-term (1000 years, see Figs. 6.45 and 6.49). In the long-term, some aqueous species may decrease to very low levels, like e.g. Mg^{2+} and AlO_2^- ions (Figs. 6.46 and 6.48).
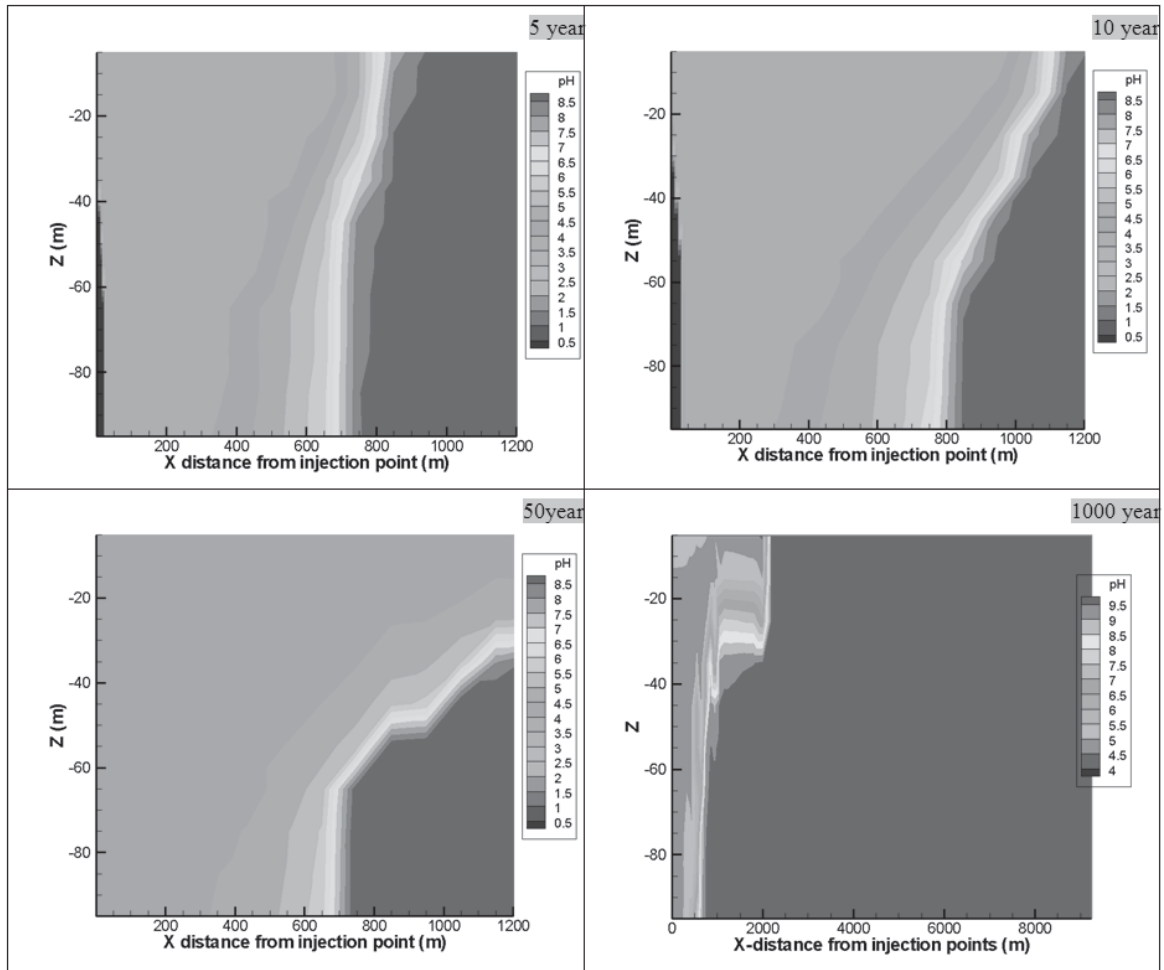
Fig. 6.44 Spatial and temporal evolution of pH in a sandstone reservoir
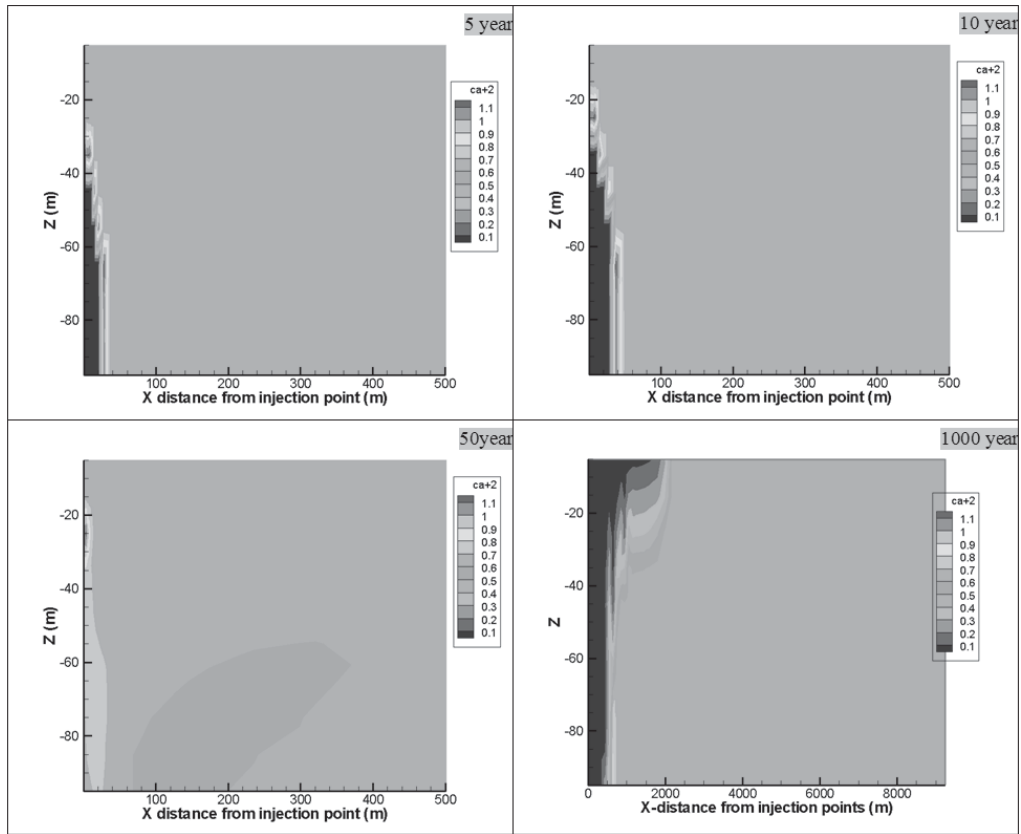
Fig. 6.45 Spatial and temporal evolution of Ca^{2+} concentration in a sandstone reservoir
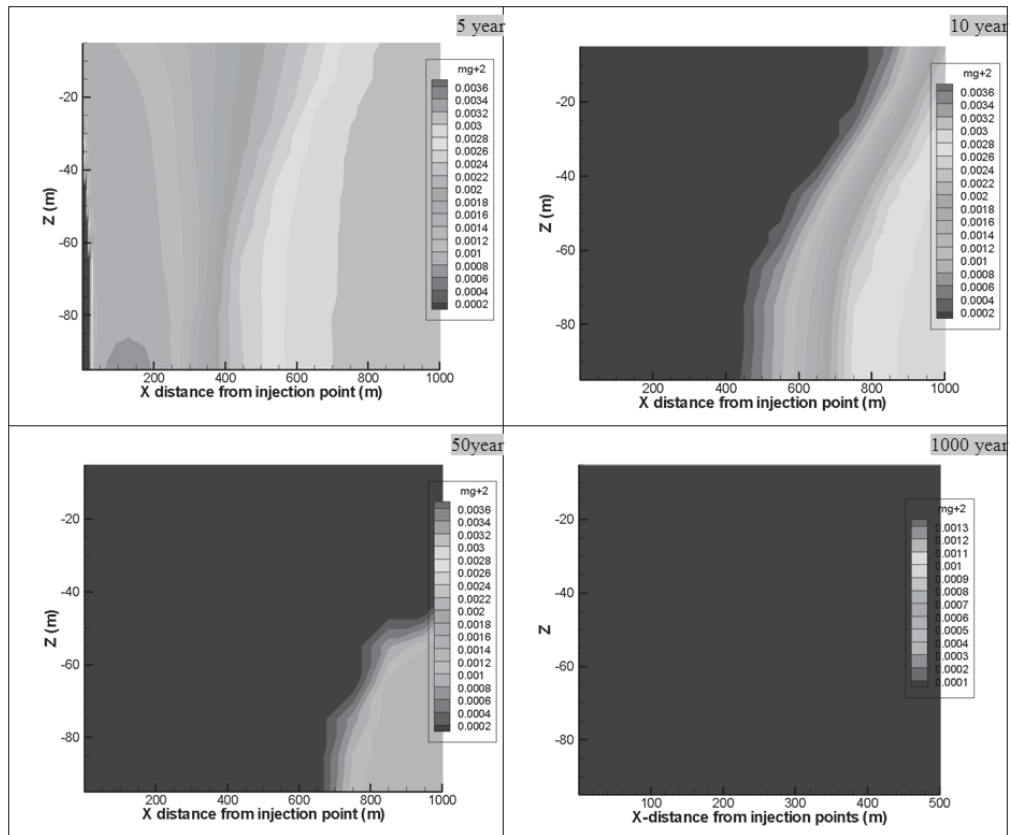
Fig. 6.46 Spatial and temporal evolution of Mg^{2+} concentration in a sandstone reservoir (x-axis is exaggerated to show details)
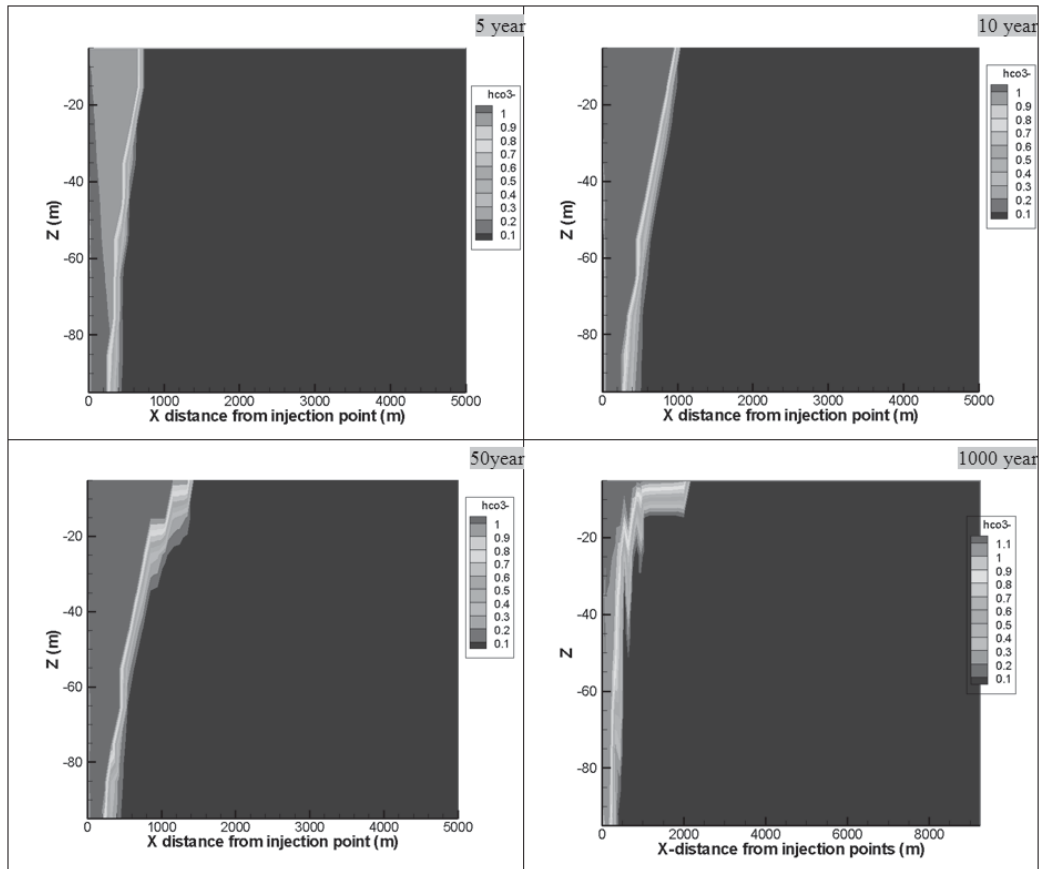
Fig. 6.47 Spatial and temporal evolution of HCO_3^- concentration in a sandstone reservoir (x-axis is exaggerated to show details)
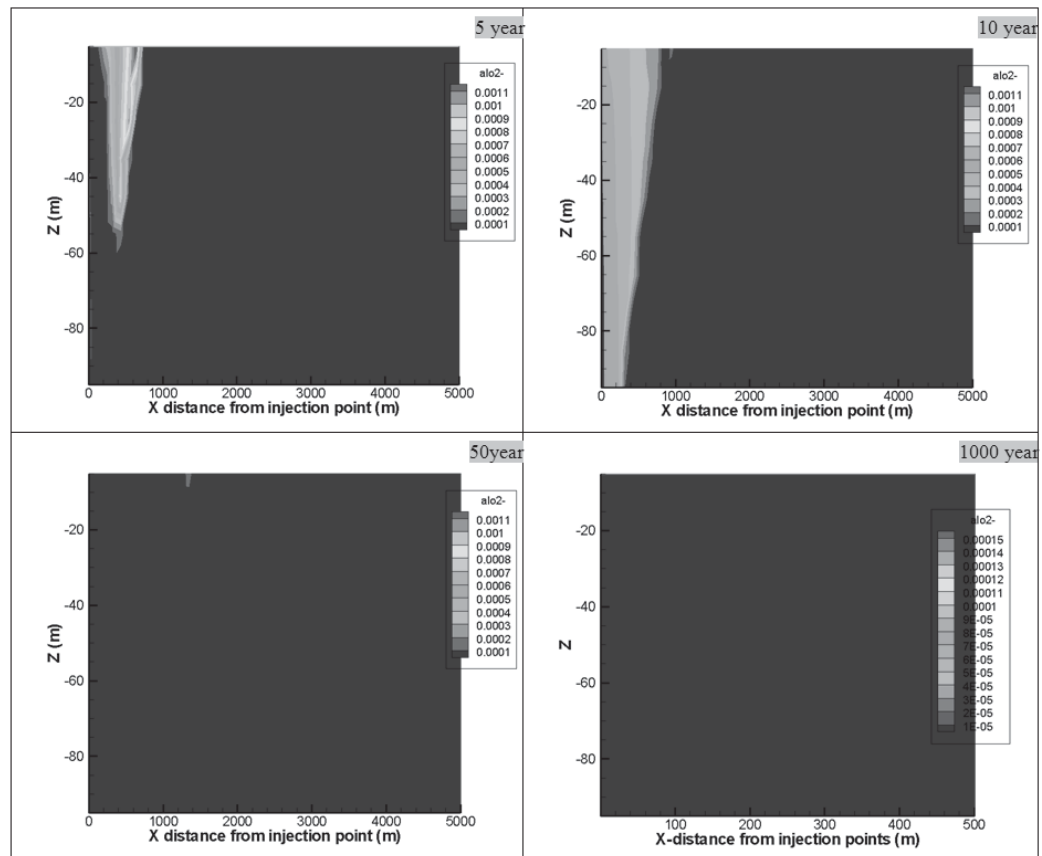
Fig. 6.48 Spatial and temporal evolution of AlO_2^- concentration in a sandstone reservoir

181
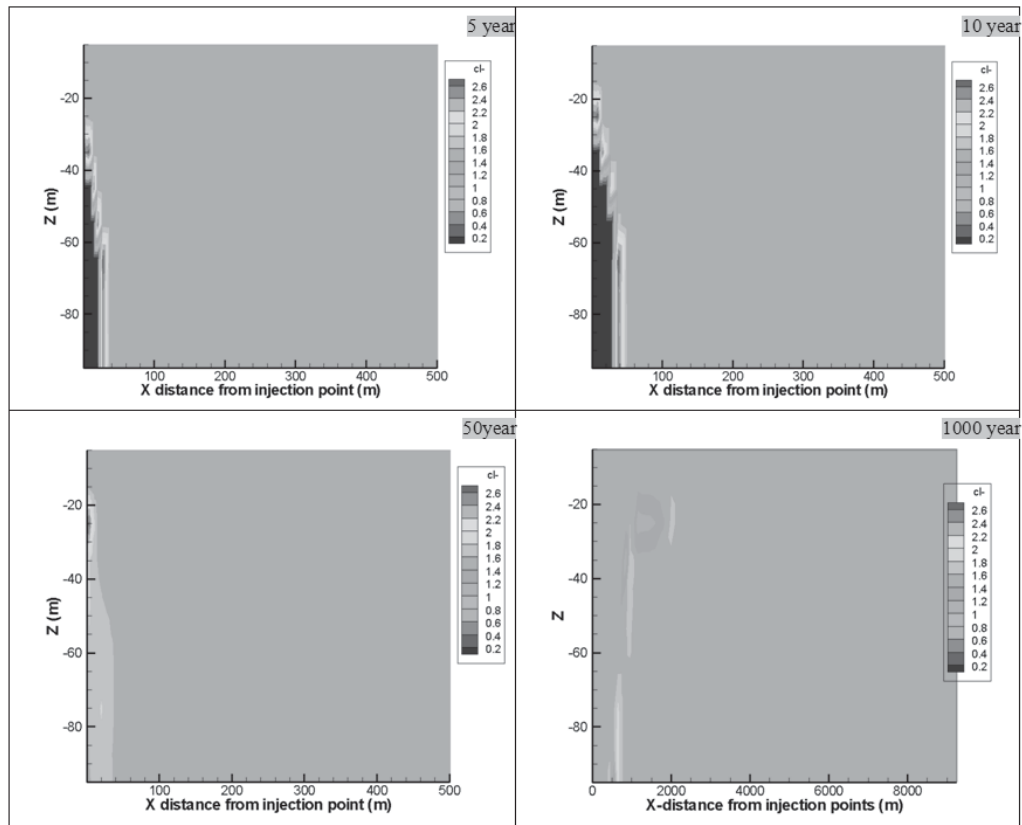
Fig. 6.49 Spatial and temporal evolution of Cl⁻ concentration in a sandstone reservoir (x-axis is exaggerated to show details)

6.5.3.3 Mineral volume fraction changes with time

It is common for all minerals that there is a narrow region existed around the near-well region for precipitation (positive values), and high concentration region for dissolution minerals (negative values) during CO_2 injection period. This is caused by the accumulation of a single CO_2 phase in the near-well region, which hinders the chemical reaction (From Figs. 6.50 to 6.58). Away from the near-well region, an active reaction region exists, illustrating the main transition zone between CO_2 migration fluid and initial water (Remoroza et al., 2012). The initial saturation states of minerals are different, for example, albite, quartz, calcite, illite, smectite-Ca, smectite-Na and kaolinite are at a precipitated state, while oligoclase and K-feldspar are at the dissolved state before CO_2 injection. In the long-term, oligoclase is further intensively dissolved in the near wellbore region (Fig. 6.50), while some K-feldspar may deposite after 1000 years (Fig. 6.51). The injected CO_2 also has a great impact on the re-distribution of low-albite. At the top of the reservoir, along the fluid flow direction, more precipitation of albite occurs (Fig. 6.52). Some illite dissolves in the aqueous phase (Fig. 6.55), especially in the near well region, while its precipitation takes place far away from the injection zone. Other clay minerals show precipitation characteristics, for instance, smectite-Ca, smectite-Na and kaolinite (Figs. 6.56 to 6.58).
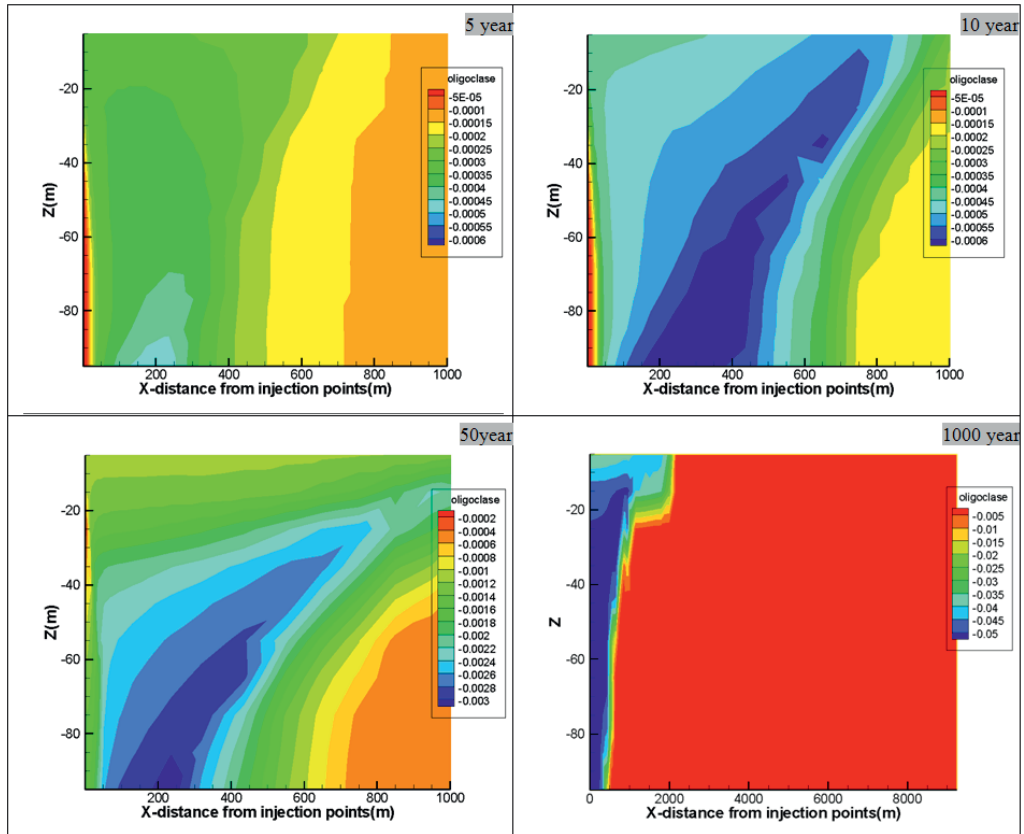
Fig. 6.50 Spatial and temporal evolution of volume fraction of oligoclase in a sandstone reservoir
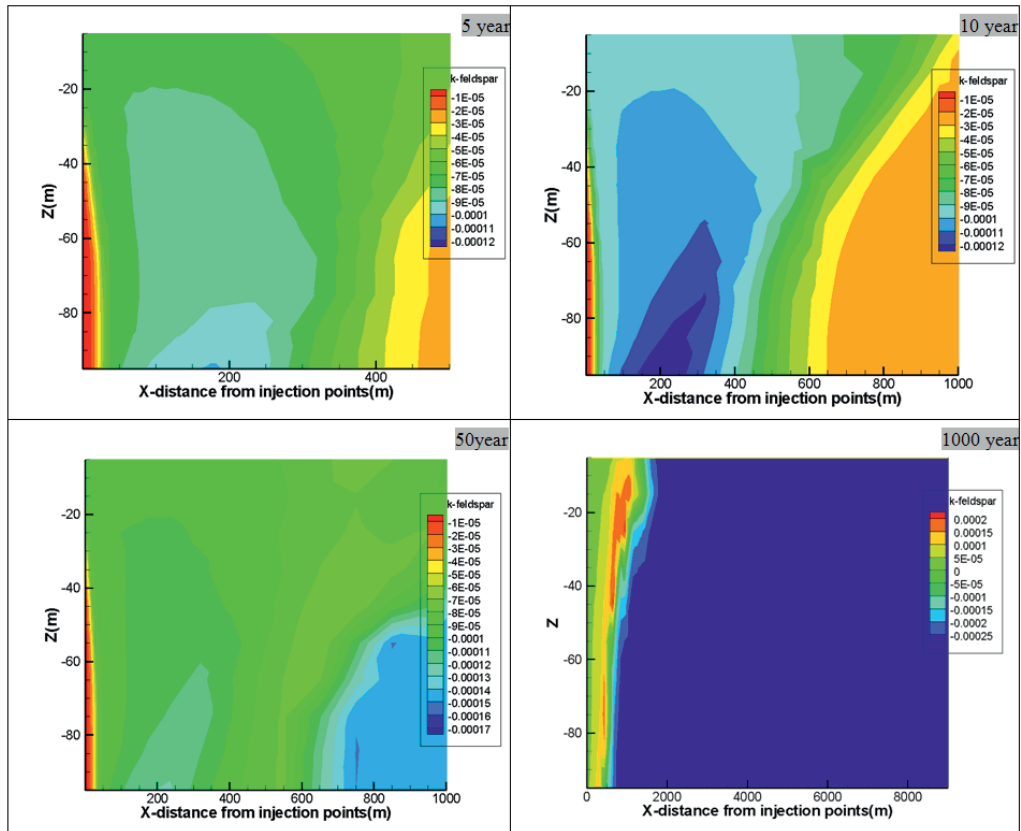
Fig. 6.51 Spatial and temporal evolution of volume fraction of K-feldspar in a sandstone reservoir
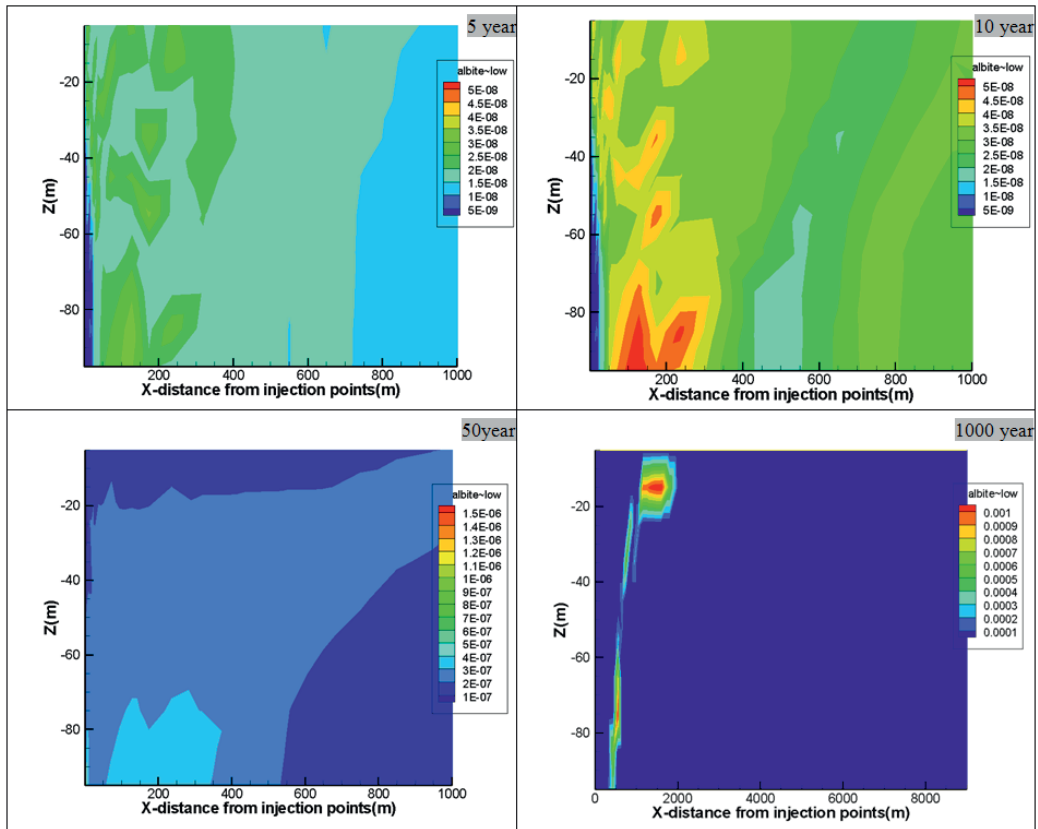
Fig. 6.52 Spatial and temporal evolution of volume fraction of low-albite in a sandstone reservoir
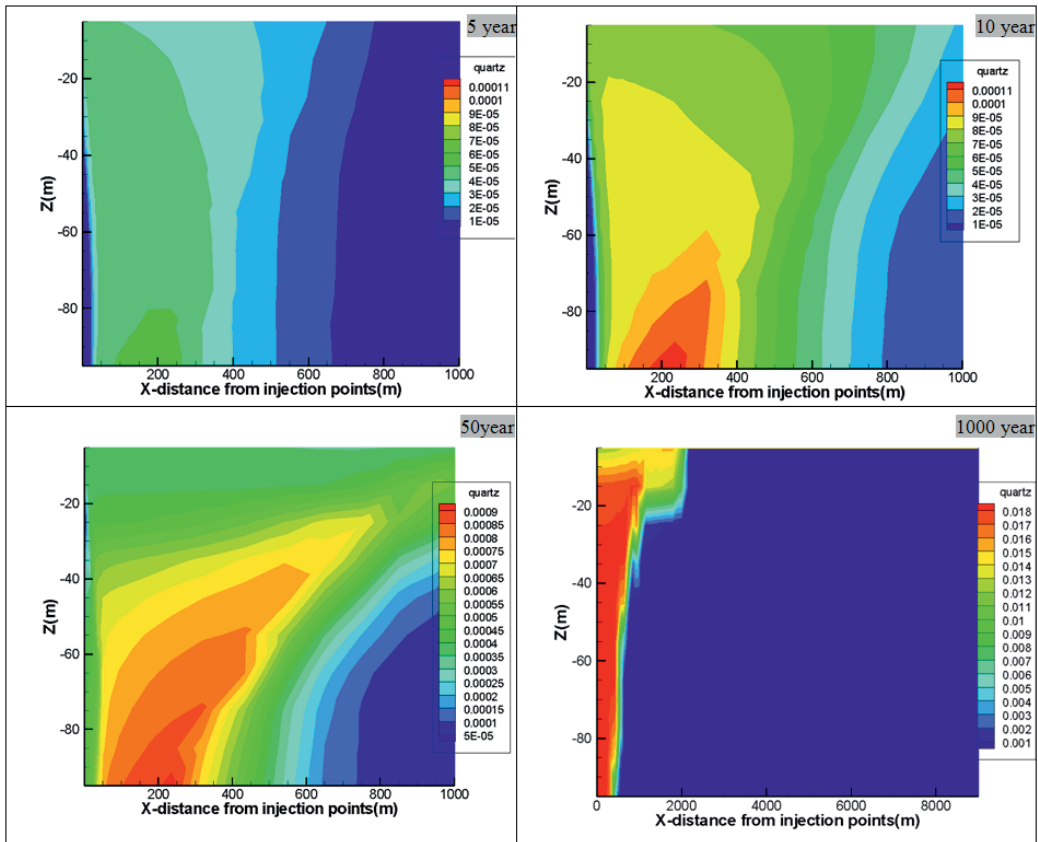
Fig. 6.53 Spatial and temporal evolution of volume fraction of quartz in a sandstone reservoir
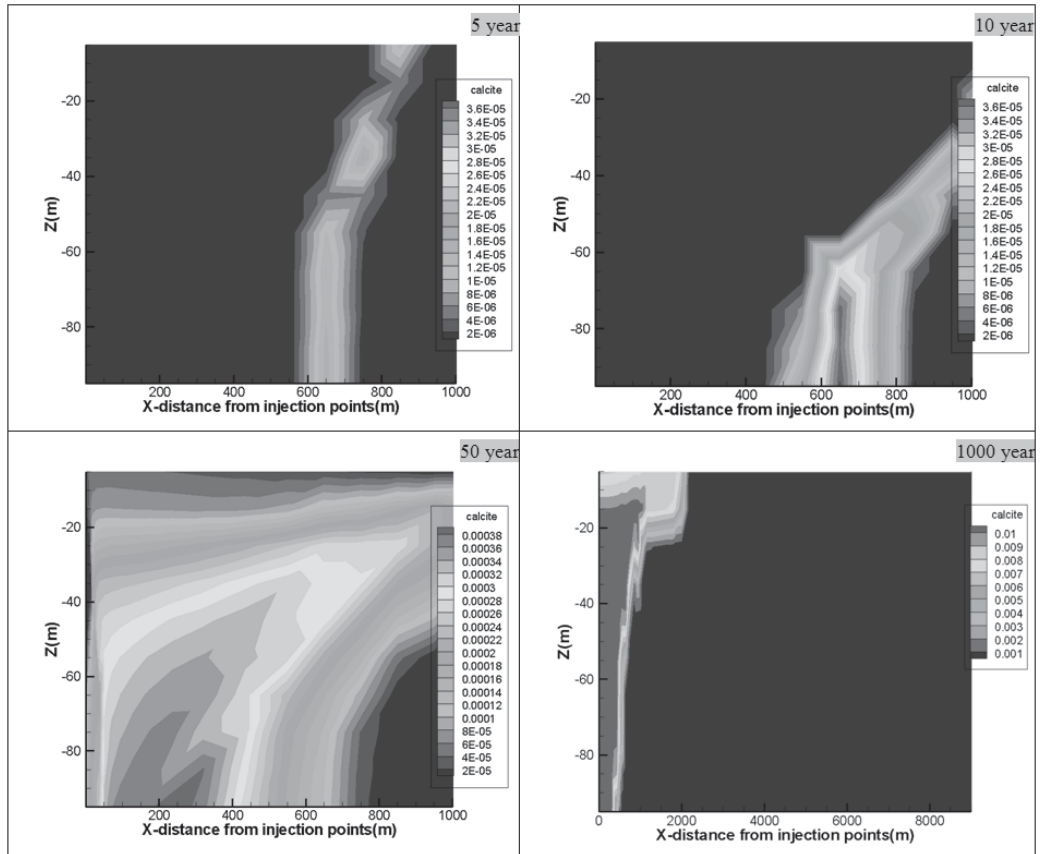
Fig. 6.54 Spatial and temporal evolution of volume fraction of calcite in a sandstone reservoir
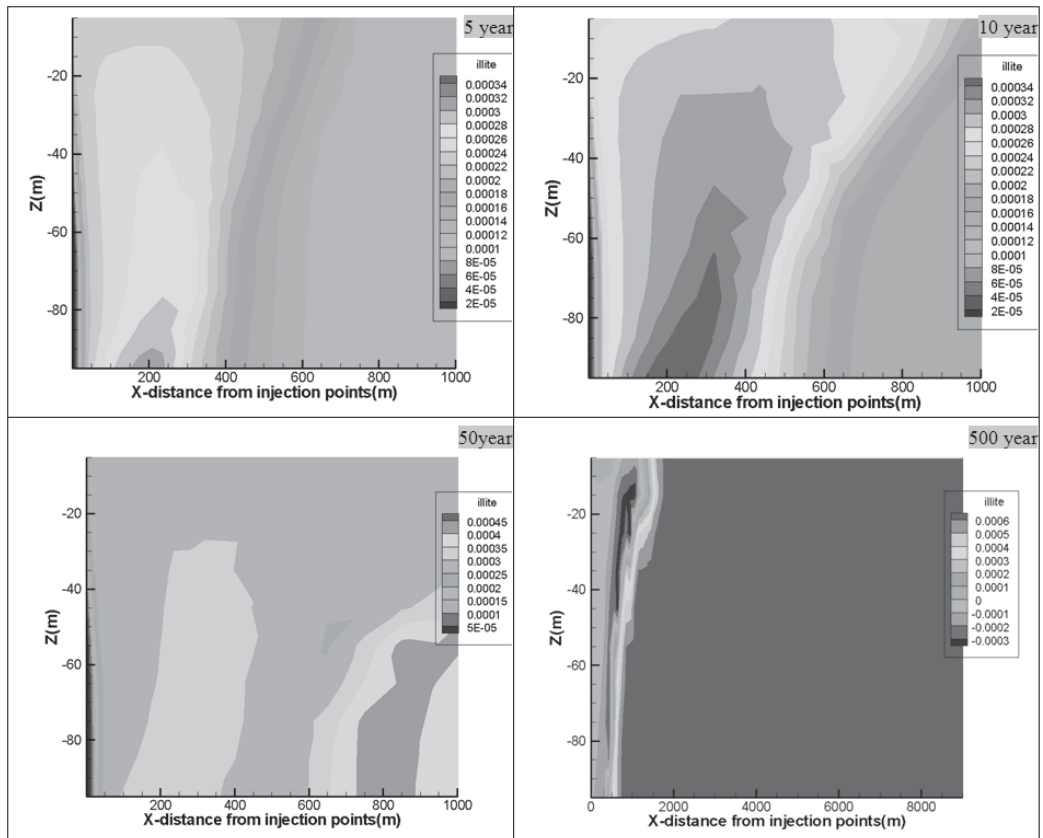
Fig. 6.55 Spatial and temporal evolution of volume fraction of illite in a sandstone reservoir

185
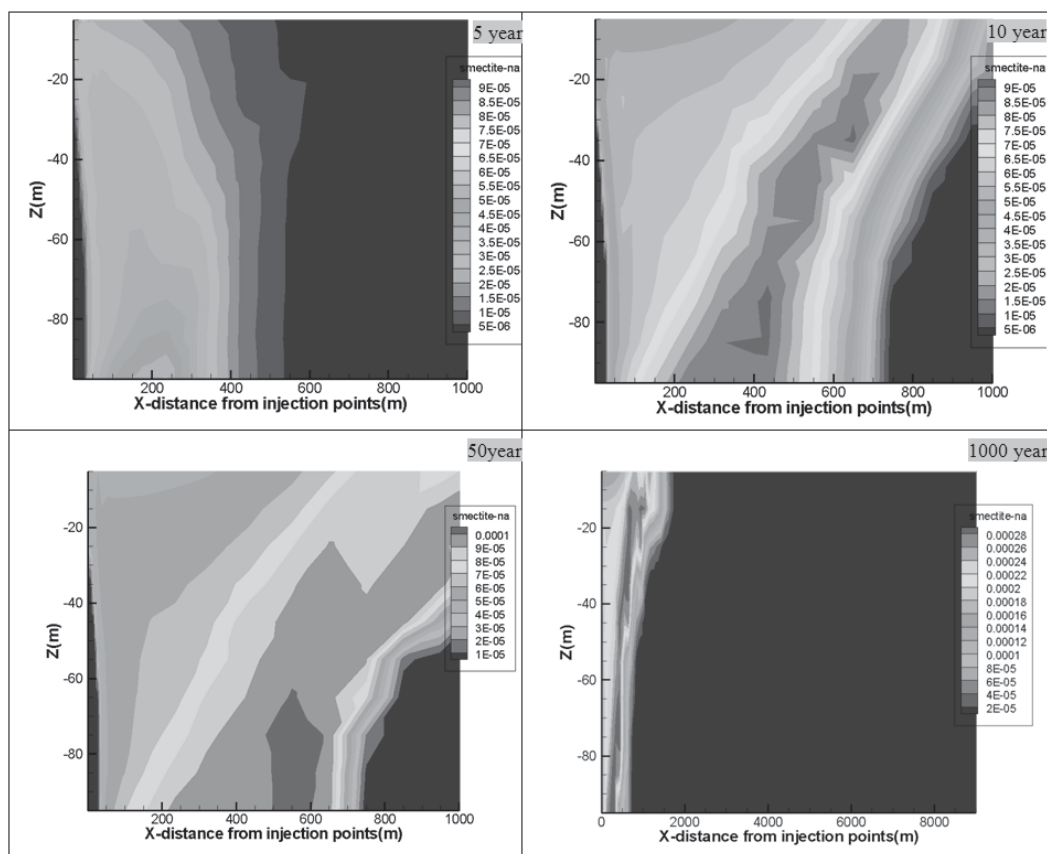
Fig. 6.56 Spatial and temporal evolution of volume fraction of smectite-Na in a sandstone reservoir
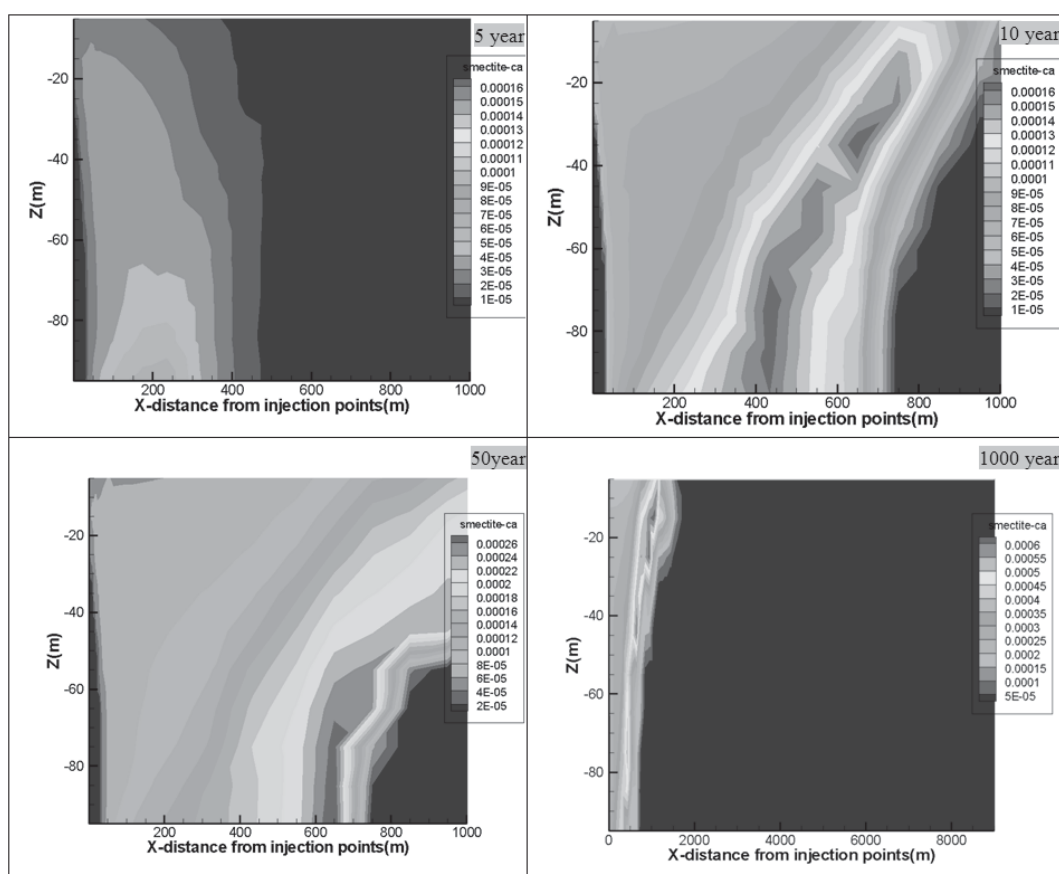
Fig. 6.57 Spatial and temporal evolution of volume fraction of smectite-Ca in a sandstone reservoir

186
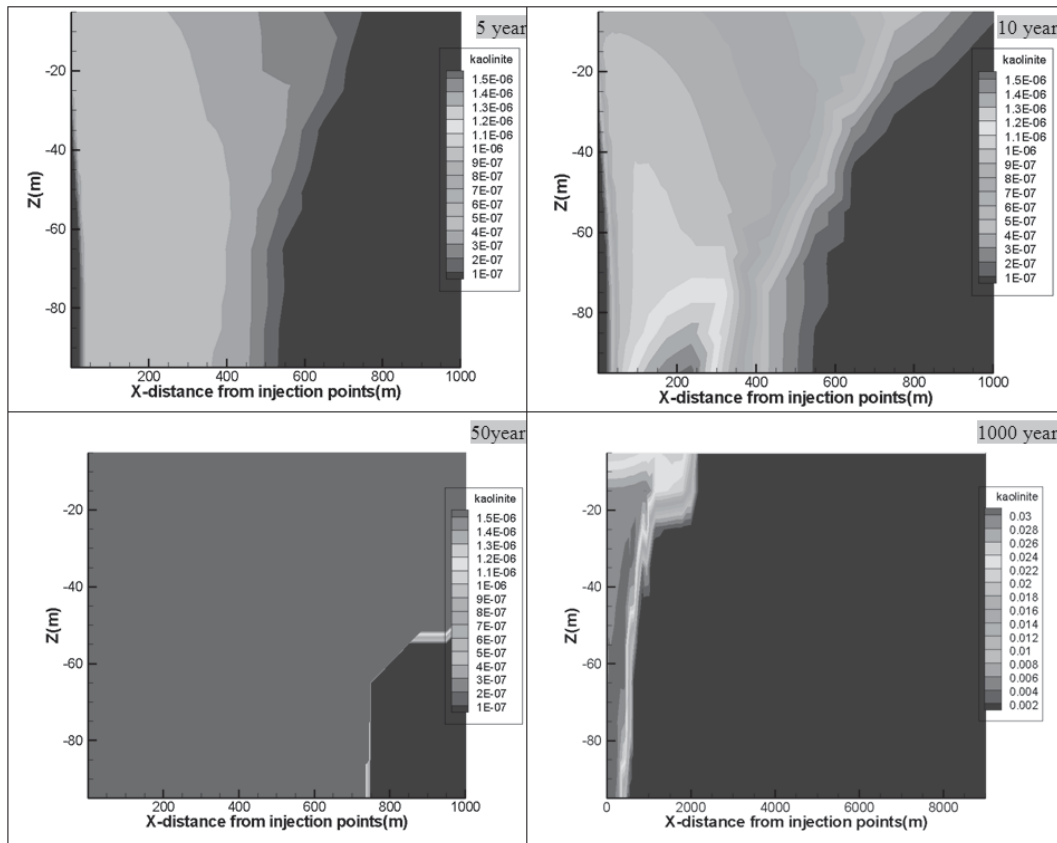
Fig. 6.58 Spatial and temporal evolution of volume fraction of kaolinite in a sandstone reservoir

6.5.3.4 Porosity and permeability changes with time

Hydrogeological parameters, especially porosity and permeability, have great impact on the fluid flow patterns (Dawson et al., 2013). In natural porous media systems, porosity and permeability of the reservoir change with time and space caused by various chemical reactions, resulting in much complex fluid flow pathways (Edmunds et al., 1982; Giles and de Boer, 1990). The simplified simulation model shows that these two reservoir properties are improved during CO_2 injection process (see Figs. 6.59 and 6.60), with the maximum porosity and permeability developing at the bottom injection zone, but less than 0.1% of the initial value. In the long-term, however, these properties become negative in the near-well zone (at 50 and 1000 years in Figs. 6.59 and 6.60, respectively). These variation trends show a clear correlation between the evolution of porosity and permeability in the reservoir.
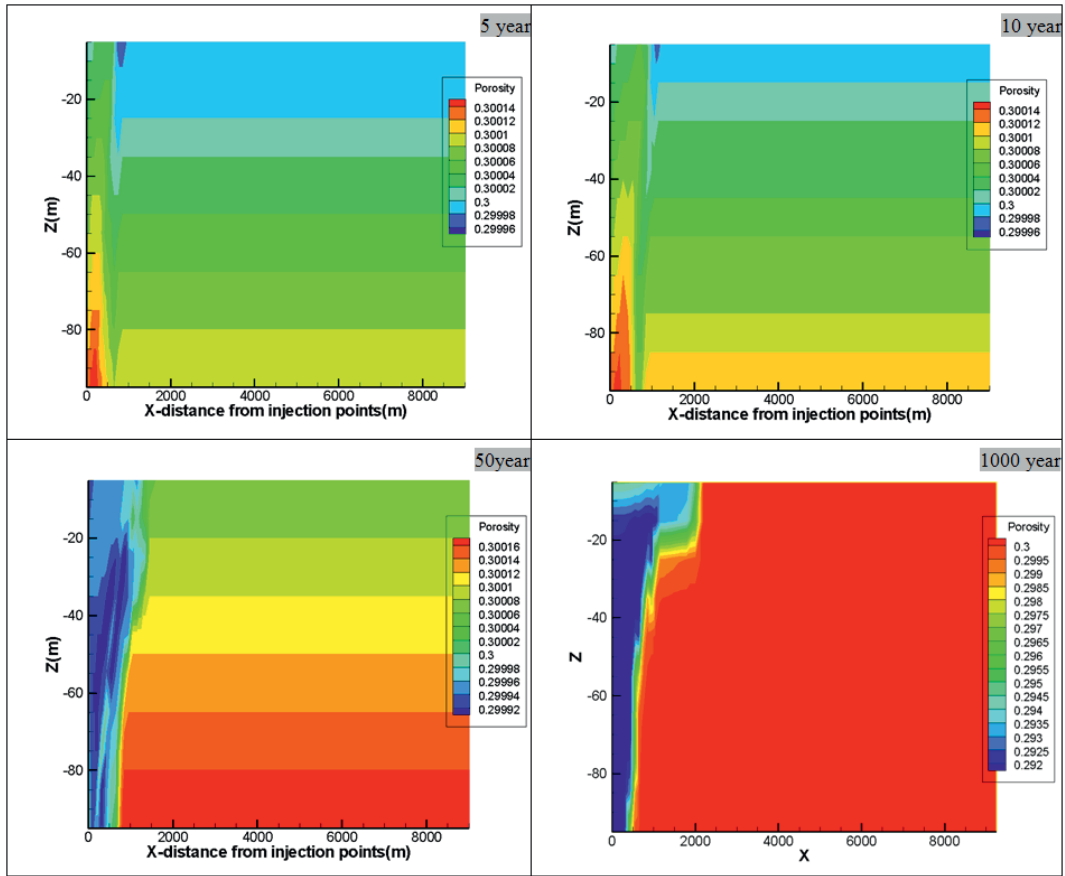
Fig. 6.59 Spatial and temporal evolution of porosity in a sandstone reservoir
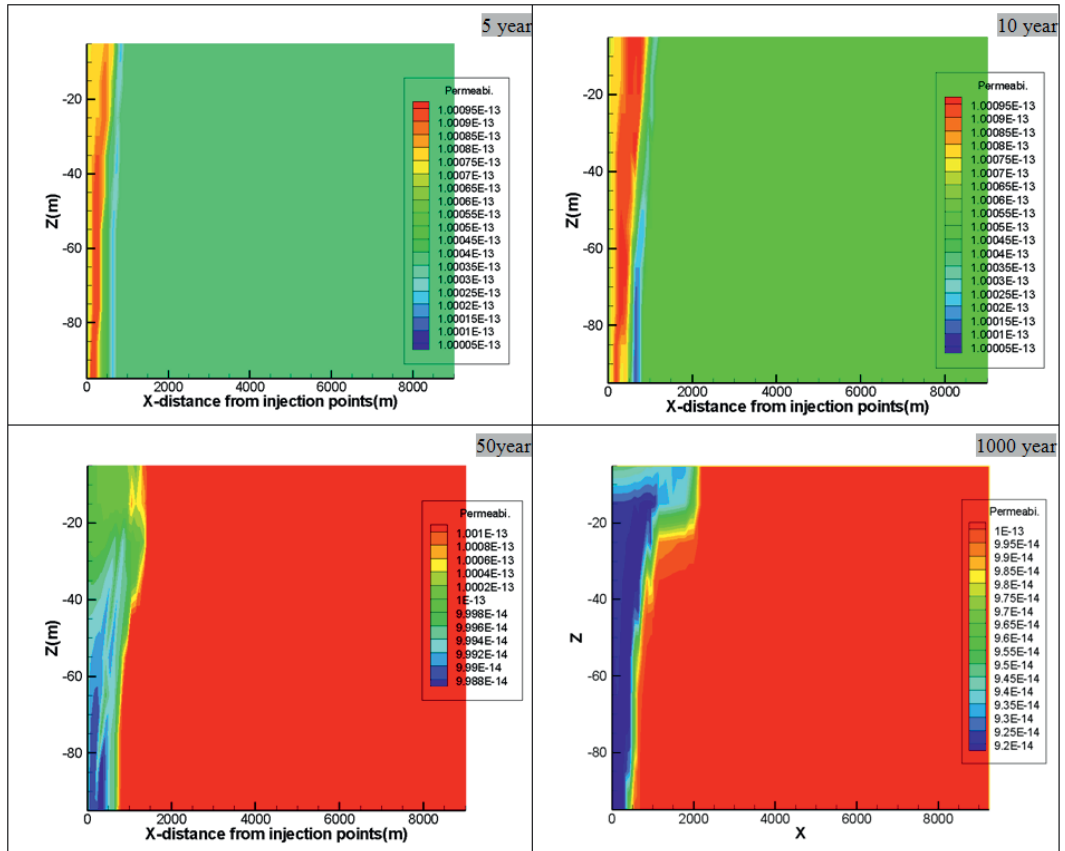
Fig. 6.60 Spatial and temporal evolution of permeability in a sandstone reservoir

7. Case study of CO$_2$–aided hydrothermal system

7.1 Characteristics of hydrothermal systems

The Earth is rich in many kinds of natural resources, including hydrocarbons, metal and non-metal ores, geothermal energy and so on. However, most of these resources are non-renewable compared to the human history. Among them, fossil fuels (oil, coal and natural gas) constitute about 79.4% of the primary energy structure (Fig. 7.1). The renewable clean energy (hydro, marine, bioenergy, solar energy, wind and geothermal) only contributes a small portion to the production of primary energy. With the development of industrialization and population increase, conventional fossil fuels have been excessively consumed posing a threat to become depleted in the near future (Lior, 2008; Shahriar and Erkan, 2009). Due to the threat of hazardous radiations from reactive nuclear waste generated by nuclear fired plants on the environment and human life (Bandlamudi and Avirneni, 2013), more and more countries in the world have taken steps to shut down nuclear power plants. For example, some European countries, especially Germany, will shut all nuclear power plants by 2022. This may give way to the development of renewable energy in the next decades. The investments in renewable energy have also increased greatly, about three times more than that in 2001 (Fig. 7.2).
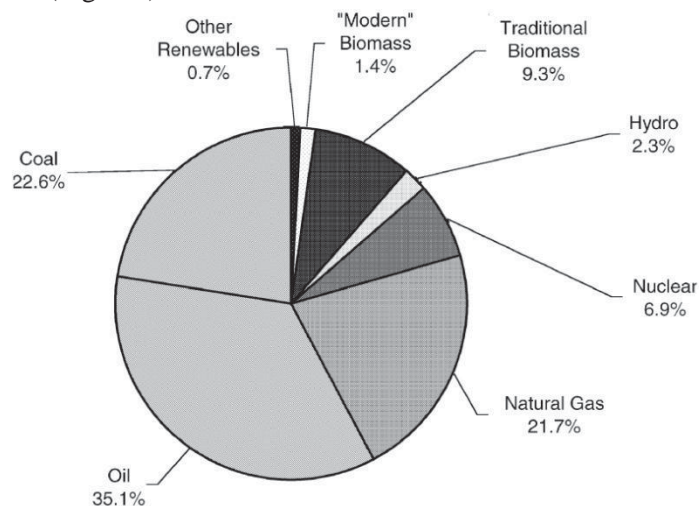
Fig. 7.1 Worldwide primary energy production in 2001 (UNDP, 2004)
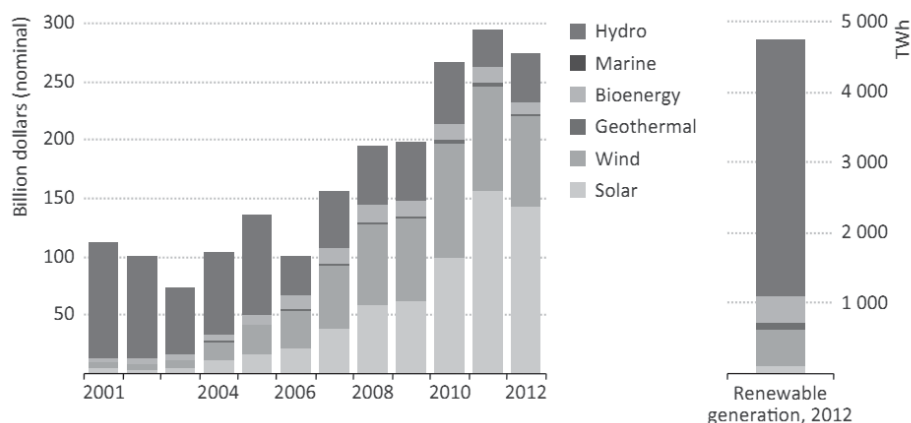
Fig. 7.2 Global investment in renewable-based power plants and total generation in the last 10 years (IEA, 2013)

Under safety, sustainability and environmental friendly concerns, geothermal energy has its advantages and can be regarded as an important supplement to the conventional fossil fuels and other renewable energies (e.g. solar energy and wind energy) (Tester et al., 2006; IEA, 2010). The available

189

geothermal energy resource is huge, estimated to be about 42×10^6 EJ, which can supply the world energy requirements, at a rate of 500 EJ/year, for about 100,000 years (Gupta and Roy, 2007; Bertani, 2010, Fig. 7.3). Therefore, extraction of geothermal energy for electricity power production has been paid more attention and rapidly developed in recent years, especially in the USA, Philippines, Indonesia, Italy, Mexico, New Zealand, Iceland and Japan (Fig. 7.4). The geothermal energy production will become a new hot spot in the near future.
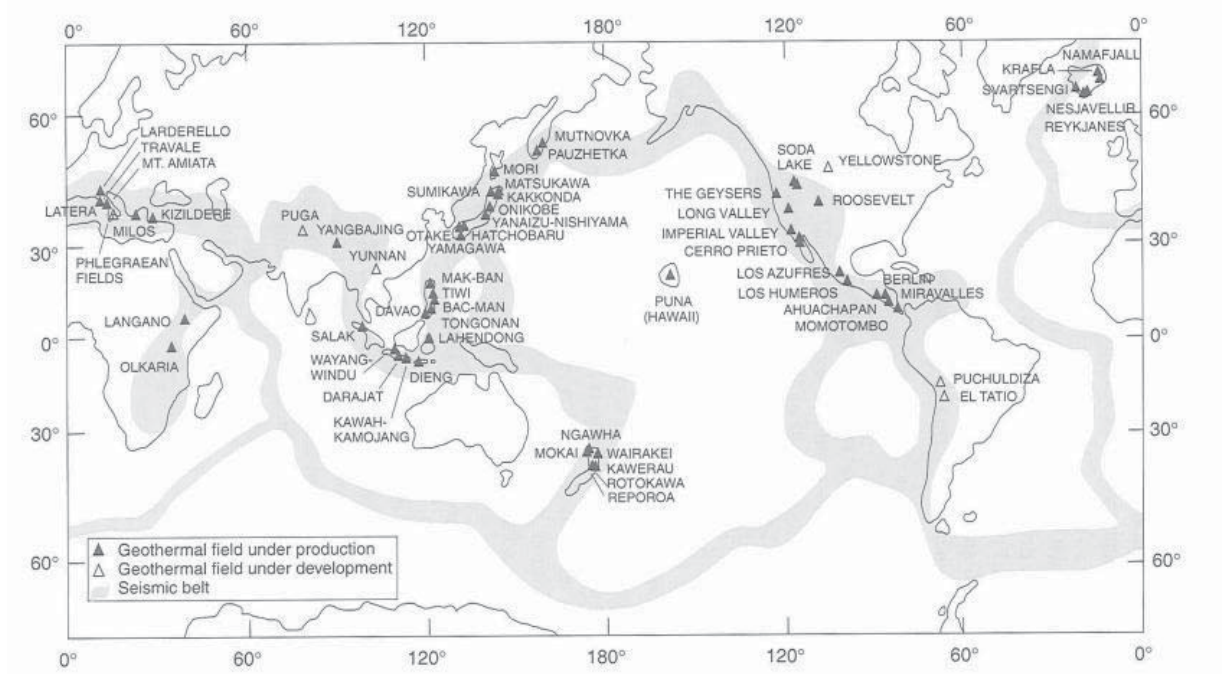
Fig. 7.3 Worldwide major geothermal fields (Gupta and Roy, 2007)
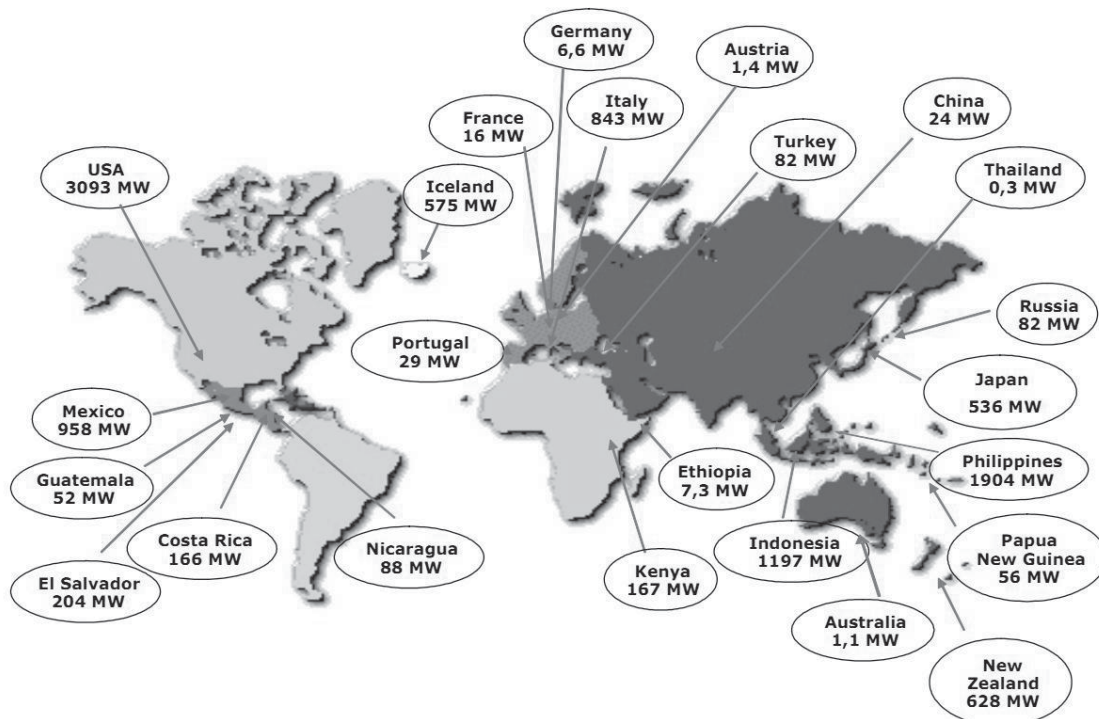
Fig. 7.4 Worldwide installed geothermal power plant with their capacities in 2010 (Bertani, 2010)

Applications of geothermal energy can be divided into three categories: 1) geothermal heat pumps with operation depth less than tens of meters; 2) circulating hot water (e.g. district heating) with the

190

operation depth of about several hundreds of meters; and 3) electric power generation, which converts heat energy into electricity through different methods (e.g. flash steam plants or binary cycle power plants) and usually pump the hot steam or hot water from a depth of three to five kilometers (Payne et al., 2008; Blodgett and Slack, 2009). According to the data from World Geothermal Congress in 2005, 54.4% of the worldwide geothermal direction use comes from the geothermal heat pumps, which accounts for about 32% of the total geothermal energy consumption (Bertani, 2009).

Geothermal electric power and heat production from hydrothermal resources has been commercialized since 1904 (Tester et al., 2006). Table 7.1 lists geothermal power plants worldwide including date of installation and type of electricity generated. The table shows that single flash and dry steam are the dominated power plant types, with a total installation capacity of 41.3 and 26.9%, respectively.

Table 7.1 Worldwide development of geothermal power plants and their types (Bertani, 2010)

country	date	Back pressure		Binary		Single Flash		Double Flash		Dry Steam		Total		Percentage	
		MW	unit	MW	unit	MW	unit	MW	unit	MW	unit	MW	unit	MW	unit
USA	1960			653	149	59	4	795	30	1585	25	3094	209	28.9%	39.8%
Philippines	1979			209	18	1330	31	365	7			1904	56	17.8%	10.7%
Indonesia	1983	2	1			735	14			460	7	1197	22	11.2%	4.19%
Mexico	1973	75	15	3	2	410	15	470	5			958	37	8.94%	7.05%
Italy	1916/1946					88	5			755	28	843	33	7.87%	6.29%
New Zealand	1958	47	5	137	24	290	12	100	1	55	1	628	43	5.86%	8.19%
Iceland	1978			10	8	474	14	90	3			575	25	5.37%	4.76%
Japan	1966			2	2	349	14	160	3	24	1	535	20	4.99%	3.81%
El Salvador	1975			9	1	160	5	35	1			204	7	1.90%	1.33%
Kenya	1981			14	3	153	7					167	10	1.56%	1.90%
Costa Rica	1994	5	1	21	2	140	3					166	6	1.55%	1.14%
Nicaragua	1983	10	2	8	1	70	2					88	5	0.82%	0.95%
Russia	1966					82	11					82	11	0.77%	2.10%
Turkey	1984			14	2	20	1	47	1			82	4	0.77%	0.76%
Papua New Guinea	2001	6	1			50	2					56	3	0.52%	0.57%
Guatemala	1998			52	8							52	8	0.49%	1.52%
Portugal	1994			29	5							29	5	0.27%	0.95%
China	1981							24	8			24	8	0.22%	1.52%
France	1984			2	1	10	1	5	1			16	3	0.15%	0.57%
Germany	2008			7	3							7	3	0.07%	0.57%
Ethiopia	1999			7	2							7	2	0.07%	0.38%
Australia	-			1	2							1	2	0.009%	0.38%
Austria	-			1	3							1	3	0.009%	0.57%
TOTAL		145	25	1178	236	4421	141	2092	60	2878	62	10715	525		
Percentage (%)		1.35%	4.76%	11.0%	45.0%	41.3%	26.9%	19.5%	11.4%	26.9%	11.8%				

Based on the type of circulating fluid and reservoir, geothermal production can be divided into four main groups (see Table 7.2): 1) Traditional H$_2$O-based reservoir type (commercial stage), e.g. Wayang Windu (in Indonesia, with a capacity of 117 MW), Socrates (in the USA, with a capacity of 113 MW), Cerro Prieto III (in Mexico, with a capacity of 110 MW), Kawerau (in New Zealand, with the capacity of 100 MW), etc; 2) H$_2$O-based fractured reservoir type-EGS (Enhanced Geothermal System, at pilot to demonstration stage, see Fig. 7.5), for example, Fenton Hill project (in the USA, with the BHT 200-300 $^{\circ}$C), the Rosemanowes (in the U.K., with the BHT 80-90 $^{\circ}$C), Hijiori (in Japan, with the BHT 150-250 $^{\circ}$C), Ogachi (in Japan, 230 $^{\circ}$C at 1000 m depth), Landau project (in Germany, a 2.5 MW plant) and Soultz project (in France, a 1.5 MW plant); 3) CO$_2$-based reservoir type (at the stage of conceptual and research), also called CO$_2$-Plume Geothermal (CPG) system, which was studied by Randolph and Saar (2011a and 2011b); and 4) CO$_2$-based fractured reservoir type (at the stage of conceptual model and research stage). For H$_2$O-based reservoir, hot water can be used directly (e.g. in households, industrial and institutional buildings). Besides, it can also be used indirectly for electric power generation. However, only electricic power generation can be considered for CO$_2$-based circulating reservoir system.

Table 7.2 Geothermal production methods

Geothermal production style	Preconditions	Problems	Usage	
			Direct use (heating)	Electricity
Traditional H_2O-based reservoir	S1. Significant amount of water S2. A permeable formation S3. Sufficient subsurface T	Water disposal and reinjection into shallow layer	T = 40 ~ 150 ^oC	T > 150 ^oC
H_2O-based EGS	1. Injection water 2. manmade S2 3. S3	Water loss (12% or more); induced seismicity; The difficulty in generating fractures in a large volume of hot rock; The difficulty in making sufficient permeability and long-circuiting pathways	T = 40 ~ 150 ^oC	T > 150 ^oC
CO_2-based reservoir (CPG)	1. Injected CO_2 2. S2 3. expand the T range	Probably leakage risk; Reinjection, small amount of CO_2 sequestration	—	T > 98.2 ^oC 65.8 ^oC CO_2 = 100 ^oC water
CO_2-based EGS	1. Injected CO_2 2. manmade S2 3. expand the T range	Reinjection, large amount of CO_2 sequestration	—	T > 98.2 ^oC

Fig. 7.5 European H_2O-based fractured reservoir type geothermal (EGS) site locations (Tester et al., 2006)

Each type has its own advantages and disadvantages. All geothermal electric power systems have to address fluid re-injection problems, which cause the clogging of formations. For a traditional H_2O-based reservoir type, water disposal should be made to remove the precipitated salts before the reinjection of water into the shallow formations (Szucs et al., 2010). As for the fractured reservoir types, H_2O-EGS, a large amount of water loss (about 12%) may occur during hot water circulation processes (Tester et al., 2006; Bertani, 2010). Moreover, significant technical and economic difficulties have to be overcome to generate fractures in a large volume of hot rock in order to sustain sufficient permeability and extend circulation pathways (Pruess, 2007). Besides, hydraulic fracturing stimulation used in EGS may have the possibility to induce microseismic events (Phillips et al., 2002; Shapiro and Dinske, 2009). CO_2-based geothermal system, can not only achieve more heat extraction than aqueous fluid (Pruess, 2007), and also becomes a mean to sequester some CO_2 at the same time. However, a series of CO_2 leakage threats and corrosion of well pipes should be addressed when CO_2 is considered as the exchange geothermal fluid just as in a CO_2 sequestration project (Court, 2011). CO_2-based EGS is similar to H_2O-based EGS, while the difference is that the circulating fluid is CO_2 instead of water (Brown, 2000; Pritchett, 2010).

192

Production of geothermal electric power by CO$_2$ can have a lower temperature requirement (98.2 $^{\circ}$C) than in the conventional water-based geothermal (150 $^{\circ}$C). It not only enables the development in a deeper hot rock, but also makes CO$_2$ sequestration become possible.

7.1.1 H$_2$O-based hydrothermal system

Almost all commercial scale geothermal power plants under operation today are H$_2$O-based reservoir type, which are only located in positive sites possessing easily developed high-grade hydrothermal resources with high average thermal gradients, high rock permeability and porosity, low salinity, plenty of fluids in place, and sufficient recharge of water (Tester et al., 2006). Unlike conventional hydrothermal reservoirs, enhanced geothermal systems (EGS) are artificially developed fractured reservoirs. Different definitions are used to describe this kind of geothermal system, including conduction dominated, low permeable resources in sedimentary and basement formations, as well as geopressured-type magma and low grade hydrothermal by MIT, and HDR, deep heating mining, hot wet rock, hot fractured rock, stimulated geothermal and hydrothermal system followed by BMU and others (Breede et al., 2013). Huenges (2010) has concluded the characteristics of geothermal systems in detail, from both theoretical and practical cases point of view. Breede et al. (2013) have systematically reviewed the development and status of EGS technology based on 31 projects worldwide. EGS technologies are still at the levels of pilot to demonstration (Bertani, 2009, 2010; DOE, 2012). It may still require a long time to achieve the commercial-scale application for EGS technology.

Table 7.3 lists the thermal efficiency of hot water with different temperatures (Qu et al., 2012). It shows that with increased temperature of hot water, the thermal efficiency will increase accordingly. Carnot cycle system offers the maximum efficiency, contributing 20% of the total electric power capacity with a water temperature of 100 $^{\circ}$C, while the efficiency at 60 $^{\circ}$C is dropped by about a half. The ideal electric efficiency is very low (< 10%) when water temperature is less than 100 $^{\circ}$C. For intermediate hot water, the ideal electric efficiency is much lower. Therefore, water temperature is a key factor affecting the electric efficiency of a geothermal system (Stefansson, 2005).

Table 7.3 The ideal thermal efficiency of hot water and generating capacity (Qu et al., 2012)

Temperature of water/$^{\circ}$C	60	70	80	90	100	180-300
Carnot cycle limited efficiency η_c/%	10.5	13.1	15.6	17.8	20	-
Ideal efficiency of hot water $\eta_{t,max}$/%	5.5	6.9	8.3	9.6	10.6	-
The maximum capacity of electricity derived from the hot water $N_{e,max}$/kWh.t^{-1}	2.20	3.7	5.56	7.25	9.26	20

To make a geothermal electric power project profitable, the production flow rate must reach 50 kg/s-150 kg/s or much higher with the generated energy larger than 5 MW, which requires a reservoir temperature higher than 150 $^{\circ}$C. A net energy capacity of 4.7 MW can be generated in the hot water of 150 $^{\circ}$C with a flow rate of 125 kg/s (Tester et al., 2006).

Large geothermal power plants (with installed capacity > 50 MW) are mainly distributed in the USA, Philippines, Indonesia, Mexico, Italy, New Zealand and Japan. Table 7.4 lists the top largest H$_2$O-based conventional geothermal power plants in the world. The table clearly shows that the USA takes up the largest share in electricity generation using the dry steam type of geothermal energy, Philippines generates electricity from both single flash and double flash type power plants, Indonesia from single flash and dry steam type power plants, Mexico from double flash type power plants, Italy from dry steam power plants. Japan takes a relative smaller contribution in large geothermal power plants, although its technology for geothermal production is already mature, considering its contribution to the market for equipments in most of the projects.

Table 7.4 The largest and earliest geothermal power plants in the world (Duchane and Brown, 2002; Monastero 2002; Lund 2004; Bertani, 2010; Breede et al., 2013)

Country	Plant	Unit	Start Time	Capacity (MWe)	Type	Operator	Manufacturer
Italy	Lardarello	-	1904	700	Dry Steam	ENEL	unknown
USA	Coso	9	1981	270	Double Flash	Coso company	Mitsubishi and Fuji
Indonesia	Wayang Windu	2	2009	117	Single Flash	Star Energy Ltd	Fuji
USA	Socrates	1	1983	113	Dry Steam	Calpine	Toshiba
USA	Quicksilver	1	1985	113	Dry Steam	Calpine	Toshiba
USA	Lake View	1	1985	113	Dry Steam	Calpine	Toshiba
USA	Grant	1	1985	113	Dry Steam	Calpine	Toshiba
Mexico	Cerro Prieto III	1	1986	110	Double Flash	CFE	Toshiba
USA	Cobb Creek	1	1979	110	Dry Steam	Calpine	Toshiba
USA	Eagle Rock	1	1975	110	Dry Steam	Calpine	Toshiba
Mexico	Cerro Prieto II	2	1987	110	Double Flash	CFE	Toshiba
Mexico	Cerro Prieto II	1	1986	110	Double Flash	CFE	Toshiba
Indonesia	Darajat	2	2008	110	Dry Steam	Chevron	Mitsubishi
Indonesia	Wayang Windu	1	2000	110	Single Flash	Star Energy Ltd	Fuji
Mexico	Cerro Prieto III	1	1986	110	Double Flash	CFE	Toshiba
USA	Sulphur Spring	1	1980	109	Dry Steam	Calpine	Toshiba
New Zealand	Kawerau	1	2008	100	Double Flash	Mighty River Power	Fuji
USA	Big Geyser	1	1980	97	Dry Steam	Calpine	GE
Indonesia	Darajat	2	1999	90	Dry Steam	Chevron	Mitsubishi
USA	Sonoma	1	1984	80	Dry Steam	Calpine	Toshiba
Philippines	Malitbog	3	1997	78	Single Flash	EDC	Fuji
USA	Sonoma	1	1983	72	Dry Steam	Calpine	Mitsubishi
Indonesia	Gunung Salak-IPP	3	1997	65	Single Flash	Chevron	Fuji
Japan	Yanaizu-Nishiyama	1	1995	65	Single Flash	Tohoku Electric Power	Toshiba
Philippines	Mak-Ban B	2	1980	63	Double Flash	Chevron	Mitsubishi
USA	Dixie Valley	1	1988	62	Double Flash	Terra Gen	Fuji
Indonesia	Gunung Salak	3	1997	62	Single Flash	PLN	Fuji
Indonesia	Gunung Salak	2	1994	60	Single Flash	PLN	Ansaldo/Tosi
Indonesia	Dieng	1	1998	60	Single Flash	PLN	
Italy	Farinello	1	2002	60	Dry Steam	Enel Green Power	Ansaldo/Tosi
Italy	Valle Secolo	2	1991	60	Dry Steam	Enel Green Power	Ansaldo/Tosi
Philippines	Tiwi A	1	1979	60	Single Flash	Chevron	Toshiba
Italy	Valle Secolo	1	1991	60	Dry Steam	Enel Green Power	Ansaldo/Tosi
Philippines	Mahanagdong B	1	1997	59	Single Flash	EDC	Toshiba
Philippines	Tiwi C	2	1982	57	Single Flash	Chevron	Toshiba
USA	Fenton Hill (first EGS)	-	1974-1995	0.5	Back Pressure	Los Alamos National Lab	unknown
UK	Rosemanowes (first EGS in EU)	-	1977-1992	Pilot	-	Camborne School of Mines	unknown
France	Soultz	-	1984	1.5	ORC	EU cooperation	unknown

7.1.2 CO₂-based hydrothermal system

The idea of using CO_2 as the heat extraction fluid was presented by Brown (2000). The CO_2-based reservoir type geothermal system (Fig. 7.6) can provide pressure for driving the CO_2 plume through the saline formation using a combination of hot brine extraction and residual brine reinjection (Buscheck et al., 2012a, 2012b, 2012c, 2012d; Court, 2011; Court et al., 2011a, 2011b, 2012). In a pure CO_2 sequestration project, this can reduce the risk of CO_2 leakage to the surface by decreasing the reservoir pressure. If geothermal production is considered after in situ water is displaced out of the working area (dry out), the geothermal production efficiency can be increased by using CO_2 as working fluid. This can extend the available range of temperature ($> 98.2\,^{o}C$) and sedimentary reservoir hydraulic characteristics (k = 20 mD ~ 200 mD) for geothermal electricity.
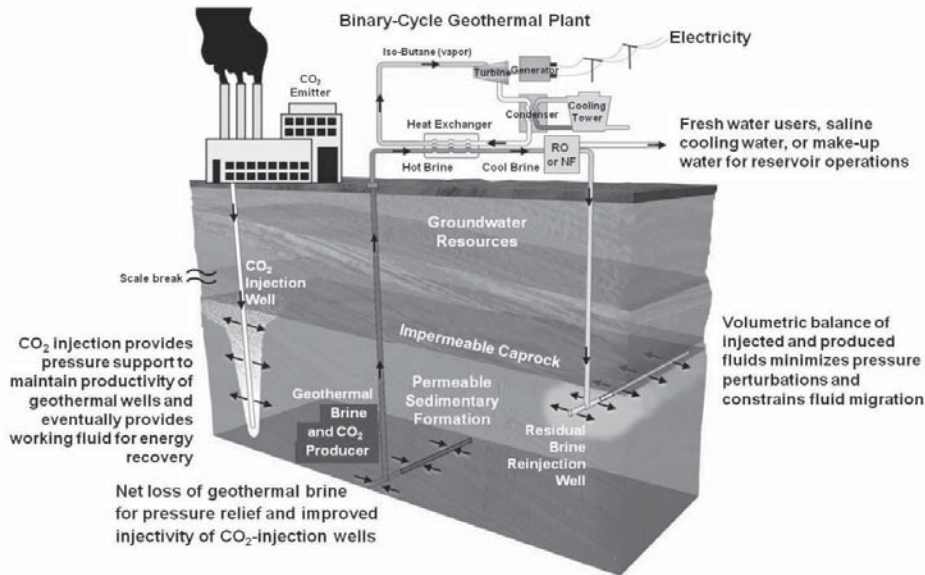
Fig. 7.6 Integrated geothermal production with CO_2 sequestration (Buscheck et al., 2012c)

Using CO_2 as the working fluid may produce larger heat extraction rates than water in the EGS system (Pruess and Azaroual, 2006; Pruess, 2006, 2007; Randolph and Saar, 2011), due to the compensation of the unfavorably smaller specific enthalpy for CO_2 compared with H_2O (Fig. 7.7). Under a given effective pressure gradient, the fluid flow rate is proportional to its mobility,

$$\bar{\bar{M}} = \frac{\rho}{\mu}, \tag{7.1}$$

where ρ and μ are density and viscosity of the fluid, respectively.

Under most conditions, CO_2 has a much larger mobility than water (Fig. 7.8). Therefore, the flow rate of CO_2 is much higher than that of water (Pruess, 2007).
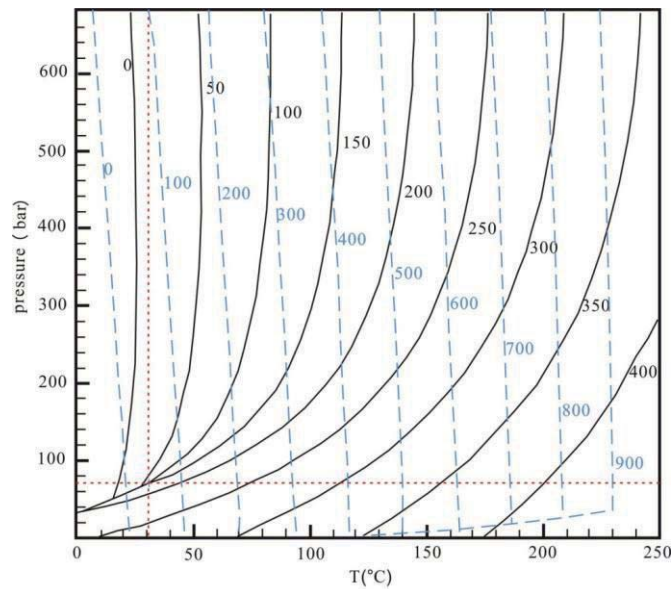
Fig. 7.7 Specific enthalpy (kJ/kg) of CO$_2$ (black line) and water (blue dotted line) under varying T and P (Pruess et al., 2006)
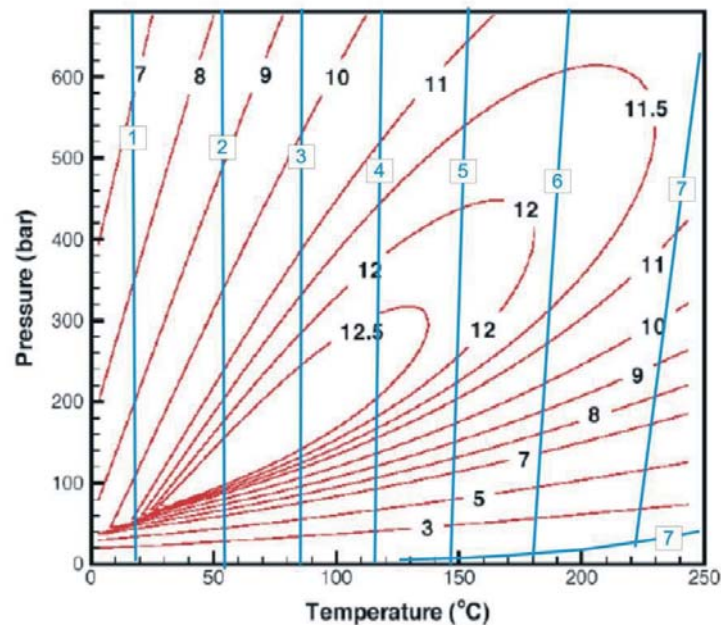
Fig. 7.8 Mobility of CO$_2$ (red line) and water (blue line) (Pruess, 2007)

Though drying out of the initial water reservoir may take a long time, the residual water content (< saturated content) in the CO$_2$ rich phase may not affect the performance of the reservoir when the temperature is high (Atrens and Gurgenci, 2013). Therefore, water content in the CO$_2$ rich phase should be limited when the CO$_2$ rich phase is considered as the working fluid, as CO$_2$ bearing water will result in the erosion of the turbine blades and tubings (Reichman et al., 2008; Atrens et al., 2011). Well spacing, permeability of reservoir and circulation fluid type may all influent heat extraction efficiency (Fig. 7.9). Though the heat extraction rate decreases with time when CO$_2$ is used as the working fluid, it is still more efficient in the long term (Randolph and Saar, 2011). CO$_2$-aided or plume geothermal production (CPG) has the most efficient heat extraction rate. Other parameters that affect the production rate include well spacing and the permeability of the reservoir. The closer the well spacing, the faster CO$_2$ breakthrough will occur in the production wells and less CO$_2$ will be sequestrated in the reservoir (Fig. 7.10). Besides, the permeability of the reservoir shows positive correlation with the heat extraction rates.
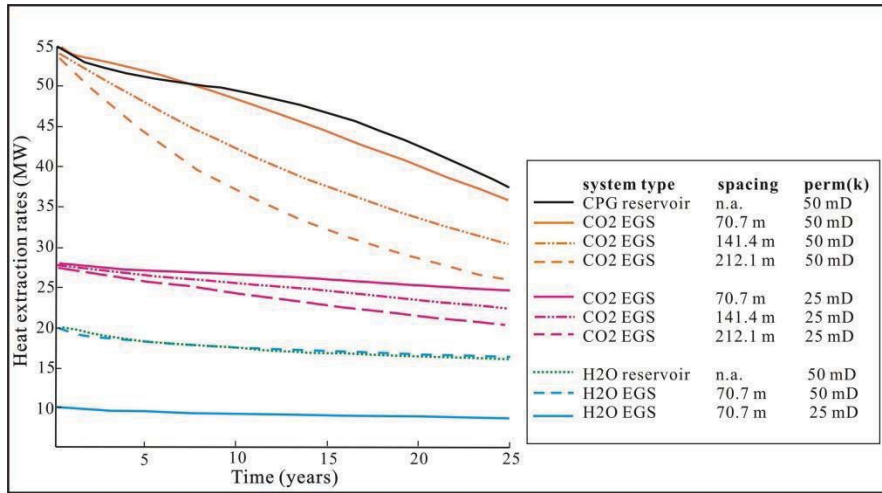
Fig. 7.9 Time series of geothermal heat extraction rates in five spot well configuration system (Randolph and Saar, 2011). Legend info includes: system type, fracture spacing and permeability
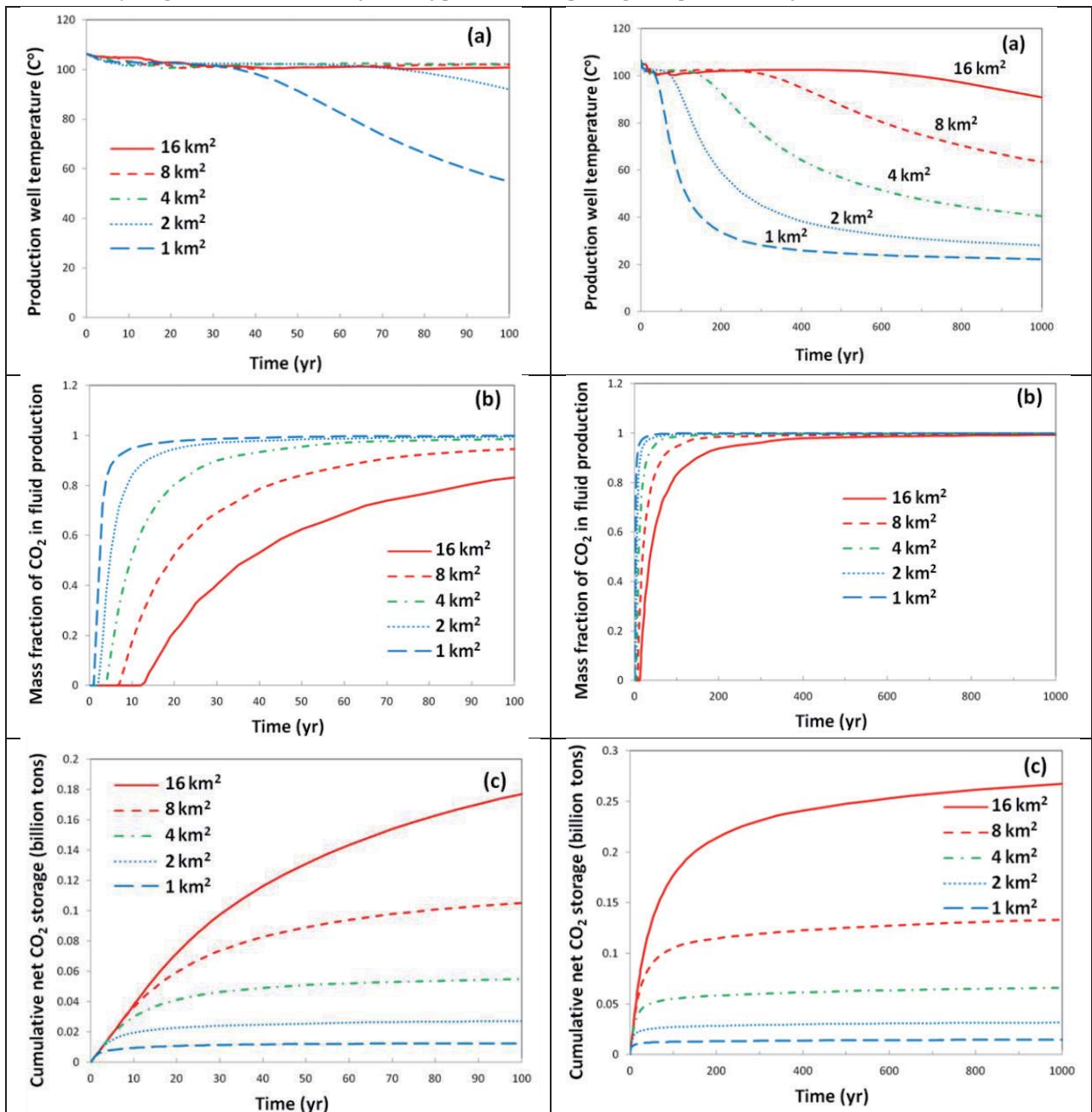
Fig. 7.10 Parameter changes with time in a five spot geothermal production (heat flux 75 mW/m^2, injection and production rate 120 kg/s) associated with CO$_2$ sequestration: left column-to the time of 100 years, right column- to the time of 1000 years (Buscheck et al., 2012c), including (a) production temperatures; (b) mass fraction of CO$_2$ in fluid phase; (c) cumulative CO$_2$ sequestration amount.

7.2 Numerical model set up

7.2.1 System geometry

Based on the understanding of the CO$_2$-based geothermal system, it is possible to investigate the distribution of CO$_2$ and pressure, including the heat extraction capacity. When CO$_2$ acts as the pressure driven fluid, but not as the heat extraction fluid, a numerical model is idealized as a three dimensional symmetric domain (Nx= 3000 m, Ny= 3000 m, Nz= 700 m) (Fig. 7.11). This is a simplified multilayered system with the thickness of sandstone and mudstone being 540 and 160 m, respectively. The model top is at 1800 m below the surface. Mesh discretization is fine in the near well region, becoming progressively coarse with distance away from the well. The injection and production wells are set at the center of y direction, and well spacing is 500 m in x direction. To show the simulation results more clearly, a ½ 3D model is set up with a total of 52,500 elements and 35 2D layers arranged.
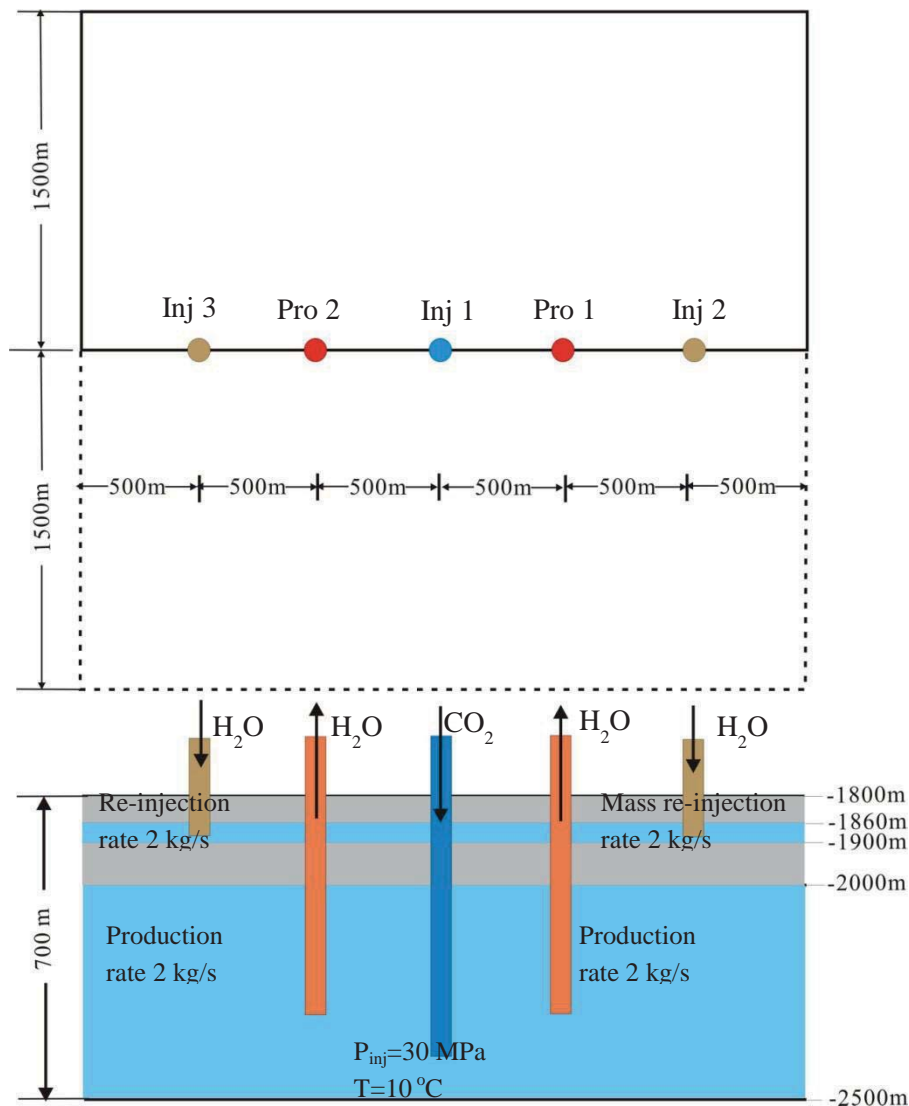
Fig. 7.11 Model used in the CO$_2$-driven geothermal production and brine re-injection system

7.2.2 Initial and boundary condition

Table 7.5 shows the reservoir and caprock hydrological properties used for simulations. Some data are obtained from petroleum and groundwater exploration companies operating in the NE Ordos Basin, such as porosity, permeability, salinity, pore pressure etc. Most of these parameters are similar to those used in the CO_2-water two phase fluid flow simulation (base case) in Chapter 4. However, the geological model used here is more simplified. Initial conditions for fluid pressure, temperature and salinity of the reservoir and caprock are assumed based on averaged values of all available data from upper Proterozoic formations of the Ordos Basin. Considering the hydrogeological characteristics in this area, reservoir boundaries are assumed to be open in the lateral directions. The top and bottom boundaries are assumed to be closed, which means that fluid and heat exchange from the reservoir is not possible.

Table 7.5 Hydrological properties and parameters used in simulation

Property	Reservoir formation	Caprock
Formation properties		
Horizontal and vertical permeability (m^2)	5.0×10^{-14}	1.0×10^{-18}
Pore compressibility (Pa^{-1})	4.5×10^{-10}	4.5×10^{-10}
Porosity	0.30	0.10
Thickness (m)	540	160
Bottom of formation(m)	-2500	-2000
Grain density (kg/m^3)	2450	2000
Rock grain specific heat (J/kg ^{o}C)	1000	1000
Thermal conductivity (W/m ^{o}C)	2.1	2.1
Relative permeability and capillary pressure		
Van Genuchten(1980) m	0.40	0.40
Van Genuchten(1980) $1/P_0$ (Pa^{-1})	2.79×10^{-4}	1.61×10^{-5}
Residual gas saturation	0.05	0.05
Irreducible water saturation	0.20	0.20
Initial conditions		
Pressure	Hydrostatic pressure gradient	
Temperature gradient (^{o}C/100 m)	3.1	
Salinity (g/L)	18	
Boundary conditions		
Top/ bottom boundary	Closed, no heat and mass flow	
Lateral boundary	Open, with heat and mass flow	
Injection and production condition		
CO_2 injection temperature (^{o}C)	10	
CO_2 injection pressure (MPa)	30	
Production rate (kg/s)	2	
Re-injection rate (kg/s)	2	

7.3 Results and discussion

The parallel version TOUGH2MP/ECO2N simulator was used in the simulation runs. The simulations were set to last 35 years, considering the general economic lifespan of a geothermal project. During this period, CO_2 is continuously injected into the reservoir at a fixed pressure of 30 MPa and temperature of 10 ^{o}C. Therefore, about a total of 1.5×10^7 ton CO_2 (15 Mt) is injected in the reservoir. The two geothermal production wells operate simultaneously when CO_2 injection starts (Fig. 7.12). At a shallow depth, two shallower wells are used for the reinjection of the tail water after the geothermal operation. The aim of this simulation is to investigate the pressure perturbations caused by CO_2 injection and geothermal production, temperature disturbance and CO_2 plume migration in the system.

Fig. 7.12 shows how the pressure evolves with time (i.e. after 0.1, 5, 10 and 35 years) since the beginning of CO_2 injection. Since the injection rate of CO_2 is larger than the production rate of water, a domelike pressure zone will progressively form between two production wells with the continuous CO_2 injection period. When the pressure transfer effect reaches the bottom confining layer of mudstone, the lateral distribution of pressure is affected. Pressure increase in the reinjection layer above the CO_2 injection formation is smaller compared with that in the main CO_2 storage aquifer layer. The pressure buildup caused by CO_2 injection propagates sequently from the near well region to the far field of the reservoir (Atrens and Gurgenci, 2013; Liu et al., 2014). The injection of CO_2 can sustain the reservoir pressure which delays the depletion of the geothermal hot water reservoir caused by continuous production (Sanyal and Enedy, 2011). On the other hand, the long-term storage of CO_2 in the geothermal reservoir also becomes possible.

Fig. 7.13 shows how temperatures progressively expand away from the injection well after 0.1, 5, 10 and 35 years. The injection of cold CO_2 causes a sharp decrease in temperature in the reservoir of the near-well region, and continuous injection enlarges the impact zone. Heat advection occurs, especially at the transition region between CO_2 dominated zone and fully H_2O saturated zone. The high temperature zone will move upward driven by the cold CO_2. Several processes affect the temperature distribution of CO_2 plume (Riano, 2012), including the convective upward flow of the warmer CO_2 from the bottom; the downward movement of the upper colder brines; CO_2 cooling down due to Joule –Thomson effect (Kopp et al., 2006); temperature increase due to the exothermal reaction of CO_2 dissolution into the brine. The redistribution of temperature is also affected by the boundary between sandstone and mudstone layers.

Fig. 7.14 displays the migration of CO_2 plume at 0.1, 5, 10 and 35 years after the start of CO_2 injection. Before CO_2 reaches the production wells, it develops as a mounded shape until it touches the bottom of the caprock layer. After breakthrough of CO_2 plume in the production wells occurs, buoyancy effect becomes much stronger, causing the development of a funnel shaped CO_2 plume (Atrens and Gurgenci, 2013). At the end of simulation time, CO_2 plume almost reaches the lateral boundary of the model, 1.5 km away from the injection well. Before breakthrough occurs, injection CO_2 acts to pressurize the geothermal reservoirs so as to improve the overall performance of the reservoir.
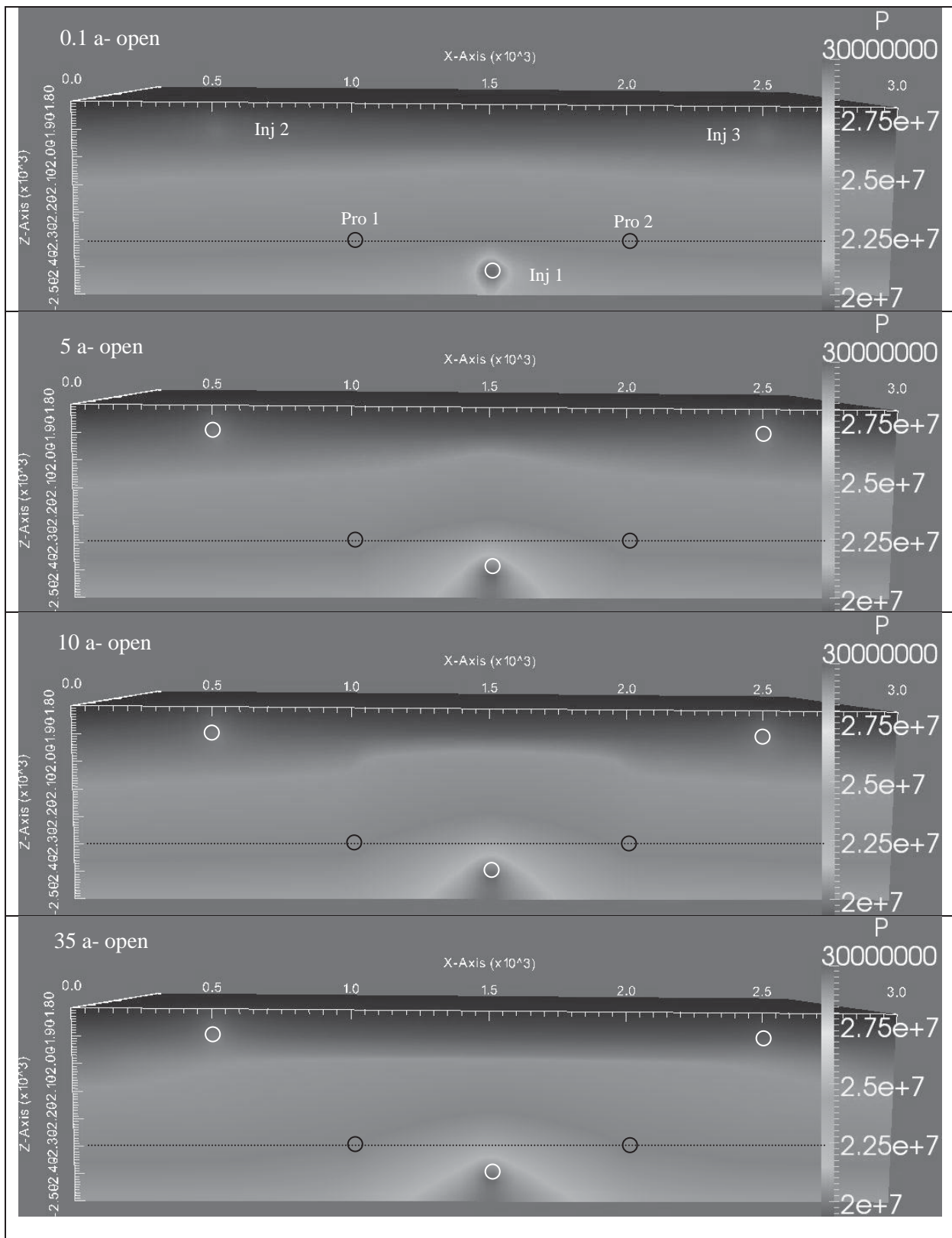
Fig. 7.12 Time evolution of the reservoir pressure in the CO$_2$ driven H$_2$O-based geothermal production system
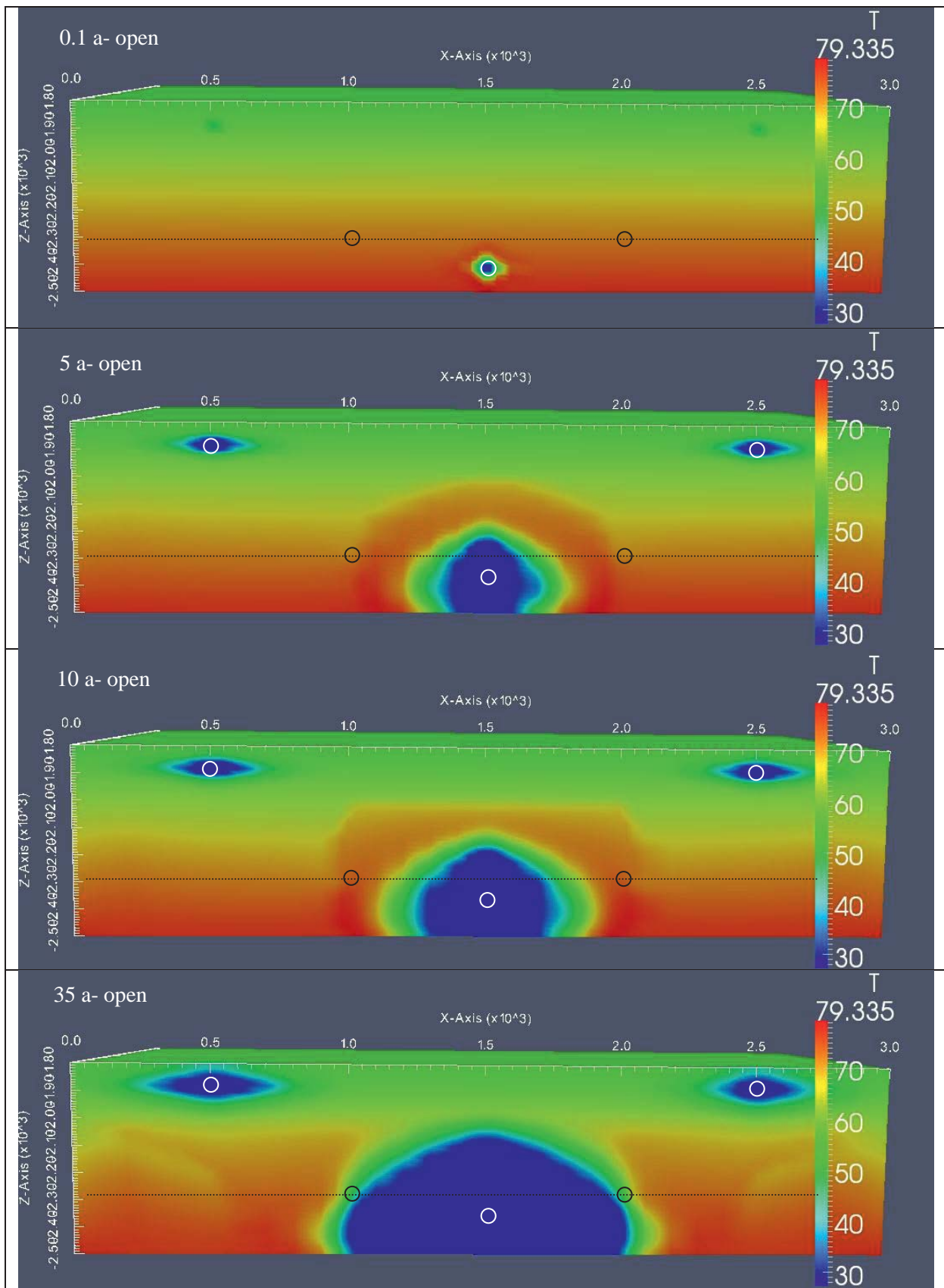
Fig. 7.13 Time evolution of the temperature in the CO$_2$ driven H$_2$O-based geothermal production system

202
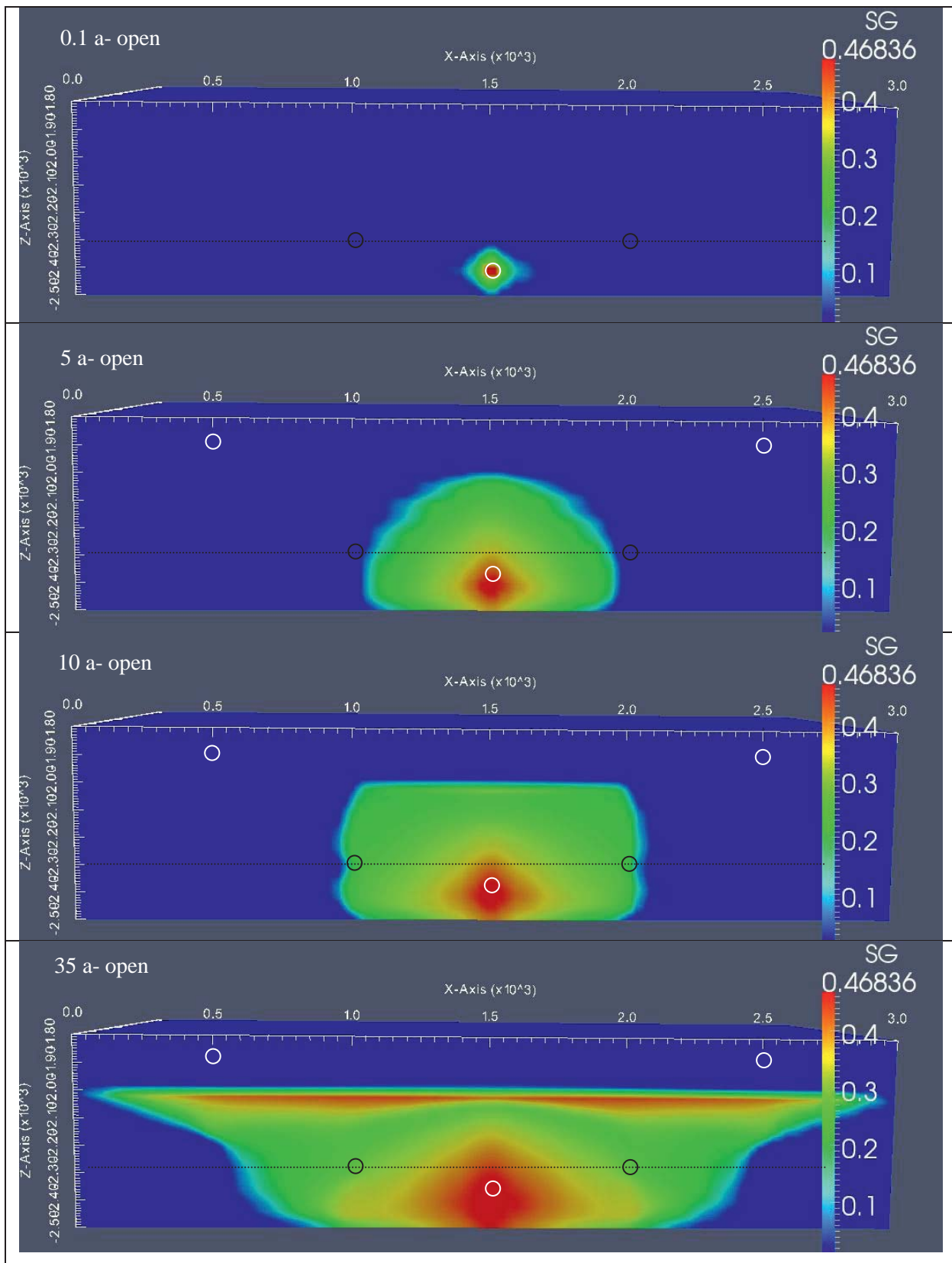
Fig. 7.14 Time evolution of the gas saturation in the CO_2 driven H_2O-based geothermal production system

Fig. 7.15 shows the evolution of CO_2 and liquid flow rates, flowing enthalpy and CO_2 mass fraction changes. The CO_2 flows radially once injected into the saline formations. However, they flow at different rates in different directions due to pressure difference. In this simulation, the CO_2 flows more easily in the vertical direction towards the bottom due to the impact of gravity effect at the beginning of injection. The flow rate of CO_2 will decrease and lasts a short period (Fig. 7.15A). When the near-well region is occupied totally by injected CO_2 (irreducible water also exists), CO_2 flow rate will increase gradually. The gravity and buoyancy effect become much stronger under influence of fluid flow (Fig. 7.15B). The breakthrough of CO_2 in the production well is shown in Fig. 7.15C. The flow rate of water will reduce sharply until CO_2 totally dominates at the bottom of production well. Note that CO_2 flow rate in the production well will decrease after CO_2 breakthrough, which may bear a relationship with imbibition of water, resulting in a trail of immobile CO_2 left behind by the plume (Kim et al., 2013). Fig. 7.15D illustrates clearly that CO_2 breakthrough occurs after about 6 years of CO_2 injection. Production at the near-well region is dominated by different fluid phases during CO_2 driven processes. Before breakthrough, the near-well region is totally water saturated. At the early stage of CO_2 breakthrough, it is dominated by two phases (i.e. water and CO_2). As time goes by, only CO_2 can be produced from the production well. The flowing enthalpy changes in the production well demonstrate that CO_2 takes priority over water when it is used as the heat extraction fluid, which has also been testified by several other researchers (Pruess, 2007; Atrens and Gurgenci, 2013).
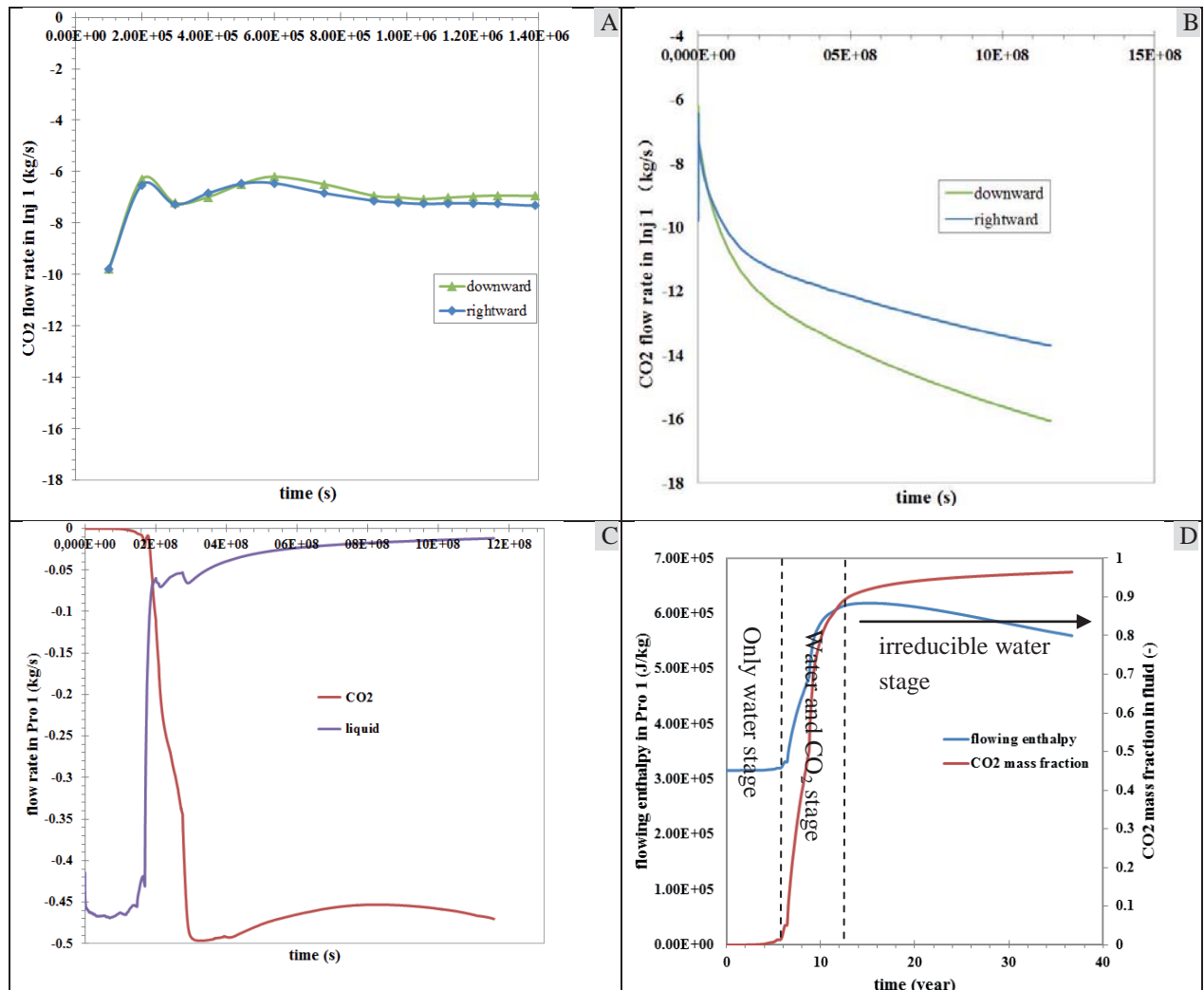
Fig. 7.15 Flow rate and flowing enthalpy changes with time (negative value represents the flow direction from element to production wells): (A) CO_2 flow rate in injection well, to the downward and right flow direction; (B) the same with (A), but the time scale is different; (C) flow rate changes from geothermal production well to downward grid; (D) flowing enthalpy and CO_2 mass fraction changes in production well

CO$_2$ breakthrough lags far behind the pressure response in the geothermal production system (Fig. 7.16A). When breakthrough of CO$_2$ takes place, strong perturbations in reservoir pressure evolution will occur as in CO$_2$-EGR and CO$_2$-ECBM processes (Oldenburg and Benson, 2001; Oudinot et al., 2007). From this time on, CO$_2$ (as the displacing fluid) has lost its efficiency in driving the water for production. During two phase fluid (CO$_2$ and H$_2$O) production period, pressure in the reservoir will decrease. When the near well region of production wells are predominantly occupied by CO$_2$, the pressure will rise again. When the production of hot water is not considered, reservoir pressure will increase gradually with the continuous injection of CO$_2$, until equilibrium state is reached (Fig. 7.16B).
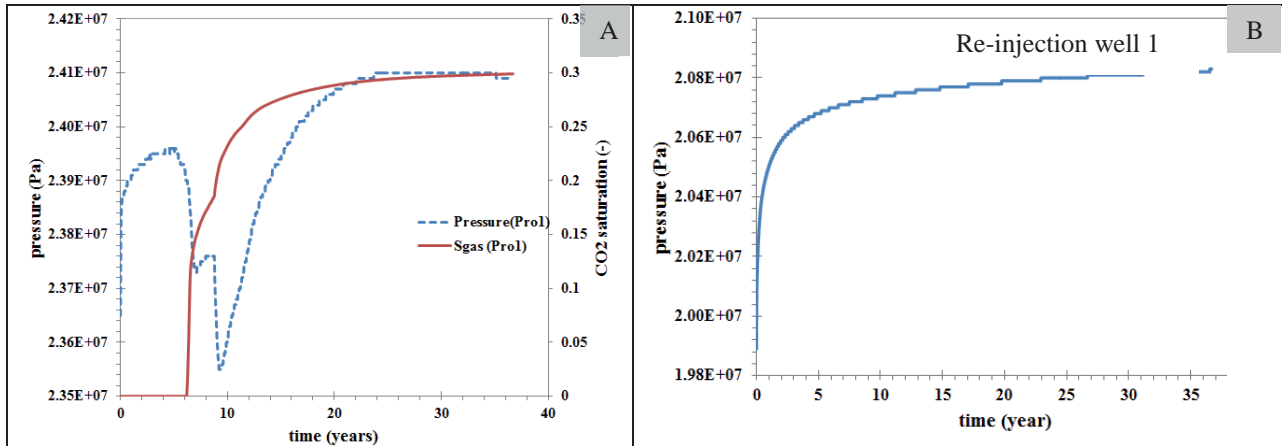
Fig. 7.16 Pressure changes in the production well (A) and in the re-injection well (B)

The configuration of the wells plays a significant role in controlling the breakthrough time (Ganjdanesh et al., 2012). For example, when production wells are completed at the bottom of the aquifers (horizontally away from injection well), breakthrough time can be delayed to 20 years, even under a high production rate (10 kg/s). A larger pressure difference between injection and production wells promotes a much faster flow of liquid and CO$_2$ towards the production well (Fig. 7.17A). The mass fraction of CO$_2$ in the production well is less compared with that when the production well is completed in the upper locations with a production rate of 2 kg/s, which enables a smaller flowing enthalpy (maximal value 370 kJ/kg) in the production well (Fig. 7.17B).
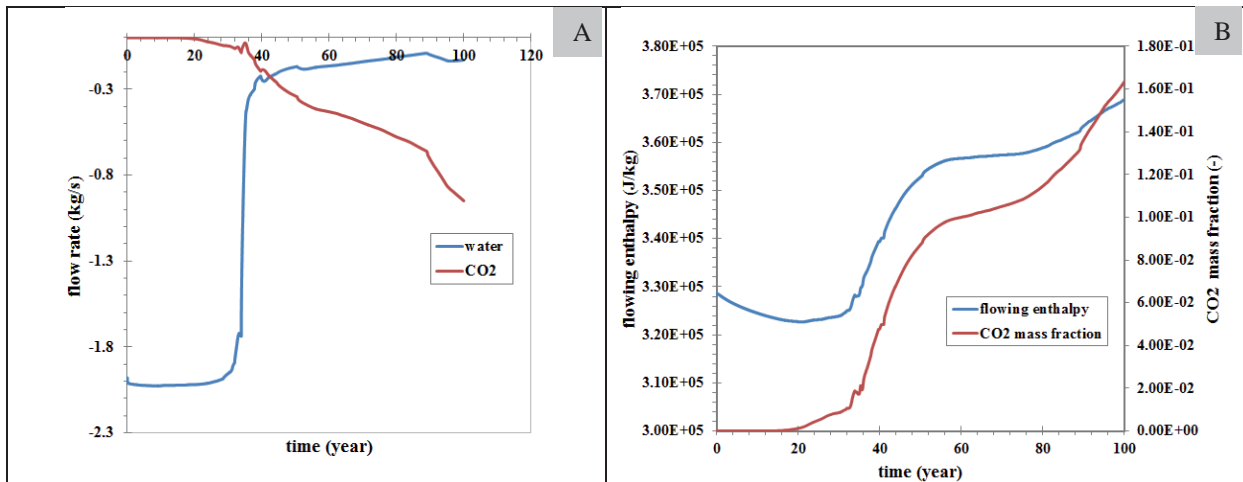
Fig. 7.17 Flow rate and flowing enthalpy changes with time in production well (negative value represents the flow direction from element to production wells): (A) CO$_2$ and water phase flow rate; (B) flowing enthalpy and CO$_2$ mass fraction changes

8. Site selection criteria for CO_2-aided hydrothermal production

When CO_2 is used to increase the reservoir pressure or as the circulating fluid in a geothermal system, it is related with a series of engineering, scientific and policy management issues. The process can be divided into four distinct stages, which is similar to a CO_2 sequestration project: site selection and development, operations, closure and post-closure.

In a specific CO_2 sequestration project, capacity, injectivity and caprock integrity are the three main factors that need to be considered (Bachu, 2003; Gibson-Poole et al., 2006; Cooper, 2008). Similarly, when CO_2 is involved in the production of geothermal energy, these three factors need to be addressed during the site selection process to guarantee the economic status (geothermal electricity generation amount, close proximity to the CO_2 point source, re-use of the existing infrastructure…), feasibility (large capacity and injectivity), safety (avoid leakage of CO_2 through abandoned wells and faults), environmental protection and social status (including population acceptance) of the whole system (CO2CRC, 2008; Grataloup et al., 2009).

In this Chapter, assessment of site suitability during different stages is introduced, including the corresponding criteria for the selection of a suitable workflow. Based on the screening and ranking methods for a suitable site selection of CO_2 sequestration developed in Bachu (2003), the weight factors can also be added to each criterion in order to improve the reasonability of the evaluation result. At the end, this evaluation method is used for a preliminary selection and ranking of several sedimentary basins in China, from two aspects (i.e. pure CO_2 sequestration and CO_2-aided geothermal production), before an engineering project is launched.

8.1 Site suitability evaluation

8.1.1 Evaluation processes

Before a geothermal plant project is approved at a specific site, detailed evaluation work must be carried out to ensure its suitability for development. This is a tough job, requiring precisely following a series of standard procedures. Based on the exploration level and accuracy of assessment, ranging from low to high, five stages (levels) are involved including: (1) country-level; (2) sedimentary basin-level; (3) target area of interest-level; (4) site-level; (5) engineering operation-level (Fig 8.1).

Several sedimentary basins are involved in country-level assessment. After the comprehensive ranking and screening processes, one or two basins are selected for further investigations.

At the stage of basin-level evaluation, many technologies applied in petroleum exploration can also be used in the establishment of more accurate 3D geological models, for instance, the remote sensing prospection, seismic data, well log, well cores, well production data and so on (Talley et al., 1998; Brady et al., 2006; Chadwick et al., 2008; Cooper, 2008; DOE, 2013).

In the third stage of assessment (target area of interest), a detailed survey and description of the area's geology, including the mapping of the stratigraphic formations, structures and reservoirs are carried out.

Under consideration of land ownership, further screening is needed for the optimization of the construction site. Site-scale comprehensive studies of geological investigation, geophysical exploration, well drilling, small scale injection experiment, dynamic monitoring and numerical simulations are carried out to make a reasonable plan of injection and production scheme.

After a successful operation of the small scale injection experiment and a better understanding of the geological characteristics of formations, long-term engineering operation will start. Geophysical exploration, geochemical prospecting, core sample collection and related experiments, improved

206

numerical simulation methods are required at this stage. Environment, safety risks and economic assessments of the engineering operation-level are needed during the whole lifespan of injection and production.
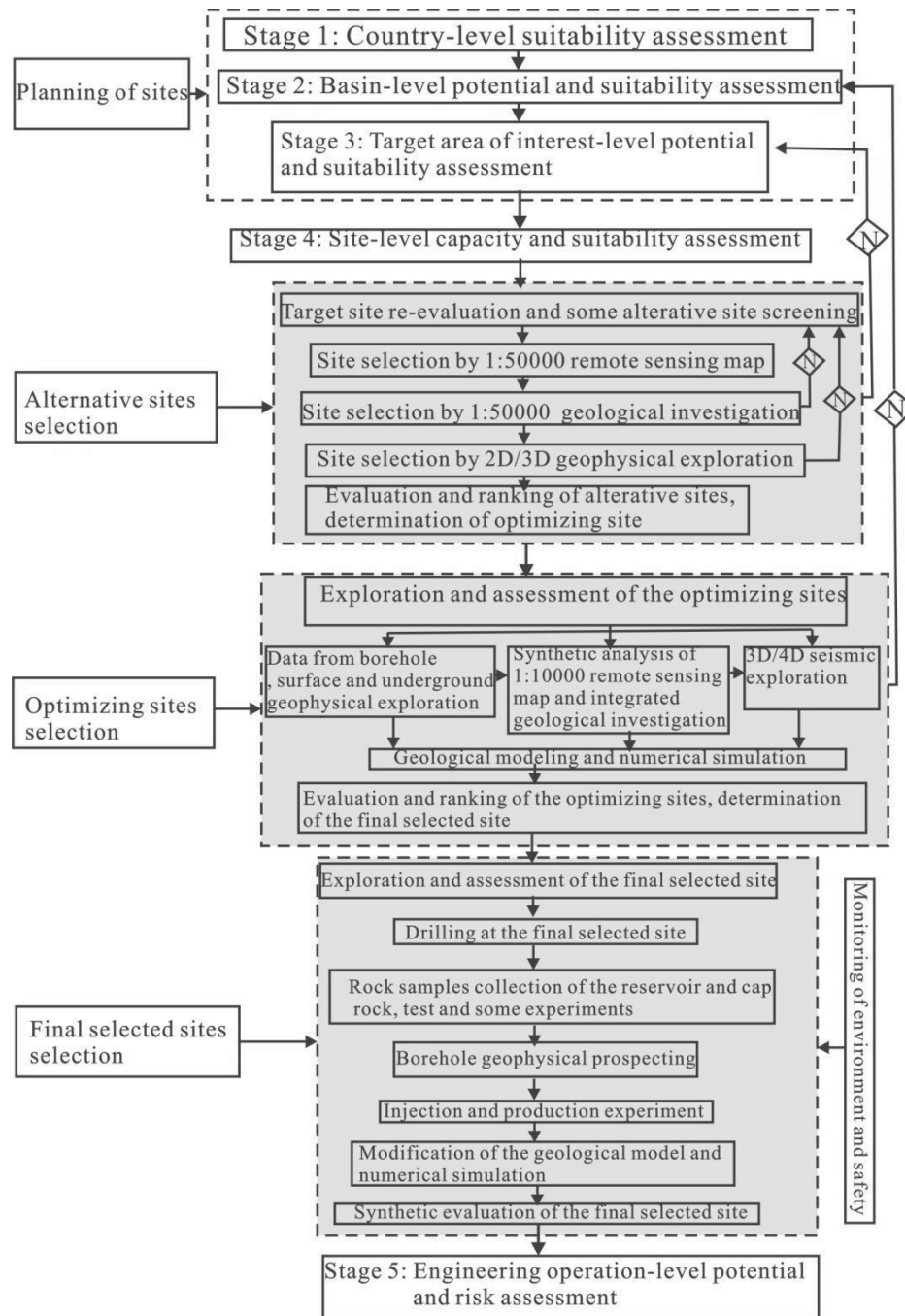
Fig. 8.1 General evaluation procedure of suitable site for geothermal production associated with CO$_2$ sequestration (Zhang et al., 2011; modified)

Based on the characteristics of a specific basin planned for geothermal production and CO$_2$ sequestration, reservoirs can be divided into four main types: **I.** low temperature hot dry rock; **II.** high temperature hot dry rock; **III.** low temperature hydrothermal type; and **IV.** high temperature hydrothermal type. Different types of reservoirs can serve different purposes and optimal site selection plan can be established accordingly (Fig 8.2). For example, type **I** reservoirs can not be used in the near future. EGS (enhanced geothermal system) technology can be adopted by type **II** reservoirs. Type **III** reservoirs can be used for pure CO$_2$ sequestration purpose and type **IV** reservoirs can be regarded as CO$_2$-driven or - aided geothermal systems. Three factors are mainly considered in evaluation processes, namely economic

status, safety and environmentally friendly consideration. Considering the beneficial demands of investors, economic calculation is necessary before the detailed operation starts, followed by site-scale, target formation-scale and engineering operation-scale assessment (safety and environmental protection).
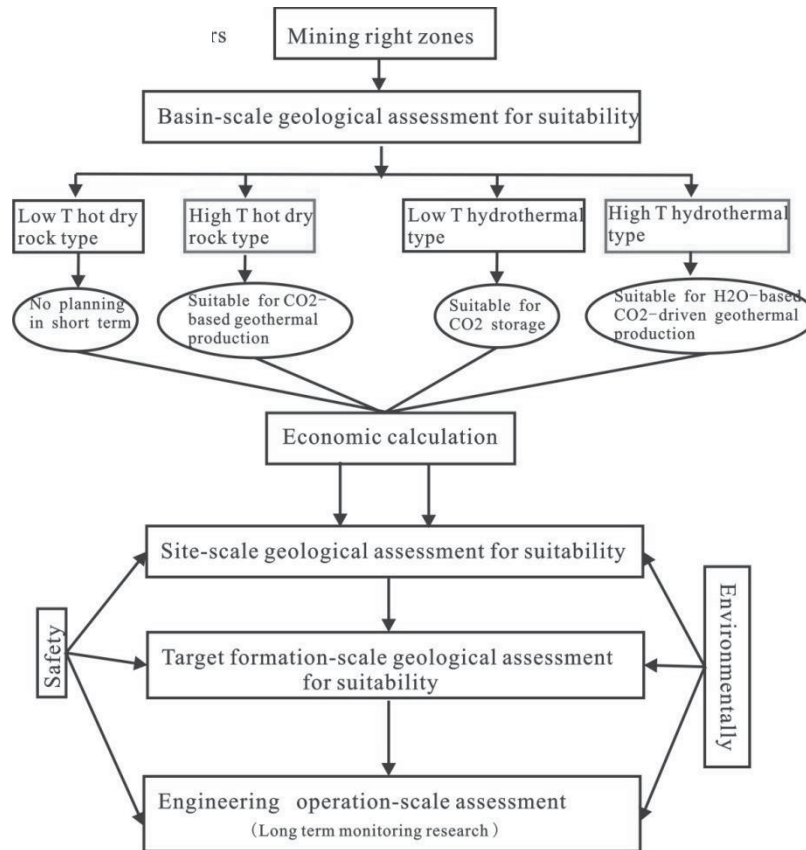
Fig. 8.2 Geological suitability evaluation system for different types of reservoirs

8.1.2 Site selection criteria

In the stepwise geological assessment for an optimum site served for two systems of CO$_2$-aided geothermal production and pure CO$_2$ sequestration purposes, three or four aspects are considered in detail, based on the degree of importance (Table 8.1). Take CO$_2$-driven or -aided geothermal reservoirs as an example, several requirements, such as efficiency, safety and environmental friendly conditions should be satisfied.

8.1.2.1 Basin-scale

Temperature gradient determines the efficiency of a geothermal system. Based on the temperature level, three types of geothermal resources are identified (Tester et al., 2006): high temperature ($T \geq 150$ $^{\circ}$C), middle temperature ($150 \, ^{\circ}$C $> T \geq 90 \, ^{\circ}$C) and low temperature (T $< 90 \, ^{\circ}$C). Geothermal resources in a specific basin should be carefully estimated before drilling and production, from different aspects, for example, storage heat capacity (J), fluid volume in the reservoir (m^3), the available production amount of geothermal fluid (m^3/day or m^3/year) and the available heat energy (J). High temperature gradients (i.e. a high enthalpy at a relative shallow depth) can save drilling costs. Thus, during basin-scale selection phase, temperature gradient is a major factor in economic evaluation. Other factors of importance include basin area, water content, permeability and porosity of the reservoir, CO$_2$ source, salinity, etc.

From the safety aspect of view, two main categories are used: crust reliability and caprock integrity. Crust reliability relys on the structural setting, density of small faults and fractures, amount of large active faults, fault sealing characteristics, frequency of seismic activity, seismic magnitude etc. Structural setting factor plays a great role in the safety assessment of CO$_2$-aided geothermal production and pure CO$_2$

208

sequestration. Extensional craton basin is the most optimal site with the highest level 5, followed by the extensional inland rift basin with a level 4, and the extensional continental shelf basin with level 3. Compressional structural setting is bad for both pure CO_2 sequestration and CO_2-aided geothermal production systems, such as compressional intromonate (level 2) and compressional oceanic basin (level 1). All other factors are ranked in the similar way as the criterion of structural setting. When integrity of caprock is assessed, mineral composition, thickness of caprock (direct or multilayered), impermeability of caprock, lateral continuity of caprock and the density of drilling wells in the basin have to be ranked and graded.

Environmental friendly considerations include two aspects: public social environment and the geographic environment. Public acceptance is the key factor determining whether a CO_2-aided geothermal production project can be successfully carried out or not. Besides, geographic environment also determines the security of a construction site and its efficiency. Some un-predicted/natural factors, especially geo-hazards (debris flow, hurricane, earthquakes, etc) will also result in a delay of the project.

8.1.2.2 Field-scale

Once an optimum site is determined, the surface engineering infrastructure will be set up for drilling wells (e.g. injection, production and monitoring wells). Therefore, geological assessment at field scale is essential for the economic evaluation of the project. Once some risks occur during long-term operations, for instance, CO_2 leakage or blowout (Wiprut and Zoback, 2000), the costs for a well workover will be very high, or even leading to abandonment of a project or a threat to life. Besides, the engineering operation at the field site will also affect the environment of the surrounding residential area. Therefore, more detailed criteria should be supplemented in the evaluation system. Several alterative field sites should be compared before the best field site is confirmed.

8.1.2.3 Target formation-scale

The properties of a target formation has a direct relationship with efficiency of both pure CO_2 storage and CO_2-aided geothermal production, which is preferred for large thickness, high porosity and permeability, large initial water content, high temperature etc. Take CO_2-aided geothermal production as an example, it is economically efficient if the heat energy can be transferred into electric power, depending on a high reservoir temperature, water content, water recharge rate and so on. Besides, the impermeable properties of the direct and multi-layered indirect caprock are vital for the safety of the project. As a result, geological assessment on target formation-scale suitability should be done more carefully. After a series of selection and ranking processes, the optimum target formation should be selected.

8.1.2.4 Engineering operation-scale

Engineering operations related with pure CO_2 sequestration and CO_2-aided geothermal production include: well number and types (horizontal, vertical, multilateral wells etc.) and operation strategies (CO_2 injection amount; injection/production rate, well head pressure; injection temperature etc). All these factors may affect the economy and safety of the project.

The field-scale and target formation-scale dynamic geological models can help to determine the plan of engineering operations. For example, reservoir characteristics will have a great impact on well configuration (e.g. well count, well density etc), and thus the injection strategy (Cooper, 2008).

A reasonable operational strategy will favor the proper flowing rates and limited pore pressure buildup in order to guarantee the safe operation (below the maximum injection pressure). When pore pressure buildup is larger than the rock fracturing pressure due to a large amount of CO_2 injected, CO_2

leakage along fractures, caprock, abandoned wells may be possible. As to the economy of geothermal production, movement of CO_2 plume and the related pressure transport may have great effect on the circulation rate of hot water. Therefore, a reasonable engineering operation scheme plays a big role in the assessment of the geothermal production well during the efficient life-span period.

Table 8.1 Evaluation indicator system for a suitable site selection of CO_2-aided geothermal production (Bachu, 2003; Zhang et al., 2011, modified)

I	II	III	Specific indicators	Good 5	Very good 4	Normal 3	Very poor 2	Poor 1
Basin scale	Safety requirement	Crust reliability	Structural setting	Extensional ~ Craton Basin	Extensional ~ Inland rift basin	Extensional Continental shelf	Compressional intromonate	Compressional Oceanic basin
			Density of small faults and fractures	Limited		Some		Large
			Density of large active faults	No				Yes
			Fault sealing characteristics	Good	Very good	Medium	Very bad	Bad
			Seismic safety level	High		Middle		Low
		cap ock integrity	Lithology	Rock salt	Mudstone	Tight limestone	Shale	Siltstone
			Direct caprock thickness / (m)	>20		10 ~ 20		<10
			Multiple caprock thickness/ (m)	>300		150 ~ 300		<150
			Lateral continuity	Regional continuity		Middle continuity		Non-continuity
			Caprock impermeability	Good		Normal		Bad
			Density of drilling wells or abandoned wells	0	1 ~ 2/10 km, shut in with cement	3 ~ 5/10 km, shut in with cement	5 ~ 10/10 km, open	>10/10 km, open
	Economic evaluation	reservoir properties	Basin area/ 10^4 km^2	Supergiant (>1000)	Giant (50 ~ 100)	Large (10 ~ 50)	Middle (1 ~10)	Small (< 1)
			Depth / m	>5000	4000 ~ 5000	2000 ~ 4000	1000 ~ 2000	< 1000
			Effective storage capacity/ 10^4 t	Large (>900)		Middle (300 ~900)		Small (<300)
			Geothermal gradient /(°C/km)	>50	40 ~ 50	30 ~ 40	20 ~ 30	< 20
			CO_2 source	Supergiant	Giant	Large	Middle	Small
			Surface temperature	>25	10 ~ 25	3 ~ 10	-2 ~ 3	< -2
			Salinity /(g/L)	< 1	1 ~ 10	10 ~ 50	50 ~ 250	> 250
	Environmental evaluation	Social support	Social approval degree	High		Normal		Low
		Geographical conditions	Distance from potential geohazard site	Far		Normal		Near
			Residential density	Scatter		Normal		Dense

211

		Field demonstration scale			
Technical issues		**Economic evaluation**			**Safety**
		Well configuration	CO$_2$ supply	Electricity capacity	General
Corrosiveness of CO$_2$ — Corrosion resistant pipeline / Normal / Low-performance pipe					
Security of supply — High safety / Normal / Low safety					
Power supplies to the pumping stations — Adequate / Normal / Lack					
Well network		4 spot / 5 spot / > 9 spot			
Well spacing		<500 / 1 ~ 2 km / >2 km?			
Distance from CO$_2$ source / km, costs			<100, low / 100 ~ 200, middle / >200, high		
Size of CO$_2$ source / (10kt·a^{-1})			>25 / 10 ~ 25 / <10		
Infrastructure situation			Complete / Middle / Uncomplete		
Ore-bearing in upper or lower layers			No / — / Yes		
Cost of connecting to the electric grid				Low / Middle / High	
Distance of electric transmission				Close / Middle / Far	
Long-term large-scale operation capacity				Yes (>50 years) / Medium (30 ~ 50) / No (<30 years)	
Large vertical active fault					No / — / Yes
Abandoned wells in the injection area					No / — / Yes
Distance from residential area / m					>1000 / 800 ~ 1000 / < 800
Governing wind direction compared with residential area					Down wind / Normal / Up wind
In recharge area of ground water					No / — / Yes
Distance from river or water reservoir /m					>150 / — / <150
Geohazard emergency					No / — / Yes

Engineering operation scale	Target saline formation scale					
Safety and Economic	Economic evaluation					Safety
Operation strategy	General					
Whether there is ground water aquifer above-CO_2 storage formation	No					Yes
Shallow reinjection layer	Yes					No
Breakthrough pressure of main caprock	Large					Small
Secondary caprock performance	Multiple, good	Single, medium				No, bad
Formation temperature	>150	90 ~ 150	60 ~ 90	32 ~ 60		<32
Formation depth	>3500	2000 ~ 3500	1500 ~ 2000			<800
Formation thickness / m	>80	30 ~ 80	30 ~ 80			<30
Formation water salinity / ($g \cdot L^{-1}$)	<3	3 ~ 10	10 ~ 50			>50
Formation porosity /% — Sandstone	>15	10 ~ 15	10 ~ 15			<10
Formation porosity /% — Carbonate	>12	4 ~ 12				<4
Formation permeability / mD — Sandstone	>50	10 ~ 50				<10
Formation permeability / mD — Carbonate	>10	5 ~ 10				<5
Geothermal use	Electricity	Direct use		Heat pumps		Heat pumps
Cost of exploration	Low	Middle				High
Distance from residential area / km	<10	10 ~ 50				>50
Effective storage amount / 10^4 t	>900	300 ~ 900				<300
Economic service life	>30					<30
Injectivity index / m^3	$>10^{-14}$	$10^{-15} \sim 10^{-14}$				$<10^{-15}$
Effective storage ratio / %	>8	2 ~ 8				<2
Well head pressure / Pa	$< P_b$ and P_f	$= P_b$ and P_f				$> P_b$ and P_f
Total injection amount / (m^3)	< Storage amount	= Storage amount				> Storage amount
Injection rate / ($m^3 \cdot s^{-1}$)	Maintain a state without fracture emergence in formation	Fracture emergence in formation				Fracture emergence in formation

where P_b is caprock breakthrough pressure and P_f is formation fracture pressure

213

8.1.3 Screening and ranking methods

According to site selection criteria at different scales, from basin scale → field demonstration scale → target saline formation scale → surface operation scale, a systematic, quantitative evaluation method for site selection at different scales in terms of their corresponding suitability is set up in order to serve CO_2-aided geothermal production. The ranking and screening method used in this thesis is based on parametric normalization and ranking system presented by Bachu (2003). It can be further developed by adding more parameters or more detailed weight factors.

Take the suitability assessment of a specific site at basin-scale for CO_2-aided geothermal extraction for an example, each criterion is listed in Table 8.2. The detailed evaluation method is similar to that described in Bachu (2003). A monotonically-decreasing numerical function S_i is assigned based on the the score grade j (where $j=5$ to $j=1$ are characterized as the best to the worst grade in terms of suitability of a particular criterion), which can be continuous or discrete. For example, scores can be assigned for all the five grades, or only three or four grade levels can be assigned scores for the corresponding criterion. Here, symbol i is the index of the criterion and j is the score grade level.

For a specific sedimentary basin k needed to be evaluated in terms of its general suitability for CO_2-aided geothermal production, the corresponding score grade j with respect to a specific criterion i is determined, resulting in a suitable score $S_{i,j}$. As the function S_i has different ranges of values for each criterion i, the comparisons between different scales of site selection assessments may be difficult. Therefore, it is vital to use a normalized value in selection of a suitable site at different scales, as in Bachu (2003). Hence,

$$P_i^k = \frac{S_{i,j} - S_{i,1}}{S_{i,n} - S_{i,1}}, \tag{8.1}$$

where $S_{i,j}$ is the specific score value for criterion i at grade level j, $S_{i,1}$ is the score under the least favorable class condition ($j=1$) for criterion i, $S_{i,n}$ is the value under the most favorable class condition ($j=n$), the normalized value $P_i=0$ stands for the least favorable class and $P_i=1$ means the most favorable class.

After evaluation of all available criteria, 18 individual scores ($P_1, P_2, P_3, ... P_{18}$) can be calculated for a specific sedimentary basin with 18 criteria. The normalization method can transform characteristics of various sites at different scales (basin, demonstration field, target formation and surface infrastructure), into dimensionless variables between 0 and 1. Considering the weight factor of each criterion, a general score R^k can be obtained which is used in ranking processes.

$$R^k = \sum_1^{18} \overline{\overline{w}}_i P_i^k, \tag{8.2}$$

where $\overline{\overline{w}}_i$ is the weight factor that is used to estimate the impact degree of criterion i, which can satisfy the following relationship:

$$\sum_1^{18} \overline{\overline{w}}_i = 1, \tag{8.3}$$

Table 8.2 Scores and weights assigned to various criteria and classes for assessing the suitability of a specific basin for CO_2-aided geothermal production (Bachu, 2003; Zhang et al., 2011, modified)

Class I	Class II	Criteria	Index i	Scores j=5	j=4	j=3	j=2	j=1	Weight
Basin scale	Safety requirement	Structural setting	1	15	15	7	3	1	0.10
		Density of small faults and fractures	2	21	13	7	3	1	0.03
		Fault sealing characteristics	3		15	7	3	1	0.04
		Seismic safety level	5		15	7	3	1	0.10
		Drilling wells or abandoned wells density	6			7	3	1	0.05
		cap rock integrity — Caprock lithology	7	11	9	7	3	1	0.05
		Direct caprock thickness	8			7	3	1	0.03
		Multiple caprock thickness	9			7	3	1	0.04
		Lateral continuity	10			5	3	1	0.03
	Economic evaluation	Basin area/ 10^4 km^2	11		9	5	3	1	0.06
		Depth / m	12			5	3	1	0.05
		Effective storage capacity/ 10^4t	13			5	3	1	0.06
		Geothermal gradient /(^{o}C/km)	14			7	3	1	0.12
		Water salinity / (g/L)	15			7	3	1	0.06
		Surface temperature	16			7	3	1	0.03
		CO_2 sources	17		15	7	3	1	0.06
		Onshore/offshore	18			7	3	1	0.10

8.2 Examples: basin-scale suitable site selection in China

China mainland is composed of several Precambrian platforms surrounded by accreted terrain and fold belts of different ages (Fig. 8.3; Wang, 2001), including the Sino-Korean platform, the Yangtze platform, and the Tarim platform. The collision of the Sino-Korean and Tarim platform with the Siberian craton in the north resulted in the Tianshan-Beishan and Hinggan-east Mongolia fold belt at the northwestern and northeastern part of China, respectively. The Qinling-Dabie fold belt formed due to the collision of the Yangtz and the Sino-Korean platforms in the early Mesozoic era (Ren, 1999).
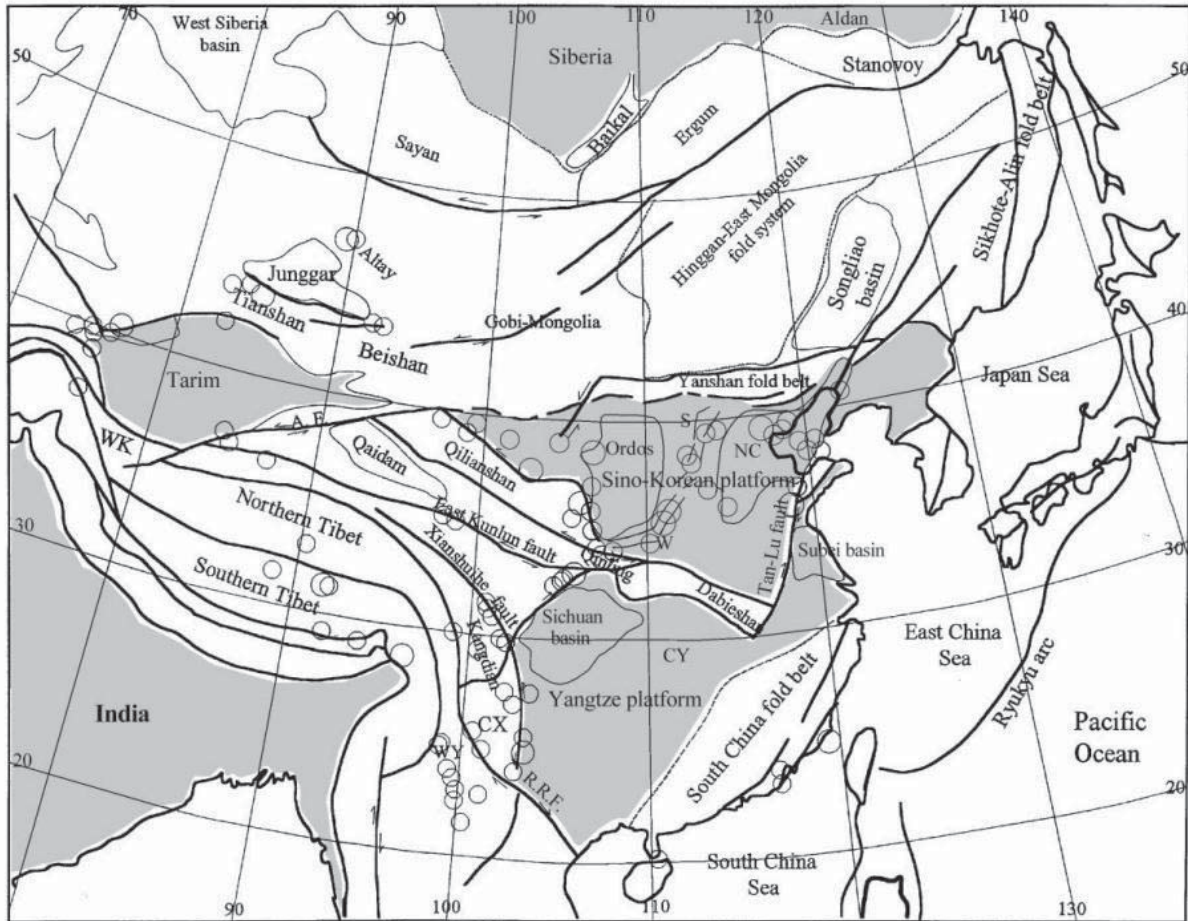
Fig. 8.3 Tectonic sketch map of China mainland and its adjacent areas (Wang, 2001) Shaded areas represent cratons or platforms; circles represent epicenters of the strong earthquakes (M $\geq$ 7). A.F.: Altyn-Tagh fault; CX: Chuxiong Basin; CY: central Yangtze; NC: North China Basin; R.R.F: Red River fault; S: Shanxi graben; WK: West Kunlun; WY: Western Yunnan.

According to the dynamic mechanism, sedimentary basins in China can be divided into five types (Zou et al., 2008): 1) East Asia island arc-marginal sea basins (e.g. the Donghai, Zhujiangkou and Yingqiong basins); 2) East continental sea back arc rift basins (e.g. the Songliao, Bohaiwan and Huanghai-Subei basins); 3) Middle stable craton basins (e.g. the Ordos Basin) and 4) Northwest compression-inversion intromonate basins (e.g. the Tarim, Zhungeer, Chaidamu and Tuha basins) and 5) Tethys type basins characterized by strong collision and uplift (e.g. the Sichuan, Kunming and Qiangtang basins).

The heat flux contour map of China (Fig. 8.4) shows a zoning characteristic (Tao and Shen, 2008): high in the east and southwest and low in the central and northwestern regions (Tao and Shen, 2008). The heat flow pattern in China is mainly controlled by the lithospheric scale tectonic activities of Meso-Cenozoic period, for instance, the India-Eurasia collision in the west and the Cenozoic tensile fracturing movement in the east (Chi, 1988; Wang, 2001). The high heat flow belt lies in southern Tibet (> 75 mW/m^2), also called the Southern Tibet-western Yunnan geothermal belt, which turns southwards into the western Yunnan (70-90 mW/m^2) in Burma and northern Taiwan (Wang, 2001). The Zhungeer and Chaidamu basins have a relatively lower geothermal flux value of about 35-45 mW/m^2; heat flow in the Tarim basin is about 45-55 mW/m^2, with a relatively higher value of 90-100 mW/m^2 along the western boundary. Basins distributed in the middle area of China have, on average, a low heat flux (e.g. about 60 mW/m^2) for the Ordos and North China basins, while the Sichuan Basin has a much lower geothermal flux of only 50-60 mW/m^2. Basins in the eastern part of China, are dominated by the Cenozoic taphrogeny, and have relatively higher average heat fluxes compared to those in the middle part of the

216

mainland: e.g. the Songliao Basin (70 mW/m^2), Hinggan-east Mongolia fold system (55 mW/m^2), Subei Basin (72 mW/m^2), South China fold belt (72 mW/m^2) etc.
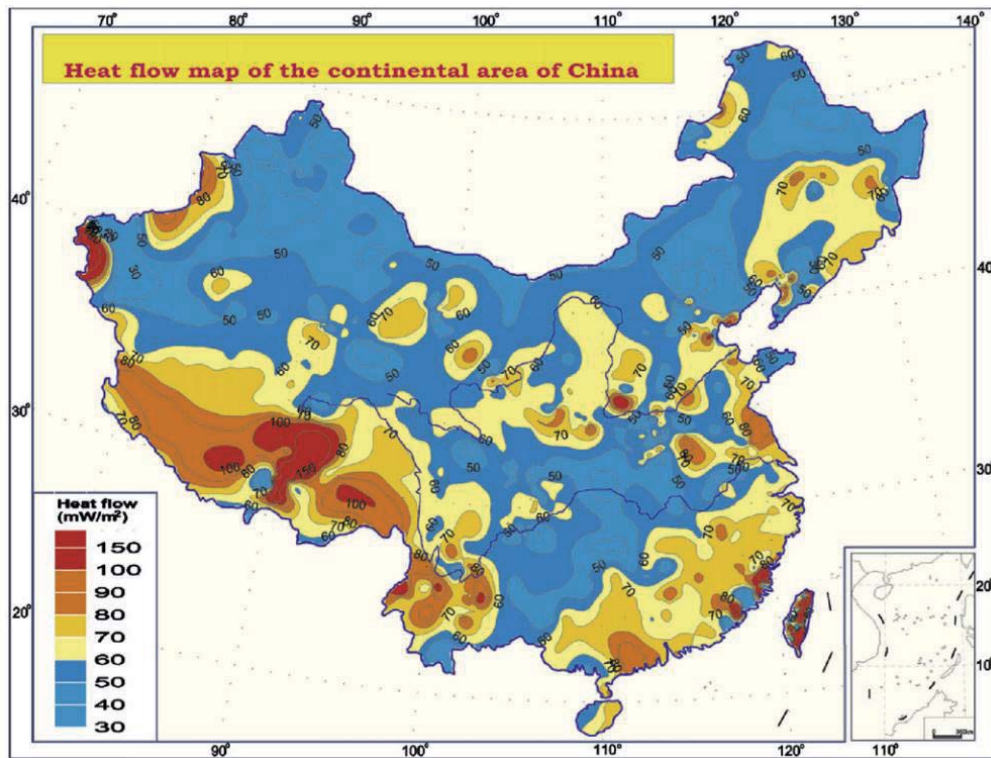
Fig. 8.4 Heat flux contour map of China (Tao and Shen, 2008)

Using the selection and ranking methods described in Section 8.2.3, 14 sedimentary basins in China have been evaluated for suitability of two purposes, i.e. CO$_2$-aided geothermal production and pure CO$_2$ sequestration based on their respective geological characteristics (Table 8.3). Temperature has totally opposite effects on these two purposes, which means, a high temperature gradient is positive for CO$_2$-aided geothermal production and negative for the storage capacity of pure CO$_2$ underground. This is the reason that the density of supercritical CO$_2$ decreases with increased temperature (Bachu, 2003). Besides, salinity of water is also a key factor affecting the economy of geothermal production, considering the costs for water disposal (Ren et al., 2011). When hot high salinity water cools down, precipitation of silica scale takes place. This precipitated scale may be problematic for the geothermal power plant (Gudmundsson and Einarsson, 1989; Sugita et al., 1999; Ueda et al., 2003; Gunnarsson and Arnorsson, 2005). In pure CO$_2$ sequestration projects, there are no rigid requirements for the salinity of water. Accessibility to electric grid is also another consideration for the economy of a geothermal power plant. For these reasons, some criteria in Table 8.2 are totally different before being used in the suitability assessment of pure CO$_2$ sequestration and CO$_2$-aided geothermal production.

Based on the characteristics of geothermal resources in different regions, other criteria are also necessary for CO$_2$-aided geothermal production and pure CO$_2$ sequestrations (Chen et al., 1994; Hu et al., 2000; Tian et al., 2006; Liu et al., 2013b). Prelimary studies have shown that some potential regions can satisfy geothermal electricity requirements, for instance, the south Tibet area and western Yunnan (Chuxiong and Kunming basins), west of Tarim basin and south China fold belt, while some other regions have the potential to produce hot water or develop the hot spring, including the Bohaiwan, south Huanghai-Subei and Songliao basins, etc., Fig 8.5. The top three basins for pure CO$_2$ sequestration are Tarim, Ordos and Chaidamu basins, considering safety, economy, environmental friendly, feasibility.
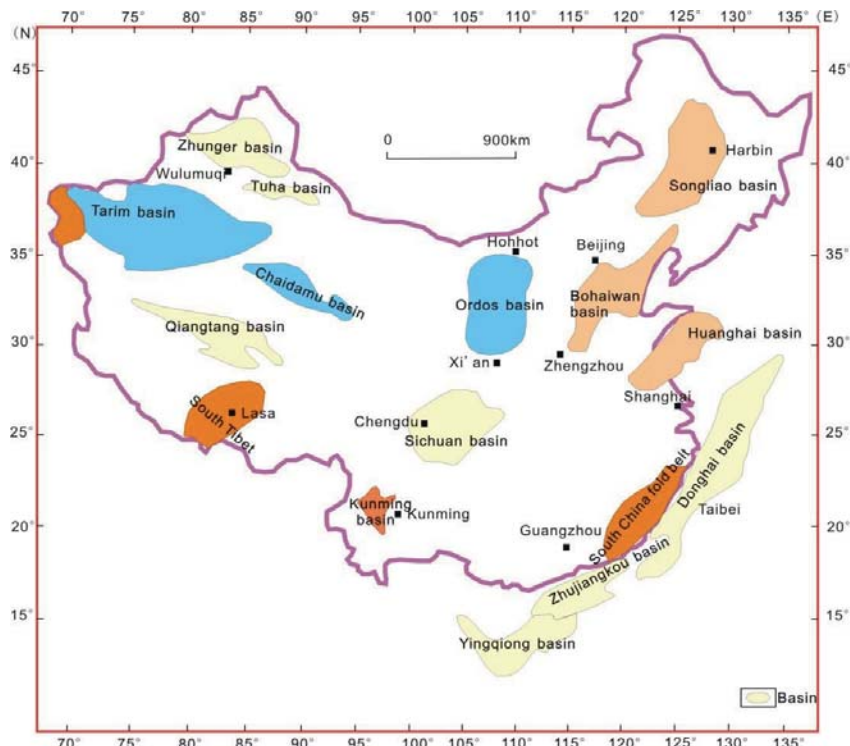
Fig. 8.5 The suitability of geothermal production of several main sedimentary basins in China (Wang et al., 2012a; Zou et al., 2008; modified) Blue color represents suitability for CO$_2$ sequestration only; dark orange color illustrates the availability of geothermal electricity requirement; light orange color is available for low-middle geothermal production (space heating or hot water use); light yellow shows the unfavorable feasibility for both in present.

Table 8.3 shows the characteristics of the main sedimentary basins and their scores based on the screening and ranking method in terms of suitability, for two different systems of CO$_2$-aided geothermal production and pure CO$_2$ sequestration. Although the table depicts that the Bohaiwan Basin has a great potential for geothermal production, however, the basin's medium geothermal gradient demonstrates that its hot water is not suitable for electric power generation. The Songliao basin also has a great potential for hot water production. Besides, large CO$_2$ point sources and hydrocarbon exploration in Songliao basin also provides its feasibility for CO$_2$-EOR or CO$_2$-EGR at the same time (Shen et al., 2007; Hao and Song, 2010). The Qiangtang basin is also possible for geothermal production (electricity purpose). However, the lack of adequate infrastructure and electricity in the local area may limit its development of geothermal production.

For pure CO$_2$ sequestration purpose, the top suitable three basins are the Ordos, Tarim and Bohaiwan Basins. If, however, storage costs and capacity are considered, the sequence should be Bohaiwan, Sichuan, Southeast Zhungeer and Subei Basins (Li et al., 2006). The evaluation results, however, do not mean that all regions in the basin have equal suitabilities. More detailed data, for instance, geological data, tectonic setting, maturity, etc., in these basins is needed for a better field-scale suitability assessment.

Table 8.3 Ranking of China's sedimentary basins in terms of their suitability for CO_2-aided geothermal production and pure CO_2 sequestration

Area	Basins	Characteristics	Reservoir type	CO_2-aided Geothermal production (score R^k)	Pure CO_2 storage (score R^k)
1	Tarim	1.5-2.5 ^oC/100 m, giant, foreland basin (compressional), rich in oil, gas, coal and salt, small point CO_2 sources, porosity 4-20%, permeability 0.1-100 mD,	Low T	0.52	0.64 ★
2	Donghai	On-offshore, giant, high geothermal flux, marginal sea basin (extensional), rich in oil, gas and methane hydrates,	Middle T	0.56	0.52
3	Zhungeer	1.5-2.5 ^oC/100 m, foreland basin (compressional), rich in oil, gas and coal, small point CO_2 sources,	Low T	0.52	0.62
4	Ordos	2.5-3 ^oC/100 m, high salinity water, cratonic basin (NE-SW compressional, NW-SE tensional), rich in oil, gas and coal, large point CO_2 sources, porosity 2-15%, permeability 0.01-10 mD,	Low to middle T	0.51	0.72 ★
5	Sichuan	2.5-3 ^oC/100 m, high salinity, foreland basin (compressional), rich in oil, gas, coal and brine, large point CO_2 sources, porosity 3-12%, permeability 0.001-100 mD, good infrastructure,	Low to middle T	0.42	0.52
6	Songliao	3.0-4.5 ^oC/100 m, 1 g/L, back-arc rift basin (extensional), large point CO_2 sources, porosity 0.5-18%, permeability 0.1-1 mD, good infrastructure,	Low to middle T	0.64 ★	0.61
7	Qiangtang	2.5-4.0 ^oC/100 m, graben basin(compressional), small point CO_2 sources, unexplored,	High T	0.52	0.52
8	Chaidamu	2.0-3.3 ^oC/100 m, foredeep basin (compressional), small point CO_2 sources, porosity 25-30%, permeability 100-600 mD,	Low to middle T	0.49	0.49
9	Bohaiwan	3.5-4.5 ^oC/100 m, back-arc rift basin (extensional), rich in oil, gas, coal and gypsum, high water quality(<1 g/L) and rich in hot water, large point CO_2 sources, large CO_2 emissions, good infrastructure	Middle T	0.71 ★	0.65 ★
10	Huanghai-Subei	On/offshore, 2.5-3.5 ^oC/100 m, rich in hot water, back-arc rift basin (extensional), rich in oil, gas, coal and salt, large point CO_2 sources, good infrastructure,	Middle T	0.58 ★	0.55
11	Zhujiangkou	On-offshore, high geothermal flux, marginal sea basin (extensional), rich in oil and gas	Middle T	0.55	0.48
12	Yingqiong	Offshore, high geothermal flux, marginal sea basin (extensional), porosity 12-25%, permeability 0.02-100 mD,	Middle T	0.42	0.30
13	Tuha	1.5-2.5 ^oC/100 m, depressed basin (compressional), small point CO_2 sources,	Low to middle T	0.30	0.40
14	Kunming	1.5-3.0 ^oC/100 m, small, graben basin (compressional),	Middle to high T	0.35	0.31

9. Conclusions

Based on the review studies on the geological characteristics of the Ordos Basin and a series of numerical realizations on the physo-chemical interactions induced by CO_2 injection from two phase fluid flow of CO_2 and water (H^2), hydro-mechanical response (H^2M), hydro-chemical interaction/CO_2-water-rock interactions, the extended application of CO_2 as a pressure-driven fluid in hydrothermal systems and the concluded site selection criteria and system for CO_2-aided hydrothermal system, some conclusions can be obtained:

9.1 Geological characteristics of the Ordos Basin

Simulations carried out in this thesis are based on parameters obtained by field investigations at a specific site in the Ordos Basin, at which an integrated CCS project "from CO_2 capture to storage in deep saline formations" was launched. The multilayer injection of CO_2 into four saline formation layers was started in 2011, and about 0.6-0.7 Mt of CO_2 has until today been injected. The efficiency and safety of CO_2 sequestration is site specific, significantly varying with the geological heterogeneities in the basin, including regional and local tectonic stress distributions, sequence stratigraphy and sedimentary paleo-geography, reservoir and caprock properties (i.e. porosity, permeability, pore structure, mineral and fluid composition) etc. A detailed study of the geological characteristics of the basin is very helpful for the selection of suitable site for the long-term storage of CO_2 in the geological underground. The uncertainty with the geological characteristics has a direct relationship with the safety of CO_2 sequestration. The presence of active faults and potential open fractures may accelerate the leakage of CO_2 in the long term. Reservoir continuity, especially the sandbody lateral connectivity may affect the movement of CO_2 plume and pressure perturbation pattern. Underground water flow/recharge rates play a great role in the solubility or mineral sequestration of the injected CO_2. Besides, pore structure type and pore volume sizes are the main factors that influence the evaluation of storage capacity of reservoir for CO_2. Mineral compositions and mechanical properties of reservoir and caprocks impart a great influence on the integrity and safety of CO_2 sequestration.

Using an extensive review from a large collection of literature including field investigations this study has been able obtain some basic geological characteristics of the Ordos Basin. Though the Ordos Basin is generally stable, there are still a lot of faults and fractures, in particular the four groups of strike faults 30 km away from the CCS pilot project, which in the long-term may offer leakage paths for the CO_2 fluid, when commercial scale storage is launched. The regional tectonic stress field is characterized as compressional (σ_H) in the NE-SW direction, and tensional (σ_h) in the perpendicular direction.

The sedimentary facies in the Upper Paleozoic strata are mainly features of the continental integrated system, i.e. the alluvial fan-alluvial delta-fluvial delta-shallow lake system. Various sub-facies have been spatially and temporally developed in the basin. Reservoir sandstone is laterally discontinuous, due to the changes in the sedimentary facies. The vertical stratigraphic sequence is made up of a multi-layer reservoir and cap rock structure.

Groundwater system in the basin is distributed (from boundary to the center) into the following patterns: the boundary karst water system, the eastern loess area ground water system (clastic rock fracture water) and the Cretaceous artesian basin ground water system. Today groundwater flows from the boundary to the center of the basin (i.e. east to west, north to south directions) with a rate of 0.0005-0.1 cm/s. The karst water in C-J reservoir system flows very slowly and and is regarded as the target storage site for the CO_2. Some low fluid pressure zones exist due to the leak off of the natural gas into the shallow formation and the slow charge rate of water.

The sandstones of the Upper Paleozoic formation in the Ordos Basin are currently in the late diagenetic stage. Their primary pores have gradually decreased and today possess an average porosity in the range of 2-10.27%, and a permeability of between 0.1 ~ 1.36 mD. Most sandstone samples are typically marked as small aperture, low areal porosity and high displacement pressure. Sandstone typically have small apertures (in the range of 0.5 ~ 400 μm), low areal porosity and high displacement pressure, between 0.75 ~ 5MPa.

Furthermore, the sandstones are mainly composed of clastic quartz grains, rock debris, feldspar and kaolinite, which is about 85-95% of the whole rock. The secondary minerals are mainly siderite, kaolinite, overgrowth quartz, calcite, and a little chlorite, illite and hydromica. In addition, two types of mudstone are observed in the Upper Paleozoic strata, i.e. one that is associated with coal seams, and the other which is associated with fluvial sandstone. The mineral compositions of these mudstones include smectite, kaolinite (27%-35%), mixed-layers of illite and smectite (37%-42%).

Sandstones and mudstones from the Ordos Basin, however, have different mechanical properties. Young's module and Possion's ratio, for example, are in the range of 20 ~ 32 GPa and 0.16 ~ 0.23 respectively, for sandstones and 20 ~ 26 GPa and 0.21 ~ 0.28 for the mudstones.

9.2 Multiphase, multi-component fluid flow in porous media

Many physical and chemical processes control the movement and mineralization of CO_2, including fluid flow (migration) in response to pressure gradients caused by CO_2 injection or the natural hydraulic gradients, buoyancy and gravity forces induced by the density contrast between CO_2 and the formation water, molecular diffusion, dispersion and fingering effect caused by heterogeneities of formation and mobility difference between CO_2 and fluid, dissolution ability, adsorption of CO_2 onto organic matter, pore space (relative permeability) trapping and mineralization.

The fundamental characteristics of porous media are helpful for us to determine the parameters used in simulation runs. For example, the pore types (single porosity or dual-porosity), compaction of porous media, compressibility of solid skeleton and the pore fluids, wettability and so on. All of these factors can affect fluid flow processes and the fluid distribution characteristics by changing some infiltration parameters, such as end point relative permeability and capillary pressure, etc.

Different scales of research can be carried out during multiphase fluid flow in a porous medium including basin scale, near-well regional scale and pore scale. The flow paths of fluids and distribution characteristics can be significantly different in macroscopic and microscopic cases. Mass and heat transport occur along with the fluid flow process, including advection and convection in the macroscopic scale and diffusion/dispersion in the microscopic scale. Darcy's law can be widely used in describing advection of mass, which has many extensions based on different assumptions. The essential parameters used in Darcy's law, such as relative permeability and capillary pressure have different empirical functions on saturations. Molecular diffusion in rocks along the zigzag path through the inter-granular pores, can be described in Fick's law.

9.3 Simulation studies of CO_2-water two phase fluid flow in deep saline formations

TOUGH2MP has been used in this thesis to simulate the two phase (CO_2-water) fluid flow processes during CO_2 sequestration in deep saline formations. Successful application of any simulation method to investigate the CO_2-water two phase fluid flow processes in the porous media, including those whereby no mass transfer occurs between the two phases at the interface separating them and no phase equilibrium exist between the two phases, demands some assumptions for use in the mathematical model.

A CCS demonstration site in the Ordos Basin of China, characterzed by a multilayered reservoir-caprock system, has been selected and simplified for study as a simulation model. The numerical model grids are finely divided in the near wellbore region, but become larger with distance away from the wellbore. A ¼ model with the dimensional size of 1 km × 1 km × 830 m in the field scale has been used in the simulations to study the CO_2 plume movement and its associated fluid flow characteristics. Each layer in the stratigraphic sequence has been assigned specific values for parameters including porosity, permeability, thickness, residual liquid saturation, CO_2 relative permeability and capillary pressure evaluated at the residual liquid saturation, etc. Values for some of these parameters are based on actual field and laboratory data, while others, such as the density, specific enthalpy of rock and so on, were obtained from literatures. Only average values for the parameters were assigned to each formation layer. The response of the multi-layer system involves a complex interplay of formation properties, fluid properties and injection scenarios.

Based on the results of the base case study in Chapter 4, characterized as a closed lateral boundary reservoir, with four layers simultaneously injected for 1 year at the rate of 0.1981 kg/s, it has been demonstrated that the CO_2 plume zone is significantly smaller than the pressure perturbation zone. CO_2 tends to migrate laterally and upward drived by pressure buildup and buoyancy, respectively. During the injection process, the CO_2 plume front accordingly moves outward, although a large amount of CO_2 still remains behind, concentrated around the near wellbore region. Pressure perturbation is strongly temporal and spatial dependent. Temporally, the following sequence from initial hydrostatic state → disturbed pressure state → unchanged state will occur for the whole system. Spatially, pressure increase first occurs around the injection zone, and then dissipates radial toward the reservoir boundaries. Reservoir properties have great impact on pressure dissipation and CO_2 plume movement. It is easier for the plume to move laterally along the higher permeable layer, with more and more CO_2 dissolving in the saline formation brine, as time goes by. The spatial distribution of dissolved CO_2 in the aqueous phase will become complex due to advection of the pure formation brine and the brine with dissolved CO_2. Besides, perturbation between layers is obvious, especially when two injection layers are close to each other.

Several scenarios have been studied to understand the impact of the CO_2-water fluid flow process on the multilayer reservoir-caprock formation, including formation properties (tight reservoir, fractured reservoir, boundary effect etc), fluid properties (residual liquid saturation dependent relative permeability and capillary pressure) and injection strategy (injection layers, injection rate).

The numerical model has been able to provide insights into the overall behavior of the system. Nevertheless, the model is clearly limited by the scope and the restrictive assumptions. After the sensitivity analysis based on different parameters modifications, some cognition about the whole system has been obtained. The influence of parameters on CO_2 plume distance from the injection point can be ranked in the following sequence: injection rate >fractured layer (high permeable layer) > multi-layer injection > tight sandstone and mudstone properties. The effect of other parameters on CO_2 plume movement is not obvious. In the course of time, however, the distribution and movement of CO_2 plume adjust with respect to pressure dissipation. The results of this simulation study, including further field data collection will allow for reductions in uncertainties and associated increases in confidence to explore and operate large-scale field sites for sequestration of CO_2 in deep saline formations. Overall, the sensitivity analysis will help in the selection of the best modeling parameters for a realistic specific project and provide some important information before an industrial scale operation is carried out.

9.4 Coupled hydro-mechanical effect in the pilot CCS project of the Ordos Basin

Long-term safety and integrity of the sealing caprock are the key criteria to guarantee the success of any specific CO_2 sequestration project. From this point of view, a critical study of the coupled hydro-

mechanical effect can provide significant guidance into understanding the engineering management and acquisition of the optimal values for the necessary scientific parameters, including the safe maximum pressure, uplift, and CO_2 migration distance. Therefore, results of the hydro-mechanical simulation study at the demonstration CO_2 sequestration site in the Ordos Basin is indeed very highly momentous for some basic ideas required for the future planning of a CO_2 storage project on commercial scale. Below are some important results that have been derived through the TOUGH2MP-FLAC3D simulator, using data from the pilot site and the surrounding area:

1. Under consideration of coupled hydro-mechanical effect, the lateral movement of the CO_2 plume can be enlarged to some extent as being a result of the volumetric expansion of the reservoir. However, the response is different in different aquifer layers depending on a number of factors including primary stress state, reservoir pressure and characteristics of the formations (porosity, permeability, depth) etc.

2. Injection of CO_2 will affect temporal and spatial changes of the primary stress state in the injection layer. Since the reservoir pore pressure is made to increase during CO_2 injection, effective primary stresses will be reduced to some extent. Initially, the near-well region develops a relatively high pore pressure during the CO_2 injection. It needs some time for the pressure buildup to dissipate to distant regions of the whole reservoir. Vertical uplift of the multilayered reservoir-caprock model occurs at different rates in different constituent layers. With a total amount of 100 ktones CO_2 injected into the multilayered reservoir-caprock system of the Ordos Basin, till the end of the injection (1 year), uplift movement of the uppermost captock and different injection points from top to bottom (Fm. LJG, Fm. SQF, Fm. SHZ and Fm. SX) attain values of 1.95, 1.70, 1.10, 0.60 and 0.38 cm, respectively.

3. Case studies (simulation runs) have been carried out to investigate the effect of varying some key parameters (e.g. primary stress state, reservoir permeabälity and injection rate) on the simulation results, including the changes in magnitudes and characteristics CO_2 migration, vertical uplift, pore pressure and effective stress during and after CO_2 injection period. However, injection rate factor causes the largest impact, followed by reservoir permeability. The simulations have also confirmed that the reservoir permeability can significantly affect the trend of uplift, especially when injection stops. In addition, a tight reservoir will hinder the dissipation of pore pressure away from the injection point.

4. Through the analytical solution for safe maximum storage pressure, it has been established that the caprocks of SHZ formation, SX formation and the uppermost caprock layer are likely to fail when the injection rate is increased to 3.17 kg/s (1.5 Mtones CO_2/year). Variations in pressure buildup in different layers is mainly affected by the thickness of the aquifer layers, demonstrating that failure of caprock begins first above the much thinner aquifer layer. In comparison with the shear failure criterion of reservoir, which permits a much larger pore pressure increase, the integrity criterion is much more important for estimation of the safe maximum injection pressure.

However, due to the lack of adequate measured data, a simplified 3D model has been used in this simulation to provide some general understanding of hydro-mechanical behaviorial effect, though not totally precise for the CO_2 sequestration at any site. With respect to the geological conditions at the Ordos site, simulation results suggest that the pressure buildup should be controlled not to exceed 13.7, 14.8, 17.0, 17.5 MPa in the four injection layers from the top to bottom, respectively, to achieve a safe long-term storage of CO_2. Nevertheless, a more realistic 3D model for the near-well region must be set up by combining more experimental, seismic, well logging data etc, in order to achieve a more reliable guidance for a practical CO_2 sequestration in the Ordos Basin.

9.5 Simulation studies on CO_2-water-rock interactions for saline formations of the Ordos Basin

The saturation state for a specific mineral at dynamic equilibrium with the surrounding pore fluid environment depends on variations in several parameters including fluid infiltration over time, element

content caused by water-rock interaction, the ambient geothermal gradient, as well as the bio-geochemistry conditions.

Current experimental studies clearly indicate that geochemical reactions caused by CO_2 injection are strongly case and site specific, mainly depending on the mineralogy of the rock, pressure, temperature, and fluid composition of the reservoir. Therefore, the laboratory experiments for each individual reservoir system have to be investigated separately, as general conclusions are mostly imprecise.

The effects of supercritical CO_2-water-rock interaction on the porosity and permeability changes become more complex under different reservoir conditions (including pressure, temperature, mineralogy and pore fluid composition) and reaction time scales: increased porosity and permeability is mainly experienced in carbonate reservoirs; decreased porosity and permeability is mainly due to migration of fine grains, mainly from illite, into pore throats; unchanged porosity and permeability may imply the offset of dissolution of minerals and the migration of fine grains.

Mineral dissolution and re-precipitation can happen in porous media, fractures and faults. CO_2 can be trapped in the form of complex ions (including HCO_3^-, $CaHCO_3^+$, $MgHCO_3^+$ and $FeHCO_3^+$) and minerals (e.g. calcite, magnesite, siderite, dawsonite, ankerite, etc). Mineral alterations can be triggered through chemical reactions. The types of the chemical reactions depend on many factors, e.g. the relative content of minerals in the rock, cation concentration in the aqueous phase, pH, temperature, CO_2 partial pressure, reservoir pressure, etc.

Generally, dissolution and precipitation of minerals are described by two different mechanisms: 1) thermodynamic mechanism (whereby the main parameters include equilibrium constant, activity coefficient and activity) and 2) kinetic mechanism (in which kinetic rate constants and specific surface areas are used). In thermodynamic mechanism, solubility constant (K_{sp}) can be used to estimate the dissolution and precipitation capacity of a mineral. Most carbonate minerals, such as magnesite, calcite, dolomite, ankerite and siderite can easily precipitate with increased temperature (since K_{sp} decreases with increasing temperature). Except chlorite, most minerals can easily dissolve when temperature is increased (i.e. K_{sp} positive correlates with temperature).

Modeling of CO_2 sequestration processes in saline formation also involves finding the solutions to a series of equations, including component transport equations, thermodynamic equilibrium equations between gas and aqueous phase or kinetic rate equations, and geochemistry equations. The latter equations involve reactions between the aqueous species and mineral precipitation and dissolution. Integral finite difference method is adopted in space discretization to solve differential equations, in which an implicit time-weighting method is used. The method uses a sequential iteration approach to solve coupled problems of fluid flow, species transport and geochemical reactions. Chemical reaction equations in each grid-block are solved by Newton-Raphson iteration method, until the convergence is achieved.

The non-isothermal reactive geochemical transport code TOUGHREACT is used in the simulation. To increase the understanding of the CO_2-water-rock interactions in the saline formations in Ordos Basin during CO_2 sequestration, the batch, 1D and 2D simulations were carried out. To enable comparison with the experimental results, an isothermal model was used at a temperature of 75 $^{\circ}$C. Data for the initial mineralogy and formation water compositions for the four layers (Liujiagou, Shiqianfeng, Shihezi and Shanxi formations) is derived from the adjacent gas fields or other collaborators of Ordos CO_2 sequestration project. Solubility of CO_2 in the four formation water samples under 75°C is obtained from experimental results. Generally, the solubility of CO_2 in formation water increases with formation depth, i.e. from Fm. Liujiagou to Fm. Shanxi, showing a good correlation between solubility and salinity (the higher the salinity, the lower the solubility of CO_2). The mineral compositions in the four layers are mainly comprise detrital feldspar and detrital quartz for the framework grains and mainly carbonate and

224

clay minerals, such as calcite, dolomite, chlorite, smectite, illite, kaolinite etc for the cements. Varied mineral contents occur in different formations.

Through batch simulations for the four sandstone samples under in situ pressure and a temperature of 75 $^{\circ}$C, some general results can be concluded. Injection of CO_2 causes a reduction in the pH, ranging from 3.0-4.6 at the starting point. Overall, however, pH shows a gradually increasing trend due to the CO_2-water-rock interaction effect. Great trend differences for different samples occur due to the difference in initial conditions (e.g. primary mineral compositions and water chemistry). The responses of different ion concentration changes and mineral volume fraction changes caused by CO_2 injection show a significant distinction. Different ions may show a time dependent characteristics, especially for K^+ and AlO_2^-, which present totally opposite variation trends for LJG and SQF chemical reaction simulation. An overall similar variation trend can be shown in four batch simulation runs, for quartz and feldspar minerals, the quartz is at precipitated state, while oligoclase and K-feldspar are at dissolved state, and low-albite may dissolve at first, but then precipitate. For carbonate minerals, great changes can be shown, for example, calcite can be dissolved or precipitated in those four simulation runs. Different mineral assemblages occur, for instance, calcite and dawsonite in LJG, only calcite in SQF, calcite, ankerite and siderite in SHZ, calcite and dawsonite in SX. For clay minerals, chlorite is more easily to dissolve in acidic environment, while kaolinite and illite are the stable precipitated clay minerals in acid environment.

Three regions exist when CO_2 is injected into a saline formation: 1) a pure CO_2 gas phase region (in the vicinity of the injection well); 2) a transition region with a mixture of CO_2 and water, i.e. two phases between the propagation front and the intensive impact zone by carbonic water; and 3) a pure water phase region beyond the CO_2 plume front. With the continuous injection of CO_2, the transition zone extends outwards from the injection zone. The concentration of all ions will be changed due to the CO_2-water-rock interactions. However, their variation extent and spatial distribution pattern will show great diversities. Due to the dissolution of CO_2 in water, the chemical interactions are enhanced. The difference in density between CO_2 bearing water and initial water promotes convective flow of fluid, especially at the boundary region between the CO_2 plume front and initial water zone.

The injected CO_2 has a great impact on the re-distribution of minerals, especially in the transition zone where the geochemical reactions are strong. The feldspar minerals, such as oligoclase and K-feldspar are usually present a dissolved state, while some clay minerals, for instance, smectite-Ca, smectite-Na and kaolinite are present in a precipited form. Dissolution or precipitation state for a specific mineral can change with time. For example, illite can dissolve in the aqueous phase, especially in the near well region, but precipitate far away from the injection zone. Minerals may occur in a sequence due to their respective saturation index. For example, in the 1D simulation, the carbonate minerals volume fraction changes demonstrate that calcite and smectite-Ca deposit first, followed by dawsonite.

To a small extent, both 1D and 2D simulation runs show that reservoir properties (i.e. porosity and permeability) are improved in the short-term during CO_2 injection process. However, in the long term, porosity and permeability are adversely impaired in the vicinity of the injection point.

9.6 Simulation studies of hydrothermal production: CO_2 as a pressure-driven fluid

Due to the imminent danger of energy crisis and environmental awareness, much more attention is now being paid on the development of renewable energy, although 80% of the current primary energy consumption still relies on supplies from the traditional fossil fuels. Among them, geothermal energy production will become a new hot spot in the next decades because of its sustainability (stability on supply), availability of extensive reserves and environmentally friendly characteristics.

Based on the temperature of the reservoir, geothermal energy can be used in the following forms: 1) geothermal electric power generation (at the depth 3-5 km, temperature > 150 $^{\circ}$C, flowing rate > 125 kg/s

225

for a net energy capacity of 4.7 MW power plant); 2) direct use geothermal energy, including two main categories: geothermal heat pumps (< 100 m at depth, used for heating and cooling systems) and circulating hot water (< 2000 m, temperature 90-150 $^{\circ}$C, used in space and district heating, industrial drying process, aquiculture etc).

Geothermal electric power and heat production from hydrothermal resources has been commercialized since 1904. Large conventional geothermal power plants (installed capacity > 50 MW) are mainly located in the USA, Philippines, Indonesia, Mexico, Italy, New Zealand and Japan. Four generalized categories of plant designs are used in geothermal generators: back pressure, binary, flash (single flash and double flash) and dry steam. The last three types constitute 98% of the total installed capacity, of which single flash and dry steam power plants are the most dominated types, weighting 41.3% and 26.9%, respectively.

Based on the type of circulating fluid and reservoir, geothermal production can be divided into four main groups: 1) Traditional H_2O-based reservoir type (commercial stage), like the Wayang Windu plant (in Indonesia, with a capacity of 117 MW), Socrates (in the USA, with a capacity of 113 MW), Cerro Prieto III (in Mexico, with a capacity of 110 MW), Kawerau (in New Zealand, with a capacity of 100 MW), etc; 2) H_2O-based fractured reservoir type-EGS (enhanced geothermal system, still at pilot and demonstration stages), for example, Fenton Hill project (in the USA, with the bottom hole tempreaure (BHT) 200-300 $^{\circ}$C), the Rosemanowes (in the U.K., with the BHT 80-90 $^{\circ}$C), Hijiori (in Japan, with the BHT 150-250 $^{\circ}$C), Ogachi (in Japan, 230 $^{\circ}$C at 1000 m depth), Landau project (in Germany, with a capacity of 2.5 MW) and Soultz project (in France, with a capacity of 1.5 MW); 3) CO_2-based reservoir type (still at the conceptual model and research stages); 4) CO_2-based fractured reservoir type (at conceptual model and research stages).

In contrast to H_2O-based geothermal production, CO_2-based geothermal production may have advantage of having a larger mobility and higher heat extraction efficiency. Most important is that it can simultaneously sequester CO_2, thus a win-win situation is achieved.

Many factors may affect the efficiency of heat extraction in the geothermal production system, such as well spacing, permeability of reservoir, circulation fluid type and so on. The closer the well spacing, the higher heat extraction rate will be. However, this will also lead to a quick CO_2 breakthrough in the production wells and therefore leaving less CO_2 to be sequestered in the reservoir. High permeability has priority over heat extraction rate.

Based on the available data from petroleum groundwater exploration in the NE Ordos Basin, a simplified 3D model has been set up for the purpose of understanding fluid flow and pressure perturbation processes in geothermal production associated with CO_2 sequestration. The parallel version of TOUGH2MP/ECO2N simulator is used in the simulation runs. The simulation lasted 35 years, considering the general economic lifespan of a geothermal project. A total of 15 Mt CO_2 are injected in the reservoir when two production wells with a rate of 2 kg/s are located 500 m horizontally away from the injection well. Two reinjection wells for disposal water are also set at a much shallower depth.

 The near-well region of a production well is dominated by different fluid phases during CO_2 driven processes. Before breakthrough, the near-well region is totally water saturated. At the early stage of CO_2 breakthrough, it is dominated by two phase fluid (water and CO_2). As time goes by, only CO_2 will be produced from the production well.

CO_2 breakthrough lags far behind the pressure response in the geothermal production system. When the pressure transfer effect reaches the bottom of the confining mudstone layer, it will affect the lateral evolution of pressure. The CO_2 plume will evolve with time. Before CO_2 reaches the production wells, the plume develops as a mounded shape until it touches the bottom of caprock. After breakthrough,

buoyancy effect becomes much stronger, with the development of a funnel shaped CO_2 plume. A continuous lateral movement of the CO_2 plume will occur along the bottom of the cap rock.

The lateral and vertical distance between injection and production wellbores plays a significant role in controlling the breakthrough time and improving of the overall performance of a geothermal reservoir. A favorable well configuration is achieved when geothermal production wells are perforated parallel or below the CO_2 injection wells. Simulation results show that the CO_2 breakthrough time can be delayed to 20 years, 14 years later than the case when production wells are setted 100 meters above the injection well with a CO_2 breakthrough time of 6 years.

9.7 Suitable site selection criteria and workflow for CO_2-aided hydrothermal system

Site suitability evaluation processes for the simultaneous production of geothermal energy and CO_2 storage and only CO_2 sequestration have different stages. Based on the exploration level and accuracy of assessment, the evaluation stages can be divided into: 1) country-level; 2) sedimentary basin-level; 3) target area of interest-level; 4) site-level; and 5) engineering operation-level. However, more data is needed when the evaluation target becomes smaller.

Based on the characteristics of geothermal production, reservoirs can be divided into four types: I. low temperature hot dry rock; II. high temperature hot dry rock; III. low temperature hydrothermal; and IV. high temperature hydrothermal reservoir types. Each type has its own corresponding development strategy. Through using a series of evaluation criteria, a feasible guidance to operaters is attained. Take CO_2-driven H_2O-based geothermal reservoirs as an example, several requirements, such as efficiency (temperature gradient, basin area, water content, permeability and porosity of reservoir, CO_2 source, salinity, accessibility to national electricity netzwork etc), safety (crust stability: structural setting, density of small faults and fractures, large active faults, fault sealing characteristics and seismic safety level; and caprock integrity: the mineral composition of the caprock, thickness, impermeability of the caprock, single direct caprock or multilayered caprock, lateral continuity of caprock and density of drilling wells, etc) and environmental friendly aspects (project approval by the people and geographic environment) should be satisfied. Therefore, each factor is classified into different grades according to its level of suitability assessment.

A set of 18 criteria has been used for the assessment and ranking of sedimentary basins in terms of their suitability for geothermal production associated with CO_2 sequestration. For each criterion, several levels have been defined and given a value based on the suitability degree. To compare the priority of different basins, a normalized score is used by multiplying the initial value of each criterion and weight factor (the degree of importance of each criterion on the results). The sum of the normalized score is given for each evaluated basin. The higher the score, the more suitable the basin is. More criteria can be added in this assessment system, when more data is available. Therefore, it is very helpful in the first and second stage of ranking and selection, when limited data is available.

Application of the ranking system in the sedimentary basins of China shows that Bohaiwan, Songliao and Qiangtang Basins have the greatest potential for geothermal production associated with CO_2 sequestration. The middle-low temperature gradient in Bohaiwan and Songliao Basins limits the electricity requirement. For geothermal use, however, the hot water can be used for heating system or domestic hot water supply. Songliao Basin has also a great potential for CO_2-EOR and CO_2-EGR due to the gradually depletion of the hydrocarbon reservoirs exploited for over 60 years. Qiangtang Basin, especially near Lasa area, has a higher temperature gradient and its geothermal water can be used for electricity, although the low local electricity demand and the poor infrastructure will restrict widespread development of geothermal production. When only CO_2 sequestration is considered based on safety,

227

economy and environmental protection evaluations, the top three basins are the Ordos, Tarim and Bohaiwan Basins.

The general score of each sedimentary basin after the assessment system does not mean that all parts of the basin have equal suitability. More criteria need to be added into the assessment system when evaluation of more detailed field-scale, target formation-scale and engineering operation-scale is considered.

References

Adepoju O.O., 2006. Coefficient of isothermal oil compressibility for reservoir fluids by cublic equation-of-state, Master Thesis in Department of Petroleum Engineering, Texas Tech University.

Alkan H., Cinar Y., Ülker E., 2010. Impact of capillary pressure, salinity and in situ conditions on CO_2 injection into saline aquifers, Transport in Porous Media 84:799–819.

Andre L., Spycher N., Xu T.F., Vuatza F.D., Pruess K., 2006. Modeling brine-rock interactions in an enhanced geothermal system deep fractured reservoir at Soultz-Sous-Forets (France): a joint approach using two geochemical codes: FRACHEM and TOUGHREACT. LBNL-62357.

Arsyad A., Mitani Y., Babadagli T., 2013. Comparative assessment of potential ground uplift induced by injection of CO_2 into Ainoura, and Berea sandstone formations. Procedia Earth Planet Science 6:278–286.

Atrens A.D., Gurgenci H., Rudolph V., 2011. Removal of water for carbon dioxide-based EGS operation, In: Proceedings Thirty-Sixth Workshop on Geothermal Reservoir Engineering, Stanford University, Stanford, California, 31 January - 2 February, 2011.

Atrens A.D., Gurgenci H., 2013. Design of CO_2-based geothermal power plant for transient reservoir dry-out or 'enhanced water recovery'. In: Proceedings Thirty-Eighth Workshop on Geothermal Reservoir Engineering, Stanford University, Stanford, California, 11-13 February, 2013.

Auriault J.L., Boutin C., Geindreau C., 2009. Homogenization of coupled phenomena in heterogeneous media, Wiley, Hoboken.

Averjanov S.F., 1950. About permeability of subsurface soils in case of incomplete saturation. Engineering Collection VII: As quoted by Polubarinova Kochina P.Ya., The Theory of Ground Water Movement. English translation by J.M. Roger De Wiest, 1962, Princeton University Press, Princeton.

Ayan C., Colley N., Wannell M., Goode P., Halford F., Joseph J., Mongini A., Pop J., 1994. Measuring permeability anisotropy: the latest approach, Oilfield Review 24-35.

Bachu S., Gunter W.D., Perkins E.H., 1994. Aquifer disposal of CO_2: hydrodynamic and mineral trapping, Energy Conversion and Management 35: 269–279.

Bachu S., 2002. Sequestration of CO_2 in geological media in response to climate change: roadmap for site selection using the transform of the geological space into the CO_2-phase space. Energy Conversion and Management 43:87-102.

Bachu S., 2003. Screening and ranking sedimentary basins for sequestration of CO_2 in geological media in response to climate change, Environmental Geology 44: 277−289.

Bachu S., Adams J.J., 2003. Sequestration of CO_2 in geological media in response to climate change: Capacity of deep saline aquifers to sequester CO_2 in solution, Energy Conversion and Management 44(20): 3151–3175.

Bachu S., Dusseault M., 2005a, Underground injection of carbon dioxide in salt beds, in: Tsang C.F., Apps J., editors, Proceedings of the Second International Symposium on Deep Well Injection, , 22–24 October 2003, Berkeley, CA.

Bachu S., Gunter W.D., 2005b. Overview of acid gas injection operations in western Canada, In: Rubin E.S., Keith D.W., Gilboy C.F., editors. In: Proceedings of the 7th international conference on greenhouse gas control technologies, London, UK: Elsevier 1: 443–448.

Bachu S., 2008. CO_2 storage in geological media: Role, means, status and barriers to deployment, Progress in Energy and Combustion Science 34: 254–273.

Bachmat Y., Bear J., 1986. Macroscopic modelling of transport phenomena in porous media: the continuum approach, Transp. Porous Media 1: 213–240.

Bandlamudi D., Avirneni S., 2013. Power plant-a scientific disaster, International Journal of Engineering Research and Applications (IJERA) 3(3): 61–65.

Bastian P., 1999. Numerical computation of multiphase flows in porous media, habilitationthesis in University of Kiel, Germany.

Bateman K., Turner G., Pearce J.M., Noy D.J., Birchall D., Rochelle C.A., 2005. Large-scale column experiment: study of CO_2, porewater, rock reactions and model test case, Oil & Gas Science and Technology 60(1): 161–175.

Bear J. 1972. Flow through porous media, Elsevier.

Bear J., Bachmat Y., 1990. Introduction to modeling of transport phenomena in porous media, Dordrecht: Kluwer pp.553.

Bennethum L.S., Murad M.A., Cushman J.H., 1997. Modified Darcy's law, Fick's law, and Terzaghi's effective stress principle for swelling clay soils, Swelling Clay Soils 1–26.

Bennion B., Bachu S., 2005. Relative permeability characteristics for supercritical CO_2 displacing water in a variety of potential sequestration zones in the western Canada sedimentary basin, SPE paper 95547. In: SPE Annual Technical Conference and Exhibition in Dallas, Texas, U.S.A., 9-12 October 2005.

Bennion B., Bachu S., 2006a. The impact of interfacial tension and pore-size distribution/capillary pressure character on CO_2 relative permeability at reservoir conditions in CO_2-brine systems, SPE paper 99325.

Bennion B., Bachu S., 2006b. Supercritical CO_2 and H_2S-brine drainage and imbibition relative permeability relationships for intergranular sandstone and carbonate formations, SPE paper 99326, SPE Europec/EAGE Annual conference and exhibition, Vienna, Austria, June 12–15.

Bennion D.B., Bachu S., 2008. Drainage and imbibition relative permeability relationships for supercritical CO_2/brine and H_2S/brine systems in intergranular sandstone, carbonate, shale and anhydrite rocks, SPE Reservoir Evaluation and Engineering 11(3):487-496.

Benson S.M., Cook P., 2005. Underground Geological Storage, IPCC Special Report on Carbon Dioxide Capture and Storage, Chapter 5. Intergovernmental Panel on Climate Change, Cambridge University Press, Cambridge, U.K.

Benson S., Hepple R., 2005. Prospects for early detection and options for remediation of leakage from CO_2 storage projects, In: Thomas D.C., Benson S.M. editors, Carbon Dioxide Capture for Storage in Deep Geologic Formations, Volume 2, Elsevier Ltd. pp. 1189–1203.

Benson S.M., 2005. Overview of geologic storage of CO_2, In: Benson S.M., Oldenburg C., Hoversten M., Imbusand S., editors. Carbon Dioxide Capture for Storage in Deep Geologic Formations-results from the CO_2 capture project (CCP), 2: 665–672.

Benson S.M., Cole D.R., 2008. CO_2 sequestration in deep sedimentary formations, Elements 4: 325–331.

Bergman P.D., Winter E.M., 1995. Disposal of carbon dioxide in aquifers in the U.S, Energy Conversion and Management 36: 523–526.

Bertier P., Swennen R., Laenen B., Lagrou D., Dreesen R., 2006. Experimental identification of CO_2–water–rock interactions caused by sequestration of CO_2 in Westphalian and Buntsandstein sandstones of the Campine Basin (NE-Belgium), Journal of Geochemical Exploration 89: 10–14.

Bertani R., 2009. Geothermal energy: an overview on resources and potential, In: International Geothermal Days Slovakia 2009, Conference and Summer School.

Bertani R., 2010. Geothermal power generation in the world 2005-2010 update report, In: Proceedings World Geothermal Congress, 2010, Bali, Indonesia, 25-29 April 2010.

Beyer C., Li D.D., De Lucia M., Bauer S., Kühn M., 2012. Modelling CO_2-induced fluid–rock interactions in the Altensalzwedel gas reservoir, Part II: coupled reactive transport simulation, Environ Earth Science 67: 573–588.

Bickle M., Chadwick A., Huppert H.E., Hallworth M., Lyle S., 2007. Modelling carbon dioxide accumulation at Sleipner: implications for underground carbon storage, Earth and Planetary Science Letters 255: 164–176.

Bieber M.T., Rasolofosaon P., Zinszner B., Zamora M., 1996. Measurement and overall characterization of permeability anisotropy by tracer injection, Revue de l'Institut Francais du Pettrole 51(3):333–347.

Biot M., 1955. Theory of elasticity and consolidation for a porous anisotropic solid, Journal of Applied Physics 26(2): 182–185.

Birkholzer J.T., Zhou Q., Tsang C.F., 2009. Large-scale impact of CO_2 storage in deep saline aquifers: a sensitivity study on the pressure response in stratified systems, International Journal of Greenhouse Gas Control 3(2):181–194.

BjΦrlzkke K., Chuhan F., Kjeldstad A., Gundersen E., Lauvrak O., HΦeg K., 2004. Modeling of sediment compaction during burial in sedimentarz basins, 699–708. In: Stephansson O., Hudson J.A., editors. Coupled thermo-hydro-mechanical-chemical processes in geo-systems-fundamentals, modelling, experiments and applications, Elsevier Geo-Engineering Book Series Volume 2.

Blodgett L., Slack K., 2009. Geothermal 101: Basics of geothermal energy production and use, Washingtone, DC, Geothermal Energy Association.

Booth R., 2008. Miscible flow through porous media, PhD thesis in University of Oxford.

Boschi C., Dini A., Dallai L., Ruggieri G., Gianelli G., 2009. Enhanced CO_2-mineral sequestration by cyclic hydraulic fracturing and Si-rich fluid infiltration into serpentinites at Malentrata (Tuscany, Italy), Chemical Geology 265: 209–226.

Bower K.M., Zyvoloski G., 1997. A numerical model for thermo-hydro-mechanical coupling in fractured rock, International Journal of Rock Mechanics and Mining Science & Geomechanical Abstracts 34: 1201–1211.

Bowker K.A., Shuler P.J., 1991. Carbon dioxide injection and resultant alteration of the Weber sandstone, Rangely field, Colorado, American Association of Petroleum Geologists Bulletin 75:1489–1499.

Brady J.L., Hare J.L, Ferguson J.F, Seibert J.E., Klopping F.J., Chen T., Niebauer T., 2006. Results of the world's first 4D microgravity surveillance of a waterflood-Prudhoe Bay, Alaska: SPE Annual Technical Conference & Exhibition , San Antonio, September (2006), Expanded Abstracts, SPE 101762.

Breede K., Dzebisashvili K., Liu X.L., Falcone G., 2013. A systematic review of enhanced (or engineered) geothermal systems: past, present and future, Geothermal Energy 1:4 doi:10.1186/2195-9706-1-4

Brooks R.H., Corey A.T., 1964. Hydraulic properties of porous media, Hydrology, Paper 3, Colorado State University, Fort Collins, pp. 27.

Brown D.W., 2000. A hot dry rock geothermal energy concept using supercritical CO_2 instead of water, 233–238, In: Proceedings of the 25th Workshop on Geothermal Reservoir Engineering, Stanford University.

Brutsaert W., 1967. Some methods of calculating unsaturated permeability, Transactions of ASAE 10:400–404.

Bunger A., McLennan J., Jeffrey R., 2013. Effective and sustainable hydraulic fracturing, Published by InTech, Croatia, pp. 1072.

Burdine N.T., 1953. Relative permeability calculations from pore-size distribution data, Transactions of the American Institute of Mining, Metallurgical and Petroleum Engineers 198: 71–78.

Burton M.M., Kumar N., Bryant S.L., 2008. Time-dependent injectivity during CO_2 storage in aquifers, SPE 113937.

Buscheck T.A., Sun Y., Chen M., Hao Y., Wolery T.J., Bourcier W.L., Court B., Celia M.A., Friedmann S.J., and Aines R.D., 2012a. Active CO_2 reservoir management for carbon storage: Analysis of operational strategies to relive pressure buildup and improve injectivity, Internationl Journal of Greenhouse Gas Control 6: 230–245.

Buscheck T.A., Elliot T.R., Celia M.A., Chen M., Hao Y., Lu C., Sun Y., 2012b. Integrated, geothermal-CO_2 storage reservoirs: adaptable, multi-stage, sustainable, energy-recovery strategies that reduce carbon intensity and environmental risk, In: Proceedings for the Geothermal Resources Council 36th Annual Meeting, 30 Sept–3 Oct, 2012, Reno, NV, USA.

Buscheck T.A., Elliot T.R., Celia M.A., Chen M., Sun Y., Hao Y., Lu C., Wolery T.J., Aines R.D., 2012c. Integrated geothermal-CO_2 reservoir systems: Reducing carbon intensity through sustainable energy production and secure CO_2 storage, In: Proceedings of the International Conference on Greenhouse Gas Technologies (GHGT-11), Kyoto, Japan, 18–22 Nov, 2012.

Buscheck T.A., Chen M.J., Sun Y.W., Hao Y., Elliot T.R., 2012d. Two-stage, integrated, geothermal-CO2 storage reservoirs: an approach for sustainable energy production, CO_2-sequestration security, and reduced environmental risk, LLNL-TR-526952.

Byerlee J., 1978. Friction of rocks, Pure and Applied Geophysics 116: 615−626.

Byer C.W., Guthrie H.D., 1997. Assessment of world coal resources for carbon dioxide (CO_2) storage potential—while enhancing potential for coalbed methane, US Department of Energy, Greenhouse Gas Mitigation, Technologies for Activities Implemented Jointly, Proceedings of Technologies for Activities Implemented Jointly, 26–29th May, Vancouver, Canada, 573–576.

Byer C.W., Guthrie H.D., 1998a. Carbon dioxide potential in coalbeds: a near-term consideration for the fossil energy industry, US Department of Energy. In: Proceedings of the 23rd International Technical Conference on Coal Utilization and Fuel Systems, 9–13 March, Clearwater, FL, 593–600.

Byer C.W., Guthrie H.D., 1998b. Coal deposits: potential resource for storing carbon dioxide emissions from power plants, US Department of Energy. In: Fourth International Conference on Greenhouse Gas Control Technologies (GHGT4), 30 August–2 September, Interlaken, Switzerland.

Campbell G.S., 1974. A simple model for determining unsaturated hydraulic conductivity from moisture retention data, Soil Science 117: 311–314.

Carrel K. D., 1987. The occurrence, prevention and treatment of sulfate scale in shell exportation, SPE 16538 presented at Offshore Europe 87, Aberdeen, Scotland, September 8-11, 1987.

Celia M.A., Bachu S., Nordbotten J.M., Gasda S.E., Dahle H.K., 2005. Quantitative estimation of CO_2 leakage from geological storage: Analytical models, numerical models and data needs, In: Proceedings of 7th international conference on greenhouse gas control technologies (GHGT-7), September 5–9, 2004, Vancouver, Canada I: 663–672.

Celia M.A., Nordbotten J.M., 2009. Practical modeling approaches for geological storage of carbon dioxide, Ground Water 47(5): 627−638.

Chadwick R.A., Noy D., Arts R., Eiken O., 2008. Quantification issues from the latest time-lapse seismic data at the Sleipner CO_2 injection operation, in: GHGT-9.

Charleston J., 1968. Scale removal in the Virden, Manitoba Area, SPE 2160 presented at the 43rd Annual Fall Meeting, Houston, TX, September 29-October 2, 1968.

Chen M.X., Wang J.Y., Deng X., 1994. The geothermal resources in China-formation characteristics and potential evaluation, Science Press, in Beijing (in Chinese).

Chen G., Li X., Zhou L., 2005. Coupled relationships between tectonics and multiple mineralizations in the Ordos Basin, Earth Science Frontiers 12: 535–541 (in Chinese).

Chen H.Y., Teufel L.W., 1997. Coupling fluid-flow and geomechanics in dual-porosity modeling of naturally fractured reservoirs, SPE 38884. In: SPE A nnual Technical Conference and Exhibition, 5-8 October 1997, San Antonio, Texas.

Chen M.X., Wang J.Y., Deng X., 1994. Geothermal resources in China-formation characteristics and potential evaluation, Science Press, Beijing (in Chinese).

Chen Y.F., Zhou C.B., Jing L.R., 2009. Modeling coupled THM processes of geological porous media with multiphase flow: theory and validation against laboratory and field scale experiments, Computers and Geotechnics 36: 1308–1329.

Chen Z.X., Huan G.R., Ma Y.L., 2006. Computational methods for multiphase flows in porous media, Society for Industrial and Applied Mathematics, 3600 University City Science Center, Philadelphia.

Cheng Y.H., Pan W.D., Sun S.L., 2003. Study on infection of fouling of oil deposit caused by CO_2 injection, Corrosion and Protection in Petrochemical industry 20(6): 21−23 (In Chinese).

Chi J.S., 1988. The study of Cenozoic basalts and upper mantle beneath eastern China, China University of Geosciences Press, Wuhan. (in Chinese with English summary).

Chiquet P., Broseta D., Pau U., Thibeau S., 2005. Capillary alteration of shaly caprocks by carbon dioxide, SPE paper 94183, in: SPE Europec/EAGE Annual Conference, Madrid, Spain, 13-16 June 2005.

Cihan A., Birkholzer J.T., Zhou Q., 2013. Pressure buildup and brine migration during CO_2 storage in multilayered aquifers, Groundwater 51(2): 252-267.

Cinar Y., Neal P., Allinson W., Sayers J., 2009. Geoengineering and economic assessment of a potential carbon capture and storage site in Southeast Queensland, Australia, SPE Reservoir Evaluation and Engineering 12:660–670.

Class H., Ebigbo A., Helmig R., Dahle H., Nordbotten J., Celia M., Audigane P., Darcis M., Ennis-King J., Fan Y., Flemisch B., Gasda S., Jin M., Krug S., Labregere D., Naderi Beni A., Pawar R., Sbai A., Thomas S., Trenty L., Wei L. 2009. A benchmark study on problems related to CO_2 storage in geologic formations, Computational Geosciences 13(4):409–434.

Coat K.H., Nielsen R.L., Terhune M.H.T., Weber A.G., 1967. Simulation of three-dimensional, two-phase flow in oil and gas reservoirs, Journal of Petroleum Science and Engineering 377–388.

Cooper C., 2008. A technical basis for carbon dioxide storage, In: GHGT-9.

Corey A.T., 1954.The interrelation between gas and oil relative permeabilities, Producers Monthly 38–41.

Court B., 2011. Safety and water challenge in CCS: modeling studies to quantify CO_2 and brine leakage risk and evaluate promising synergies for active and integrated water management, PhD thesis, in Department of Civil and Environmental Engineering, Princeton University.

Court B., Elliot T. R., Dammel J., Buscheck T.A., Rohmer J., Celia, M.A., 2011a. Promising synergies to address water, sequestration, legal, and public acceptance issues associated with large-scale implementation of CO_2 sequestration. Special Issue on Carbon Capture and Storage (CCS) "Five years after the IPCC Special Report on CCS: state of play, Mitigation and Adaptation of Strategies for Global Change Journal.

Court B., Celia M.A., Nordbotten J.M., Elliot T.R., 2011b. Active and integrated management of water resources throughout CO2 capture and sequestration operations, Energy Procedia 4: 4221–4229.

Court B., Bandilla K., Celia M.A., Buscheck T.A., Nordbotten J.M., Dobossy M., and Jansen A., 2012. Initial evaluation of advantageous synergies associated with simultaneous brine production and CO_2 geological sequestration, International Journal of Greenhouse Gas Control, accepted for publication.

CO2CRC, 2008. Storage capacity estimation, site selection and characterization for CO_2 storage projects. Cooperative Research Centre for Greenhouse Gas Technologies, Camberra. CO2CRC Report Number RPT08-1001.

Dahle H.K., Eigestad G.T., Nordbotten J.M., Pruess K. 2009. A model-oriented benchmark problem for CO_2 storage, available at http://org.uib.no/cipr/Workshop/2009/CO2/benchmark_definition.pdf.

Dane J.H., Vrugt J.A., Unsal E., 2011. Soil hydraulic functions determined from measurements of air permeability, capillary modeling and high-dimensional parameter estimation, Journal of Vadose Zone 10:1–7.

Dawson G.K.W., Sidiq H., Gao J-F., Golding S.D., Rudolph V., Li Q., Xing H., 2013. ANLEC Project 3-1110-0101 Report: Review of laboratory-scale geochemical and geomechanical experiments simulating geosequestration of CO_2 sandstone, and associated modeling studies, Australian National Low Emissions Coal Research and Development, Manuka, ACT.

De Lucia M., Bauer S., Beyer C., Kühn M., Nowak T., Pudlo D., Reitenbach V., Stadler S., 2012. Modelling CO_2-induced fluid-rock interactions in the Altensalzwedel gas reservoir, Part I: from experimental data to a reference geochemical model, Environmental Earth Science 67:563–572.

De Silva P.N.K., Ranjith P.G., 2012. A study of methodologies for CO_2 storage capacity estimation of saline aquifers, Fuel 93:13–27.

De Visser E., de Vos R., Hendriks-Ecofys C., 2009. Catching carbon to clear the skies (CATO)- experience and highlights of the Dutch R&D programme on CCS.

Deng J., Wang, Q.F., Gao B.F., Huang D.H., Yang L.Q., Xu H., Zhou Y.H., 2005. Evolution of the Ordos Basin and its distribution of various energy and mineral resources, Geoscience 19 (4): 538–545(in Chinese with English abstract).

Dentz M., Tartakovsky D.M. 2009. Abrupt-Interface Solution for carbon dioxide injection into porous media, Transport in Porous Media 79(1): 15–27.

DOE, 2012. Annual report on geothermal technologies.

DOE, 2013. Site screening, selection and initial characterization for storage of CO_2 in deep geologic formations.

Dong J.G., Fan X.M., 2006. A method to calculate porosity of compact sandstone, Journal of Jilin University (Earth Science Edition) 36:193–196 (In Chinese).

Doughty C., Pruess K., Benson S.M., Hovorka S.D., Knox P.R., Green C.T., 2001. Capacity investigation of brine-bearing sands of the Frio Formation for geologic sequestration of CO_2, In: Proceedings of first national conference on carbon sequestration, 14–17 May 2001, Washington, D.C., United States Department of Energy, National Energy Technology Laboratory, CD-ROM USDOE/NETL-2001/1144, Paper P.32, pp. 16.

Doughty C., 2007. Modeling geologic storage of carbon dioxide: comparison of non-hysteretic and hysteretic characteristic curves, Energy Conversion and Management 48(6):1768–1781.

Doughty C., Freifeld B., Trautz R., 2008. Site characterization for CO_2 geologic storage and vice versa: the Frio brine pilot, Texas, USA as a case study, Environmental Geology 54(8):1635–1656.

Doughty C. 2010. Investigation of CO_2 plume behavior for a large-scale pilot test of geologic carbon storage in a saline formation, Springer Netherlands.

Duchane D., Brown D., 2002. Hot dry rock(HDR) geothermal energy research and development at Fenton Hill, New Mexico, GHC Bulletin 13–19.

Ebigbo A., Class H., Helmig R., 2007. CO_2 leakage through an abandoned well: problem-oriented benchmarks, Computational Geosciences 11(2):103–115.

Economides M.J., Boney C., 2000. Reservoir stimulation in petroleum production, In: Economides M.J., Nolte K.G., editors, Reservoir stimulation, 3rd edition, Chichester: Wiley, 2000.

Edmunds W. M., Bath A.H. and Miles D.L., 1982. Hydrochemical evolution of the East Midlands Triassic sandstone aquifer, England, Geochimica et Cosmochimica Acta 41: 1097–1103.

Ehlig-Economides C., Ecomomides M. J. 2010. Sequestering carbon dioxide in a closed underground volume, Journal of Petroleum Science and Engineering 70:123–130.

El-Naqa A., 2001. The hydraulic conductivity of the fractures intersecting Cambrian sandstone rock masses, central Jordan, Environmental Geology 40:973-982.

Enick R.M., Klara S.M., 1990. CO_2 solubility in water and brine under reservoir conditions, Chemical Engineering Communications 90: 23−33.

Ennis-King J.P., Paterson L., 2001. Reservoir engineering issues in the geological disposal of carbon dioxide, In: Proceedings of the 5th international conference on greenhouse cas control technologies (GHGT-5), Williams D., Durie D., McMullan P., Paulson C. and Smith A., editors, 13–16 August 2000, Cairns, Australia, CSIRO Publishing, Collingwood, Victoria, Australia, pp. 290–295.

Ennis-King J.P., Paterson L., 2003. Role of convective mixing in the long-term storage of carbon dioxide in deep saline formations, SPE J 10:349–356, In: Society of Petroleum Engineers Annual Technical Conference and Exhibition, Denver, Colorado, 5–8 October 2003, SPE paper no. 84344.

Ennis-King J., Gibson-Poole C.M., Lang S.C., Paterson L., 2003. Long term numerical simulation of geological storage of CO_2 in the Petrel sub-basin, North West Australia, In: Proceedings of the 6th International Conference on Greenhouse Gas Control Technologies (GHGT-6), J. Gale and Y. Kaya (eds.), 1–4 October 2002, Kyoto, Japan, Pergamon, v.I, 507–511.

Faigle B., 2009. Two phase flow modeling in porous media with kinetic interphase mass transfer processes in fractures, Master thesis in University of Stuttgart.

Fan M., Jiang X.Q., Liu W.X., Zhang J.Y., Chen H.Y., 2007. Dissolution of carbonate rocks in CO_2 solution under different temperatures, ACTA Sedimentologica Sinica 25(6): 825–830.

Fatt I., 1958. Pore volume compressibilities of sandstone reservoir rocks, Transactions of AIME 213: 362–364.

Feng Z.Z., Zhang Y.S., Jin Z.K., 1998. Type, origin, and reservoir characteristics of dolostones of the Ordovician Majiagou Group, Ordos, North China platform; carbonate platform sediments, Sedimentary Geology 118 (1-4):127−140.

Fenghour A., Wakeham W.A., Vesovic V., 1998. The Viscosity of Carbon Dioxide, Journal of Phys. Chem. Ref. Data, 27(1): 31−44.

Fischer S., Zemke K., Liebscher A., Wandrey M., and the CO2SINK Group., 2011. Petrophysical and petrochemical effects of long-term CO_2-exposure experiments on brine-saturated reservoir sandstones, Energy Procedia 4487–4494.

Flaathen T.H., Gislason S.R., Oelkers E.H., Sveinbjornsdottir A.E., 2009. Chemical evolution of the Mt. Hekla, Iceland, groundwaters: A natural analogue for CO_2 sequestration in basaltic rocks, Applied Geochemistry 24: 463–474.

Flett M., Taggart I., Lewis J., Gurton R., 2003. Subsurface sensitivities study of geologic CO_2 sequestration in saline formations, in: 2 nd Annual Conference on Carbon Sequestration, Alexandria, VA 5-8 May 2003.

Flett M., Beacher G., Brantjes J., Burt A., Dauth C., Koelmeyer F., Lawrence R., Leigh S., Mckenna J., Gurton R., 2008. Gorgon Project: Subsurface evaluation of carbon dioxide disposal under Barrow Island, SPE Asia Pacific Oil and Gas Conference and Exhibition 20-22 October, Perth, Australia.

Flett M.A., Gurton R.M., Taggart I.J., 2005. Heterogeneous saline formations: long-term benefits for geo-sequestration of greenhouse gases, In: Proceedings of the 7th International Conference on Greenhouse Gas Control Technologies (GHGT-7), September 5–9, 2004, Vancouver, Canada, v.I, 501–510.

Förster A., Norden B., Zinck-Jϕrgensen K., Frykman P., Kulenkampff J., Spangenberg E., Erzinger J., Zimmer M., Kopp J., Borm G., Juhlin C., Cosma C.G.; Hunter S., 2006. Baseline characterization of the CO2SINK geological storage site at Ketzin, Germany, Environmental Geosciences 13(3):145-161.

Freiboth S., Class H., Helmig R., et al. A model for multiphase flow and transport in porous media including a phenomenological approach to account for deformation-a model concept and its validation within a code intercomparison study, Computational Geosciences 2009, 13(3): 281–300.

Friedmann S.J., 2007. Geological carbon dioxide sequestration, Elements 3: 179–184.

Fu S.T., Tian J.C., Chen H.D., Hou Z.J., Yang H., Fu J.H., Fan Z.P., Shi X.Y., 2003. The delta depositional system distribution of later Paleozoic era in Ordos Basin, Journal of Chengdu University of Technology (Science and Technology Edition) 30(3): 236–241.

Ganjdanesh R., Bryant S.L., Orbach R.L., Pope G.A., Sepehrnoori K., 2012. Coupled CO_2 sequestration and energy production from geopressured geothermal aquifers, CMTC 151351, In: Carbon Management Technology Conference, Orlando, Florida, USA, 7-9 February 2012.

Garcia A.V., Thomsen K., Stenby E.H., 2006. Prediction of mineral scale formation in geothermal and oilfield operations using the extended UNIQUAC model: Part 2. Carbonate-scaling minerals Geothermics 35(3): 239−284.

Garcia J.E., 2003. Fluid dynamics of carbon dioxide disposal into saline aquifers, PhD thesis in Department of Civil and Environmental Engineering, University of California, Berkeley.

Garven G., 1995. Continental-scale groundwater flow and geologic processes, Annual Review of Earth and Planetary Sciences 23: 87–117.

Gasda S.E., Nordbotten J.M., Celia M.A. 2010. The impact of local-scale processes on large-scale CO_2 migration and immobilization, International Conference on Greenhouse Gas Technologies (GHGT 10), Elsevier/Energy Procedia.

Gaupp R., Pudlo D., Kohlhepp B., et al., 2009. Investigation of reservoir facies and fluid-rock interaction in the Rotliegend sandstones of the Altensalzwedel Block, Altmark, Middle Clean report.

Geertsma J., 1957. The effect of fluid pressure decline on volume changes of porous rocks, Transactions of AIME 210:331−339.

Gibson-Poole C.M., Edwards S., Langford R.P., Vakarelov B., 2006. Review of geological storage opportunities for carbon capture and storage (CCS) in Victoria. Cooperative Research Centre for Greenhouse Gas Technologies, December 2006, Report Number ICTPL-RPT06-0506.

Gilbert Z., Pyrak-Nolte L., 2004. Seismic montinoring of fracture alteration by mineral deposition, ARMA/NARMS04-512, in: the 6th North America Rock Mechanics Symposium (NARMS): Rock Mechanics Across Borders and Disciplines, Houston, Texas, June 5-9, 2004.

Giles M.R., de Boer R.B., 1990. Origin and significance of redistributional secondary porosity, Marine and Petroleum Geology 7: 378–397.

Goerke U.J., Park C.H., Wang W., Singh A.K., Kolditz O., 2011. Numerical simulation of multiphase hydromechanical processes induced by CO_2 injection into deep saline aquifers, Oil & Gas Science and Technology 66(1): 105–118.

Gou Y., Hou Z.M., Liu H.J., Zhou L., Were P., 2014. Numerical simulation of carbon dioxide injection for enhanced gas recovery (CO_2-EGR) in Altmark natural gas field, Acta Geotechnica 9:49–58.

Graf H., 2004. Experimental investigations on multiphase phenomena in porous media, PhD dissertation in Rupertus Carola University of Heidelberg, Germany.

Grataloup S., Bonijoly D., Brosse E., Garcia D., Hasanov V., Lescanne M., Renoux P., Rigollet C., Thoraval A., 2009. PICOREF: A site selection methodology for saline aquifer in Paris Basin, Energy Procedia 1(1): 2929–2936.

Grathwohl S., Lemp O., Schnell U., Maier J., Scheffknecht G., Kluger F., 2009. Highlz flexible burner concept for oxyfuel combustion, in: 1st International Oxyfuel Combustion Conference Cottbus, Germany 7-11 September 2009.

Gray G., 1983. Constitutive theory for vertically averaged equations describing steam-water flow in porous media, Water Resources Research 19(6): 1501–1510.

Grigg R.B., Svec R.K., Lichtner P.C., Carey W., and Lesher C.E., 2005. CO_2-brine-carbonate rock interactions: dissolution and precipitation. Poster presented at the Fourth Annual Conference on Carbon Capture & Sequestration, Alexandria, Virginia, May 2–5.

Gudmundsson S.R., Einarsson E., 1989. Controlled silica precipitation in geothermal brine at the Reykjanes geo-chemical plant, Geothermics 18: 105–112.

Gunnarsson I., Arnorsson S., 2005. Treatment of geothermal waste water to prevent silica scaling. In: Proceedings World Geothermal Congress, Antalya, Turkey, 24-29 April 2005.

Gunter W.D., Perkins E.H., McCann T.J., 1993. Aquifer disposal of CO_2-rich gasses: reaction design for added capacity, Energy Conversion and Management 34: 941–948.

Gunter W.D., Bachu S., Law D.H.-S., Marwaha V., Drysdale D.L., MacDonald D.E., McCann T.J., 1996.Technical and economic feasibility of CO_2 disposal in aquifers within the Alberta sedimentary basin, Canada, Energy Conversion and Management 37: 1135–1142.

Gunter W. D., Wiwchar B., Perkins E. H., 1997. Aquifer disposal of CO_2-rich greenhouse gases: extension of the time scale of experiment for CO_2-sequestering reactions by geochemical modeling, Mineral and Petrology 59: 121–140.

Guo L., Ling Y., Zhang S., Zhang F., 2012. Effects of stimulation treatment on reservoir characterization and reservoir simulation- a case study, in: 74th EAGE Conference and Exhibition incorporating SPE EUROPEC.

Guo Z., Pan L., Liu X., 2001. Formation conditions and distribution law of Jurassic ancient landform oil field in Ordos basin, China Petroleum Exploration 6 (4): 20–27 (in Chinese).

Guo Z., Zhang J., Yu Z., 1994. The evolutional characteristics f structure of the oil and gas bearing areas in Ordos massif. Petroleum Exploration and Development 21 (2): 22–29 (in Chinese).

Gupta H., Roy S., 2007. Geothermal energy–an alterative resource for the 21st century, Elsevier, Amsterdam, the Netherlands.

Hall H.N., 1953. Compressibility of reservoir rocks, Transactions of AIME 1953: 309–311.

Halvorsen C., 1993. Probe permeametry applied to a highly laminated sandstone reservoir, Marine and Petroleum Geology 10: 347-351.

Hao M., and Song Y.C., 2010. Research status of CO_2-EOR. Drilling and Production Technology 33(4): 59-63 (in Chinese).

Hardy J.A., Barthorpe R.T., Plummer M.A., Rhudy J.S., 1992. Control of scaling in the south Brae field, OTC 7858 presented at the 1992 Offshore Technology Conference, Houston, TX, May 4-7, 1992.

Harrison B., Falcone G., 2014. Carbon capture and sequestration versus carbon capture utilization and storage for enhanced oil recovery, Acta Geotechnica 9:29-38.

Hassanizadeh S.M., Gray W.G., 1979. General conservation equations for multi-phase systems 2: mass, momenta, energy, and entropy equations, Advances in Water Resources 2: 191–208.

Hassanizadeh M., Gray W., 1980. General conservation equations for multi-phase systems: 3.Constitutive theory for porous media flow, Advances in Water Resources 3(1): 25–40.

Hassanizadeh S.M., 1986a. Derivation of basic equations of mass transport in porous media, Part I, Macroscopic balance laws, Advances in Water Resources 9:196–206.

Hassanizadeh S.M., 1986b. Derivation of basic equations of mass transport in porous media, Part II, Generalized Darcy's law and Fick's law, Advances in Water Resources 9: 207–222.

Hawkes C.D., McLellan P.J., Zimmer U., Bachu S., 2004. Geomechanical factors affecting geological storage of CO2 in depleted oil and gas reservoirs: risks and mechanisms, In: Proceedings of Gulf Rocks 2004, the 6th North America Rock Mechanics Symposium (NARMS): Rock Mechanics Across Borders and Disciplines, Houston, Texas.

Heath J.E., McKenna S.A., Dewers T.A., Roach J.D., Kobos P.H., 2014. Multiwell CO_2 injectivity: impact of boundary conditions and brine extration on geological CO_2 storage efficiency and pressure buildup, Environmental Science Technology 48: 1067-1074.

Heeschen K., Risse A., Ostertag-Henning C., Stadler S., 2011. Importance of co-captured gases in the underground storage of CO_2: Quantification of mineral alterations in chemical experiments, Energy Procedia 4: 4480−4486.

Heinemann Z.E., 2005. Textbook series volume 1-fluid flow in porous media, Leoben.

Helgeson H.C., Kirkham D.H., Flowers G.C., 1981.Theoretical prediction of the thermodynamic behavior of aqueous electrolytes at high pressures and temperatures: IV. Calculation of activity coefficients, osmotic coefficients, and apparent molal and standard and relative partial molal properties to 600°C and 5 kbar, American Journal of Sciences 281: 1249–1516.

Hellevang H., 2006. Interactions between CO_2, saline water and minerals during geological storage of CO_2, PhD thesis in University of Bergen, Norway.

Helmig R., 1997. Multiphase flow and transport processes in the subsurface, Springer, 1997.

Hendriks C.A., Blok K., 1993. Underground storage of carbon dioxide, Energy Conversion and Management 34 (9–11): 949–957.

Hettema M.H.H., Schutjens P.M.T.M., Verboom B.J.M., Gussinklo H.J., 1998. Production-induced compaction of sandstone reservoirs: the strong influence of field stress, SPE 50630, In: SPE European Conference, The Hague, The Netherlands, 1998.

Hillel D., 1998. Environmental soil physics, Academic Press, the USA.

Holloway S., Savage D., 1993.The potential for aquifer disposal of carbon dioxide in the UK, Energy Conversion and Management 34: 925–932.

Holt T., Jensen J.I., Lindeberg E., 1995. Underground storage of CO_2 in aquifers and oil reservoirs, Energy Conversion and Management 36 (N6–9): 535–538.

Holtz M.H., 2002. Residual gas saturation to aquifer influx: A calculation method for 3-D computer reservoir model construction, SPE Paper 75502, presented at the SPE Gas Technologies Symposium, Calgary, Alberta, Canada. April 2002.

Horne R.A., 1969. Marine Chemistry: the structure of water and the chemistry of the hydrosphere, Wiley, New York, USA.

Horne N.R., 1990. Modern well test analysis: a computer-aided approach: Petroway, Inc, 257.

Hou Z., Tadongmo F.A., Pusch G., 2009. Secondary in-situ stresses resulting from change of pore pressure and their influence on the maximal storage pressure of CO_2 or natural gas in depleted reservoirs. DGMK/ÖGEW-Frühjahrstagung 2009, Fachbereich Aufsuchung und Gewinnung Celle, 27-28 April 2009.

Hou Z., Gou Y., Taron J., Gorke U.J., Kolditz O., 2012a. Thermo-hydro-mechanical modeling of carbon dioxide injection for enhanced gas-recovery (CO_2-EGR): a benchmarking study for code comparison. Environmental Earth Science 67(2):549–561.

Hou Z., Kracke T., Zhou L., Wang X., 2012b. Gebirgsmechanische Auswirkungen von Fracs im tiefen Untergrund des Norddeutschen Beckens: geologische Steinsalzbarriereintegrität und maximale Magnitude induzierter Mikrobeben anhand der GeneSys-Stimulation im Mai 2011. Erdöl Erdgas Kohle 11:457–460.

Hou Z., Zhou L., 2013. Numerical investigation and optimiyation of multiple fractures in tight gas reservoirs. Oil Gas-European Magazin 39(3):129–135.

Hu S.B., He L.J., Wang J.Y., 2000. Heat flow in the continental area of China: a new data set. Earth and Planetary Science Letters 179: 407–419.

Hu J.N., Zhang S.N., Li D.M., 2001. The influence of diagenesis on reservoir quality in Shihezi-Shanxi formation in northern Ordos Basin, Journal of Chengdu University of Technology 28(2): 170–173(In Chinese).

Huenges E., 2010. Geothermal Energy Systems: Exploration, Development and Utilization, Viley-VCH 2010.

Huppert H.E., 2000. Geological fluid mechanics, In: Batchelor G.K., Moffat H.K., Worster M.G., editors, Perspectives in Fluid Dynamics: A Collective Introduction to Current Research, Cambridge University Press, Cambridge, 2000, pp. 447–506.

Hussain F., Cinar Y., Michael K., 2013. Impacts of Surat Basin geological CO_2 storage on groundwater flow (generic and Wandoan area simulations), CO2CRC Report No: RPT13-4161.

Huq F., Blum P., Marks M.A.W., Nowak M., Haderlein S.B., Grathwohl P., 2012. Chemical changes in fluid composition due to CO_2 injection in the Altmark gas field: preliminary results from batch experiments. Environmental Earth Sciences 67(2):385–394.

IEA Greenhouse Gas R&D Programme, 2000. Capture of CO_2 using water scrubbing. Report Ph3/26, IEA Greenhouse gas R&D Programme, Cheltenham, UK.

IEA, 2010. Geothermal energy, annual report 2010.

IEA, 2011. Caprock systems for CO_2 geological storage.

IEA, 2013. Redrawing the energy-climate map. World Energy Outlook Special Report.

IPCC, 2005. In: Metz B., Davidson O., de Coninck H.C., Loos M., Mayer L.A., editors, Special report on carbon dioxide capture and storage. Cambridge, UK, and New York, NY, USA: Cambridge University Press.

IPCC, 2007. In: Parry M., Canziani O., Palutikof J., van der Linden P., Hanson C., 2007, climate change: impacts, adaptation and vulnerability.

Itasca, 2009. FLAC3D version 4.0 manual, advanced, three dimensional continuum modeling for geotechnical analysis of rock, soil and structural support.

Jaeger J.C., Cook N.G.W., 1979. Fundamentals of rock mechanics, 3rd edition, Chapman and Hall, London.

Jalalh A.A., 2006. Compressibility of porous rocks: part II new relationships, Acta Geophysica 54(4): 399–412.

Jambhekar V.A., 2011. Forchheimer porous-media flow models-numerical investigation and comparison with experimental data, Master Thesis in Institute of water and environmental system modeling, University of Stuttgart.

Joekar-Niasar V., Hassanizadeh S.M., 2011. Specific interfacial area: the missing state variable in two-phase flow equations, Water Resources Research 47, W05513.

Johnson J.W., Nitao J.J., Steefel C.I., Knauss K.G., 2001. Reactive transport modeling of geologic CO_2 sequestration in saline aquifers: the influence of intra-aquifer shales and the reactive effectiveness of structural, solubility and mineral trapping during prograde and retrograde sequestration, First National Conference on Carbon Sequestration, National Energy Laboratory, Washington, DC.

Kabera T., Li Y.L., 2011. Impact of CO_2 injection in deep saline aquifers: a study on pressure evolution in stratified formation of Qianjiang sag, China, International Journal of Chemical Engineering and Applications, 2(2): 122-129.

Kaszuba J.P., Janecky D.R., Snow M.G., 2003. Carbon dioxide reaction processes in a model brine aquifer at $200^{o}C$ and 200 bars: Implications for geologic sequestration of carbon, Applied Geochemistry 18: 1065–1080.

Kaszuba J.P., Janecky D.R., Snow M.G., 2005. Experimental evaluation of mixed fluid reactions between supercritical carbon dioxide and NaCl brine: Relevance to the integrity of a geologic carbon repository, Chemical Geology 217: 277–293.

Keith D., Hassanzadeh H., Pooladi-Darvish M., 2005. Reservoir engineering to accelerate dissolution of stored CO_2 in brines, In: Proceedings of the 7th International Conference on Greenhouse Gas Control Technologies (GHGT-7), September 5–9, 2004, Vancouver, Canada, 2:2163–2168.

Ketzer J.M., Iglesias R., Einloft S., Dullius J., Ligabue R., de Lima V., 2009. Water–rock–CO_2 interactions in saline aquifers aimed for carbon dioxide storage: Experimental and numerical modeling studies of the Rio Bonito Formation (Permian), southern Brazil, Applied Geochemistry 24: 760–767.

Kim J., Nam M.J., Matsuoka T., 2013. Estimation of CO_2 saturation during both CO_2 drainage and imbibition processes based on both seismic velocity and electrical resistivity measurements, Geophysical Journal International 195: 292–300.

Klimetz M.P., 1983. Speculations on the Mesozoic plate-tectonic evolution of eastern China, Tectonics 2:129–166.

Klubertanz G., Bouchelaghem F., Laloui L., Vulliet L., 2003. Miscible and immiscible multiphase flow in deformable porous media, Mathematical and Computer Modelling 37:571-582.

Kobus H., de Haar U., 1995. Perspektiven der Wasserforschung, DFG.

Kohl A.L., Nielsen R.B., 1997. Gas Purification, Gulf Publishing Company, Houston, TX, USA.

Koide H., Tazaki Y., Noguchi Y., Iijima M., Ito K., Shindo Y., 1993. Underground storage of carbon dioxide in depleted natural gas reservoirs and in useless aquifers, Engineering Geology 34 (3–4): 175–179.

Koide H.G., Takahashi M., Tsukamoto H., 1995. Self-trapping mechanisms of carbon dioxide, Energy Conversion and Management 36(6–9): 505–508.

Kolditz O., 2002. Multiphase flow in deformable porous media, Computational Methods in Environmental Fluid Mechanics 333-372.

Kolditz O., Goerke U., Shao H., Wang W., 2011. Benchmarks and examples for THMC processes in porous media, 1st edition, Springer: Berlin.

Kolditz O., Bauer S., Bilke L., Böttcher N., Delfs J.O., Fischer T., Görke U.K., et al., 2012. OpenGeoSys: an open-source initiative for numerical simulation of thermo-hydro-mechanical/chemical (THM/C) processes in porous media, Environmental Earth Sciences 67(2): 589–599.

Kool J.B., Parker J.C., 1987. Development and evaluation of closed form expressions for hysteretic soil hydraulic properties, Water Resources Research 23: 105–114.

Kopp A., Bielinski A., Ebigbo A., Class H., Helmig R., 2006. Numerical investigation of temperature effects during the injection of carbon dioxide into brine aquifers. In: GHGT 8, Trondheim, Norway.

Korbol R., Kaddour A., 1995. Sleipner vest CO_2 disposal—injection of removed CO_2 into the Utsira Formation, Energy Conversion and Management 36(6–9): 509–512.

Kovscek A.R., 2002. Screening criteria for CO_2 storage in oil reservoirs, Petroleum Science and Technology 20(7–8): 841–866.

Kumar A., Noh M.H., Sepehrnoori K., Pope G.A., Bryant S.L., Lake L.W., 2005. Simulating CO_2 storage in deep saline aquifers, in: Benson SM, editor. Carbon dioxide capture for storage in deep geologic formations - results from the CO_2 capture project, vol. 2, geologic storage of carbon dioxide with monitoring and verification. London, UK: Elsevier; pp. 877–898.

Kühn M., Tesmer M., Pilz P., Meyer R., Reinicke K., Förster A., Kolditz O., Schäfer D., CLEAN Parterners, 2012. CLEAN: project overview on CO_2 large-scale enhanced gas recovery in the Altmark natural gas field (Germany). Environmental Earth Science 67: 311–321.

Labus K., Bujok P., 2011. CO_2 mineral sequestration mechanisms and capacity of saline aquifers of the Upper Silesian Coal Basin (Central Europe) - Modeling and experimental verification, Energy 36: 4974–4982.

Lake L.W., 1989. Enhanced oil recovery, Prentice Hall, New Jersey.

Lasaga A.C., 1984. Chemical kinetics of water-rock interactions, Journal of Geophysical Research 89: 4009–4025.

Lasaga A.C., Rye D.M., 1993. Fluid flow and chemical reaction kinetics in metamorphic systems, American Journal of Science 293: 361–404.

Lasaga A.C., Soler J.M., Ganor J., Burch T.E., Nagy K.L., 1994. Chemical weathering rate laws and global geochemical cycles, Geochimica et Cosmochimica Acta 58(10): 2361–2386.

Law D.H-S., Bachu S., 1996. Hydrogeological and numerical analysis of CO_2 disposal in deep aquifers in the Alberta sedimentary basin, Energy Conversion and Management 37: 1167–1174.

Le G.Y., Fillacier S., Lecomte A., Munier G., Hanot F., Quisel N., Rampnoux N., 2011. Technical challenges in characterization of future CO_2 storage site in a deep saline aquifer in the Paris basin, lessons learned from practical application of site selection methodology, Energy Procedia 4: 4599–4606.

Lenhard R.J., Johnson T.G., Parker J.C., 1993. Experimental observations of nonaqueous-phase liquids subsurface movement, Journal of Contaminant Hydrology 12: 79–101.

Leverett M.C., 1939. Flow of oil-water mixtures through unconsolidated sands, Transaction of AIME 132: 381–401.

Lewis J.J.M., 1988. Outcrop-derived quantitative models of permeability heterogeneity for genetically different sand bodies, SPE Paper 18153, in: 63rd Annual Technical Conference and Exhibition of the Society of Petroleum Engineers, Houston, Texas, Oct 2-5, 1988, 449-463.

Li C., Kong X., Xu X., Li P., 1999. Double effective stresses of porous media, Ziran Zazhi 21(5): 288–292.

Li C.L., Chen X.F., Du Z.M., 2004. A new relationship of rock compressibility with porosity, SPE 88464, in: SPE Asia Pacific Oil and Gas Conference and Exhibition held in Perth, Australia, 18-20 October 2004.

Li G., Lu M., 2002. Atlas of Chinese Petroliferous Basins, Petroleum Industry Press, Beijing (in Chinese).

Li M., Gao J.R., 2010. Basement faults and volcanic rock distributions in the Ordos Basin, Science China (Earth Sciences) 1–9.

Li Q., Liu G.Z., Liu X.H., Li X.C., 2013. Application of a health, safety, and environmental screening and ranking framework to the Shenhua CCS project, International Journal of Greenhouse Gas Control 17: 504–514.

Li J., Teixeira M., Salim P., Fan Y., 2012. Performance evaluation of a new transient two-phase flow model, IADC/SPE 151034

Li S., Xiao Y., Liou D., Chen Y., Ge N., Zhang Z., Sun S., Cong B., Zhang R., Hart S.R., Wang S., 1993. Collision of the north China and Yangze and formation of coesite-bearing eclogites: timing and processes, Chemical Geology 109: 89–111.

Li X.C., Liu Y.F., Bai B., Fang Z.M., 2006. Ranking and screening of CO_2 saline aquifer storage zones in China, Chinese Journal of Rock Mechanics and Engineering 25(5): 963–968 (in Chinese).

Lichtner P.C., 1985. Continuum model for simultaneous chemical reactions and mass transport in hydrothermal systems, Geochimica et Cosmochimica Acta 49(3): 779–800.

Lichtner P.C., 1992.Time-space continuum description of fluid/rock interaction in permeable media, Water Resources Research 28:3135–3155.

Lide D.R., 2000. Handbook of Chemistry and Physics, the Chemical Rubber Company, CRC Press LLC, Boca Raton, FL, USA.

Lindeberg E., Wessel-Berg D., 1997. Vertical convection in an aquifer column under a gas cap of CO_2, Energy Conversion and Management 38(Suppl.): S229–S234.

Lior N., 2008. Energy resources and use the present situation and possible paths to the future, Energy 33: 842–857.

Liu H.H., Zhang Y.Q., Zhou Q., Molz F.J., 2007. An interpretation of potential scale dependence of the effective matrix diffusion coefficient, Journal of Contaminant Hydrology 90: 41–57.

Liu H.J., Hou Z.M., Gou Y., Were P., 2013a. Simulation of CO2-water-rock interaction processes: mineral scaling problems in saline formations 233-248. In: Hou M.Z., Xie H.P., Were P., editors. Clean energy systems in the subsurface: production, storage and conversion. In: Proceedings of the 3rd Sino-German conference on Underground storage of CO2 and energy, Goslar, Germany: Springer series in Geomechanics and Geoengineering, 21-23 May 2013

Liu H.J., Hou Z.M., Were P., Gou Y., Sun X.L., 2014. Simulation of CO_2 plume movement in multilayered saline formations through multilayer injection technology in the Ordos Basin, China. Environmental Earth Science 71:4447–4462.

Liu H.J., Hou Z.M., Were P., Gou Y., Xiong L., Sun X.L., 2014b. Modelling CO_2-brine-rock interactions in the Upper Paleozoic formations of Ordos Basin used for CO_2 sequestration, DOI 10.1007/s12665-014-3571-4.

Liu L.Q., Liu C.X., Wang J.S., 2013b. Deliberating on renewable and sustainable energy policies in China, Renewable and Sustainable Energy Reviews 17: 191–198.

Liu Z.H., Wolfgang D., 2002. Physicochemical mechanisms of rate-determining of calcite deposition and their implications for paleo-environmental reconstruction, Academica Sinica 21(1): 252–257(in Chinese).

Liu Z.Q., Gao Q.S., Zhang J., 2001. Pore structural features of Shanxi formation reservoir in Daniudi gas field, Natural Gas Industry (supplementary issue) 21: 53–56(In Chinese).

Logan J.D., 2001. Transport modeling in hydrogeochemical systems, Springer Publisher, pp. 225.

Lohuis J.A.O., 1993. Carbon dioxide disposal and sustainable development in the Netherlands, Energy Conversion and Management 34: 815–821.

Louis C.A., Dessenne J.L., Feuga B., 1977. Interaction between water flow phenomena and the mechanical behavior of soil or rock masses, In: Gudehus G, eds. Finite Elements in Geomechanics, New York: Wiley 479–511.

Louis L., David C., Metz V., Robion P., Menéndez B., Kissel C., 2005. Microstructural control on the anisotropy of elastic and transport properties in undeformed sandstones, International Journal of Rock Mechanics and Mining Sciences 42(7/8): 911–923.

Lu C., Lee S.Y., Han W.S., Mcpherson B.J., Lichtner P.C., 2009. Comments on "abrupt-interface solution for carbon dioxide injection into porous media" by Dentz M., Tartakovsky D.M., Transport in Porous Media 79: 29–37.

Lucia M.D., Bauer S., Beyer C., Kühn M., Nowak T., Pudlo D., Reitenbach V., Stadler S., 2012. Modelling CO_2-induced fluid-rock interactions in the Altensalzwedel gas reservoir, Part I: from experimental data to a reference geochemical model, Environmental Earth Science 67:563–572.

Lund J.W., 2004. 100 years of geothermal power production, GHC Bulletin 11–19.

Luquot L., Gouze P., 2009. Experimental determination of porosity and permeability changes induced by injection of CO_2 into carbonate rocks, Chemical Geology (1-2): 148–159.

Ma R.Y., Zhu H.P., Zhang D.F., Pan A.F., 2009. Basement faults and their recent activity in Ordos Basin, Chinese Journal of Earth Science and Environment 31(4): 400–408 (in Chinese).

Ma Z., Chen A., Wang J., 1998. A study on the conditions of forming the fossil weathered residuum gas reservoir in the center of Eerduosi basin, Natural Gas Industry 18 (1): 9–13 (in Chinese).

Mangold D.C., Tsang C.F., 1991. A summary of subsurface hydrological and hydrochemical models, Review of Geophysics 9: 51–79.

Martens S., Kempka T., Liebscher A., Lüth S., Möller F., Myrttinen A., Norden B., Schmidt-Hattenberger C., Zimmer M., Kühn M., The Ketzin Group, 2012. Europe's longest-operating on-shore CO_2 storage site at Ketzin, Germany: a progress report after three years of injection, Environmental Earth Science 67:323–334.

Mathiassen O.M., 2003. CO_2 as injection gas for enhanced oil recovery and estimation of the potential on the Norwegian Continental Shelf, PhD thesis, Norwegian University of Science and Technology, Trondheim/Stavanger, May, 2003.

McCaln W.D., Gillespie C., Assocs. Inc, 1991. Reservoir-fluid property correlations-state of the art, SPE 18571.

McKee C.R., Bumb A.C., Koenig R.A., 1988. Stress-dependent permeability and porosity of coal and other geologic formations, SPE Formation Evaluation 3: 81–91.

McPherson B.J.O.L., Cole B.S., 2000. Multiphase CO_2 flow, transport and sequestration in the Powder River basin, Wyoming, USA, Journal of Geochemical Exploration 69–70(6): 65–70.

Mcpherson B., Lichtner P., 2001. CO_2 Sequestration in deep aquifers, Los Alamos National Laboratory (LANL), Los Alamos, NM.

Meng Z.P., Lan Q., Liu C.L., Ji Y.M., Li S.N., Zhang X.M., 2013. In-situ stress and coal reservoir pressure in Southeast margin of Ordos Basin and their coupling relations, Journal of China Coal Society 38(1): 122−128 (in Chinese).

Meyer J.P., 2012. Linear failure criteria with three principal stresses, Master Thesis in the University of Minnesota.

Meyer R., 2002. Anisotropy of sandstone permeability, CREWES Research Report 14:1–12.

Monastero F.C., 2002. Model for success-an overview of industry-military cooperation in the development of power operations at the Coso Geothermal Field in Southern California, GRC Bulletin 188–194.

Moritis G., 2006. CO_2 injection gains momentum, Oil Gas J 104(15): 37–57.

Morozova D., Zettlitzer M., Let D., Würdemann H., CO2SINK group, 2011. Monitoring of the microbial community composition in deep subsurface saline aquifers during CO_2 storage in Ketzin, Germany, Energy Procedia 4:4362–4370.

Morris J.P., Hao Y., Foxall W., McNab W., 2011. In Salah CO_2 storage JIP: hydromechanical simulations of surface uplift due to CO_2 injection at In Salah, Energy Procedia 4:3269–3275.

Mualem Y., 1974. A conceptual model of hysteresis, Water Resources Research 10: 514–520.

Mualem Y., 1976. A new model for predicting the hydraulic conductivity for unsaturated porous media, Water Resources Research 12: 513–522.

Muskat M., Meres M.W., 1936. The flow of heterogeneous fluids through porous media, Physics 7: 346–363.

Neal P. R., Cinar Y., Allinson W. G. 2011. The Economics of pressure-relief with CO_2 injection, Energy Procedia 4:4215–4220.

Nicot J.P., Oldenburg C.M., Bryant S.L., Hovorka S.D., 2008. Pressure perturbations from geologic carbon sequestration: area-of-review boundaries and borehole leakage driving forces, in: 9th International Conference on Greenhouse Gas Control Technologies (GHGT-9), Washington, D.C., 16-20 November, 2008.

Nishikawa N., Morishita M., Uchiyama M., Yamaguchi F., Ohtsubo K., Kimuro H., Hiraoka R., 1992. CO_2 clathrate formation and its properties in the simulated deep ocean, Energy Conversion and Management 33: 651−658. In: Proceedings of the first international conference on carbon dioxide removal.

Nooner S.L., Eiken O., Hermanrud C., Sasagawa G., Stenvold T., Zumberge M.A., 2007. Constraints on the in situ density of CO2 within the Utsira formation from time-lapse seafloor gravity measurements, International Journal of Greenhouse Gas Control 1:198–214.

Nordbotten J.M., Celia M.A., Bachu S., 2005. Injection and storage of CO_2 in deep saline aquifers: Analytical solution for CO_2 plume evolution during injection, Transport in Porous Media 58: 339–360.

Nordbotten J.M., Celia M.A., 2006. Similarity solutions for fluid injection into confined aquifers, Journal of Fluid Mechanics 561:307–327.

Obdam A., van der Meer L.G.H., May F., Kervevan C., Bech N., Wildenborg A., 2003. Effective CO2 storage capacity in aquifers, gas fields, oil fields and coal fields. I: 339–344. In: Gale J. and Kaya Y. editors, Proceedings of the 6th International Conference on Greenhouse Gas Control Technologies (GHGT-6), 1–4 October 2002, Kyoto, Japan, Pergamon.

Olafuyi O.A., 2008. Capillary pressure and relative permeability of small cores, in: Proceedings -SPE Symposium on Improved Oil Recovery, 20-23 April, Tulsa, Oklahoma, USA.

Oldenburg C.M., Benson S.M., 2001. CO_2 injection for enhanced gas production and carbon sequestration, SPE 74367, in: SPE International Petroleum Conference and Exhibition, Villahermosa, Mexico, 10-12 Feb 2002.

Oldenburg C.M., Pruess K., Benson S.M., 2001. Process modeling of CO_2 injection into natural gas reservoirs for carbon sequestration and enhanced gas recovery, Energy and Fuels 15: 293–298.

Oldenburg C. M., Rinaldi A. P. 2011. Buoyancy effects on upward brine displacement caused by CO_2 injection, Transport in Porous Media 87:525–540.

Omole O., Osoba J.S., 1983. Carbon dioxide-dolomite rock interaction during CO_2 flooding process, Paper 83-34-17, Petrol. Soc. Canadian Inst. Min. Metal. 1–13, Ban, Alberta.

Ortoleva P.J., Dove P., Richter F., 1998. Geochemical perspectives on CO_2 sequestration, Manuscript prepared for U. S. Department of Energy Workshop on "Terrestrial Sequestration of CO_2 - An Assessment of Research Needs," Gaithersburg, MD, May 10–12.

Ostrowski L., 2011. Well test analysis in practice, training courses in the TU Clausthal, 14–17 February 2011.

Oudinot A.Y., Schepers K.C., Reeves S.R., 2007. Gas injection and breakthrough trends as observed in ECBM sequestration pilot projects and field demonstrations, No 0714, in: 2007 International Coalbed Methane Symposium.

Palandri J.L., Kharaka Y.K., 2004. A compilation of rate parameters of water-mineral interaction kinetics for application to geochemical modeling, U.S. Geological Survery, Open File Report 2004-1068.

Pankow J.F., Cherry J.A., 1996. Dense chlorinated solvent and other DNAPLs in groundwater: History, behavior and remediation, Waterloo Educational Services, Rockwood, ON, Canada.

Parlange J.-Y. , 1976. Capillary hysteresis and the relationship between drying and wetting curves, Water Resources Research 12: 224–228.

Payne D.J.B., Ward M., King R.L., 2008. Position paper: direct use geothermal applications. AGEA

Pearce J.M., Holloway S., Wacker H., Nelis M.K., Rochelle C., Bateman K., 1996. Natural occurrences as analogues for the geological disposal of carbon dioxide, Energy Conversion and Management 37 (6–8): 1123–1128.

Pentland C.H., Al-Mansoori S., Iglauer S., Bijeljic B., Blunt M.J., 2008. Measurement of non-wetting phase trapping in sand packs, SPE 115697.

Perry K.F., 2005. Natural gas industry experience and technology: potential applications to CO_2 geological storage, 815–826. In: Benson SM, editor. Carbon dioxide capture for storage in deep geologic formations-results from the CO_2 capture project, vol. 2: geologic storage of carbon dioxide with monitoring and verification. London, UK: Elsevier.

Phillips W.S., Rutledge J.T., House L.S., Fehler M.C., 2002. Induced microearthquake patterns in hydrocarbon and geothermal reservoirs: six case studies, Pure and Applied Geophysics 159: 345–369.

Plotkowiak M., 2005. Hydro-mechanical coupling in porous media with emphasis on poroelasticity, paper in University of Hannover, ISEB.

Pritchett J. W., 2010. On the relative effectiveness of H_2O and CO_2 as reservoir working fluids for EGS heat mining, Geothermal Resources Council Transactions 33: 235–239.

Pruess K., 1991. TOUGH2: A general numerical simulator for multiphase fluid and heat flow, Lawrence Berkeley Laboratory Report LBL-29400, Berkeley, California.

Pruess K., Oldenburg C., Moridis G., 1999. TOUGH2 user's guide, Version 2.0, Lawrence Berkeley Laboratory Report LBL-43134, Berkeley, California.

Pruess K., Xu T.F., Apps J.A., Garcia J., 2001. Numerical modeling of aquifer disposal of CO_2, paper SPE 66537. In: Proceedings SPE/EPA/DOE Exploration and Production Environmental Conference, San Antonio, Texas, February 26–28, 2001.

Pruess K., Garcia J., Kovscek T., Oldenburg C., Rutqvist J., Steefel C., Xu, T. 2002. Intercomparison of numerical simulation codes for geologic disposal of CO_2, LBNL 51813, United States.

Pruess K., Garcia J., Kovscek T., Oldenburg C., Rutqvist J., Steefel C., Xu T.F., 2004. Code intercomparison builds confidence in numerical simulation models for geologic disposal of CO_2, Energy 29:1431–1444.

Pruess K., 2005. Geologic storage of greenhouse gases: multiphase and non-isothermal effects, and implications for leakage behavior, LBNL 58633.

Pruess K., 2006. Enhanced geothermal dystems (EGS): using CO_2 as working fluid – a novel approach for generating renewable energy with simultaneous sequestration of carbon, Geothermics 35(4): 351–367, August.

Pruess K., Azaroual M., 2006. On the feasibility of using supercritical CO_2 as heat transmission fluid in an Engineered Hot Dry Rock Geothermal System. In: Proceedings of the Thirty-First Workshop on Geothermal Reservoir Engineering,Stanford University, Stanford, CA, USA, pp. 386–393.

Pruess K., 2007. Enhanced geothermal systems (EGS) comparing water with CO_2 as heat transmission fluids. Paper LBNL 63627.

Pruess K., Muller N., 2009. Formation dry-out from CO_2 injection into saline aquifers: effects of solids precipitation and their mitigation, Water Resources Research 45: pp.W03402.

Pudlo D., Reitenbach V., Albrecht D., Ganzer L., Gernert U., Wienand J., Kohlhepp B., Gaupp R., 2012. The impact of diagenetic fluid-rock reactions on Rotliegend sandstone composition and petrophysical properties (Altmark area, central Germany), Environmental Earth Sciences 67: 369–384.

Qin Y.Y., He Q., Cui T.X., Deng H.L., Yuan L.H., 2005. Application and development of production technology for Daniudi gas field, In: 1st Sinopec oil and gas production technology meeting, 27 May, Beijing, 285–302 (in Chinese).

Qu Y., Luo C., Gong Y.L., 2012. The study of mid-low temperature geothermal power system, Renewable Energy Resources 30(1): 88–91(in Chinese).

Randolph J.B., Saar M.O., 2011a. Impact of reservoir permeability on the choice of subsurface geothermal heat exchange fluid: CO_2 versus water and native brine. In: Proceedings for the Geothermal Resources Council 35th Annual Meeting: 23–26 Oct, 2011, San Diego, CA, USA.

Randolph J.B., Saar M.O., 2011b. Combining geothermal energy capture with geologic carbon dioxide sequestration, Geophysical Research Letters 38: L10401.

Reeves H.W., Abriola L.M., 1994. An iterative compositional model for subsurface multiphase flow. Journal of Contaminant Hydrology 14: 249–276.

Reichman J., Bresnehan R., Evans G., Selin C., 2008. Electricity generation using enhanced geothermal systems with CO_2 as heat transmission fluid, in: Proceedings of the Sir Mark Oliphant International Frontiers of Science and Technology Australian Geothermal Energy Conference, Rydges Hotel, Melbourne.

Remoroza A., Doroodchi E., Moghtaderi B., 2012. CO_2-EGS in hot dry rock: preliminary results from CO_2-rock interaction experiments, in: Proceedings of 37th Workshop on Geothermal Reservoir Engineering, Stanford University, Stanford, California, 30 January-1 February, 2012, SGP-TR-194.

Ren J.S., 1999. The geotectonic map of China and its adjacent area (1:5000,000) and its explanatory text. Geological Publishing House, Beijing (in Chinese and English).

Ren J.S., Xiao L.W, 2002. Tectonic settings of petroliferous basins in continental China, Episodes 25(4): 227–235.

Ren X.K., Cui Y.J., Bu X.P., Tan Y.J., Zhang J.Q., 2010. The potential analysis of CO_2 geological sequestration of Ordos basin, Chinese Energy 32(1): 29–32 (in Chinese).

Ren Z., 1996. Thermal history of the Ordos Basin and its relationship to oil and gas generation, Acta Petrolei Sinica 17: 17–24 (in Chinese with English abstract).

Rhodes M.E., Bijeljic B., Blunt M.J., 2009. A rigorous pore-to-field-scale simulation method for singel phase flow based on continuous time random walks, SPE 106434, 88–94.

Riano V.V., 2012. Thermo−hydro−mechanical impacts of carbon dioxide (CO_2) injection in deep saline aquifers, PhD Thesis in Technical University of Catalonia.

Rimmelé G., Barlet-Gouédard V., Renard F., 2010. Evolution of the petrophysical and mineralogical properties of two reservoir rocks under thermodynamic conditions relevant for CO_2 geological storage at 3 km depth, Oil Gas Science and Technology – Review IFP 65: 565–580.

Rochelle C.A., Bateman K., Pearce J.M., 2002. Geochemical interactions between supercritical CO_2 and the Utsira formation: and experimental study, British Geological Survey Commissioned Report, CR/02/060, pp. 62.

Rohmer J., Bouc O., 2010. A response surface methodology to address uncertainties in cap rock failure assessment for CO_2 geological storage in deep aquifers, International Journal of Greenhouse Gas Control 4(2): 198−208.

Roht Y.L., Boschan A., Ippolito I., Chertcoff R., 2012. Experimental study of solute dispersion in macroscopic suspension flow, Journal of Contaminant Hydrology 145:10–16.

Rosenbauer R., Koksalan T., Palandri J.L., 2005. Experimental investigation of CO_2–brine–rock interactions at elevated temperature and pressure: implications for CO_2 sequestration in deep-saline aquifers, Fuel processing technology 86:1571–1597.

Rutqvist J., Tsang C.F., 2002. A study of caprock hydromechanical changes associated with CO_2-injection into a brine formation, Environmental Geology 42: 296–305.

Rutqvist J., Wu Y.S., Tsang C.F., Bodvarsson G., 2002. A modeling approach for analysis of coupled multiphase fluid flow, heat transfer, and deformation in fractured porous rock, International Journal of Rock Mechanics and Mining Sciences 39:429-442.

Rutqvist J., Stephansson O., 2003a. The role of hydromechanical coupling in fractures rock engineering, Hydrogeology Journal 11:7-40.

Rutqvist, J., Tsang C-F., 2003b. TOUGH-FLAC: a numerical simulator for analysis of coupled thermal–hydrologic–mechanical processes in fractured and porous geological media under multiphase flow conditions. In: Proceedings of the TOUGH Symposium 2003, Lawrence Berkeley National Laboratory, Berkeley, May 12– 14.

Rutqvist J., Birkholzer J.T., Tsang C.F., 2008. Coupled reservoir-geomechanical analysis of the potential for tensile and shear failure associated with CO_2 injection in multilayered reservoir-caprock systems, Rock Mechanics and Mining Sciences 45:132−143.

Rutqvist J., 2012. The geomechanics of CO_2 storage in deep sedimentary formations, Geotechnical and Geological Engineering 30:525−551.

Sanyal S.K., Enedy S.L., 2011. Fifty years of power generation at the geysers geothermal field, California- the lessons learned, in: Thirty-sixth workshop on geothermal reservoir engineering, Stanford, California.

Sayegh S.G., Krause F.F., Girard M., DeBree C., 1990. Rock-fluid interactions of carbonated brines in a sandstone reservoir: Pembina Cardium, Alberta, Canada, SPE Formation Evaluation 5: 399–405.

Scatter A., Iqbal G.M., Buchwalter J.L., 2007. Practical enhanced reservoir engineering-assisted with simulation software, PennWell Corporation, USA.

Schrefler B.A., Gawin D., 1996. The effective stress principle: incremental or finite form? International Journal for Numerical and Analytical Methods 20: 785–815.

Scislewski A., Zuddas P., 2010. Estimation of reactive mineral surface area during water–rock interaction using fluid chemical data, Geochimica et Cosmochimica Acta 74: 6996–7007.

Scott P. S., Farquhar G. J., Kouwen N., 1983. Hysteretic effects on net infiltration, Advances in Infiltration 11: 163–170.

Settari A.T., Walters D.A., 1999. Advances in coupled geomechanical and reservoir modeling with applications to reservoir compaction, SPE 51927, In: Reservoir Simulation Symposium, Houston, Texas, 14-17 February 1999.

Sevougian S.D., Lake L.W., Schechter R.S., 1992. A new geochemical simulator to design more effective sandstone acidizing treatments. Paper SPE 24780. In: Proceedings 67th SPE Annual Technical Conference and Exihibition, Washington, DC, October 4–7, 1992.

Shahriar S., Erkan T., 2009. When will fossil fuel reserves be diminished? Energy Policy 37(1): 181–189.

Shapiro S.A., Dinske C., 2009. Scaling of seismicity induced by nonlinear fluid-rock interaction, J.Geophys. Res. 114, B09307

Shen P.P., Jiang H.Y., Chen Y.W., 2007. EOR study of CO_2 injection, Special Oil and Gas Reservoirs 14 (3): 14–20 (in Chinese).

Shiraki R., Dunn T.L., 2000. Experimental study on water-rock interactions during CO_2 flooding in the Tensleep Formation, Wyoming, USA. Applied Geochemistry 15: 265–279.

Snow D.T., 1969. Anisotropic permeability of fractured media, Water Resources Research 5(6):1273–1289.

Solomon S., 2006. Criteria for intermediate storage of carbon dioxide in geological formations, Bellona.

Solomon S., Kristiansen B., Stangeland A., Torp T.A., Karstad O., 2007. A proposal of regulatory framework for carbon dioxide storage in geological formations, Bellona, pp. 1–10.

Solomon S., Carpenter M., Flach T.A., 2008. Intermediate storage of carbon dioxide in geological formations: A technical perspective, International Greenhouse Gas Control 2(4):502–510.

Soltanzadeh H., Hawkes C.D., 2009. Assessing fault reactivation tendency within and surrounding porous reservoirs during fluid production or injection, International Journal of Rock Mechanics & Mining Sciences 46: 1–7.

Somomon S., Kristiansen B., Stangeland A., Torp T.A., Karstad O., 2007. A proposal of regulatory framework for carbon dioxide storage in geological formations, Bellona, January 2007.

Sonnenthal E.L., Bodvarsson G.S., 1998. Percolation flux estimates from geochemical and thermal modeling, 130–132. In: Proceedings of the Eighth International Conference on High-Level Radioactive Waste Management, American Nuclear Society.

Sorensena J.A., Holubnyaka Y.I., Hawthornea S.B., Millera D.J., Eylandsa K., Steadmana E.N., Harju J.A., 2009. Laboratory and numerical modeling of geochemical reactions in a reservoir used for CO_2 storage, Energy Procedia 3391–3398.

Span R., Wagner W., 1996. A new equation of state for carbon dioxide covering the fluid region from the triple-point temperature to 1100 K at pressures up to 800 MPa, Journal of Physical and Chemical Reference Data 25(6): 1509 −1596.

Spycher N., Pruess K., 2005. CO_2-H_2O mixtures in the geological sequestration of CO_2 –partitioning in chloride brines at 12–100 ˚C and up to 600 bar, Geochimica et Cosmochimica Acta 69(13): 3309–3320.

Steefel C.I., Lasaga A.C., 1992. Putting transport into water–rock interaction models, Geology 20: 680–684.

Steefel C.I., Lasaga A.C., 1994. A coupled model for transport of multiple chemical species and kinetic precipitation/dissolution reactions with application to reactive flow in single-phase hydrothermal systems, American Journal of Science 294: 529–592.

Steefel C.I., MacQuarrie K.T., 1996. Approaches to modeling reactive transport in porous media- reavtive transport in porous media, In: Lichtner P.C., Steefel C.I., Oelkers E.H., editors, Reviews in Mineralogy 34, Mineralogical Society of America 83–129.

Stephansson O., Hudson J.A., Jing L.R., 2004. Coupled thermo-hydro-mechanical-chemical processes in geo-systems, Elsevier Geo-Engineering Book Series, Elsevier Ltd., Oxford, UK.

Stefansson V., 2005. World geothermal assessment, In: Proceedings of the World Geothermal Congress, Antalya, Turkey, April 24-29, 2005.

Stevens S.H., Spector D., 1998a. Enhanced coalbed methane recovery: worldwide applications and CO_2 storage potential, Report prepared for IEA Greenhouse Gas R&D Programme, IEA/CON/97/27.

Stevens S.H., Kuuskraa J.A., Spector D., 1998b. CO_2 storage in deep coal seams: pilot results and worldwide potential, In: Fourth International Conference on Greenhouse Gas Control Technologies, 30 August–2 September, 1998, Interlaken, Switzerland.

Stone H.L., 1973. Estimation of three-phase relative permeability and residual oil data, Journal of Canadian Petroleum 53−61.

Streit J.E., Hillis R.R., 2004. Estimating fault stability and sustainable fluid pressures for underground storage of CO_2 in porous rock, Energy 29:1445−1456.

Subedi D.P., 2011. Contact angle measurement for the surface characterization of solids, The Himalayan Physics 2:1–4.

Sugita H., Kato K., Ueda A., Matsunaga I., Sakurai Y., Yasuda K., Bando Y. and Nakamura M., 1999. Field tests on silica removal from geothermal brines in Sumikawa and Onuma geothermal areas, Journal of Chemical Engineering of Japan 32: 696–700.

Suman A., 2009. Uncertainties in rock pore compressibility and effects on seismic history matching, Master Thesis in the Department of Petroleum Engineering of Stanford University.

Sung W.M., Lee Y.S., Kim K.H., Jang Y.H., Lee J.H., Yoo I.H., 2011. Investigation of CO_2 behavior and study on design of optimal injection into Gorae-V aquifer, Environmental Earth Science 64: 1815 −1821.

Swanson S.E., 1977. Relation of nucleation and crystal-growth rate to the development of granitic textures, American Mineralogist 62: 966–978.

Swenson D., Gosavi S., Hardman B., 2004. Integration of poroelasticity into TOUGH2, in: Proceedings of Twenty-Ninth Workshop on Geothermal Reservoir Engineering, Stanford University, Stanford, California, 2004.

Szucs P., Kovacs B., Bobok E., Toth A., Madarasz T., 2010. Technological review of geothermal energz utilization, in: 1st Knowbrige Conference on Renewable.

Szulczewski M.L., 2009. Storage capacity and injection rate estimates for CO_2 sequestration in deep saline aquifers in the conterminous United States, Master Thesis in Massachusetts Institute of Technology.

Szymkiewicz A., 2013. Modelling water flow in unsaturated porous media accounting for nonlinear permeability and material heterogeneity, Springer.

Taheri A., Zahedzadeh M., Masoudi R., et al., 2011. Simulation and experimental studies of mineral scale formation effects on performance of Sirri-C oil field under water injection, Iran Journal of Chemistry and Chemistry Engineering 30(3): 9–24.

Tallakstad K.T., Knudsen H.A., Ramstad T., Løvoll G., Malφy K.j., 2009. Steady-state two-phase flow in porous media: statistics and transport properties, Physical Review Letters No. 074502, 102(7): 1–4.

Talley D.J., Davis T.L., Benson R.D., Roche S.L., 1998. Dynamic reservoir characterization of vacuum field, The Leading Edge 17(10): 1396–1402.

Tang M., He S.M., Xing J.B., Zheng F.H., Deng H.L., Cao S.S., Zhou H.G., 2010. Practices and knowledge from nitrogen foam drilling at the well DP-14 in the Daniudi gas field. Natural Gas Industry 30(3):74–76 (in Chinese).

Tao W., Shen Z.K., 2008. Heat flow distribution in Chinese continent and its adjacent areas, Progress in Natural Science 18: 843–849.

Taron J., Elsworth D., Min K.B., 2009. Numerical simulation of thermal-hydrologic-mechanical-chemical processes in deformable, fractured porous media, International Journal of Rock Mechanics and Mining Science 46: 842−854.

Teng H., Zhao T.S., 2000. An extension of Darcy Law to non-Stokes flow in porous media, Chemical Engineering Science 55:2727–2735.

Tester J. et al., 2006. The future of geothermal energy – impact of enhanced geothermal systems (EGS) on the United States in the 21th century, Massachusetts Institute of Technology, Cambridge, MA, USA.

Tian T.S., Li M.L., Bai Z., 2006. The geothermal resources of China and its development. China Environmental Science Press, in Beijing (in Chinese).

Tong F.G., Jing L.R., Zimmerman R.W., 2010. A fully coupled thermo-hydro-mechanical model for simulating multiphase flow, deformation and heat transfer in buffer material and rock masses, International Journal of Rock Mechanics and Mining Sciences 47: 205–207.

Treiber L.E., Archer D.L., Owens W.W., 1972. A laboratory evaluation of the wettability of fifty oil producing reservoirs, SPE Journal of Transaction of AIME 253: 531−540.

245

Ueda A., Kato K., Mogi K., Mroczek E., Thain I. A., 2003. Silica removal from Mokai, New Zealand, geothermal brine by treatment with lime and a cationic precipitant, Geothermics 32: 47–61.

Ueda A., Kato K., Ohsumi T., Yajima T., Ito H., Kaieda H., Metcalfe R., Takase H., 2005. Experimental studies of CO_2-rock interaction at elevated temperatures under hydrothermal conditions, Geochemical Journal 39: 417–425.

UNDP, 2004. World energy assessment—energy and the challenge of sustainability overview: 2004 update. United Nations Development Programme, New York.

Van der Meer L.G.H., 1992. Investigations regarding the storage of carbon dioxide in aquifers in The Netherlands, Energy Conversion and Management 33 (5–8): 611–618.

Van der Meer L.G.H., 1993. The conditions limiting CO_2 storage in aquifers, Energy Conversion and Management 34(9–11): 959–966.

Van der Meer L.G.H., 1995. The CO2 storage efficiency of aquifers, Energy Conversion and Management 36(6–9): 513–518.

Van der Meer L.G.H., Arts R.J., Peterson L., 2000. Prediction of migration of CO_2 injected into a saline aquifer: reservoir history matching to a 4D seismic image with a compositional gas/water model. In: Williams D.J., Durie R.A., McMullan P., Paulson A.J., Smith A.Y., editors, Greenhouse Gas Control Technologies, CSIRO Publishing, Collingwood, 2000, pp. 378–384.

Van der Meer B., 2005. Carbon dioxide storage in natural gas reservoir, Oil & Gas Science and Technology 60 (3): 527–536.

Van Genuchten M. T., 1980. A closed-from equation for predicting the hydraulic conductivity of unsaturated soils, Soil Science Society of America Journal 44: 892–898.

Van Pham T.H., Aagaard P., Hellevang H., 2012. On the potential for CO_2 mineral storage in continental flood basalts-PHREEQC batch-and 1D diffusion-reaction simulations, Geochemical Transactions 13:5 doi:10.1186/1467-4866-13-5.

Verruijt A., 1969. Elastic storage of aquifers, in: Dewiest R.J.M., editor, Fow through Porous Media, Academic Press: New York.

Verruijt A., 2008. Consolidation of soils, Encyclopedia of Hydrological Sciences, John Wiley and Sons, Ltd., Chichester, UK.

Vilarrasa V., 2012. Thermo-Hydro-Mechanical impacts of carbon dioxide (CO_2) injection in deep saline aquifers, PhD thesis in Technical University of Catalonia (UPC-BarcelonaTech).

Von Eynatten H., Barcelo-Vidal C., Pawlowsky-Glahn V., 2003. Composition and discrimination of sandstones: a statistical evaluation of different analytical methods, Journal of Sedimentary Research 73(1): 47–57.

Walsh J.B., Grosenbaugh M.A., 1979. A new model for analyzing the effect of fractures on compressibility, Journal of Geophysical Research 84(B7): 3532–3536.

Wan Y.Y., 2012. Migration and transformation of CO_2 in CO_2 geological sequestration process of Shiqianfeng saline aquifers in Ordos Basin, PhD thesis in Jilin University, China (in Chinese).

Wang B.Q., AL-Aasm I.S., 2002. Karst-controlled diagenesis and reservoir development: example for the main-reservoir carbonate rocks on the east margin of Ordos Basin, China, American Association of Petroleum Geologists Bulletin 86 (9): 1539–1658.

Wang D.Q., Liu Z.Z., Yin L.H., 2005. Hydrogeological characteristics and groundwater systems of the Ordos Basin, Quaternary Science 23(1): 6–14.

Wang H.F., 2000. Theory of linear poroelasticity with applications to geomechanics and hydrogeology, Princeton University Press.

Wang J., Huang S.Y., Huang G.S. Wang J.Y.,., 1990. The fundamental characteristics of the geothermal distribution in China, Seismological Publishing House, in Beijing (in Chinese).

Wang J.Y., Hu S.B., Pang Z.H., He L.J., Zhao P., Zhu C.Q., Rao S., Tang X.Y., Kong Y.L., Luo L., Li W.W. , 2012a. Estimation of geothermal resources potential for hot dry rock in the continental area of China, Science & Technology Review 30(32):25–31(in Chinese).

Wang S.J., Wang E.Z., 2004. Recent study of coupled processes in geotechnical and geoenvironmental fields in China, In: Stephansson O., Hudson J.A., Jing L., editors, 2004. Coupled thermo-hydro-mechanical-chemical processes in geo-systems, Elsevier.

Wang Y., 2001. Heat flow pattern and lateral variations of lithosphere strength in China mainland: constraints on active deformation, Physics of the Earth and Planetary Interiors 126: 121–146.

Wang Y., Xu Y.Q., Zhang K.N., 2012. Investigation of CO_2 storage capacity in open saline aquifers with numerical models, Procedia Energy 31:886–892.

Wang Y.X., Mao X.M., DePaolo D., 2011. Nanoscale fluid-rock interaction in CO_2 geological storage, Earth Science-Journal of China University of Geosciences 36(1): 263–171(in Chinese).

Wang Z.L., Zhang L.K., Sun M.L., Fu J.H., Xi S.L., Liu B., 2004. Natural gas accumulation mechanism in Upper Shihezi and Shiqianfeng formations of Shenmu-Yulin district in northeastern Ordos Basin, Acta Petrolei Sinica 25(3): 37–43(in Chinese).

Watanabe N., McDermott C.I., Wang W.Q., Taniguchi T., Kolditz O., 2009. Sensitivity analysis of thermo-hydro-mechanical (THM) coupled processes in a hot-dry-rock reservoir, in: Proceedins of Thirty-Fourth Workshop on Geothermal Reservoir Engineering, Stanford University, Stanford, California, February 9-11.

Wateson M.P., Hayward A.B., Parkinson D.N., Zhang Z.M., 1987. Plate tectonic history, basin development and petroleum source rock deposition onshore China, Marine and Petroleum Geology 4: 205–225.

Wei G.Q., Cheng M.J., Sheng H.J. et al., 2003. Gas pool formation pattern of the tight sandstone reservoir from the Ordos Basin, an Internal Report of Exploration and Development Institute of Chinese Petroleum 89–123 (in Chinese).

Wei H., Li W., Shao L., 2002. Characteristics and controlling factors of the Permian reservoirs in the Suligemiao region, Journal of Mineralogy and Petrology 22(3): 42–46 (in Chinese).

Wei Y., Wang Y., 2004. Comparison of enrichment patterns of various energy and mineral resources in the Ordos Basin, Oil & Gas Geology 25: 385–392 (in Chinese).

Wei Z.Q., Hudson J.A., 1988. Permeability of jointed rock masses, in: ProcInt Symp Rock Mech and Power Plants. Balkema, Rotterdam 613–625.

Wei Z.Q., Egger P., Descoeudres F., 1995. Permeability predictions for jointed rock masses. International Journal of Rock Mechanics and Mining Sciences & Geomechanics Abstracts 32(3): 251–261.

Weir G.J., White S.P., Kissling W.M., 1995. Reservoir storage and containment of greenhouse gases, Energy Conversion and Management 36 (6–9): 531–534.

Western Governors' Association (January 2006). Geothermal Task Force Report http://www.westgov.org/wga/initiatives/cdeac/Geothermal-full.pdf

Whitaker S., 1986. Flow in porous media I: A theoretical derivation of Darcy's law, Transport in Porous Media 1(1): 3–25.

White S., Weir G., Kissling W., 2001a. Numerical simulation of CO_2 sequestration in natural CO_2 reservoirs on the Colorado Plateau, in: Proceedings of the First National Conference on Carbon Sequestration, Washington DC, May 2001.

White S.P., Allis R.G., Moore J., Chidsey T., Morgan C., Gwynn W., Adams M., 2001b. Injection of CO2 into an unconfined aquifer located beneath the Colorado Plateau, Central Utah, in: Proceedings of the First National Conference on Carbon Sequestration, Washington DC, May 2001.

Wigand M., Carey J.W., Schütt H., Spangenberg E., Erzinger J., 2008. Geochemical effects of CO_2 sequestration in sandstones under simulated in situ conditions of deep saline aquifers, Applied Geochemistry 23: 2735–2745.

Williams G.D., Collins I.R., SPE, BP Amoco Exploration et al., 1999. Enhancing mineral scale dissolution in the near-wellbore region, SPE No.56774.

Winter E.M., Bergman P.D., 1993. Availability of depleted oil and gas reservoirs for disposal of carbon dioxide in the United-States, Energy Conversion and Management 34 (9–11): 1177–1187.

Wiprut D., Zoback M.D., 2000. Fault reactivation and fluid flow along a previously dormant normal fault in the northern North Sea, Geology 28: 595–598.

Wu W.L., Yin X.Y., 2008. The study on the relationship between petrophysical parameters and geophysical characteristics: take QHD326 oil field as an example, Geophysical Prospecting for Petroleum 47(3): 235–243 (in Chinese).

www.ipcc.ch

Xiao X.M, Zhao B.Q., Thu Z.L., Song Z.G., Wilkins R.W.T., 2005. Upper Paleozoic petroleum system, Ordos Basin, China, Marine and Petroleum Geology 22: 945–963.

Xie H.P., Li X.C., Fang Z.M., Wang Y.F., Li Q., Shi L., Bai B., Wei N., Hou Z.M., 2014. Carbon geological utilization and storage in China: current status and perspectives, Acta Geotechnica 9:7-27.

Xie X., Economides M.J., 2009. The impact of carbon geological sequestration, Journal of Natural Gas Science and Engineering 1: 103–111.

Xu T.F., Apps, J.A., Pruess K., 2001. Analysis of mineral trapping for CO_2 disposal in deep aquifers, Lawrence Berkeley National Laboratory Report LBNL-46992, July 2001.

Xu T.F., Apps J.A., Pruess K., 2003. Reactive geochemical transport simulation to study mineral trapping for CO_2 disposal in deep arenaceous formations, Journal of Geophysical Research 108(B2): 2071–2084.

Xu T.F., Sonnenthal E., Spycher N., Pruess K., 2004a. TOUGHREACT User's Guide: A Simulation Program for Non-isothermal Multiphase Reactive Geochemical Transport in Variably Saturated Geologic Media.

Xu T.F., Pruess K., 2004b. Numerical simulation of injectivity effects of mineral scaling and clay swelling in a fractured geothermal reservoir, LBNL 2004.

Xu T.F., Apps J.A., Pruess K., 2005. Mineral sequestration of carbon dioxide in a sandstone-shale system, Chemical Geology 217: 295–318.

Xu T.F, Sonnenthal E., Spycher N., Pruess K., 2006. TOUGHREACT- A simulation program for non-isothermal multiphase reactive geochemical transport in variably saturated geologic media: applications to geothermal injectivity and CO_2 sequestration, Computers and Geosciencs 32(2): 145−165.

Xu T.F., Apps J.A., Pruess K., Yamamoto H., 2007. Numerical modeling of injection and mineral trapping of CO_2 with H_2S and SO_2 in a sandstone formation, Chemical Geology 242:319−346.

Xu T.F., Li T., 2013. Reactive transport modeling to address the issue of CO_2 geological sequestration, Procedia Earth and Planetary Science 7: 912-915.

Xue C.J., Xue W., Kang M., Tu Q.J., Yang Y.Y., 2008.The fluid dynamic processes and its uranium mineralization of sandstone-type in Ordos basin, China, Earth Science: Journal of China University Geoscience 22(1):1–8 (in Chinese).

Xue C.J, Chi G.X, Xue W., 2011. Effects of hydrocarbon generation on fluid flow in the Ordos Basin and its relationship to uranium mineralization, Geoscience Frontiers 2(3): 439–447.

Yang H., Fu S.T., Wei X.S, 2004. Geology and exploration of oil and gas in the Ordos Basin, Applied Geophysics 1(2): 103–109.

Yang H., Fu J.H., Wei X.S, Liu X.S., 2008. Sulige field in the Ordos Basin: Geological setting, field discovery and tight gas reservoirs, Marine and Petroleum Geology 25: 387–400.

Yang H., Fu J.H., Wie X.S., Ren J.F., 2009. Tight sandstone gas reservoirs (exploration) in upper Paleozoic of Ordos Basin, Report.

Yang Q. J., 2008. Dynamic modelling of CO_2 injection in a closed saline aquifer in the Browse Basin, Western Australia, Presented at the SPE Asia Pacific Oil and Gas Conference and Exhibition, Perth, Western Australia, Australia, 20–22 October.

Yang Y.H., Nan J.X., He J., Wang X.F., 2001. The microscopic characteristic of the sandstone reservoir of upper Paleozoic of the Ordos basin and the affected factors of reservoir property, China Petroleum Exploration 6(4): 37–43(In Chinese).

Yang Z., Ma X., Besse J., Courtillot V., Xing L., Xu S., Zhang J., 1991. Paleomagnetic results from Triassic sections in the Ordos basin, north China, Earth and Planetary Science Letters 104: 258–277.

Yeh G.T., Tripathi V.S., 1989. A critical evaluation of recent developments in hydrogeochemical transport models of reactive multichemical components, Water resources Research 25(1): 93–108.

Yeh G.T., Tripathi V.S., 1991. A model for simulating transport of reactive multispecies components: model development and demonstration, Water resources Research (27): 3075–3094.

Yin A., Nie S., 1996. A Phanerozoic palinspastic reconstruction of China and its neighboring regions, In: Yin, A., Harrison, T.M., editors, The Tectonic Evolution of Asia. Cambridge University Press, Cambridge, pp. 442–485.

Yin Z.J., Yu X.Y., Lu G.Y., 2006. Sedimentary facies of 8th member of Shihezi formation in block Su6 in sulige gas field, Natural Gas Industry 26(3): 26–27(in Chinese).

Yin S.D., 2008. Geomechanics-reservoir modeling by displacement discontinuity-finite element, PhD thesis in University of Waterloo.

Yin S.D., Dusseault M.B., Rothenburg L., 2012. Coupled THMC modeling of CO_2 injection by finite element methods, Journal of Petroleum Science and Engineering 80: 53−60.

Yuan K., Zhou W., Guan S., 2009. Characteristics of He 8 sandstone reservoir in the Jinbian gas field of Ordos Basin, Computing Techniques for Geophysical and Geochemical Exploration 31(3): 271–276 (in Chinese).

Yuan Y.H., Lee T.R., 2013. Contact angle and wetting properties, in: Bracco G., Holst B., editors, Surface Science Techniques, Springer Series in Surface Sciences 51, doi 10.1007/978-3-642-34243-1_1, Springer-Verlag Berlin Heidelberg.

Zeng L.B., Gao C.Y., Qi J.F., Wang Y.K., Li L., Qu X.F., 2008. The distribution of fractures and their seepage effect in the ultra-low permeability sandstone reservoir of Longdong district in Ordos Basin, China Science D: Earth Science 38 supplementary I: 41–47(in Chinese).

Zhao J.Z., Fu J.H., Wie X.S., Liu X.S., Wang X.M., Cao Q., Ma Y.P., Fan Y.F., 2011. Quasi-continuous lithologic accumulation system: a new model for tight gas occurrence in the Ordos Basin, China, in: oral presentation at AAPG International Convention and Exhibition, Milan, Italy, 23-26, October, 2011.

Zhao Y.S., Yang D., Feng Z.C., Liang W.G., Kang Z.Q., 2008. Multi-field coupling theory of porous media and its applications to resources and energy engineering, Chinese Journal of Rock Mechanics and Engineering 27(7): 1321-1328 (in Chinese).

Zhang K.N., Wu Y.S., Pruess K., 2008. User's Guide for TOUGH2-MP-A massively parallel version of the TOUGH2 code, LBNL-315E.

Zhang S.Q., Guo J.Q., Li X.F., Fan J.J., Diao Y.J., 2011. Geological conditions of CO_2 sequestration and geological assessment of site selection in China. Beijing: Geological Publishing House (in Chinese).

Zhang X., Tian J.C., Chen H.D., Hou M.C., Hou Z.J., 2009. The lithofacies-paleographic and spatiotemporal evolution of Upper Permian Shiqianfeng Formation in Ordos Basin, China, Journal of Chengdu University of Technology 36(2): 165–171(in Chinese).

Zhang L.Y., 2013. Aspects of rock permeability, Frontiers of Structural and Civil Engineering 7(2):102–116.

Zheng B.Y., Liu F.H., Ye J., Fan Z.P., 1999. The sedimentary facies analysis on the mudstone of Carboniferous and Permian of Ordos Basin, Northwestern Geology 32(1): 1–4(in Chinese).

Zheng G.Z., 2008. Dynamic mechanism of transition from basin to plateau in Ordos, Journal of Earth Science and Environment 30(2): 144–148 (in Chinese).

Zhou D., Graham, S.A., 1996. The Songpan–Ganzi complex of the West Qinling Shan as a Triassic remnant ocean basin, In: Yin, A., Harrison, T.M., editors, The Tectonic Evolution of Asia. Cambridge University Press, Cambridge, pp. 281–299.

Zhou Q.L., Birkholzer J.T., Tsang C.F., Rutqvist J., 2008. A method for quick assessment of CO_2 storage capacity in closed and semi-closed saline formations, International Journal of Greenhouse Gas Control 2(4): 626−639.

Zhou Q.L., Birkholzer J.T., Mehnert E., Lin Y.F., Zhang K.N., 2010. Modeling basin- and plume-scale processes of CO_2 storage for full-scale deployment, Ground Water 48(4): 494−514.

Zhou Q.L, Birkholzer J., 2011. On scale and magnitude of pressure build-up induced by large-scale geologic storage of CO_2, Greenhouse Gas Science Technology 1:11−20.

Zhou X.G., Zhang, L.Y., Fan, K., Huang, C.J., Liu, G.Y., Hou, Q.H., 2009. The measurement of the present stress field of the Ordos Basin and its application in the petroleum production, Journal of Xi'an Shiyou University (Natural Science Edition) 24(3): 7−12 (in Chinese).

Zhu R., Lou Z.H., Jin A.M., Wei X.S., 2003. Analysis on fluid dynamics and formation process of deep basin gas trap in Upper Paleozoic of the Ordos Basin, Chinese Journal of Geology 38(1): 31–43.

Zimmermann R.W., 1991. Compressibility of sandstones, Elsevier Science Publishers, Amsterdam, Netherlands.

Zou C.N., Tao S.Z., 2008. Geological characteristics of large gas provinces and large gas fields in China, Science in China Series D: Earth Sciences 51(1): 14–35.

Zweigel P., Hamborg M., Arts R., Lothe A.E., Sylta Ø., Tømmerås A., 2000. Prediction of migration of CO_2 injected into an underground depository: reservoir geology and migration modelling in the Sleipner case. SINTEF SACS.

Appendix

A1.1 Properties of CO_2

A1.1.1 Physical properties of CO_2

(1) Phase state of CO_2

From the phase diagram of CO_2 in Fig. A1.1a, we can see that carbon dioxide is a gas phase at ambient conditions. The physical state of CO_2 varies with temperature and pressure (IPCC, 2005). It is noted that there are two important points for CO_2, one is the triple point (p=5.1 bar, T=−56.5 ^{o}C), and the other is the critical point (p=73.9 bar, T=31.1^{o}C). At the triple point, three phases (gas-solid-liquid) will exist at the same time. At critical point, all the three phases of exist simultaneously. Except along the sublimation line, melting line and saturation line, where two phases exist in equilibrium, only one phase exists at any given temperature and pressure conditions. For example, CO_2 is a solid under low temperature and high pressure conditions, and the solid will sublime directly into the vapor state under decreased pressure (constant temperature) and increased temperature conditions (constant pressure). At intermediate temperatures (−56.5 ^{o}C <T< 31.1 ^{o}C), CO_2 may be transformed from vapor state into liquid state by compressing it to the corresponding liquefaction pressure (pressure above the vaporization curve/saturation line). At temperatures higher than 31.1 ^{o}C (p>73.9 bars), CO_2 turns into a supercritical state when it behaves as a gas (IPCC, 2005; Bachu, 2003). In supercritical state, its property is different from gas or liquid CO_2, as it has the characteristic of both, i.e. its density is close to liquid, and the viscosity is close to gas. Therefore, its diffusivity coefficient is a hundred times that of liquid.

During phase changes, e.g., across the solid-gas (sublimation), solid-liquid (melting) and liquid-gas (evaporation) boundaries (see Fig. A1.1a), heat can be released or absorbed. However, the phase changes from the supercritical state to liquid or to gas phase do not require the release or absorption of heat.

(2) Density, vapor pressure, viscosity, enthalpy of CO_2

A lot of important information available for the physical properties of CO_2 can be found in the references (Fenghour et al., 1998; IEA, 2000; Bachu, 2003; IPCC, 2005; Pruess et al., 2005). Selected physical properties of CO_2 are given in Table A1.1. Many authors have investigated the equation of state for CO_2 (Span and Wagner, 1996). Under high pressure condition, the density of supercritical CO_2 is very large, reaching or even exceeding the density of liquid water, which is an important property for its underground storage and sequestration (Fig. A1.1b).

The understanding of thermodynamic properties of CO_2 (including density, viscosity, specific enthalpy, vapor pressure, solubility and so on) is very important for the successful CO_2 sequestration. The variations of CO_2 density correlating with temperature and pressure is displayed in Fig. A1.1b, vapor pressure with temperature in Fig. A1.1c, and viscosity with temperature and pressure in Fig. A1.1d. Further information on viscosity was provided in Fenghour et al. (1998). The specific enthalpy of CO_2 and water under different temperatures and pressures is described in Fig. A1.2.
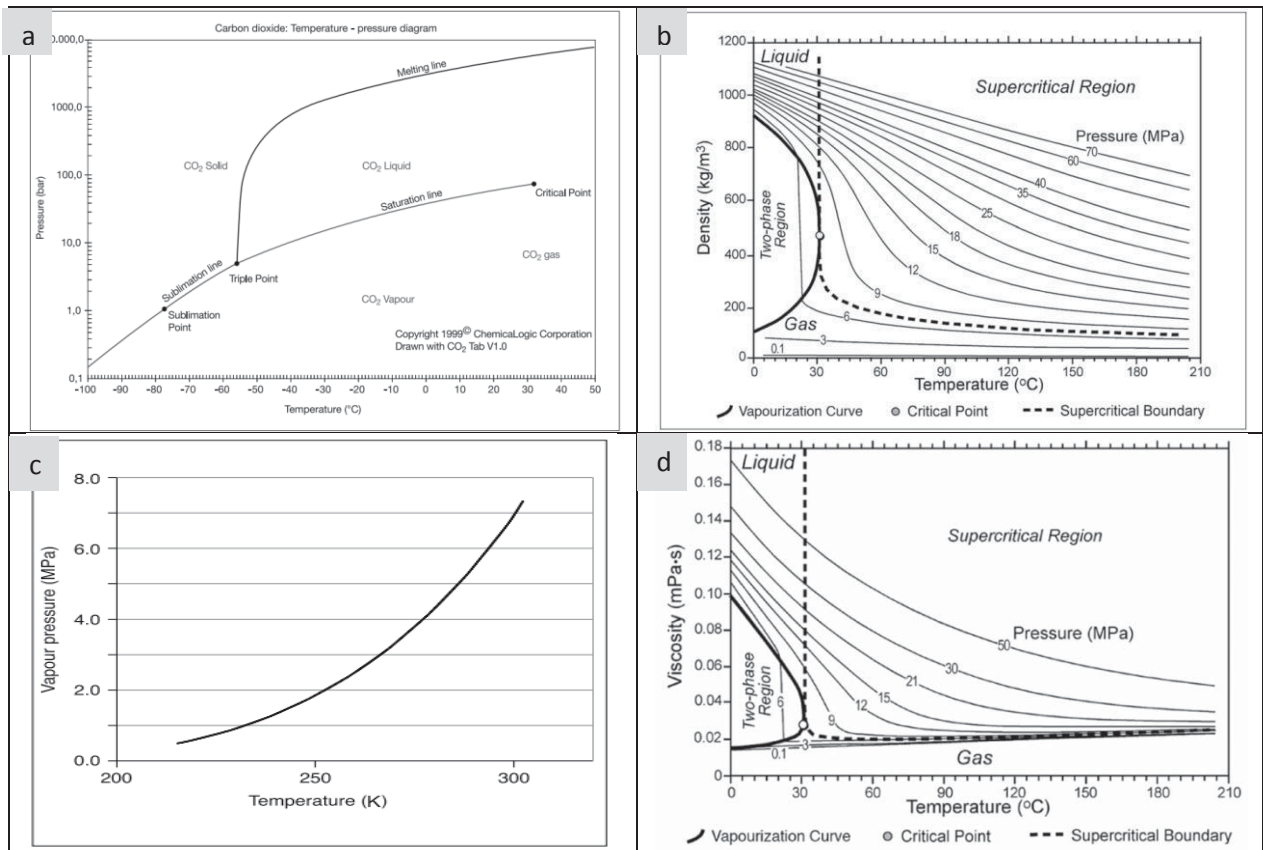
Fig. A1.1 Physical properties of CO_2, **a)** Phase diagram for CO_2: pressure against temperature (chemicallogic corporation, 1999); **b)** density against temperature (Bachu, 2003); **c)** Vapor pressure against temperature (Span and Wagner, 1996); **d)** viscosity against temperature (Bachu, 2003)

Specific enthalpy of CO2 and H2O under different T and P conditions(KJ/kg)
(blue dotted line: water; black solid line:CO2)
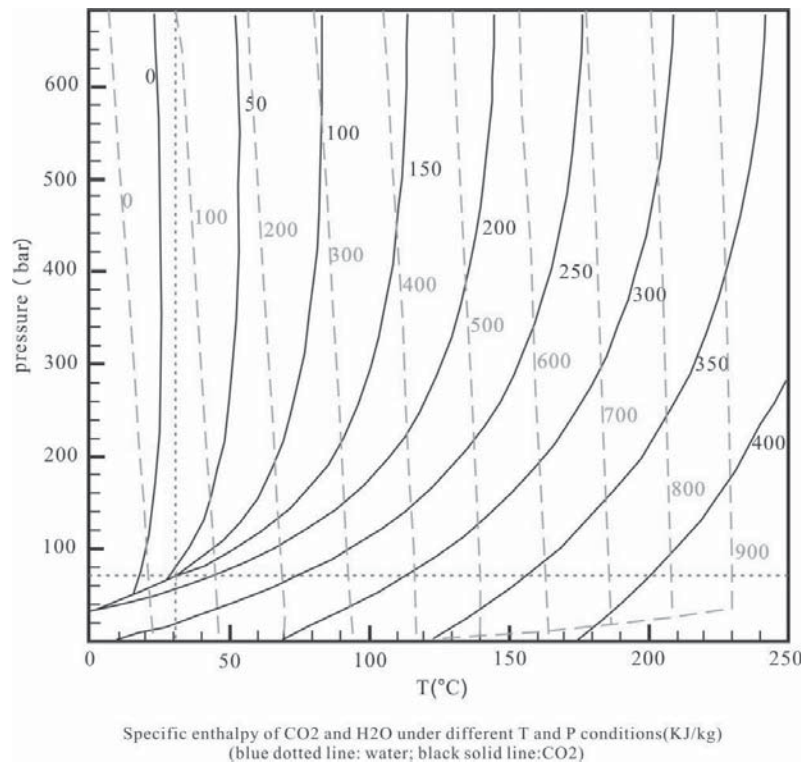
Fig. A1.2 Specific enthalpy diagram of CO_2 and water under T and P (Pruess et al., 2005)

**Table A1.1** Physical properties of CO_2 (IPCC, 2005), at standard conditions

Property	Value
Molecular weight	44.01
Critical temperature	31.1 °C
Critical pressure	73.9 bar
Critical density	467 kg/m^3
Triple point temperature	-56.5 °C
Triple point pressure	5.18 bar
Boiling(sublimation) point (1.013 bar)	-78.5 °C
Gas phase	
Gas density(1.013 bar at boiling point)	2.814 kg/m^3
Gas density (@ STP)	1.976 kg/m^3
Specific volume (@ STP)	0.506 m^3/kg
Cp (@ STP)	0.0364 kJ.mol/K
Cv (@ STP)	0.0278 kJ.mol /K
Cp/Cv (@ STP)	1.308
Viscosity (@ STP)	13.72 µN.s/m^2 or µPa.s
Thermal conductivity (@ STP)	14.65 mW
Solubility in water (@ STP)	1.716 vol/vol
Enthalpy (@ STP)	21.34 kJ/mol
Entropy (@ STP)	117.2 J.mol/K
Entropy of formation	213.8 J.mol/K
Liquid phase	
Vapour pressure (at 20 °C)	58.5 bar
Liquid density (at -20 °C and 19.7 bar)	1032 kg/m^3
Viscosity (@ STP)	99 µN.s/m^2 (or µPa.s)
Solid phase	
Density of carbon dioxide snow at freezing point	1562 kg/m^3
Latent heat of vaporization (1.013 bar at sublimation point)	571.1 kJ/kg

(3) Solubility of CO_2

Solubility of CO_2 in water is greatly affected by temperature and pressure, i.e. generally decreasing with temperature and increasing with pressure (Fig. A1.3A). It also decreases with increasing water salinity by about as much as one order of magnitude (Fig. A1.3B). Calculations demonstrate that, depending on the water salinity and depth of reservoir, about 20–60 kg CO_2 can dissolve in 1 m^3 of formation fluid (Holt et al., 1995; Koide et al., 1995; IPCC, 2005). The following empirical function (Enick and Klara, 1990) can be applied in the estimation of CO_2 solubility in brackish water and brine:

$$\widetilde{w}_{CO2,b} = \widetilde{w}_{CO2,w} \times (1.0 - 4.893414 \times 10^{-2}\bar{\bar{S}} + 0.1302838 \times 10^{-2}\bar{\bar{S}}^2 - 0.1871199 \times 10^{-4}\bar{\bar{S}}^3)$$

$$(A1.1)$$

where $\widetilde{w}_{CO2}$ is solubility of CO_2, $\bar{\bar{S}}$ is brine salinity and the subscripts w and b are used to describe pure water and brine respectively.
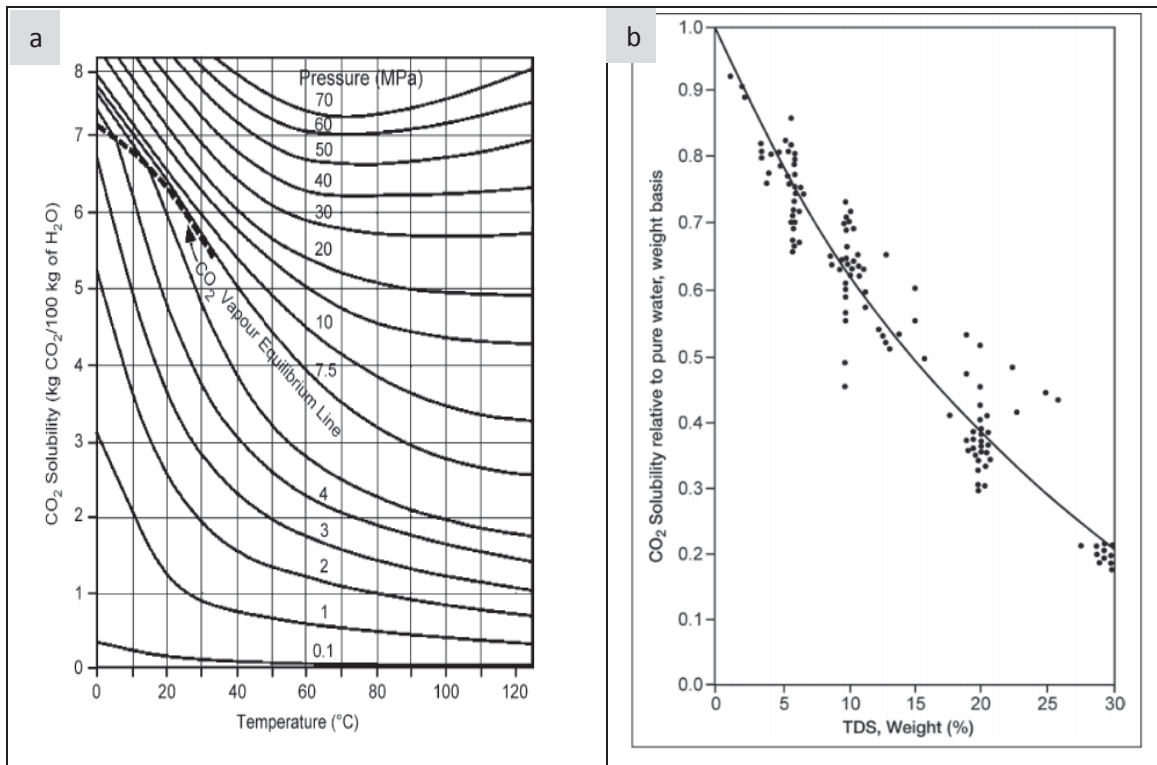
Fig. A1.3 Solubility of CO_2 in water, **(a)** temperature and pressure effect (Kohl and Nielsen, 1997); **(b)** salinity effect (Enick and Klara, 1990), *TDS* stands for total dissolved solids

Dissolution of CO_2 occurs at the interface of the CO_2 bubble and formation water. The amount of CO_2 dissolved will be proportional to the total area of the CO_2-water interface (van der Meer, 2005). When CO_2 is injected into underground formations, some of it will dissolve in the formation water. In slowly flowing water systems, simulation results show that, over tens of years, up to 30% of the injected CO_2 will dissolve in formation water, while centuries are needed for the entire CO_2 to dissolve in the formation water (McPherson and Cole, 2000; Doughty et al., 2001; Ennis-King et al., 2003; Solomon et al., 2008). If the injected CO_2 is trapped in a closed system, it will need much longer time for CO_2 to totally dissolve because of limited contact area with unsaturated formation water (IPCC, 2005). After CO_2 dissolved in the formation fluid, it will migrate along with the regional groundwater flow.

Water dissolved with CO_2 is slightly denser (about 1%) than the initial formation water, which is strongly affected by water salinity (Enick and Klara, 1990; Bachu and Adams, 2003; IPCC, 2005). It is expected that during the total CO_2 injection activity only a small amount (~10%) of the water present would be affected by the dissolution process and this process will be dominated by local circumstances affecting the efficiency of the process. With high vertical permeability, free convection and more mixing will take place than molecular diffusion alone (van der Meer et al., 1992), replacing the CO_2-saturated water from the vicinity of the plume with unsaturated water, therefore promoting faster dissolution of CO_2 in water (Lindeberg and Wessel-Berg, 1997; Ennis-King and Paterson, 2003; Solomon et al., 2008). If the CO_2 mobility is relatively high, the displacement of the water by the CO_2 is entirely dominated by multiple viscous fingering and the area of the CO_2-water will be enlarged.

A1.1.2 Chemical properties of CO_2

The dissolution of CO_2 in formation water gives rise to a series of chemical reactions. First, the dissolved CO_2 will react with water to form carbonic acid (H_2CO_3), and then dissociates to bicarbonate ions (HCO_3^-), which further dissociates into carbonate ions (CO_3^{2-}).

$$CO_{2(g)} \leftrightarrow CO_{2(aq)}, \tag{A1.2}$$

$$CO_{2(aq)} + H_2O \leftrightarrow H_2CO_{3(aq)}, \tag{A1.3}$$

$$H_2CO_{3(aq)} \leftrightarrow H^+_{(aq)} + HCO^-_{3(aq)}, \tag{A1.4}$$

$$HCO^-_{3(aq)} \leftrightarrow H^+_{(aq)} + CO^{2-}_{3(aq)}, \tag{A1.5}$$

(1) pH on the transformation of H_2CO_3 hydrolysate

By convention, pH is an indicator to measure the acidity or alkalinity of an aqueous solution., the solution can be said to be acidic with pH<7, while alkaline with pH>7. The pH can be given as

$$pH = -log(\bar{\bar{a}}_{H^+}), \tag{A1.6}$$

where $\bar{\bar{a}}_{H+}$ is the hydrogen ion activity. The pH of pure water decreases with increasing temperatures. For example, the pH of pure water at 50 ^{o}C is decreased to 6.55. The adsorption of CO_2 of water can cause the decrease of pH for the slowing conversion of CO_2 into bicarbonate and hydrogen ions:

$$CO_{2(g)} + H_2O \leftrightarrow H^+_{(aq)} + HCO^-_{3(aq)}, \tag{A1.7}$$

The pH of the water has great impact on the concentration of hydrolysate and H_2CO_3. Fig. A1.4 shows that there is only a small amount of CO_2 dissolved in the water and forms H_2CO_3 when pH is below 6; with pH increased, more HCO_3^- and CO_3^{2-} will form; when pH is higher than 11, there is only CO_3^{2-} in water.

(2) pH changes caused by the CO_2 concentration in water

For sea water, the typical value of pH is 8.1−8.4 at 0 ^{o}C and 7.8−8.1 at 25 ^{o}C. The data values are strongly dependent on carbonate/bicarbonate buffering (Nishikawa et al., 1992). Based on the theoretical calculations using activity coefficients in the equilibrium reaction between carbonic acid-bicarbonate-carbonate (Horne, 1969; IEA, 2000), the relationship of pH and dissolved CO_2 concentration is shown in Fig. A1.4. It demonstrates that the pH will reduce when the concentration of CO_2 increases. Temperature shows a minor effect on the reduction in pH that results from dissolution of CO_2 (see Fig. A1.5). Influence of pressure on pH can be neglected based on some experimental results (Lide, 2000).
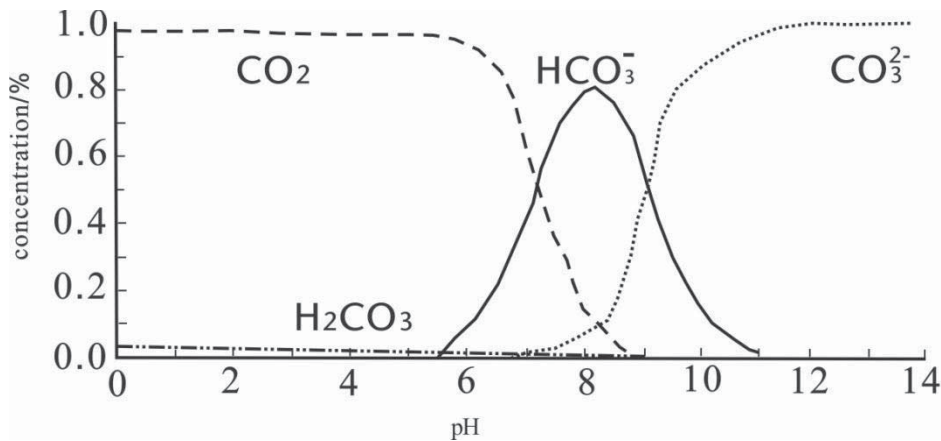

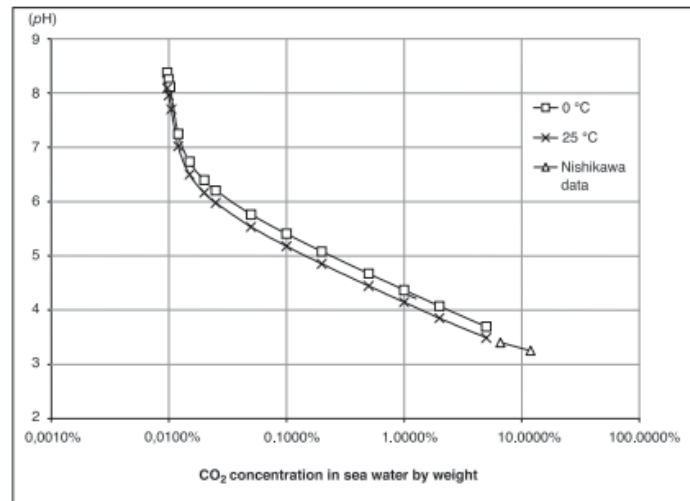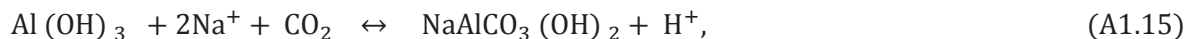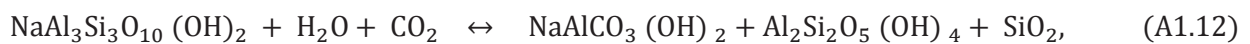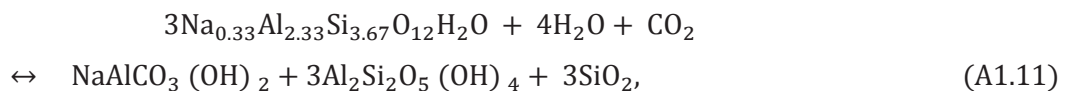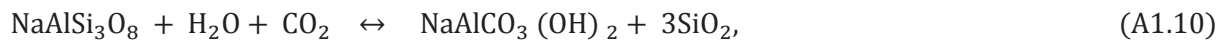**Fig. A1.4** pH of water on the transformation of hydrolysate of H_2CO_3 concentration (Cheng, et al., 2003)

Fig. A1.5 Influence of temperature on pH and CO_2 concentration in sea water (IEA, 2000)

(3) P_{CO2} on the dissolution of minerals

The pressure of CO_2 in reservoir can affect the dissolution and precipitation of minerals in reservoir. From the following equation, we can see that with increasing P_{CO2}, the reaction will move towards the positive direction. Different minerals have different response to the injection of CO_2 in the fluid-rock system, for example, the dissolution of calcite, magnesite, albite and illite, corresponds with the precipitation of dawsonite and kaolinite. When sodium is sufficient in the solution, dawsonite forms at the expense of CO_2. The reactants can be albite, kaolinite, K-keldspar etc.

$$CaCO_3 + H_2O + CO_2 \leftrightarrow Ca^{2+} + 2HCO_3^-, \tag{A1.8}$$

$$MgCO_3 + H_2O + CO_2 \leftrightarrow Mg^{2+} + 2HCO_3^-, \tag{A1.9}$$

$$NaAlSi_3O_8 + H_2O + CO_2 \leftrightarrow NaAlCO_3(OH)_2 + 3SiO_2, \tag{A1.10}$$

$$3Na_{0.33}Al_{2.33}Si_{3.67}O_{12}H_2O + 4H_2O + CO_2$$
$$\leftrightarrow NaAlCO_3(OH)_2 + 3Al_2Si_2O_5(OH)_4 + 3SiO_2, \tag{A1.11}$$

$$NaAl_3Si_3O_{10}(OH)_2 + H_2O + CO_2 \leftrightarrow NaAlCO_3(OH)_2 + Al_2Si_2O_5(OH)_4 + SiO_2, \tag{A1.12}$$

$$Al_2Si_2O_5(OH)_4 + 2Na^+ + H_2O + 2CO_2 \leftrightarrow NaAlCO_3(OH)_2 + 2SiO_2 + 2H^+, \tag{A1.13}$$

$$CaAl_2Si_2O_8 + 2Na^+ + 3H_2O + 2CO_2 \leftrightarrow 2NaAlCO_3(OH)_2 + 3CaCO_3 + 2SiO_2 + 2H^+, \tag{A1.14}$$

$$Al(OH)_3 + 2Na^+ + CO_2 \leftrightarrow NaAlCO_3(OH)_2 + H^+, \tag{A1.15}$$

Dissolution and precipitation rate of a specific mineral depends on CO_2 partial pressure, temperature, ion concentration and so on. Fig. A1.6 shows that with the higher P_{CO2}, the deposition rate of calcite will be slower than at lower P_{CO2} conditions. Dissolution of calcite, however, shows completely contrasting results. Increasing the temperature will accelerate the precipitation rate of calcite.

255
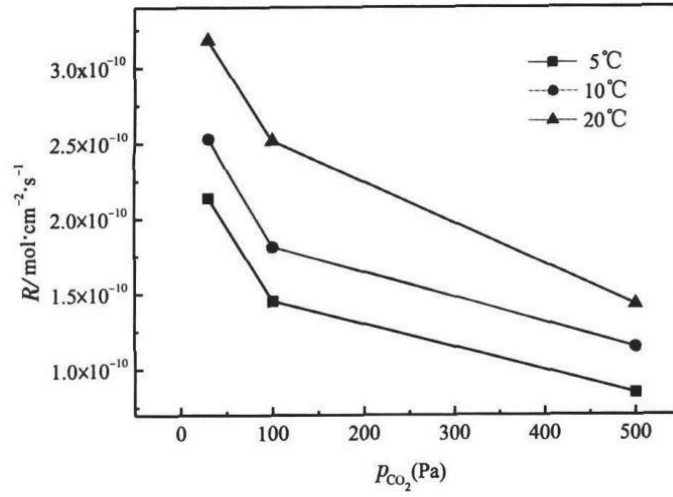
Fig. A1.6 The precipitation rate of calcite under different temperature and pressure conditions (Liu and Wolfgang, 2002)

Resume

Last Name: Liu
First Name: Hejuan
Birth: 30/12/1983, Hebei, China
Nationality: Chinese

01/09/2003-01/07/2007	Bachelor study of Geology in China University of Geosciences (Beijing)
01/09/2007-01/07/2010	Master study of Mineral Resource Prospecting and Exploration in China University of Geosciences (Beijing)
01/11/2010-30/10/2014	Doctoral study of Petroleum Engineering in Clausthal University of Technology (Clausthal-Zellerfeld), Germany

Publications during PhD studies:

LIU H.J., HOU Z.M., Were P., GOU Y., SUN X.L., 2014. Simulation of CO_2-brine-rock interactions in upper Paleozoic formations at Ordos CO_2 sequestration site, China. Environmental Earth Science DOI 10.1007/s12665-014-3571-4

LIU H.J., HOU Z.M., Were P., GOU Y., SUN X.L., 2013. Simulation of CO_2 plume movement in multilayered saline formations through multilayer injection technology in the Ordos Basin, China. Environmental Earth Science 71:4447-4462, DOI 10.1007/s12665-013-2839-4

LIU H.J., HOU Z.M., GOU Y., Were P, 2013. Simulation of CO_2-water-rock interaction processes: mineral scaling problems in saline formations, 233-248. In: Hou M.Z., Xie H.P., Were P., editors. Clean energy systems in the subsurface: production, storage and conversion. In: Proceedings of the 3rd Sino-German conference on Underground storage of CO_2 and energy, Goslar, Germany: Springer series in Geomechanics and Geoengineering, 21-23 May 2013, DOI 10.1007/978-3-642-37849-2_20

LIU H.J., SUN X.L., WAN D.H., 2013. The thought on some special sedimentary structures of Precambrian: an example from Jixian section of Tianjin. Journal of Earth Science and Environment, 35(3): 44-54 (in Chinese).

GOU Y., HOU Z.M., **LIU H.J.**, ZHOU L., Were P., 2014. Numerical simulation of carbon dioxide injection for enhanced gas recovery (CO_2-EGR) in Altmark natural gas field. Acta Geotechnica, 9:49-58, DOI 10.1007/S11440-013-0221-z

LIU H.J., MENG X.H., GE M., 2012. The study of microsparite carbonates (Molar Tooth) of Dalongkou formation in the central of Yunnan. Acta Petrologica Et Mineralogica 31(2):181-190(in Chinese).